LBL-24580
CONF-8711116--
UC-34C

January 1988

Proceedings of the 8th High Energy Heavy Ion Study

November 16–20, 1987

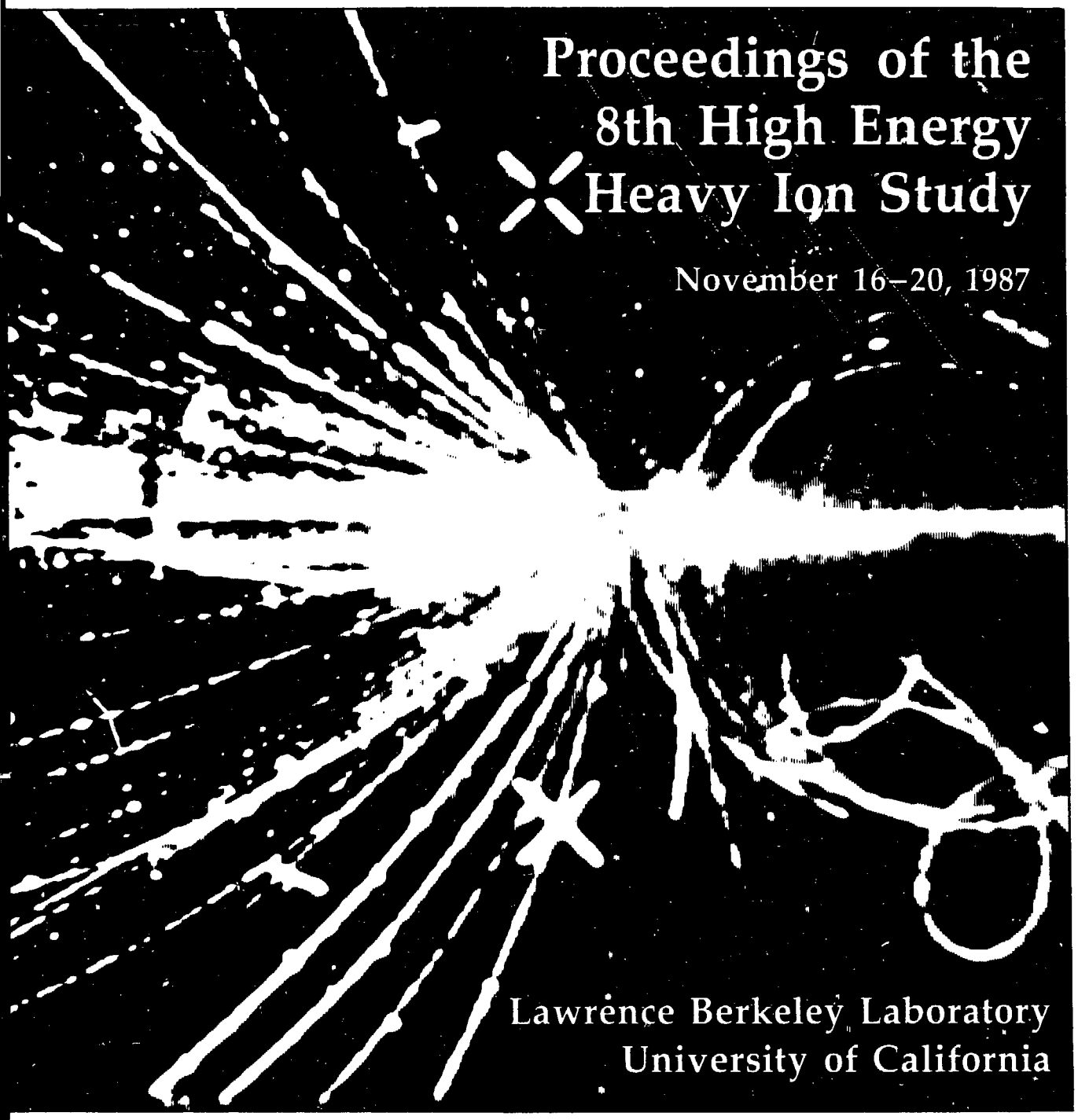

Lawrence Berkeley Laboratory
University of California

Prepared for the U.S. Department of Energy under Contract No. DE-AC03-76SF00098

Cover Caption: Reaction products detected in the streamer chamber from a collision of a 1.1 GeV/nucleon ^{165}Ho beam from the Bevalac with a ^{165}Ho target.

Printed in the United States of America
Available from
National Technical Information Service
U.S. Department of Commerce
5285 Port Royal Road
Springfield, VA 22161
Price Code: A24

LBL--24580

DE88 014053

Proceedings of the 8th High Energy Heavy Ion Study

Lawrence Berkeley Laboratory
November 16-20, 1987

Jointly sponsored by

Nuclear Science Division
Lawrence Berkeley Laboratory
University of California
Berkeley, CA 94720
USA

and

Gesellschaft für Schwerionenforschung MBH
Planckstraβe 1
D-6100 Darmstadt
Federal Republic of Germany

Edited by

J.W. Harris
G.J. Wozniak

Organizing Committee

R. Bock, GSI
H.J. Crawford, LBL
J.W. Harris, LBL
J. Randrup, LBL
L.S. Schroeder, LBL
G.J. Wozniak, LBL, Chairman

This work was supported by the U.S. Department of Energy under Contract No. DE-AC03-76SF00098

Preface

This was the eighth in a series of conferences jointly sponsored by the Nuclear Science Division of LBL and the Gesellschaft für Schwerionenforschung in West Germany. Over 130 scientists attended from 26 institutions. Sixty papers on current research at both relativistic and intermediate energies were presented. Topics covered consisted of: Equation of State of Nuclear Matter, Pion and High Energy Gamma Emission, Theory of Multifragmentation, Intermediate Energies, Fragmentation, Atomic Physics, Nuclear Structure, Electromagnetic Processes, and New Facilities planned for SIS-ESR. The latest design parameters of the Bevalac Upgrade Proposal were reviewed for the user community. Also, the design of a new electronic 4π detector, a time projection chamber which would be placed at the HISS facility, was presented.

Some highlights of the conference included: (a) vigorous discussions on whether a hard or soft equation of state (EOS) agrees better with the experimental data, (b) demonstration of direct lepton production at Bevalac energies by the Dilepton Spectrometer collaboration, (c) vigorous discussions between theorists and experimentalists on the appropriate experimental signature of multifragmentation at intermediate energies, (d) the production of very hot compound nuclei at excitation energies approaching their binding energy/nucleon, (e) new HISS data on the fragmentation of very heavy beams, and (f) the use of secondary beams to extract interaction radii of exotic nuclei such as ^{6}He, ^{8}He, and ^{11}Li.

It is remarkable how rapidly this field has progressed since the last workshop. We now have a reasonably well-accepted picture of an early division into spectators and participants, with partial penetration of the participant matter, accompanied by some compression, leading to stopping and an approach to local equilibrium, followed by expansion and flow. The evolution of the experimental situation in this regard has been most impressive. In fact at present the extraction of physics from this data is hampered by the lack of detailed quantitative theoretical calculations. Hopefully, by the next conference we will see great improvements in the theoretical models.

In putting on this conference the organizing committee was extensively aided by local LBL staff members. Extraordinary help was given by Ann Fitzgerald, who oversaw all stages of the preparation and conduction of the conference. Linda Davis helped with the travel arrangements of the speakers. Bill O'Conner and Peggy Little, the Conference Coordinators, provided expertise that saved us a great deal of time and worry. Loretta Lizama has done an excellent job of editing the Proceedings.

The success of this conference was due to the excitement that the speakers and participants brought to the discussions. A key ingredient to the vigorous examinations of the data and theoretical models was provided by the session chairpersons, who both stimulated and facilitated the discussions. For

their contributions to the success of the conference, the organizing Committee would like to thank the session chairpersons: L.S. Schroeder, R. Bock, H.H. Gutbrod, T.J. Symons, N.K. Glendenning, A.C. Mignerey, H.C. Britt, K. Hildenbrand, J. Wefel, and A M. Poskanzer.

Gordon J. Wozniak,
Chairman, Organizing
Committee

List of Participants

Jorg Aichelin
Universitat Heidelberg
Institut Fuer Hochenergiephysik
Schroederstrasse 90
D-6900 Heidelberg
Federal Republic of Germany

Jose Alonso
Lawrence Berkeley Laboratory
1 Cyclotron Road
Berkeley, CA 94720

Wolfgang W. Bauer
106-38
Kellogg Radiation Lab.
California Institute of Technology
1201 E. California Blvd.
Pasadena, CA 91125
(818) 356-4256

Klaus H. Berkner
50-149
Lawrence Berkeley Laboratory
1 Cyclotron Road
Berkeley, CA 94720
(415) 486-5501

Thomas Blaich
M/S J-519
Los Alamos National Laboratory
P. O. Box 1663
Los Alamos, NM 87545
(505) 667-0064

Charles Bloch
IUCF
Indiana University
Bloomington, IN 47405
(812) 335-9365

David Boal
Simon Fraser University
Burnaby, B.C. V5A 1S6 Canada

Rudolf Bock
Gesellschaft fur Schwerionenforschung
Postfach 11 05 52
D-6100 Darmstadt 11 Germany

Helmut Bossy
Lawrence Berkeley Laboratory
1 Cyclotron Road
Berkeley, CA 94720

David R. Bowman
71-259
Lawrence Berkeley Laboratory
1 Cyclotron Road
Berkeley, CA 94720
(415) 486-6471

F. Paul Brady
Physics 1050
Univ. of California, Davis
Davis, CA 95616
(916) 752-1580

Harold C. Britt
L-397
Lawrence Livermore National Lab
Livermore, CA 94550
(415) 422-0684

Gerald E. Brown
SUNY, Stony Brook
State Univ. of New York
Stony Brook, NY 11794
(516) 632-7989

Jim Carroll
Univ. of California, Los Angeles
Los Angeles, CA 90024

Yuen dat Chan
Lawrence Berkeley Laboratory
1 Cyclotron Road
Berkeley, CA 94720

Scott Ira Chase
Lawrence Berkeley Laboratory
1 Cyclotron Road
Berkeley, CA 94720
(415) 285-4817, x5697

Junsei Chiba
National Lab. for HEP, Tsukuba
KEK
Oho-machi, Tsukuba-gun
Ibaraki 305, Japan
0298-64-1171

Jim Clayton
Michigan State University
East Lansing, MI 48824-1321

Nelson Claytor
Lawrence Berkeley Laboratory
1 Cyclotron Road
Berkeley, CA 94720

S. Costa
Universita di Catania
Dipartimento di Fisica
57, Corso Italia
I 95129 Catania

Jim Costales
Massachusetts Inst. of Technology
1 Amherst Street
Cambridge, MA 02139

Henry J. Crawford
Lawrence Berkeley Laboratory
1 Cyclotron Road
Berkeley, CA 94720

Laszlo Csernai
Michigan State University
East Lansing, MI 48824-1321

Francis A. Cucinotta
M/S 493
Old Dominion Univ.
NASA
Langley Research Center
Hampton, VA 23365
(804) 865-4218

Janis M. Dairiki
70A-3307
Lawrence Berkeley Laboratory
1 Cyclotron Road
Berkeley, CA 94720
(415) 486-5673

Lieseu Dieter
Gesellschaft fur Schwerionenforschung
Postfach 11 05 52
D-6100 Darmstadt 11 Germany

Hans E. Emling
Gesellschaft fur Schwerionenforschung
Postfach 11 05 52
D-6100 Darmstadt 11 Germany
6151-359-669

George Fai
Kent State University
Kent, OH 44242
(415) 486-5466

David Fields
L-396
Lawrence Livermore National Lab
Livermore, CA 94550

Dan Fox
P-2, MS D456
Los Alamos National Laboratory
P. O. Box 1663
Los Alamos, NM 87545
(505) 667-1594

Jurgen Friese
Technische Universitat Munchen
D-8046 Garching
West Germany
089/3209-2439

Sun Yiu Fung
University of California, Riverside
Riverside, CA 92521

Charles Gale
University of Minnesota
111 Church Street, S.E.
Minneapolis, MN 55455

Hans Geissel
Gesellschaft fur Schwerionenforschung
Postfach 11 05 52
D-6100 Darmstadt 11 Germany

W. Geist
Lawrence Berkeley Laboratory
1 Cyclotron Road
Berkeley, CA 94720

Konrad Gelbke
Michigan State University
East Lansing, MI 48824-1321

Giles Gerbier
Lawrence Berkeley Laboratory
1 Cyclotron Road
Berkeley, CA 94720

Norman Glendenning
Lawrence Berkeley Laboratory
1 Cyclotron Road
Berkeley, CA 94720

Jean Gosset
Centre d'Etudes Nucleaires, Saclay
B. P. no. 2
F-91191 Gif-sur-Yvette, France

Edward E. Gross
MS 368
Oak Ridge National Laboratory
P. O. Box X
Oak Ridge, TN 37831-6371
(615) 574-4725

Charles Gruhn
Lawrence Berkeley Laboratory
1 Cyclotron Road
Berkeley, CA 94720

Hans H. Gutbrod
CERN
CH-1211 Geneva 23, Switzerland
0041-22-835938

Miklos Gyulassy
Lawrence Berkeley Laboratory
1 Cyclotron Road
Berkeley, CA 94720
(415) 486-5239

Hongyin Han
Academia Sinica
Inst. of Atomic Energy
P. O. Box 275-46
Beijing, China
(415) 486-6471

Luisa F. Hansen
L-405
Lawrence Livermore National Lab
Livermore, CA 94550
(415) 422-4512

John Harris
Lawrence Berkeley Laboratory
1 Cyclotron Road
Berkeley, CA 94720

Walter F. Henning
Gesellschaft fur Schwerionenforschung
Postfach 11 05 52
D-6100 Darmstadt 11 Germany
(0) 6151-359664

Klaus Hildenbrand
Gesellschaft fur Schwerionenforschung
Postfach 11 05 52
D-6100 Darmstadt 11 Germany

Huan Zhong Huang
Massachusetts Inst. of Technology
1 Amherst Street
Cambridge, MA 02139

Kexing Jing
Academia Sinica
Inst. of Atomic Energy
P. O. Box 275-46
Beijing, China
(415) 486-6471

Karl-Heinz Kampert
CERN
CH-1211 Geneva 23, Switzerland
(CET) (4) 22-835920

Yasha J. Karant
Visiting at:
Lawrence Berkeley Laboratory
1 Cyclotron Road
Berkeley, CA 94720

Declan Keane
University of California, Riverside
Riverside, CA 92521

Walter L. Kehoe
University of Maryland
College Park, MD 20742

Ferdous Khan
Old Dominion Univ.
Physics & Geophysical Sci. Dept.
Norfolk, VA 23508
(804) 865-2297

Paul Kienle
Gesellschaft fur Schwerionenforschung
Postfach 11 05 52
D-6100 Darmstadt 11 Germany
(0) 6151-359648

C. M. Ko
Texas A&M University
College Station, TX 77843

Volker Koch
SUNY, Stony Brook
State Univ. of New York
Stony Brook, NY 11794

Hans-Joachim Korner
Argonne National Laboratory
9700 So. Cass Ave.
Argonne, IL 60439

Gary F. Krebs
Lawrence Berkeley Laboratory
1 Cyclotron Road
Berkeley, CA 94720
(415) 486-5575

Kris Kwiatkowski
Cyclotron Facility
Indiana University
Bloomington, IN 47405
(812) 335-8212

Robert Lanier
Lawrence Livermore National Lab
Livermore, CA 94550

H. Liesen
Gesellschaft fur Schwerionenforschung
Postfach 11 05 52
D-6100 Darmstadt 11 Germany

Peter Lindstrom
Lawrence Berkeley Laboratory
1 Cyclotron Road
Berkeley, CA 94720

Walter Loveland
Oregon State University
Corvallis, OR 97331-5503

Uli Lynen
Gesellschaft fur Schwerionenforschung
Postfach 11 05 52
D-6100 Darmstadt 11 Germany
001/49/6151/359763

Dick Madey
Kent State University
Kent, OH 44242

Michael R. Maier
Cyclotron Laboratory
Michigan State University
East Lansing, MI 48824-1321

Howard S. Matis
50D-105
Lawrence Berkeley Laboratory
1 Cyclotron Road
Berkeley, CA 94720
(415) 486-5031

Kensaku Matsuta
Osaka University
Toyonaka
Osaka 560
Japan

Paolo R. Maurenzig
Instituto Nationale di Fisica Nucleare
Largo E. Fermi 2
Sezione di Firenze, 50125 Italy
0039-55-2298141

Thomas McAbee
Lawrence Livermore National Lab
Livermore, CA 94550

Margaret A. McMahan
71-259
Lawrence Berkeley Laboratory
1 Cyclotron Road
Berkeley, CA 94720
(415) 486-6471

Volker W. Metag
University of Giessen
Institut fur Theor. Physik
der Justus-Liebig Universitat
6300 Giessen
Heinrich Buff Ring, 16, W. Germany
49-641-702-2760

Alice C. Mignerey
Dept. of Chemistry
University of Maryland
College Park, MD 20742
(301) 454-4423

Jack Miller
70A-3307
Lawrence Berkeley Laboratory
1 Cyclotron Road
Berkeley, CA 94720
(415) 486-6492

Dennis M. Moltz
Bldg. 88
Lawrence Berkeley Laboratory
1 Cyclotron Road
Berkeley, CA 94720
(415) 486-5088

Luciano Moretto
Lawrence Berkeley Laboratory
1 Cyclotron Road
Berkeley, CA 94720

Arialdo Moroni
INFN, Frascati
Lab. Nazionali di Frascati
Casella Postale 13
I-00044 Frascati (Rome)
Italy
2-2392251

Ulrich Mosel
Institut fur Theor. Physik
der Justus-Liebig Universitat
6300 Giessen
Heinrich Buff Ring, 16, W. Germany

Walter F. J. Mueller
Lawrence Berkeley Laboratory
1 Cyclotron Road
Berkeley, CA 94720
(415) 486-7366

Walter Müller
Lawrence Berkeley Laboratory
1 Cyclotron Road
Berkeley, CA 94720

M. N. Namboodiri
L-234
Lawrence Livermore National Lab
Livermore, CA 94550
(415) 423-8159

Grazyna Odyniec
Lawrence Berkeley Laboratory
1 Cyclotron Road
Berkeley, CA 94720
(415) 486-7128

Alessandro Olmi
Instituto Nationale di Fisica Nucleare
Largo E. Fermi 2
Sezione di Firenze, 50125 Italy
0039-55-2298141

Doug Olson
University of California, Riverside
Riverside, CA 92521

Herbert Orth
Gesellschaft fur Schwerionenforschung
Postfach 11 05 52
D-6100 Darmstadt 11 Germany

Robert Palmer
Stanford Linear Accelerator Center
P. O. Box 4349
Stanford, CA 94305

Art Poskanzer
Lawrence Berkeley Laboratory
1 Cyclotron Road
Berkeley, CA 94720
(415) 486-5618

R. Potenza
Universita di Catania
Dipartimento di Fisica
57, Corso Italia
I 95129 Catania

Buford Price
Lawrence Berkeley Laboratory
1 Cyclotron Road
Berkeley, CA 94720

Gulshan Rai
Lawrence Berkeley Laboratory
1 Cyclotron Road
Berkeley, CA 94720

Jorgen Randrup
Nuclear Science Div.
Lawrence Berkeley Laboratory
1 Cyclotron Road
Berkeley, CA 94720
(415) 486-6157

John O. Rasmussen
70A-3307
Lawrence Berkeley Laboratory
1 Cyclotron Road
Berkeley, CA 94720
(415) 486-6318

Wolfgang Hans Rauch
Lawrence Berkeley Laboratory
1 Cyclotron Road
Berkeley, CA 94720
(415) 486-6460

Hans Georg Ritter
Lawrence Berkeley Laboratory
1 Cyclotron Road
Berkeley, CA 94720
(415) 486-4138

Guy R. Roche
Lawrence Berkeley Laboratory
1 Cyclotron Road
Berkeley, CA 94720
(415) 486-6983

Thomas Craig Sangster
L-397
Lawrence Livermore National Lab
Livermore, CA 94550
(415) 422-8176

Hans Sann
Gesellschaft fur Schwerionenforschung
Postfach 11 05 52
D-6100 Darmstadt 11 Germany

Rainer M. Schicker
70A-3307
Nuclear Science Div.
Lawrence Berkeley Laboratory
1 Cyclotron Road
Berkeley, CA 94720
(415) 486-5413

Walter Schimmerling
29-100
Lawrence Berkeley Laboratory
1 Cyclotron Road
Berkeley, CA 94720
(415) 486-5518

Hans Rudolf Schmidt
CERN
CH-1211 Geneva 23, Switzerland
22-83-6297

Karl-Heinz Schmidt
Gesellschaft fur Schwerionenforschung
Postfach 11 05 52
D-6100 Darmstadt 11 Germany
6151-359739

Lee Schroeder
Lawrence Berkeley Laboratory
1 Cyclotron Road
Berkeley, CA 94720

Berndt Schürmann
Technische Univ. Munchen
Physics Dept.
D-8046 Garching,West Germany

Peter Seidl
Lawrence Berkeley Laboratory
1 Cyclotron Road
Berkeley, CA 94720

Susumu Shimoura
Department of Physics
Kyoto University
Kyoto 606
Japan

Philip J. Siemens
Physics Building
University of Tennessee
Knoxville, TN 37996-1200
(615) 974-2288

Horst Stöcker
Univ. Frankfurt
Inst. fur Theor. Phys.
Robert-Mayer Str. 8-10
D-6000 Frankfurt-am-Main, Germany

Robert G. Stokstad
Lawrence Berkeley Laboratory
1 Cyclotron Road
Berkeley, CA 94720

Herbert W. Strobele
Gesellschaft fur Schwerionenforschung
Postfach 11 05 52
D-6100 Darmstadt 11 Germany

Hans Stroeher
Gesellschaft fur Schwerionenforschung
Postfach 11 05 52
D-6100 Darmstadt 11 Germany
6151-359535

John Sullivan
Texas A&M University
College Station, TX 77843

T. James Symons
70A-3307
Lawrence Berkeley Laboratory
1 Cyclotron Road
Berkeley, CA 94720
(415) 486-5670

Lawrence P. Teitelbaum
Lawrence Berkeley Laboratory
1 Cyclotron Road
Berkeley, CA 94720

Mark Tincknell
Lawrence Berkeley Laboratory
1 Cyclotron Road
Berkeley, CA 94720

Wolfgang Trautmann
Gesellschaft fur Schwerionenforschung
Postfach 11 05 52
D-6100 Darmstadt 11 Germany

Craig Tull
Lawrence Berkeley Laboratory
1 Cyclotron Road
Berkeley, CA 94720

Flemming Videbaek
Argonne National Laboratory
9700 So. Cass Ave.
Argonne, IL 60439
(312) 972-3619

Victor E. Viola
Department of Chemistry & IUCF
Indiana University
Bloomington, IN 47405

C. Jake Waddington
School of Physics & Astronomy
University of Minnesota
111 Church Street, S.E.
Minneapolis, MN 55455
(612) 624-2566

Wolfgang Wagner
Technische Universitat Munchen
D-8046 Garching
West Germany
089/3209-2439

Laurie Waters
SUNY, Stony Brook
State Univ. of New York
Stony Brook, NY 11794

Michael Webb
Lawrence Livermore National Lab
Livermore, CA 94550

John P. Wefel
Nicholson Hall
Physics & Astr.
Louisiana State University
Baton Rouge, LA 70803
(504) 388-8696

Howard H. Wieman
Lawrence Berkeley Laboratory
1 Cyclotron Road
Berkeley, CA 94720
(415) 486-6953

L. Wilets
University of Washington
Seattle, WA 98105

Jerry B. Wilhelmy
MS J-514
Los Alamos National Laboratory
P. O. Box 1663
Los Alamos, NM 87545
(505) 667-4785

James Ricker Wilson
L-35
Lawrence Livermore National Lab
Livermore, CA 94550
(415) 422-1659

Kevin L. Wolf
MSD-456, P-2
Los Alamos National Laboratory
P. O. Box 1663
Los Alamos, NM 87545
(505) 665-1512

Gordon J. Wozniak
71-259
Lawrence Berkeley Laboratory
1 Cyclotron Road
Berkeley, CA 94720

Russ Wright
Lawrence Berkeley Laboratory
1 Cyclotron Road
Berkeley, CA 94720

Jonathan Z. Zingman
L-18
Lawrence Livermore National Lab
Livermore, CA 94550
(415) 423-8458

TABLE OF CONTENTS

Pion and High Energy Gamma Emission

*Manuscript not received

Theory — Multifragmentation

Intermediate Energies

*Manuscript not received.

Fragmentation

*Manuscript not received.

Atomic Physics, Nuclear Structure, and Electromagnetic Processes

Summary and Epilogue

*Manuscript not received.

New Facilities

THE BEVALAC UPGRADE *

Jose Alonso
Lawrence Berkeley Laboratory
University of California
Berkeley, California 94720

Introduction

The field of medium-to-high energy heavy ion physics, pioneered by the Bevalac, is now entering into the era of second generation machines. Construction of SIS-18 and the ESR in Darmstadt, serious proposals for a superferric machine in Dubna, operations at Saturne II, construction start for a heavy-ion medical synchrotron at Chiba in Tokyo, and the recent commissioning of heavy ions at the AGS in Brookhaven and in the SPS at CERN all speak to the growing interest in the field, and in increasing commitments to very substantial investments in the hardware needed to actively pursue it.

It is very clear that an aggressive, innovative initiative is needed at Berkeley to ensure the continued excellence of the Bevalac program. We have designed the Bevalac Upgrade project with such a goal in mind: building on the very strong base of available facilities and resources, we are proposing an extensive modernization program which will guarantee forefront performance well into the next century.

The primary goals of the Upgrade project are to provide very substantial increases in beam intensity over present Bevalac performance, by a factor of 100 at light masses and 1000 for heavier masses; to provide beams of much higher quality and duty factor than are presently available; to improve operational flexibility allowing for pulse-to-pulse variability in ion, energy and beamline; and to allow for significant reduction in operations and maintenance costs.

In this paper we will discuss briefly the technical scope of the project, how we expect to achieve the above-stated goals; our planned accelerator improvement programs and upgrade-specific R & D projects which will not only increase our readiness for the upgrade, but will also move us quite a ways along in achieving the

* This work was supported by the Director, Office of Energy Research, Office of High Energy and Nuclear Physics, Nuclear Science Division, U.S. Department of Energy under Contract No. DE-AC03-76SF00098.

performance goals of the project. Finally we will give a brief assessment of our present thinking on future directions for carrying the Bevalac facility beyond the scope of the present project.

Technical Scope

The basic concept of the project is to replace the Bevatron with a modern, strong-focusing synchrotron capable of achieving the stated performance goals. Figure 1 shows the new synchrotron installed in place of the Bevatron, inside the Bevatron's shielding enclosure, and mated to existing injection and extraction channels. It is planned that the new synchrotron will by mounted directly onto the bottom yoke of the Bevatron magnet, a sturdy, highly-adjustable platform. By utilizing the existing shielding, as well as the available injectors, transport lines, external beam lines, experimental facilities, power distribution systems and physical plant capabilities, the cost and scope of providing this modern, high-performance facility is a small fraction of what it would otherwise be.

The configuration of the new synchrotron is shown in Figure 2, a classical FODO lattice whose basic cell includes two long and one short dipole, allowing adequate open space for RF, correction elements, injection and extraction channels, and beam diagnostic devices. The constraint of placing the ring inside the present Bevatron shielding requires a reduction in the maximum rigidity available, from 19.2 tesla-meters for the Bevatron to 17 T-m, this being due to the smaller fraction of the total ring circumference which can be filled with bending magnets. The accelerator will be capable of pulsing at 0.5 Hz, a factor of three higher than the Bevatron, but can also extend flattops indefinitely, reducing repetition rate, but allowing for very high duty factors for experiments not requiring the maximum intensity. Injection and extraction efficiencies will be very significantly higher than at present; control of extracted beam quality will also be vastly improved, guaranteeing low-emittance, essentially structure-free beam spills for high-quality experiments. The vacuum system for the new machine will be modeled after the present cryo-liner utilized in the Bevatron, but because of much-reduced magnet apertures must be engineered very differently. A composite fiber guard-vacuum box is planned, integrated with the magnet pole-tips to minimize eddy currents. Inside this guard-vacuum enclosure will be nested boxes held at liquid nitrogen and 12 K. Profiles of these boxes will be designed to conform to the changing beam envelope through the magnets, thus making maximum utilization of available space. Key to meeting the performance specifications for the new

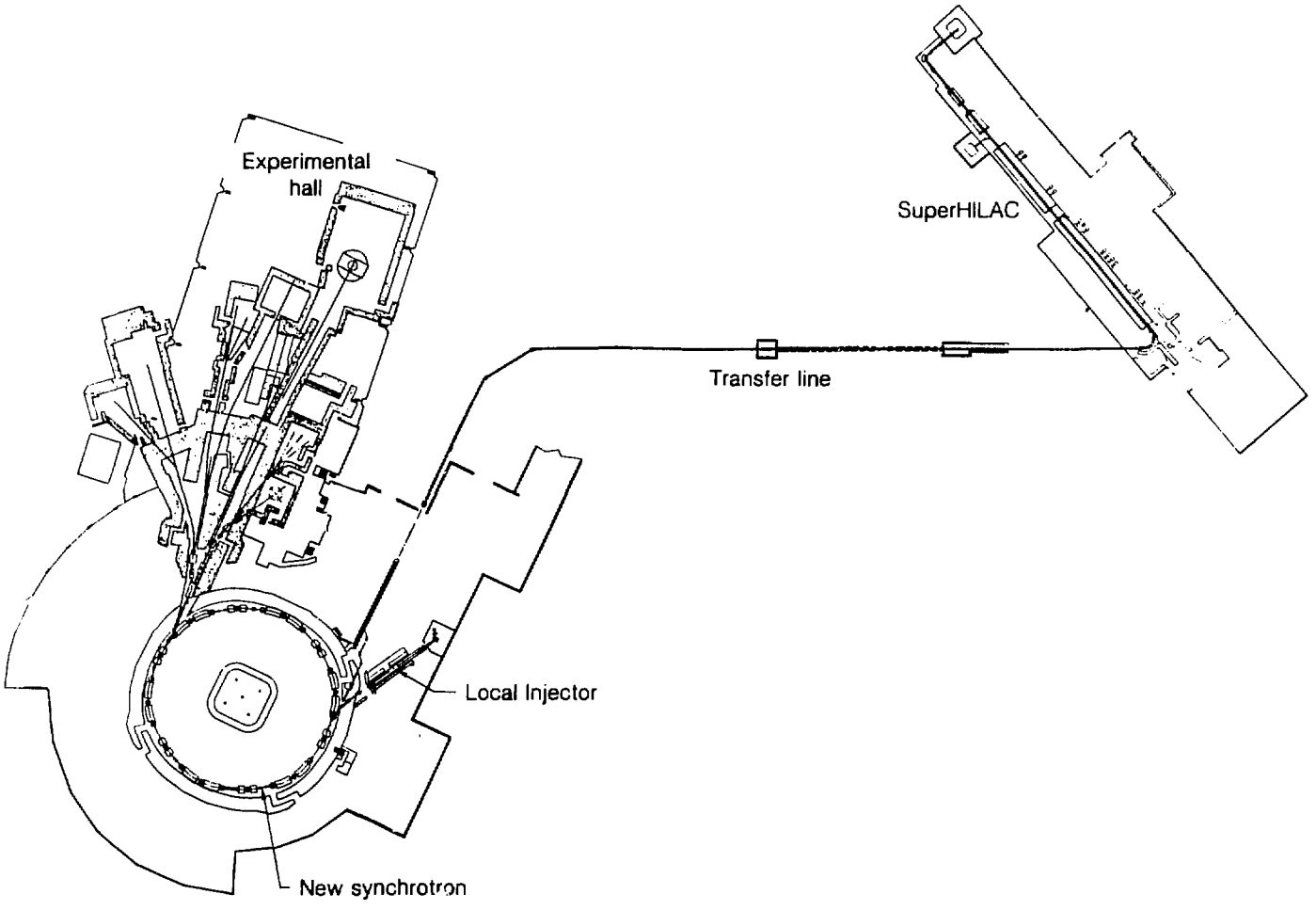

Fig. 1 The Upgraded Bevalac, including the unmodified SuperHILAC, transfer line, Local Injector, and experimental facilities.

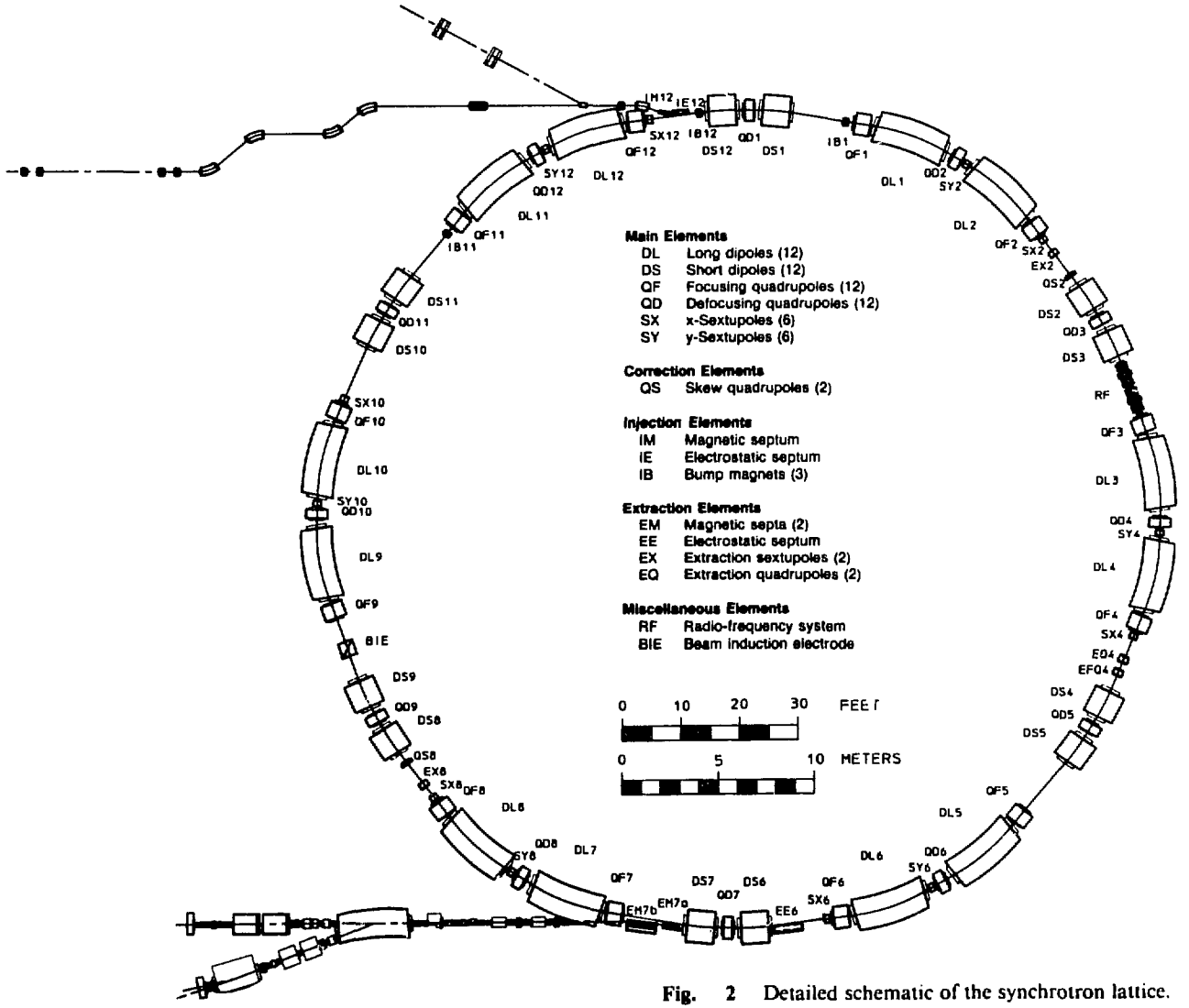

Fig. 2 Detailed schematic of the synchrotron lattice.

synchrotron is an integrated modern control system. Elements of this system are being built and installed now as an Accelerator Improvement Project (see below), and further integration of the new components into this control system will serve to accomplish the stated goals of reliability, efficiency and flexibility.

The project is estimated to require three years to complete, and to cost $39.2 M in then-year dollars (i.e. costs are corrected for anticipated escalation in the actual year the expense is incurred), assuming a construction start in FY89. A construction plan has been developed which calls for building and assembly of components in the first two years in such a way that operation of the existing Bevalac is not impacted. Then in the third year the Bevatron will be shut down and dismantled, and the new machine installed and commissioned.

Details of the technical design and specifications, magnet and power supply designs, operational performance, and a detailed cost breakdown are given in the Conceptual Design Report published in May of 1987 (LBL-PUB 5183 Rev), copies are available from the ARC Office at the Bevalac.

Ongoing Activities and Plans

For many years now, the normal course of developments at the Bevalac has consisted of a series of modest, but meaningful Accelerator Improvement Projects aimed at providing new or improved capabilities for the facility, interspersed with very significant upgrade projects about once every ten years. The recent larger projects have included the Transfer Line leading to the creation of the Bevalac in 1973, the Uranium Beams capability in 1981, and now the new synchrotron project. AIP projects have fallen into two categories: utilization of new technologies (RFQ installation at the Bevatron Local Injector; MEVVA source for the SuperHILAC Abel Injector; hybrid drift-tube quads "laced" with permanent magnet material for higher field strengths), and direct modernization and improvement of components (External Beam Line rebuilding for improved vacuum, instrumentation, and elimination of aperture restrictions; Transfer Line instrumentation; replacement of faulty SuperHILAC drift tube magnets; and rebuilding of Local Injector Alvarez linacs). The sum total of these projects is manifested in the constantly improving performance of the Bevalac, and the expanding community of experimenters basing their research efforts at our facility.

Our program for the near-term future is designed to carry on in the same vein. We have developed a list of AIP projects for the next six years, summarized in Table I, which will continue the tradition of expanding the capabilities of the Bevalac. Before detailing these projects, however, a few words are in order about the R&D activities we are embarked on. These efforts are directed primarily to developing the justification and technical basis for the AIP projects listed below, but also serve to lay groundwork for solidification of the Bevalac Upgrade design.

R & D Activities for Enhancement of Bevalac Performance

Fast-Pulsing Magnet Designs. We are developing and building a new switching magnet for the front end of the External Particle Beam area. This large laminated magnet, by virtue of its ability to rapidly pulse, will offer tremendous savings in power consumption, paying for itself in less than three years of operation. It will allow for pulse-to-pulse switching, being capable of being reversed in about half a second. In addition, this magnet shares many of the design features of the planned Upgrade synchrotron magnets, being comparable in size and design, allowing for developing relevant information on design, and fabrication and assembly techniques.

Vacuum Tanks in Transport Magnets. In the spirit of reducing power consumption and providing the utmost in flexibility of operating conditions, a program has been initiated to study novel vacuum vessels for dipole magnets. As shown in Figure 3, the proposed vacuum tank is open both top and bottom, using the pole faces of the dipole magnet as a vacuum interface. Such a design concept reduces the necessary magnet gap by twice the required thickness of the vacuum tank, and also eliminates the problem of eddy currents in the vacuum tank walls, a definite concern for rapidly pulsing magnets. To further reduce eddy currents, the tank will be made entirely from fiberglass. Such tanks have wide applicability, both in the external beam lines allowing for smaller magnet gaps and more rapid beam line switching, as well as for the guard-vacuum enclosure in the Bevalac Upgrade dipole magnets. Of concern in this design concept is the reliability of the complicated seals between the tank and the magnet. A prototype tank is in fabrication at present; it is planned that a full-scale box will be built and installed in the above-mentioned rapid-pulsing magnet to be located in the external beam lines.

Power Supply Tests. Modernization of the Bevatron main-magnet power supply can pay handsome dividends in improved flexibility and operational reliability. To gain

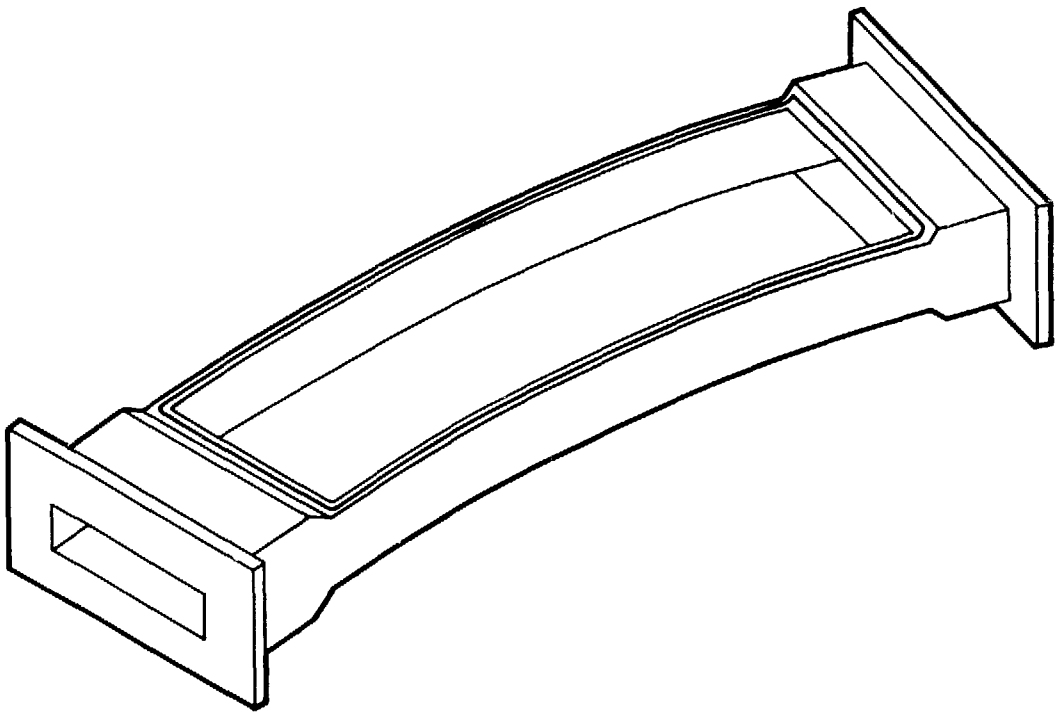

Fig. 3. The fiberglass guard-vacuum chamber, which uses the dipole magnet faces as the top and bottom "walls".

Table I - Accelerator Improvement Projects

Year	Principal Activity
FY 88	Control System Upgrade
FY 89	Pulse-to-pulse switching in External Beam Area
FY 90	Main magnet power supply improvements
FY 91	RF system upgrade - enhancement
FY 92	Bevatron injection lines upgrade
FY 93	Upgrade of Eve injector at SuperHILAC for uranium

experience with present-day high-power rectification technologies we are building a small (3 MVA) SCR supply capable of driving the Bevatron at a reduced ramp rate to a field of about 4 kG. Using our SCR designs under actual operating conditions will allow us to explore stability and ripple behavior of the Bevatron driven by these solid-state components, their performance and reliability under field conditions, and perhaps most importantly their behavior under fault conditions to ensure adequate protection for the main power components. Experience gained with this small test supply will be of great benefit for proper specifications and designs of the supplies for the Upgrade.

Accelerator Improvement Projects

The control system upgrade, the main project for this present year, includes implementation of a workstation-based highly distributed system operating in a Unix-ethernet environment. By drawing on the by-now extremely sophisticated packaged hardware and software available commercially which can be directly applied to our control needs, a most powerful system can be assembled at a very reasonable cost. We will be integrating operations of both accelerators, placing many more control points under computer control, implementing autotune algorithms, improving auto-diagnostic capabilities, and generally improving reproducibility and stability of machine operation. Implementation of the new system will be phased so as to cause minimum impact on operations, but the eventual goal will be the elimination of the Modcomp computers which have been in service now for almost 15 years.

Building on the base of the rapid-pulsing magnet to be installed this year at the front of the switchyard, we intend to upgrade other components to allow for pulse-to-pulse switching in the entire beam line system. This capability, essential for the upgrade, will provide much needed flexibility into the present Bevalac operation. It will allow the diversion of an occasional pulse into a new beam line, for tuning, calibration, or keep-alive operation of an ongoing experiment. Although this project will not provide ion-species and beam-energy switching on a pulse-to-pulse basis, it is still a very significant step towards the kind of flexibility which will be the hallmark of the future operation with the upgraded Bevalac.

It is expected that a logical outgrowth of the 3 MW power supply test will be the construction of a 30 MW supply, capable of driving the Bevatron (possibly directly off of the power grid, thus bypassing the MG sets) to fields adequate to service most of its low-energy program. This new supply would significantly improve flexibility of field-

setting for the Bevatron, perhaps allowing pulse-to-pulse switching of beam energies. Bypassing the mercury rectifiers (and possibly the MG sets) would provide very great benefits in operational costs for power and staff.

Improving the RF system will be geared towards modernization of components in service now for about 30 years. It is also desired to extend the range of the frequency swing of the present system, to allow for injection of lower velocity ions. We have recently experienced operational limitations because the RF frequency would not go down to low enough values to capture and accelerate very slow ions. This capability, in addition to improving system reliability, will open up research with accelerated ions from which very few electrons have been removed.

The design of the injection lines developed for the Upgrade Project has many very appealing features for matching of the beams from the two linear accelerators into the new synchrotron. Closer investigation has revealed that these same advantages also apply for the present Bevatron, and furthermore, that the actual designs and layouts for the Upgrade injection lines can be directly used for the Bevatron. It is proposed to build these beam lines, providing about a factor of five improvement in the captured beam intensity in the Bevatron through better dispersion and transverse matching of the beam to the synchrotron. The new lines will also allow for pulse-to-pulse ion switching at the inflection point.

Upgrading the Eve injector at the SuperHILAC for uranium beams will provide two injectors with full-mass capability. The scope will be to install a MEVVA source in this terminal, move the column and transport line so the beam from the Cockcroft Walton is transferred to the Wideroe entrance instead of directly into the SuperHILAC. Having dual heaviest-ion capability will greatly improve scheduling flexibility options, as well as providing backup reliability for ion source performance. Already today we are finding that much of the demand for beams requires the use of the Abel injector; having a second uranium injector will become more critical as the years progress.

Future plans

Thinking beyond the scope of the present Upgrade Project, it is clear that the next logical step is the implementation of a Storage Ring with as flexible a design as possible. As is now seen with the emerging plans at GSI, such a ring adds so much to the experimental capabilities of a heavy-ion accelerator complex that it must be

included in the ultimate plans for any world-class facility in this field. There are two difficulties with proposing to build a storage ring as the first stage of a Bevalac upgrade; first the Bevatron is not a suitable injector, beam emittance is too large and single turn extraction is not now possible; and second the projected experimental programs on such a ring all place very different constraints on the ring parameters; providing a ring which is flexible enough to satisfy all these requirements is very difficult. It was our feeling that building a synchrotron which would serve as a high quality injector would be the most effective first step in ultimately providing a first-class storage ring facility, and also that in a few years, when the new synchrotron was well along and the experimental programs requiring storage ring capabilities had further matured, a clearer definition of the design parameters could be made, and at that time a serious proposal could be written to build such a ring.

Siting for such a ring in the Bevalac complex has received much thought, with a logical solution emerging as an expanded high-bay in the Building 64 area. By using the 64 high-bay area enhanced by roofing over the space between the EPB hall and Bldg 64, adequate floor space is made available, with excellent access to utilities, as well as to both high and low energy transport lines to and from the synchrotron. We shall be seriously studying this question in the next years.

Summary

The Bevalac Upgrade is a timely, cost-effective project which will preserve a leading role for the US in the field of medium energy heavy ion physics. In preparation and support of this project there are numerous R & D activities and Accelerator Improvement Projects all geared to improving the performance of the Bevalac. In fact, several of the direct goals of the Upgrade Project can be partially met with these ancillary projects, such as increased operational flexibility, higher intensity, and better beam stability for low field applications. With active interest in continuing to Phase II, the Storage Ring, there is little doubt that the Bevalac will be a vital, world-class facility well into the next century.

PRESENT STATUS OF THE GSI-SIS/ESR PROJECT

Paul Kienle
Gesellschaft für Schwerionenforschung mbH.
D-6100 Darmstadt, West-Germany.

This is a short report on the status of the construction of the SIS/ESR facility as it stands in November 1987. Recent decisions concerning the facilities for first experiments are sketched.

1. SIS/ESR Project

Fig. 1 gives an overview of the heavy ion acceleration complex under construction at GSI[1]. It consists of an upgraded UNILAC used as an injector into a medium energy (1-2 GeV/u) heavy ion synchrotron SIS 18[2,3] which is connected with a storage cooler ring ESR[4] of half the circumference of SIS 18. The combination of these two rings should allow to produce completely stripped heavy ion beams up to U^{92+} with the highest possible phase space densities achievable by various beam cooling techniques. In addition SIS/ESR will provide beams of radioactive nuclei in the energy range from several MeV/u up to 1-2 GeV/u again cooled to the highest possible phase space densities. The beams in the ESR may be used either circulating with high currents or extracted with a great variety of time structures and intensities. They may be also reinjected into SIS for further acceleration or deceleration. There will be a large experimental area with several experiments set up on beams from both SIS and ESR. Further experimental areas are located directly behind SIS, between SIS and ESR and around the ESR. In future one can think of injecting the high phase space density completely stripped beams in superconducting collider rings with small apertures, modest size and prize to achieve very high c.m. energies ($>$ 20 GeV/u) at as high as possible luminosities.

Very recently we changed our injector concept into the UNILAC, such that we can run a truly independent low energy program with a free choice of ion species and energy parallel to a low duty factor high current injection cycle into SIS 18.

The SIS injection is based on recently developed high intensity ion sources[5] for low charge states (U^{2+}) which will be accelerated by 27 MHz RFQ structures up to 130 keV/u and after stripping injected straight into the second Wideröe tank. This high current injector will be operated with a duty factor of 1 %, which is sufficient for synchrotron injection. It can provide 100-1000 times more injection current than the present UNILAC.

For the low energy UNILAC program we plan to construct an independent injector[6] consisting of a 10 or 16 GHz ECR-source, a RFQ linac up to energies of 300 keV/u, followed by an interdigital line structure up to the injection energies of the Alvarez section (1.4 MeV/u). These

structures will be operated at 108 MHz with 50 % duty factor. Because no stripping is foreseen the ECR source has to produce U^{28+} ions with sufficient intensities. First tests with the 10 GHz CAPRICE ECR source gave 7μA Pb^{25+} and up to 2μA U^{28+} ions[6]. We plan to do further R&D work to achieve the specified current of 5μA U^{28+}. This new injector will be installed in the present stripper hall.

The heavy ion beam accelerated in the UNILAC up to 11.4 MeV/u, and stripped to an adequate high charge state for the desired energy and intensity, is injected into SIS 18 during 10 to 30 turns and accelerated with a repetition rate between 3 Hz (up to 1.2 T) and 1 Hz (up to 1.8 T) to maximum energies, depending on the charge states of the ions as shown in Fig. 2.

For uranium ions with a charge state of $q = 78$, after stripping at 11.4 MeV/u with a foil target, 1 GeV/u is achieved as maximum energy. The maximum beam intensities from SIS 18 are shown in Fig. 3 for Ne- and U-ions of various ionic charges, depending on the stripping procedure, as function of their specific energies. The decrease of the intensities towards higher energies is caused by a small decrease of the synchrotron repetition rate; the drop for 1 GeV/u Ne and 500 MeV/u U is due to a change of the repetition rate from 3 to 1 Hz.

Between SIS 18 and ESR the beam may be stripped once more to the highest desired charge state. The ESR with a bending power of $B\rho = 10$ Tm allows to store ions up to U^{92+} with the following maximum energies: Ne^{10+} (834 MeV/u), Ar^{18+} (709 MeV/u), Kr^{36+} (656 MeV/u), Xe^{54+} (609 MeV /u) and U^{92+} (556 MeV/u). The uranium ions can be fully stripped at this energy with an efficiency of 60 % in a Cu-target of 100 mg/cm² thickness.[7] The stripping yield increases strongly with decreasing nuclear charge charge, thus one expects a yield of 70 % for Pb^{82+}-ions (574 MeV/u) and already 100 % for Xe^{54+}-ions (609 MeV/u). Alternatively one can install a reaction target for projectile fragmentation. The favourable kinematic focussing of the products around the beam direction and velocity allows effective mass-separation in a special mass-separator between SIS and ESR, followed by accumulation of radioactive beams with the ESR, which accepts beams with $\delta p/p = \pm 0.5$ % and transverse emittances of 20 π mm mrad.

The ESR (Fig. 4) has two 9.5 m long straight experimental sections, in one of which an electron cooling device will be installed. The other 4 straight sections will be used for the installation of rf cavities, slow and fast extraction elements. The rf cavities are used for acceleration, deceleration and especially also for bunching of the beam together with the electron cooling for reduction of the occupied longitudinal phase space volume. With the fast extraction system of the ESR one can transfer a highly ionized and cooled beam back to SIS 18 for further acceleration or specially also deceleration. The optics of the ring allows three modes of operation, one with moderate dispersion along the ring specially suited for accumulation of beams with large momentum spread ($\delta p/p = \pm 0.5$ %) and emittance ($\varepsilon_{hv} = 20$ π mm mrad), one with zero dispersion in the straight sections, which allows multi-charge operation (U^{89+} - U^{92+}) and one with large dispersion to accomodate two beams of slightly different momenta, which

then may be brought to merge with a well defined angle of about 100 mrad.[8] This can be used to study collisions of *two* highly ionized beams at fixed target equivalent energies of up to 7.2 MeV/u and an energy definition of better than 10 %.

The most important facilities of the ESR are various cooling devices which can be applied complementary. For low phase space density secondary beams stochastic pre-cooling may be used. For cooling to very high phase space density, electron cooling of completely stripped heavy ions is foreseen in an interaction zone of 2 m length. A "cool" electron beam of 5-10 A is focused within an area of 5 cm diameter collinearly along the ion beam at the corresponding average velocity. For cooling of beams between 30 MeV/u and 560 MeV/u, electron energies in the range of 16.5 keV and 310 keV are required. With an electron beam current density of up to 1 A/cm^2 and ion beams of initially $\delta p/p = 0.1$ % and $\varepsilon = 4\pi$ mm mrad cooling times of 30 ms for U^{92+} at 500 MeV/u respectively are expected. Heavy ion beams with emittances as small as 0.1 π mm mrad and momentum spreads of less than 10^{-5} may be produced. Space charge effects limit the number of ions to be cooled in a circulating beam[9]

While the cooled beam circulates in the ring, it may be used in the second straight section for the study of collision processes with internal targets, which may be atomic or electron beams (unpolarized or even polarized), gas jets or fibres. For all experiments which need thin targets a high gain in luminosity may be achieved compared with a single pass experiment due to the increase of the circulating beam current ($\sim 2\times10^6$). Also the interaction of collinear laser and electron beams with the circulating ions of high intensity and small momentum spread may be favourably studied.

The building construction started in November 1986 and will be completed in middle of 1988. The SIS tunnel is ready for installation of the synchrotron components, the installation of which will start in February 1988. Most of the magnets including the vacuum system are manufactured and have been tested and accepted. Some quadrupoles need unforeseen readjustments. Despite some delay we expect the synchroton to be completely assembled by the end of 1988, followed by a commissioning period of about half a year. Thus we anticipate that the experimental program may start in fall 1989.

The ESR is constructed parallel to SIS. The magnets, power supplies, UHV systems and the electron cooling device are under construction. In summer 1988 we plan to begin the installation of the ESR magnets with the goal to start commissioning and first cooling experiments only shortly after SIS has taken up production.

2. EXPERIMENTAL FACILITIES FOR FIRST NUCLEAR PHYSICS EXPERIMENTS AT SIS/ESR

a) Projectile Fragment Separator (FRS)

In the experimental area between SIS and ESR (Fig 5) a high resolution projectile fragment isotope separator (FRS) will be installed[10]. Radioactive beams can be transported into a small cave close to the FRS, into all experimental facilities of the large target hall and most important into the ESR. The FRS is constructed following a scheme which has been successfully used by the separator LISE at GANIL[11]. A high energy, high intensity beam from SIS hits a target in which projectile fragments are produced with similar velocities as the beam and well focused in the direction of the beam ($\Theta_{1/2} < 0.5\text{-}1^{o}$). The first two dipole magnets separate fragments with a certain A/Z values, from the projectiles and fragments with different A/Z. For an isotope separation from a selected A/Z-fraction, the nuclei are passed through an absorber, in which they loose energy proportional to Z^2. Thus nuclei with a certain Z can be separated completely by the following two dipole magnets. By shaping the absorber chromaticity corrections may be introduced.

The physics programs at the FRS is expected to become very diversified. First we will focus on the study of the fragmentation process especially with heavy masses. Beside the measurement of A and Z distributions the study of the momentum and energy transfer on the fragment should shed light on the reaction dynamics. With separated isotopes detailed nuclear structure studies of heavy neutron rich nuclei should be possible. Then of course high energy radioactive beams may be produced and used for reaction studies, especially also in context with the ESR, in which they may be cooled and decelerated.

A very different class of reactions which may be favourably investigated in the FRS are fusion reactions[12] at high energies using inverse kinematics, like $^{12}C\ (p;\ \gamma,\ \pi^{o})^{13}N$. The heavy fusion products emitted in a small forward cone may be identified and completely momentum analyzed with 100 % detection efficiency. Thus very rare processes may be studied. Another interesting field is connected with the proposed study of Δ-production in quasielastic collisions, for which the FRS may be used as a high resolution spectrometer. Very rare processes like the subthreshold production of K^- and antiprotons can advantageously be studied at the FRS as well as the search for exotics like neutrons bound by negative pions.

b) Nuclear Physics Experiments with the ESR

The radioactive beams of the FRS may be injected into the ESR, accumulated and cooled by stochastic precooling and electron fine cooling to the highest phase space densities possible. Their energies may be adjusted in a large range by acceleration or deceleration in the ESR

These radioactive beams may be used as high current circulating beams in the ESR or they may be slowly extracted and transported in the experimental hall. The ESR may be also favorably used as a high resolution mass spectrometer or mass separator. With a scan of the revolution frequencies of cooled coasting radioactive beams in the ESR, high resolution mass measurements may be performed. The relative (A/Z) resolution given by the expression $\delta(A/Z)/(A/Z) = (< \delta B/B >^2 + (1/\gamma^2 - 1/\gamma_t^2)\,\gamma_t^4 < \delta p/p >^2)^{1/2}$ is determined by the variation of the magnetic field $\delta B/B$ and the momentum spread ($\delta p/p$). Note that the contribution from the momentum spread becomes very small if one could store the ions with a relativistic factor γ close to the transition point (γ_t). With well controlled magnetic fields and well cooled beams, mass resolutions of 10^{-5} to 10^{-6} may be achieved. The ESR is also equipped with a resonance extraction system, which may be used as a mass separator. In such an operation the electron energy of the cooling system would be used for fine adjustment of the revolution frequency to the extraction resonance for one particular isotope which would be kicked out of the ring.

It was suggested[13] to use cooled circulating radioactive beams of 200 - 400 MeV/u energy for high resolution nuclear reaction spectroscopy on nuclei far off stability. All standard quasi elastic reactions, like inelastic scattering and transfer reactions may be investigated by bombarding atomic beam targets of H, D, T, ^{3}He, ^{4}He, ^{6}Li,^{7}Li etc. with circulating cooled, radioactive beams and detecting the light recoils at angles, which correspond to forward angles in the c.m.-system. The resolution is critically dependent on the accuracy to measure the recoil angle and thus on the emittance of the cooled beam. With an emittance of 0.1 π mm mrad one expects for inelastic scattering at 160 MeV/u a Q-value resolution of about 50 keV.

One class of ESR experiments is concerned with the β-decay of a completely stripped nucleus to its isobar with the decay electron becoming bound in the 1s state. This process which is interesting for the nuclear synthesis[13] and neutrino physics[14] has not been observed before. Because the final state is energetically favoured relative to the initial one by about the binding energy of the 1s electron, nuclei which are stable as atoms may decay if the following condition is fulfilled:

$$Q = [m(Z) - m(Z+1)]\ c^2 + [B(Z) - B(Z+1)] + |B(1s)|_{Z+1} > 0.$$

In this expression $[m(Z) - m(Z+1)]c^2$ is equal to the mass difference of the neutral atoms, $[B(Z) - B(Z+1)]$ denotes the total binding energy difference of the electrons in the atom Z and Z+1,and $|B(1s)|_{Z+1}$the binding energy of the electron captured in the atomic 1s-state of the nucleus with atomic number Z+1.

There is an interesting proposal to study the groundstate hyperfine splitting of hydrogen-like ions either by detection of the M1-transitions between the hyperfine levels after production of the hydrogen-like ions in a stripper foil or more ambitiously by collinear laser spectroscopy. The transition energies are in the optical region and one can also use the large Doppler shifts

for tuning purposes. The radiative lifetimes of typical groundstate hyperfine structure transitions are between 100 ms and 100 μs

Studies of nuclei far off stability were proposed using complete fusion and possibly transfer reactions with radioactive beams of fragmented projectiles, cooled in the ESR and decelerated to energies close to the Coulomb-barrier. Such reactions will allow to reach the proton dripline for many isotopes.

c) Hot Dense Nuclear Matter

Following the exploring work on the properties of heated, compressed, and baryon excited nuclear matter studied by medium energy nucleus-nucleus collisions at the Bevalac, second generation experiments are designed to study the dynamics of dense and hot matted including the rare processes like the production of γ-rays, strange hadrons and antiprotons in the SIS target hall.

Fig. 6 shows the tentative lay out of the beam transport system leading to three large caves in which the first experimental facilities will be installed during the next two years. Two caves are anticipated for nucleus-nucleus collision studies at the beginning. The third cave is reserved for biology, atomic physics and smaller nuclear physics experiments.

For the study of central collisions we decided to construct an advanced 4π-detector for charged particles including a forward-spectrometer and large BaF_2-detector arrays for high energy photon spectroscopy. This device is designed to measure the complete momentum flow ($d^3\sigma/d\vec{p}$) of <u>all</u> charged particles originating from a hard collision, which will allow to analyze in substantial detail the collective nuclear matter flow first observed in exclusive experiments by Gustafson et al.[15]

A schematic lay out of the 4π-detector is shown in Fig. 7. The target B is surrounded by a drift chamber E placed within the magnetic field (0.5T) of a superconducting solenoid J. Particles emitted in a forward cone between 30^O and 7^O are identified with three planes of tracking detectors F, a detector to measure energy loss H and the TOF plastic wall G, placed about 4 m downstream the target. For handling high multiplicity events the plastic wall is segmented into about 1500 thin plastic scintillators recording ΔE and the time of flight of particles. A complete particle identification is aimed at by measuring the magnetic rigidity (Bρ), the velocity v, and the energy loss ΔE through several detectors. The momentum vector $\vec{p}$ can also be determined for each charged particle. In order to also cover the forward cone $\Theta < 7^O$ a forward spectrometer (FS) using a large magnetic dipole field is under discussion. Such a device would complete the momentum flow analysis in the important forward direction. The

complete 4π-detector can of course also be used to study in detail certain selected particle-particle correlations including multifragmentation

The production of γ-rays, π^o and η^omesons will be studied with a Two Arm Photon Spectrometer "TAPS" consisting of at least two arrays of 64 BaF_2crystals each being 12 radiation lengths deep. High energy γ-spectroscopy may be a useful probe to investigate the temperature and possibly the energy density of the hot matter in an unambiguous way. It may also the possible to study directly the production and decay of baryonic resonances. At higher bombarding energies the combinatorial background of many γ-rays from π^o decay may prevent single photon spectroscopy or will make it very difficult. In this energy regime complete π-meson creation studies seem to be most important. At still higher bombarding energies, the complete 4π-detector should allow to observe also K^+-production. The forward spectrometer of the 4π-detector will be extremely useful for nuclear reactions, in which lighter target nuclei are bombarded with heavy projectiles. The projectile fragments should be all contained within a forward cone and can be analyzed simultaneously by a spectrometer with large angular acceptance. For first experiments moderate momentum resolution might be adequate.

There are also plans to construct a detector for high energy neutrons, having very high efficiency and the best possible time of flight resolution to study Coulomb break up of relativistic projectiles. Such a detector (N) consisting of a sandwich structure of iron converter plates and plastic scintillators could be put 15 m downstream from the target.

With the highest SIS energies and high beam intensities it will be possible to study the subthreshold production of strange particles like K^+ and K^- and hopefully also antiprotons as function of bombarding energy and mass of the colliding nuclei. These rare processes should give further information on collective effects, like compression and correlations of quarks and antiquarks in the high density fireballs produced in medium energy nucleus-nucleus collisions. Several magnetic spectrometers and transport devices are suggested for these investigations, including the use of the projectile fragmentation isotope separator for the measurement of K^- and $\bar{p}$-production in forward direction. Fig. 8 shows the design values of a Kaon Spectrometer, which is discussed to study specially K^+-production at energies as far as possible below the threshold.

3. CRYSTALLINE BEAMS

At the end of my review I like to draw attention on a phenomenon which seems to open up very exciting physics with cold heavy ion beams available.

It was pointed out[16] that by cooling beams of highly stripped high Z ions (U^{92+}) in the ESR to low enough temperatures a phase transition to an ordered state should occur. if the order

parameter[17] $\Gamma = (Z^2e^2/a)/kT$ exceeds 170. Molecular dynamics simulations[18] (Fig. 9) show that in such a beam a novel form of ordering occurs with the particles being placed on cylindrical shells encircling the beam axis. New crystallographic symmetries occur that differ from those in an infinite Coulomb lattice. The lattice constants are in the order of several tens of micrometer, thus a piece of condensed ordered matter is formed with a density 10^{15} times smaller than ordinary matter. The practical absence of Doppler broadening will be extremely beneficial for some nuclear physics experiments discussed above. A momentum spread $\Delta p/p$ of 10^{-6}, characteristic for crystalline beams, would allow high precision mass measurements (Schottky scan) and resonance laser spectroscopy with lower power requirements.

REFERENCES

1. Die Ausbaupläne der GSI, March 1984
2. SIS - Ein Beschleuniger für schwere Ionen hoher Energie, GSI-Bericht 82-2
3. K. Blasche, D. Böhne, B. Franzke, H. Prange, 1985 Particle Acc. Conf. 1985, Vancouver, IEEE Trans. NS32, (1985)
4. B. Franzke et al. Zwischenbericht zur Planung des Experimentier-Speicherrings (ESR) der GSI, GSI-SIS-INT/84-5 August 1984 and Information about ESR. GSI-ESR-TN/87-02.
5. R. Keller et al., Proc. Int. Ion Engineering Congress, Kyoto (1983)
6. N.Angert, internal report
7. H. Gould et al., Phys. Rev. Lett. 52, 180 (1984)
8. B. Franzke, Ch. Schmelzer, GSI-Scientific Report 1984, p.341
9. I. Hofmann, GSI Scientific Report, 1985, p. 387
10. G. Münzenberg, GSI-Nachrichten 11-87, p. 3
11. M. Langevin et al. Phys. Lett. 150B, 71 (1985)
12. J. Homolka et al., Nucl. Instr. Meth. A260, (1987) 418
13. K. Takahashi and K. Yokoi, Nucl. Phys. A404 578 (1983)
14. P. Kienle in Proc. of "10 Years of Uranium Beams" GSI Conference 86-19 and Proc. of "Int. Conf. on Solar Neutrino Detection" GSI preprint 86-57
15. H.A. Gustafson et al., Phys.Rev.Lett. 52, 1590(1984)
16. J.P. Schiffer and P. Kienle, Z. f. Physik, A321, 181 (1985)
17. J.P. Hansen, Phys. Rev. A11, 1025 (1975)
18. A. Rahman, J.P. Schiffer, Phys. Rev. Letters 57, 1133, (1986)

Figure captions

Fig. 1 Layout of the upgraded UNILAC, SIS and ESR.

Fig. 2 Maximum achieveable energies at SIS 18 as a function of nuclear charge, the energies are given for a gas- or a foil-stripper at an energy of 1.4 MeV/u, resulting in relatively low degrees of ionization. If a second stripper at 11.4 MeV/u is added or if completely ionized particles from the experimental storage ring ESR are reinjected into the synchrotron higher energies can be achieved.

Fig. 3 Beam currents for various charge states of Ne- and U-ions, gained with the stripping procedures described in Fig. 2 as function of the energy. The intensity drops by a factor of 3 for Ne^{10+} and U^{78+} are due to a decrease of the repetition rate from 3 Hz to 1 Hz.

Fig. 4 The magnetic lattice lay out of the ESR ring, with stochastic and electron cooling devices, rf-cavities and a straight section with an optional gas jet target.

Fig. 5 Experimental area between SIS and ESR with the fragment mass separator FRS and its various experimental areas and the connection line between SIS and ESR in which a final stripper for production of completely stripped heavy ions may be placed. There are additional high dose and high intensity irradiation facilities foreseen.

Fig. 6 One version of a possible layout of the beam transport system and three experimental caves in the target hall. Other versions are in study.

Fig. 7 Schematic lay out of the 4π-detector. The target B is surrounded by a central drift chamber E in a magnetic field produced by a superconducting solenoid J. The forward cone between 7^{o} and 30^{o} is covered with tracking chambers F, a cluster detector H and a time of flight wall G. The products emitted in beam direction are analyzed with a forward spectrometer, neutrons are measured with a time of flight detector N. High energy γ-rays are detected with BaF_2 arrays K.

Fig. 8 Design schematic of a Kaon Spectrometer

Fig. 9 Crystalline beams.
Upper part: Projection of 2000 particles in a molecular-dynamics calculation[19] onto the plane perpendicular to the beam (x-axis) for $\Gamma = 170$. Lower part: distribution of particles in the outer shell with the shell unfolded into a plane. All shells but the innermost show a similar pattern.

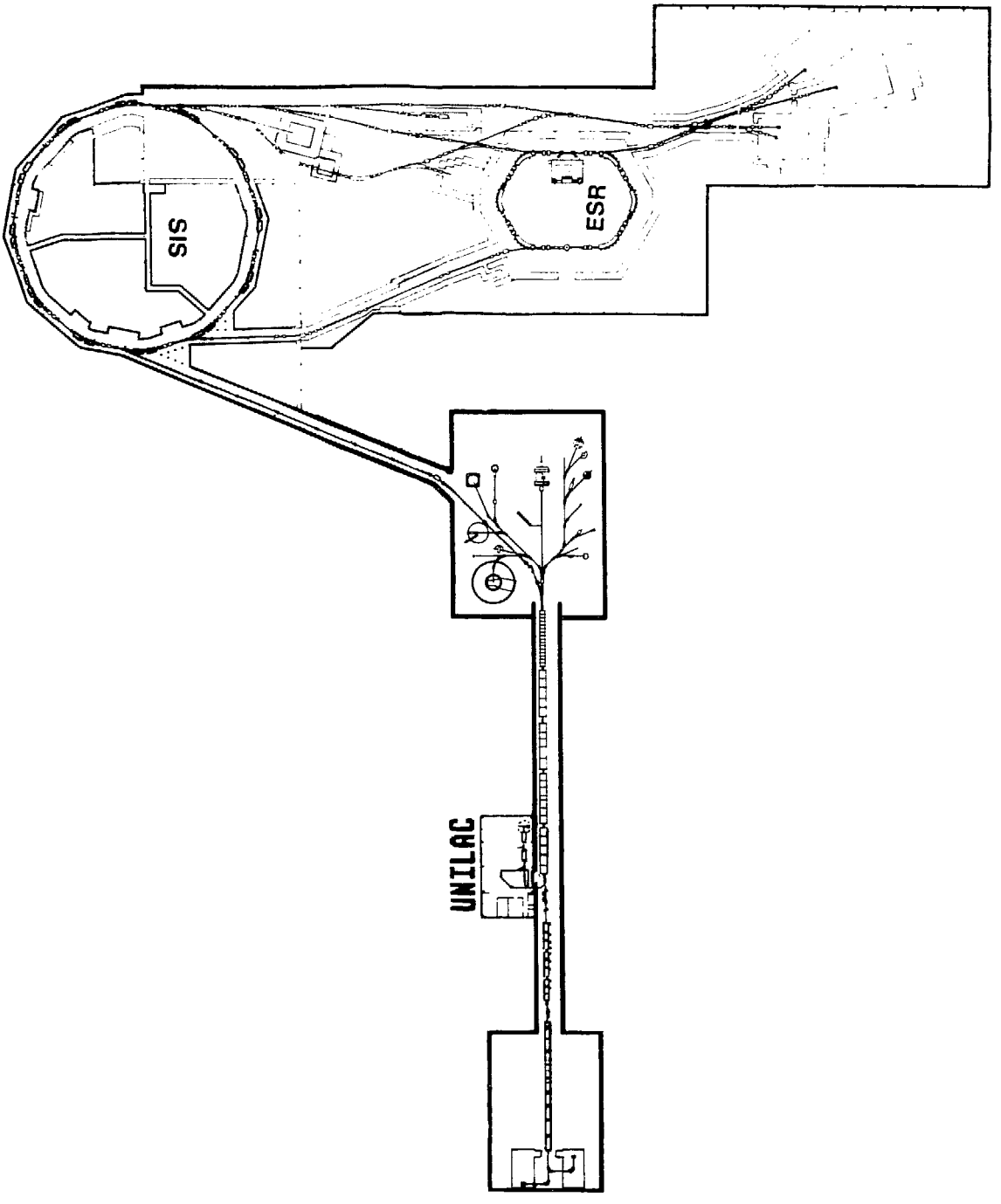

Fig. 1

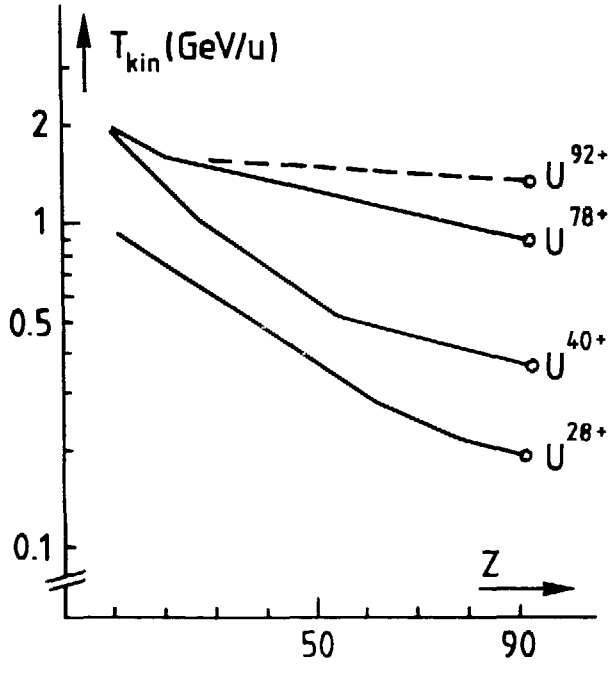

Stripping

Fig. 2

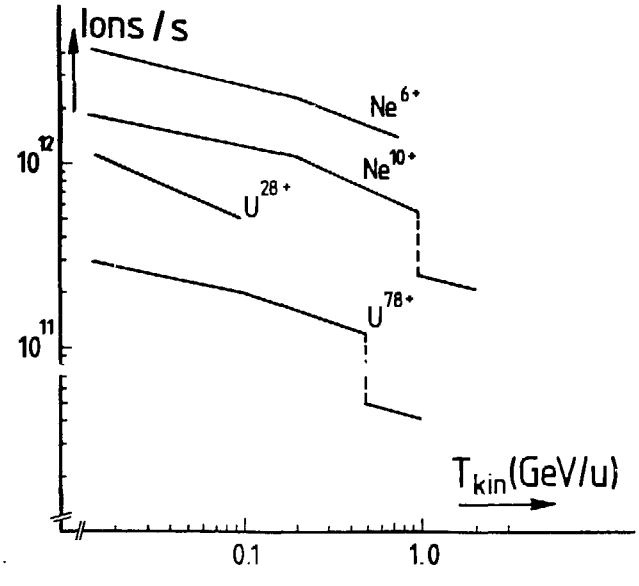

Fig. 3

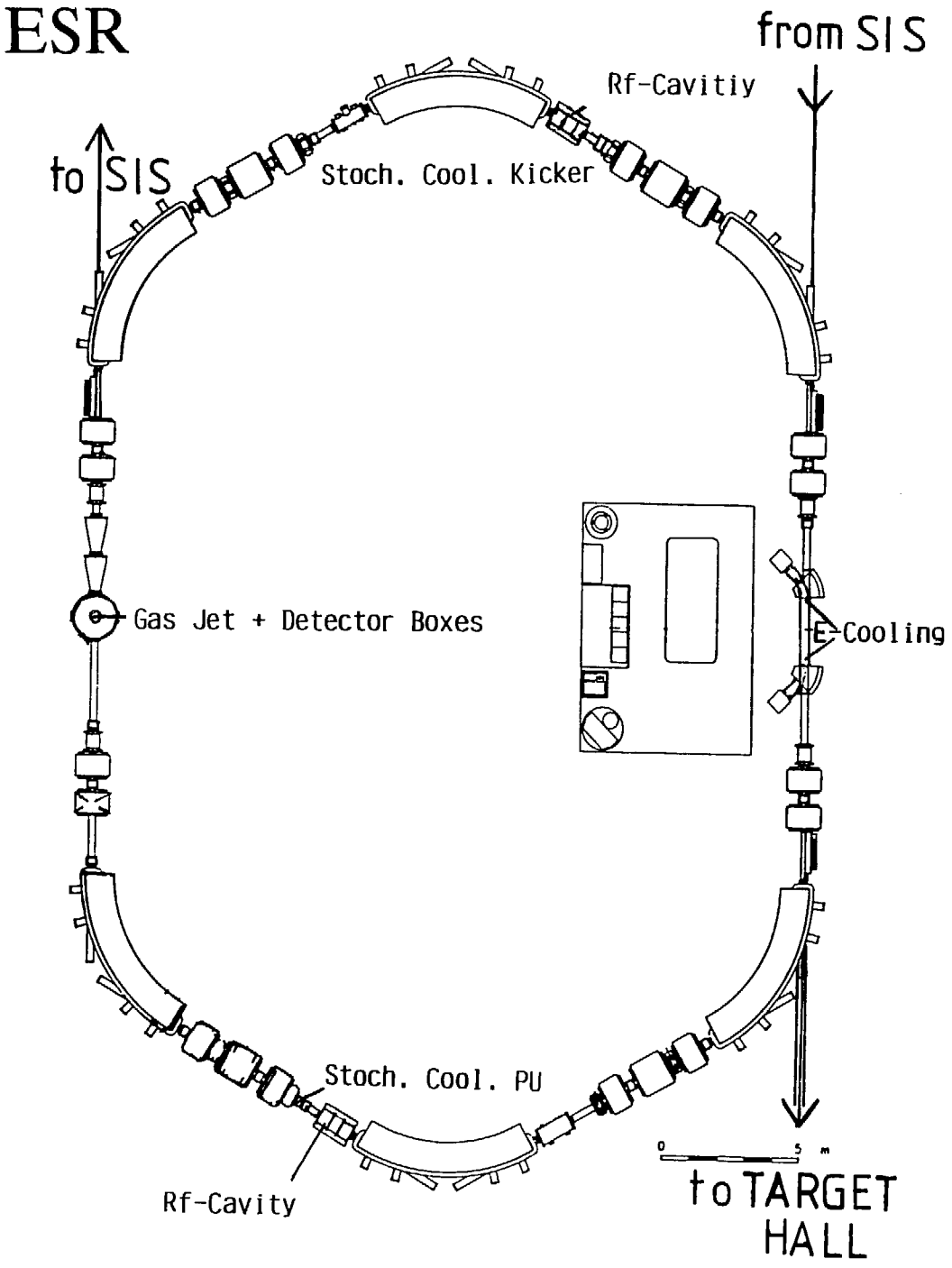
ESR
from SIS
Rf-Cavitiy
to SIS
Stoch. Cool. Kicker
Gas Jet + Detector Boxes
Cooling
Stoch. Cool. PU
Rf-Cavity
0
5 m
to TARGET HALL

Fig. 4

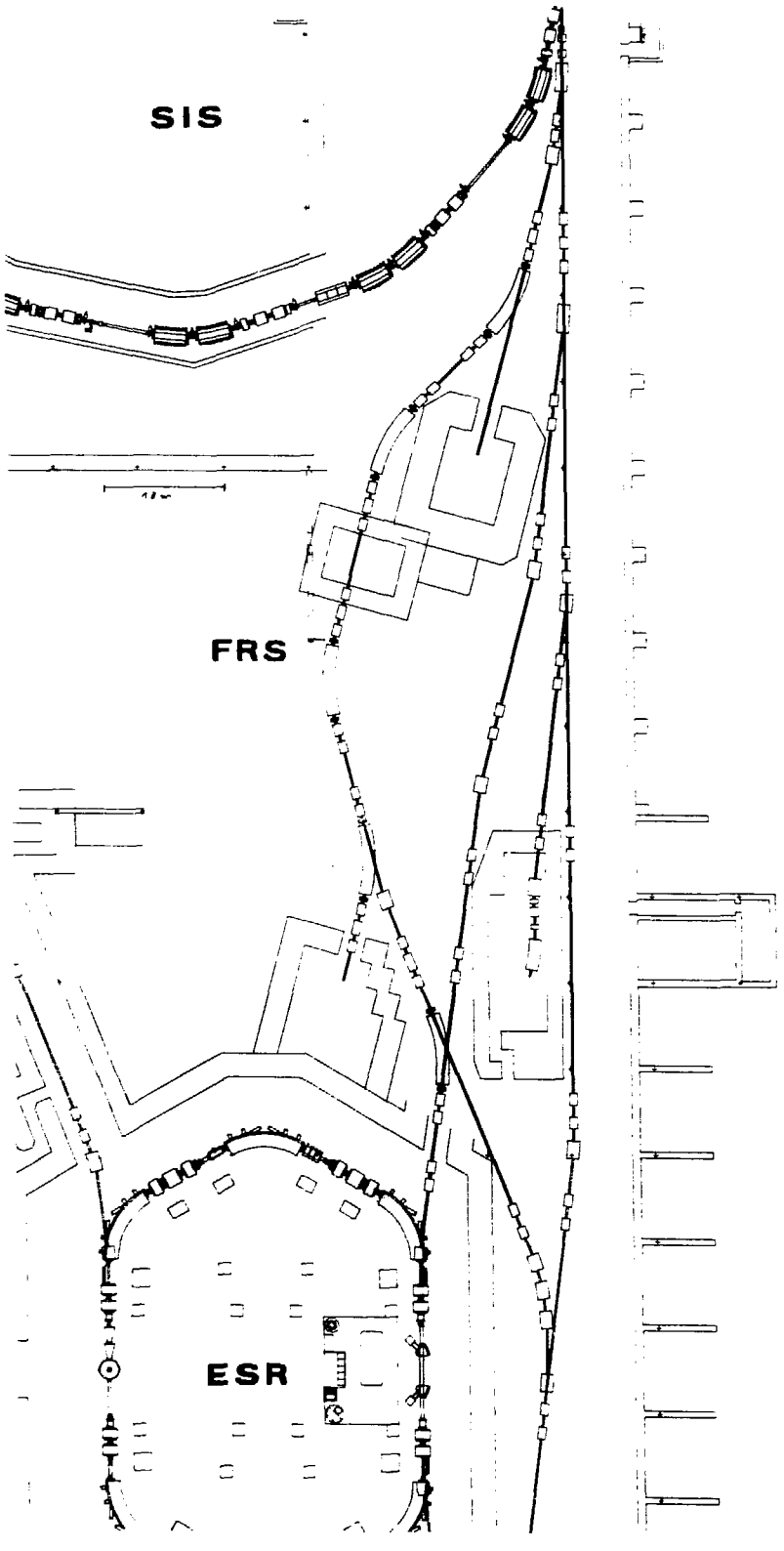

Fig. 5

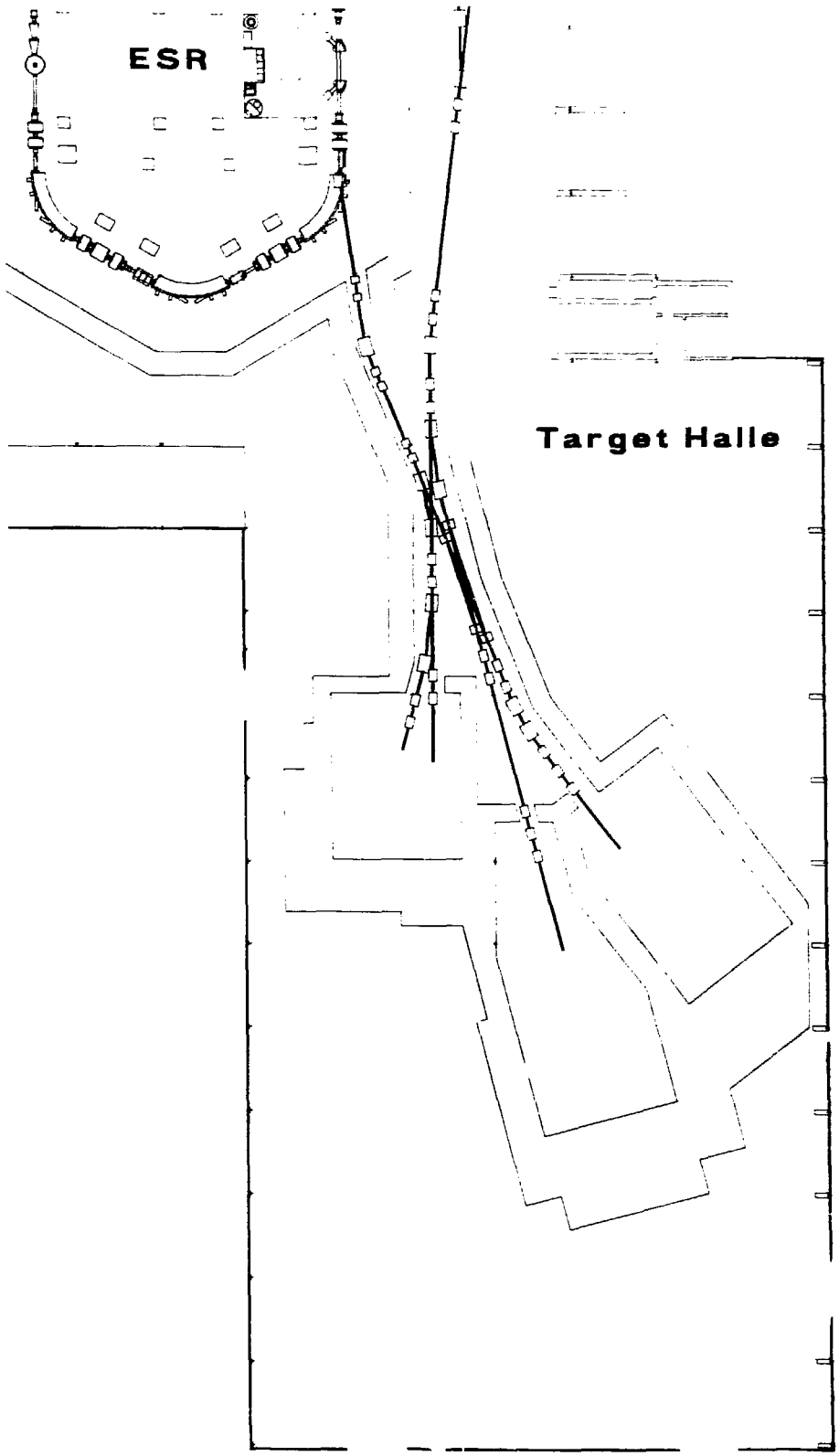

Fig. 6

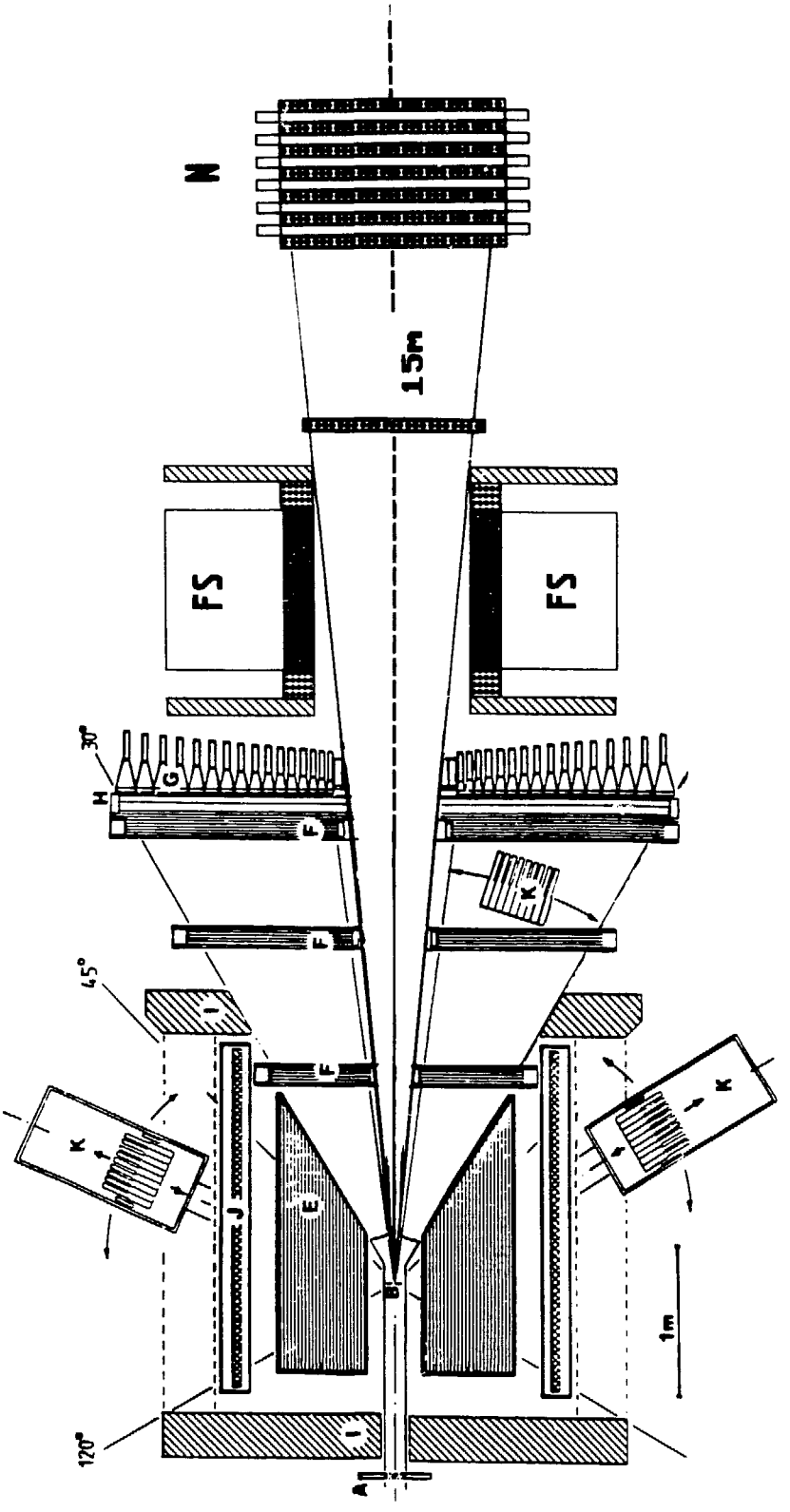

Fig. 7

Kaon Spectrometer

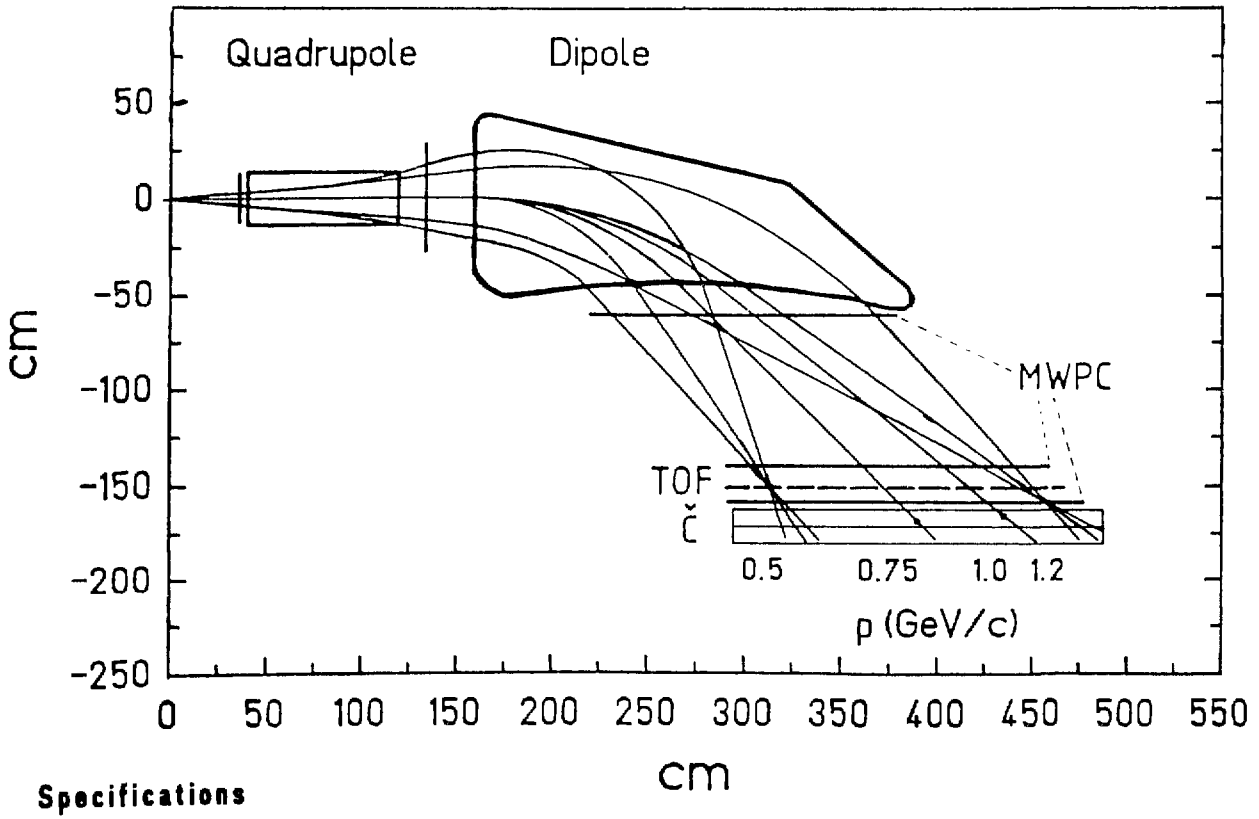

Specifications

B_{max}	1,7 T		
Solid angle Ω	20 - 35 mrad		
	min	central	max
Momentum range at B_{max}	570	750	1200 MeV
Dispersion along focal plane	3,5	2,0	1,3 cm/% p
Total length (target focal plane)	3,7	4,5	5,7 m
Total weight	90 t		

Fig. 8

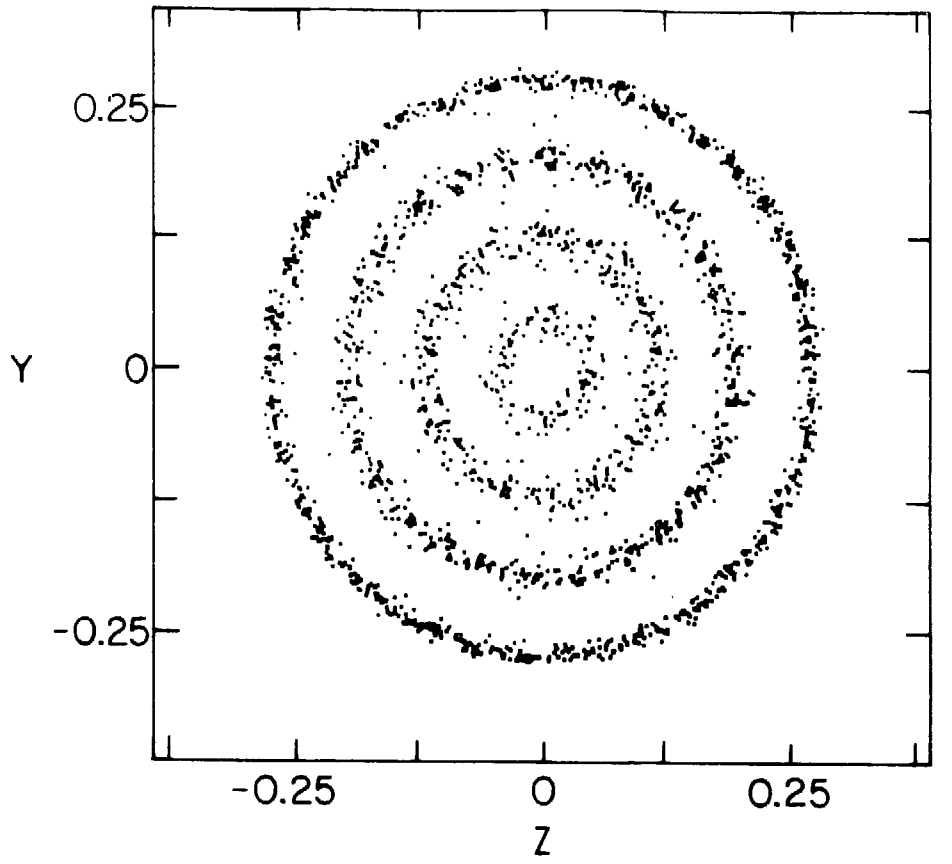
0.25
Y
0
-0.25
-0.25
0
0.25
Z

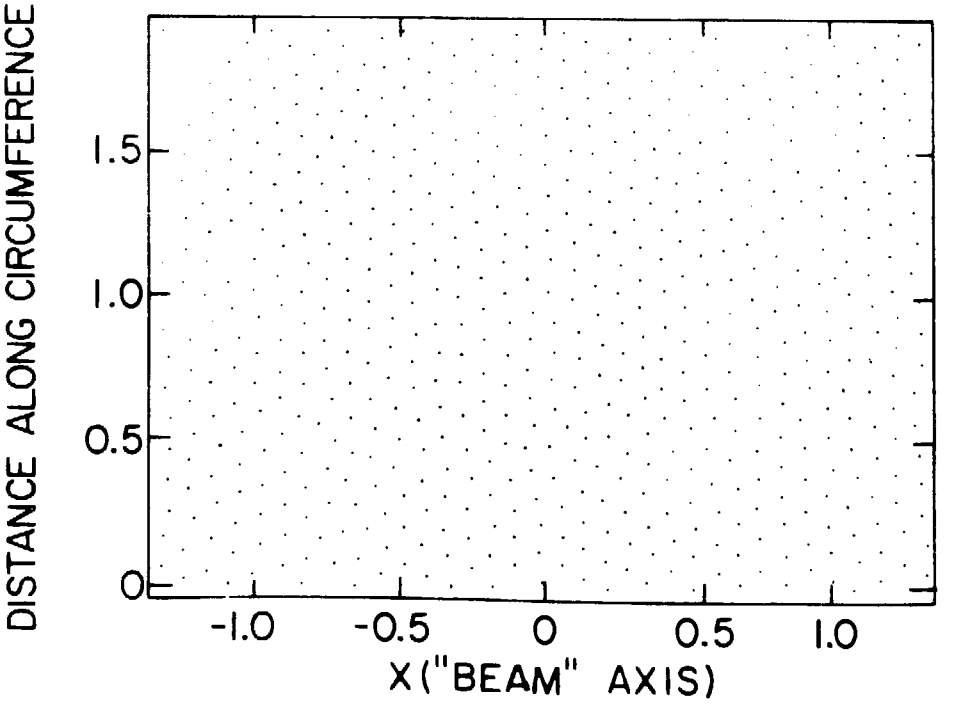
DISTANCE ALONG CIRCUMFERENCE
1.5
1.0
0.5
0
-1.0
-0.5
0
0.5
1.0
X("BEAM" AXIS)

Fig. 9

The Equation of State of Nuclear Matter

MEDIUM EFFECTS IN NUCLEAR STOPPING AND THE TRANSVERSE FLOW*

G. E. Brown and Volker Koch†

Physics Department
State University of New York at Stony Brook,
Stony Brook, New York, 11794.

ABSTRACT

We study medium effects on the nuclear stopping, with special reference to laboratory energy $E/A \simeq 800\,MeV$. Effects on virtual pions and, especially, on pions emitted in nucleon-nucleon scattering increase the stopping power substantially, so that equilibration results. We study other changes, due to the medium, of the properties of nucleons in nuclear matter.

*Supported in part by the US Department of Energy under Contract No. DE-AC02-76ER13001.
† Institute of Theoretical Physics, University of Giessen, D-63 Giessen, F.R. Germany; Supported by the German Accademic Exchange Service (DAAD)

1. Introduction

In a preprint of the title Rosenhauer et al. [1] calculate the effect of in medium corrections to two-nucleon cross sections in heavy-ion collisions at Bevalac energies. The included corrections for Pauli blocking, etc. lower the two-nucleon cross sections somewhat and decrease the speed of thermalisation.

We employ here a different picture when we look at the initial collision of two heavy ions in terms of the projectile consisting of a loosely bound wave packet of fermions, each nearly independently incident on the stationary target nucleus, and discuss the first collisions that take place. Then, since the Fermi spheres representing the momentum distribution of the two nuclei are far apart, initially the Pauli principle will play no role. Later, after thermalisation, it will come into play, but with effects substantially smaller then those discussed here.

We tackle first the problem of energy degradation at the maximum energy, $800 MeV$ ($^{197}Au + ^{197}Au$) discussed in ref. [1]. This is a common energy for Bevalac experiments. Sobel et al. [2] pointed out that with increasing energy, the transport mean free path increased, reaching the nuclear radius by $E/A \geq 1\ GeV$. We shall, however, show that the cross section for nucleon- nucleon scattering are greatly increased in medium and that equilibration certainly results up to quite high energy, as high as we can calculate. We shall consider relatively central collisions, which can be selected experimentally by triggering on high-multiplicity events.

2.Medium Dependence of Pion Production

We put off the discussion of elastic scattering, which mainly results in relatively forward scattering, and is therefore not so important for the transport mean free path, until later. We begin considering pion production, which proceeds mostly through isobar formation. Since the center of mass energy in the two-body collision is only 365 MeV, and we shall assume the dominant process to go through the on-shell exitation of the Δ-resonance on the right-hand-side of fig.1 at 300 MeV, nearly all of the energy is used up and the two final nucleons go off with little energy. This is accentuated by the optical model potential which is repulsive at these energies, so even more of the incident energy must be used up in mounting this barrier. Thus, if p is the momentum on the left, roughly the same momentum p will be carried by the pion, which has virtual energy $\sqrt{p^2 + m_\pi^2} \simeq 600 MeV$.

We consider the Tamm-Dankoff sum, the first term of which is shown in fig. 1b). In this sum, virtual pions are not present at the same time as isobars. Therefore, we have the largest parts. The ratio of b) to a) is found, following the formalism reviewed in ref. [3] to be

$$R = \frac{1}{2} \frac{f_{\pi N\Delta}^2}{m_\pi^2} \left(g'_{N\Delta} \frac{p^2}{p^2 + m_\pi^2} \right) \left(\frac{4}{9} \right) \frac{\rho}{250 MeV} \qquad (1)$$

We now explain the factors. The $\frac{1}{2}$ arises because for each pion we can have only one out of the two time orderings which would give equal contribution in the nucleon-nucleon

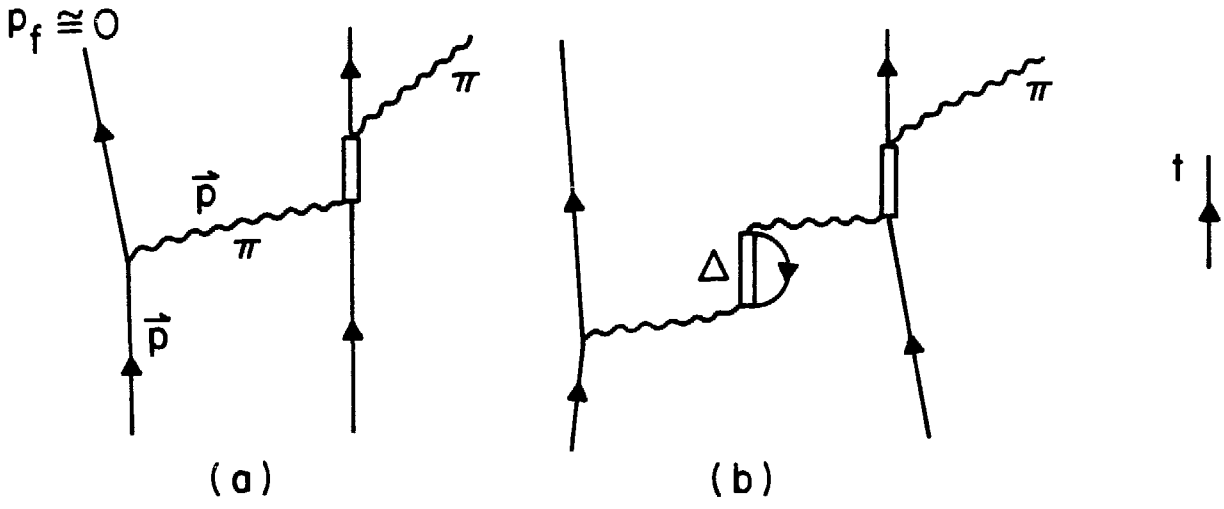

Figure 1: Pion production through isobar formation: a) Production amplitude in a nucleon-nucleon collision. b) Medium-dependent correction to a). We show only the optimal time ordering for the process. There are many other time orderings, especially of b).

interaction (where the isobar on the right is not present). The $\frac{4}{9}$ is a product of spin and isospin projection operators, projecting on the space of isobars. The 250 MeV in the denominator is $E_\Delta - E_N$ lowered by 50 MeV because of the lower kinetic energy of the isobar, due to its larger mass than the initial nucleon.

We chose [4] $g' = 0.4$. Certainly, from the absence of multiple scattering in low-energy pion-nucleus scattering, g' must be in the neighborhood of 1/3 [5]. The coupling constant $f_{\pi n\Delta} = 2$. With these values we find $R = 0.135\,(\rho/\rho_0)$.

Since the virtual pions are quite hard, i.e. , $\sqrt{p^2 + m_\pi^2}$ is large compared with $E_\Delta - E_N$, the diagrams we have drawn are the large ones. However, for different time orderings of fig.1a) one can draw various corresponding time orderings of fig.1b) and, roughly speaking, we expect the ratio to be about the same. For $\rho = 2\rho_0$ we expect, then, the cross section to be increased by a factor of $\sim (1.27)^2 \geq 1.5$ because of the medium corrections. From our later considerations, we shall see that our estimated increase here is quite modest.

The process we have employed here to enhance the virtual pion exchange is reminiscent of those employed in the days when pion condensation or critical opalescence was en vogue (e.g., see ref.[6]). Here the main attention was often paid to nucleon particle-hole bubbles. The measurement [7,8] that g'_{NN} had to be ≥ 0.9 destroyed this mechanism for condensation or softness. However, the smallness of $g'_{N\Delta} \sim 0.4$ noted earlier means that isobar-nucleon holes take over the role.

A number of authors [9,10] have considered the effect of medium corrections in the final pion emitted in the $(N + N \rightarrow N' + N' + \pi)$ process. The main effect here comes from the

uncrossed absorption and emission of a pion through an isobar intermediate state. The nucleon particle hole intermediate states give small contributions for two reasons: i) The crossed and uncrossed graphs tend to cancel. ii) The large local field corrections expressed through $g'_{NN} \simeq 0.9$ supresses them, as noted above. We have

$$\omega_\pi^2 = m_\pi^2 + k^2 + \Pi(k,\omega) \tag{2}$$

where $\Pi(k,\omega)$ is the in medium pion polarisation diagram. This is [10]

$$\Pi(k,\omega) = \frac{k^2\,\Lambda^2(k^2)\,\chi_R(k,\omega)}{1 - g'_{N\Delta}\,\Lambda^2(k^2)\,\chi_R(k,\omega)} \tag{3}$$

where

$$\chi_R(k,\omega) = -\frac{4a\,\omega_R\,\rho}{\omega_R^2 - \omega^2} \tag{4}$$

ω_R is the difference between isobar and nucleon energies. These authors chose $g'_{N\Delta} = 0.6$, $a = 1.13/m_\pi^2$, and the cut off $\Lambda(k) = exp(-k^2/b^2)$ with $b = 7m_\pi$. For $\omega = m_\pi$ and small k and $\rho = 2\,\rho_0$,

$$\Pi(k,\omega) \simeq -1.03\,k^2 \tag{5}$$

With the parameters we used to obtain R in eqn.(1) we would have $\Pi(k,\omega) = -1.15\,k^2$. In any case, the curve of $\omega(k)$ versus k is relatively flat, for small k, as function of k, and possibly decreases a bit at first. As we remark later on, because of the cut-off $\Lambda(k)$ and recoil effects in ω_R, later on the curve will go up.

Now, the density of final pion states, which enters into the pion production cross section, involves $|d\omega_\pi/dk_\pi|^{-1}$. (This comes in evaluating the integral $\int \delta(E_{N_1} + E_{N_2} - E'_{N_1} - E'_{N_2} - \omega_\pi)\frac{d^3k_\pi}{(2\pi)^3}$.) Because of the attractive interaction of the pion with the medium, expressed through Π, this density of states will be increased by a factor

$$F = \frac{|d\omega_\pi/dk_\pi|_{\Pi=0}}{|d\omega_\pi/dk_\pi|} \tag{6}$$

Such an enhancement factor has recently been considered by Charles Gale and J. Kapusta [11].

In order to see what the factor (6) means, let us consider the situation where $\Pi(k,\omega)$ begins, for small k, as $-k^2$. Then $\omega = m_\pi$, for as long as this holds. In this case, $F \to \infty$. As long as we can neglect the recoil energy of the final nucleon resulting from the isobar decay, energy conservation can be achieved for pions up to where ω begins taking on an appreciable k dependence. In fact, since the isobar has a large width (even larger in nuclear matter than in vacuum because of the possibility of mesonless decays with formation of particle-hole pairs) energy conservation is not a problem.

Now ω will move away from m_π as $\Lambda^2(k^2)$ starts to cut off and as $\omega_R = m_\Delta - m_N + k^2/2m_\Delta$ begins to be affected by the final term, the recoil energy. The scale here is m_N, but one can see from Friedman et al. [10] that ω_π reaches $2m_\pi$ already at $k \simeq m_N/2$.

Now the phase space accompanying the δ-function of energies involves a $\left(\frac{d^3p_N}{(2\pi)^3}\,\frac{4\pi k_\pi^2}{(2\pi)^3}\right)$, the dk_π having been converted into a $d\omega_\pi$.

Without medium effects, the k_π of the pion in the decay of an isobar is $\simeq \sqrt{3}\, m_\pi$ (since $\omega_\pi \sim 2m_\pi$). In medium, $k_\pi \sim 3m_\pi$. In the center of mass system of the isobar, which is close to being formed at rest in our case of $E/A = 800\, MeV$, $\vec{p}_N = -\vec{k}_\pi$, so p_N has the same magnitude as k_π. Thus, the phase space is increased, by medium effects, by the factor

$$\tilde{F} = \frac{\left[\frac{d^3p_N}{(2\pi)^3}\frac{4\pi k_\pi^2}{(2\pi)^3}\right]_{in\ medium}}{\left[\frac{d^3p_N}{(2\pi)^3}\frac{4\pi k_\pi^2}{(2\pi)^3}\right]_{vacuum}} \simeq \left(\sqrt{3}\right)^5 \simeq 15 \tag{7}$$

We must multiply this factor, however, by the renormalization of the pion pole of the excitation, $(1 - \partial\Pi/\partial\omega^2)^{-1}_{\omega_\pi}$ which we calculate to be $\simeq 0.4$. Thus, our net factor is ~ 6. Multiplying by our previous ~ 1.5 we have ~ 9. This looks disgracefully large, but replaces the factor $F = \infty$ which would result from eqn. (6) with our schematic $\omega = m_\pi$, all k.

Lest the reader think the factor ~ 9 ridiculous we remark that Ainsworth et al [12] found that for $\rho = 2\rho_0$, the pion to nucleon ratio in equilibrium was increased a factor ~ 10 by the medium interactions.

Of course, our medium effects increase the pion production cross section for protons going through nuclei, although the effect is not large here, going with some $< \rho > /\rho_0 < 1$ More pions are seen generally than cascade programs, which do not include these medium dependent effects, predict. However, most of the true pion absorption is not included in cascade calculations [13]. In a more complete calculation, most of these excess pions would be expected to be absorbed before they get out.

It seems clear that medium effects, through the change in pion energies in the medium, dramatically increase the stopping power for $E/A = 800\, MeV$. In sections 5 and 6 we indicate that we believe that this will continue to substantially higher energies, although this has not been worked out in detail yet.

Having settled, to our satisfaction, the question that nuclei colliding with nuclei equilibrate, we go on in sections 3 and 4 to have fun and play games to see what might happen with nucleons in dense matter. These sections will not be important for stopping, however.

3. The Nucleon-Nucleon Cross sections in Medium and Three-Body-Forces

In this section we begin by showing that relativistic calculations with effective nucleon masses m^* should give medium corrections to the nucleon-nucleon cross section σ_{NN}.

In perturbation theory, which we shall improve upon later, the effective mass in relativistic mean field theories on the nucleon on the left hand side in fig. 2 can be thought of as arising from process shown [14]. We shall here estimate the ratio of this amplitude to the vacuum two-nucleon amplitude, fig.3. In this ratio $R_{2/3}$, the bubble on the left of fig.2 brings in a scalar mean field U_s. Each vertex for pair creation and annihilation brings in [14] a p/m, and the energy denominator with the virtual pair present is $\simeq 2m_n$. Thus, this ratio is

$$R_{2/3} = 2 \times 2\left(\frac{U_s}{m_n}\right)\frac{p^2}{2m_n^2} \tag{8}$$

One factor of 2 here comes from the two possible time orderings of the σ-fields originating

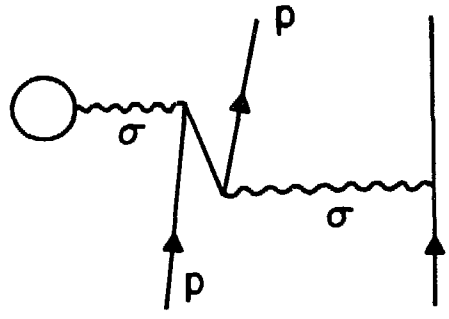

Figure 2: Here the backward-going line represents an antinucleon

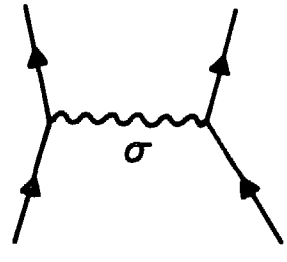

Figure 3: Standard mean field σ exchange

from the Z-diagram on the left; the other factor 2 because the bubble can occur on either the left or the right line. Here $p^2/2m_n$ is the (nonrelativistic) energy of one of the nucleons in the center of mass system, $p^2/2m_n = T_{lab}/4$ nonrelativistically. Thus, we have

$$R_{2/3} = \left(\frac{U_s}{m_n}\right)\frac{T_{lab}}{m_n} \tag{9}$$

Dirac phenomenology requires [15] $|U_s| \simeq 300\,MeV$ for $T_{lab} = 800\,MeV$ whereas the two-nucleon phase shifts give [16] $|U_s| \simeq 200\,MeV$. We shall use the latter, smaller, number but assume that it scales linearly with density since we are using mean field theory in our estimates. We thus find

$$R_{2/3} = -0.32 \tag{10}$$

Without recourse to perturbation theory, we could have made the same calculation in the following way. At each vertex of the scalar coupling we have (This argument applies only for forward scattering. Since the chief scattering is through small angles, it should be indicative. The calculations reported here use the relativistic Feynman formalism and continue correctly away from zero angle.)

$$g_\sigma\bar{\psi}\psi \simeq g_\sigma\psi^+\psi < \gamma_0 >= g_\sigma\psi^+\psi\,\frac{m_n^*}{\sqrt{k^2+m_n^{*2}}} = g_\sigma\psi^+\psi/\gamma^* \tag{11}$$

where γ^* is the in medium boost factor. Thus, each vertex is modified in medium by the factor

$$F = \frac{m_n^*/\sqrt{k^2+m_n^{*2}}}{m_n/\sqrt{k^2+m_n^2}} = 0.82 \tag{12}$$

where we have chosen $m_n^* = 0.6\,m_n$, appropriate for $T_{lab}/A = 800\,MeV$ and $\rho = 2\,\rho_0$, i.e., for the case of no compression. Squaring this, we find $F^2 = 0.67$, or a reduction of 0.33 to be compared with the 0.32 reduction found from perturbation theory.

This is a complicated way to proceed, because in eqn.(11) we have essentially divided by the in medium boost, and this will just be cancelled by the contraction of $\psi^+\psi$. However, we will use our knowledge of the size of the process, fig.2, later. Also, the $\psi^+\psi$ here and the $\psi^+\psi$ which enters into the vector coupling get a common compression by γ^*, so our factor of $1/\gamma^*$ in eqn.(11) is useful in seeing how the scalar interaction decreases with respect to the vector with increasing energy.

Empirically, the vector forward scattering just cancels the scalar forward scattering for $T_{lab}/A \simeq 300\,MeV$, and above this energy the vector predominates, because of the growing γ^*. However, the empirical σ_{NN} is only a fraction what it would be from either vector or scalar interaction separately, because of the near cancellation. Thus, one would expect the cross section from the process, fig.2, alone to be comparable with σ_{NN}.

We can calculate the cross section that would come from only σ exchange in mean field approximation using the values for the meson masses of Serot and Walecka [17], $g_\sigma^2/4\pi = 3.18$, $m_\sigma = 0.55\,m_n$. We find

$$(\sigma_{NN})_\sigma = 80\,mb \tag{13}$$

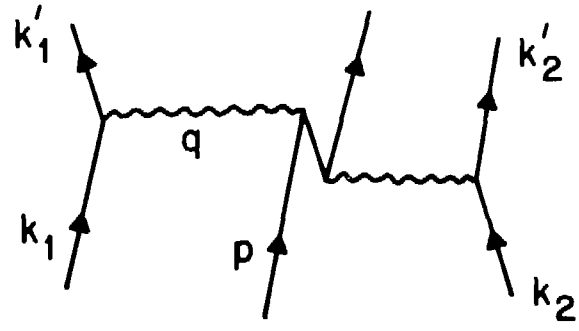

Figure 4: The three-body force arising from the process, fig.2.

Then including the ω, with $g_\omega^2/4\pi = 3.9$, $m_\omega = 0.825\, m_n$

$$(\sigma_{NN})_{\sigma+\omega} = 12.9\, mb \tag{14}$$

Finally, we can calculate the cross section with inclusion of $m^* = 0.6\, m$ (for density $2\rho_0$) giving

$$(\sigma_{NN})_{\sigma+\omega,m^*} = 19.7\, mb \tag{15}$$

As compared with standard scenarios, we already have increases in the cross section, but we now point out that there is a large three-body force which has not yet been put into calculations. Cutting the nucleon loops in the process of fig.2, gives the three-body process fig.4

Now we estimate the ratio of the cross section from the process, fig.4 to that from fig.2. The three-body cross section involves a factor of $(q^2 + m_\sigma^2)^{-2}$ which is $(m_\sigma^2)^{-2}$ in the two-body one, fig.2. There is a final integration over $4 \int \frac{d^3 k_1'}{(2\pi)^3}$ in which the magnitude of k_1' will be limited to $\sim m_\sigma$. Therefore, the ratio of cross sections of the process fig.4 and 2 is

$$\frac{\sigma_3}{\sigma_2} = \frac{m_\sigma^3}{k_f^3} \simeq 4 \tag{16}$$

so that

$$\sigma_3 \simeq 4\, [(\sigma_{NN})_{\sigma,m^*} - (\sigma_{NN})_{\sigma,m}] \tag{17}$$

With the parameters given above, we can evaluate the right-hand side to give

$$\sigma_3 \simeq 27.2\, mb \tag{18}$$

This is not large, but a three-body interaction may be effective in forming deuterons, since a neutron and proton can be scattered in one direction, the third particle taking off the momentum.

4. Nucleons "Swell" with Increasing Density

The question as to whether or not nucleons swell in the nucleus has proved to be an elusive one, but arguments have been given that the masses of the scalar [18] and vector [19,20] mesons scale in medium roughly as the nucleon effective mass, i.e.,

$$\frac{m_i^*}{m_i} \simeq \frac{m_n^*}{m_n} \tag{19}$$

This conclusion is inescapable in the Nambu-Jona-Lasinio theory of dynamical mass generation [21]. In this calculation the nucleon mass comes from that of the constituent quarks, the meson masses - other than that of the pion - come chiefly from the sum of constituent quark and antiquark masses. Therefore, very roughly

$$m_\sigma \simeq \frac{2}{3} m_n \tag{20}$$

and the same relation holds in medium [21], $m_\sigma^* \simeq \frac{2}{3} m_n^*$. Whether the models in refs. [18,19,20,21] are correct in detail or not, it is clear from general constraints imposed by chiral restoration at higher densities that constituent quark masses, and, therefore, meson masses, as well as the nucleon mass, must drop with increasing density. This is because the σ- and π- mesons become degenerate at the chiral restoration point, so m_σ must go down to m_π by the time $\rho \rightarrow \rho_c$, the critical density.

It is hard to pin down this swelling in electron scattering. In refs.[20] the apparent swelling of nucleons is interpreted in terms of the virtual γ-ray coupling part of the time through vector mesons which have a lowered in medium mass. This follows along the lines of the swelling of the pion cloud in medium [22] . However , in standard many-body theory [22] the graphs which describe this swelling of the pion cloud are only several among many, such as those coming from Pauli blocking and exchange current effects. In particular, there are strong cancelations between the "swelling" diagrams and the Pauli blocking ones [23] . We expect something similar to happen in our problem. Initially, as two nuclei start to go over each other, the Fermi spheres in momentum space are well separated, but later, as the movement towards equilibration proceeds, Pauli blocking will enter in and cancel much , if not most of the increase in cross section resulting from increased nucleon size. In the transport mean free path [2] the differential cross section is weighted with $(1 - cos\Theta)$. It is this mean free path that describes momentum degradation. However, at the lower energies important for equilibration, the transport mean free path is low, $\lambda_{tr} \ll R$ where R is the nuclear dimension, so equilibration will proceed without any in medium enhancement of cross section.

We have the amusing situation that in the initial nucleon-nucleon collisions, the range of interaction is larger because of the density $\rho \simeq 2\rho_0$. The small-angle scattering amplitudes, which go as $(m_i^*)^{-2}$ are also increased. However, the larger-angle scattering, which is more important for the transport mean free path, will go primarily as q^{-2}, where q is the momentum transfer, since the amplitude goes as $(q^2 + m_i^{*2})^{-1}$. In any case, the lower meson masses should increase the σ_{NN} somewhat in medium and this will further contribute to the increased stopping.

Since higher densities are achieved in nucleus-nucleus collisions than in nucleon-nucleus ones, the forward scattering amplitude in the former case should be increased substantially more than in the latter, by a factor of $(0.6/0.4)^2 = \frac{9}{4}$ greater, using our m_n^*'s from the last section. This should increase the momentum dependence substantially for the nucleus-nucleus collisions, over that obtained by folding the nucleon-nucleus dependence [24].

Note that the "swelling" discused in this section dependes only on the ambient density and should take place essentially immediately, with time scale $\tau \simeq \hbar/m_\sigma c$.

Our discussion of the "swelling" of nucleons in medium and our bringing up of the three-body force are quite "jazzy" but the reader should not be misled. The pion production and its increase because of medium dependence is by far the most important ingredient in producing the large stopping power. This is, of course, because the pion production produces the large-angle scattering which is so effective [2] in shortening the transport mean free path.

In the copious recent literature on heavy ion collisions in the several hundred $MeV/nucl.$ region, stiff equations of state are often adduced to produce strong sideways flow, large flow angles. Although adding momentum dependence to soft EOS's mocks up many effects of a stiffer EOS, it does not produce a large enough flow angle [24], chiefly because the degradation of longitudinal momentum is insufficient [24].

Now the sideways flow in a equilibrated system depends on the pressure per particle in the overlapping region of the two nuclei, divided by the average velocity with which they go through each other [25]. Larger two-body cross sections will give the colliding nuclei a larger time to push each other apart. Beautiful examples of this are shown in ref. [26]. For small impact parameters it is shown here that doubling the nucleon-nucleon cross section produces a larger increase in transverse momentum than changing from a soft to a stiff EOS. These calculations are carried only to $E/A = 400\,MeV$, but our simple picture [25] convinces us that this will hold true to higher energies.

5. Higher Energies

Three-body forces are small at low momenta because of chiral constraints [27]. There is no need for them to remain small with increasing energy and, indeed, in the stopping, one might expect many-body interactions and many-body effects to take over from the two-body interactions

As the momentum increases away from the soft-pion limit, at low energies contributions from the isobar take over. Let us consider energies $\simeq 1.8\,GeV/nucleon$, where some Bevalac experiments are already done. We can expect pion production through the double-isobar process, fig.5, to play a dominant role in the stopping here. Indeed, for $E_{lab} = 1.8\,GeV/nucleon$, $E_{cm} = 750\,MeV$ just a bit above the peak at $600\,MeV$ of the double-delta intermediate state. (It has been suggested [28] that even at much lower energies, where the double delta state is far off shell, that this state plays as important a part in pion absorption as the single delta.) It is known that the double-delta state, excited only virtually, provides much, if not most, of the intermediate-range absorption between nucleons [29]. The large coupling constant $f_{\pi N\Delta} = 2$ appears at every vertex in fig.5.

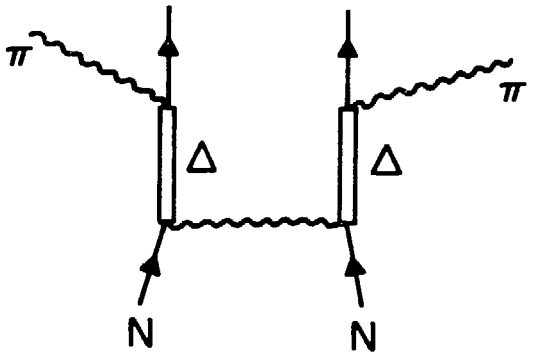

Figure 5: Pion production through double isobar production

Furthermore, both virtual and the two on-shell pions will be substantially enhanced by the medium dependent effects outlined in section 2.

Given the strong coupling betwen nucleon and isobar, one can manufacture a plethora of many-body interactions, one of which is given in fig.6. This interaction can proceed so that essentially all energy denominators are close to the double isobar energy, so that they are nearly on-shell for an incident energy of $E/A \simeq 1.8\,GeV$.

Although we noted several many-body forces earlier, we believe those involving intermediate Δ's to be most important because it is the easiest to produce on-shell pions. Producing one on-shell pion will virtually ensure the equlibration in a collision at $E_{lab}/A \simeq 800\,MeV$, and producing two will ensure that at $E_{lab}/A \simeq 1.8\,GeV$. It may be that the stopping goes down in between these energies, since in this region neither one nor two isobar states can quite put on shell, although the recoil and nucleon energies may wash this out.

Relatively few experimental results are available at $E_{lab}/A \simeq 1.8\,GeV$, but a recent preprint [30] gives very interesting results. Sophisticated methods are employed to remove anticorrelations, and the treatment of data is thoroughly tested, so the data should be relatively free of biases. The results show that in the collision of relatively light systems $Ar + KCl$ the transverse momentum of $56 \pm 5\,MeV$ for high multiplicity events at $800\,MeV$ per particle nearly doubles to $95 \pm 5\,MeV$ at $1.8\,GeV/nucleon$. Furthermore, the flow angle changes but little, dropping from $9.6 \pm 0.8\,degrees$ at $0.8\,GeV/nucleon$ (for all nucleons) to $8.5 \pm 1.0\,degrees$ at $1.8\,GeV/nucleon$. Thus a doubling of the center of mass energy produces essentially no difference in the angle of the flow, indicating a congruence between the situation at these two energies. We interpret this as meaning nearly complete equillibration. This would not be expected to result from the transport mean free path of Sobel et al. [2] which decreases rapidly with increasing energy, especially in the region above $1\,GeV/nucleon$.

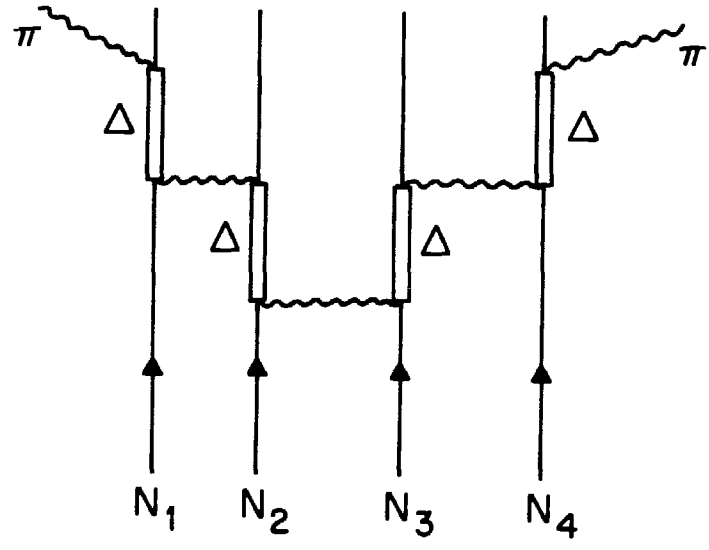

Figure 6: A many-body interaction involving four initial nucleons and two final pions

6. Per Ardua Ad Alta

Maybe we won't go over so rapidly to strings and somewhat reduced stopping power with increasing energy into the GeV region. Presumably we can manufacture more and more complex processes involving more Δ's etc. to give greater stopping at higher energies. Given a lot of energy, there is no need that the isobars return to nucleons, but one can have [28] a local predominance of Δ's. We know from Regge pole descriptions, esp. duality, that direct channel momenta may be high, but that if crossed channel momenta are low, boson-exchange works well for this latter channel. Of course the type of stopping we discuss here would only be expected to apply in projectile and target fragmentation regions, because the projectile is well out of the nucleus before it decays in central rapidity regions at high energies.

After completion of our note we were referred to the contribution by H. Stöbele et al. to the 7^{th} High Energy Heavy Ion Study. They show that the angular distribution of pions approaches an isotopic one in the limit of zero impact parameter (completely central collision) to *Ar + KCl* at 1.8 *GeV/nucleon*. This is precisely what our picture would suggest. The isobars in our double isobar are nearly at rest in the cms and give off pions isotropically. (The same should be true for the single isobar at an energy of $0.8\,GeV/nucleon$.)

Note that at an energy midway between $800\,MeV/nucleon$ and $1.8\,GeV/nucleon$, where the energy is roughly equally off-shell (in opposite directions) for single and double delta intermediate states, the single delta will not be formed at rest, but equally forward and backward. However, the velocities are not large.

Acknowledgements

We would like to thank Subal Das Gupta and M. Prakash for many discusions. One of the authors (G.E.B) would like to thank Horst Stöcker for "holding his nose to the data", and for many helpful discussions. Together with Horst Stöcker, he derived the test of what two colliding light systems would do at $1.8 GeV/nucleon$. Following the report of ref. [30] at the 8^{th} High Energy Heavy Ion Study at Berkeley, Nov. 18-20, 1987 by H. Ströbele we saw that this confirmed the large stopping power at this energy. To the extent that our treatment of stopping power adds new perspectives , we believe that Horst Stöcker should share in the credit. Of course, if we are wrong, he should not be blamed. We would like to thank Charles Gale, who reported on his work with Joe Kapusta, at the Berkeley meeting. This report confirmed the possible increase in pionic production due to interaction with the medium. Finally, we would like to thank Phil Siemens for continued advice and insight into the mechanisms we discuss here.

References

[1] A. Rosenhauer, G. Peilert, H. Stöcker, W. Greiner, and J. Aichelin. 1987. Univ. of Frankfurt Theoretical Physics Preprint 203/1987.

[2] M.I. Sobel, P.J. Siemens, J. Bondorf, and H.A. Bethe. *Nucl.Phys*, **A251**,502, 1975.

[3] G.E. Brown and W. Weise. *Phys. Repts.*, **22C**,280, 1975.

[4] A. Arima, T. Cheon, K. Shimizu, H. Hyuga, and T. Suzuki. *Phys. Lett.*, **63B**,43, 1976.

[5] M. Thies. *Phys. Lett.*, **63B**,43, 1976.

[6] M. Gyulassy. In *Proccedings of Falls Creek Falls Meeting on Heavy Ion Collisions, Falls Creek Falls, Tennessee*, June 13 - 17, 1977.

[7] T.A. Carey, K.W. Jones, J.B. McClelland, J.B. Moss, L.B. Rees, N. Tanaka, and A.D. Backer. *Phys. Rev. Lett.*, **53**,144, 1984.

[8] J.M. Moss. In *Int. Conference on Antinucleon and Nucleon -Antinucleon Interactions, Telluride, CO*, March 18 - 22, 1985.

[9] I.M. Mishustin, F. Myhrer, and P.J. Siemens. *Phys. Letts.*, **95B**,361, 1980.

[10] B. Friedmann, V.R. Pandharipande, and Q.N. Usmani. *Nucl. Phys.*, **A372**,483, 1981.

[11] C. Gale and J. Kapusta. *Phys. Rev.*, **C 35**,2107, 1987.

[12] T.L. Ainsworth amd E. Baron, G.E. Brown, J. Cooperstein, and M. Prakash. *Nucl. Phys.*, **A 464**,740, 1987.

[13] G.E. Brown, P. Siemens, and J. Zimanyi. to be published.

[14] G.E. Brown, W. Weise, G. Baym, and J. Speth, *Comments Nucl. Part. Phys.* **17**,39, 1987.

[15] B.C. Clark. In *Los Alamos Workshop on Relativistic Dynamics and Quark-Nuclear Physics*, June 2 - 14,1985.

[16] J.A. Tjon and S.J. Wallace. In *Workshop on Dirac Approaches to Nuclear Physics, Los Alamos, NM*, 1985.

[17] B.D. Serot and J.D. Walecka. *The Relativistic Many-Body Problem in "Advances in Nuclear Physics ", eds. J.W. Negele and E. Vogt.* 1986.

[18] T.L. Ainsworth, G.E. Brown, M. Prakash, and W. Weise. *Phys. Lett.* to be published.

[19] G.E. Brown. *Proc. Theor. Phys. (Japan).* to be published.

[20] G.E. Brown, C. Dover, P. Siegel, and W. Weise. to be published.

[21] V. Bernard, U. G. Meißner, and I. Zahed. *Phys. Rev. Lett.*, **59**,966, 1987.

[22] Magda Ericson and M. Rosa-Clot. *Z. Phys*, **A324**,373, 1986.

[23] S. Krewald. private communication.

[24] J. Aichelin, A. Rosenhauer, G. Peilert, H. Stöcker, and W. Greiner. *Phys. Rev. Letts.*, **58**,1926, 1987.

[25] G.E. Brown. Phys. Repts., to be published (Bethe Birthday Volume). This argument was made earlier in 1981 in a preprint by Horst Stöcker and Bernd Mueller which was, however, rejected for publication as being too simple. We find that is illustrates our point beautifully.

[26] G.F. Bertsch, W.G. Lynch, and M.B. Tsang. *Phys. Letts.*, **189B**,384, 1987.

[27] G.E. Brown, A.M. Green, and W.J. Gerace. *Nucl. Phys.*, **A115**,435, 1968.

[28] G.E. Brown, H. Toki, W. Weise, and A. Wirzba. *Phys. Letts.*, **118B**,39, 1982.

[29] J.W. Durso, M. Saarela, G.E. Brown, and A.D. Jackson. *Nucl. Phys.*, **A278**,445, 1977.

[30] P. Danielewicz et al. 1987. Univ. of Warsaw Preprint ITF/42/87.

The Nuclear Equation of State, Viscosity and Fragment Flow in High Energy Heavy Ion Collisions*

G.Peilert[a], A.Rosenhauer[a], T.Rentsch[a], H.Stöcker[a]†, J.Aichelin[b] and W.Greiner[a]

[a)] Institut für Theoretische Physik
Johann Wolfgang Goethe–Universität
D–6000 Frankfurt am Main, Germany
[b)] Institut für Theoretische Physik, Universität Heidelberg and
Max Planck Institut für Kernphysik
D-6900 Heidelberg,Germany

Abstract: The Quantum Molecular Dynamic Method is used to study multifragmentation in the bombarding energy interval from 100 A MeV to 800 A MeV. We find that the inclusive fragment mass distributions exhibit a power law behaviour with an exponent $\tau \approx -2.3$ in agreement with the data. The transverse momentum flow of the complex fragments is shown to depend sensitively on the nuclear equation of state (EOS). In nuclear fluid dynamics, we find a strong sensitivity also on the nuclear viscosity, which is related to the in–medium scattering cross sections used in microscopic calculations. At 200 MeV/n there are only minor effects of momentum dependent interactions. We conclude that the EOS is quite hard.

* This work has been funded in part by the German Federal Minister for Research and Technology (BMFT) under the contract numbers 06 OF 772, 06 HD 776 and by the Gesellschaft für Schwerionenforschung (GSI).

† invited speaker at the 8th High Energy Heavy Ion Study, LBL Berkeley, November 1987.

There has been considerable recent interest in the production of intermediate mass fragments ($A > 4$) in intermediate and high energy heavy ion collisions [1]–[10]. The mass distributions of inclusive measurements exhibit a power law form which has been interpreted as evidence for a liquid–vapour phase–transition[1]–[5]. Exclusive measurements established the collective flow in such reactions [11,12,13,14]. In one of the last Plastic Ball experiments it has been shown that intermediate mass fragments up to Z = 10 are abundantly produced in Au (200 A MeV) + Au reactions and preferentially emitted in the flow direction[9,10]. This correlation is stronger for more massive fragments as predicted by fluid dynamic calculations [15,16].

Fig. 1 shows the importance of the nuclear viscosity for the entropy (light particle production) and for the collective flow. Observe the strong increase of S/A, when viscosity is included, and the factor ~ 2 decrease of the transverse momentum transfer p_x/A. It turns out, that the effects of the nuclear EOS and of the nuclear viscosity are compatible in hydrodynamics. Therefore we now switch to a microscopic theory, which takes the nonequilibrium effects (e.g. viscosity) into account via the in–medium scattering cross sections.

We study multifragmentation in the reaction $^{197}Au + ^{197}Au$ at an energy of 200 A MeV, using the QMD model defined in refs. [17,18,19].

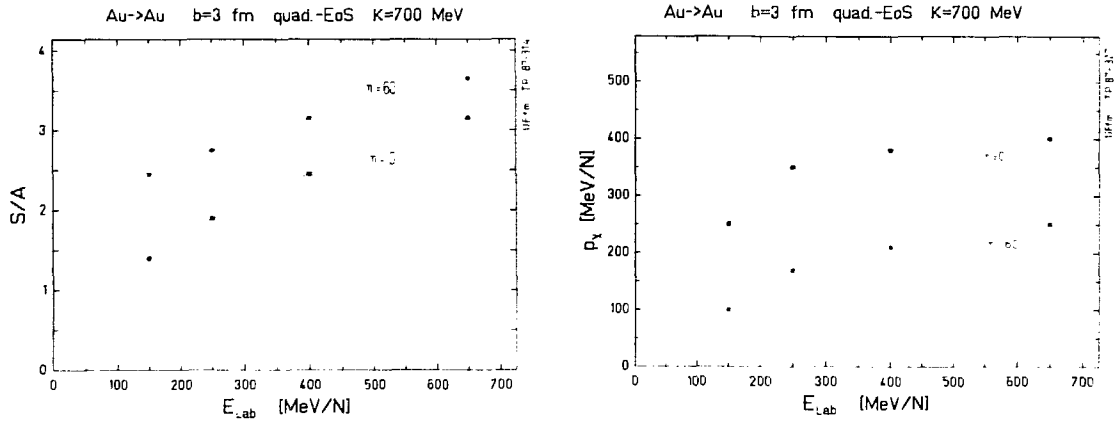

Figure 1: Viscous hydrodynamic predictions of entropy and transverse momentum transfer vs. energy in the reaction Au + Au. Observe the strong dependence on the viscosity coefficient η $(MeV/fm^2\ c)$

We determine the cluster distributions, using a common *minimum spanning tree* procedure. The upper part of *Fig. 2* shows the inclusive, i.e. impact parameter averaged mass yield curves for the hard and the soft equation of state. Both curves exhibit a clear power law behaviour $A^{-\tau}$. For the constant τ we find $\tau \approx 2.3$. Such a power law dependence with a value of τ between 2 and 3 has been interpreted as an evidence for a liquid–vapour phase–transition [1]–[5]. In the present fully dynamic model we can investigate to what extent this conclusion is conclusive.

Therefore we display in the lower part of Fig. 2 the final fragment yields for four different impact parameters. We observe a steep decrease in the yield of the fragments with $A \leq 10$. Large differences become evident for the heavier fragments. For central collisions (b = 1 fm) there are no $A > 40$ fragments. For b = 5 fm the distribution exhibits a flat plateau between A = 40 - 70. At b = 7 fm a U–shaped curve with a peak at $A \approx 120$ and almost no fragments in the $A = 20 - 80$ region results. We find that for non-central collisions the fragments of different masses reside in different rapidity bins in each event.

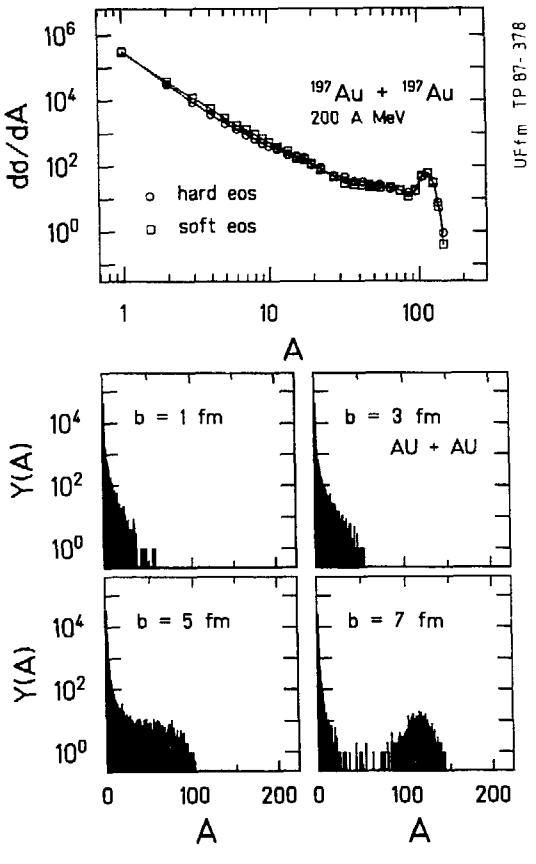

Fig. 2: Inclusive mass yield σ_A (upper part) and impact parameter dependence of the mass yields (lower part) for the reaction Au (E = 200 A MeV) + Au.

Hence we conclude that impact parameter averaging (rather than a liquid–vapour phase–transition) leads to an accidental power law dependence of the inclusive mass yield. The question of the liquid–vapour phase–transition could, however, be studied by measuring the fragment yield excitation function for E = 10–200 A MeV in very central collisions

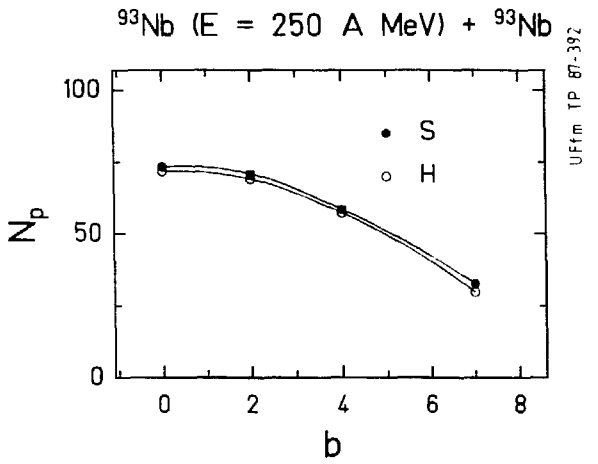

Figure 3: The connection between the impact parameter b and the multiplicity of participant protons N_p for the reaction Nb + Nb.

of the heaviest projectiles available.

In analogy to the experimental results we define the total participant proton multiplicity N_p. The impact parameter dependence of the participant proton multiplicities N_p for the reaction Nb + Nb at 250 A MeV beam energy, using a soft and a hard EOS, is shown in *Fig. 3*. For not central collisions (b = 2,4,7 fm) there is a nearly linear increase of N_p, but there is no significant increase of the participant proton multiplicities when going from b=2 fm to b=0 fm collisions. From this one can conclude that all collisions up to a relativ impact paramter of about 40 % of the radius are experimentally considered as central collisions and can not be distinguished. It shows also that the different forms of the EOS leads to almost no difference in N_P.

Let us now come back to the Au + Au system and study the behaviour of the intermediate mass fragments in more detail. To compare our results with the data [9,10] we included only those fragments in our calculations which could also be measured by the Plastic Ball. Therefore we applied a low-energy cut-off of 35 A MeV to all particles. The intermediate mass fragments were only registered if they were emitted to angles $< 30°$ in the lab, as done in the Plastic Mall. Fragments with $A > 20$ were not included into the analysis.

In *Fig. 4* we present the fragment multiplicity distributions of the fragments at four

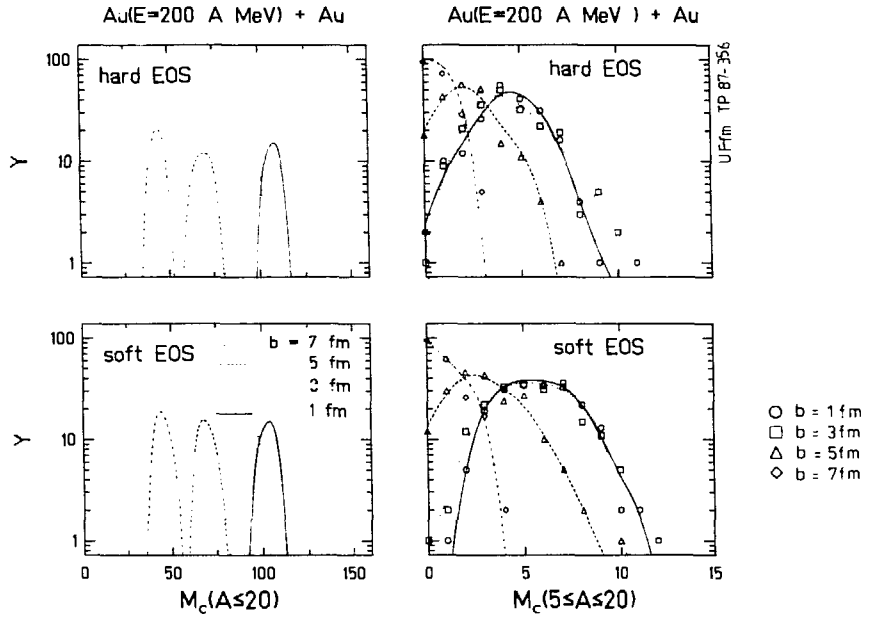

Figure 4: Multiplicity distributions of the reaction Au(E = 200 A MeV) + Au applied with a Plastic Ball filter.

different impact parameters and for a hard and a soft EOS. The right column shows the multiplicities of intermediate mass fragments $M_c(5 \leq A \leq 20)$. One observes in both cases (S and H) that the central collisions (b= 1,3 fm) lead to almost the same distributions. Both curves are peaked at a mean value of about five intermediate mass fragments per event. The real multiplicity is about double that value, the target hemisphere fragments can, however, not be detected in the Plastic Ball. The number of these fragments decreases if one goes to more peripheral collisions. The left column shows the total charged particle distribution $M_c(A \leq 20)$ for the soft and the hard EOS for the different impact parameters. The calculation shows, that the impact parameters from 1 to 7 fm result in multiplicity distributions which cover the region of $30 \leq M_c \leq 120$ completely. There is no overlap for the peripheral collisions (b = 7,5,3 fm), only the central collisions (b= 3,1 fm) show some overlap in the multiplicity distributions.
Let us now turn to the collective flow which can be used to study the properties of nuclear matter at high density. In this context it has long been proposed that complex fragments should exhibit flow effects more clearly, since they are subjected to less random thermal motion [15,16]. Therefore we now study the dependence of collective flow effects on the

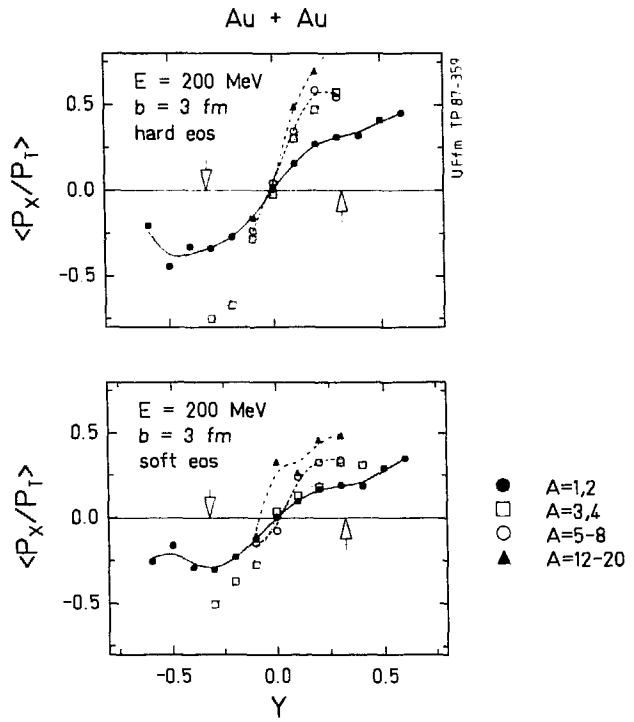

Figure 5: Transverse momentum alignment $< p_x/p_T >$ for the reaction Au(E = 200 A MeV, b = 3 fm) + Au

fragment size. In order to compare our results with the data we applied the efficiancy cuts as used above for the multiplicity distributions. Then we sampled those fragments in different mass bins. The first bin contains now all the fragments with A = 1 and 2, the second the A = 3,4 fragments then follow the intervals with A = 5–8, 9–11 and 12–20. The values of the transverse momentum alignment $< p_x/p_T >$ of the so selected fragments, which can now be compared with the data, are shown in *Fig. 5* for the hard and the soft EOS. Observe the increasing transverse momenta with increasing fragment mass. The differences between the hard and the soft EOS comes out clearly.

The influence of the momentum dependent interactions on the transverse momentum transfer is shown in *Fig. 6* for the reaction Au + Au. Here is shown the time evolution of the transverse momentum for the three interactions S, H, and SM(= soft EOS + momentum dependent interactions (MDI)) for this reaction at 200 and 800 MeV bombarding energy. Observe the clear difference between the cases S and SM for the high

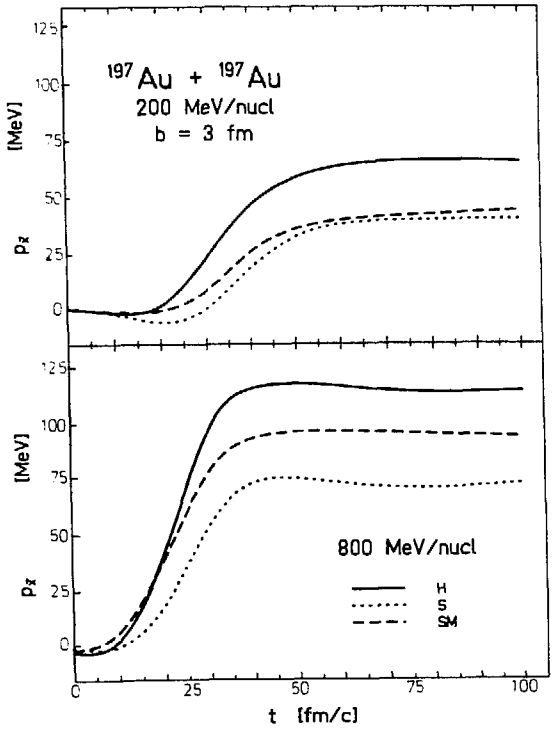

Figure 6: Transverse momentum transfer for the Au + Au reaction for the hard and the soft EOS without momentum dependent interactions (S, H) and with MDI included (SM).

energy case, while at 200 MeV bombarding energy the MDI have almost no influence on the transverse momentum.

In order to compare this flow effects with experimental data one has to have one common definition for a quantitative collective nuclear flow. One possibility is to use the slope of the p_x–Y distribution in the midrapidity zone [13]. The present data include only the single nucleons and the very light fragments in this distributions, because the intermediate mass fragments are not measured, except for the 200 A MeV Au + Au collision of ref. [10]. But we have seen that the intermediate mass fragments show the flow more clearly. For these fragments we cannot define the slope of the p_x/A–Y distribution because they are peaked in the projectile and target rapididity zone.

Fig. 7 shows in the upper part the excitation function of the flow for the reaction Au (b = 3 fm, E = 200-800 A MeV) + Au for the hard and the soft local potential with

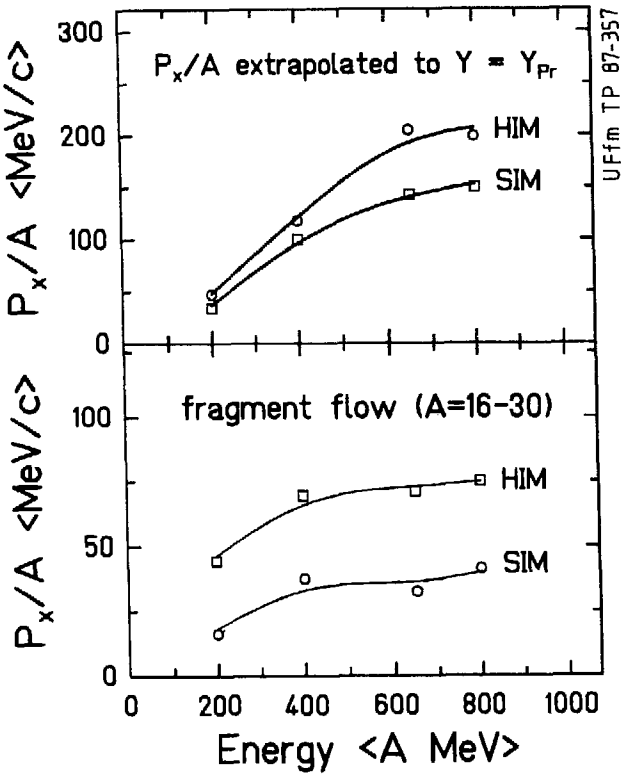

Figure 7: Excitation functions of the flow

in–medium effects included (for the details of these in–medium effects see refs. [18] and [19]). Here we defined the flow by extrapolating the linear, midrapidity part part of the p_x/A–Y distribution to the projectile rapidity. For the determination of the p_x/A–Y distribution we took all nucleons, thus making no difference between single nucleons and such ones bound in fragments. Because of this construction, and the fact that the massive fragments are centered at projectile and target rapidity, the midrapidity region contains, similar to the experiment, only the single nucleons and the very light fragments. As a result one observes for the low energy (E = 200 and 400 A MeV) only a small difference between the case HIM and SIM.

For the high energy part the flow obtained with the hard local potential exceeds that obtained with the soft local potential by approximately 40%.

In contrast to this definition we present in the lower part of Fig. 7 the excitation function of the *fragment flow* (for fragments with $A = 16 - 30$),taken at those rapidity values were the dN/dY distribution for those fragments shows a maximum (practically this values

are identical with the beam rapidity $Y = \pm Y_{beam}$), for the cases SIM and HIM. Notice the clear difference between the case with an underlying soft local potential and the hard local potential. The hard local potential leads to p_x/A values which are more as double as high as for a soft local potential for all energies.

The same distributions obtained without the in–medium effects yield even higher transverse momenta, so we find in the reaction $Au(E = 200MeV, b = 3fm) + Au$ p_x/A values of about 80 MeV for the hard EOS without MDI. The same value is shown in the data [9] for the fragments with $6 \leq Z \leq 10$ in central Au + Au collisions. Such high p_x–values cannot be obtained with our soft EOS. From this we conclude that the nuclear EOS is quite hard.

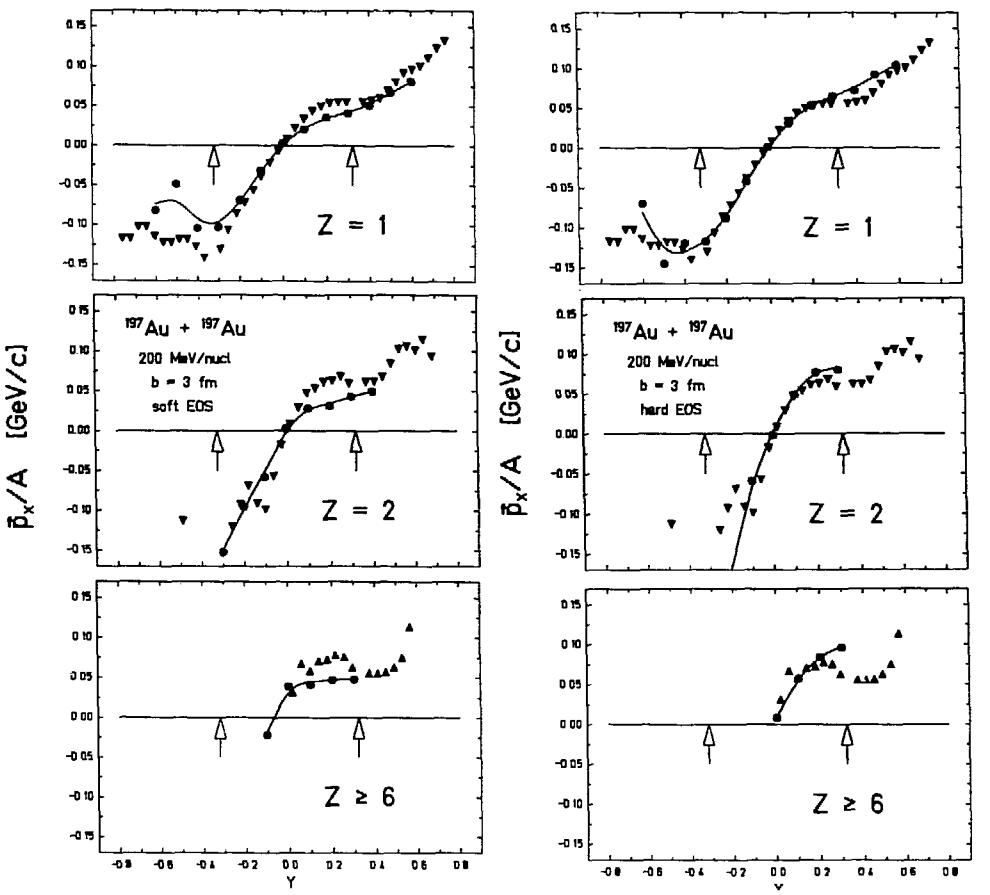

References

[1] R.W.Minich et al., Phys. Lett. 118B (1982) 458;

[2] J.E.Finn et al., Phys. Rev. Lett. 49 (1982) 1321;

[3] A.S. Hirsch et al., Phys. Rev. C29 (1984) 508;

[4] A.D. Panagiotou et al., Phys. Rev. Lett. 52 (1984) 496;

[5] L.Csernai and J.Kapusta, Phys. Rep. 131 (1986) 223.

[6] B.Jakobsson, G.Jönsson, B.Lindkvist and A.Oskarsso n, Z. Phys. A307 (1982) 293;

[7] B.V.Jacak et al., Phys. Rev. Lett. 51 (1983) 1846 and Phys. Rev. C35 (1987) 1751;

[8] A.I.Warwick et al., Phys. Rev. C27 (1983) 1083.

[9] K.H.Kampert, Thesis, University of Münster (1986);

[10] K.G.R. Doss et al., Phys. Rev. Lett. in press

[11] H.A.Gustafsson, et al., Phys. Rev. Lett. 52 (1984) 1590 ;

[12] H.G.Ritter et al., Nucl. Phys. A447 (1985) 3c;

[13] K.G.R.Doss et al., Phys. Rev. Lett. 57 (1986) 302;

[14] P.Danielewicz and G.Odyniecz, Phys. Lett. 157B (1985) 146.

[15] W.Scheid, H.Müller and W.Greiner, Phys. Rev. Lett. 32 (1974) 741;

[16] H.G.Baumgardt et al., Z. Phys. A273 (1975) 359.

[17] A.Rosenhauer, J.Aichelin, H.Stöcker and W.Greiner, J. Physique C4 (1986) 395;

[18] G. Peilert et al., to be published.

[19] J. Aichelin et al., to be published.

SUBTHRESHOLD KAON PRODUCTION IN HEAVY ION COLLISIONS: AN OVERVIEW

B. Schürmann and W. Zwermann
Physik-Department, TU München, D-8046 Garching, W. Germany

1. INTRODUCTION

The emphasis of this overview is on the rôle of kaons as probes for strong compression of nuclear matter. We concentrate on the production of kaons from heavy ion collisions down to beam energies of several hundred MeV per nucleon, far below the lowest threshold of 1.6 GeV/nucleon for kaon production in free baryon-baryon (BB) encounters. In this energy domain strong compression of nuclear matter is to be expected and hence information can be obtained on the equation of state (EOS) of nuclear matter far away from its ground state. Energies of a few GeV/nucleon seem less appropriate since, at least for inclusive reactions and medium mass colliding systems, the nucleon differential cross sections exhibit a large degree of transparency as is illustrated in fig. 1. The figure also shows that with decreasing beam energy the anisotropy ratio diminishes.

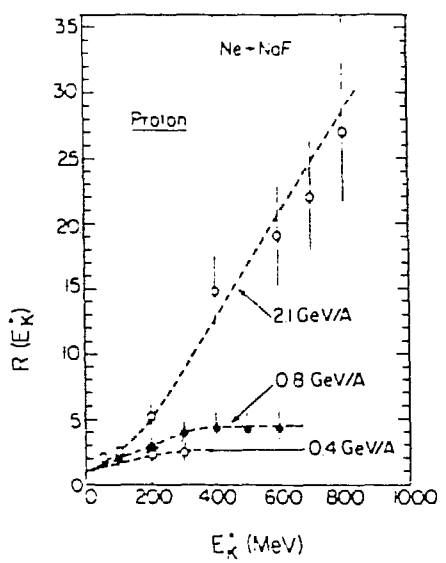

Fig. 1. Ratios of the proton inclusive cross sections at 30 and 90 degrees for Ne+NaF at various beam energies. From ref.[1].

For theoretical descriptions of subthreshold kaon production we have to get some guidance from kaon production *above* threshold because of the lack of experimental data *below* threshold. The data for K^+-production at 2.1

GeV/nucleon[2] have been compared with various theoretical models. For a review see ref.[3]. The less complete data for subthreshold antikaon production, at the same energy of 2.1 GeV/nucleon[4] may serve as a further test of theoretical models[3]. The most detailed comparisons of the 2.1 GeV/nucleon K^+-data have been performed with cascade models, which differ in detail, but are based on the same physical picture: a heavy ion reaction is viewed as a sequence of independent free BB collisions; at any BB encounter kaons can be created with their (small) free-space probability. The baryon distributions are assumed to be unperturbed by the kaons. They can be tested by the experimental proton differential cross sections. A typical result obtained with the model of transport theory[5] is shown in fig. 2a. The corresponding kaon spectra are displayed in fig. 2b together with two other cascade approaches[6,7] and with the experimental data[2]. The calculations yield very

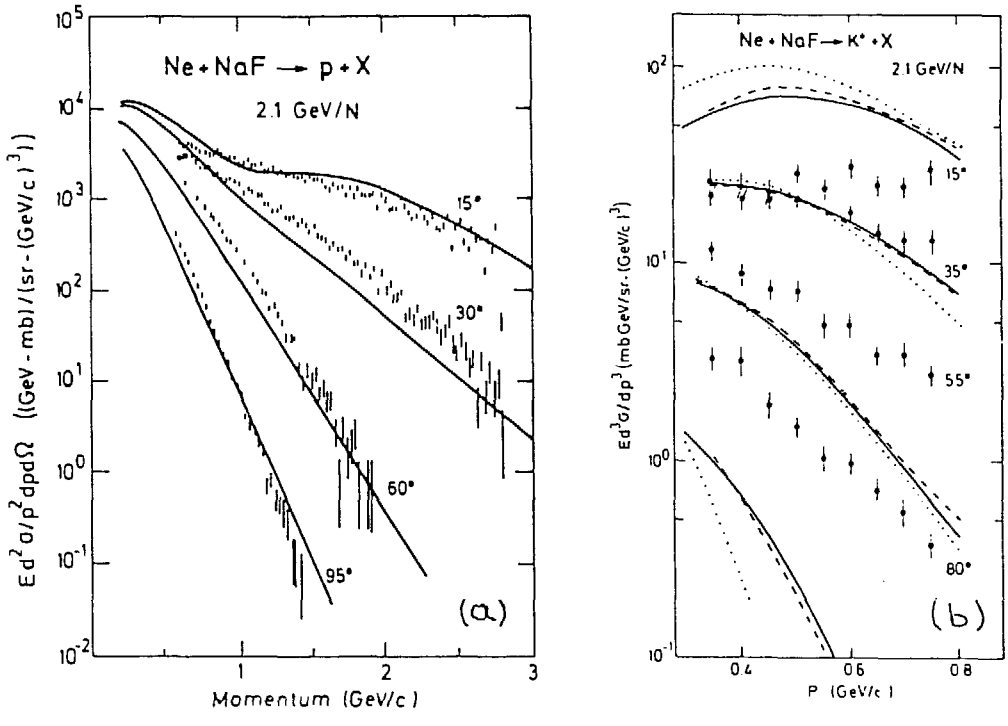

Fig. 2. (a) Proton inclusive differential cross section for Ne+NaF at 2.1 GeV/N. From ref.[5]. Data from ref.[1]. (b) Kaon inclusive differential cross section for the same reaction. Data from ref.[2]. Full lines: transport theory[5]; dotted lines: rows on rows[6]; dashed lines: Cugnon cascade[7].

similar results. The data are, however, badly reproduced because in the c.m. system the calculated kaon spectra, though isotropic like the data, are fall-

ing off much too steeply. The inclusion of kaon rescattering on the surrounding baryons looks like an improvement in the laboratory system, but it destroys the isotropy of the kaon cross section in the c.m. system. The failure of theoretical models to satisfactorily explain the data [2] has been a long standing puzzle which, however, may have been resolved recently[6].

In the cascade models the reaction channel

$$BB \rightarrow BYK \tag{1}$$

is the dominant one. The baryon B is either a nucleon (N) or a delta resonance (Δ), and Y denotes either a Λ or a Σ hyperon. The calculated total kaon yield on the basis of (1) indeed agrees within the experimental uncertainties with the data point of ref.[2]

We briefly outline the contents of this overview. In section 2 we present a closed expression for the kaon excitation function which we use for describing its mass number and energy dependences. An essential input in the cascade approaches, the elementary kaon cross section, is discussed in section 3. The implications of the different parametrizations for the elementary on the heavy ion induced kaon yields are addressed in section 4. The rôle of subthreshold kaons as probes for the compressional part of the equation of state is taken up next. A summary and conclusions are given in the final section 6.

2. FEATURES OF THE KAON EXCITATION FUNCTION

We start with a closed expression for the yield of a particle produced perturbatively in individual BB encounters in a mass-symmetric system with mass number A at a beam energy/nucleon E_0,

$$\sigma_\lambda(A,E_0) = \sum_{i,j=1}^{\infty} N_A(i)\, N_A(j) \sum_{m,n=1}^{i,j} \sum_{\mu,\nu} \sigma_{\lambda;m,n}^{\mu\nu}(E_0). \tag{2}$$

Here, λ denotes the created particle which may be a kaon, a subthreshold pion, or a photon, $N_A(i)$ [$N_A(j)$] denotes the number of baryons which encounter precisely i(j) collisions, and $\sigma_{\lambda;m,n}^{\mu\nu}$ denotes the partial yield for particle λ produced by the baryons μ and ν (μ,ν stand for N and Δ) in their mth and nth collisions. The geometrical weights N_A depend on the free nucleon-nucleon cross section σ_{NN}, and on the nuclear matter density ϱ_0. The yields $\sigma_{\lambda;m,n}^{\mu\nu}$ are the momentum integrated foldings of the elementary λ-yield with the respective baryonic momentum distributions[5]. The functions N_A obey the sum rules:

$$\sum_i N_A(i) \approx \pi R^2/\sigma_{NN}, \tag{3}$$

$$\sum_i i\, N_A(i) = A. \qquad (4)$$

Relation (3) is exact for sharp surface nuclei with radius R. Expression (2) has first been derived for kaons in ref.[6]. The partial yields in the transport model[5] differ, however, from those of ref.[6] in the baryonic momentum distributions which in our model can become thermal for a sufficiently large m(n).

Expression (2) contains two interesting limiting cases with respect to the mass number dependence of σ_λ: (i) if particle λ is produced only in first chance encounters m=n=1, then

$$\sigma_\lambda \propto A^{4/3} \qquad (5)$$

because of (3). Such an A-dependence seems to apply for pion production far below threshold[3]. (ii) There is no restriction on m and n. Then approximately

$$\sigma_\lambda \propto A^2 \qquad (6)$$

This applies for kaon production at several hundred MeV per nucleon and above[6,7,3].

Finally, we discuss the *size* of the kaon yields expected below threshold. An example is shown in fig. 3 for the reaction Ne+Ne. At 700 MeV per nucleon we still obtain a value of about 10^{-2} mb. For a heavy system like Pb on

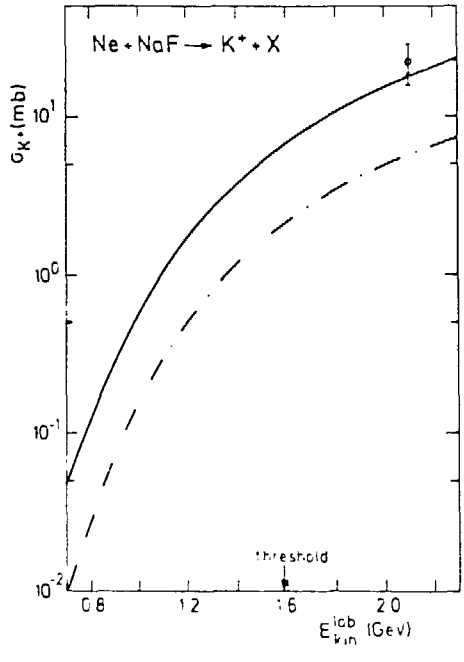

Fig. 3. Kaon inclusive yield for Ne+NaF. Data point from ref.[2]. Full line: transport theory[5]; dashed-dotted line: first chance collisions only. From ref.[5].

Pb, the yield will be, because of the A^2-dependence, about 1 mb. Such values will be accessible to the high intensity accelerator SIS under construction at GSI as well as to the upgraded Bevalac.

3. THE ELEMENTARY KAON PRODUCTION CROSS SECTION

An essential ingredient in cascade model calculations is the cross section for kaon production from free BB collisions. So far the parametrization of ref.[6] has been almost exclusively used. It reads

$$\sigma_{NN\to f} = 72\ [p^f{}_{max}/(GeV/c)]\ \mu b \qquad (7)$$

where f is one of the four exit channels $N\Lambda K^+$, $N\Sigma K^+$, $\Delta\Lambda K^+$, and $\Delta\Sigma K^+$, and $p^f{}_{max}$ is the maximum c.m. momentum of the produced kaon. For delta resonances in the entrance channel, the cross sections are

$$\begin{aligned} \sigma_{N\Delta\to f} &= (3/4)\ \sigma_{NN\to f}, \\ \sigma_{\Delta\Delta\to f} &= (1/2)\ \sigma_{NN\to f}. \end{aligned} \qquad (8)$$

The kaon yield as obtained from (7) is shown in fig. 4 together with the experimental data as compiled in ref.[10]. The cross section is plotted as a function of p_{max} for the lowest lying channel $NN\to N\Lambda K^+$. The parametrization (7) provides a reasonable fit to the data which, however, is far from being unique

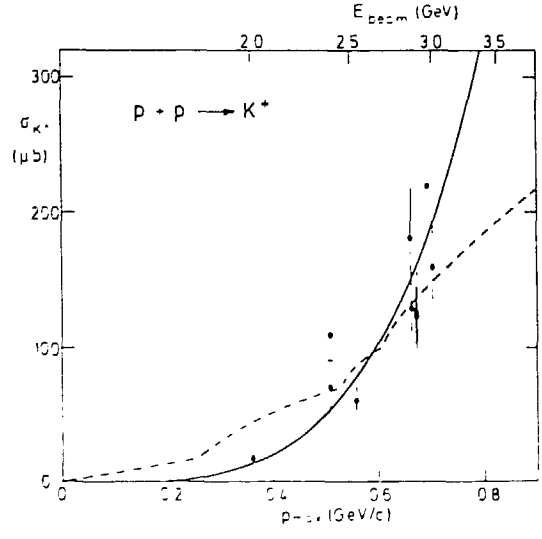

Fig. 4. Total kaon production cross in proton-proton collisions. Data from ref.[10]. Full line: parametrization (9); dashed line: parametrization (7). From ref.[11].

due to the lack of experimental points in the immediate neighbourhood of the threshold. A different parametrization which fits the scarce data points equally well has been proposed in ref.[11]:

$$\sigma_{NN\to K^+} = 800\ [p_{max}/(GeV/c)]^4\ \mu b. \qquad (9)$$

It is also displayed in fig. 4. Eq. (9) has been obtained by employing three particle phase space. The same functional dependence also results from a one meson exchange calculation[12].

4. INFLUENCE OF THE ELEMENTARY KAON PRODUCTION CROSS SECTION ON THE TOTAL KAON YIELD

The influence of the elementary on the total kaon yield is shown in fig. 5 for the parametrizations (7) and (9) for Ne on Ne. Both curves fit the data point at 2.1 GeV/nucleon. At low energies the differences become as large as a factor of 2.5. This is also true for heavier mass-symmetric systems because the approximate A^2-dependence of σ_{K^+} (6) holds for both parametrizations (7) and (9) (cf. ref.[11]).

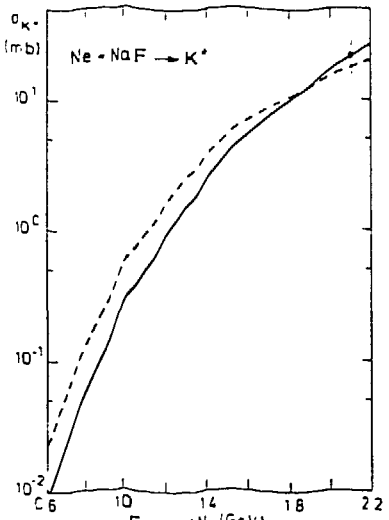

Fig. 5. Kaon inclusive yield for Ne+NaF, obtained with the parametrizations (7) and (9) (dashed and full lines, respectively). From ref.[11]. Data point from ref.[2].

5. SUBTHRESHOLD KAON PRODUCTION AND COMPRESSION EFFECTS

We first discuss the rôle of kaons for revealing compression effects along the lines of arguments given for pion production[13]. If compression effects are detectable for heavy systems the *measured* number of kaons should be substantially smaller than our *calculated* one because part of the energy otherwise available for K production is then stored in compression. This difference may still be visible as is indicated in fig. 6 for the system Nb on Nb: shifting the kaon excitation function by a c.m. energy of 40 MeV/nucleon,

being a rough estimate for the compressional energy[13], we predict at a beam energy of 800 MeV/nucleon a difference of a factor 4 which exceeds the uncer-

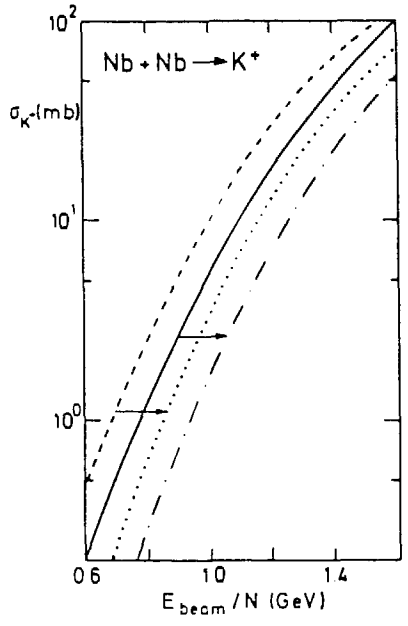

Fig. 6. Same as in fig. 5, but for Nb+Nb. Dotted and dashed-dotted lines: excitation functions shifted by 40 MeV/N c.m. energy, indicated by the arrows. From ref.[11].

tainties introduced by the elementary cross section. Moreover, the actual uncertainties are possibly smaller than estimated because in contrast to the parametrization (7), the phase space formula (9) satisfactorily explains the data[2], cf. fig. 7, and may therefore be more appropriate.

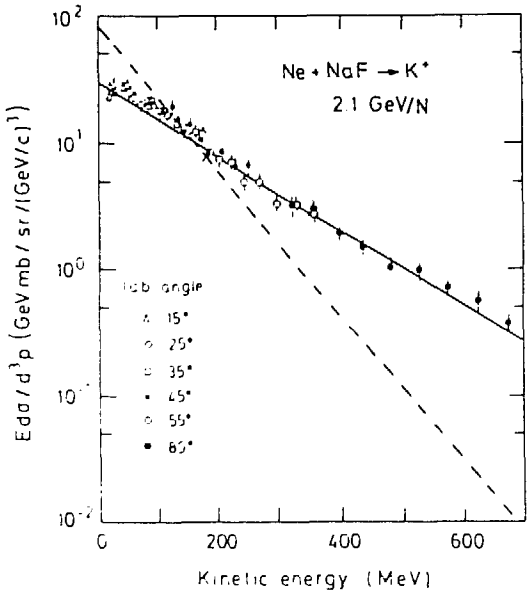

Fig. 7. The inclusive K^+-spectrum for Ne+NaF at 2.1 GeV/N calculated with the parametrizations (7) and (9) (dashed and full lines, respectively). Data from ref.[2].

An alternative way is to consider *ratios* of the kaon yields from collisions of heavy and light equal mass nuclei. The kaon yield ratios for Nb on Nb and Ne on Ne essentially eliminate the uncertainties introduced by the elementary kaon production cross section[11]. We expect such a behaviour also in future experiments if there is *no sensitivity to compression.* If *there is* the mass number dependence is expected to be largely reduced, since compression effects should be small for light but large for heavy systems. Such a reduction should clearly be measurable. To strengthen these arguments one has to go beyond the analytic model of transport theory and study numerically the space-time evolution of kaon production. This has been done in ref.[14], on the basis of the Boltzmann-Uehling-Uhlenbeck equation. In such an approach the variation of the nuclear density and the kaon production rate with collision time as well as the influence of the nuclear mean field on the kaon yield can be investigated. The kaons are produced during the compression phase, with an appreciably larger number for a soft than for a stiff EOS[14]. Unfortunately, in ref.[14] no *cross sections* are given, but only *production probabilities* for several mass-symmetric systems at a fixed impact parameter instead of a fixed b/R. Denoting the production probabilities by $P^{A}_{K,\delta}$ for an A+A collision where δ stands for either a soft or a stiff EOS, we obtain from ref.[14]

$$P^{Nb}_{K,soft}/P^{Ne}_{K,soft} \approx 23,\quad P^{Nb}_{K,stiff}/P^{Ne}_{K,soft} \approx 8,\quad P^{Nb}_{K,stiff}/P^{Ne}_{K,stiff} \approx 13 \qquad (10)$$

which supports our conjecture.

For the ratio $P^{Nb}_{K,soft}/P^{Nb}_{K,stiff}$ as a function of the bombarding energy the sensitivity on the EOS decreases with increasing energy[14] consistent with the growing transparency of the collision with increasing energy.

6. SUMMARY AND CONCLUSIONS

In continuation of a review on strange particle production in the few GeV/nucleon region[3] we have summarized the present situation for subthreshold kaon production. Experimental data are not yet available, and so far the theoretical studies are almost exclusively based on cascade-type approaches.

It is tempting to "unify" subthreshold kaon and pion production by relating one subthreshold energy region to the other by the relation $E^{\pi}_{0}/E^{\pi}_{thr} = E^{K}_{0}/E^{K}_{thr}$ (cf. ref.[15]) where E^{λ}_{0} and E^{λ}_{thr} denote the beam and the threshold energies of particle λ. For cascade models such a scaling is only meaningful if (i) the elementary production cross section is similar in both cases, and

(ii) if the number of contributing multiple scattering components to σ_K and σ_π [cf. eq. (2)] is similar. We have performed a corresponding study with elementary production cross sections based on 3-particle phase space as input[9]. The result is shown in fig. 8. Below 100 MeV the scaling prescription completely fails: at 70 MeV the pion yield is two orders of magnitude larger than the kaon yield. Above threshold, the differences become smaller, being only a factor 4 at 400 MeV. The reasons for such a behaviour are discussed in ref.[9].

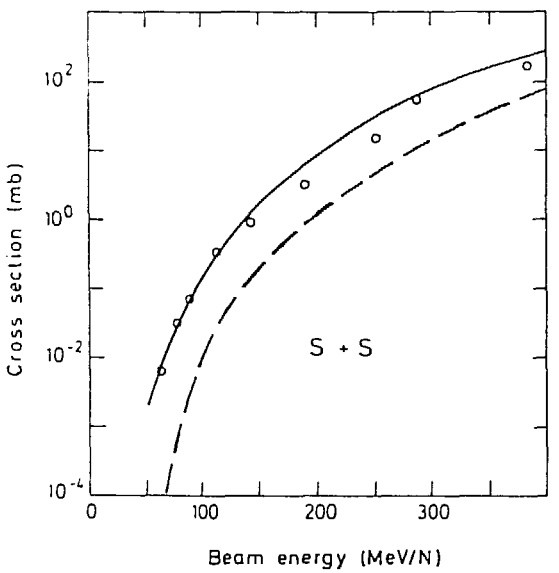

Fig. 8. Pion and kaon inclusive yields (full and dashed lines, respectively) for S+S. The energy scale is the one for pions. Data points from ref.[15].

Subthreshold kaons are produced in still measurable number in an energy region where strong compression of nuclear matter occurs and hence, they in principle can give us information on the nuclear matter equation of state. Admittedly in addition to the uncertainties addressed there are others like the complication introduced by the momentum dependent terms of the nuclear mean field. Despite this, subthreshold strange particle production will, with the event of experimental data, add an exciting new facet to heavy ion collisions.

1. S. Nagamiya et al., Phys. Rev. C24 (1981) 971.

2. S. Schnetzer et al., Phys. Rev. Lett. 49 (1982) 989.

3. B. Schürmann and W. Zwermann, 7th High Energy Heavy Ion Study, GSI-report 85-10 (1985) 275.

4. E. Barasch et al., Phys. Lett. B161 (1985) 265.

5. W. Zwermann et al., Phys. Lett. B134 (1984) 397; W. Zwermann and B. Schürmann, Nucl. Phys. A423 (1984) 525.

6. J. Randrup and C.M. Ko, Nucl. Phys. A343 (1980) 519; A411 (1983) 537.

7. J. Cugnon and R.M. Lombard, Phys. Lett. B134 (1984) 392; Nucl. Phys. A422 (1984) 635.

8. W. Zwermann, Mod. Phys. Lett. (1987), in press.

9. B. Schürmann and W. Zwermann, in preparation.

10. V. Flaminio et al., CERN-HERA-report 84-01.

11. B. Schürmann and W. Zwermann, in: Hadronic Matter in Collision, p. 351, World Scientific (1986); Phys. Lett. B183 (1987) 31.

12. E. Ferrari, Nuovo Cim. 15 (1960) 652.

13. R. Stock et al., Phys. Rev. Lett. 49 (1982) 1236; J.W. Harris et al., Phys. Rev. Lett. 58 (1987) 463.

14. J. Aichelin and C.M. Ko, Phys. Rev. Lett. 55 (1985) 2661.

15. E. Grosse, 7th High Energy Heavy Ion Study, GSI-report 85-10 (1985) 169.

LATEST RESULTS ON SUBTHRESHOLD KAONS AND ANTIPROTONS*

Jim Carroll
University of California at Los Angeles
Los Angeles, California 90024

By 'subthreshold production' we refer to those nuclear reactions yielding particles whose production threshold (in free nucleon-nucleon collisions) is significantly higher than the energy available in the average N+N collision. Some sort of collectivity is thus required by this definition. It is useful to distinguish between two types of 'collectivity' - that which is intrinsic to the initial state nuclei (such as Fermi motion, clusters of nucleons or quarks...); and that which is characteristic of the collision itself (possible equilibration of the various kinetic and chemical degrees of freedom for example). One expects to be able to measure the intrinsic nuclear effects by studying q + A → q + X reactions, where q represents a 'non-composite' probe, thus it is primarily the collisional collectivity that is the object of study in nucleus-nucleus subthreshold production. By choosing to detect particles of various masses (eg pions, kaons, antiprotons) one may study these collisional collective effects in a range of excitation energies, where the dynamics of the collision process may be expected to change significantly. Tables 1 and 2 give relevant kinematic information. Much work has been done in the past few years in studying subthreshold pion production[1]. Our effort has focussed on studies at higher excitation energies with the aim of understanding how, and how far, the collision dynamics proceeds toward equilibration when the excitation energies are far removed from the realm of conventional nuclear physics. In the following, due simply to considerations of time, I will present only our recent results[2] and must leave until another occasion interesting comparisons with relevant work of others, both experimental and theoretical.

Our initial measurements showed that in Si + Si collisions at 2.1 GeV K^- are produced at a level more than 10 times higher than that obtained from a somewhat careful calculation which included the effects of internal nuclear motion, and that the invariant cross section shows the usual exponential behavior with a slope of about 95 MeV.[3] Our program

*Supported by USDOE under Contract No. DE-AT03-81ER40027,
PA DE AM03-765SF00034

since then has been to outline, within the capabilities of available facilities, the systematics governing this process. We thus set out to measure the variation of the K^- yield with incident energy and with projectile/target mass combinations; to measure the K^- yield at a cm angle of 90^o; and to measure subthreshold K^+ production. We have accomplished these goals, although we did not achieve as large a range in mass and energy as we had originally hoped for. The data presented in this report are still preliminary in the sense that not all systematic corrections have been identified and carried out, nor have systematic errors been calculated - all errors shown represent counting statistics only.

Figure 1 shows center of mass cross sections at 0^o for Si + Si → K^- + X. Points belonging to the same incident energy have been connected by straight lines to indicate the groupings, with the exception of the data at 2.1 GeV/A, where the dots indicate a fit to the combined data from several past measurements. Note that the measurements cover more than two orders of magnitude in cross section, but that no large changes are apparent in the slope (at least for low values of kaon cm kinetic energy). There are increases in the slope in the region where incident energies are low and kaon cm energies are high. This is the behavior which would be expected from phase space limitations. In Figure 2, the similarity of the initial slopes has been emphasized by passing a line parallel to the 2.1 GeV/A data through the first two data points of each of the other data sets. From these lines we have made a crude estimate of the total cross section (assuming isotropy) that is shown in Figure 3, plotted against the available excitation energy in the center of mass. No error bars are given at this stage of analysis. The slope of the exponentially rising part of the curve is 54 MeV. Speculation is invited. When I look at this curve I see only the effect of the K^+K^- threshold and no influence of the Λ threshold, suggesting that the contribution of the strangeness exchange channel is small.

Figure 1 also contains the first result of our measurement of the

cross section for subthreshold production of K^+, taken at an incident energy such that the Q (available cm energy) for the $NN \rightarrow N\Lambda K^+$ channel was the same as that for the $NN \rightarrow NNK^+K^-$ channel at 2.1 GeV/A. Note that the K^+ cross section is higher than that for the K^-, even though no strangeness exchange channel is available to contribute to this yield. It may prove to be possible to account for the larger K^+ cross section by noting that the absorbtion of K- in nuclear matter is larger than for K^+, while the 3-body K^+ phase space is larger than the 4-body K^- phase space at the same value of Q. This approximate equality of cross sections suggests that the production mechanism is directly related to the Q of the NN collisions rather than to secondary (or tertiary) production mechanisms such as strangeness exchange.

Figure 4 show the cm spectra for three equal-mass projectile-target combinations C+C, Si+Si, and Ca+Ca, all at 2.1 GeV/A incident energy. (One of the yet unresolved systematics problems also shows itself.) Again we note that there is no appreciable change in slope when going from carbon to silicon to calcium. (The lines simply connect the points and are not fits.) This same data is shown in another form in Figure 5, where the cross section at fixed kaon cm energy is plotted versus the mass number of the target. When interpreted as an A^k dependence the lower two points give a value of $k = 3.6$, while the upper points give a value $k = 1.2$. Again, at this stage of analysis we prefer not to assign errors to these derived quantities. Attempts were made to measure the yields from the Nb+Nb and La+La systems, but the combined effects of lower beam intensity and lower beam energy, and the need for thinner targets to maintain a fixed fragmentation loss reduced the yield below that measurable in the allotted time. This apparent saturation, or roll-over, of the cross section is one of the tantalizing features that will remain for future workers in this field to explore.

The kaon data which are still being analyzed include:

subthreshold K^+ to give a momentum spectrum for
1.26 GeV/A Si+Si → K^+ + X

K^+ momentum spectrum for
2.1 GeV/A Si+Si → K^+ + X (compare with Schnetzer)

subthreshold K- momentum spectrum for $\Theta^* = 90^o$
2.1 GeV/A Si+Si → K^- + X

and some data on target mass dependence, momentum spectra for

2.1 GeV/A Si+Mo → K^- + X
Si+La → K^- + X
Si+Pb → K^- + X

This experimental program began as a search for anti-proton production in relativistic heavy ion collisions, and during each of experiments we have usually produced a single event with the characteristics of an anti-proton, but have never had sufficient integrated flux to collect a number of such events, nor particle ID quite sufficient to completely persuade ourselves that the identification was correct. During our last data acquisition period, however, we have accumulated 5 such events, all other events being clearly identified as either pions, or kaons; that is to say, no background. These 5 events have the timing characteristics of anti-protons; the mean time-of-flight of the group is within 50ps of the measured time-of-flight of protons under the same experimental conditions, and the width of this distribution is also consistent with the 50ps sigma we measure for pions under these conditions. (The pion-proton time-of-flight difference is 2.9 ns.) The

tof measured by a third high-resolution detector, placed roughly mid-way between the other two, is consistent, for each event, with that of protons, and inconsistent with that of pions or kaons. A lead glass calorimeter shows that 4 out of the 5 events give pulse heights much larger than those produced by pions and kaons. (Since the calorimeter does not absorb all of the incident energy, this ratio of 4/5 is what is expected.) Auxillary apparatus shows that the events in question are 'clean', with no pile up in crucial detectors, or multiple particles traversing the detector assemblies. The collaboration feels that the present level of evidence that these events are in fact anti-protons is at least as good as that on which the discovery of the anti-proton was based, but we are still working on ways of making this more quantitative. The observed yield (p-bar/π^-) is about 4 10^{-7} (at 1.89 GeV/c), corresponding to a laboratory cross section of about 80 nb/sr/(GeV/c).

References

(1) See Stachel, et al, Phys. Rev. C 57 (198??) and references therein.

(2) The collaboration which has done the work presented here:
UCLA - S. Carlson, J. Carroll, J. Gordon, G. Igo, S. Trentalange, J-F Wang, K. Ganezer, S. Abachi
LBL - B. Keay, G. Krebs, P. Lindstrom, V. Perez-Mendez, T. Mulera
BNL - A. Shor
LSU - P. Kirk
Johns Hopkins U. - T. Hallman
UC Davis - E. Barasch

(3) Shor, et al, Phys. Rev. Lett. 48 (1982)
Barasch, et al, Phys. Lett. 161B (1985)

Table 1 Thresholds kinematics for the reaction N + N ->

Channel	S_{thr}	T^*	P^*	T^{lab}_{thr}	
$NN\pi$	2015	70	369	288	
$N\Lambda K^+$	2548	336	862	1585	(note 1)
NNK^+K^-	2864	494	1082	2496	(note 2)
$NNNN^-$	3752	938	1624	5628	(N^- = anti-N)

(all energies in MeV)

(1) There also exists a two-step process for making the K^+,

$N + N \rightarrow NN\pi$; $\pi + N \rightarrow K^+ + \Lambda$.

(2) There is also a three-step process for making the K^-,

$N + N \rightarrow NN\pi^-$;

$N + N \rightarrow NK^+\Lambda$; $\pi^- + \Lambda \rightarrow NK^-$.

Table 2 Available energies in NN center of mass for the reaction $NN \rightarrow NNK^+K^-$. (All MeV)

$(T/A)_{inc}$	T^*	P^*	ΔT^*	ΔP^*	$(T/A)_{inc}$ (π-prod.)
2100	430	990	-65	-90	282
1700	360	890	-140	-190	
1550	330	850	-165	-229	
1400	301	810	-190	-270	
				-350	35
1000	223	685	-271	-397	

(T^*, P^*, ΔT^*, and ΔP^* are the kinetic energy, momentum, and their deficits per nucleon in the center of mass.)

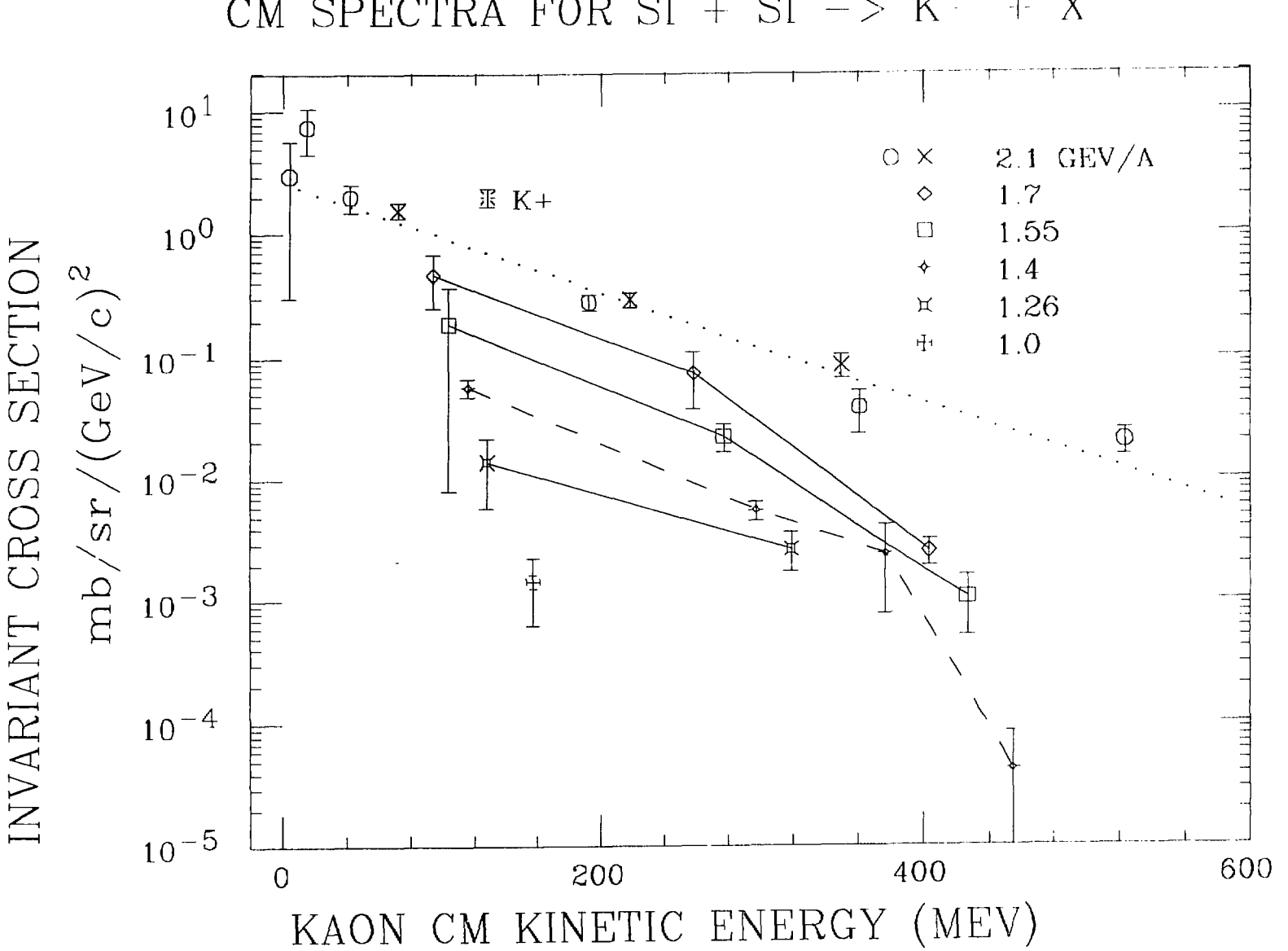
CM SPECTRA FOR SI + SI -> K+ + X
INVARIANT CROSS SECTION
mb/sr/(GeV/c)^2
10^1
10^0
10^{-1}
10^{-2}
10^{-3}
10^{-4}
10^{-5}
K+
2.1 GEV/A
1.7
1.55
1.4
1.26
1.0
0
200
400
600
KAON CM KINETIC ENERGY (MEV)

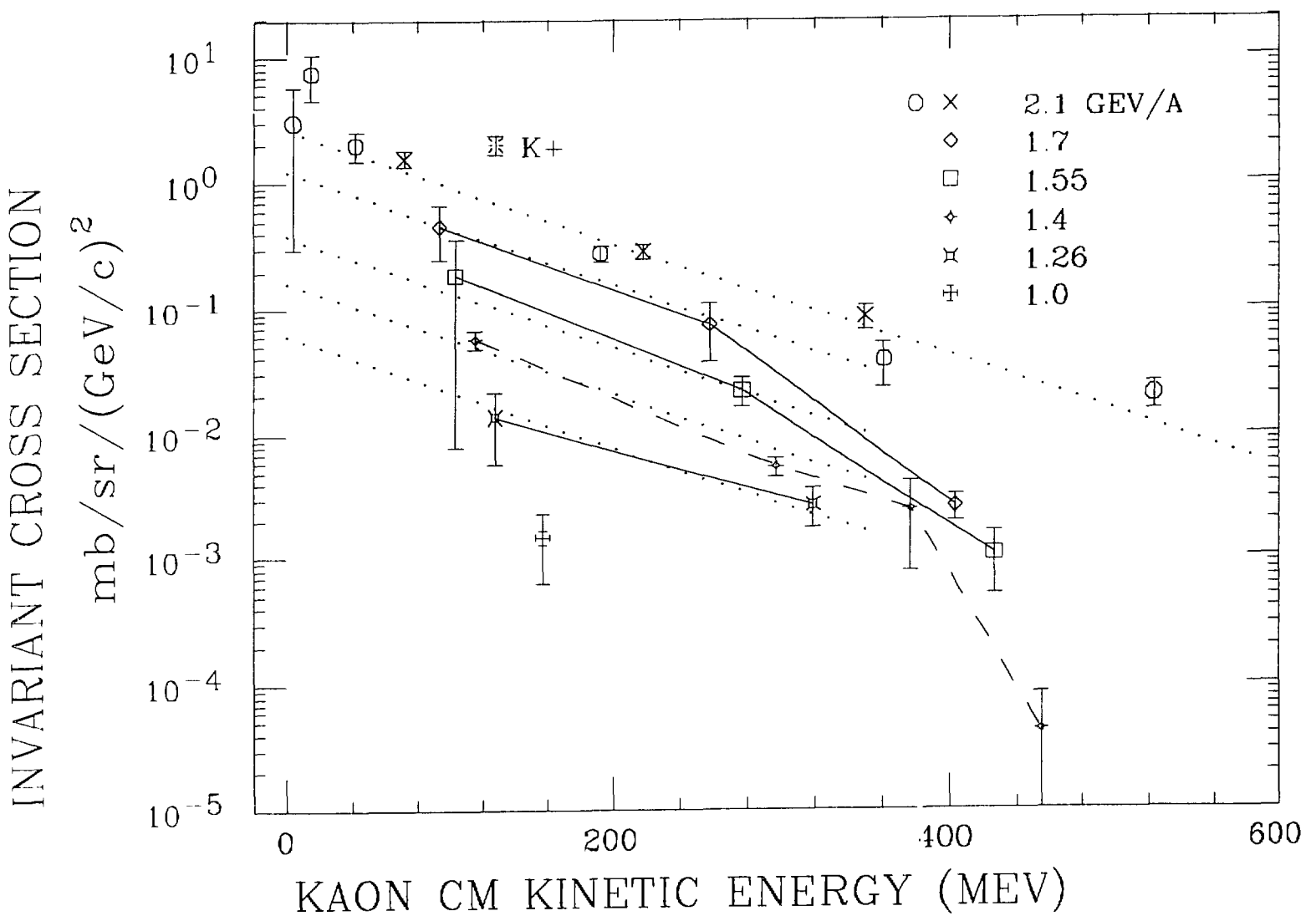
CM SPECTRA FOR SI + SI -> K- + X
INVARIANT CROSS SECTION
mb/sr/(GeV/c)^2
10^1
10^0
10^{-1}
10^{-2}
10^{-3}
10^{-4}
10^{-5}
K+
2.1 GEV/A
1.7
1.55
1.4
1.26
1.0
0
200
400
600
KAON CM KINETIC ENERGY (MEV)

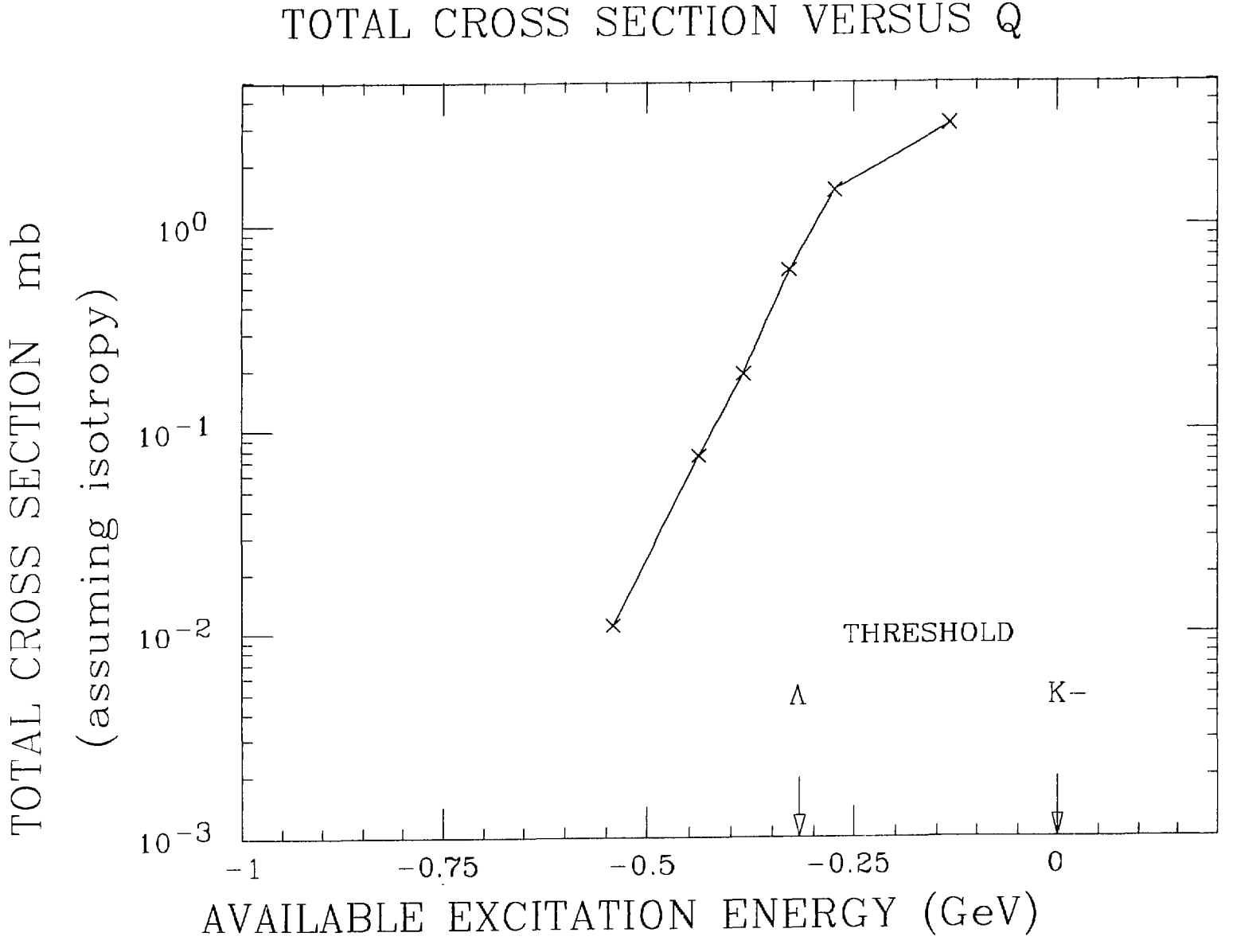
TOTAL CROSS SECTION VERSUS Q
TOTAL CROSS SECTION mb
(assuming isotropy)
10^0
10^{-1}
10^{-2}
10^{-3}
THRESHOLD
Λ
K−
−1
−0.75
−0.5
−0.25
0
AVAILABLE EXCITATION ENERGY (GeV)

MASS DEPENDENCE AT 2.1 GEV/A
INVARIANT CROSS SECTION
mb/sr/(GeV/c)^2
10^1
10^0
10^{-1}
10^{-2}
10^{-3}
0
100
200
300
400
500
KAON CM KINETIC ENERGY (MEV)
Ca + Ca
Si + Si
C + C

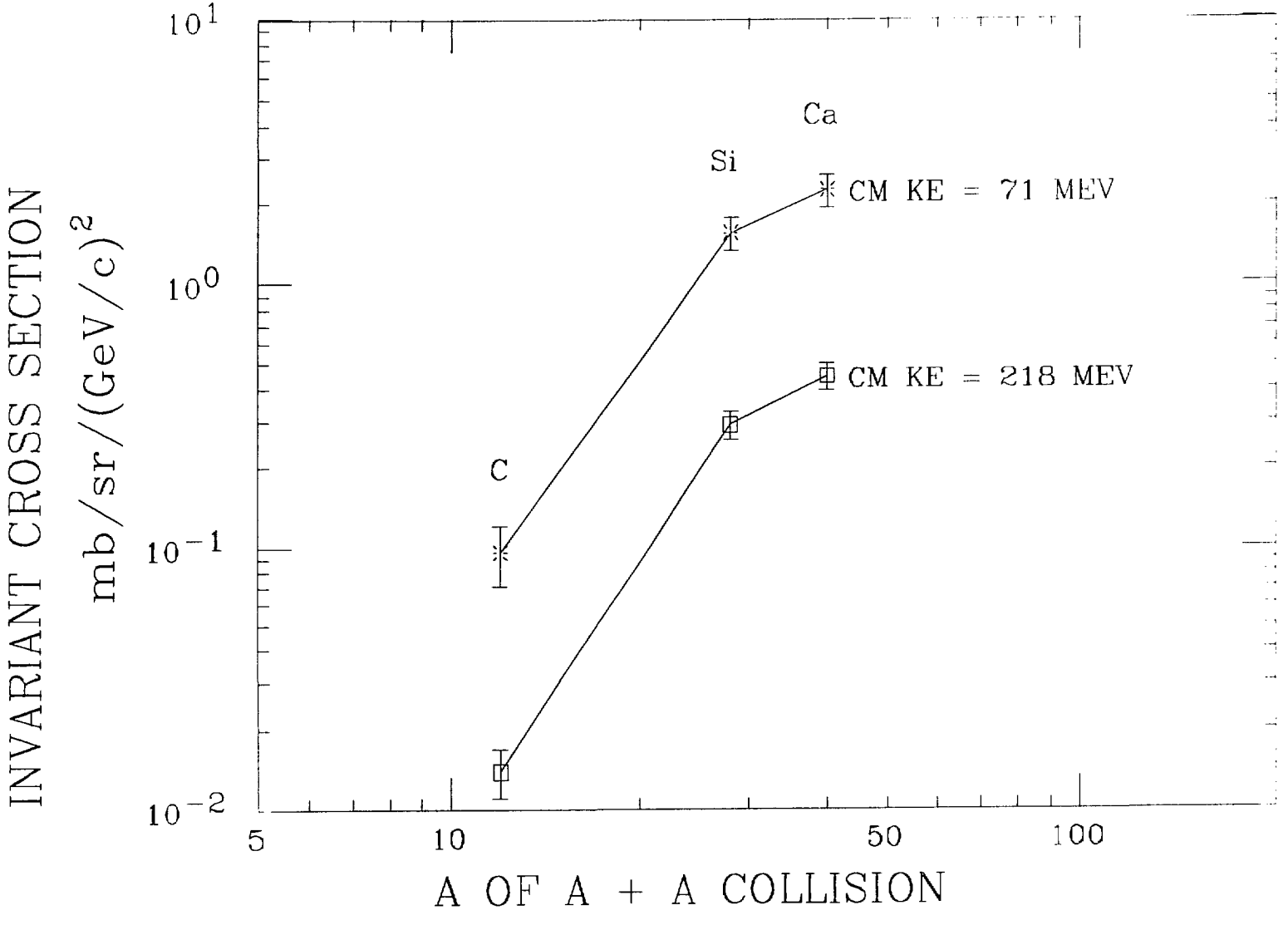
MASS DEPENDENCE AT 2.1 GEV/A
INVARIANT CROSS SECTION
mb/sr/(GeV/c)^2
10^1
10^0
10^{-1}
10^{-2}
5
10
50
100
A OF A + A COLLISION
C
Si
Ca
CM KE = 71 MEV
CM KE = 218 MEV

PLANS FOR A MAGNETIC KAON SPECTROMETER AT SIS

Darmstadt - Frankfurt - LBL - Marburg - Collaboration*

Presented by Walter Henning
Gesellschaft für Schwerionenforschung mbH
6100 Darmstadt, West-Germany

Abstract

A design is presented for a double-focussing QD magnetic spectrometer at SIS with the primary purpose to study in detail kaon production in energetic collisions between nuclei. The proposed compact design is matched to the requirements for kaon detection with short flight path (<5 m), large solid angle (>30 msr), wide momentum acceptance ($\approx 60\%$), maximum momentum well above 1 GeV/c (1.8 GeV/c at reduced solid angle), and reasonable momentum resolution ($\approx 10^{-2}$ without, and $\approx 10^{-3}$ with raytracing). The focal-plane dimensions of <1.5 m length and <0.6m height allow the efficient construction of detectors necessary for particle identification and raytracing, involving wire chambers, time-of-flight scintillators, aerogel and water Cerenkov counters and segmented calorimeters for particle decay. While the primary purpose of the spectrometer is the measurement of kaons, it can be used as a general purpose magnetic spectrometer for other hadrons and for leptons. Its large solid angle and relatively open geometry also allow the study of two-particle correlations.

I. Introduction

The specific properties of kaons, in particular of the K^+, have suggested them as a major tool in our attempt to extract information from nuclear collisions up to 1-2 GeV/nucleon about the nuclear equation of state. At these energies, the number of degrees of freedom from nucleonic resonances and from hadronic particle creation is still limited and a detailed study of the pressure-density-temperature dependence of the equation of state in the nucleonic regime can be envisioned.

Kaons are considered of importance in studies of central collisions and the extraction of the equation-of-state for the following reasons:

- The weakly interacting K^+ ($\sigma_{inel}(K^+N) \leq 15$ mb for $p_K < 1$ GeV/c) will emerge from the reaction zone without reabsorption and essentially unscattered except for the long-range Coulomb force. Consequently, it is expected to carry information about the primary collision zone.
- because of strangeness conservation in the strong interaction kaons are produced in K^+K^- and $K^+\Lambda$ pairs with nucleon-nucleon thresholds of 2.48 GeV and 1.58 GeV, respectively. For SIS energies therefore the production is sub- or near-threshold and thus particularly sensitive to the specific multinucleon collision processes. The threshold energies fall into an energy region

where the onset of major compressional effects in nuclear matter is expected to occur in nuclear collisions.

In measurement of kaons one therefore would like to achieve the following goals:

- a (preferably simultaneous) measurement of a large range of kaon momenta to allow unambiguous extraction of temperature(s) in the production zone from the energy spectra.
- excitation functions over a wide range of incident energies, from far below the nucleon-nucleon threshold to well above where K^+/K^- (Λ) ratios and possible correlations can be well established at sufficient production rates.
- measurements of kaon production over a large range of nuclear systems in comparison to production cross sections of, for example, strongly absorbed pions in order to assess the relative importance of surface and bulk effects in the nuclear interaction zone.
- detailed measurements as a function of impact parameter, requiring an event-characterizer in form of a multiplicity and/or nucleon-flow array at forward angles.
- the necessity of a system which can tolerate high beam currents (up to at least 10^9/sec) on targets of modest thickness (to minimize secondary reactions in the target by the copiously emitted nucleons), with good momentum resolution and reasonable solid angle, and with at the same time excellent background suppression and particle identification.
- an instrument which allows measurements over a wide angular range ($10^0 \leq \theta_{lab} \leq 120^0$) to fully cover the kinematical region for meson (and possibly lepton or antiproton) emission.

We consider the magnetic spectrometer described here a reasonable solution to these requirements. The unambiguous identification of kaons - in particular below the nucleon-nucleon threshold - from a huge background of other particles, and the need for a reliable momentum measurement have resulted in a modest solid angle, compact-size magnetic dipole spectrometer as the most reasonable choice.

II. General Layout of the Spectrometer System

The general layout of the kaon spectrometer is shown in Figure 1. The design was derived from ion-optical calculations to third order with the codes TRANSPORT[1] and RAYTRACE[2] optimizing the configuration for the following requirements:

- compact spectrometer geometry to minimize the kaon flight path and hence losses through decay in flight. For 500 MeV/c the mean decay length is 3.7 m, for example.
- large solid angle at acceptable momentum resolution for the low-cross section processes at sub-threshold energies. At 500 MeV/nucleon incident energy the kaon production rate per incident nucleon is estimated at about 10^{-5}-10^{-6}.
- maximum momentum well above 1 GeV/c, preferably approaching 1.5 GeV/c. For nucleus-nucleus collisions at 1 GeV/nucleon, the maximum of the kaon emission spectrum from a simple fireball

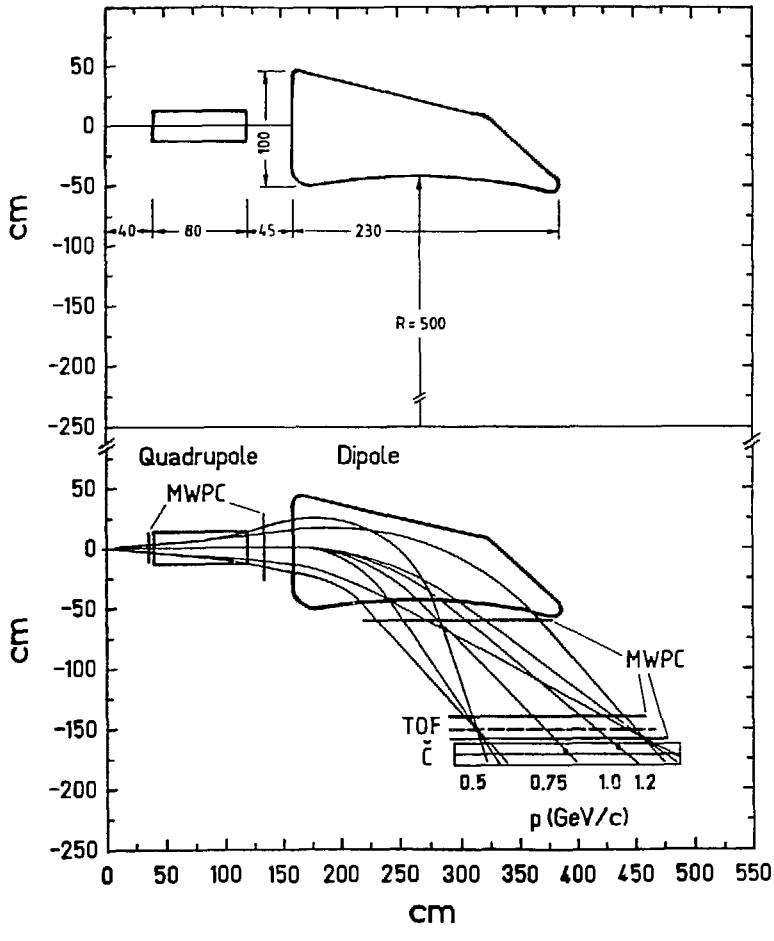

Fig 1: Upper part: Schematic of the QD-spectrometer configuration with dimensions. The target position is at (0,0), the pole face area of the dipole is approximately 1.5 m^2.
Lower part: Spectrometer configuration with detector system and central trajectories for 4 different momenta. For p = 0.5 GeV/c and p = 1.2 GeV/c, the trajectories for full acceptance are also shown.

prediction is near 600 MeV/c kaon momentum. The spectra should be measurable to at least twice this value.

- reasonable momentum resolution over the full solid angle without raytracing ($\approx 10^{-2}$) and good resolution ($< 10^{-3}$) with raytracing corrections.

- double focussing and acceptable focal-plane dimensions. Particle identification and detection at the momenta under consideration require a complex focal plane detector system and thus reasonable focal plane dimensions are necessary to make it affordable.

Various combinations of optical elements were investigated. The most promising configuration to account for the requirements listed above consists of a quadrupole singlet and a dipole. The limited number of elements, small deflection angle and limited resolution minimizes the size of the device

and thus losses by decay in flight while still providing double focussing and acceptable focal plane dimensions. The detailed specifications are listed in Table I and discussed in detail in the subsequent sections. Figure 1 illustrates the overall geometrical layout and dimensions of the magnetic field regions and, in the lower part, ion trajectories and detector positions.

III. Specifications and Performance Characteristics

The QD Spectrometer (Quadrupole Singlet plus Dipole) is characterized by a mean deflection angle of $\alpha = 45^0$. All coils are normal conducting and, at the fields considered, the iron is not saturated. For the central momenta the proposed configuration accepts a solid angle of slightly above 35 msr and has a path length of 450 cm.

The quadrupole provides vertical focussing, whereas horizontal focussing is achieved by a pole-face rotation ($\beta_2 = -45^0$) at the exit of the dipole, resulting in an image distance of $\approx$180 cm which is well matched to the required detector configuration. The exit pole-face boundary is curved with a radius of R = 5.0 m to partially correct for 2nd order aberrations x/θ^2. Due to this relatively large radius of curvature the focal plane is slightly curved and tilted by 37° with respect to the central ray. Such inclination has an advantage for the position determination in a multiwire chamber and seems not to cause problems for the other detectors envisaged.

In order to minimize the distance between the quadrupole and dipole, the entrance pole-face boundary is neither rotated nor curved. However, this has only minor influence on the ion optics, as no additional focussing is needed and the second order aberrations x/θ^2 are already as low as $\approx 2 \times 10^{-5}$ cm/mrad^2. The small bending angle of $\alpha = 45^0$ results in a moderate dispersion of $x/\delta \approx 2$ cm/%p, varying along the focal plane. However, in combination with $\beta_2 = -45^0$ and $R_2 = 5$ m a very large momentum bite of 500 MeV/c < p < 1200 MeV/c is analyzed in one setting. In this case the total length of the focal plane is about 1.5 m. Even higher momenta up to 1.8 GeV/c can be measured at reduced solid angle by moving the focal plane detector.

The quadrupole has a length of 80 cm and an aperture of 26 cm accepting horizontal angles of $\theta = \pm 70$ mrad at p = 750 MeV/c. Due to the vertical dipole gap of 20 cm, vertical angles up to $\varphi = \pm 140$ mrad are accepted. In Fig. 2 the resulting solid angle is shown versus momentum (open circles). The decrease towards lower and higher momenta is due to the dipole gap, which cuts the trajectories in the case of overfocussing (low momenta) or too weak focussing (high momenta). The dashed line illustrates the effective solid angle with the kaon decay in flight taken into account.

Figure 3 shows the aberrations of the spectrometer calculated with the code RAYTRACE. The horizontal angle θ_{foc} at the focal plane is plotted versus the horizontal position for five different particle momenta (x = 0 corresponds to the position of the first order focus for each momentum). The target angle θ is varied from $\theta = -60$ mrad to +60 mrad; the vertical angle is $\varphi = 0$ (upper part) and $\varphi = 100$ mrad (lower part). A dominant 3rd order aberration is obvious; a simultaneous correction

for all momenta by a simple 3rd order exit pole-face boundary, however, turns out to be not possible because of a change in sign of the third order term for different momenta.

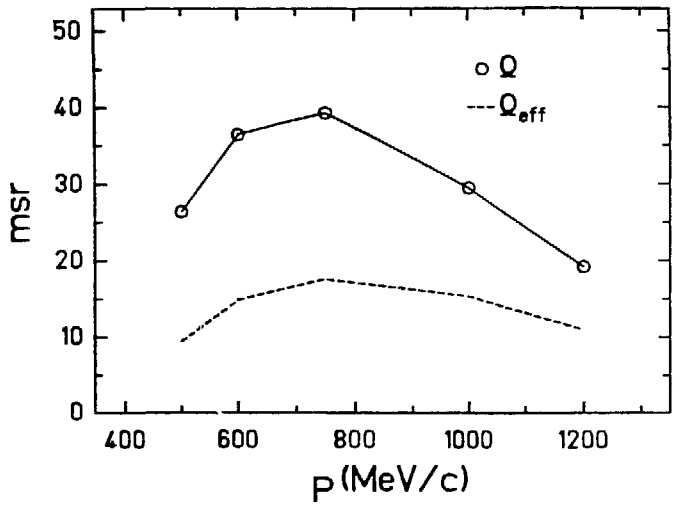

Fig. 2: Geometric solid angle Ω of the spectrometer as a function of particle momentum (circles). Ω_{eff} (dashed line) takes into account kaon decay in flight over a distance L: $\Omega_{eff} = \Omega \times \exp(-L/\beta\gamma c\tau)$ with: $\beta \times c$ = particle velocity; $\gamma = 1/\sqrt{1-\beta^2}$; $c\tau$ = 3.7 m (kaons).

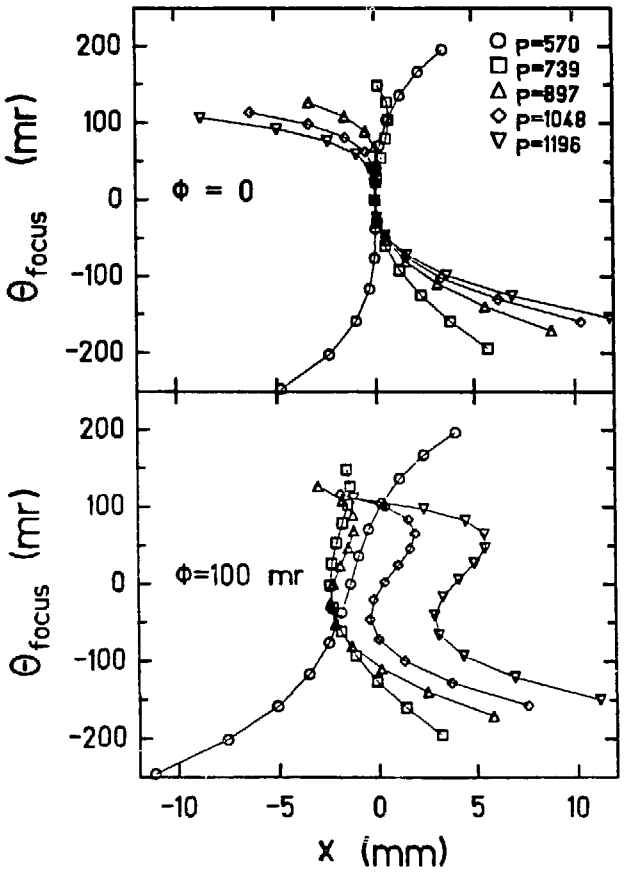

Fig. 3: Aberrations of the spectrometer for 5 different momenta calculated with the code RAYTRACE. The horizontal angle θ_{focus} relative to the central ray is plotted as a function of the focal-plane position x. For each momentum, trajectories are calculated for a horizontal acceptance at the target between ±60 mrad in steps of 10 mrad.

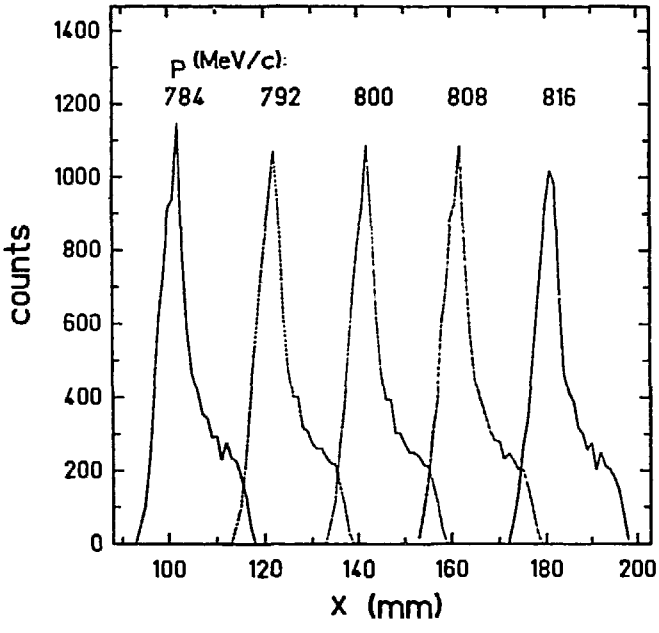

Fig. 4: Focal-plane position spectra for 5 momenta which differ by $\delta p/p = 1$ %. Here x is the position along the focal plane tilted by 37° with respect to the central ray and calculated with θ and φ statistically sampled between ± 60 mrad and ± 100 mrad, respectively, using RAYTRACE.

Table I: Spectrometer Specifications

Quadrupole:	Length	80 cm
	Aperture	26 cm ⌀
	B_{max} at pole tip	0.84 T
Dipole:	Field area	$\approx$ 1.5 m²
	Gap	20 cm
	Pole face tilt at entrance (β_1)	0°
	at exit (β_2)	45°
	Radius of curvature at exit	5 m
	Central ray bending radius	1.5 m
	bending angle	45°
	B_{max}	1.7 T
QD-Spectrometer:	Horizontal opening angle $\Delta\theta$	$\pm$ 70 mrad
	Vertical opening angle $\Delta\varphi$	$\pm$ 100 - 140 mrad
	Solid angle Ω	20 - 35 mrad
	Focal plane length	1.5 m
	height	20-60 cm
	tilt angle	37°

	min	mean	max	
Momentum at B_{max}	570	900	1200	MeV/c
Dispersion along focal plane	2.1	1.9	1.6	cm/%p
Total length (target-focal plane)	3.9	4.5	5.3	m
Resolution (intrinsic)		$\approx 10^{-2}$		
(w. raytracing)		$< 10^{-3}$		
Angular range	0°,10°-120°			

Coils are normal conducting, the dipole yoke is C-shaped, total weight is less than 80 tons

To study the line shapes and intrinsic resolution of the spectrometer, 10000 rays with randomly distributed angles between -60 mrad $< \theta <$ +60 mrad and -100 mrad $< \varphi <$ +100 mrad were calculated for five momenta around 800 MeV/c using the code RAYTRACE. The line shapes calculated for each momentum are shown in Fig. 4. Here the focal plane is tilted by $\varphi_{rot} = 37^{0}$ with respect to the central ray and the distance from the dipole is chosen such as to optimize the resolution for each momentum. Figure 4 also demonstrates a momentum resolution of $\approx 10^{-2}$ since the five spectra correspond to momenta differing by $\delta p/p = 1\%$. In addition, although high resolution is not the primary aim of the design, the momentum resolution can be improved considerably to $\delta p/p < 10^{-3}$ if raytracing is applied. This will be discussed in section IV. Finally, the vertical position spectra are shown in Fig. 5 for different momenta. The spread at high and low momenta is due to the fact. that the spectrometer is fully double focussing only for the central momentum.

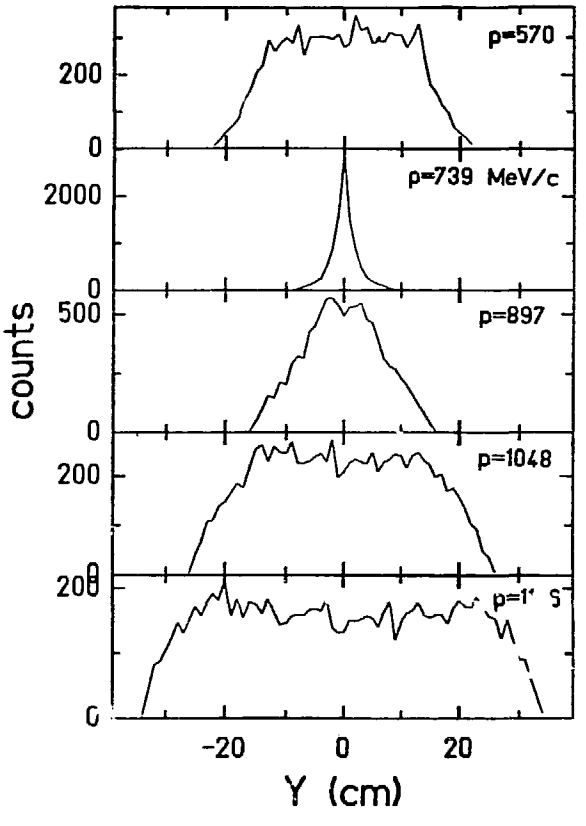

Fig. 5: Vertical position spread at the focal plane for 5 different momenta.

IV. Detector System

At SIS energies the predominant particle species are baryons with an admixture of roughly 10% pions. At 1.8 GeV/nucleon a K^{+}/π^{+} ratio of about 1/100 has been observed[3] at the BEVALAC. For experiments extending well below the N-N threshold for K production a further suppression by a factor 10 or more is expected for the kaon yield. Thus ratios are expected of the order K^{+}: π^{+}: p $\approx$ 1:10^{3}(10^{5}):10^{4}(10^{6}).

The design aim of the detector system is the separation of p, π and K in the momentum range from 0.5 to 1.8 GeV/c. First, the system has to provide a fast on-line trigger for the selection of events containing kaons or pions. Then, in the off-line analysis incorporating tracking, we have to be able to identify K, π and p uniquely. The fast trigger condition will be achieved mainly from the time-of-flight measurements and the threshold Cerenkov counters with electronic hard ware. More stringent software trigger conditions can be obtained depending on the capability of the micro-processors to be used with the front-end electronics. The off-line identification will additionally use the position information from multiwire proportional chambers to track the path of the particle. For an additional background suppression in experiments with very low kaon rates we envisage the installation of existing large volume scintillators behind the other detectors; there the kaons will be stopped and their delayed decay will be observed.

a) Multiwire Proportional Chambers

The determination of the particle tracks in the spectrometer will be made by multiwire proportional chambers (MWPC), designed for 1 mm spatial resolution. The two large chambers at the focal plane and one chamber 1 m in front of these yield a directional resolution of 1.5 mrad. Multiple scattering in the vacuum window at the exit of the dipole and in the wire chambers leads to an additional directional uncertainty of about 1-2 mrad. The total angular spread of about 2 mrad when combined with the transport matrix elements, and the magnification and dispersion of the spectrometer results in a variance in focal plane position of about 1 mm. Hence tracking will not worsen the intrinsic resolution of 1 mm of the focal plane detector, and therefore the momentum resolution of the spectrometer with tracking can be $\leq 10^{-3}$, depending on beam spot size and beam divergence.

To allow for high total particle rates and a proper detection of multiple hits in the focal plane detector, the wires of the MWPC's have to be read out directly in both coordinates. Two cathode wire planes will be used for x and y determination. Anode wires will be inclined by 45^0 and will allow to reduce multiple-hit ambiguities via pattern read out. Optional low-pressure chambers before the dipole allow to select rays coming from an area of less than 3x3 mm^2 on the target and thus to reduce background. In experiments with very high particle rates and multiplicities they can be deactivated. The total number of signal channels is mainly determined by the large focal plane MWPC's; overall a total of about 1500 readout channels has to be equipped with preamplifiers and ADC's.

b) Time-of-Flight Measurement

Figure 6 illustrates the expected particle separation between K, π, p and d in the momentum range of 0.2 to 1.2 GeV/c calculated for a momentum resolution of 1% and a time resolution of 250 ps (FWHM) and a total flight path of 4.5 m from target to focal plane. The bars represent a 6 σ variance. The flight time will be measured between a start detector near the target and 20-50 plastic scintillator paddles inbetween the last two MWPC's. The start detector is a segmented scintillator which is sensitive to any charged reaction product. The stop detector scintillators consist of PILOT-U and are read out via ultra fast photomultipliers at both ends to compensate for light propagation.

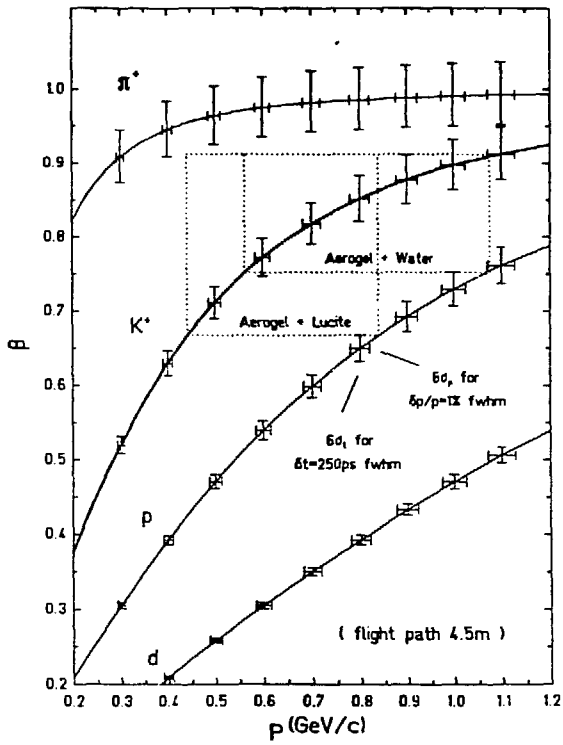

Fig. 6: Separation of π, K, p, and d passing through the spectrometer by time of flight. The area enclosed by the dotted lines corresponds to velocities and momenta, where a unique trigger signal can be derived from Cerenkov light in aerogel and water or lucite, respectively.

c) Cerenkov Detectors

As material for the threshold Cerenkov counters we propose water and Silica Aerogel[4], whose index of refraction can be varied according to need. In addition a lucite radiator[5] is foreseen for K/p separation at low momenta. The essential components of a detector module are thus: Silica Aerogel Cerenkov-detector for pion tagging, a water (lucite) radiator for kaon tagging (it also registers pions of course), and a scintillator to detect all charged particles; the latter is identical to the time-of-flight stop detector. In principal the combination of the corresponding three signals gives a unique separation of K, π, p, as is indicated by dotted lines in Fig. 6. For kaon momenta above 1 GeV/c a lower density Aerogel radiatior will be used. To avoid background in the kaon spectra, the Aerogel detector must be very efficient in tagging pions. An efficiency of $1\text{-}10^{-4}$ corresponds to 9 photoelectrons detected which requires a thickness of the radiator of 9 cm. For the lucite radiator the corresponding thickness is only 4 cm.

V. Two-Particle Correlation Measurements

The spectrometer layout in Figure 1 indicates the magnetic field region without return yoke From a preliminary engineering design we expect that the dipole magnet can be constructed as a C-type magnet with still moderate weight. This would leave most of the forward direction and left-

hand side of the magnet (when looking downstream) with an open gap allowing detection of particles with opposite charge and thus measurement of corresponding two-particle correlation function. (Since the quadrupole will be defocussing for such opposite-charge particles it will have to be turned off, reducing the solid angle). Similarly, the large solid angle will allow correlation studies between like particles and possibly also between charged and neutral particles. Two particle correlation functions $R(\vec{q})$ have been of particular interest in nuclear reaction studies. $R(\vec{q})$ is defined by

$$R(\vec{q}) = C_{12} \cdot \frac{Y_{12}(\vec{p}_1, \vec{p}_2)}{Y_1(\vec{p}_1) \cdot Y_2(\vec{p}_2)} - 1$$

where $Y_1(\vec{p}_1)$ and $Y_2(\vec{p}_2)$ are the singles yields and $Y_{12}(\vec{p}_1, \vec{p}_2)$ the coincidence yield for two particles of momenta $\vec{p}_1$ and $\vec{p}_2$, with $\vec{q} = \vec{p}_1 - \vec{p}_2$. C_{12} is a normalization constant, determined by the requirement that $R(\vec{q}) = 0$ for large relative momenta. In the limit of a thermal model and under the assumption that the interaction between the two particles dominates over the one with the rest of the system, R(q) has been found to be given by the following approximate expression[6].

$$R(q) = \frac{2\pi}{(2s_1+1)(2s_2+1) \cdot V \cdot q^2} \sum_{J,\alpha} (2J+1) \frac{\partial \delta_{J,\alpha}}{\partial q}$$

Here the factor $(2s_1+1)(2s_2+1)$ is a statistical spin factor, J is the total angular momentum, $\delta_{J,\alpha}$ the scattering-phase shift for channel α, and V the volume of the emitting system.

In the past, the expression has generally been viewed as a means to deduce V and therefore the space (and time) extend of the emitting system in nuclear reaction studies. (In analogy to the correlations arising from the quantum statistics of a system obeying Bose-Einstein statistics as first deduced by Hanbury-Brown & Twiss[7] for interferometry of photons and applied to size determinations of stars). Of course, any system may be studied for correlations and under the assumption of knowing V, the scattering-phase shifts can in principle be extracted. This might be of particular interest for shortlived elementary particles where such studies are otherwise not possible. In this sense - of providing a thermal source emitting elementary particles whose final-state interactions can be measured - heavy ion reactions in the GeV/u range may provide an unique opportunity. The design of the spectrometer will allow some such studies within the limits mentioned.

Footnotes and References

* Proposal for a QD-Magnetic Kaon Spectrometer at SIS; R. Bock, H. Bokemeyer, R. Brockmann, H. Grein, E. Grosse (co-spokesperson), W. Henning, T. Humanic, D. Miskowiec, A. Sandoval, D. Schüll, P. Senger, H. Stelzer, H. Ströbele (GSI Darmstadt); H. Oeschler (Technische Hochschule Darmstadt); W. Heck, R. Renfordt, K. Stiebing, R. Stock (co-spokesperson), S. Wenig (University of Frankfurt); J.W. Harris, S. Chase (Lawrence Berkeley Laboratory); B. Kohlmeyer, F. Pühlhofer, H. Stege (University of Marburg).

1. K.L. Brown and S.K. Howry, SLAC Report No. 91 (1970).
2. S. Kowalski and H.A. Enge, MIT Report (1985).
3. J.W. Harris et al., Phys. Rev. Lett. 47 (1981) 229.
4. P. De Brion et al., NIM 179 (1981) 61; P.J. Carlson, NIM A248 (1986) 110; G. Poelz, NIM A248 (1986) 118.
5. C.R. Brower et al., NIM A252 (1985) 112.
6. Z. Chen et al., MSU preprint; B.K. Jennings et al., P.R. C33 (1986) 1303, and references therein.
7. R. Hanbury-Brown and R.Q. Twiss, Nature 178 (1956) 1046.

What is Interesting about Dilepton Production at Bevalac/SIS/AGS Energies?§ †

Charles Gale‡ and Joseph Kapusta

School of Physics and Astronomy
University of Minnesota
Minneapolis, MN 55455

Abstract

The general features of electron-positron emission from hot nuclear matter are discussed. Estimates are made for dileptons arising from incoherent nucleon-nucleon bremsstrahlung and from annihilation reactions. We focus on the following processes: $np \rightarrow np e^+e^-$, $\pi^+\pi^- \rightarrow e^+e^-$, $K^+K^- \rightarrow e^+e^-$ and $N\bar{N} \rightarrow e^+e^-$.

1. Introduction

The main purpose of colliding heavy nuclei at high energy is to study the properties of nuclear matter in temperature and density regions far from equilibrium. We then hope to learn about the behavior of excited nuclear matter and perhaps to reveal some exotic new phenomena. The conjectured liquid-gas phase transition [1] and QCD phase transition [2] are often mentioned in this context. It is the purpose of this communication to show that the emission spectrum of dileptons in high energy heavy ion collisions can serve as an ideal probe of the relativistic many-body system.

Recently much attention has been drawn by the observation of copious direct photon production in nucleus-nucleus collision [3]. Depending on the energy and angle of the emitted photons, this should provide information on nuclear stopping power [4] and on the dynamics of the cascading baryons in hot and dense nuclear matter [5,6]. The theoretical study of dilepton production in high energy heavy ion collisions was initiated with the suggestion that it might serve as a thermometer of quark-gluon plasma formed at ultrarelativistic energies [7]. However, dileptons should be produced at lower energies as well, where no quark- gluon plasma formation is expected. The reasoning behind this argument is simple: whenever a charged particle is accelerated it will radiate photons. It can just as well radiate virtual photons which internally convert to e^+e^- pairs. Electromagnetic signals offer obvious advantages over strongly interacting probes:

a) They do not interact much, i.e. they will travel relatively unscathed from the interaction zone. If the pairs are formed mainly in incoherent processes at the single baryon level, they carry valuable information about the space-time region where those interactions are the most frequent: the high temperature/high density phase.

b) Their coupling to other particles is very well known.

The main drawback is of course the extremely low counting rates, mainly because of the size of

§ Work supported by the US Dept. of Energy under contract DE-FG02-87ER40328.

† Invited talk presented at the 8th High Energy Heavy Ion Study, Lawrence Berkeley Lab., November 16-20, 1987.

‡ Fellow of the Minnesota Supercomputer Institute and of the NSERC of Canada, Speaker.

α. Note that the rate of dilepton emission is of order α^2 whereas photon emission goes as α.

A rigorous study of e^+e^- production is extremely difficult primarily because of the strongly interacting nature of nuclear matter: for example, there are complications from two and three particle correlations, three body collisions, identification of the relevant degrees of freedom (nucleons, baryonic resonances, mesons, collective degrees of excitation, quarks, etc.) and finite temperature and density corrections to form factors, widths and so on. Therefore our analysis will be at times quite phenomenological and our studies will be based on relativistic kinetic theory, for the most part.

2. General Discussion

2.1 Nucleon-Nucleon Bremsstrahlung

Let us first consider bremsstrahlung in hadron-hadron collisions. For example, in the reaction $np \rightarrow np$, photons (both real and virtual) can be radiated. In the soft photon approximation one retains only radiation from the external charged lines on the corresponding diagram [8]. This approximation is valid if the energy carried by the photon is less than the inverse of the strong interaction collision time. The latter is usually estimated as about 1-2 fm/c, so that this mechanism is dominant if $E_\gamma < \tau_{NN}^{-1} = 100$-$200$ MeV. For hard photons we must in addition look inside the strong interaction region. For example, the dilepton pair emitted from an exchanged boson is show in figure 1.

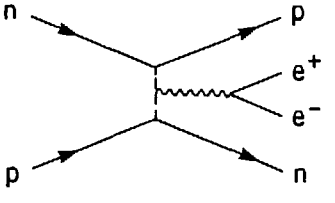

Figure 1. Radiation from an internal charged pion line in np scattering.

In the soft photon approximation, the connection between the spectrum of dileptons and that of real photons has been known for some time [9]. It is given by:

$$E_+E_-\frac{d^6\sigma^{e^+e^-}}{d^3p_+d^3p_-} = \frac{\alpha}{2\pi^2}\frac{1}{q^2}q_0\frac{d^3\sigma^\gamma}{d^3q}, \tag{1}$$

where $q^\mu = p_+^\mu + p_-^\mu$.

In general, a number of micro-processes will contribute to the production of electron-positron pairs but in the region of interest (dilepton invariant masses of a few hundred MeV) the dominating contributions will be those of np bremsstrahlung and of two-particle annihilation [10]. We start by the first of these. The cross-section for an np collision to make an e^+e_- with invariant mass M is (in the soft photon approximation) [10]

$$\frac{d\sigma_{np}^{e^+e^-}}{dM^2} = \frac{\alpha^2}{3\pi^2}\frac{\bar{\sigma}(s)}{M^2}\ln[\frac{\sqrt{s}-2m_N}{M}], \tag{2}$$

$$\bar{\sigma}(s) = \int_{-(s-4m_N^2)}^{0}(\frac{-t}{m_N^2})\frac{d\sigma_{np}}{dt}\,dt. \tag{3}$$

where t is the 4-momentum transfer and $\bar{\sigma}(s)$ is the momentum transfer weighted cross section. We have implicitly assumed that $|t| < 4m_N{}^2$, a reasonable approximation. In the independent particle approximation of kinetic theory, the rate for producing dilepton pairs is

$$\frac{dR_{np}^{e^+e^-}}{dM^2} = \iint \frac{d^3k_1}{(2\pi)^3}\frac{d^3k_1}{(2\pi)^3} f_n(\mathbf{k_1}) f_p(\mathbf{k_2}) \frac{d\sigma_{np}^{e^+e^-}}{dM^2}(s, M^2)\, v_{rel}, \tag{4}$$

where

$$v_{rel} = \frac{\sqrt{(k_1 \cdot k_2)^2 - m_N^4}}{E_1 E_2}.$$

Here f's are the occupation probabilities in momentum space. For our purposes it is sufficient to use the Maxwell-Boltzmann form:

$$f_i = 2e^{\mu_i/T} e^{-E/T}, \tag{5}$$

where $E = \sqrt{\mathbf{k}^2 + m_N^2}$, μ is the chemical potential, i is associated with the proton or neutron and the 2 is a spin factor.

It will be usefull later to evaluate the rate of emission of back-to-back dilepton pairs i.e. pairs with total momentum $\mathbf{q} = 0$ in the nuclear matter rest frame. The cross section for this reaction is:

$$\frac{d^4\sigma_{np}^{e^+e^-}}{d^3q dM}\Big|_{\mathbf{q}=0} = \frac{\alpha^2}{6\pi^3}\frac{\bar{\sigma}(s)}{M^4}. \tag{6}$$

The formulae displayed above are only approximate but they are simple. In the energy region appropriate to theses estimates, the main improvement lies surely in going beyond the soft photon approximation. We will discuss such improvements later.

2.2 $\pi^+\pi^-$ Annihilation

The most important annihilation channel for the production of e^+e^- pairs in heavy ion collisions is $\pi^+\pi^- \to e^+e^-$ [7]. The cross section is well known to be

$$\sigma_{\pi\pi}^{e^+e^-}(M) = \frac{4\pi}{3}\frac{\alpha^2}{M^2}\sqrt{1 - 4m_\pi^2/M^2}\,|F_\pi(M)|^2, \tag{7}$$

where $F_\pi(M)$ is the pion electromagnetic form factor. We use a relativistic Breit-Wigner type fit to the Gounaris-Sakurai formula [10, 11]. The rate is obtained by inserting equation 7 into equation 4.

Before we compute the bremsstrahlung and pion annihilation contributions to $dR^{e^+e^-}/dM$ let us consider the thermal rates for back- to-back dilepton emission, first in $\pi^+\pi^- \to e^+e^-$. It can be shown that the rate of emission of electron-positron pairs with zero total momentum is [10]

$$\frac{d^4R_{\pi^+\pi^-}^{e^+e^-}}{d^3q dM}\Big|_{\mathbf{q}=0} = \frac{\alpha^2}{3(2\pi)^4}\frac{|F_\pi(M)|^2}{\left(e^{\omega/T}-1\right)^2}\sum_k{}' \frac{k^4}{\omega^4}\left|\frac{d\omega}{dk}\right|^{-1}, \tag{8}$$

where the prime denotes that the sum is restricted to those values of k satisfying $2\omega(k) = M$. The important point is to notice that this rate is inversely proportional to the group velocity of the pion and to the fourth power of k/ω. The group velocity appear simply as the Jacobian of the transformation between energy and momentum.

The true pion dispersion relation in hot and dense nuclear matter is not known. The pion will be dressed by many-body effects and the in-medium and vacuum propagators will differ. Some

studies [12] make it plausible that the dispersion relation develops a dip at finite momentum because of the strong p-wave interaction with the nucleons. We will adopt a parametrization exhibiting this behavior and investigate its consequences. We take the functional form

$$\omega(k) = [(k - k_0)^2 + m_0^2]^{1/2} - U. \tag{9}$$

In general the parameters k_0, m_0 and U are all temperature and density dependent. However it is safe to assume that the main effect will be the density dependence since this is what causes the interaction in the first place. The choice of parameters in equation 9 is dictated by the following considerations:

(i) The group velocity $d\omega/dk$ should never exceed the speed of light.

(ii) At high momenta many-body effects should be of negligible importance such that $\omega \to k$ as $k \to \infty$.

(iii) The energy first decreases as the momentum increases, corresponding to a strong p-wave attraction, and then goes up again (see point (ii)).

We use equation 9 in actual calculations. Note however that a more rigorous derivation of the pionic dispersion relation in a dense nucleon medium is in progress.

One then sees the great advantage of studying back-to-back emission. Since we are dealing with a two body process there is a one to one correspondence between the energy and momentum carried by the electron-positron pair and that of the colliding pions. We are directly probing the pion dispersion relation. This is made clear by the following argument: if the pion total energy has a minimum at a finite value of momentum one realizes that at this point the rate for dilepton emission will be greatly enhanced because the group velocity is reduced. See equation 8. In this ideal situation, a dip in the pionic dispersion relation is then signaled by a sharp peak in the dilepton spectrum. By this reasoning we also see why we favor the study of e^+e^- pairs over that of $\mu^+\mu^-$ pairs: an emitted muon pair has a lower threshold to its invariant mass of $2m_\mu$. If $\omega_{min}(k) < m_\mu$, then the peak in the dimuon spectrum would lie below threshold. This does not happen with electrons because they are essentially massless.

Let us now put our formalism to use and integrate numerically our rate equations to compare the relative contributions of the processes we have discussed so far.

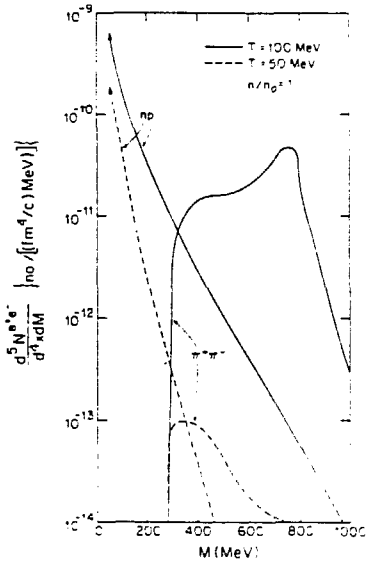

Figure 2. The thermal rates for producing e^+e^- pairs of invariant mass M at two different temperatures and at normal nuclear matter density. Contributions from np bremsstrahlung and from $\pi^+\pi^-$ annihilation are shown separately.

On figure 2 we show e^+e^- production rates at T=50 and 100 MeV using a free pion dispersion relation. These two temperatures span the upper range of excitation energies one expects to reach at the Bevalac and SIS. The bremsstrahlung contributions are unsurprisingly featureless. However at both 50 and 100 MeV temperature, the spectrum is dominated by the pion annihilation channel for $M > 400$ MeV. At the higher temperature, the ρ peak is clearly visible. From plots like this one one might be able to deduce how many real pions were present in the strongly interacting system since the rate for $\pi^+\pi^- \rightarrow e^+e^-$ should be proportional to n_π^2, the square of the pion density. Furthermore it has been conjectured that, as the phase transition to the QCD plasma is approached, the shape and position of the ρ peak will change [13]. With dilepton probes, the onset of the QCD phase transition could be studied from the hadronic side.

On figure 3, we witness the dramatic enhancement in back-to-back emission caused by our interacting dispersion relation. Even if the bremsstrahlung had been underestimated by an order of magnitude, the pion signal would still shine through. The qualitative features of this figure are independent of our specific parametrization and constitute a striking signature of a modified pionic dispersion relation. However, we must realize that in actual heavy ion collisions those peaks will be broadened due to finite size and dynamical effects.

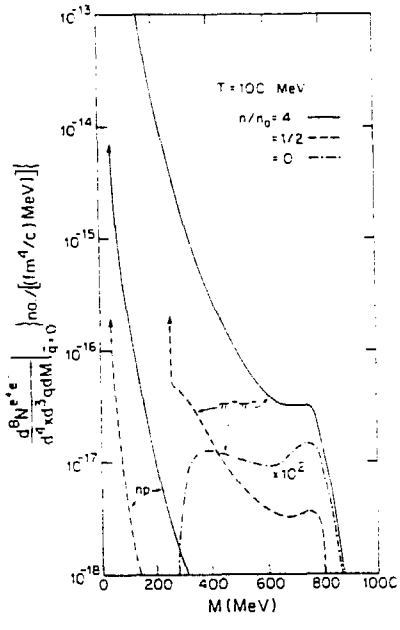

Figure 3. Comparison of the thermal rates for producing e^+e^- pairs of invariant mass M and zero total momentum coming from np bremsstrahlung and from $\pi^+\pi^-$ annihilation.

2.3 $N\bar{N}$ Annihilation

We have seen that the emission of dilepton pairs can reveal intimate features of the interacting pions. We might then ask if there is a chance of learning about the nucleons at high temperature and density? It turns out that formally there is a connection between the dilepton spectrum coming from $N\bar{N} \rightarrow e^+e^-$ and the nucleon effective mass, m_N^*. This can be illustrated, for example, by Walecka's mean field Lagrangian [14]:

$$\mathcal{L}_{MFT} = \bar{\psi}[i\gamma_\mu\partial^\mu - g_v\gamma^0 V_0 - (m_N - g_s\phi_0)]\psi. \qquad (10)$$

One can then define $m_N^* = m_N - g_s\phi_0$. By usual methods, the above Lagrangian yields a Dirac equation

$$[i\gamma_\mu\partial^\mu - g_v\gamma^0 V_0 - m_N^*]\psi = 0.$$

with single particle energy

$$\epsilon^\pm(k) = g_v V_0 \pm \sqrt{\mathbf{k}^2 + m_N^{*2}}.$$

Relying on relativistic kinetic theory we obtain the following rate equation:

$$\left.\frac{d^4 R_{N\bar{N}}^{e^+e^-}}{d^3q dM}\right|_{q=0} = \frac{\alpha^2}{12\pi^4}\left[\,|G_M(M)|^2 + 2\left(\frac{m_N^*}{M}\right)^2 |G_E(M)|^2\,\right] f_N f_{\bar{N}} \sqrt{1 - 4\left(\frac{m_N^*}{M}\right)^2}. \qquad (11)$$

The familiar electromagnetic nucleon form factor [15] appears in equation 11. Further note that in the Maxwell-Boltzmann limit we can write:

$$f_N f_{\bar{N}} \approx e^{-\beta M}. \qquad (12)$$

We plot the result of a calculation done with $T = 100$ MeV and $m_N^* = 500$ MeV on figure 4. We also compare with the pion contribution. Unfortunately, the nucleon signal is totally drowned by the pions, even in the most favorable case where the free pionic dispersion relation is used. From equation 11 we see that the main effect of the effective mass is to lower the threshold, not so much to affect the height of the spectrum.

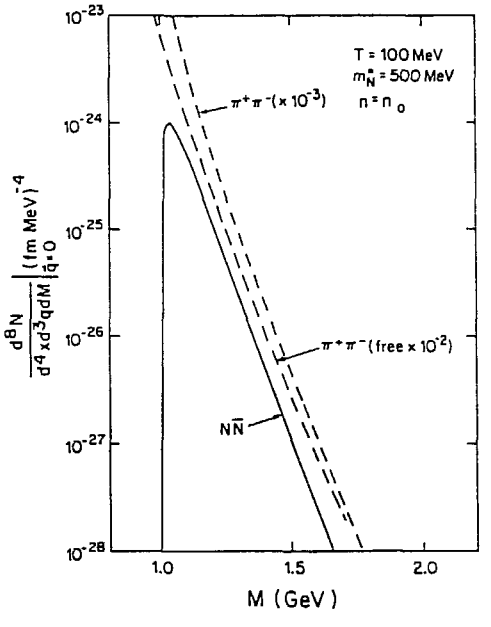

Figure 4. Thermal dilepton production rates from $N\bar{N} \rightarrow e^+e^-$ and $\pi^+\pi^- \rightarrow e^+e^-$.

2.4 K^+K^- Annihilation

The reaction $K^+K^- \rightarrow e^+e^-$ may be especially interesting in light of the recent enticing concept that kaon condensation may occur at *moderate* nuclear densities [16]. Furthermore the dilepton spectrum will explore the kaon electromagnetic form factor which, in the vector dominance

hypothesis, is due to the superposition of the ρ, ω and ϕ vector mesons resonances. The approach to kaon condensation may be modeled very simply by a vanishing mass at the critical density:

$$m_K = m_K^0 \sqrt{(1 - (\frac{n}{n_c})}. \tag{13}$$

This will allow us to talk of a modified kaon dispersion relation via

$$\omega(k) = \sqrt{\mathbf{k}^2 + m_K^2}.$$

Using our familiar techniques, we get

$$\frac{d^4 R^{e^+e^-}_{K^+K^-}}{d^3 q dM}\Big|_{\mathbf{q}=0} = \frac{\alpha^2}{3(2\pi)^4} |F_K(M)|^2 f_{K^+} f_{K^-} \frac{[M^2/4 - m_K^2]^{3/2}}{M^3}, \tag{14}$$

where the kaon electromagnetic form factor is

$$F_K(s) = \frac{1}{2}\frac{m_\rho^2}{m_\rho^2 - s - im_\rho\Gamma_\rho} + \frac{1}{6}\frac{m_\omega^2}{m_\omega^2 - s - im_\omega\Gamma_\omega} + \frac{1}{3}\frac{m_\phi^2}{m_\phi^2 - s - im_\phi\Gamma_\phi}.$$

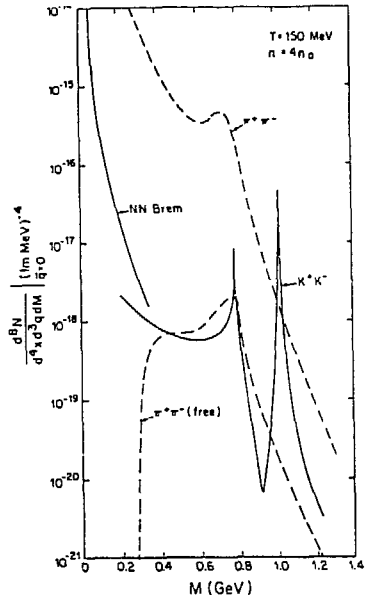

Figure 5. Dilepton rates for the reactions $K^+K^- \rightarrow e^+e^-$, $np \rightarrow npe^+e^-$ and $\pi^+\pi^- \rightarrow e^+e^-$. Both interacting and free pion dispersion relations are used.

On figure 5 we display our calculation for a nuclear density equal to the critical density, and at a temperature of 150 MeV. The former was chosen to be $n_c = 4n_0$. As in the nucleon-antinucleon case, the main effect of lowering the kaon mass is to shift the threshold, revealing more features of the kaon electromagnetic form factor. The ϕ and $\rho - \omega$ peaks are clearly visible. We show the signal from colliding pions in the cases where $\omega_\pi = \omega_{free}$ and where ω_π is defined by equation 9. These two scenarios are the "best" and "worst" situations as far as the kaon signal is concerned. In both

of these, the ϕ peak clearly sticks out. One could then imagine doing analogous studies as the ones proposed for the ρ peak in the pion signal. However at $M = 1$ GeV the experimental difficulties are obvious: we are in a very low counting rate region and furthermore the ϕ meson has an extremely narrow width. Such difficulties will no doubt greatly hinder observations. In the low invariant mass region, our kaon contribution lies below the bremsstrahlung continuum. At present, it is difficult to predict the consequences of kaon condensates, but our "best" scenario does suggest an enhancement of the ρ peak. Bear in mind that these approaches are undoubtedly oversimplified but nevertheless they contain more than enough interesting features to fuel additional experimental and theoretical investigations.

3. Outlook and Conclusion

Clearly, improved calculations will go beyond the soft photon approximation in the nucleon-nucleon process. We will relax this simplification by actually evaluating diagrams such as the one displayed in figure 1. The coupling constants and *NNBoson* form factors are found in relativistic one-boson exchange models such as the Bonn potential approach [17]. There the coupling to a pseudo-scalar meson, for example, is described by $\mathcal{L}_{NNps} = \frac{f_{ps}}{m_{ps}} \bar{\psi}\gamma^5\gamma^\mu\psi\partial_\mu\phi_{ps}$. Such approaches constitute effective relativistic field theories and are a good basis for off-shell extrapolations. The cross sections derived in such theories can be then used as input to the dynamical simulation models that are available, such as the BUU scheme [18]. The calculations described above are under way.

There are exciting times ahead. A large amount of additional work needs to be done, both theoretically and experimentally. In the latter sector, the DLS (DiLepton Spectrometer) experiment at the Bevalac has already produced some promising results. It is important to support endeavors such as the DLS collaboration and its proposed AGS extension, as the study of dileptons in heavy ion collisions will reveal features of strongly interacting many-body systems that were up to now inaccessible.

3. References

[1] See, for example, L.P. Csernai and J.I. Kapusta, Phys. Rep. 131 (1986) 223.

[2] See, for example, *Quark Matter 86*, Nucl. Phys. A461 (1987).

[3] K.B. Beard *et al.*, Phys. Rev. C32 (1985) 111; E. Grosse *et al.*, Europhys. Lett. 2 (1986) 9; N. Alamanos *et al.*, Phys. Lett. 173B (1986) 392.

[4] J.I. Kapusta, Phys. Rev. C15 (1977) 1580; M.P. Budiansky, S.P. Ahlen, G. Tarle and P.B. Price, Phys. Rev. Lett. 49 (1982) 361; D. Vasak *et al.*, Nucl. Phys. A428 (1984) 291c.

[5] H. Nifenecker and J.P. Bondorf, Nucl. Phys. A442 (1985) 478; C.M. Ko, G. Bertsch and J. Aichelin, Phys. Rev. C31 (1985) 2324; W. Cassing *et al.*, Phys. Lett. 181B (1986) 217; W. Bauer, G.F. Bertsch, W. Cassing and U. Mosel, Phys. Rev. C34 (1986) 2127; K. Nakayama and G.F. Bertsch,*ibid*, 34 (1986) 2190.

[6] D. Neuhauser and S.E. Koonin, Nucl. Phys. A462 (1987) 163.

[7] G. Domokos and J.I. Goldman, Phys. Rev. D23 (1981) 203; G. Domokos, *ibid*, 23 (1983) 123; K. Kajantie and H.I. Miettenen, Z. Phys. C 9 (1981) 341; 14 (1982) 357.

[8] J.D. Jackson, *Classical Electrodynamics* (Wiley, New York, 1975).

[9] R. Rückl, Phys. Lett. 64B (1976) 39.

[10] C. Gale and J. Kapusta, Phys. Rev. C35 (1987) 2107.

[11] G.J. Gounaris and J.J. Sakurai, Phys. Rev. Lett. 21 (1968) 244.

[12] A.B. Migdal, Rev. Mod. Phys. 50 (1978) 107; I.M. Mishustin, F. Myrher and P.J. Siemens, Phys. Lett. 95B (1980) 361; B. Friedman, V.R. Pandharipande and Q.N. Usmani, Nucl. Phys. A372

(1981) 483
[13] R.D. Pisarski, Phys. Lett. 110B (1982) 155.
[14] J.D. Walecka, Ann. Phys. (N.Y.) 83 (1974) 491.
[15] See, for example, M.L. Perl, *High Energy Hadron Physics* (Wiley, New York, 1974).
[16] D.B. Kaplan and A.E. Nelson, Phys. Lett. 175B (1986) 57; G.E. Brown, K. Kubodera and M. Rho, Saclay preprint PhT/87-09.
[17] R. Machleidt, K. Holinde and Ch. Elster, Phys. Rep. 149 (1987) 1.
[18] G.F. Bertsch, H. Kruse and S. Das Gupta, Phys. Rev. C29 (1984) 673; H. Kruse, B. Jacak and H. Stöcker, Phys. Rev. Lett. 54 (1985) 289; C. Gale, G.F. Bertsch and S. Das Gupta, Phys. Rev. C35 (1987) 1666.

FIRST RESULTS ON DILEPTON PRODUCTION AT THE BEVALAC

G. Roche(a), G. Claesson(b), D. Hendrie(c), G. Krebs(d),
E. Lallier, H. Matis, J. Miller, T. Mulera(e), C. Naudet,
L. Schroeder, P. Seidl, A. Yegneswaran, Z.F. Wang
Nuclear Science Division, Lawrence Berkeley Laboratory,
University of California, Berkeley, CA 94720

J. Bystriky(f), J. Carroll, J. Gordon, G. Igo, S. Trentalange(g)
Department of Physics, University of California at
Los Angeles, Los Angeles, CA 90024

T. Hallman, L. Madansky
Department of Physics, The Johns Hopkins University,
Baltimore, MD 21218

S. Christo(h), J.F. Gilot(i), P. Kirk
Department of Physics and Astronomy, Louisiana State University,
Baton Rouge, LA 70803

D. Miller
Department of Physics, Northwestern University,
Evanston, IL 60201

G. Landaud
Universite de Clermont II-Institut National de Physique Nucleaire
et de Physique des Particules, 63170 Aubiere, France

(a) On leave from the Universite de Clermont II, Aubiere, France
(b) Present address: Gesellschaft fur Schwerionenforschung, Darmstadt West Germany
(c) Present address: Department of Energy, ER-23/GTN, Washington, DC 20545
(d) Accelerator and Fusion Research Division, Lawrence Berkeley Laboratory
(e) Present address: Perkin Elmer Co., Hayward, CA 94545
(f) On leave from Institut National de Physique Nucleaire et de Physique des Particules, France
(g) Present address: Rutgers University, New Brunswick, NJ 08903
(h) Present address: CEBAF, Newport News, VA 23606
(i) Present address: Eidgenossische Technische Hochschule, Zurich, Switzerland

ABSTRACT

We report on preliminary results of direct electron pair measurements in p+Be at 4.9 GeV and 2.1 GeV and Ca+Ca at 1.95 GeV/A collisions at the Bevalac. The results are compared to existing data in p+Be at 12.1 GeV and π^-p at 15.9 and 16.9 GeV.

PHYSICS OBJECTIVES

The dilepton spectrometer (DLS) program deals with the study of electron pair production in p-nucleus and nucleus-nucleus collisions at the Bevalac. Dileptons have been extensively studied in hadron-hadron and hadron-nucleus collisions at high incident energies. A typical mass spectrum exhibits the vector meson resonance peaks on top of a continuum which, for the high mass domain, is well understood in term of the Drell-Yan mechanism. Below 2-3 GeV, the continuum is much larger than that calculated from the Drell-Yan formula or from the decays of known resonances. Lepton production has also been investigated in single-particle inclusive experiments. The direct lepton production rate (after subtraction of the contributions from the decays of known particles or resonances) is expressed in term of the lepton-to-pion ratio at a given Pt. The e/π ratio (electron/pion) has been measured at the level of 10^{-4}, with a rise at low Pt, for various hadronic projectile-target combinations and for energies from about 10 GeV up to the ISR domain. A low energy experiment on pp at 800 MeV (ref. 1) has observed no direct single electron signal within the sensitivity of the apparatus of $e/\pi \simeq 10^{-6}$. Both low mass dileptons and low Pt single direct leptons are assumed to be of the same origin. The calculations which have been most successful in understanding the production rates and the features of the distributions are done in the framework of the soft parton models in which one considers that wee quarks and antiquarks centrally produced during the collision annihilate (with or without radiative corrections) and generate the dileptons (see for instance ref. 2).

The first objective of the DLS program follows the above considerations. It aims to establish the existence of direct electron pairs at Bevalac energies and to help in clarifying the mechanism(s) of their production. The second objective of the program is to use the dilepton

signal as a probe to gather information on the first stage of nucleus-nucleus collisions which has been well discussed in the talk by the previous speaker.

THE DILEPTON SPECTROMETER

The DLS experimental setup is installed on the Beam 30 line at the Bevalac. It consists of a segmented target (5 segments) and two symetric arms (Fig. 1), each arm including a large aperture dipole magnet, two scintillator hodoscopes for accurate time of flight measurement and triggering purposes, two segmented gas Cerenkov counters working at one atmosphere for electron identification and three drift chamber stacks for tracking (the stack D3 on each arm has at present not been implemented). The segmentation of the detector was designed for intermediate mass systems (Ca+Ca). It will be tested in an upcoming experiment on Fe+Fe and Nb+Nb collisions. Movable arrays of lead glass blocks located behind each arms are used for the Cerenkov counter calibration (electron efficiency and pion rejection power). The conical scattering chamber provides a minimum amount of material along the particle trajectories into the spectrometer and will facilitate the installation of a multiplicity detector (which will be done in 1988). The central ray of each arm is set at 40 deg to the beam direction, which roughly corresponds to electrons emitted at 90 deg in the nucleon-nucleon center-of-mass frame (for incident energies from 1.5 to 5 GeV/A).

The DLS simulation program makes use of the CERN GEANT3 library. It presently includes most of the characteristics of the detectors and in particular the tracking of the Cerenkov photons. It is used for the acceptance calculations which are run both on the LBL VAX's and on the Cray X-MP at the MFE Computer Center. Fig. 2 shows the DLS acceptance for electron pairs as a function of mass and Pt, integrated over rapidity Y. Our present evaluation of the acceptance (and therefore the

Fig. 1

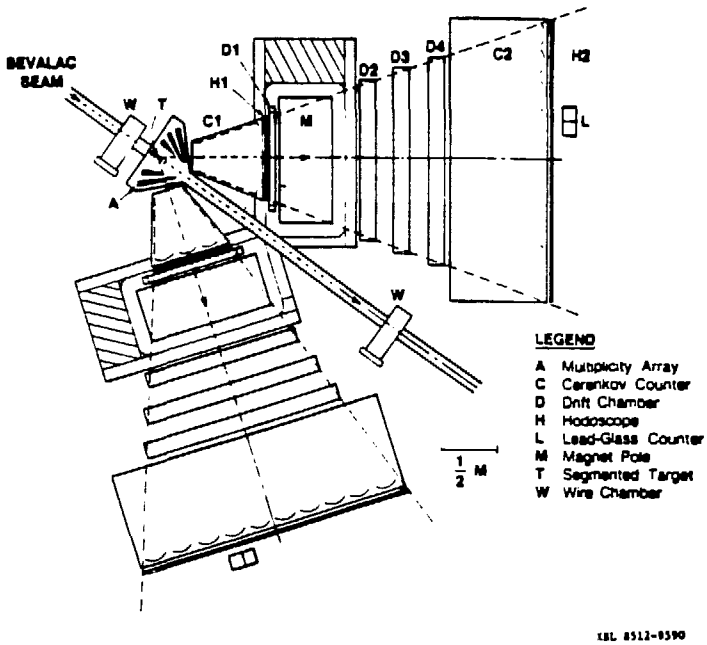
BEVALAC BEAM
D1
H1
W
T
C1
A
M
D2
D3
D4
C2
H2
L
W
LEGEND
A Multiplicity Array
C Cerenkov Counter
D Drift Chamber
H Hodoscope
L Lead-Glass Counter
M Magnet Pole
T Segmented Target
W Wire Chamber
1/2 M
XBL 8512-9590

Fig. 2

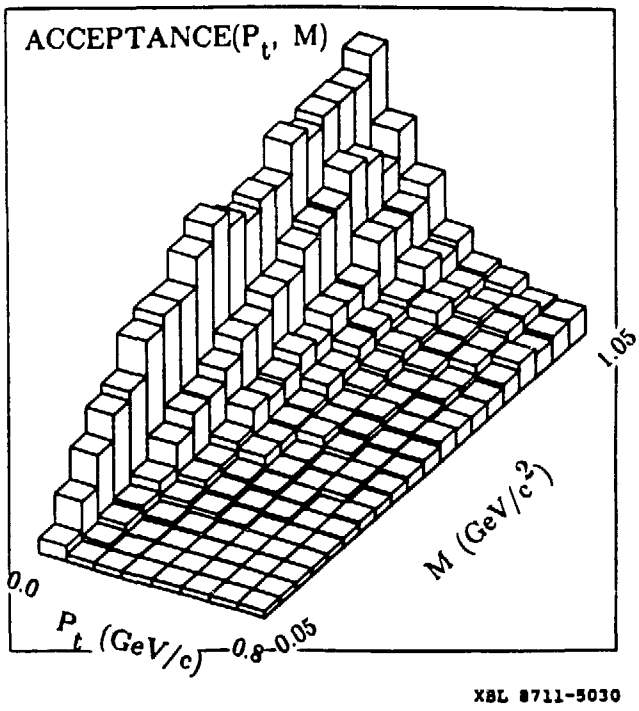
ACCEPTANCE(P_t, M)
1.05
M (GeV/c^2)
0.0
P_t (GeV/c) 0.8-0.05
XBL 8711-5030

cross section) suffers from low Monte Carlo statistics in the region where the acceptance is low (at low mass and high Pt).

PRELIMINARY PHYSICS RESULTS

The installation of the DLS was completed and tests were done in November 1986. Data were taken on the reaction p+Be at 4.9 GeV in December 1986, and p+Be at 2.1 GeV and Ca+Ca at 1.95 GeV/A in May 1987. The table below shows the pair statistics for the different runs. Because of a problem with the beam, we had to subtract an empty target contribution in the p+Be run at 2.1 GeV.

OS = number of opposite sign pairs
LS = number of like sign pairs
F = number of false pairs in the OS sample (F = LS)
T = number of true pairs (T = OS - LS)
σ_T = sigma of T

Reaction	OS	LS	T +/- σ_T	T/F	T/σ_T
p + Be at 4.9 GeV	732	201	531+/-31	2.6	17.4
p + Be at 2.1 GeV	567	148	419+/-27	2.8	15.7
MT	144	112	32+/-16	0.3	2.0
Ca + Ca at 1.95 GeV/A	94	45	49+/-12	1.1	4.2

The acquisition times and average beam intensities were:

Reaction	Time (hrs)	Intensity (p/spill)
p + Be at 4.9 GeV	33	2 X 10**8
p + Be at 2.1 GeV	20	3 X 10**8
Ca + Ca at 1.95 GeV/A	27	2-5 X 10**7

Fig. 3 shows the cross section $d\sigma/dM$ (per nucleon, assuming an $A^{q/3}$ dependence) for the p+Be reaction at 4.9 GeV. The main features of the mass distribution are a rapidly decreasing continuum above 300 MeV, a slight enhancement in the ρ region and a shoulder at low mass. The slope of the continuum agrees with the KEK data on p+Be at 12.1 GeV (3). The shoulder below 300 MeV is still under investigation and might be

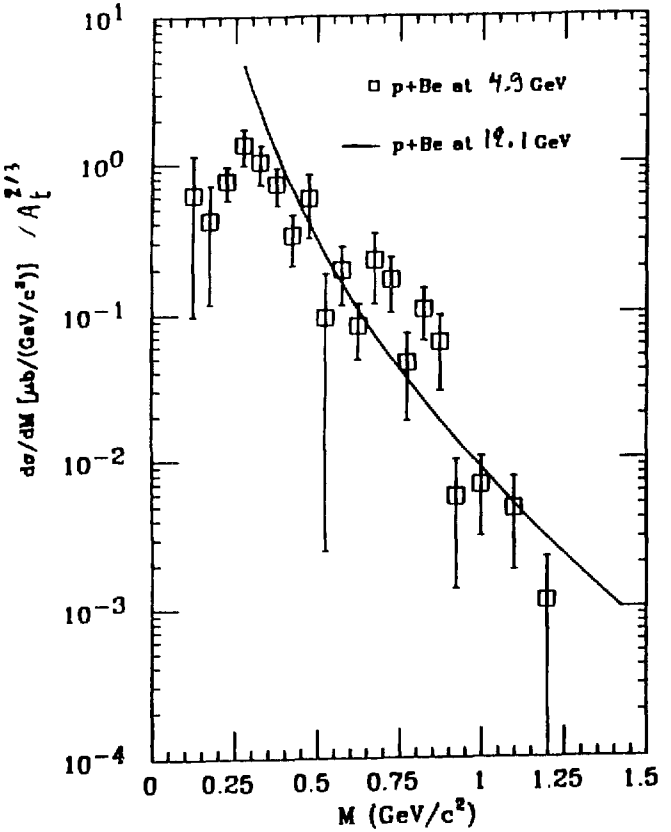
p+Be at 4.9 GeV
p+Be at 19.1 GeV
dσ/dM [μb/(GeV/c²)] / A_t^{2/3}
M (GeV/c²)

Fig. 3

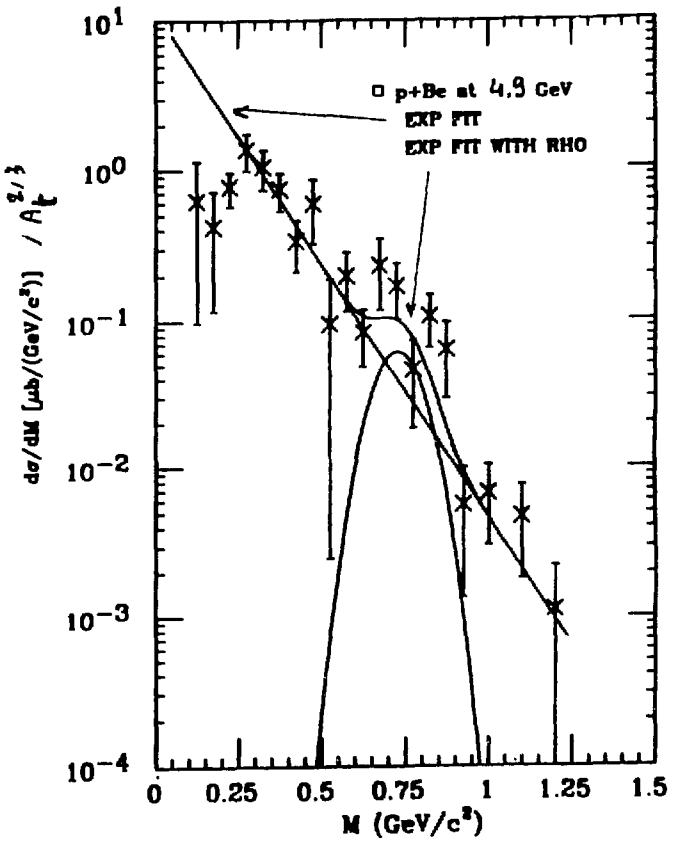
p+Be at 4.9 GeV
EXP FIT
EXP FIT WITH RHO
dσ/dM [μb/(GeV/c²)] / A_t^{2/3}
M (GeV/c²)

Fig. 4

due to an acceptance problem. Because of our decision to increase the DLS sensitivity and emphasize the detection of low mass pairs, the field in the dipoles was set quite low (1.5 kG) and thus the momentum resolution of the DLS was not optimized to see the ρ. We are planning a specific measurement with a higher field setting in the dipoles (3 or 5 kG). However, from the enhancement in the ρ region, we have estimated the cross section for the process p+Be --> ρ --> e^+e^- (see Fig. 4). This estimate compares well with existing data as shown below.

Existing data at 5.52 GeV/c (4):

$$\sigma(pp \rightarrow \omega) = .126 \pm .023 \text{ mb}$$
$$\sigma(pp \rightarrow \rho) = .07 \pm .05 \text{ mb}$$
$$\Longrightarrow \sigma(pp \rightarrow \{\omega, \rho\} \rightarrow e^+e^-) = 11.6 \pm 3. \text{ nb}$$

DLS at 4.9 GeV (5.8 GeV/c):

$$\sigma(pN \rightarrow \{\omega, \rho\} \rightarrow e^+e^-) = 10.4 \pm 5. \text{ nb}$$

Fig. 5 compares the cross section per nucleon $d\sigma/dPt^2$ from our measurement at 4.9 GeV (5.8 GeV/c) to the data points of Blockus et al. (ref. 5: π^-p at 15.9 GeV) and to a fit given by Adams et al. (ref. 6: π^-p at 16.9 GeV, fit given in arbitrary units). Both sets of data points have similar general features.

Fig. 6 shows the cross section per nucleon $d\sigma/dM$ for the p+Be reaction at 2.1 GeV. There may be a shoulder at low mass. The ρ contribution is no longer visible (note that the threshold in a free nucleon -nucleon collision is at 1.86 GeV incident kinetic energy). The shape of the continuum above 300 MeV is in qualitative agreement with the KEK data. Fig. 7 shows $d\sigma/dPt^2$ as a function of Pt^2 for the reaction Ca+Ca at 1.95 GeV/A. Adams' fit is also given on the figure for comparison.

Finally, the total cross sections have been obtained by integration of our differential cross section $d\sigma/dM$ above 100 MeV. The given values

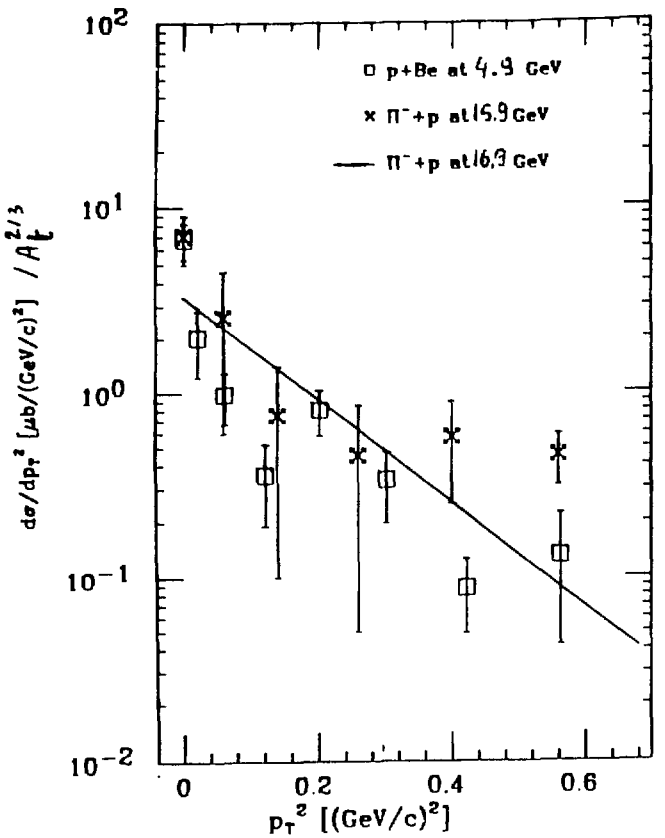
p+Be at 4.9 GeV
π⁻+p at 16.9 GeV
π⁻+p at 16.9 GeV
dσ/dp_T² [μb/(GeV/c)²] / A_t^{2/3}
p_T² [(GeV/c)²]

Fig. 5

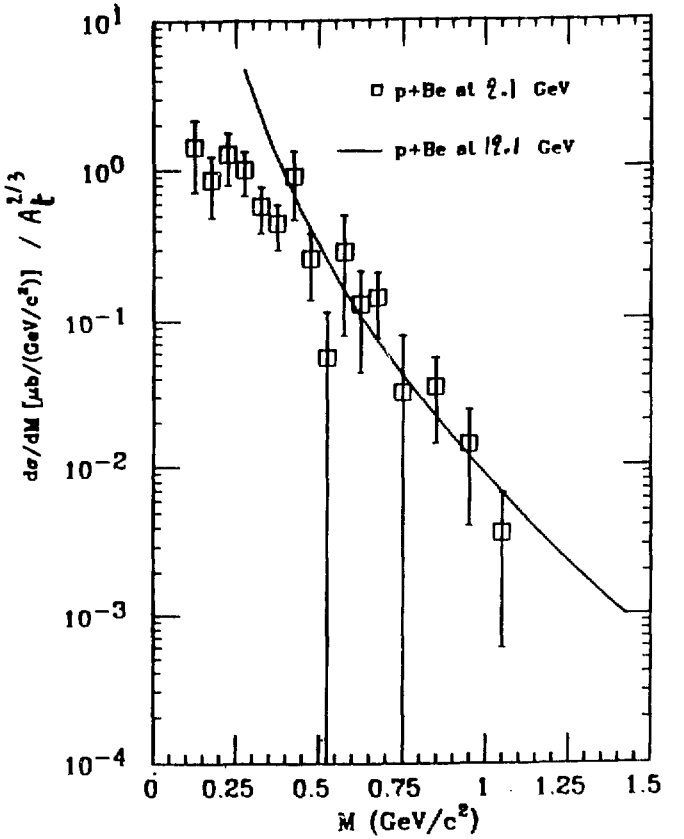
p+Be at 2.1 GeV
p+Be at 12.1 GeV
dσ/dM [μb/(GeV/c²)] / A_t^{2/3}
M (GeV/c²)

Fig. 6

below are actually the cross sections divided by $A_p \times A_t^{1/3}$, where A_p is the projectile mass and A_t the target mass. For comparison, we report the KEK cross section given in the paper and an estimate calculated from their fit.

Reaction	Total cross section (μb)
p + Be at 4.9 GeV	0.343 +/- 0.045
p + Be at 2.1 GeV	0.372 +/- 0.105
Ca + Ca at 1.95 GeV/A	0.771 +/- 0.196

KEK data: p + Be at 12.1 GeV

paper ---> .38 +/- .14 μb for 0.3 < mass < 0.7 GeV

integration of their fit above 0.2 GeV ---> 0.50 μb

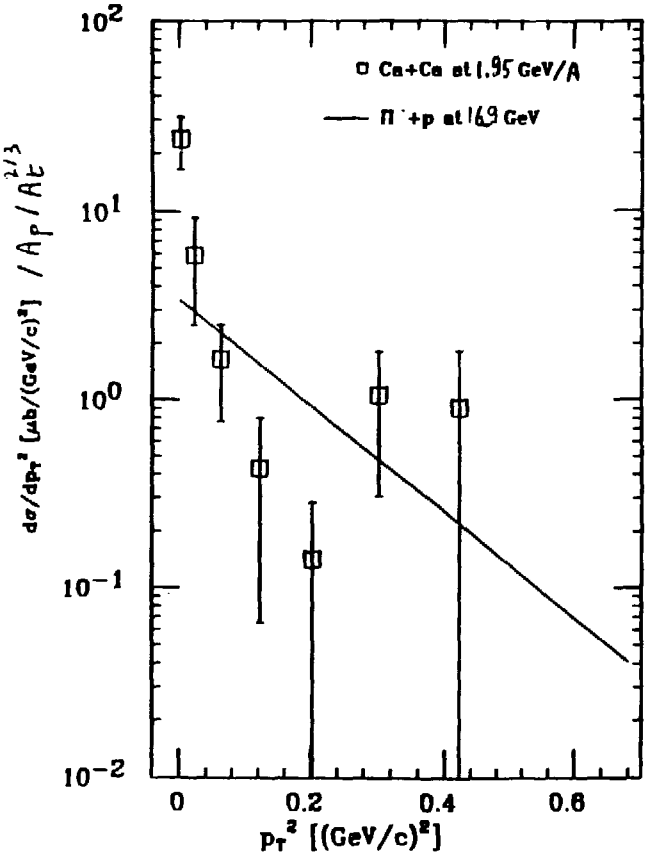

Fig. 7

CONCLUSION

We have established the existence of a direct electron pair signal down to about 2 GeV incident kinetic energy per nucleon, for both incident protons and Calcium nuclei. The cross sections are similar to what has been measured at higher energies. More work has to be done on the DLS acceptance and efficiency calculations before the figures are finalized and we can perform detailed comparisons and interpretation. The Ca+Ca data supports the feasability of measurement of intermediate mass systems in 100 to 150 hrs of Bevalac beam time.

ACKNOWLEDGMENTS

This work was supported by the Director, Office of Energy Research, Division of Nuclear Physics of the Office of High Energy and Nuclear Physics of the U.S. Department of Energy under Contract DE-AC03-76SF00098.

REFERENCES

(1) A. Browman et al., Phys. Rev. Lett. 37, 246 (1976)
(2) V. Cerny et al., Phys. Rev. D24, 652 (1981)
(3) S. Mikamo et al., Phys. Lett. 106B, 428 (1981)
(4) Particle Data Group, UCRL-20000 NN, August 1970
(5) D. Blockus et al., Nucl. Phys. B201, 205 (1982)
(6) M.R. Adams et al., Phys. Rev. D27, 1977 (1983)

NUCLEAR MATTER FLOW - THEORETICAL OVERVIEW *

George Fai
Kent State University, Kent OH 44242
Lawrence Berkeley Laboratory, Berkeley CA 94720

1 Introduction

The properties of the equation of state of nuclear matter influence the results of carefully chosen nuclear collision experiments. One manifestation of the equation of state, and probably the least controversial one, is the collective ordered motion, the **flow** of nuclear matter in the final stage of a nuclear collision. A large fraction of the discussion at this meeting is devoted to this phenomenon; and indeed, the flow should get a lot of attention, since, in my opinion, the observation of this collective behavior is the most important outcome of the experimental heavy ion program to date.

I was asked to give a theoretical overview on nuclear matter flow. There are two issues here: one is related to the prediction and observation of the flow, and the other concerns the relation of the *observed* collective flow to the basic physical properties of nuclear matter. The second subject, the connection of the flow to the static and dynamic properties of hot, dense nuclear matter, provides the main motivation for studying the flow. My contribution is divided into two parts corresponding to these two topics. Since however, nuclear matter properties and their implications are extensively discussed elsewhere in these Proceedings, and also because I don't want to be bogged down in arguments on the precise value of the nuclear incompressibility K, or of the critical temperature T_c, or of the viscosity η, I will mostly focus today on the phenomenological aspect of the question, the prediction and observation of nuclear matter flow.

This is a beautiful example of the continuing interaction between theory and experiment and illustrates how this interaction produces the advances in the field. Therefore, I feel obliged to review some history. I find it necessary to display the experimental development parallel to the theoretical work. I will cite selected steps in the process—only those, of course, that best fit in my line of argument. By no means should this be taken as a complete review.

2 Prediction and Observation of Nuclear Matter Flow

My broad picture of the history of predicting and observing nuclear matter flow is divided into the 'beginning' (through around 1980), and more recent history (from approximately 1981).

The successes of the liquid-drop description in explaining nuclear properties prompted the application of fluid-dynamics to nuclear collisions. Several people predicted collective, fluid-like behavior of nuclear matter in this framework [1–3]. Siemens and Rasmussen [4] argued that the sudden creation of hot dense matter leads to a blast wave associated with the explosion.

I wish to exploit the early predictions to give a qualitative definition of nuclear matter flow. The common feature of the models is that, in addition to the random, thermal motion of the products of a nuclear collision, they predict a collective (ordered) component in the motion of nuclear matter. I will call this ordered motion in the final state of a nuclear collision the **flow**.

Obviously, some ordered motion in the final state is trivial and uninteresting. For instance, the presence of spectators means ordered motion in the final state. Coulomb effects also introduce an ordering of the velocities. These effects should be separated from genuine consequences of nuclear matter properties. Although the blast-wave type radial expansion is very important, in this talk I will concentrate on collective sidewards emission or transverse flow.

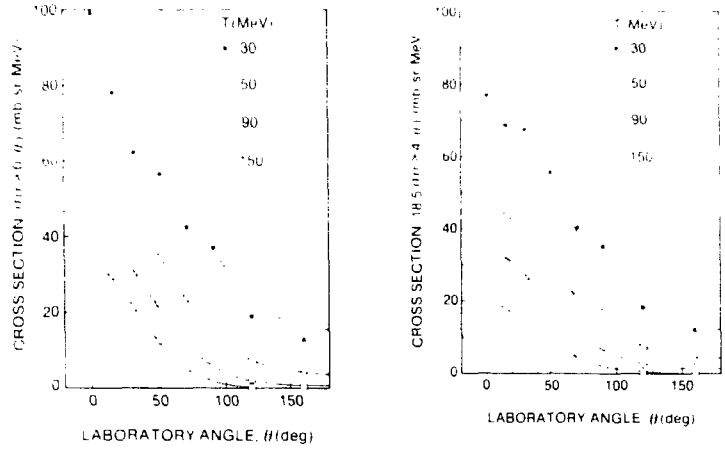

Figure 1: Inclusive (left) and multiplicity selected (right) neutron angular distributions for Ne + Pb at 390 MeV/nucleon.

Experimentally, the 'beginning' meant the measurement of inclusive single-particle spectra and claims that collective behavior is apparent from these [5,6].

Recent history is marked by the evolution of more exclusive experiments. I will only give a partial list of the most characteristic devices here. Many successful measurements were carried out at LBL with the Plastic Ball/Wall detector system. These data are nicely augmented by the data taken with the Streamer Chamber by several groups, including GSI-LBL, Riverside and MSU. The Diogene detector is collecting similar information at Saturne. Emulsion experiments (Minneapolis, Grenoble-Lund, Buffalo ...) provide additional insight.

2.1 Coulomb effects on inclusive proton spectra

The forward suppression of proton emission in central Ne + U collisions at 393 MeV/nucleon was observed in 1980 [6]. It was tempting to interpret the suppression as evidence for nuclear matter flow and this 'evidence' was used until recently in comparisons to fluid-dynamical calculations. However—as I will now show— it was premature to conclude at the time that collective flow has been observed.

First of all, the question can be addressed experimentally. Fig. 1. shows inclusive and multiplicity selected *neutron* angular distributions from Ne + Pb collisions at 390 MeV/nucleon, measured by the Kent State Users Group [7]. The different symbols represent the data at different outgoing neutron energies as indicated. The associated multiplicity of charged particles is denoted by r. The curves are the (normalized) result of a simple model calculation [8] to be discussed shortly. Comparing the slopes of the inclusive and multiplicity-selected neutron angular distributions, one can see that neutron emission does not show any forward suppression in central collisions.

One immediately suspects that Coulomb effects are (at least partly) responsible for the forward suppression of proton emission in central collisions. This was of course realized by a large number of people, e.g. Refs. [9–12]. I will show a couple more figures from Ref.[8]. Fig. 2a. displays calculated proton angular distributions for inclusive and central ($b \leq R_T - R_P$) Ne + U collisions at 393 MeV/nucleon with arbitrary normalization. The 'forward suppression' is evident for central collisions. Moreover, as shown in Fig. 2b, these simple calculations approximately reproduce the measured [6] shape of the angular distributions in central collisions.

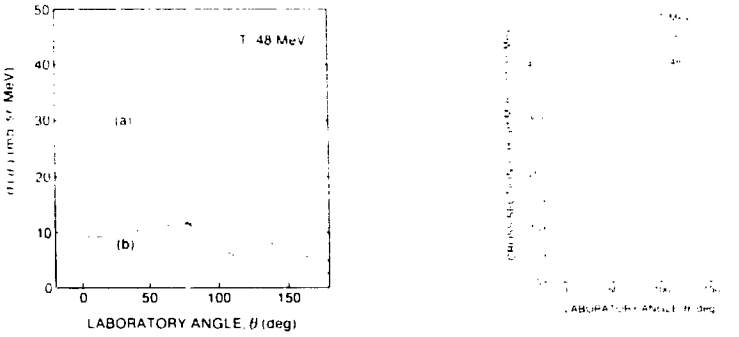

Figure 2: Central proton angular distributions for Ne + U at 393 MeV/nucleon, compared to inclusive angular distributions (left), and to data [6](right), as calculated in the simple model of Ref. [8].

The lesson to be learned from these figures is that more exclusivity is needed in the experiments in order to draw conclusions on the flow of nuclear matter. The response of the community to this (and other similar experiences) was to take a big step forward, to turn to more exclusive devices. Note, however, that the failure of inclusive single particle spectra (double differential cross sections) to reveal collective behavior does not tell us quantitatively *how much more* exclusivity is needed. I will return to this question.

2.2 First observation of collective flow and new methods of analysis

Fig. 3. is an example of the famous Plastic Ball/Wall results [13,14] representing the first observation of sidewards nuclear matter flow in sufficiently *heavy systems* and sufficiently *central collisions* (i.e. sufficiently high multiplicities). Note on the other hand, that there is no effect for exactly central ($b = 0$) collisions. The azimuthal symmetry is preserved in this case, and only radial flow is expected. The analysis displayed in Fig. 3. was carried out in terms of the kinetic flow tensor

$$F_{ij} = \sum_{\nu} \frac{p_i(\nu)p_j(\nu)}{2m(\nu)} \qquad (1)$$

introduced in Ref. [15] Here $p_i(\nu)$ denotes the i^{th} component of the three-momentum of fragment ν, whose mass is $m(\nu)$. The summation goes for as many detected fragments as possible (pions excluded). The flow tensor (1) is diagonalized, and the aspect ratios and orientation of the corresponding ellipsoid are used to characterize the flow [15]. In particular, the polar angle θ of the longest principal axis is called the flow angle. Note that this definition has inherent difficulties associated with it for close to spherical (and in particular for oblate) shapes. A given angle θ has to be weighted in a proper Jacobian-free manner; this was first pointed out in Ref. [16], and is reflected in the abscissa in Fig. 3. being $dN/d\cos\theta$.

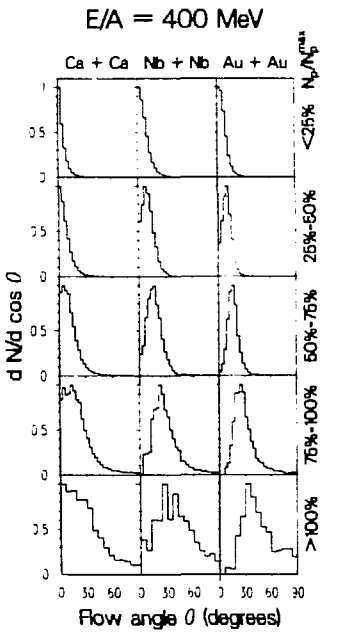

Figure 3: Flow angles [14]

In the first Plastic Ball/Wall paper reporting the observation of collective sidewards flow [13] approximately 50000 events of Nb + Nb collisions at 400 MeV/nucleon were analysed. Two separate phenomena, both representing ordered collective motion in the final state, were isolated: the

'bounce-off' of the spectators, and the 'side-splash' of the participants. In my opinion, these two important effects should be kept separate as much as experimentally possible. Unfortunately, the distinction gets less emphasis in later analyses and calculations.

Based on many similar experiments for different systems and different energies, the energy and mass number dependence of the flow angle can be studied. A compilation of the experimental results can be found in Ref. [17]. Moreover, introducing dimensionless variables and using fluid-dynamical concepts [18,19], the scaling behavior of the flow properties can be analysed. Ref. [17] contains the most complete such analysis to date.

Recently, more sensitive methods of analysis have been introduced. The transverse-momentum analysis of Danielewicz and Odyniec [20] is the most widely used today. In this method, one first obtains the approximate reaction plane for each event. This is done by constructing

$$\mathbf{Q}^{\perp} = \sum_{\nu} \omega(\nu)\mathbf{p}^{\perp}(\nu) \tag{2}$$

where $\omega(\nu)$ is a weight factor. If $\omega(\nu)$ was one for each fragment and all fragments were detected, then $\mathbf{Q}^{\perp} = \mathbf{0}$ by transverse momentum conservation. If, however, $\omega(\nu)$ is chosen to be ± 1 for fragments emitted in the forward and backward hemispheres in the center of mass, respectively, then, in case of a sidewards emission pattern, $\mathbf{Q}^{\perp}$ will lie in the (approximate) reaction plane. Each event can then be rotated around the beam axis and the projected transverse momenta

$$p_x(\nu) = (\mathbf{p}^{\perp}(\nu) \cdot \frac{\mathbf{Q}^{\perp}}{\mid \mathbf{Q}^{\perp} \mid}) \tag{3}$$

can be defined. Finally, p_x/A is averaged in a rapidity bin and plotted as a function of the rapidity (in units of the beam rapidity in the center of mass). The characteristic S-shape of the emerging curve is a clear sign of nuclear matter flow, as shown in Ref. [20].

This method exhibits the flow in much smaller samples, and is therefore more appropriate for the analysis of e.g. emulsion and streamer chamber data. It was used successfully (with some modifications) e.g. in Refs. [21–23]. In [21], where emulsion data were examined with a pseudorapidity analysis (angles only) around 400 events proved to be sufficient to obtain the flow. In U + U collisions [22] 80 events in the streamer chamber produce a clear signal. The equivalence of the analyses based on the kinetic flow tensor (1) and the one based on projected transverse momenta (3) was experimentally demonstrated for sufficiently large samples (where both methods work) [24].

The transverse-momentum analysis was also used [14] to give a quantitative definition of the flow in terms of the slope of the above S-shaped curve at midrapidity:

$$F = \left(\frac{d\langle p_x/A \rangle}{d(y/y_p)} \right)_{y=0} \tag{4}$$

The quantity F has the dimensions MeV/c. The relation of the flow F to the flow angle θ and the aspect ratio R (length ratio of longest to shortest principal axes of the flow tensor (1)) was recently obtained in the framework of an almost-analytic transport model [25] as

$$F = y_p(R-1)\sin\theta\cos\theta \tag{5}$$

This relation, which is actually more general than the model in which it was deduced, shows that F vanishes if $\theta = 0$, $\theta = \pi/2$, or $R = 1$. In other words: (i) central ($b = 0$) collisions preserve azimuthal symmetry and don't lead to sidewards emission, and (ii) a completely spherical source does not produce sidewards flow.

Another method, the W_2 analysis was also introduced recently [26] for the study of collective effects. In this technique the variables

$$W_1 = \frac{\mid \sum_\nu \mathbf{p}^\perp(\nu) \mid}{\sum_\nu \mid \mathbf{p}^\perp(\nu) \mid} \tag{6}$$

and

$$W_2 = \frac{\mid \sum_\nu \mathbf{p}^\perp(\nu)/m(\nu) \mid}{\sum_\nu \mid \mathbf{p}^\perp(\nu)/m(\nu) \mid} \tag{7}$$

are first constructed. Then the summation is restricted to specific groups of particles (e.g. forward and backward hemispheres). The amount of collective azimuthal alignment between the groups and within the groups, respectively, is determined.

The W_2 analysis was used in a recent preprint [27] to demonstrate that the observed collective azimuthal alignment is not simply a consequence of momentum conservation. For this purpose a model calculation was required, that conserves momentum in each individual event. The authors utilized the standard version of the *FREESCO* event generator, available from the library of Computer Physics Communications [28]. In the next Section, I will describe a modified version of this event generator, designed to accommodate sideward collective flow.

2.3 The flow in *FREESCO*

The approximate microcanonical event generator *FREESCO* was developed in collaboration with Jørgen Randrup [29]. It is a statistical background model with minimal dynamical input. Our purpose in developing the model was to provide a tool for quick reference calculations, not to fit data. Experimental results and dynamical theories can be checked against this background calculation. The event generator is extensively used in the design of new experiments, too.

The physical input parameters of the model are related to the transport properties of nuclear matter, and should ideally be taken from a transport theory. These parameters, x, y and z, as we denote them, vary between zero and one, and describe a wide range of physical scenarios with respect to energy- and momentum-sharing among the subsystems (participants and spectators) created in the collision. In particular, the parameter z, related to transverse momentum sharing, describes the 'bounce-off' of the spectators. The values of the parameters are expected to depend on the beam energy, since the efficiency with which the nuclear system equilibrizes energy and momentum clearly depends on the beam energy. In lieu of a transport-theoretical derivation, these parameters were tuned to Plastic Ball/Wall data at 400 MeV/nucleon by Art Poskanzer [14]. It turned out that additional parameters were required to describe the 'side-splash' of the participants. These input parameters have been introduced as the flow velocity vector $\mathbf{w}$ in the reaction plane. (The theoretically generated events of course always have a well-defined reaction plane.) The polar angle θ_w is taken to be

$$\tan\theta_w = \sqrt{\frac{1-\bar{b}}{\bar{b}}} \tag{8}$$

where $\bar{b} = b/(R_P + R_T)$ is the dimensionless impact parameter. This form was found to best fit the data in Ref. [13]. The magnitude of $\mathbf{w}$ should be separately fitted at all energies. To model the 'side-splash', an energy, corresponding to $\mathbf{w}$ is removed from the available energy of the participant source. The participant source is assumed to disassemble with this energy. After the randomly oriented (statistical) component of the velocity of a given fragment $\mathbf{v}_{0\alpha}$ is assigned according to the available microcanonical phase space, the fragment is also endowed with an ordered velocity

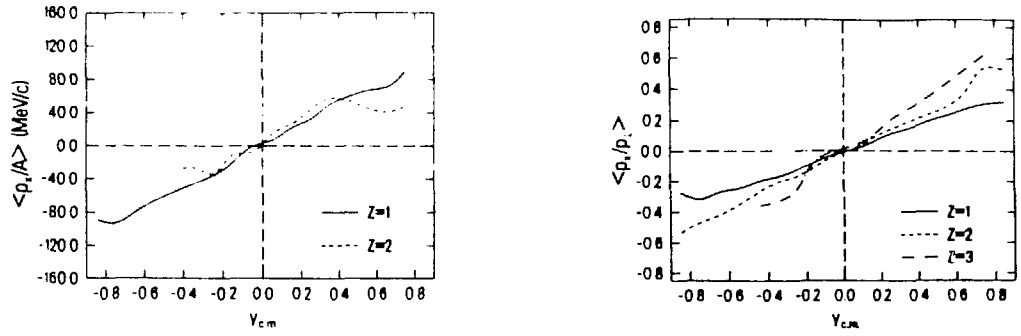

Figure 4: Transverse momenta per nucleon $\langle p_x/A \rangle$ (a) and transverse momentum alignment $\langle p_x/p_\perp \rangle$ for 200 MeV/nucleon Au + Au collisions. Data are from Ref. [34,35].

component ensuring total energy and momentum conservation. The total velocity of fragment α is taken to be

$$\mathbf{v}_\alpha = \mathbf{v}_{0\alpha} + (\hat{\mathbf{v}}_{0\alpha} \cdot \hat{\mathbf{w}})\mathbf{w} \tag{9}$$

where $\hat{\mathbf{v}}_{0\alpha}$ and $\hat{\mathbf{w}}$ denote unit vectors in the respective directions.

The apparent need to introduce the flow velocity vector w in *FREESCO* illustrates the usefulness of a phase-space model. The characteristic deviation of the data from the statistical background provides evidence for the flow. Once a new phenomenon is well understood, it is of course useful to incorporate it in the background to facilitate the search for other deviations, potentially signaling other interesting effects.

2.4 Fragment flow

It is expected that heavier fragments exhibit a stronger collective sidewards flow than protons: 'the fragments go with the flow'. This expectation is borne out in the framework of fluid-dynamical calculations [30,31] as well as in *FREESCO* [32] and in Quantum Molecular Dynamics (QMD) [33]. There are at least two simple reasons for this behavior: (i) at a given temperature, the thermal smearing of $p^\perp$ is larger for lighter fragments, and (ii) the assumption of a constant temperature is a simplification even in the case of one source; in colder regions, which produce heavier fragments more abundantly, the contribution of ordered motion is more important than in regions of higher temperature. The first effect is incorporated in *FREESCO*.

In Ref. [32] the analysis was carried out in terms of the flow angle. Recently, new data became available [34,35] in terms of the transverse momentum analysis. In Fig. 4. I display the prediction of *FREESCO* for $\langle p_x/A \rangle$ and for $\langle p_x/p_\perp \rangle$ for 200 MeV/nucleon Au + Au collisions in a selected multiplicity bin (MUL3 of the experiment), [1] to facilitate comparison with the data. I show $Z = 1, 2$ and 3 fragments only, since for for fragments with $Z \geq 6$ the statistics becomes very poor in the 10000 events generated. Comparison to the data [34–36] indicates that *FREESCO* produces the right trend of the Z-dependence. The fact that the flow (in particular for heavier fragments) appears quantitatively too small, while the alignment for protons is about right, is consistent with the observation that *FREESCO* does not incorporate all effects responsible for this behavior.

[1] Note, however, that the data refer to the multiplicity of detected fragments, while the cut is made on the total multiplicity in the calculation.

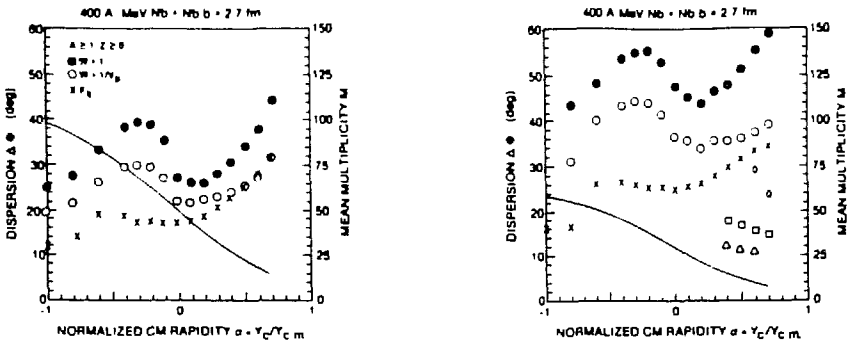

Figure 5: Fluctuations of the estimated reaction plane as a function of the rapidity cut using all fragments (left) and with cuts on the fragment mass and charge (right).

2.5 Optimal degree of exclusivity

Notice that in the transverse momentum analysis the exclusive information is only used to obtain the azimuth of the reaction plane. More generally, the main observables used to date to extract information on the nuclear equation of state (pion excitation functions, composite fragment yields and in-plane transverse momenta) require the determination of *triple differential* **single particle** cross sections. This prompted Miklos Gyulassy, Wei-ming Zhang and myself to compare the efficiency of different methods to extract the reaction plane [37]. Once the azimuth of the reaction plane is determined, we have the necessary reference frame to measure triple differential single particle cross sections. The methods we compared are basically the ones mentioned earlier: the kinetic flow analysis [15], a transverse velocity analysis that is a simplified version of the transverse momentum analysis [20], the pseudorapidity analysis [21] and an analysis using the fragments of the projectile [38].

Based on the experimental results [13,14,22,39] and on the theoretically required sensitivity [40] we estimate [37] that the reaction plane needs to be determined with an accuracy of $\Delta\Phi \leq 35 - 45$ degrees. In Fig. 5. I show the accuracy reached by several methods listed above (crosses: kinetic flow tensor analysis, dots and open symbols: transverse velocity analysis with weight factors as shown in Fig. 5a.) in an illustrative example of 2500 *FREESCO* events for 400 MeV/nucleon Nb + Nb collisions at $b = 2.7$ fm impact parameter with the event generator tuned to Plastic Ball/Wall data [14]. A rapidity cut y_c was introduced to study the effects of less than 4π acceptance by measuring fragments with $y > y_c$. Fig. 5a. displays the dependence of the root mean squared fluctuation of the estimated reaction plane as a function of the rapidity cut, taking all fragments (except pions) into account in the analysis, while Fig. 5b. contains similar results with more restrictive cuts on the fragment mass and charge. Also shown is the multiplicity of fragments used in the analysis for a given rapidity cut (solid line, right scale).

The projectile fragment transverse velocity analysis can provide the required resolution for intermediate impact parameters in collisions involving $A > 100$ nuclei. For more central collisions, the transverse velocity method can be used with a judicious choice of the weight factor and the rapidity cut. It is therefore possible to devise an experiment that is conceptually simpler than 4π measurements and may be able to provide more detailed information on nuclear matter flow than has been possible up to now. An optimal experiment would involve a high-resolution single-particle spectrometer together with a multiplicity array to constrain the magnitude of the impact parameter and a time-of-flight wall to determine the azimuth of the reaction plane. An experiment of the Kent State Users Group [41] along these lines has now been approved at the Bevalac.

3 Collective Flow and Basic Properties of Nuclear Matter

We study the flow in order to learn about the static and dynamic properties of hot and dense nuclear matter. The static properties can be thought about as expressed in the equation of state of nuclear matter. Present discussion mostly focuses on the incompressibility K [42,43], but there are further interesting quantities, like e.g. the specific heat C of nuclear matter, or the sound speed in nuclear matter u_s, that should be calculated in different models. The models should be used to connect the flow to these properties, and additional information about them should be sought from other observables.

A particularly interesting property of the equation of state is the liquid-vapor phase transition of nuclear matter. Since the phase diagram of any system interacting via van der Waals-type two-body forces possesses the characteristic two-phase structure, the question here is not the existence or non-existence of the phase transition, but, rather, the value of the critical temperature T_c and how we can observe the consequences of this structure in nuclear collision experiments. This problem is widely discussed both experimentally [44] and theoretically (e.g. [45]), and it would take a separate contribution to do justice to its literature. Let me only point out that, clearly, the phase transition is related to the fragmentation of nuclear matter [46].

With respect to the dynamic properties of nuclear matter, the transport coefficients (viscosity, heat conductivity, diffusion coefficients) need to be reliably calculated. The transport properties determine e.g. the physical input parameters of *FREESCO*. Again, there is a large amount of activity in this direction, and the spatial limitations of this contribution preclude a review.

Let me emphasize that the task is to evaluate the static and dynamic properties of nuclear matter away from the ground state, and determine the relationship of these properties to the flow data.

4 Concluding remarks

I have demonstrated that double differential single particle cross sections are insufficient to learn about the flow and the equation of state of nuclear matter. This is not meant to say that these relatively simple cross sections should not be measured! Quite to the contrary: ***absolute*** double differential cross sections need to be measured for heavy systems, in particular in the energy range best suited to the application of Boltzmann-equation based dynamical models (one to several hundred MeV/nucleon beam energy). Any dynamical model should reproduce these cross sections **simultaneously** with more complicated data.

Triple differential single particle cross sections carry most information utilized to date in connection with the flow and the equation of state of nuclear matter. To obtain the triple differential cross sections the reaction plane needs to be identified in each event with sufficient accuracy; several methods exist for this purpose which are conceptually simpler than 4π measurements. An experiment using the transverse-velocity method will be done at the Bevalac in 1988, but a wide range of similar systematic studies of triple differential cross sections is needed.

For specific investigations (in particular with higher intensity beams) more exclusive data will undoubtedly be useful. The HISS TPC [47], as a general purpose electronic streamer chamber, appears to be a very attractive device for this type of research at the present beam intensities.

The above three points indicate the need for more experimental work. On the theory side we need *clear* dynamical model calculations that consistently fit all available data and connect them to nuclear matter flow, the equation of state, and, in general, to the basic physical properties of hot and dense nuclear matter.

Discussions with A.F. Barghouty, W.M. Zhang and L.P. Csernai are gratefully acknowledged. This work was supported by the Director, Office of Energy Research, Division of Nuclear Physics of the Office of High Energy and Nuclear Physics of the U.S. Department of Energy under Grant No. DE-FG02-86ER40251 and under Contract No. DE-AC03-76SF00098.

References

[1] G.F. Chapline, M.H. Johnson, E. Teller and M.S. Weiss, Phys. Rev. **D8**, 4302 (1973).

[2] W. Scheid, H. Müller and W. Greiner, Phys. Rev. Lett. **32**, 741 (1974).

[3] A.A. Amsden, G.F. Bertsch, F.H. Harlow and J.R. Nix, Phys. Rev. Lett. **35**, 905 (1975).

[4] P.J. Siemens and J.O. Rasmussen, Phys. Rev. Lett. **42**, 880 (1979).

[5] H.G. Baumgardt, J.U. Schott, Y. Sakamoto, E. Schopper, H. Stöcker, J. Hofmann, W. Scheid and W. Greiner, Z. Phys. **A273**, 359 (1975).

[6] R. Stock, H.H. Gutbrod, W.G. Meyer, A.M. Poskanzer, A. Sandoval, J. Gosset, C.H. King, G. King, Ch. Lucker, Nguyen Van Sen, G.D. Westfall and K.L. Wolf, Phys. Rev. Lett. **44**, 1243 (1980).

[7] R. Madey, J. Varga, G. Fai, A.F. Barghouty, B.D. Anderson, A.R. Baldwin, R.Cecil, J.W. Watson and G.D. Westfall, Phys. Rev. **C34**, 1342 (1986).

[8] A.F. Barghouty and G. Fai, Phys. Rev. **C35**, 950 (1987).

[9] M. Gyulassy and S.K. Kauffmann, Nucl. Phys. **A362**, 503 (1981).

[10] M. Bawin and J. Cugnon, Phys. Rev. **C25**, 387 (1982).

[11] O. Scholten, H. Kruse and W.A. Friedman, Phys. Rev. **C26**, 1339 (1982).

[12] W.A. Friedman, Phys. Rev. **C29**, 139 (1984).

[13] H.A. Gustafsson, H.H. Gutbrod, B. Kolb, H. Löhner, B. Ludewigt, A.M. Poskanzer, T. Renner, H. Riedesel, H.G. Ritter, A. Warwick, F. Weik and H. Wieman, Phys. Rev. Lett. **52**, 1590 (1984).

[14] K.G.R. Doss, H.A. Gustafsson, H.H. Gutbrod, K.H. Kampert, B. Kolb, H. Löhner, B. Ludewigt, A.M. Poskanzer, H.G. Ritter, H.R. Schmidt and H. Wieman, Phys. Rev. Lett. **57**, 302 (1986).

[15] M. Gyulassy, K. Frankel and H. Stöcker, Phys. Lett. **110B**, 185 (1982).

[16] P. Danielewicz and M. Gyulassy, Phys. Lett. **129B**, 283 (1983).

[17] A. Bonasera, L.P. Csernai and B. Schürmann, preprint, MSUCL-601 (1987).

[18] N. Balázs, B. Schürmann, K. Dietrich and L.P. Csernai, Nucl. Phys. **A424**, 605 (1984).

[19] A. Bonasera and L.P. Csernai, Phys. Rev. Lett. **59**, 630 (1987).

[20] P. Danielewicz and G. Odyniec, Phys. Lett. **157B**, 146 (1985).

[21] L.P. Csernai, P. Freier, J. Mevissen, H. Nguyen and L. Waters, Phys. Rev. **C34**, 1270 (1986).

[22] D. Beavis, S.Y. Chu, S.Y. Fung, W. Gorn, D. Keane, Y.M. Liu, R.T. Poe, G. VanDalen and M. Vient, Phys. Rev. **C33**, 1113 (1986).

[23] J. Gosset *et al.*, Saclay preprint, DPh-N/Saclay 2469B (1987).

[24] H.G. Ritter, K.G.R. Doss, H.A. Gustafsson, H.H. Gutbrod, K.H. Kampert, B. Kolb, H. Löhner, B. Ludewigt, A.M. Poskanzer, A. Warwick and H. Wieman, Nucl. Phys. **A447**, 3c (1985).

[25] B. Schürmann and W. Zwermann, preprint, TUM-TP 200 (1987).

[26] P. Beckmann, H.A. Gustafsson, H.H. Gutbrod, K.H. Kampert, B. Kolb, H. Löhner, A.M. Poskanzer, H.G. Ritter, H.R. Schmidt and T. Siemiarczuk, Mod. Phys. Lett. **A2**, 163 (1987).

[27] R. Bock, H.H. Gutbrod and T. Siemiarczuk, preprint, GSI-87-48 (1987).

[28] G. Fai and J. Randrup, Comp. Phys. Comm. **42**, 385 (1986).

[29] G. Fai and J. Randrup, Nucl. Phys. **A404**, 551 (1983).

[30] H. Stöcker, A.A. Ogloblin and W. Greiner, Z. Phys. **A303**, 259 (1981).

[31] L.P. Csernai, H Stöcker, P.R. Subramanian, G. Graebner, A. Rosenhauer, G. Buchwald, J.A. Maruhn and W. Greiner, Phys. Rev. **C28**, 2001, (1983).

[32] L.P. Csernai, G. Fai and J. Randrup, Phys. Lett. **140B**, 149 (1984).

[33] G. Peilert, A. Rosenhauer, H. Stöcker, W. Greiner and J. Aichelin, preprint, UFTP 202 (1987).

[34] K.G.R. Doss *et al.*, preprint, LBL-23758 (1987).

[35] K.H. Kampert, Ph. D. Thesis, Univ. of Munster (1986), and these Proceedings (1987).

[36] J.W. Harris, these Proceedings (1987).

[37] G. Fai, W. Zhang and M. Gyulassy, Phys. Rev. **C36**, 597 (1987).

[38] J.P. Bondorf, J.N. De, G. Fai and A.O.T. Karvinen, Nucl. Phys. **A430**, 445 (1984).

[39] R.E. Renfordt *et al.*, Phys. Rev. Lett. **53**, 763 (1984).

[40] H. Stöcker and W. Greiner, Phys. Rep. **137**, 278 (1986).

[41] R. Madey *et al.*, Bevalac Experiment 848H (1987).

[42] G.E. Brown, these Proceedings (1987).

[43] H. Stöcker, these Proceedings (1987).

[44] J.E. Finn *et al.*, Phys. rev. Lett. **49**, 1321 (1982).

[45] J. Aichelin, these Proceedings (1987).

[46] G. Fai, L.P. Csernai, J. Randrup and H. Stöcker, Phys. Lett. **164B**, 265 (1985).

[47] H. Wieman, these Proceedings, (1987).

FLOW ANALYSIS FROM STREAMER CHAMBER DATA*

H. Ströbele,[a] P. Danielewicz,[e] G. Odyniec,[b] R. Bock,[a]
R. Brockmann,[a] J. W. Harris,[b]+ H. G. Pugh,[b]++
W. Rauch,[d] R. E. Renfordt,[c] A. Sandoval,[a] D. Schall,[c]
L. S. Schroeder,[b] and R. Stock[d]

[a]Gesellschaft für Schwerionenforschung
Planckstrasse 1, D-6100 Darmstadt 11, West Germany

[b]Lawrence Berkeley Laboratory, University of California
Berkeley, CA 94720, USA

[c]Institut für Hochenergiephysik, Universität Heidelberg
D-6900 Heidelberg, West Germany

[d]Fachbereich Physik, Universität Frankfurt
D-6000 Frankfurt, West Germany

[e]Institute of Theoretical Physics, Warsaw University
ul. Hoza 69, 00-681 Warsaw, Poland

*This work was supported in part by the Director, Office of Energy Research, Division of Nuclear Physics U. S. Department of Energy under Contract DE-AC03-76SF00098, and by the Polish Ministry of Science and Higher Education Research Problem CPBP 01.09.

+A.v. Humboldt Foundation Fellow with University of Frankfurt

++A.v. Humboldt Foundation
U.S. Senior Scientist award recipient with University of Frankfurt

Collective flow is now a well established phenomenon in high energy nucleus-nucleus collisions[1,2]. This is mainly due to the advent and successful operation of 4π-detectors like the Plastic Ball[3,4] and the Streamer Chamber[5]. In this contribution we present results from the Streamer Chamber with Ar, La beams at 800 MeV/nucleon on KCL, La and Pb targets[6]. We analyze the data in the spirit of a reformulated transverse momentum method. The evaluation[7] of mean transverse momenta in the true reaction plane is based on the presumption that a dominant correlation between particle transverse momenta, contributing to the scalar product of momenta, is due to the anisotropies of momentum distributions associated with the reaction plane. This is equivalent to the requirement that the mean two-particle scalar product factorizes. In this framework the in-plane transverse momentum and the mean sphericity matrix are determined free of finite particle number effects. For a detailed description of the method see Reference [6].

The data were taken with the streamer chamber facility at the BEVALAC. The standard trigger on the absence of leading fragments selected central collision events ($b < 2.4$ fm for Ar+KCl, $b < 8.5$ fm for La+La and $b < 5.5$ fm for Ar+Pb). An unbiased sample of events in each reaction was selected for a measurement of all charged particles. Table I gives details of the event samples. Particle identification in all three reactions is based on two independent methods which cover different regions in phase space[8,9]. The first method relies on the correlation between the velocity of a charged particle and the energy loss in the streamer chamber gas exhibited in track brightness and streamer density. Visual inspection of track density permits separation of π^+ from proton up to laboratory momenta of 500 MeV/c. Protons are separated from deuterons in the momentum range of 800 MeV/c to 1700 MeV/c. The latter separation, however, is not completely quantitative because of smaller differences in ionization[8] combined with problems from track superposition in high multiplicity events.

The second method of particle identification is based on kinematic considerations, together with the fact that in the interesting energy range the particle spectra from central collisions are fairly well described by a thermal fireball formed from participating baryons. For symmetric collisions at 800 MeV/nucleon, the kinematic particle identification proceeds in several

Table I. Track statistics in the reactions at 0.8 GeV/nucleon and at 1.8 GeV/nucleon. (a) All tracks. (b) Tracks in the forward c.m.s. hemisphere.

Reaction	Ar + Pb		Ar + KCl		La + La		Ar + KCl
	a	b	a	b	a	b	(1.8 GeV/nucl)
Number of events	956		1206		217		496
Number of tracks per event							
... extrapolated (see text)	58.0	25.7	31.0	18.3	103.0	59.0	42.3
... seen	49.6		29.3		80.2		40.7
... reconstructed	46.4		28.3		71.1		38.0
Percentage of rejected tracks							
due to measuring errors	2.0%	1.1%					1.5%
due to $\Delta p_{lab} > p_{lab}/3$	2.0%	1.9%					0.2%
due to a bad vertex	1.8%	1.6%					2.0%
due to other reasons	3.2%	1.5%					2.7%
Number of π^- per event	2.4		1.3		4.0		4.6
Expected number of tracks in the forward c.m.s. hemisphere				19.3		61	

steps: (1) Laboratory momenta of the baryons are Lorentz transformed into the c.m. system, assuming that the baryons are protons. (ii) A cut in the c.m. momentum put at 780 MeV/c selects those particles that are likely not to be protons. (iii) The laboratory momenta of those particles are now transformed again into the c.m. system, assuming the deuteron mass. A similar procedure with a cut in the c.m. momentum put at 1560 MeV/c separates the particles that are considered tritons. The kinematic cuts lead to proton-deuteron separation for laboratory momenta above 1700 MeV/c in the very forward direction and above 1100 MeV/c at a laboratory angle of 45^{o}, with a certain overlap with the range of separation according to ionization. Figure 1 displays the proton and deuteron c.m. spectra in the c.m. angular range of 66^{o} to 90^{o}, for the Ar+KCl reaction. The smoothness of the deuteron spectrum indicates the consistency of the identification procedure, as otherwise the cut in proton c.m. momenta at 780 MeV/c should yield a discontinuity in the deuteron spectrum at around 100 MeV deuteron kinetic energy. Figure 2 displays the spectra for the La+La reaction. Here a discontinuity around 100 MeV is visible, due to reduced efficiency of particle separation by ionization measurement in pictures with high track density.

Figure 3 summarizes the deuteron identification in the symmetric reactions at 800 MeV/nucleon. The phase space of deuterons is projected onto the $y-p^{\perp}$ plane (y being determined in the laboratory frame assuming the deuteron mass). The shaded area represents the part of phase space in which the deuterons are identified. Specifically, in most of the forward hemisphere and at large transverse momenta in the backward hemisphere, deuterons are identified by the kinematic cut procedure. This leaves a ~ 10% contamination by protons. In the remaining part of the forward hemisphere, and some of the backward hemisphere, deuterons are identified by the visual inspection procedure.

The results on the mean transverse momenta in the reaction plane are given in Table II and Fig. 4. The average forward in-plane transverse momenta per nucleon are seen to increase with the mass of the colliding system, from about 50 MeV/c for the Ar+KCl system, through 70 MeV/c for La+La, up to about 140 MeV/c for Ar+Pb, cf. Table II. For the flow defined as a slope of $\langle p^{x}/a \rangle$, with respect to the normalized rapidity, we find ~ 100 MeV/c for the Ar+KCl reaction, and ~ 140 MeV/c for the La+La reaction.

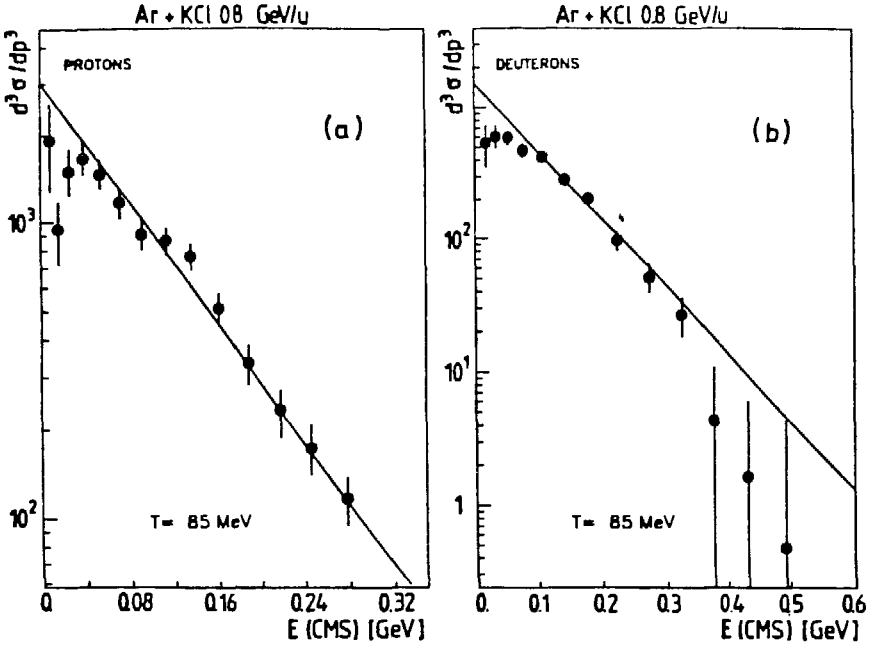
Ar + KCl 0.8 GeV/u
PROTONS
(a)
T= 85 MeV
E (CMS) [GeV]
Ar + KCl 0.8 GeV/u
DEUTERONS
(b)
T= 85 MeV
E (CMS) [GeV]

Fig. 1

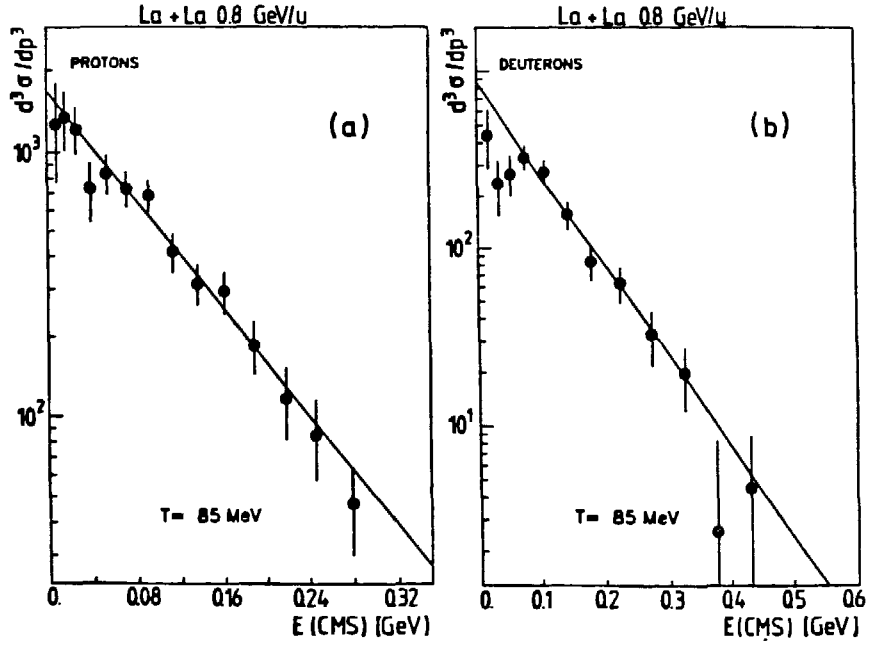
La + La 0.8 GeV/u
PROTONS
(a)
T= 85 MeV
E (CMS) [GeV]
La + La 0.8 GeV/u
DEUTERONS
(b)
T= 85 MeV
E (CMS) [GeV]

Fig. 2

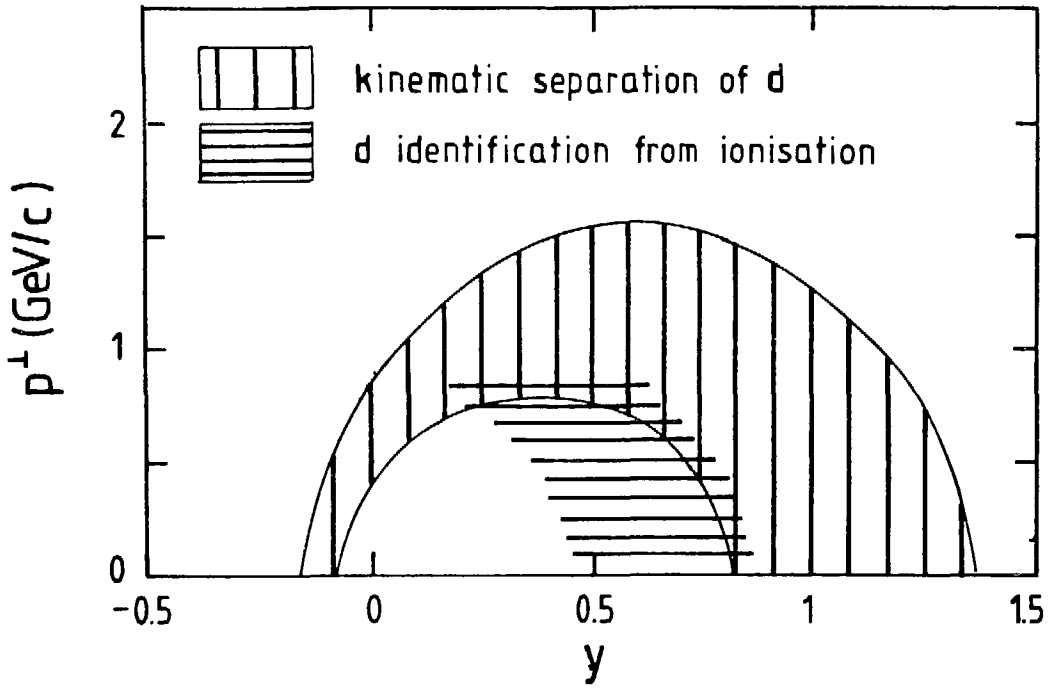

Fig. 3

Table II Mean transverse momenta in the reaction plane in the forward rapidity region $y > y_c + \delta$. For the reactions at 0.8 GeV/nucleon, transverse momenta are evaluated from deuterons only and $\delta = 0.15$. For the Ar+KCl reaction at 1.8 GeV/nucleon $\delta = 0.3$ (cf. Ref. 7). Mean pion momenta evaluated with same weighting as used for baryons, are also given. The adopted multiplicity criteria approximately halve the samples of events for the reactions.

Reaction	Events	$\langle p^x/a \rangle_{y>y_c+\delta}$ [MeV/c/nucl]	$\langle \omega p^x \rangle_{\pi^-}$ [MeV/c]	$\langle \omega p^x \rangle_{\pi^+}$ [MeV/c]
Ar + KCl	all	50 ± 4	-4 ± 7	4 ± 6
0.8 GeV/nucl	$M_p \leq 21$	44 ± 4		
	$M_p > 21$	56 ± 6		
La + La	all	72 ± 6	0 ± 5	7 ± 9
0.8 GeV/nucl	$M_p \leq 55$	78 ± 8		
	$M_p > 55$	66 ± 8		
Ar + Pb	all	139 ± 7	4 ± 5	11 ± 6
0.8 GeV/nucl	$M_p \leq 37$	122 ± 6		
	$M_p > 37$	156 ± 11		
Ar + KCl	all	95 ± 5	12 ± 8	4 ± 8
1.8 GeV/nucl				

As for the variation with bombarding energy, we observe that the average momenta in the Ar+KCl reaction rise from 50 MeV/c at 0.8 GeV/nucleon, through 70 MeV/c at 1.2 GeV/nucleon,[10] up to 95 MeV/c at 1.8 GeV/nucleon.[7] At the last bombarding energy[7] the average momenta $\langle p^x/a \rangle$ were determined from all identified nuclear fragments, as the kinematic conditions for particle separation were more favorable, and the number of deuterons was lower than in the reaction at 0.8 GeV/nucleon. In the asymmetric Ar+Pb reaction at 0.8 GeV/nucleon, it is seen in Fig. 4 that the results for $\langle p^x/a \rangle$ agree well with the predictions of the VUU calculation[11,12] with a stiff equation of state.

Transverse momenta in the reaction plane do not represent a complete picture of the momentum flow. Out of plane transverse momenta as well as longitudinal momenta have to be taken into account, which is achieved by constructing a sphericity tensor from the c.m. momenta. Table III summarizes the parameters of the average per nucleon sphericity matrix with a weight W = 1/p. Given are Θ, the angle between the longest tensor axis and the beam direction, and the ratios between the three tensor axes ($r = 2f_3/(f_1 + f_2)$, $r_{31} = f_3/f_1$ etc.) The relation between angle and elongation of the tensor is further shown in Fig. 5. Comparison with the Cugnon Cascade model[13] shows that the values of the flow angle from the cascade fall below the values inferred from the data for a given elongation of the tensor. With exception of the La+La reaction the average momenta in the reaction plane are significantly lower in the cascade model than in the data. For the symmetric reactions studied at 0.8 GeV/nucleon (Ar+KCl and La+La), the discrepancies are not as large as for the Ar+Pb or Ar+KCl reactions[7] at 1.8 GeV/nucleon. The measured momenta and angles are considerably lower than those from the ideal-fluid hydrodynamic model[14-17] at respective impact parameters or tensor elongations.

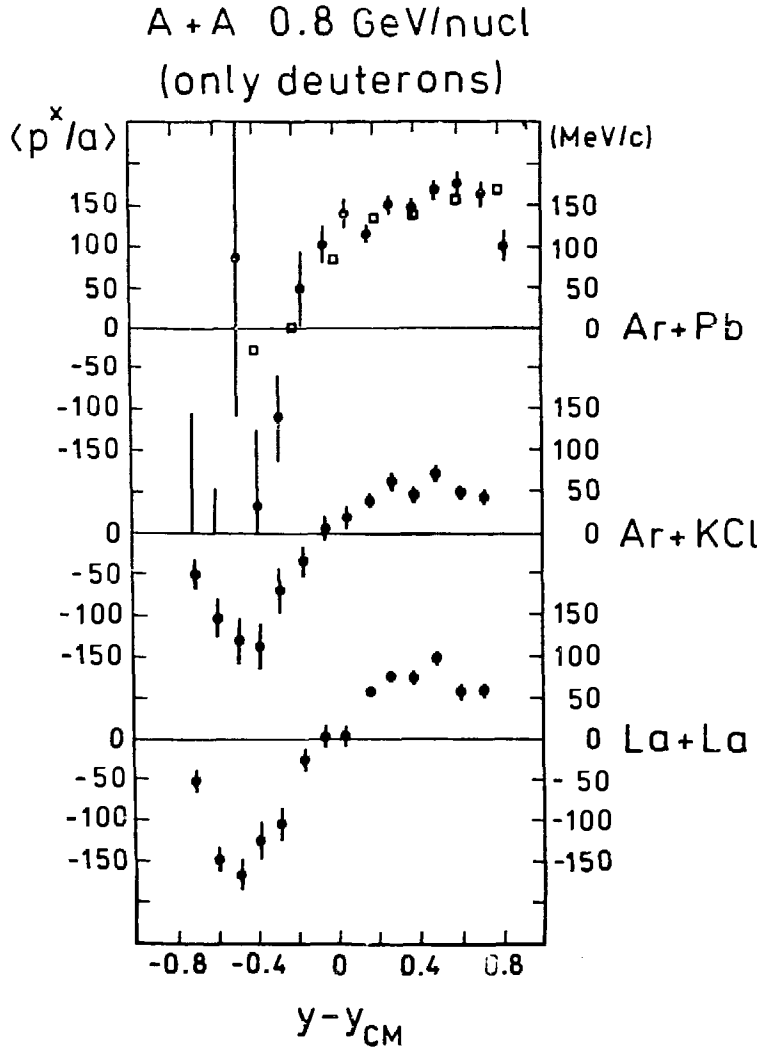
A + A 0.8 GeV/nucl
(only deuterons)
⟨p^x/a⟩
(MeV/c)
150
100
50
0
-50
-100
-150
Ar+Pb
Ar+KCl
La+La
-0.8
-0.4
0
0.4
0.8
y-y_CM

Fig. 4

Table III. Parameters of the average per-nucleon sphericity matrix with a weight w = 1/p.

Reaction	Events	θ_f [deg]	r_{31}	r_{32}	r_{21}	r
Ar + KCl 0.8 GeV/nucl	all	9.6 ± 0.8	2.96 ± 0.10	2.68 ± 0.07	1.11 ± 0.06	2.81 ± 0.04
	$M_p \leq 21$	7.2 ± 0.6	4.36 ± 0.20	3.75 ± 0.14	1.16 ± 0.09	4.03 ± 0.06
	$M_p > 21$	13.7 ± 1.2	2.17 ± 0.09	2.00 ± 0.07	1.09 ± 0.08	2.08 ± 0.04
La + La 0.8 GeV/nucl	all	16.5 ± 1.7	2.24 ± 0.10	2.09 ± 0.05	1.07 ± 0.05	2.16 ± 0.06
	$M_p \leq 55$	14.5 ± 1.7	2.69 ± 0.14	2.51 ± 0.08	1.07 ± 0.07	2.60 ± 0.08
	$M_p > 55$	19.3 ± 1.7	1.94 ± 0.08	1.80 ± 0.06	1.08 ± 0.06	1.87 ± 0.06
Ar + Pb 0.8 GeV/nucl	all	35.6 ± 1.8	1.96 ± 0.26	1.52 ± 0.07	1.28 ± 0.12	1.71 ± 0.14
	$M_p \leq 37$	28.8 ± 1.2	2.24 ± 0.15	1.85 ± 0.06	1.21 ± 0.07	2.03 ± 0.07
	$M_p > 37$	42.4 ± 1.4	1.8 ± 0.3	1.34 ± 0.10	1.36 ± 0.18	1.55 ± 0.18
Ar + KCl 1.8 GeV/nucl	all	8.5 ± 1.0	3.20 ± 0.11	3.16 ± 0.11	1.01 ± 0.06	3.18 ± 0.05

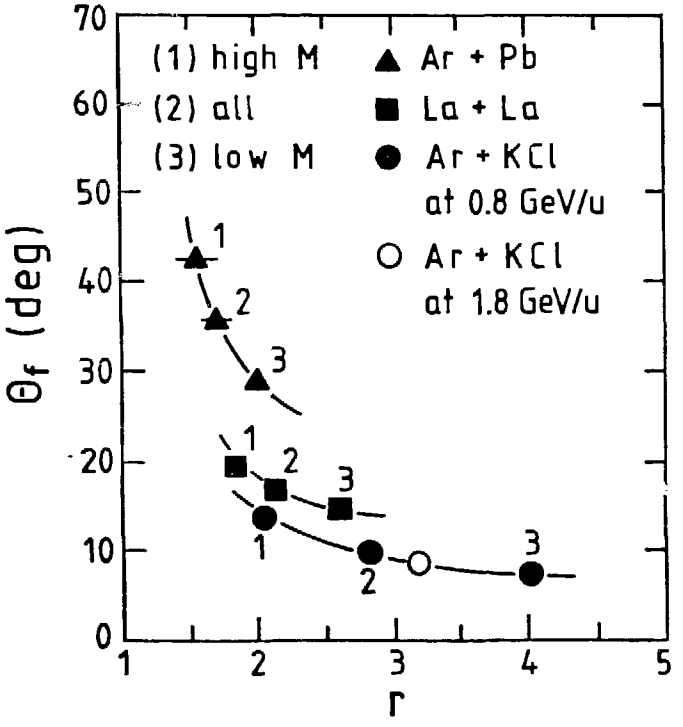

Fig. 5

FIGURE CAPTIONS

Fig. 1. C.m. energy spectra (in arbitrary units) for protons (a) and deuterons (b) emitted between 66° and 90° c.m. angle for the Ar+KCl reaction at 0.8 GeV/nucleon. The straight line is for a Maxwell-Boltzmann distribution with a temperature of 85 MeV. The spectra are corrected for contaminations with p(b), d(a), t, and He particles.

Fig. 2. C.m. energy spectra (in arbitrary units) for protons (a) and deuterons (b) emitted between 66° and 90° c.m. angle for the La+La reaction at 0.8 GeV/nucleon. The straight line is for a Maxwell-Boltzmann distribution with a temperature of 85 MeV. The spectra are corrected for contaminations with p(b), d(a), t, and He particles.

Fig. 3. The deuteron identification for symmetric reactions at 800 MeV/nucleon is illustrated by projecting the phase space of deuterons onto the $y\text{-}p^{\perp}$ plane (y being the laboratory rapidity); the horizontally shaded area results from the kinematic cuts (see text) and the vertically shaded area indicates the region of phase space where deuterons can be separated from protons on the basis of their ionisation.

Fig. 4. Mean transverse momenta per nucleon in the reaction plane as a function of rapidity. Open squares for the Ar+Pb reaction indicate a prediction of the VUU calculation (Refs. 11 and 12).

Fig. 5. Variation of the flow angle θ_f with elongation of the flow tensor $r = 2f_3/(f_1 + f_2)$.

REFERENCES

[1] H. A. Gustafsson, H. H. Gutbrod, B. Kolb, H. Löhner, B. Ludewigt, A. M. Poskanzer, T. Renner, H. Riedesel, H. G. Ritter, A. Warwick, F. Weik, and H. Wieman, Phys. Rev. Lett. 52, 1590 (1984).

[2] R. E. Renfordt, D. Schall, R. Bock, R. Brockmann, J. W. Harris, A. Sandoval, R. Stock, H. Ströbele, D. Bangert, W. Rauch, G. Odyniec, H. G. Pugh, and L. S. Schroeder, Phys. Rev. Lett. 53, 763 (1984).

[3] A. Baden, H. H. Gutbrod, H. Löhner, M. R. Maier, A. M. Poskanzer, T. Renner, H. Riedesel, H. G. Ritter, H. Spieler, A. Warwick, F. Weik, and H. Wieman, Nucl. Instr. and Meth. 203, 189 (1982).

[4] H. H. Gutbrod, H. Löhner, A. M. Poskanzer, T. Renner, H. Riedesel, H. G. Ritter, A. Warwick, F. Weik, and H. Wieman, Nucl. Phys. A400, 343c (1983).

[5] A. Sandoval, R. Bock, R.Brockmann, A. Dacal, J. W. Harris, M. Maier, M. E. Ortiz, H. G. Pugh, W. Rauch, R. E. Renfordt, F. Reiss, L. S. Schroeder, R. Stock, H. Ströbele, and K. L. Wolf, Nucl. Phys. A400, 365c (1983).

[6] P. Danielewicz et al., IFT/42/87, University of Warsaw Preprint.

[7] P. Danielewicz and G. Odyniec, Phys. Lett. 157B, 146 (1985) LBL-18600 Report.

[8] H. Ströbele, Nucl. Instr. and Meth. 221, 523 (1984).

[9] H. Ströbele, Kernmaterie in Schwerionenstössen, GSI-86-10 Report.

[10] D. Beavis, S. Y. Chu, S. Y. Fung, W. Gorn, D. Keane, Y. M. Liu, G. VanDalen, and M. Vient, Phys. Rev. C 33, 1113 (1986).

[11] J. J. Molitoris, D. Hahn, and H. Stöcker, Nucl. Phys. A447, 13c (1985).

[12] J. J. Molitoris and H. Stöcker, Phys. Lett. 162B, 47 (1985).

[13] J. Cugnon, Phys. Rev. C 22, 1885 (1980).

[14] H. Stöcker, L. P. Csernai, G. Graebner, G. Buchwald, H. Kruse, R.Y. Cusson, J. A. Maruhn, and W. Greiner, Phys. Rev. C 25, 1873 (1982).

[15] G. Buchwald, G. Graebner, J. Theis, J. Maruhn, W. Greiner, H. Stöcker, K. Frankel, and M. Gyulassy, Phys. Rev. C 28, 2349 (1983).

[16] L. P. Csernai, W. Greiner, H. Stöcker, I. Tanihata, S. Nagamiya, and J. Knoll, Phys. Rev. C 25, 2482 (1982).

[17] H. Stöcker and W. Greiner, Phys. Reports 137, 277 (1986).

Fragment Formation and Fragment Flow

J.W. Harris,[a] B.V. Jacak,[b] K.-H. Kampert,[c†] K.G.R. Doss,[a††] H.-A. Gustafsson,[c‡]
H. Gutbrod,[c] B. Kolb,[c] A.M. Poskanzer,[a] H.-G. Ritter,[a] H.R. Schmidt,[c] L. Teitelbaum,[a]
M. Tincknell,[a] S. Weiss[a] and H. Wieman[a]

[a] Lawrence Berkeley Laboratory, University of California, Berkeley, CA 94720, USA
[b] Los Alamos National Laboratory, Los Alamos, NM 87545, USA
[c] Gesellschaft für Schwerionenforschung, Darmstadt, West Germany

Abstract

Experimental results are presented on the production of light nuclei (Z = 1,2) and intermediate mass nuclear fragments ($3 \leq Z < 10$) over a large solid angle. The reactions Au + Au and Au + Fe were studied at 200 MeV/nucleon to provide information on fragment formation and fragment flow. In peripheral collisions most fragments are produced near the projectile and target rapidities. The fragment rapidity distributions shift toward midrapidity as the collisions become more central. An increased flow and alignment, both in momentum and position space, relative to the reaction plane is observed as the fragment mass increases: i.e., the fragments exhibit stronger flow effects than light particles.

1. Introduction

The study of fragment production in intermediate energy nucleus-nucleus collisions has recently become extremely interesting, particularly with the capability to study systems using very heavy nuclear beams from the Bevalac. A variety of models has been proposed predicting widely differing mechanisms for fragment formation with very little experimental data to distinguish between them. These mechanisms include fragment formation in a nuclear liquid-vapor phase transition,[1,2] in a gas of nucleons and fragments in equilibrium,[3,4,5] as a result of dynamic instabilities,[6] from partial- or non-equilibrium processes, [7,8] and from purely statistical processes.[9,10,11] Furthermore, a sidewards flow of light particles (Z=1,2) observed[12,13] in such collisions has been interpreted as evidence for the presence of collective phenomena in the form of decompression. A collective nuclear flow in relativistic nucleus-nucleus collisions was initially predicted in theoretical nuclear fluid dynamics[14,15,16]. Several calculations predict stronger collective flow effects for nuclear fragments than observed for light particles.[5,17,18] Previous experiments identifying heavier fragments have only studied single fragment inclusive distributions or correlations[19] other than fragment flow. In this work we present results from a large solid angle study [20] on the production of light particles (Z = 1,2) and intermediate mass fragments ($3 \leq Z \leq 9$). The results provide the first conclusive evidence that the fragments exhibit stronger flow effects than light particles as well as initial information on possible fragment formation mechanisms.

2. Experiment

The LBL/GSI Plastic Ball detector system [21] was upgraded to measure light and intermediate mass fragments ($2 < Z < 10$) over a large solid angle in reactions of 200 MeV/nucleon Au + Au and Au + Fe. The Plastic Ball consists of 815 CaF_2(ΔE)-Plastic Scintillator(E) telescope modules covering the angular region $10° \leq \theta_{lab} \leq 160°$ with hydrogen and helium isotope identification. Computer-controlled high voltage modules were implemented on the 160 Ball modules with $\theta_{lab} \leq 30°$, allowing online gain-matching and extension of the energy loss spectra to neon fragments. Unit separation of nuclear charges for $1 \leq Z < 10$ is obtained with isotope separation for $Z = 1$ and 2 as observed in Fig.1. In order to be identified, fragments must traverse the 4 mm thick CaF_2 which produces a low energy cut-off in the laboratory of approximately 35-40 MeV/nucleon. Since the velocity of the c.m. system corresponds to a 50 MeV/nucleon energy in the laboratory, the low energy cut-off is unimportant in the forward direction of the c.m. system ($\theta_{lab} \leq 30°$). In addition, there was a zero degree gas proportional chamber [22] covering 0 +/- 2 degrees in the laboratory. This detector with its five wire planes enabled extremely high position resolution for large projectile remnants.

3. Fragment Formation

Multiplicity distributions of fragments with $3 \leq Z < 10$, observed in the forward hemisphere of the center-of-mass frame in the Au + Au system, are displayed in Fig. 2. Events are divided into five bins of participant proton multiplicity[23] M, corresponding to $0 < M \leq 23$, $23 < M \leq 46$, $46 < M \leq 69$, $69 < M \leq 92$ and $M > 92$. These multiplicity bins are labelled MUL1, MUL2, MUL3, MUL4, and MUL5, respectively and range from peripheral collisions with few observed charges to central collisions with very high multiplicities. As seen in Fig.2 most peripheral collisions (MUL1) result in a low multiplicity of intermediate mass fragments. These fragments are observed to have energies close to that of the projectile, and a large projectile remnant is usually observed in the zero degree detector. Smaller remnants are observed as the charge multiplicity increases, corresponding to decreasing impact parameter.

In central collisions (MUL4 and MUL5) practically all of the projectile charge is observed in the form of light and intermediate mass fragments, with no large projectile remnant remaining. Many fragments produced in central collisions are emitted at large angles and with rapidities intermediate between those of the projectile and target. A near isotropic emission pattern is observed in the c.m. of single fragment inclusive distributions for near-central collisions (MUL4) with a smooth transition to isotropy in the most central ones(MUL5). This is expected for fragment production from the participant region of projectile-target overlap. As seen in Fig. 2

there are on the average 3-4 fragments in the forward hemisphere per event for central collisions. Extrapolation of this measurement to 4π leads to 8 or more intermediate mass fragments in central collisions, with a significant number of events producing as many as 20 fragments. These numbers are slight underestimates due to the low β cut-off for fragments at $\theta_{lab} < 10$. However, the total charge measured in the forward c.m. hemisphere for these two multiplicity bins sums to 80 to 90 percent of the projectile charge signifying that most of the fragments are observed. Further event-by-event fragment and light particle analysis will be necessary to learn details about the dynamics of these reactions.

4. Fragment Flow

In order to study the flow of fragments, the transverse momentum analysis technique[24] was employed to determine the reaction plane of each event. In this method the vector difference of the transverse momentum components of particles going forward and those going backwards in the c.m. is used together with the beam axis to define the reaction plane. This difference corresponds to the collective transverse momentum transfer in the c.m. The transverse momentum p_t of each particle is then projected onto the reaction plane, where the particle of interest has been excluded from determination of the plane (i.e. autocorrelations are removed), yielding the inplane transverse momentum, p_x. Displayed in Fig.3 is the inplane transverse momentum per nucleon p_x/A for light particles (Z = 1,2) and for fragments with $6 \leq Z \leq 9$ as a function of their rapidity. Positive and negative values of p_x/A correspond to opposite sides of the beam in the reaction plane. The forward-backward asymmetry is an artifact of experimental biases for low particle energies (near target rapidity) and spectator cuts made using the prescription of Ref. 23 in the projectile rapidity region. Since participant-spectator discrimination is not unique, the slopes of the curves at midrapidity in Fig.3 best characterize the flow.[25] The inplane transverse momentum per nucleon is observed to increase as a function of the mass of the observed particle or fragment.

For each particle the fraction of the particle's transverse momentum that lies in the reaction plane can be calculated. Displayed in Fig.4 is the mean value of the transverse momentum alignment $< p_x/p_t >$ in the MUL3 multiplicity bin for particles as a function of their rapidity for Z = 1,2,3 and 6. Fig.4 clearly shows that a larger part of the fragment's transverse momentum lies in the reaction plane as the fragment mass increases. The Z = 3,6 fragments are more aligned in the plane than the Z = 1,2 particles which have been interpreted to flow collectively[12,13,24,26–29].

The spatial correlation of the fragments with the reaction plane is presented in Fig.5. Shown are directivity plots of the azimuthal correlation of emitted light particles and fragments with the reaction plane. The angle plotted is the azimuthal emission angle of each particle or fragment with

respect to the reaction plane defined by the Z =1,2 light particles with autocorrelations removed. The left-hand column labelled MUL2 contains relatively peripheral collisions, and the right, MUL4, relatively central ones. Collisions at extremely large or small impact parameters result in poorly defined reaction planes and are not shown here. The two curves in each box correspond to rapidities of the emitted particles and fragments: near-midrapidity $0.32 < y < 0.42$ (circles) and near-projectile rapidity $0.52 < y < 0.62$ (crosses), where the projectile rapidity is 0.64. A strong azimuthal correlation is observed between all $Z \geq 2$ nuclei and the azimuthal direction of maximum collective momentum transfer in the flow plane, $\phi = 0$. The correlation is rather flat for $Z = 1$ and becomes increasingly stronger for heavier fragments. Projectile rapidity fragments are more correlated than midrapidity ones. The effect on projectile rapidity fragments is larger in central collisions than peripheral ones, whereas the midrapidity fragment correlations have very little dependence upon the centrality of the collision. In the limit of complete thermalization, azimuthally symmetric emission of midrapidity particles is expected. However, the presence of a correlation between fragments and the reaction plane suggests this picture to be too simple; dynamic compression-decompression effects are present for the midrapidity fragments and high multiplicity (central) events.

The observed correlations are predicted to arise from collective flow of matter in the collision. This should be more important for central collisions than peripheral ones, and a stronger correlation is indeed seen on the right side of Fig.5. The mass dependence of the correlation is also consistent with predictions of flow.[5,17,18,30] Studies of fragment flow may distinguish between the various proposed fragment formation mechanisms described earlier. One might expect that the correlations from collective motion would be somewhat diminished by the random thermal motion generated in such energetic collisions. However, this is not always the case. For a system of nucleons and fragments in thermal equilibrium at a fixed freezeout temperature, the thermal energy is equally partitioned. Thus, the thermal energy per nucleon in a fragment of mass A has a 1/A dependence. The flow energy, which is originally compressional energy built up in the early stages of the collision, should have a linear A dependence, i.e. the compressional energy per nucleon is independent of A. The final fragment energy will be the sum of the thermal and flow energies. Thus, the flow energy is an increasingly larger fraction of the fragment energy and the thermal energy less important as the fragment mass A increases. The observations in Figs.3-5 unambiguously demonstrate that the fragments exhibit stronger flow effects, both in momentum and position space, than do the lighter particles. Note, however, that it may not be possible to distinguish production of fragments in equilibrium models from coalescence of nucleons using the flow data alone, since the A dependence in both approaches is the same.[31]

5. Summary

Results from the first large solid angle measurement of fragment formation in peripheral and central heavy ion collisions have been presented. The events are characterized through the 4π measurement of the light charged particles, allowing the identification of multifragmentation events and analysis of the flow of the emitted nucleons and nuclear fragments. On the mean, 8-9 intermediate mass fragments ($Z \geq 3$) are produced in central Au + Au collisions at 200 MeV/n, with up to 20 possible. The transverse momentum per nucleon characterising the flow and the alignment of the fragments both in coordinate and momentum space relative to the reaction plane is observed to increase with the mass of the fragment. The observation of a stronger flow of fragments than that previously observed in light particles is particularly exciting and supports the early predictions of fluid dynamics of the existence of an enhanced collective flow of the heavier nuclear fragments in intermediate energy nucleus-nucleus collisions.

Acknowledgements

The authors wish to thank G. Claesson, R. Ferguson, A.I. Gavron, and J. Wilhelmy for assistance during the experiment, H. Crawford for assistance in the in-beam fragment calibration tests and F. Lefebvres for his contributions to data analysis. The continuous support of R. Bock is gratefully acknowledged. J.W.H. and A.M.P. acknowledge support from the Alexander von Humboldt Foundation of West Germany during part of this work. This work was supported by the Director, Office of Energy Research, Division of Nuclear Physics of the Office of High Energy and Nuclear Physics of the U.S. Department of Energy under contract DE-AC03-76SF00098.

†Permanent address: University of Münster, D-4400 Münster, West Germany.

††Present address: Linear Accelerator Laboratory, University of Saskatchewan, Saskatoon, Saskatchewan Canada S7N 0W0.

‡Present address: University of Lund, Solvegaton 14, S-22362 Lund, Sweden.

References

1. M.W. Curtin, H. Toki and D.K. Scott, Phys. Lett. 123B (1983) 289.
2. G. Bertsch and P.J. Siemens, Phys. Lett. 126B (1983) 9.
3. A.Z. Mekjian, Phys. Rev. Lett. 38 (1977) 640 and Phys. Rev. C17 (1978) 1051.
4. H.H. Gutbrod, A. Sandoval, P.J. Johansen, A.M. Poskanzer, J. Gosset, W.G. Meyer,

G.D. Westfall and R. Stock, Phys. Rev. Lett. 38 (1976) 667.
5. L.P. Csernai, H. Stöcker, P.R. Subramanian, G. Graebner, A. Rosenhauer, G. Buchwald, J. A. Maruhn and W. Greiner, Phys. Rev. C28 (1983) 2001.
6. B. Strack and J. Knoll, Z. Phys. A315 (1984) 249; J. Knoll and B. Strack, Phys. Lett. 149B (1984) 45; and B. Strack, Phys. Rev. C35 (1987) 691.
7. J.J. Molitoris, D. Hahn and H. Stöcker, Nucl. Phys. A447 (1985) 13c.
8. J. Randrup and S.E. Koonin, Nucl. Phys. A356 (1981) 223.
9. G. Fai and J. Randrup, Nucl. Phys. A404 (1983) 551.
10. S.P. Bondorf, R. Donangelo, I.N. Mishustin, C. Pethick and K. Sneppen, Phys. Lett. 150B (1985) 57.
11. H. Stöcker, G. Buchwald, G. Graebner, P. Subramanian, J.A. Maruhn, W. Greiner, B.V. Jacak and G.D. Westfall, Nucl. Phys. A400 (1983) 63.
12. H.-A. Gustafsson, H.H. Gutbrod, B. Kolb, H. Löhner, B. Ludewigt, A.M. Poskanzer, T. Renner, H. Riedesel, H.-G. Ritter, A Warwick, F. Weik and H. Wieman, Phys. Rev. Lett. 52 (1984) 1590.
13. R.E. Renfordt, D. Schall, R. Bock, R. Brockmann, J.W. Harris, A. Sandoval, R. Stock, H. Ströbele, D. Bangert, W. Rauch, G. Odyniec, H.G. Pugh and L.S. Schroeder, Phys. Rev. Lett. 53 (1984) 763.
14. W. Scheid, H. Müller and W. Greiner, Phys. Rev. Lett. 32 (1974) 741.
15. A. A. Amsden, G.F. Bertsch, F.H. Harlow and J.R. Nix, Phys. Rev. Lett. 35 (1975) 905.
16. H. Stöcker, J. Maruhn and W. Greiner, Phys. Rev. Lett. 44 (1980) 725.
17. H. Stöcker, A.A. Ogloblin and W. Greiner, Z. Phys. A303 (1981) 259.
18. L.P. Csernai, G. Fai and J. Randrup, Phys. Lett. 140B (1984) 149.
19. A.I. Warwick, H.H. Wieman, H.H. Gutbrod, M.R. Maier, J. Peter, H.G. Ritter, H. Stelzer, F. Weik, M. Freedman, D.J. Henderson, S.B. Kaufman, E.P. Steinberg and B.D. Wilkins, Phys. Rev. C27 (1983) 1083.
20. see also R. Bock, G. Claesson, R.L. Ferguson, H.A. Gustafsson, H.H. Gutbrod,A.I. Gavron, J.W. Harris, B.V. Jacak, K.H. Kampert, B. Kolb, A.M. Poskanzer, H.G. Ritter, H.R. Schmidt, T. Siemiarczuk, L. Teitelbaum, M. Tincknell, S. Weiss, H. Wieman and J.B. Wilhelmy, GSI preprint GSI-87-25 (1987), submitted to Mod. Phys. Lett. A (1987).
21. A. Baden, H.H. Gutbrod, H. Löhner, M.R. Maier. A.M. Poskanzer, T. Renner, H. Riedesel, H.G. Ritter, H. Spieler, A. Warwick, F. Weik and H. Wieman, Nucl. Inst. and Meth. 203, (1982) 189.
22. K.H. Kampert, Ph.D. Thesis, Univ. Muenster 1986.
23. K.G.R. Doss, H.A. Gustafsson, H.H. Gutbrod, B. Kolb, H. Löhner, B. Ludewigt, A.M. Poskanzer, T. Renner, H. Riedesel, H.G. Ritter, A. Warwick and H. Wieman,

Phys. Rev. C32 (1985) 116.
24. P. Danielewicz and G. Odyniec, Phys. Lett. 157B, (1985) 146.
25. K.G.R. Doss, H.A. Gustafsson, H.H. Gutbrod, K.H. Kampert, B. Kolb, H. Löhner, B. Ludewigt, A.M. Poskanzer, H.G. Ritter, H.R. Schmidt, and H. Wieman, Phys. Rev. Lett. 57 (1986) 302.
26. H. Kruse, B.V. Jacak and H. Stöcker, Phys. Rev. Lett. 54 (1985) 289.
27. J. Aichelin and H. Stöcker, Phys. Lett. 176 (1986) 14.
28. R.Y. Cusson, P.G. Reinhardt, J.J. Molitoris, H. Stöcker, M. Strayer and W. Greiner, Phys. Rev. Lett. 55 (1985) 2786.
29. C. Gale, G. Bertsch and S. DasGupta, Phys. Rev. C35 (1987) 1666.
30. see H. Stöcker, Proceedings of this Conference.
31. J. Gosset, H.H. Gutbrod, W.G. Meyer, A.M. Poskanzer, A. Sandoval, R. Stock and G.D. Westfall, Phys. Rev. C16 (1977) 629.

Figure Captions

1. Particle identification spectrum with hydrogen isotope identification insert.

2. Fragment ($Z \geq 3$) multiplicity distributions for 200 MeV/n Au + Au for five participant proton multiplicity bins increasing from MUL1 to MUL5. These multiplicities correspond to fragments emitted in the forward hemisphere of the c.m. system.

3. The inplane transverse momentum per nucleon p_x/A for light particles (Z = 1,2) and for fragments with $6 \leq Z \leq 9$ as a function of their rapidity. Positive and negative values of p_x/A correspond to opposite sides of the beam in the reaction plane.

4. The mean value of the transverse momentum projected onto the reaction plane (defined in text) divided by the transverse momentum vector modulus as a function of c.m. rapidity for 200 MeV/nucleon Au + Au. Displayed are the values for Z = 1,2,3 and $Z \geq 6$.

5. Directivity plots (azimuthal angular correlations) for Z = 1,2,3 and 6 relative to the reaction plane ($\phi = 0$) determined by the Z = 1,2 particles with autocorrelations removed. The left-hand column corresponds to peripheral collisions (MUL2) and the right-hand column to relatively central ones. The data are plotted for 200 MeV/nucleon Au + Au for two rapidity intervals (0's) $.32 < y \leq .42$ and (x's) $.52 < y \leq .62$.

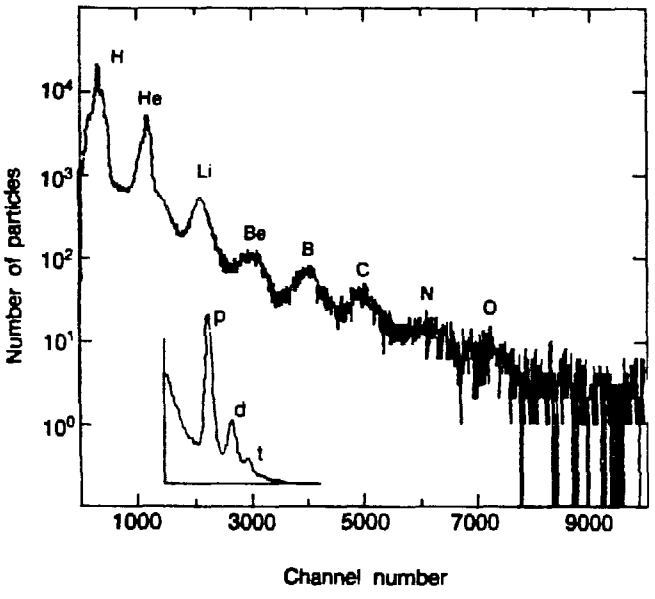

Figure 1

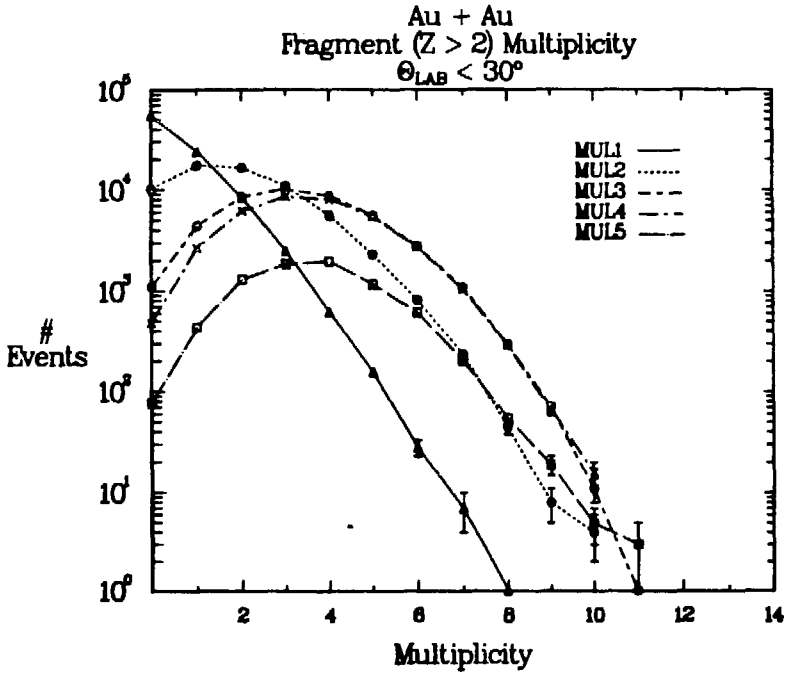

Figure 2

Figure 3

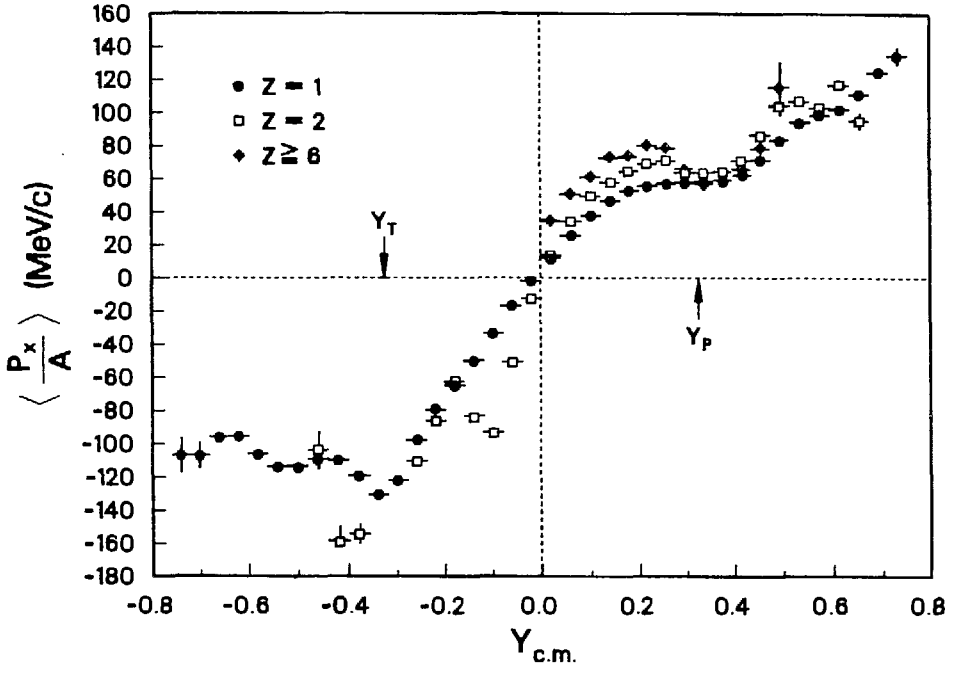

Figure 4

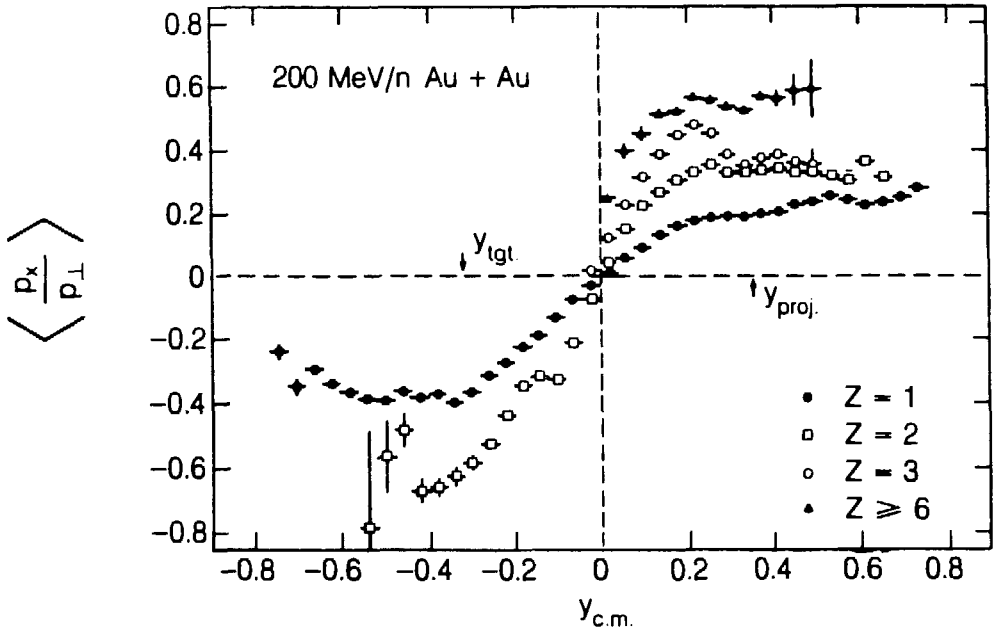

Figure 5

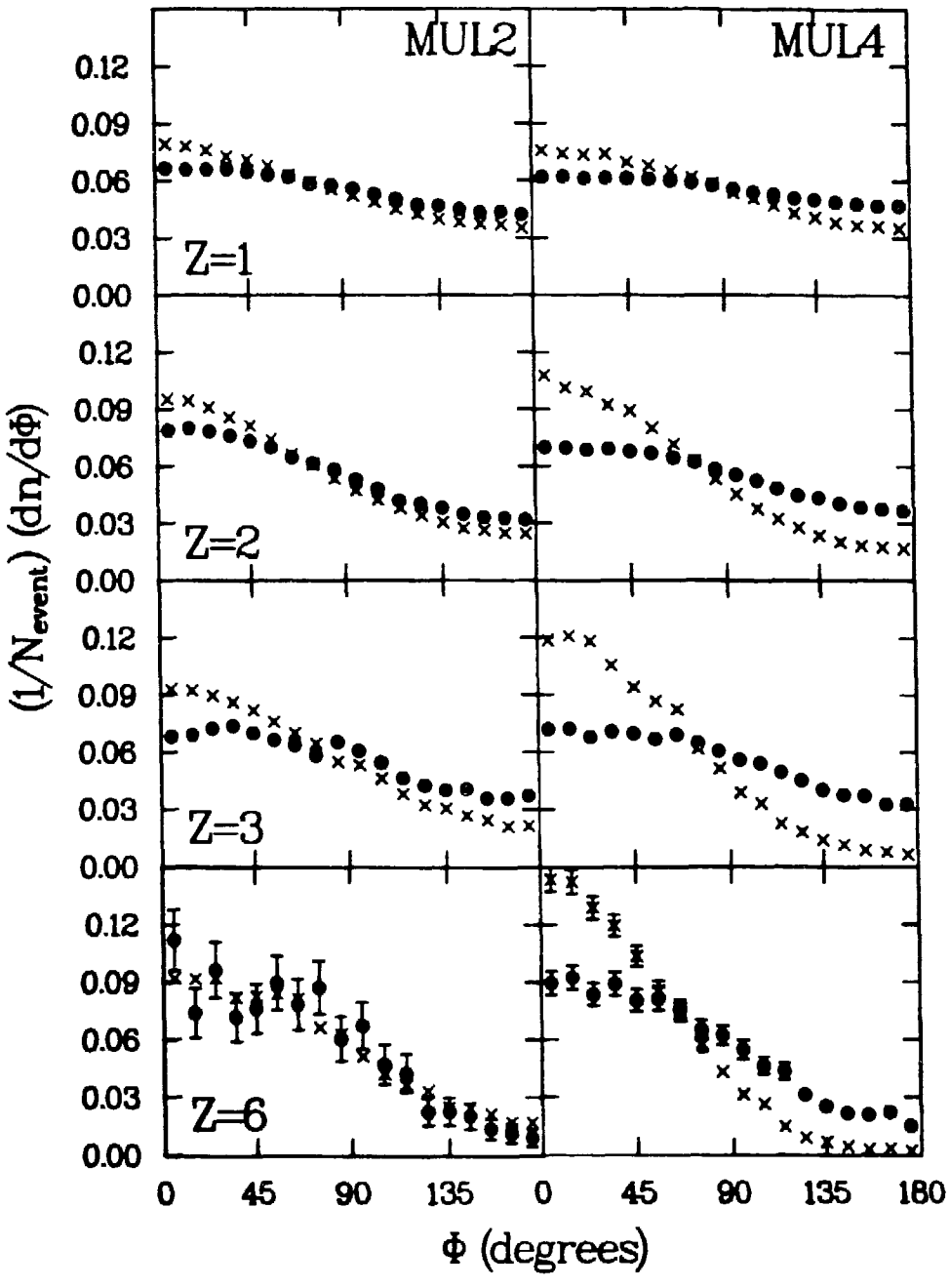
MUL2
MUL4
Z=1
Z=2
Z=3
Z=6
0.12
0.09
0.06
0.03
0.00
0
45
90
135
180
(1/N_event) (dn/dΦ)
Φ (degrees)

COLLECTIVE FLOW EFFECTS IN NE + PB COLLISIONS AT E/A=400 AND 800 MEV

J. Gosset, R. Babinet, N. De Marco[1], H. Fanet, Z. Fodor[2], M.C. Lemaire, D. L'Hôte, B. Lucas, J. Poitou, W. Schimmerling[3], Y. Terrien, O. Valette.

DPhN, C.E.N. Saclay, 91191 Gif sur Yvette Cedex, France

J.P. Alard, J. Augerat, N. Bastid, P. Dupieux, L. Fraysse, G. Montarou, M.J. Parizet, J. Valéro[4].

LPC Clermont-Ferrand, B.P. 45, 63170 Aubière, France

F. Brochard, P. Gorodetzky, C. Racca.

CRN, B.P. 20 CR, 67037 Strasbourg Cedex, France

Triple differential cross sections in momentum p, polar angle θ, and azimuthal angle φ with respect to the reaction plane, have been measured at the Saturne synchrotron in Saclay for collisions between neon and lead nuclei at incident energies of 400 and 800 MeV per nucleon, using the pictorial drift chamber (PDC) of the Diogene 4π detector[(1)]. A barrel-shaped set of 30 plastic scintillator slats surrounds the PDC; at least 2 of these must be hit in order to trigger an accepted event. The PDC and trigger acceptances used in this analysis were:

PDC: $20° < \theta < 132°$

pions	baryons	
$\eta > 0.66 + 0.77\ y$	$\eta > 0.36 + 0.72\ y$	for $y<0$
$\eta > 0.66 - 0.63\ y$	$\eta > 0.36 - 0.80\ y$	for $y>0$

TRIGGER: $37° < \theta < 119°$

pions	baryons	
$\eta > 0.81 + 0.33\ y$	$\eta > 0.41 + 0.30\ y$	for $y<0$
$\eta > 0.81 - 0.33\ y$	$\eta > 0.41 - 0.40\ y$	for $y>0$

where η is the transverse momentum divided by the mass and y is the rapidity.

---

[1] Present address: INFN, 10125 Torino, Italy

[2] Present address: CRIP, 1525 Budapest. Hungary

[3] Present address: LBL, Berkeley, CA 94720. U.S.A. Supported by the Public Health Service of the U.S. Department of Health and Human Services (grant CA 23247 awarded by the National Cancer Institute) and by the National Aeronautics and Space Administration(grant L 22395A).

[4] Present address: European Spatial Agency. Noortwijk. Holland

The experimental results are compared with the intranuclear cascade model (INC)[2]. As shown in Ref.3, the cascade calculation does not reproduce correctly the pseudo-proton multiplicity distributions, $M_{\tilde{p}}$, where pseudo-protons $\tilde{p}$ consist of free protons and protons bound in fragment nuclei. Consequently, the impact parameter selection must be made in a manner independent of the shape of this distribution. Since the cascade does reproduce the integral under the $M_{\tilde{p}}$ distribution, impact parameters were defined by dividing the area under this distribution into five bins of approximately equal cross section, starting with the highest value of $M_{\tilde{p}}$ and corresponding to increasing impact parameter values such that $(b/b_{trig})^2 = 0.1, 0.3, 0.5, 0.7$, and 0.9, where b_{trig} is the maximum impact parameter corresponding to the trigger requirement. Results will be presented only for the first 4 bins, where there is a number of particles per event sufficient to define the reaction plane.

We have used the procedure suggested by Danielewicz and Odyniec[4] to evaluate the azimuthal angle φ of each particle with respect to the (coalescence invariant) impact parameter vector, defined event-by-event as:

$\vec{Q} = \Sigma(Z_i/A_i)(y_i - \langle y \rangle)\vec{p}_{\perp i}$ with $\langle y \rangle = (\Sigma(Z_i/A_i)m_i y_i)/(\Sigma(Z_i/A_i)m_i)$, and where the subindex refers to baryons with mass m_i, rapidity y_i, transverse momentum $\vec{p}_{\perp i}$, atomic number Z_i, and atomic mass A_i. For each particle, the transverse momentum p_x in the reaction plane is calculated as the projection of the transverse momentum in the direction of $\vec{Q}$; autocorrelations are suppressed as in Ref.4. The center of mass rapidity, $\langle y \rangle$, is not known a priori for the asymmetric system described here and is thus calculated for each event. The continuous function $(y_i - \langle y \rangle)$ replaces the weights originally proposed in Ref.4. Triple differential cross sections are obtained by adding particles from all events with a given multiplicity. For each rapidity interval, the average p_x/m is calculated from the projection of the cross section onto the p_x-axis.

Figure 1 shows $\langle p_x/m \rangle$ as a function of rapidity for Ne + Pb at E/A = 800 MeV, for pseudo-protons $\tilde{p}$ emitted in events with multiplicity $M_{\tilde{p}}$ ranging from 13 to 17, which corresponds to $(b/b_{trig})^2 = 0.3$. For the same value of impact parameter, the INC calculations use $M_{\tilde{p}}$ ranging from 19 to 26. The y dependence of $\langle p_x/m \rangle$ is almost linear, especially near the rapidity y_o where $\langle p_x/m \rangle$ is zero. This point can be interpreted as the rapidity of the emitting system, and the slope S at y_o is taken as a measure of the collective particle flow in this reaction.

The flow F is obtained from S as in Ref.4 after correction for effects due to the finite number of particles in each event. The ratio F/S varies between 1.3

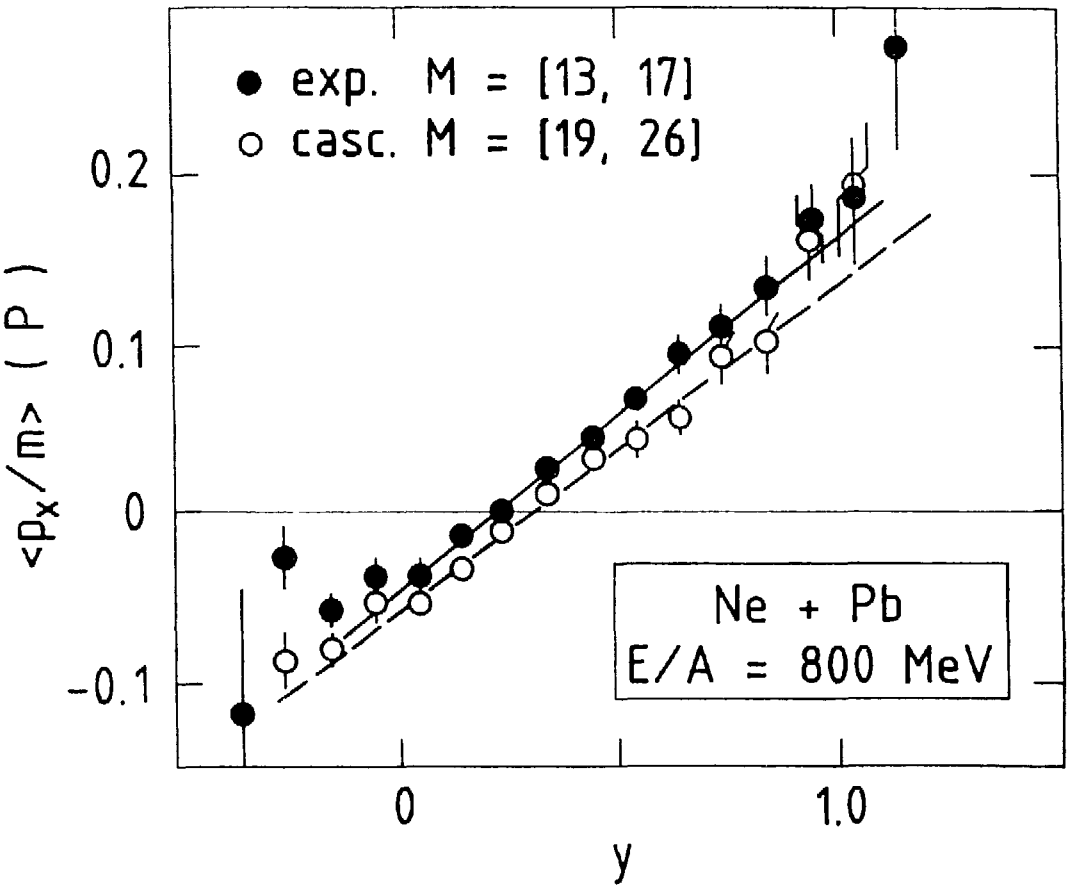

Fig.1. $\langle p_x/m \rangle$ versus rapidity, for pseudo-protons.

and 2.5 . Figure 2 shows the resultant flow obtained from experiment and from the cascade calculation at both incident energies. The flow increases as a function of impact parameter, but the experimental flow is bigger than the INC calculation, and the difference increases at small impact parameters. The experimentally observed flow is bigger at the higher incident energy; this is not true for the INC calculation.

The flow carried by deuterons was found to be slightly bigger than the flow carried by protons. The biggest difference occurred at small impact parameters for 400 MeV per nucleon neon and at large impact parmeters for 800 MeV per nucleon neon. This kind of analysis needs to be pursued with better statistics before more definite conclusions can be drawn.

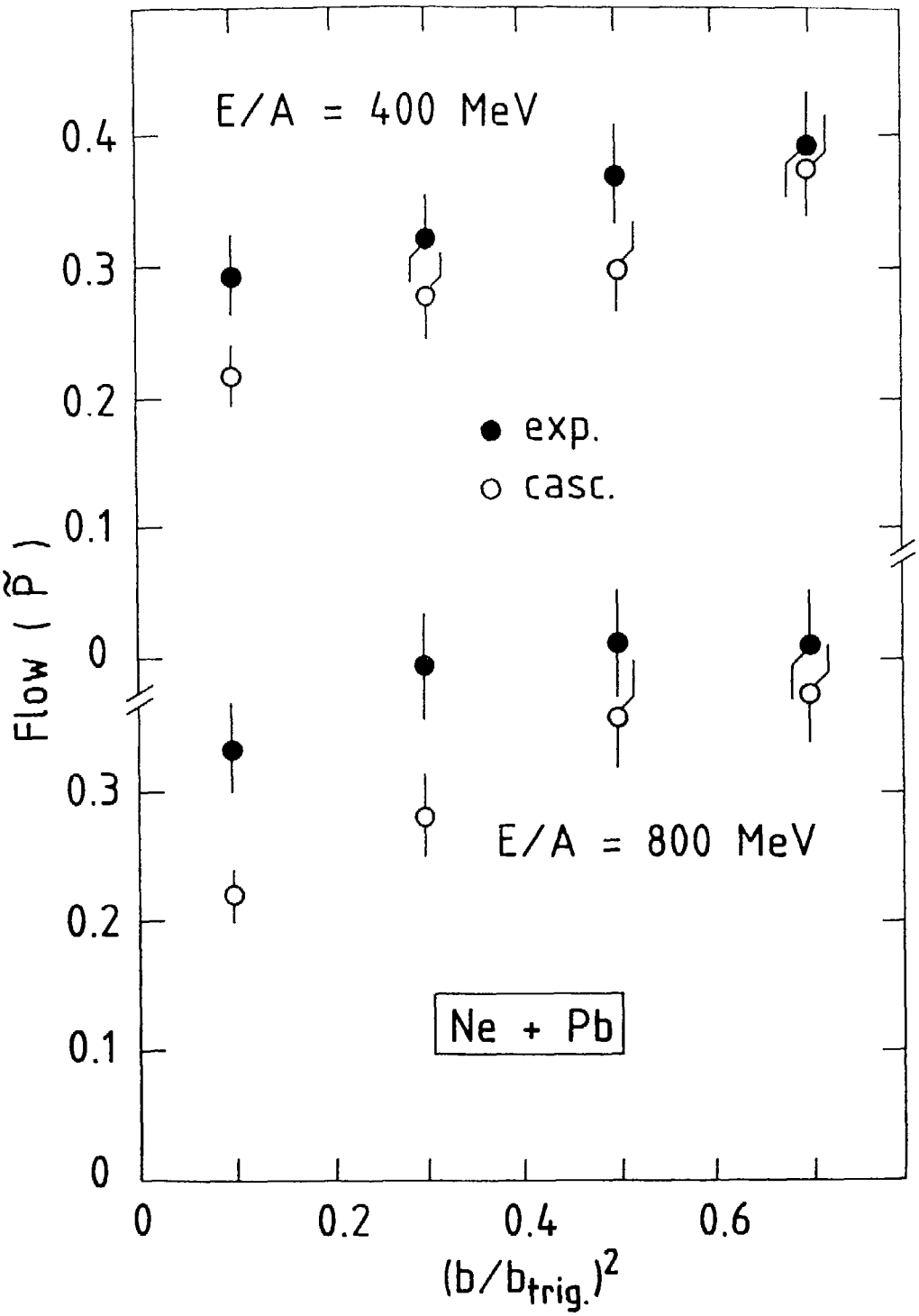

Fig.2. Flow versus impact parameter, for pseudoprotons.

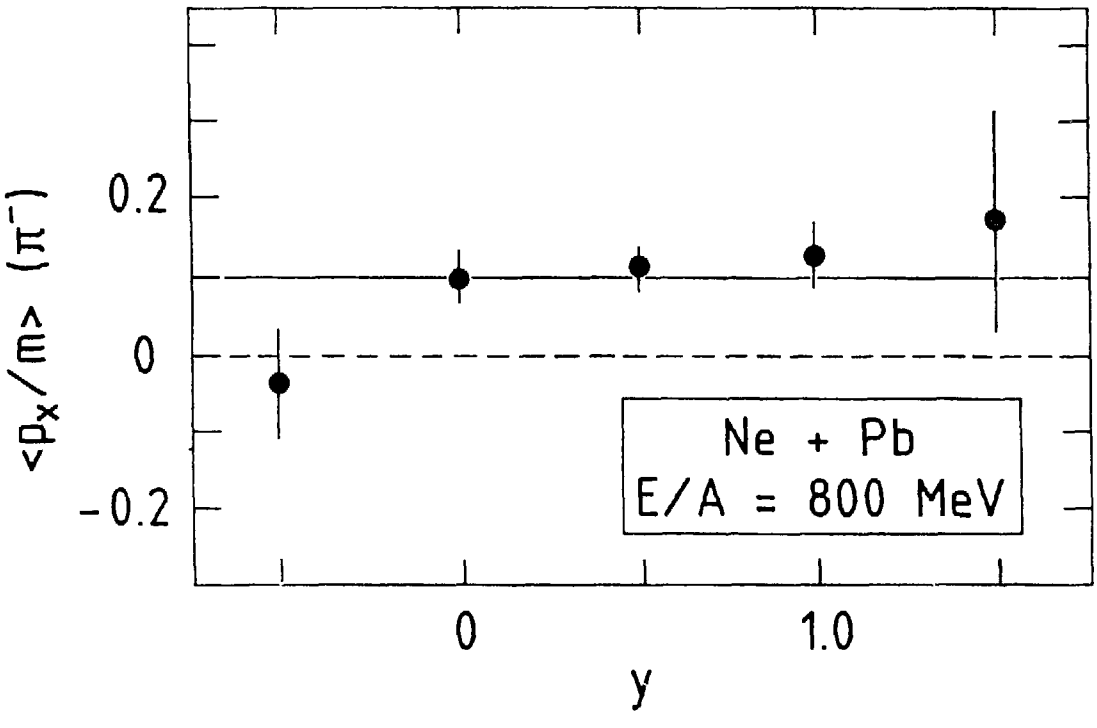

Fig.3. $\langle p_x/m \rangle$ versus rapidity, for π^-.

An example of the flow carried by pions is shown in Fig. 3, where $\langle p_x/m \rangle$ is positive for all values of the rapidity. The statistics are not adequate for a determination of the flow angle from a straight line fit to the data. Instead, the values of p_x/m, averaged over the rapidity, were binned by impact parameter. The results obtained at 800 MeV per nucleon are shown in Fig. 4, where the averaged $\langle p_x/m \rangle$ has been plotted as a function of impact parameter, for both π^+ and π^-. The average value of $\langle p_x/m \rangle$ is always positive and greater for π^+ than for π^-, especially at intermediate impact parameters. The unidirectionality of the flow is further ilustrated by the ratio between the number of pions emitted at positive values and the number emitted at negative values of $\langle p_x/m \rangle$, which is equal to 1.3 . This property of the pion flow was already observed for π^- emitted in asymmetric collisions[5], but this constitutes the first observation of unidirectional π^+ flow. The unidirectionality can be understood qualitatively as a consequence of preferential absorption, by the heavy target nucleus, of pions emitted in the direction opposite to the impact parameter vector.

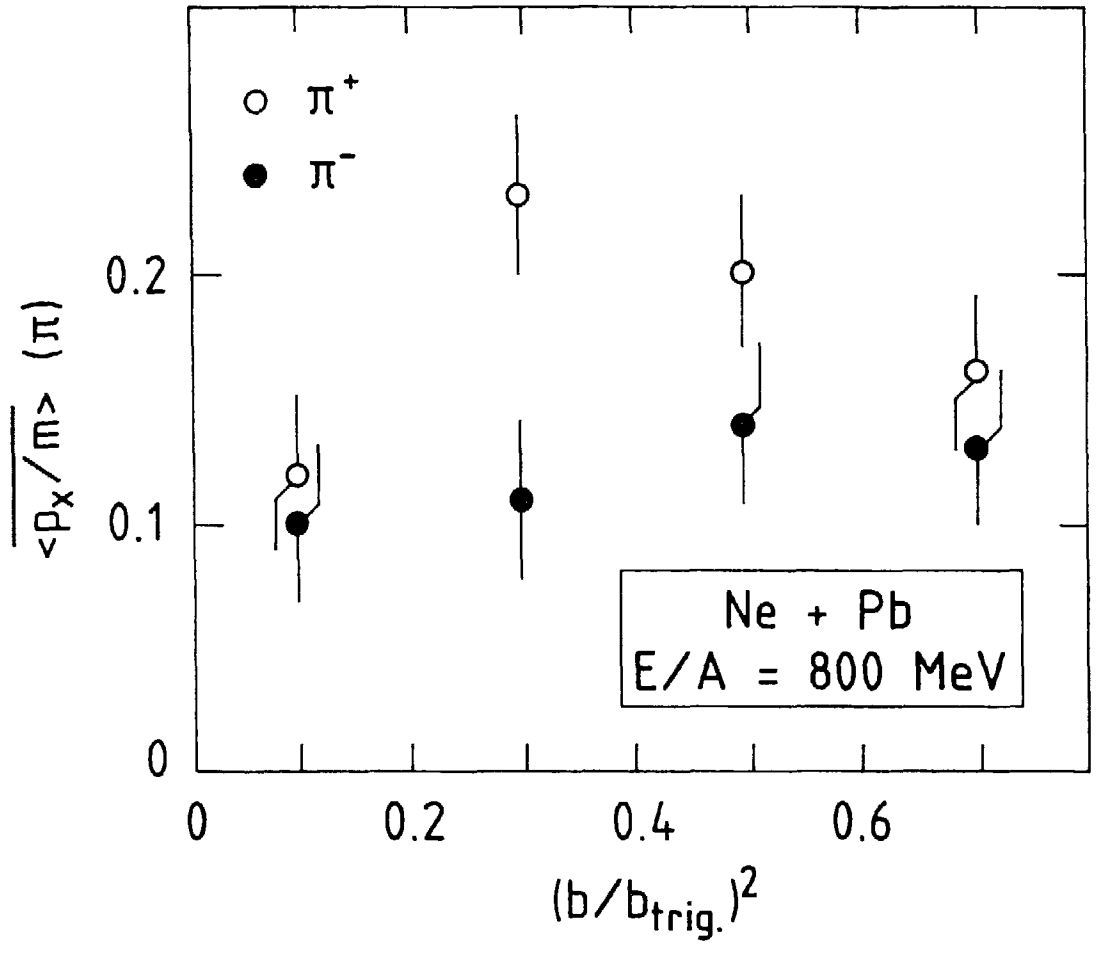

Fig.4. y-averaged $<p_x/m>$ versus impact parameter, for $\pi^{\pm}$.

Flow represents only part of the information contained in the triple differential cross sections. More information can be obtained by removing the acceptance dependence of the data and reconstructing the entire $(p_x/m,y)$ distributions. The result of such a reconstruction is shown in Fig. 5, for pseudo-protons at E/A = 800 MeV per nucleon. The $(p_x/m,y)$ distribution for three cuts in $M_{\tilde{p}}$ has been fitted to a 2-dimensional gaussian distribution tilted at some angle θ_1 from the beam axis. The 1/e-contour of this distribution in the $(p_x/m,y)$ plane is an ellipse with semi-axes σ_1 and σ_2 $(\sigma_1>\sigma_2)$.

A large amount of information can be easily obtained from Fig. 5. The rapidity at the center of each ellipse, which reflects the velocity of the emitting source, increases with increasing impact parameter, in qualitative agreement with a clean

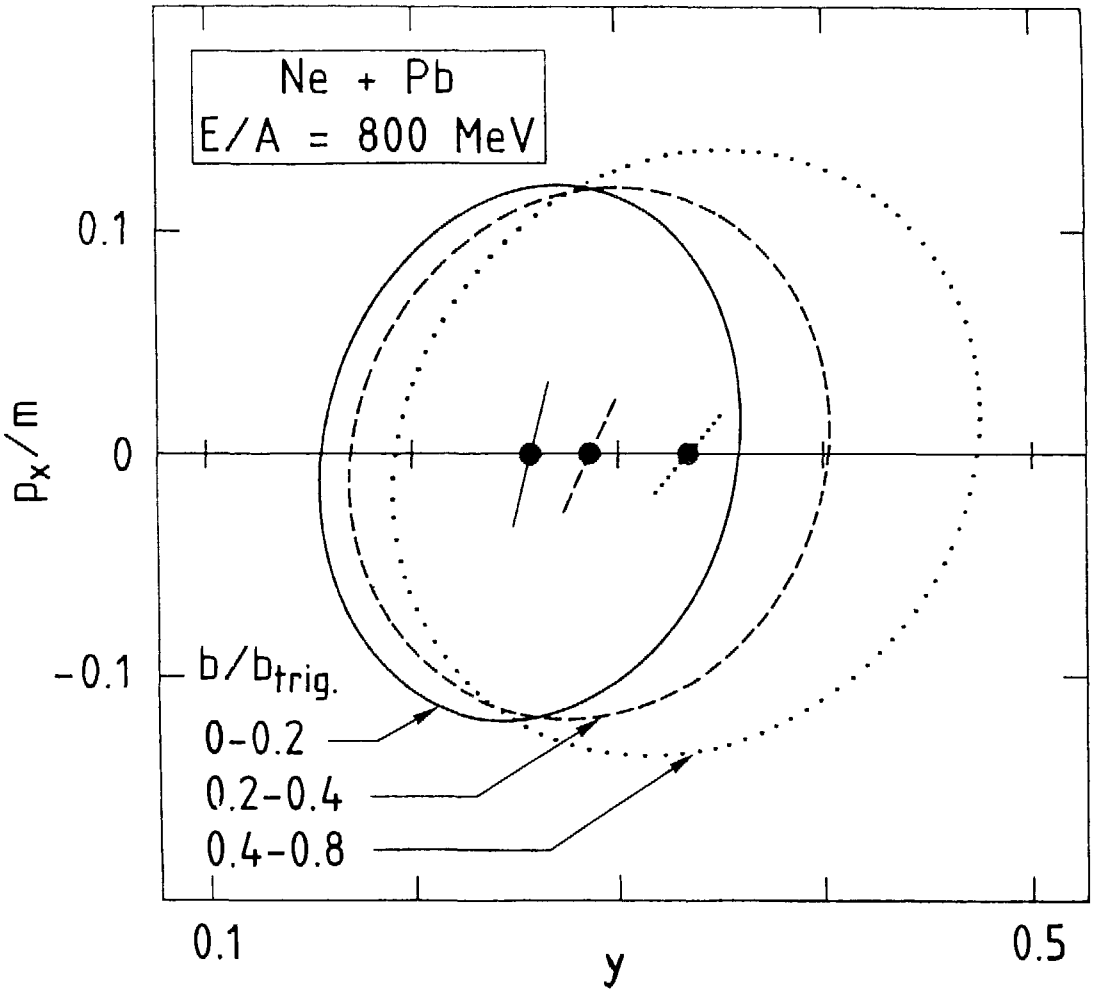

Fig.5. Contour plots in the (p_x/m,y) plane, at the 1/e-level of the maximum, of the 2-dimensional gaussian fit for pseudoprotons and three impact parameters at E/A=800 MeV.

cylindrical cut picture of the collision for the asymmetric Ne + Pb system. Also in agreement with such a geometrical model is the fact that the area of the ellipses increases with increasing impact parameter. If the slope of the major axis of the ellipses shown in Fig. 5 is taken to represent a better measure of the flow angle, it can be seen that the "real" flow angle varies from a large value of 75° at small impact parameter to a smaller value of 40° at large impact parameter. This information could not have been deduced from the usual flow measurements, which

must yield a value of 0 for purely central collisions due to the symmetry for that case.

References

1) J.P. Alard et al., submitted to Nucl. Instr. and Meth.

2) J. Cugnon et al., Nucl. Phys. A379(1982)553, J. Cugnon and D.L'Hôte, Nucl. Phys. A452(1986)738; a new version including isospin effects, Pauli blocking and prescriptions for simulating binding energy has been used.

3) J.Poitou et al., Proc. of 8th International Balaton Conference, Balatonfured, Hungary, 1987.

4) P. Danielewicz and G. Odyniec, Physics Letters 157B(1985)146.

5) D. Keane et al., Proc. of Workshop on Nuclear Dynamics, Copper Mountain, Colorado, 1986.

ENTROPY PRODUCTION IN HEAVY-ION REACTIONS FROM 150 AMEV TO 200 AGEV BOMBARDING ENERGY

H.R. Schmidt[a] for Plastic Ball [a,b] and WA-80[a,b,c,d,e] Collaborations,
D. Hahn[b] and H. Stöcker[f]

(a) Gesellschaft für Schwerionenforschung, Darmstadt, West Germany
(b) Lawrence Berkeley Laboratory, Berkeley, California, USA
(c) University of Lund, Lund, Sweden
(d) University of Münster, Münster, West Germany
(e) Oak Ridge National Laboratory, Oak Ridge, Tennessee, USA
(f) University of Frankfurt, Frankfurt, West Germany

The yield ratios of light clusters (d,t,^{3}He,a) to protons were measured with the Plastic Ball spectrometer for the reactions Nb+Nb and Au+Au for incident beam energies of 150, 250, 400 and 650 MeV/nucleon and for oxygen and sulphur induced reactions at 200 GeV/nucleon. The ratios are analyzed in the framework of the Quantum Statistical Model and the specific entropy is extracted as a function of the centrality of the collisions. The results for Nb+Nb and Au+Au are compared with predictions of the fireball model and relativistic mean field calculations and the importance of compressional effects is emphasized. The entropy produced in 200 GeV/nucleon oxygen and sulphur induced reactions in the target rapidity region is found to be similar to the entropy produced in central Nb+Nb or Au+Au collisions.

I. Introduction

There are only few observables that preserve the signatures of the early high density and high temperature phase of relativistic heavy ion collisions. One of them is considered to be the entropy per nucleon (S/A) produced in the collision. Over the last years a lively debate took place about the mechanisms and significance of entropy and the relationship to nuclear cluster production in high energy heavy ion collisions[1]. On the basis of hydrodynamics[2,3] or Monte Carlo cascade calculations[4,5] it has been argued that during the expansion phase there is only little change of the entropy which was produced in the initial phase of the heavy ion collision. After the collisions among the constituents of the expanding system have ceased at a certain freeze-out or break-up density the phase space density stays constant due to Liouville's theorem and the entropy determines the abundances of the produced clusters. Therefore the specific entropy measured via cluster abundances can help to determine the equation of state (EOS) of dense and hot matter. Furthermore, the sudden liberation of new degrees of freedom due to phase transitions - liquid to vapor at low and hadronic to quark matter at high energies - should manifest itself by the extra entropy produced at such a transition[6-10]

The translation of experimentally measured abundance ratios to values of entropy, however, is model dependent. In the early work of Siemens and Kapusta[11] the yields of composite particles were inferred from inclusive measurements and the deuteron-to-proton ratio R_{dp} was related to the specific entropy via the simple formula $S/A \approx 3.95 - \ln(R_{dp})$. This gives significantly larger entropy values than predicted by

dynamic models. This so-called "entropy puzzle" was resolved later by Stöcker et al.[3,7], who showed that the above relation is not appropriate for the (low) bombarding energies considered, and by Gutbrod et al.[12] and Doss et al.[13] who in exclusive experiments showed that the cluster-to-proton ratios increase steadily with the participant proton multiplicity, i.e. with decreasing impact parameter. From these measurements it became evident that the naive use of impact parameter averaged data had been one of the sources of the incorrect entropy determination.

The paper is organized as follows: In Sec. II we shall present the results of the measurement of the production of light clusters in the systems Nb+Nb and Au+Au as a function of multiplicity at various bombarding energies. In Sec. III we will employ the QSM (Quantum Statistical Model) to extract entropy information, which will be discussed in Sec. IV. In Sec. V we shall present and discuss the results for light cluster production in the target rapidity region for oxygen and sulphur induced reactions at 200 GeV/nucleon. Sec. VI is a summary.

II. Experiment and Results for Nb+Nb and Au+Au

The experiments to study the production of light fragments (A<5) at energies ranging from 150 to 650 MeV/nucleon were performed at the Berkeley Bevalac, using the Plastic Ball/Wall spectrometer[14]. This detector system has full particle identification capability, in the angular range from 9 to 160 degrees in the laboratory system, for singly and doubly charged particles as well as positively charged pions. The forward direction (0-9 degrees in the laboratory system) is covered by the Plastic Wall, measuring time of flight, ΔE and the angle of the particles, thus identifying the nuclear charge and the velocity of the particles. The inner part of the Plastic Wall is also used to define the trigger of the whole spectrometer. The data discussed here were taken both with a minimum bias trigger and a central collision trigger which enhances the sample of high multiplicity events.

The results on composite particle production (Figs. 1,2) are given in ratios x/p as a function of N_p, where x=(d,t,^{3}He,α), respectively and N_p is the participant proton multiplicity {N_p=p+d+t+2(^{3}He+α)}. The curves are fits to data in the framework of the QSM described below. The experimental ratios are extracted in the region of phase space where the yields of the different species overlap each other. The underlying assumptions are the validity of the basic idea of the coalescence-model, namely $D/N \propto N$, and a boltzmann-like momentum distribution of the particles. Here D and N stand for the number of deuterons and nucleons, respectively. The choice of an overlap area in phase space, where the particle momenta have been scaled by $(1/m)^{1/2}$ ensures that the above relation is also fulfilled locally. This procedure is necessary since the Plastic Ball does not have full particle identification in the full phase space. N_p is on the other hand determined from all well identified particles except for the spectators. These were excluded by applying software cuts to the data. A detailed description of the procedure for extracting the ratios and the N_p numbers is given in Ref. 13.

The abundance ratios of Figs. 1 and 2 exhibit the following features:

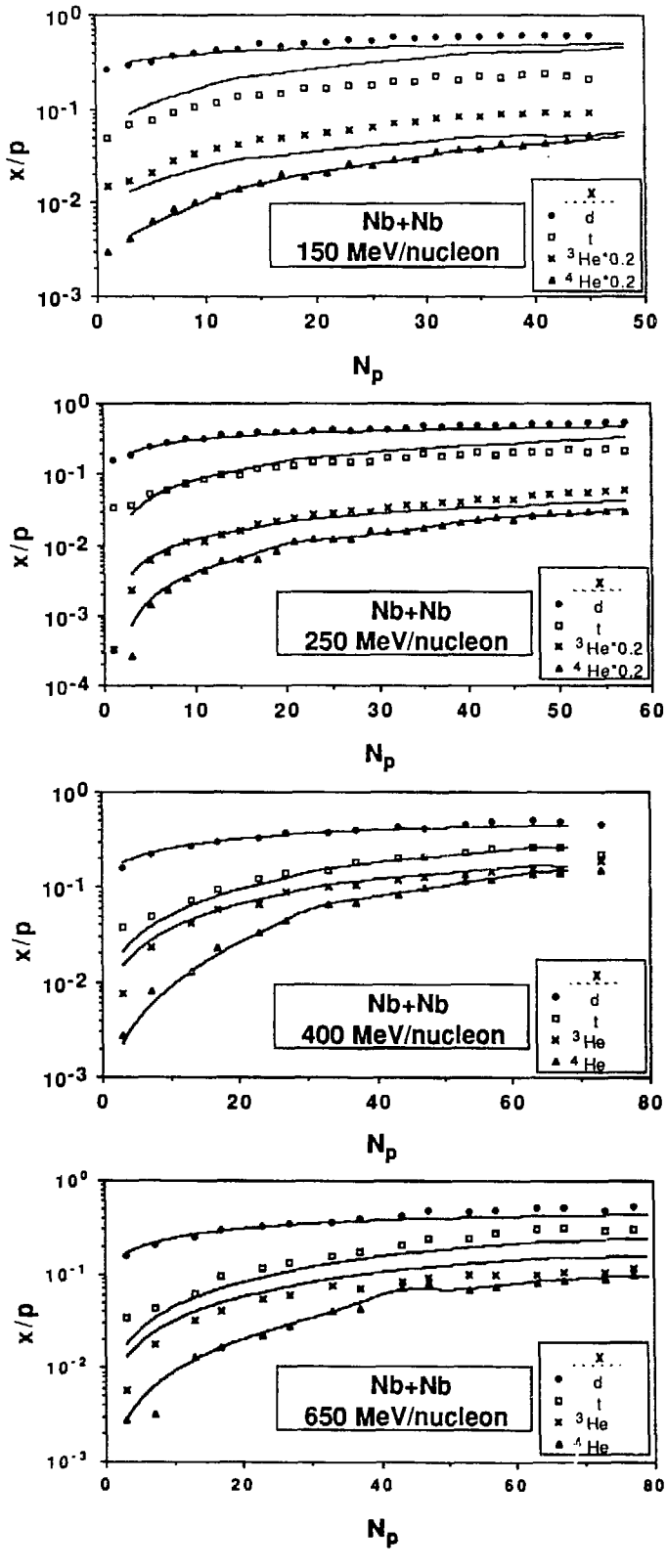

i) they all show the same behavior of increasing production of composite particles with increasing N_p,

ii) the curves tend towards an asymptotic value at high N_p values. The asymptotic limit is reached faster for the curves corresponding to the higher projectile energies.

This can qualitatively be explained by simple phase space considerations[12] taking both the size of the light fragment and the participant volume into account. The saturation at high N_p values is, however, a very reassuring result, because it indicates that we are close to an infinite volume, thermodynamic limit, where finite source size effects[15] should be negligible.

III. Entropy in the Framework of the Quantum Statistical Model

The quantum statistical model (QSM)[3,7,16] takes into account simultaneously particle unstable nuclides up to mass 20 and ground state nuclei up to mass 130, as well as Bose condensation of the integer

Fig. 1 x/p ratios for the reaction Nb+Nb, where x stands for d,t, ^{3}He, ^{4}He, as a function of the participant proton multiplicity N_p. The solid curves are fits within the framework of the QSM as described in the text.

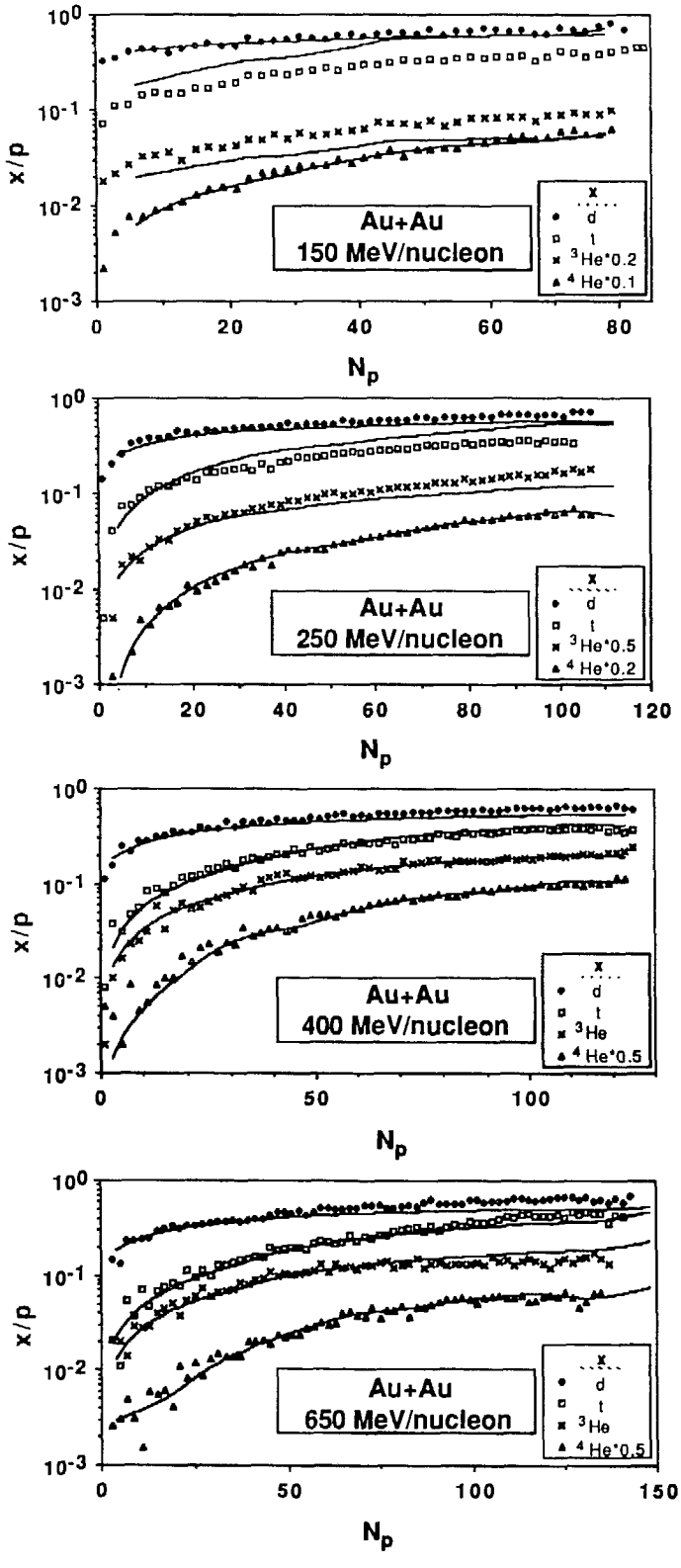

spin nuclides and excluded volume effects. In particular, the model describes the dependence of the ratios of deuteron-like to proton-like particles (d_{like}/p_{like}), as defined in Ref.13 and x/p as a function of the specific entropy of the system. The dependence of this relation on the breakup temperature T_b and the breakup density ρ_b is extensively discussed in Ref. 16. Here we only want to point out that the curve x/p(S/A), which is calculated for a grandcanonical ensemble, i.e. for infinite nuclear matter, can also be employed at finite multiplicities. It has been shown[16] that only at very low particle numbers the deviations from a classical microcanonical treatment are worth mentioning; for A=10 they are of the order of 20 %. This demonstration of the applicability of the QSM at finite multiplicities constitutes a decisive improvement over previous methods to extract specific entropies from experimental data:

Fig. 2 x/p ratios for the reaction Au+Au where x stands for d,t, ^{3}He, ^{4}He, as a function of the participant proton multiplicity N_p. The solid curves are fits within the framework of the QSM as described in the text.

i) in a previous publication[13] the ratio d_{like}/p_{like} was extrapolated to infinity employing a coalescence-model inspired formula. Due to the lever arm from finite to infinite multiplicities the extracted values S/A^{∞} were insensitive to fine differences in the experimental ratios at different bombarding energies or colliding systems.

ii) at lower bombarding energies the fraction of clusters heavier than A=4 contributing to the participant proton multiplicity N_p becomes increasingly important. These clusters, however, were not measured in the Plastic Ball spectrometer in the experiments under consideration. Therefore the coalescence formula, which relies on the measurement of the "true" N_p values must fail at lower bombarding energies.

iii) fitting all cluster ratios *simultaneously* puts a very stringent condition on the finally extracted S/A values.

The solid curves in Figs. 1 and 2 are fits to the data with the QS model. The least square fits were done simultaneously for all four ratios at 10 selected multiplicities. The lines are interpolated between the fitted values. Since the QSM treats clusters explicitly, the multiplicity N_p used in the model calculations could be defined in the same way the participant proton number is defined experimentally, not imposing any restrictions due to non-measured heavy clusters at lower bombarding energies. The breakup temperature T_b and the breakup density ρ_b were the only free parameters.

IV. Discussion

Generally the fits to the data are quite satisfactory considering the fact that only two parameters were adjusted to fit simultaneously the relative yields of the different fragments. However, at the lower bombarding energies the model does not fit the t/p and ^{3}He/p ratios. The theory predicts $t/^3He>1$ at all energies for the neutron rich systems Au + Au and Nb + Nb, in agreement with the data except for 150 MeV/nucleon incident energy. As the bombarding energy is increased the agreement gets better. At the highest energies the model yields too little tritium and too much ^{3}He. Also in a coalescence picture it is not conceivable that in neutron rich systems like Au + Au and Nb + Nb the neutron poor ^{3}He is produced more abundantly than tritium. Therefore we look for possible experimental causes for this discrepancy:

i) The phase space acceptance of the Plastic Ball is best at the lower bombarding energies and therefore the overlap regions in phase space, where the ratios were taken are largest at these energies. Therefore the discrepancy of experiment and QS model at the lower bombarding energies for the t/p and ^{3}He/p ratios is unlikely to be due to simple experimental cuts.

ii) The overlap region was chosen in the space were the particle momenta have been scaled by $(1/m)^{1/2}$, where m is the mass of the different species (p,d,t,^{3}He,α). This scaling is introduced by the assumption that the particle momenta are Boltzmann distributed in momentum space coming from a common source with temperature parameter T (see Ref. 13 for a detailed description). Recently, it has been observed[17] that ^{3}He is emitted with almost twice the mean transverse energy per particle than tritium, which has the same transverse energy per particle as the p-, d- and α-particles. If this translates into a higher

"temperature" for the ^{3}He source this would have the following consequence: at low bombarding energies, where the excluded region cuts into the low side of the momentum distribution, relatively more ^{3}He then tritium would be inside the overlap region due to the "boost" of the higher apparent temperature. At the highest bombarding energy, the excluded region cuts into the high energy tail of the momentum distribution and we would have relatively more tritium than ^{3}He in the overlap zone. This is

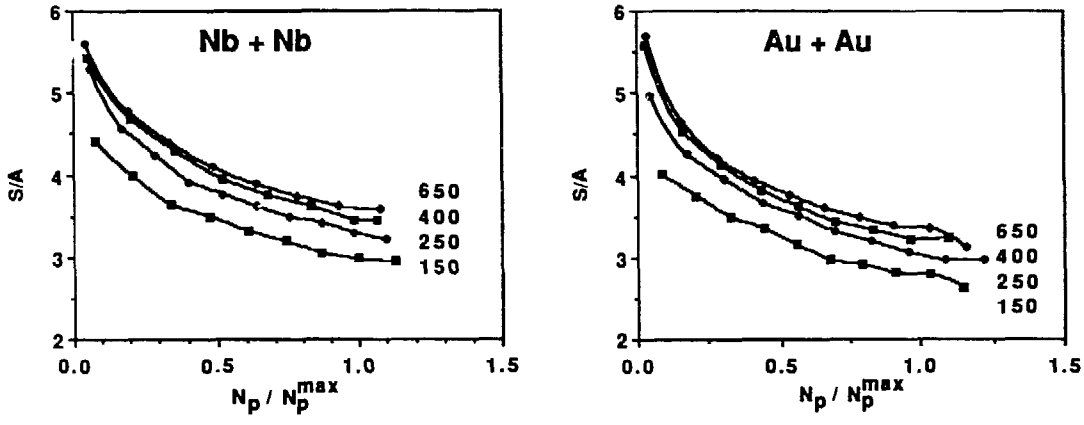

Fig. 3 Entropy values (S/A) extracted from the x/p ratios as a function of the reduced multiplicity N_p/N_p^{max}.

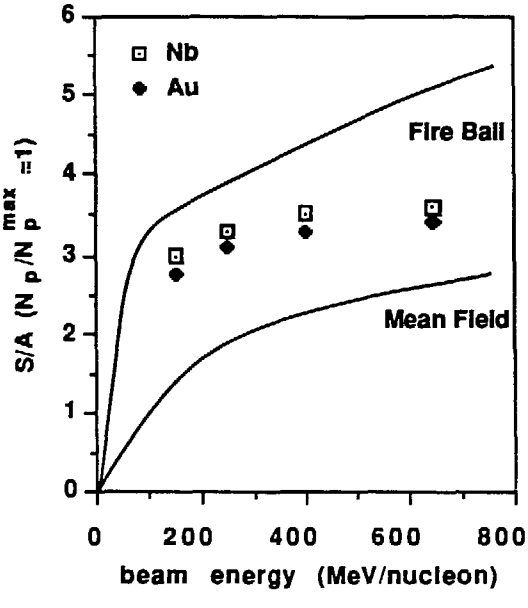

exactly what is observed experimentally. If this explanation holds it constitutes a very interesting observation in itself.

At the low energy the extracted entropies are based on the d/p- and α/p-ratios only. The resulting specific entropies as a function of the reduced multiplicity N_p/N_p^{max} are shown in Figs. 3a and b for the systems Nb+Nb and Au+Au,

Fig. 4 Comparison of the bombarding energy dependence of S/A with the fireball and a hydrodynamic mean field model. The experimental points cannot be compared directly with the theoretical models, because the data are for finite multiplicities, i.e. $N_p/N_p^{max}=1$.

respectively. For a definition of N_p^{max} see Ref.18. The reduced multiplicity has been chosen in order to compare the S/A-value for a given system at about the same impact parameter. Observe that there is an increase of S/A with bombarding energy at all multiplicities. In this plot no indication of significant extra entropy production due to a phase transition at the lowest bombarding energy can be seen. From these curves we extract the entropy per nucleon at a finite multiplicity, i.e. $N_p/N_p^{max}=1$ for the various bombarding energies. The result is shown in Fig. 4 together with two model calculations. The experimentally extracted entropy is smaller than the one predicted by the fireball model, where *all*

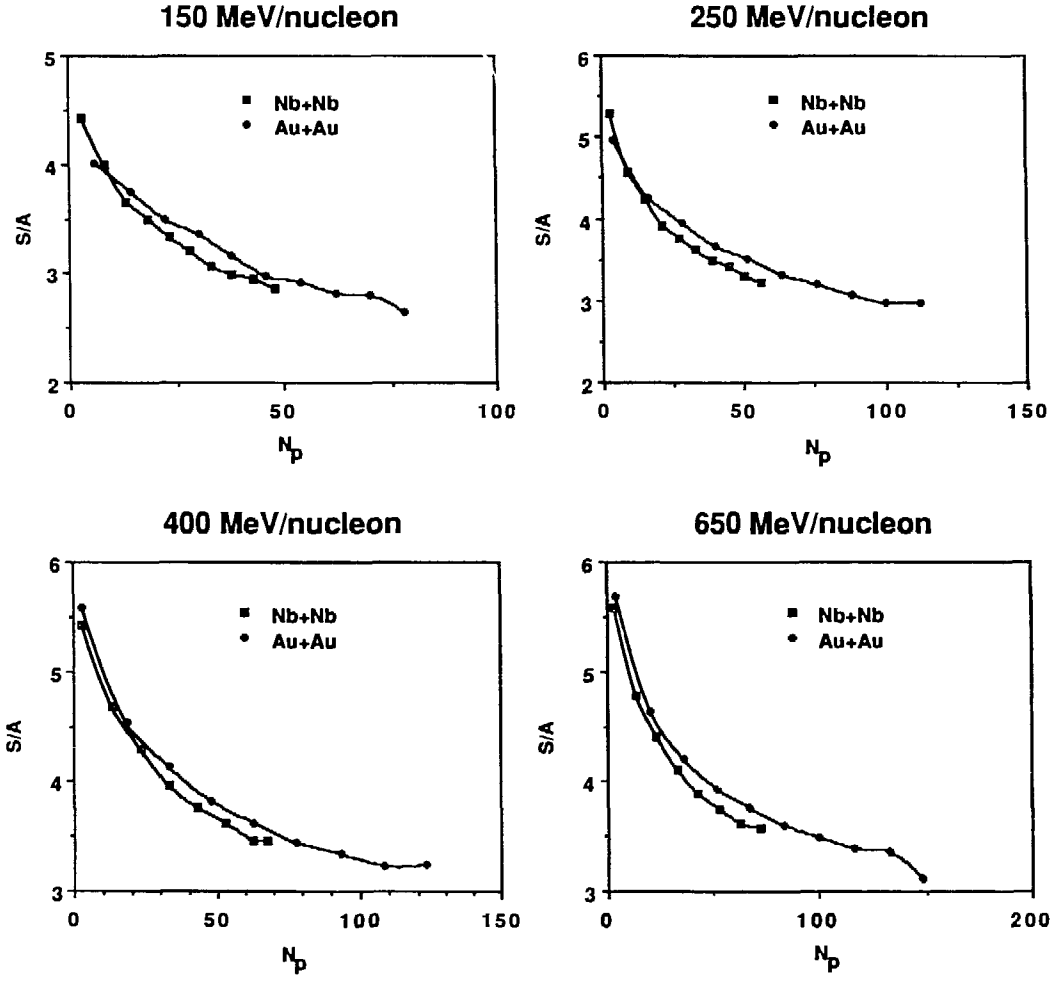

Fig. 5 Comparison of the mass dependence of S/A as a function of the participant proton multiplicity N_p.

available kinetic energy is converted into random thermal motion. The fact that this model yields too high entropy values indicates that compressional effects play an important role for the entropy production in heavy ion reactions. The curve, labeled as mean field, is a hydrodynamical calculation using an equation of state based on the relativistic mean field theory of Ref. 19. It lies below the data, reflect mainly the lower entropy per nucleon for infinite nuclear matter, for which the calculation was done. An extrapolation of S/A to infinite multiplicities[16], subject to the aforementioned uncertainties, would yield, e.g. for Nb+Nb at 400 MeV/nucleon a value of 1.6+/-0.4 in agreement with the hydrodynamical prediction. The error of 0.4 units of entropy is estimated form the the variation of S/A with the breakup density ρ_b.

While the S/A-value as a function of the impact parameter (or the reduced multiplicity) is appropriate for comparisons within one system, it is instructive to choose the participant proton multiplicity for the comparison of different systems at the same bombarding energy. The similarity of the extracted entropy values for the two systems (Fig. 5) at a given bombarding energy shows that the specific entropy is mainly dependent on the number of particles in the reaction volume. Since the reaction volumes are also proportional to first order to the number of particles, the relevant variable for S/A is the mean particle density. The slight excess of S/A for Au+Au over Nb+Nb at the highest multiplicities might indicate an effect of contributions of less central collisions: At a given (high) multiplicity the two nuclei nearly fully overlap for Nb+Nb while at the same multiplicity the reaction Au+Au is still more peripheral resulting in a less dense participant region and hence a higher entropy.

In a recent paper, studying the effects of momentum-dependent interactions[20], it was claimed that the deuteron-to-proton ratio, at least for heavy systems, is sensitive to the nuclear equation of state. The theoretical value of $(d/p)_{max} \approx 0.62$, assuming a rather hard equation of state without momentum-dependent forces is in perfect agreement with our data at all projectile energies.

V. Experiment and Results for ^{16}O and ^{32}S induced reactions at 200 GeV/nucleon

The experiments at the ultrarelativistic energies were performed at the CERN SPS. The data presented in this section were again taken with the Plastic Ball detector, now incorporated into the WA80 experimental setup. The forward part of the Plastic Ball, - the Wall and Mall -, is no longer appropriate at ultrarelativistic bombarding energies and was therefore replaced by other detectors which are described elsewhere[21]. The pseudorapidity range covered by the Plastic Ball ($-1.7 < \eta < 1.3$) can therefore be associated with the domain of target fragmentation processes. The centrality of the reaction is classified be means of the remaining energy of the projectile at ±0.3 degree, as measured in the Zero Degree Calorimeter (ZDC) of the WA80 experiment.

Fig. 6 shows a representative plot of the ratio of deuteronlike to protonlike particles from the reaction O+Au at 200 GeV/nucleon. The ratios are, as described in Sec. II, extracted only from well identified particles in a certain overlap area in phase space. As for the cluster ratios from symmetric collision at

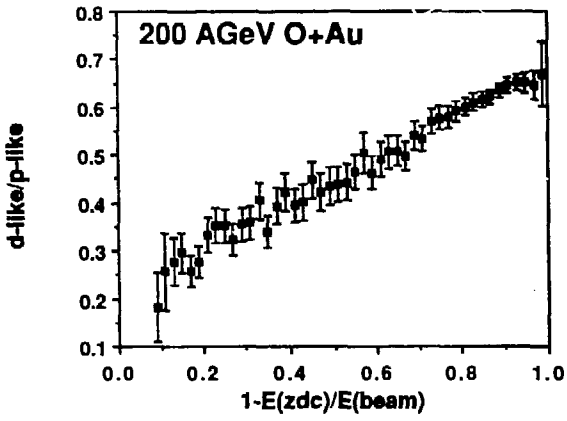

relativistic energies we observe a strong increase of the cluster ratio with the centrality of the collision.

The dependence on the mass of the target is shown in Figs. 7a,b, where the ratio of deuteronlike to protonlike particles is plotted

Fig. 6 Ratio of deuteronlike to protonlike particles of the reaction O+Au at 200 GeV/nucleon as a function of the centrality of the reaction.

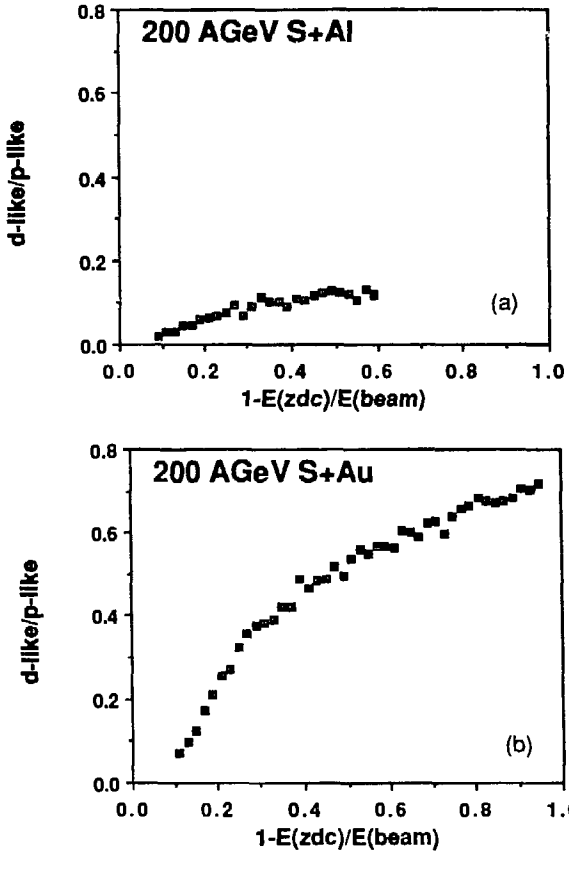

for the reaction S+Al and S+Au. We see a strong dependence on the target, while, comparing Fig. 6 and 7b, there is apparently no distinct dependence on the projectile.

The corresponding entropies, extracted at the maximum of the d-like/p-like curve, are plotted in Fig. 8a as a function of the target mass. The decrease of entropy with increasing target mass, which resembles the dependence of the entropy on the multiplicity as shown in Figs. 3 and 5 for symmetric collisions, is likely to be of the same nature: in both cases the "active" volume becomes larger and hence an decreased surface to volume ratio allows for

Fig. 7 Ratio of deuteronlike to protonlike particles of the reaction S+Al (a) and S+Au (b) at 200 GeV/nucleon as a function of the centrality of the reaction.

less entropy production. This observation suggests a strong coupling between the projectile and the target as a whole also at ultrarelativistic beam energies.

Part of the entropy produced during the collision process will be carried by pionic degrees of freedom. We have roughly estimated this fraction by assuming:

(i) The non-observed neutral pions amount to half the number of the observed charged pions.

(ii) The entropy per pion is about four units of entropy.

The result for the entropy carried by pions, normalized to the number of baryons, is shown in Fig. 8b. Differently from the case of the cluster ratios we account here for all baryons and pions falling into the acceptance window of the Plastic Ball. The error bars represents the systematic error due the lack of particle identification for very energetic protons and pions. We see again the decrease of entropy with increasing target mass as already observed for the cluster ratio.

It is instructive to compare the extracted entropies of "ultra-relativistic target matter" with the entropy of "relativistic participant matter". Fig. 9 shows a calculation of the dependence of S/A on the bombarding energy for symmetric systems taken from Ref. 16. We have included the experimental entropy per baryon for the reaction O+Au at 200 GeV/nucleon as the open and closed squares. Hereby the open and closed squares stand for S/A with and without the inclusion of the fraction of entropy carried by pions, respectively. The corresponding bombarding energy was determined by requiring the same ratio of the nucleonic and the full S/A for the experiment and for the calculation. As a result we obtain the surprising fact that the entropy of "ultrarelativistic target matter" is as high as the entropy of "participant matter" created in head-on collision of heavy symmetric systems at about 2±0.5 GeV/nucleon. A similar conclusion, however, can be drawn based on an analysis of the transverse energies[22] of the target fragments.

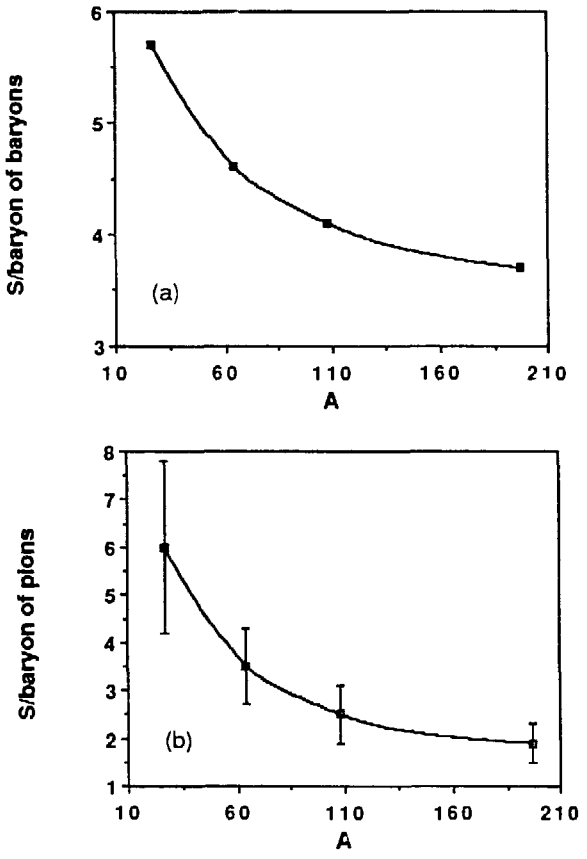

Fig.8 Dependence of the entropy per baryon for the fraction carried by baryons (a) and by pions (b) on the target mass.

VI. Summary

We have measured the multiplicity dependence of light cluster production for the medium heavy and heavy systems Nb+Nb and Au+Au at bombarding energies ranging from 150 to 650 MeV/nucleon.

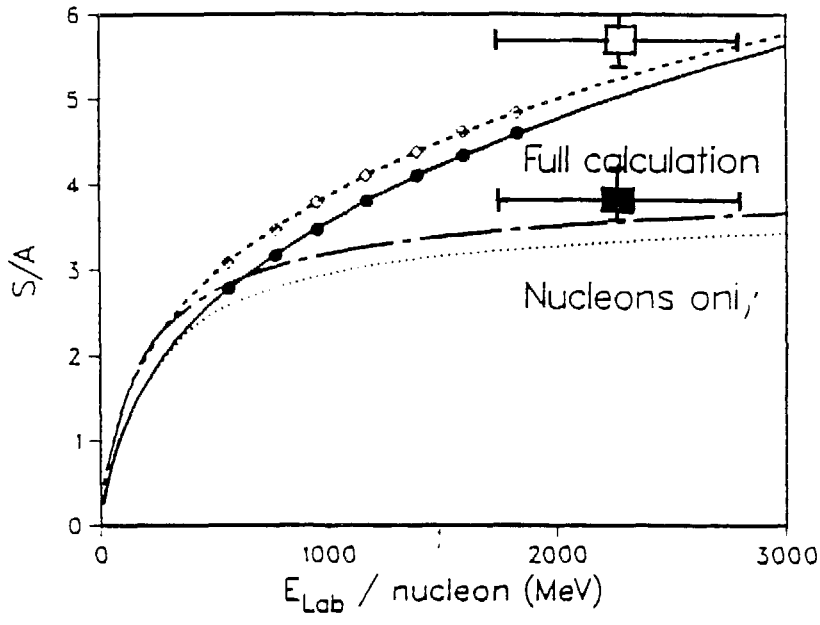

Fig. 9 Comparison of the experimental entropy per baryon produced in 200 GeV/nucleon O+Au carried by baryons only (closed squares) and by baryons and pions (open squared) with calculations. The calculations (Ref. 16) are done for symmetric collisions as a function of the bombarding energy. The lower and upper curve is for the nucleonic and full (nucleonic and pionic) entropy per baryon, respectively.

The specific entropy production has been extracted using the Quantum Statistical Model by Hahn and Stöcker[16]. A comparison of S/A at different bombarding energies gave no evidence for a significant amount of extra entropy at the lowest bombarding energy (150 MeV/nucleon) as would be expected from a phase transition, as far as this can be judged from the monotonically decreasing experimental entropies. A comparison of S/A for the two colliding systems shows at all energies only little dependence on the system. A comparison with models gives further evidence for significant compression effects in relativistic heavy ion reactions and for a rather stiff equation of state.

The entropy, produced in the target rapidity region in collisions of 200 GeV/nucleon ^{16}O and ^{32}S on various targets turns out to be comparable with the entropy of the participant fireball from central collisions of heavy nuclei at 2±0.5 GeV/nucleon. This, together with the dependence of the entropy on the target mass indicates a strong coupling of the projectile with the target as a whole.

Acknowledgements

We would like to thank Professor R. Bock for his continuous support. This work was supported in part by the U.S. Departments of Energy under Contract No. DE-AC03-76SF00098.

References

1 L.P. Csernai and J.I. Kapusta, Phys. Rep. 131 (1986) 223, and Refs. therein
2 J.I. Kapusta, Phys. Rev. C24 (1981) 2545
3 H. Stöcker, G. Buchwald, G Graebner, P. Subramanian, J.A. Maruhn, W. Greiner, B.V. Jacak and G.D. Westfall, Nucl. Phys. A400 (1983) 63c
4 G. Bertsch and J. Cugnon, Phys. Rev. C24 (1981) 2514
5 K.K. Gudima, V.D. Toneev, G. Röpke and H. Schulz, Phys. Rev. C32 (1985) 1605
6 H.W. Barz, B. Kämpfer, B. Lukás and L.P. Csernai, Phys. Rev. C31 (1985) 268
7 H. Stöcker, J. Phys. G: Nucl. Phys. 10 (1984) L111
H. Stöcker, Nucl. Phys. A418 (1984) 587c
8 J.I. Kapusta, Phys. Rev. C29 (1984) 1735
9 L. P. Csernai and B. Lukás, Phys. Lett. 132B (1983) 295
10 H. Stöcker and W. Greiner, Phys. Rep. 137 (1986) 277
11 P.J. Siemens and J.I. Kapusta, Phys. Rev. Lett. 43 (1979) 1486
12 H.H. Gutbrod, H. Löhner, A.M. Poskanzer, T. Renner, H. Riedesel, H.G. Ritter, A. Warwick, F. Weik and H. Wieman, Phys. Lett. 127B (1983) 317
13 K.G.R. Doss, H.-Å. Gustafsson, H.H. Gutbrod, B. Kolb, H. Löhner, B.Ludewigt, A.M. Poskanzer, T. Renner, H. Riedesel, H.G. Ritter, A. Warwick and H. Wieman, Phys. Rev. C32 (1985) 116
14 A. Baden, H.H. Gutbrod, H. Löhner, M.R. Maier, A.M. Poskanzer, T. Renner, H. Riedesel, H.G. Ritter, H. Spieler, A. Warwick, F. Weik and H. Wieman, Nucl. Inst. and Meth., 203 (1982) 189
15 H. Sato and K. Yazaki, Phys. Lett. 98B (1981) 153
16 D. Hahn and H. Stöcker, LBL-22378 preprint (1986)
17 K.-H. Kampert et al., to be published and private communication
18 K.G.R. Doss, H.-Å. Gustafsson, H.H. Gutbrod, K.-H. Kampert, B. Kolb, H. Löhner, B.Ludewigt, A.M. Poskanzer, H.G. Ritter, H.R. Schmidt and H. Wieman, Phys. Rev. C57 (1986) 302
19 J. Boguta and H. Stöcker, Phys. Lett. 102B (1983) 289
20 J. Aichlin. A. Rosenhauer, G. Peilert, H. Stöcker and W. Greiner, Phys. Rev. Lett. 58 (1987) 1926
21 H.R. Schmidt et al, GSI-87-64 preprint (1987)
22 K.H. Kampert et al., contribution to this conference

TRANSVERSE ENERGY PRODUCTION AND THE EQUATION OF STATE OF NUCLEAR MATTER

Karl Heinz Kampert * **for GSI - LBL Plastic Ball Collaboration and**
LBL-GSI-Lund-Münster-ORNL WA80 Collaboration

Abstract

In nuclear collisions of Au+Au, Nb+Nb and Ca+Ca at bombarding energies between 150 and 800 MeV per nucleon transverse energy and transverse momenta of light particles are studied event by event at $\theta = 90°$ in the center of mass system. At all energies a rise of the mean transverse energy per nucleon is observed with increasing charged particle multiplicity. Particularly large values of $E_\perp$ have been found for ^{3}He - fragments. The hydrodynamical picture is discussed for a possible separation of the collective flow and the thermal parts of the $E_\perp$ - spectrum. From this, evidence for a rather stiff equation of state is found. Transverse particle energies, measured in the target rapidity region of 60 and 200 AGeV oxygen and sulphur induced reactions, indicate a surprisingly high energy transfer to the target spectator.

1. Introduction

The possibility to investigate nuclear matter at high density and excitation energy and to derive an equation of state for this form of matter is one of the major motivations for performing relativistic heavy ion experiments.

Recently, collective sidewards flow of nuclear matter has been established [1] and interpreted as a signature of compressional effects, as predicted by the hydrodynamical model [2,3]. The amount of energy contained in the *directed* collective motion was estimated to be 10-20 % of the total available kinetic energy in the center of mass (c.m.) system. Furthermore, an increasing cluster production was observed with increasing multiplicities of charged particles, indicating that particles are more correlated in phase space the more central the collision, pointing towards another collective phenomena [4]. Previous investigations of spectra at 90° in the c.m.-system in Ca+Ca and Nb+Nb collisions [5] have given support to the picture of a blast-wave containing an ordered radial expansion- and an uncorrelated thermal part [6]. This superposition of different contributions to the transverse energy spectra makes the extraction of temperatures via ad hoc Boltzmann parameterizations of the measured proton spectra very problematic and the inverse slope-parameters extracted by this method can represent only an *upper limit* for the temperature [6]. This has again been confirmed by a recent analysis, where the thermal energy of a colliding system was cal-

*) Institut für Kernphysik D-4400 Münster, West Germany
Present address: CERN, EP-Division, C-1211 Geneva 23

culated from the observed pion yields [7]. The temperatures, as calculated by this thermodynamical model which includes also the compressional energy, are significantly lower than those extracted from the spectra via Boltzmann fits. The goal of this study is to investigate in detail the transverse energy, $E_\perp$, carried out by the various light fragments, p, d, t, ^{3}He and ^{4}He and to derive information about the equation of state (EOS) of nuclear matter from the discrepancy between the measured and calculated thermal mean transverse energies.

2. Results

2.1 Symmetric systems at bombarding energies of 150-800 AMeV

Collisions of Au+Au, Nb+Nb and Ca+Ca at several beam energies between 150 and 800 MeV per nucleon have been measured with the Plastic Ball detector-system [8] at the Bevalac in a minimum bias trigger mode. In the Plastic Ball charged reaction products up to ^{4}He are well identified. Their high multiplicity measured over the full 4π solid angle of the detector system allows one to evaluate mean values of the transverse energies and momenta of protons and light composites with sufficient statistical significance in each single event and to directly relate these values to other event specific observables like particle multiplicities (i.e. impact parameters) or flow angles, for example.

In fig. 1 contour lines of the event yield accumulated in the minimum bias trigger are shown in the $< E_\perp /particle >_{event}$ versus participant proton multiplicity (N_p) plane for the reaction Au+Au at 250 MeV per nucleon. N_p is defined to include also the protons bound in clusters up to ^{4}He, but to exclude particles in the projectile and target spectator regions [4]. Apart from the very low multiplicity events ($N_p < 10$ in fig. 1), a narrow distribution of the means analyzed event by event and a strong rise with increasing multiplicity is observed, demonstrating a strong correlation between the centrality of the event and the mean transverse energy per particle. Since the main interest is in the properties of participant matter, the following analysis has been restricted to particles observed at $\theta_{cm} = 90°$ where spectator contributions are minimal for kinematical reasons. A systematic study of the bombarding energy dependence of the mean transverse proton energy is shown in fig. 2 for Au+Au collisions at E_{lab} = 150, 250, 400, 650 and 800 MeV per nucleon. Since the average multiplicity depends on the bombarding energy and the projectile-target mass, the events have now been classified according to the normalized participant proton multiplicity, N_p/N_p^{max} [9], which allows a meaningful comparison of the different systems. At all energies a significant increase of the mean transverse proton energy with multiplicity is observed. The maximum values, attained in most central collisions, rise from $E \cong 70$ MeV at 150 MeV per nucleon up to $\cong$ 160 MeV at 800 MeV per nucleon incident energy. Systematic errors increase

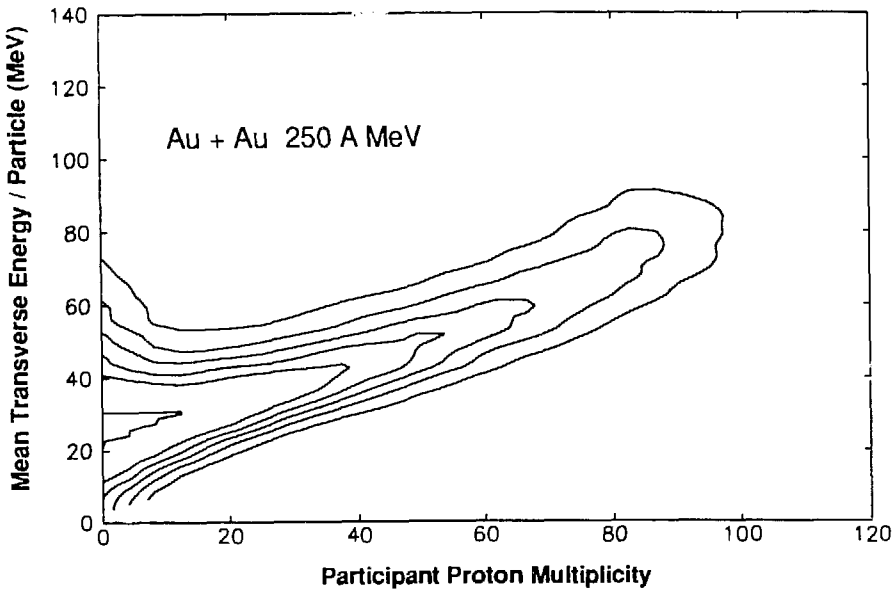

Figure 1: Contour plot (linear contours) of the mean transverse energy per particle ($<Et/particle>_{event}$) vs participant proton multiplicity (N_p) for Au+Au collisions at 250 MeV per nucleon.

with bombarding energy from <7 % up to ≈15 % at the highest energies.

It has been suggested in a previous paper [5] that the increase of the apparent temperature, i.e. the mean transverse energy per particle, with multiplicity may be caused partly by the increasing formation of composite particles which reduces the number of particles and therefore the number of degrees of freedom, thus raising the energy per particle. Let us study therefore the transverse energy of protons and composites individually. Since the formation of bound nuclei reduces only the number of *particles*, but not the number of *nucleons* emerging from the hot system, the mean kinetic energy per nucleon, $< E_{\perp}/nucleon >_{event}$ should - in a simple coalescence or fireball picture - stay constant as a function of multiplicity. Some representative results of such an analysis are shown in fig. 3 for Au+Au and Nb+Nb collisions at 250 MeV per nucleon incident energy. Here the mean transverse energies of p, d, t, ^{3}He and ^{4}He (upper half of the figure) are compared to their transverse energies per nucleon (lower part of the figure). Also, the average transverse energy per nucleon calculated from the sum of protons and the light composites is shown in the lower part of the figure. The Au+Au system still shows a significant increase of $< E_{\perp}/nucleon >_{event}$ of about 20 % when taking into account all particles up to ^{4}He. Only a weak dependence is found for Nb+Nb collisions. This difference might be explained, both, by the lower composite particle to proton ratios and by the weaker increase of the latter ones as a

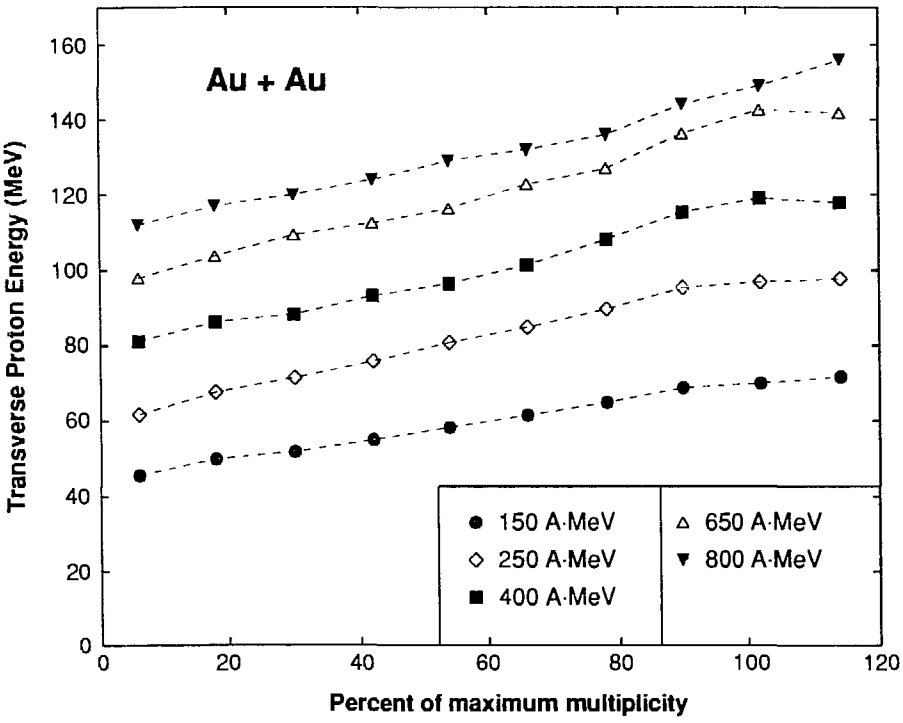

Figure 2: Mean transverse proton energy at θ_{cm} = 90° as a function of the normalized participant proton multiplicity (N_p/N_p^{max}) for Au+Au collisions at different beam energies between 150 and 800 MeV per nucleon. (The statistical errors are of the order of the size of the drawn symbols. Systematic errors increase with bombarding energy from <7 % up to 15 % at the highest energies.)

function of multiplicity in the Nb+Nb system [10]. It should be mentioned that in this calculation of $< E_\perp/nucleon >$ the free neutrons, that cannot be detected in the Plastic Ball, have been ignored. If the mean transverse energy of neutrons as a function of multiplicity would be assumed to be comparable to that of protons, then this contribution to the sum would result in a slight increase in the curve of Nb+Nb as well.

Inspecting now the transverse energies of the different particles themselves (upper part of fig. 3), we observe no significant differences in $< E_\perp/particle >$ between hydrogen isotopes (p, d, t) as one would expect from a pure fireball picture when the different particle species are in thermal equilibrium. However, ^{4}He and in particular ^{3}He - fragments exhibit a strong deviation to higher values. It should be pointed out that the selected θ_{cm}= 90° spectra are, due to the c.m.-boost, not affected by the particle dependent low-energy cutoffs in the detector, so that detector biases can be ruled out to cause this effect. Systematic errors, however, may be introduced by the limited particle identification of ^{3}He and ^{4}He in the Plastic Ball (see. ref. [8]). This effect could result in an uncertainty in the transverse energy of about 10-15 %

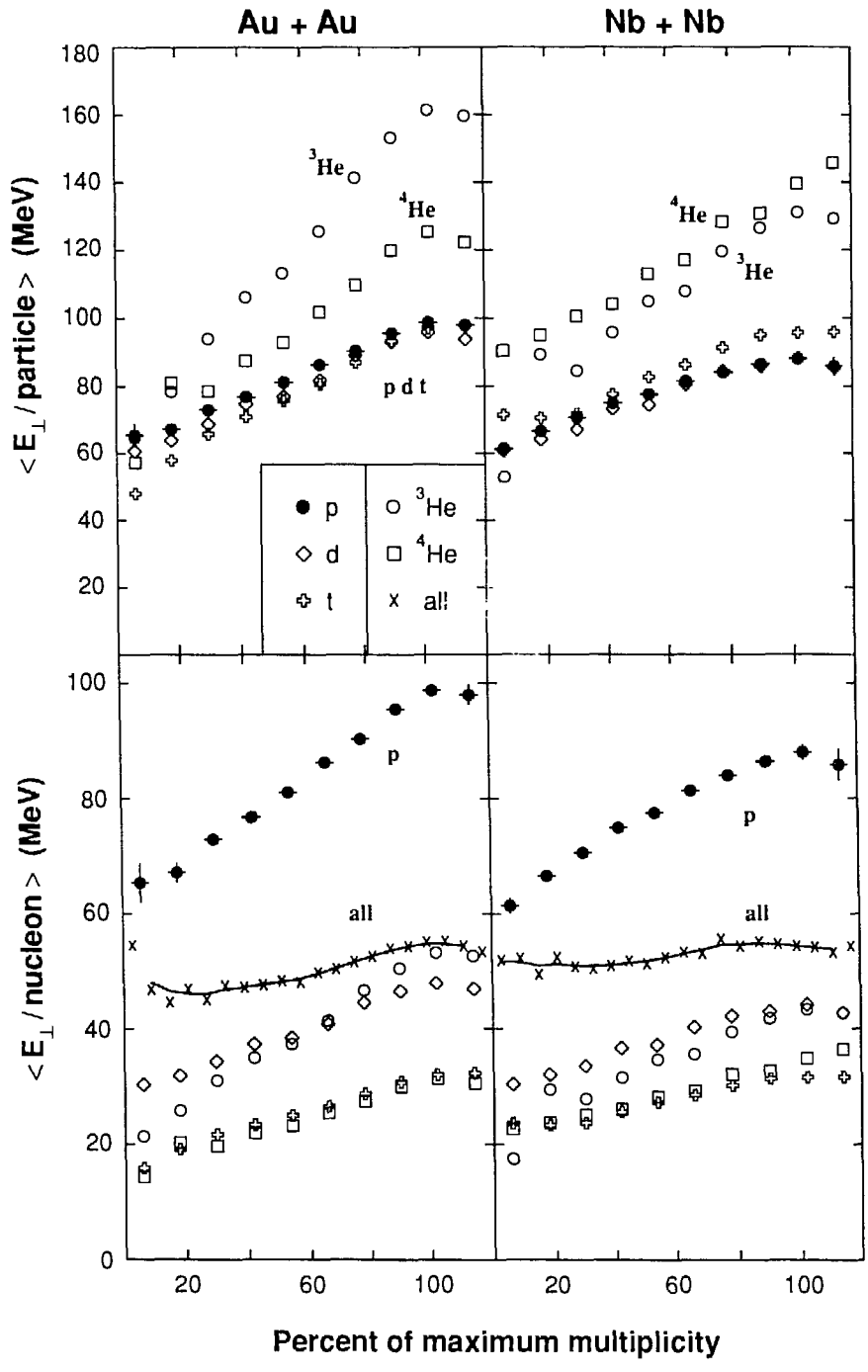

Figure 3: *Mean transverse energy per particle (upper half) and per nucleon (lower half) of p,d,t,^{3}He and ^{4}He at θ_{cm} = 90° as a function of normalized multiplicity and the mean transverse energy per nucleon for the whole set of particles for collisions of Au+Au and Nb+Nb at 250 MeV per nucleon, respectively. (For errors see fig. caption 2)*

when the yields of ^{3}He and ^{4}He are very different. A possible explanation for this "^{3}He-puzzle", also observed in asymmetric heavy-ion collisions, was proposed in ref. [11]. It was argued that ^{3}He may predominantly be emitted from the hot parts of the nucleus, thus being created in an early stage of the reaction, whereas the emission of ^{4}He and heavier particles was considered to come from a later stage. In addition, neutron rich systems, like Au+Au, are affected by the "proton robbing" of the light cluster production, i.e. the emission of p, d, ^{3}He and ^{4}He increases the *N/Z* -ratio in the remaining residue of the emitting system, thus reducing the yield of neutron poor isotopes with low kinetic energies. The latter seems to be confirmed by the observation that the strikingly high transverse energy of ^{3}He drops by more than 20 % when going from Au+Au to Nb+Nb collisions. The ^{4}He and proton spectra on the other hand do not show any significant projectile-target dependence. Coulomb repulsion, which could be considered a possible source of the increased transverse energies of the Helium isotopes, seems therefore to be of minor importance only. The situation is somewhat different for Ca+Ca, which is the lightest system investigated here. The transverse energies, attained in central collisions of the two heavier systems cannot be reached for any of the fragments, as may be due to insufficient stopping and transparency effects. This finding would be interesting to compare with recent model calculations of ref. [12] where momentum dependent interactions are reducing the effective number of nucleon-nucleon collisions in the reaction. In the following analysis only data of the more massive Au+Au and Nb+Nb systems have therefore been used. As discussed above, the mean transverse energy per particle cannot be related directly to the temperature, because of the different contributions to the energy spectra. However, if we ignore for the following discussion the ^{3}He puzzle and concentrate on the fact that the mean transverse energy per particle is the same for all hydrogen isotopes, i.e. for the major part of the cross section, and make the assumption that nearly all of the available c.m.-energy resides exclusively in thermal and compressional energy at the moment of highest density then

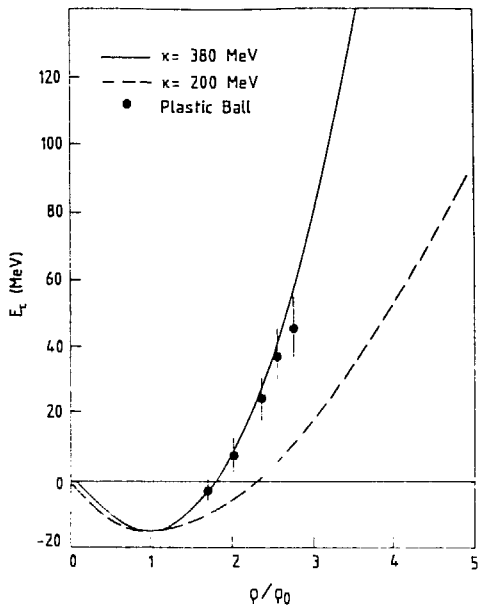

Figure 4: Equation of state from the present date compared to Skyrme equations of state with κ=200 MeV and κ=380 MeV as used in the VUU theory [14].

one may interpret the observed transverse energy as being the sum of

$$E_{\perp} = E_{therm} + E_{compr} + E_{coul}$$

where E_{therm} is the thermal excitation energy and $E_{compr} + E_{coul}$ is the potential energy associated with the initial compression and the repulsive Coulomb forces. For the reasons discussed above, the latter is assumed to be negligible. Using this formula and a reliable model providing us with the thermal energy as a function of bombarding energy, one may calculate the ratio between thermal and compression energy to derive information on the EOS of nuclear matter. The model that has been used for this purpose is that of Hahn and Stöcker [7] which has been able to reproduce measured pion multiplicities over about eight orders in magnitude in the bombarding energy range from 30 MeV per nucleon up to 4 GeV per nucleon. The temperature, i.e. the thermal energy, predicted by that model, and the sum of the compressional and thermal energy taken from the present set of data, are listed in Table 1 for all bombarding energies studied here. With these model dependent assumptions we then interpret ≈ 40 % of the total kinetic c.m. energy being converted into compressional energy in the moment of highest density. The resulting equation of state is plotted in fig. 4 as a function of the density achieved in the shock zone, as obtained in the same way from solving the Rankine-Hugoniot shock compression equations as done in the model of ref. [7]. The data-points are fairly in line with the stiff EOS plotted as a solid line in this figure, which is the same EOS as used in recent VUU-calculations that were able to describe the transverse energy flow [13,14] and the pion yield.

Table1: Transverse energies of protons at $\theta_{cm} = 90°$ and temperatures, calculated from ref. [7], at different beam energies.

E_{lab} (MeV)	$E_{\perp}^{data}$ (MeV)	T^{π} (MeV)
150	70	27
250	97	37
400	119	46
650	142	62
800	157	69

2.2 Asymmetric systems at bombarding energies of 60 and 200 AGeV

In the second part of this talk we will present some preliminary results on oxygen and sulphur induced reactions at 60 and 200 AGeV, measured with the Plastic Ball detector in the WA80 setup [16] at the CERN SPS. Because of the strongly forward focussed particle emission pattern in ultrarelativistic heavy-ion collisions and also due to the limited geometrical acceptance of the Plastic Ball ($30° \leq \theta_{lab} \leq 160°$), fragments were only measured in the

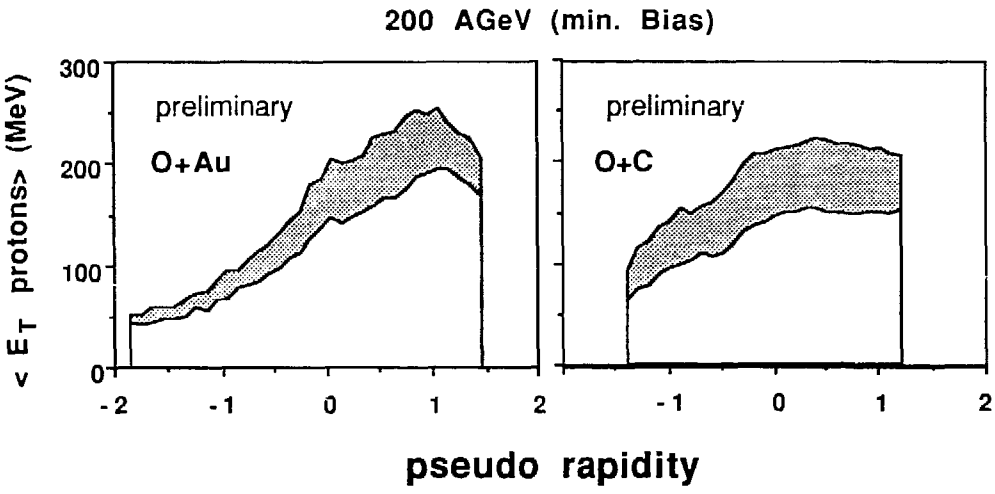

Figure 5: Mean transverse proton energy as a function of pseudorapidity for 200 AGeV O+Au and O+C collisions. Shadowed area indicates the systematic error.

target rapidity for this type of reactions. The analysis may therefore be regarded as an extension of the detailed studies of "participant" matter at relativistic energies to the study of "spectator" matter formed at ultrarelativistic heavy-ion collsions. Since neither the effective center of mass of the asymmetric systems nor the rest frame of the target spectator are known a priory, particle spectra were investigated in the laboratory system only. Figure 5 shows as an representative example the mean transverse proton energies from 200 AGeV minimum bias O+Au and O+C reactions as a function of the pseudorapidity, η , ($\eta = -\ln \tan(\theta_{lab}/2)$). The shadowed areas indicate the systematic error of these measurements which is mainly due to inability to separate very high energetic protons from punch through pions. For both systems, there is an indication of a maximum of about 200 MeV. Assuming that this structure is due to underlying physics, i.e. due to the target spectator source and not only caused by detector limitations, a longitudinal momentum transfer to the target residue of ≈ 500 MeV/c per nucleon can be estimated. Figure 6 shows the mean transverse proton energy, measured in the target rapidity region of 200 AGeV O+Au reactions, as a function of the centrality of the event, defined by the energy loss of the projectile [16]. For comparison, transverse proton energies measured in the central rapidity region of 800 AMeV Au+Au collisions are included. Evidently, there is a surprisingly high energy transfer to the target spectator which makes its excitation energy comparable to that of a fireball created at top Bevalac energies. Similar conclusions have also been drawn from the observed high entropy production [17]. Counting the number of baryons emitted into the target rapidity reveals furthermore a complete desintegration of the target matter into light fragments in very central collisions.

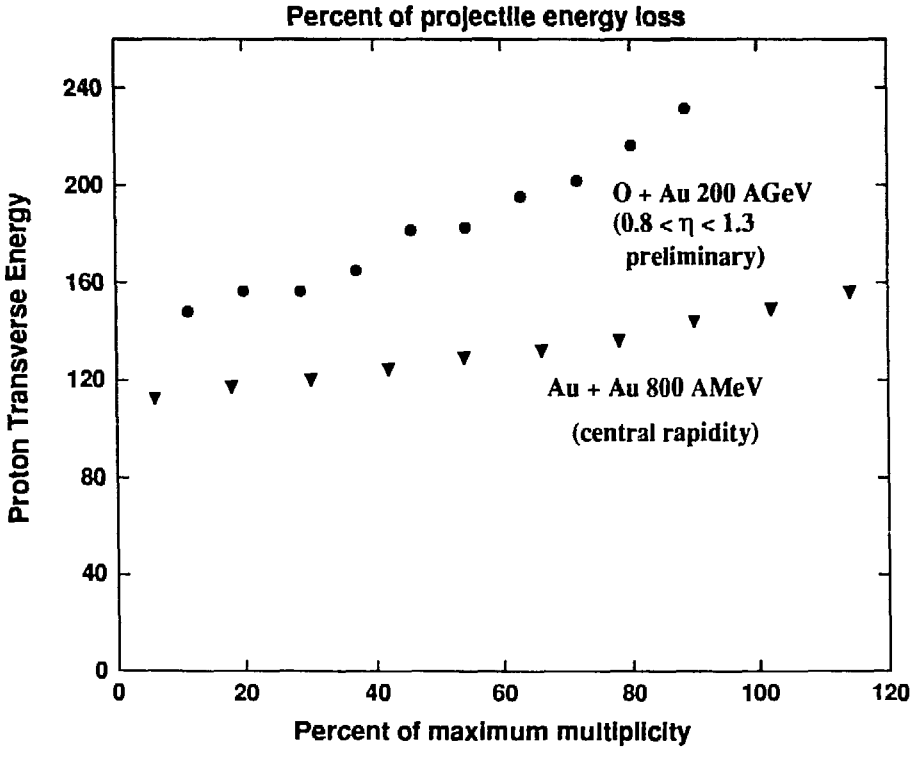

Figure 6: Mean transverse proton energy as a function of the centrality of the event for 200 AGeV O+Au reactions in the target rapidity region and for 800 AMeV Au+Au reactions at central rapidities.

Comparing different systems at 60 and 200 AGeV, we find only a very weak dependence of the transverse proton energies on the bombarding energy and a general trend of increasing values with increasing projectile and target mass.

3. Conclusion

We have presented data on transverse particle energies as a function of multiplicity and projectile-target mass at bombarding energies ranging from 150 MeV per nucleon up to 200 GeV per nucleon. For each particle type a strong increase in $E_\perp$ / *particle* as a function of multiplicity has been observed. At Bevalac energies this effect is strongest for helium isotopes. The hydrogen isotopes seem to be in thermal equilibrium since they show the same mean transverse energy per particle. ^{3}He exhibits strong anomalies, i.e. particular high $E_\perp$-values with respect to tritons and α - particles for the heaviest Au+Au system.

A model dependent way was proposed for extracting the equation of state at lower energies than was done earlier (see for example ref. [15]), down to densities $\rho / \rho_0 = 1.5$. The results

are another confirmation of a model employing a rather stiff equation of state, which is already tested with data on collective flow and on pion production. It is necessary, however, to point out several problems which must be addressed for a more quantitative discussion; i) the model which has been used to deduce the thermal energy from experimental pion yields assumes a global thermal equilibrium over the whole participant volume and calculates the temperatures in the moment of chemical freeze-out of the π/Δ-degree of freedom, whereas the measured proton transverse energies are influenced also by the clustering to composite particles which increases the temperature of the thermal bath. However, based on measured abundance ratios [4,10] and assuming ideal thermalization in the moment of particle freeze-out one can estimate this effect to cause a maximum increase of the transverse particle energy of about 15-20 % at the lowest bombarding energy and to be less important (≤10 %) at the highest bombarding energy, studied here. ii) A certain part of the transverse momentum may be transmitted via Coulomb repulsion from the large number of protons in the participant volume, and iii) experimentally, the calibration and detector inefficiencies at the highest bombarding energies may introduce some additional uncertainties. Recently, it has also been suggested that a consideration of the momentum dependent interactions in theories used so far, may affect the sensitivity of the information obtained from pion yields to the EOS quite strongly [12].

First results on 60 and 200 AGeV oxygen and sulphur induced reactions indicate a remarkable longitudinal and transverse energy transfer to the target spectator. The excitation energy is comparable to a fireball formed in head on collisions of Au+Au at top Bevalac energies and is sufficient to completely desintegrate the target nucleus into light fragments.

Acknowledgement

We are grateful for the continuous support of Professor R. Bock. This work was supported in part by the U.S. Departments of Energy under Contract No. DE-AC03-76SF00098.

References

1 H.Å. Gustafsson, H.H. Gutbrod, B. Kolb, H. Löhner, B. Ludewigt, A.M. Poskanzer, T.Renner, H. Riedesel, H.G. Ritter, A. Warwick, F. Weik, H. Wieman, Phys. Rev. Lett. 52, 1590 (1984).

2 W. Scheid, H. Müller and W. Greiner, Phys. Rev. Lett. 32, 741 (1974).

3 G. Buchwald, G. Graebner, J. Theis, J. Maruhn, W. Greiner, and H. Stöcker, Phys. Rev. Lett. 52, 1594 (1984).

G.R. Doss, H.Å. Gustafsson, H.H. Gutbrod, B. Kolb, H. Löhner, B. Ludewigt, A.M.Poskanzer, T. Renner, H. Riedesel, H.G. Ritter, A. Warwick, H. Wieman, Phys. Rev. C32, 116 (1985).

5 H.Å. Gustafsson, H.H. Gutbrod, B. Kolb, H. Löhner, B. Ludewigt, A.M. Poskanzer, T.Renner, H. Riedesel, H.G. Ritter, A. Warwick, F. Weik, H. Wieman, Phys. Lett. 142B, 141 (1984).

6 P.J. Siemens and J.O. Rasmussen, Phys. Rev. Lett. 42. 880 (1979).
7 D. Hahn and H. Stöcker, Nucl. Phys. A452, 723 (1986).
8 A. Baden, H.H. Gutbrod, H. Löhner, M.R. Maier, A.M. Poskanzer, T. Renner, H. Riedesel, H.G. Ritter, H. Spieler, A. Warwick, F. Weik, and H. Wieman, Nucl. Instr. and Meth. 203, 189 (1982).
9 K.G.R. Doss, H.Å. Gustafsson, H.H. Gutbrod, K.H. Kampert, B. Kolb, H. Löhner, B. Ludewigt, A.M. Poskanzer, H.G. Ritter, H.R. Schmidt and H. Wieman, Phys. Rev. Lett. 57, 302 (1986).
10 K.G.R. Doss, H.Å. Gustafsson, H.H. Gutbrod, D. Hahn, K.H. Kampert, B. Kolb, H. Löhner, A.M. Poskanzer, H.G. Ritter, H.R. Schmidt and H. Stöcker, Phys. Rev. C 36 (1987)
11 H.H. Gutbrod, A.I. Warwick and H. Wieman, Nucl Phys. A387, 177c (1982).
12 G.E. Brown, et al., Stony Brook preprint (1986), and J. Aichelin, A. Rosenhauer, G. Peilert, H. Stöcker and W. Greiner, Phys. Rev. Lett. 58 (1987) 1926
13 J.J. Molitoris, D. Hahn and H. Stöcker, Nucl. Phys. A447, 13c (1985).
14 H. Kruse, B.V. Jacak and H. Stöcker, Phys. Rev. Lett. 54 (1985) 289, and Phys. Rev. C31 (1985) 1770.
15 R. Stock, R. Bock, R. Brockmann, J.W. Harris, A. Sandoval, H. Ströbele, K.L. Wolf, H.G. Pugh, L.S. Schroeder, M.Maier R.E. Renford, A. Dacal and M.E. Oritz, Phys. Rev. Lett. 49 (1982) 1236.
16 H.H. Gutbrod et al, GSI preprint GSI-85-32, August 1985
17 H.R. Schmidt et al, proceedings to this conference

COMPARISONS OF VUU PREDICTIONS WITH STREAMER CHAMBER DATA

D. Keane, S.Y. Chu, S.Y. Fung, Y.M. Liu,[†] L.J. Qiao,
G. VanDalen, M. Vient, and S. Wang[†]
Department of Physics, University of California,
Riverside, California 92521

J.J. Molitoris[‡] and H. Stöcker
Institut für Theoretische Physik, Goethe Universität,
D-6000 Frankfurt am Main, West Germany

Abstract

Experimental charged particle inclusive and exclusive parameters for several nuclear systems are compared with microscopic model predictions based on the Vlasov-Uehling-Uhlenbeck equation, for various density-dependent nuclear equations of state (EOS). Inclusive variables and multiplicity distributions are in good agreement, and are not sensitive to the EOS. Rapidity spectra show evidence of being useful in determining whether the model uses the correct cross sections for binary collisions in the nuclear medium, and whether momentum dependent interactions are correctly incorporated. Sideward flow parameters do not favor the same nuclear incompressibility at all multiplicities, and there are indications that the present model may provide only an upper limit on the true stiffness of the EOS. Findings relating to impact parameter averaging and the mass and energy dependence of transverse flow are also presented.

Theoretical estimates of the peak density attained during the compressional phase of relativistic nucleus-nucleus collisions are typically in the range 2 to 4 times normal nuclear matter density. Model simulations indicate that certain observables stabilize at about the same time that the nuclear density reaches its maximum, and remain essentially unchanged during the subsequent stages of the collision process.[1,2] Collective sideward flow is one such observable, and shows promise of providing valuable information about the equation of state (EOS) of compressed nuclear matter. Fluid dynamic models[3] were the first to predict collective nuclear flow, but lack the detailed predictive power of a microscopic approach. The intranuclear cascade,[4] which neglects compressional potential energy, was the first microscopic model to successfully reproduce a wide range of experimental results;

however, the current consensus is that the cascade model yields a collective flow signature that is finite,[5-8] but consistently smaller than experimentally observed.[9,10,5-8] There have been previous comparisons[11-13,8] between experimental flow data and microscopic models with realistic EOS implementation over the full range of nuclear densities. Due to statistical errors, or uncertainties associated with filtering the predictions to simulate experimental sample selection criteria and detector inefficiencies, these comparisons yielded only preliminary estimates of EOS properties. In addition, more basic questions have yet to be resolved - uncertainties in the nucleon-nucleon cross section in the nuclear medium,[14,15] and the neglect of momentum dependence[16-18] in models with EOS implementation through a local density-dependent mean field potential.

The model[12.2] used in this study is a microscopic simulation which can be considered a solution of the Vlasov-Uehling-Uhlenbeck[19] (VUU) equation. It proceeds in terms of a cascade of binary collisions between nucleons, Δ resonances, and pions according to the experimental scattering cross sections for free particles, corrected by a Pauli blocking factor. The isospin of each particle is explicitly incorporated. The dependence on the equation of state enters via the acceleration of nucleons in the nuclear mean field. It is assumed that the local potential, U, is determined by the density of nucleons within a radius of 2 fm, with a functional form $U(\rho) = a\rho + b\rho^{\gamma}$. The parameter γ fixes the incompressibility, K, and the remaining two parameters are constrained by nuclear equilibrium conditions. $\gamma = 2$ corresponds to $K = 380$ MeV, and implies a "stiff" EOS, while $\gamma = 7/6$ corresponds to $K = 200$ MeV, usually characterized as either a "medium" or "soft" EOS. A special "supersoft" case, in which $\partial U/\partial\rho = 0$ above $\rho = \rho_o$ (equilibrium nuclear density), conforms to the assumptions of the intranuclear cascade model. Since K is defined in terms of the second derivative of the binding energy at ρ_o, both the K value *and* the functional form $U(\rho)$ must be specified in order to fix the EOS at higher densities.

Before making detailed comparisons of charged particle exclusive parameters, it is appropriate to verify that inclusive spectra are adequately reproduced by the model. Accordingly, we first present a comparison of inclusive parameters for two experimental samples from the Bevalac streamer chamber and a relatively large set of VUU model events. In order to minimize the difficulty of correctly filtering model predictions to simulate the experimental sample selection criteria and detector distortions, cuts have been imposed to remove the projectile and target spectator regions. These cuts (see below) remove $Z \geq 2$

spectator fragments which are not correctly identified in the streamer chamber, and for which a production mechanism is not incorporated in most models. The experimental samples contain a total of 1357 1.2 GeV/nucleon ^{40}Ar beam events with observed charged multiplicity $M \geq 30$. 571 of the collisions were on a KCl target, the remaining 786 on a BaI_2 target. The condition $M \geq 30$ selects just over 20% of the inelastic cross section in the case of the KCl target, and just under 40% in the case of the BaI_2 target. The streamer chamber, trigger, particle identification criteria, and additional experimental particulars are described elsewhere.[8,9,20] For each of the three values of EOS stiffness mentioned above, we have generated model statistics amounting to typically 5 times the experimental samples, using a total of about 50 hours of Cray X-MP CPU time.

The kinematic cuts remove particles with momentum (momentum per nucleon in the case of composites) < 0.27 GeV/c in the rest frames of the target and projectile. Fig. 1 shows distributions of M', the multiplicity of charged particles after imposition of these cuts. In correcting for observational losses and remaining $Z \geq 2$ composites, the detector filtering process reduces M' for each VUU event by about 12%; otherwise, the plotted VUU spectra are unaffected by filtering. Below $M' \sim 25$, the sample selection criterion $M \geq 30$ causes the roll-off in the M' spectra, and events in this lower tail of M' are discarded in the subsequent analysis. The consistently good agreement between experiment and VUU in Fig. 1 is an indication that matching M' distributions is an effective way to establish correct impact parameter averaging for a model.

Fig. 2 shows rapidity distributions, after applying the above spectator cuts and the condition $M' \geq 24$. The dotted curves (labeled $0.7\sigma_{2-body}$) correspond to a version of the VUU model in which all binary collision cross sections have been reduced by 30%. The total number of 2-body collisions decreases by about the same factor. Likewise, the dot-dash curve demonstrates the effect of an increase in collision cross sections. These curves demonstrate that rapidity spectra are useful both for determining whether the model uses the correct 2-body collision cross sections,[14,15] and for addressing questions about momentum dependent interactions[16–18] (MDI), which influence the number of collisions. Thus, these spectra can fulfill the need[18] for collective flow signatures (sensitive to both the EOS and MDI) to be supplemented by another parameter sensitive to just one of these. The factors 0.7 and 1.4 were chosen in light of the study by Bertsch *et al.*[15] of the effect of varying the cross sections over a 2 to 1 range, and the finding of Aichelin *et al.*[18] that MDI reduce the number of

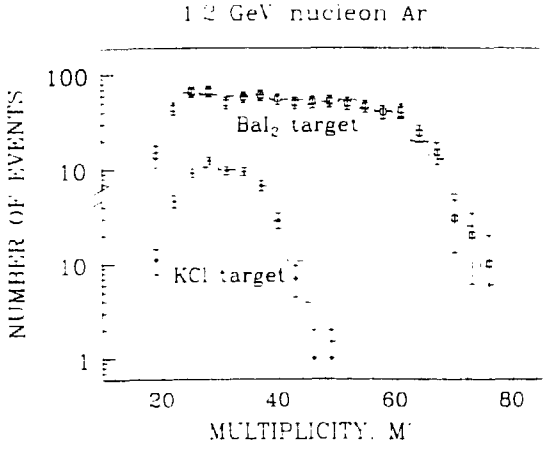

FIG. 1: Distributions of M', the total multiplicity of charged particles after cuts (see text). The dashed lines are the predictions of the VUU model, normalized to the same total number of events. Since the 3 VUU equations of state give essentially the same spectra, the 3 predictions have been averaged together in this plot. (The same is true for Figs. 2 and 3.)

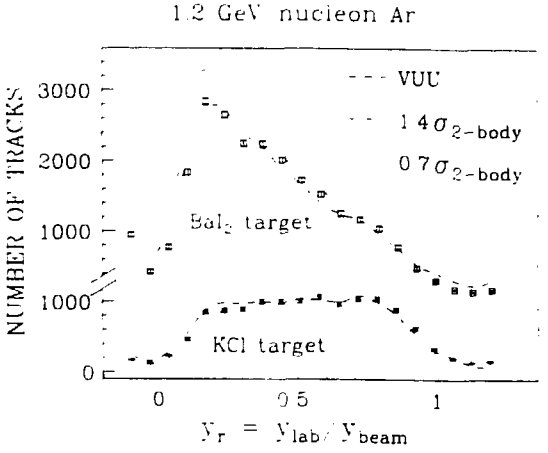

FIG. 2: Nucleon rapidity distributions for $M' \geq 24$, with spectator cuts. The results for the modified binary collision cross sections are shown only at rapidities where there is a significant difference between this calculation and the unmodified VUU model.

nucleon-nucleon collisions by 30% in the case of La + La at 0.8 GeV/nucleon. The current agreement between VUU (which does not incorporate MDI) and the experimental rapidity spectra suggests that any reduction in collisions due to MDI may need to be counteracted by an increase in the collision cross sections, possibly attributable to in-medium effects.

Fig. 3 presents distributions of transverse momentum per nucleon in three rapidity intervals. The good overall agreement between predictions and experiment again confirms that the VUU model accurately reproduces parameters which are not sensitive to the nuclear EOS.

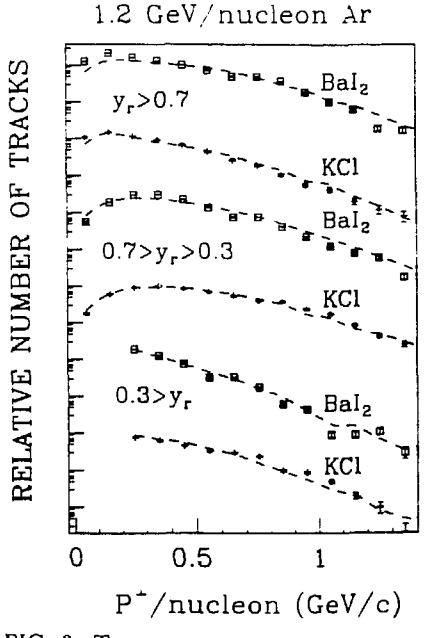

FIG. 3: Transverse momentum spectra for experiment and VUU in three rapidity intervals, where $y_r = y_{lab}/y_{beam}$. The vertical scale is in arbitrary logarithmic units.

The plot of $\langle p^x(y) \rangle$,[6] the mean transverse momentum/nucleon in the reaction plane as a function of rapidity, is now widely accepted[12,8,13,21–23] as the most useful parametrization of sideward flow. Fig. 4 shows $\langle p^x(y) \rangle$ for the same samples as in Figs. 1 to 3, along with VUU predictions for the 3 equations of state. While the multiplicity M' is still defined as in Fig. 1, with [illegible] and projectile spectator cuts, the projectile spectator cut has been omitted when calculating p^x. This has been done because the best sensitivity to the EOS coincides with rapidities $y_r \gtrsim 0.7$ in the upper half of the available multiplicity range as plotted in Fig. 1, and this region is excessively depopulated when the projectile spectator cut is applied. Ionization measurements on comparable samples confirm that the level of $Z \geq 2$ spectator like fragments in this region is not large enough to distort the p^x comparisons.

Over the relatively narrow multiplicity interval available for Ar + KCl, no significant dependence of $\langle p^x \rangle$ on M' can be detected. We have confined the VUU comparisons to the rapidity region where the overall detector efficiency is high, and there is useful sensitivity to K. The Ar + KCl results in Fig. 4 favor incompressibilities in the medium to stiff range.

Fig. 4 also shows $\langle p^x(y) \rangle$ for Ar + BaI_2 in three M' intervals. Here, the VUU predictions show the same qualitative multiplicity trend as the experimental data, with the directed flow effect reaching a maximum at intermediate multiplicity, as expected. The extent of the agreement between the model and experiment is not affected by changing the definition of M' (i.e., changing the cuts). Over most of the M' spectrum, K values in the medium

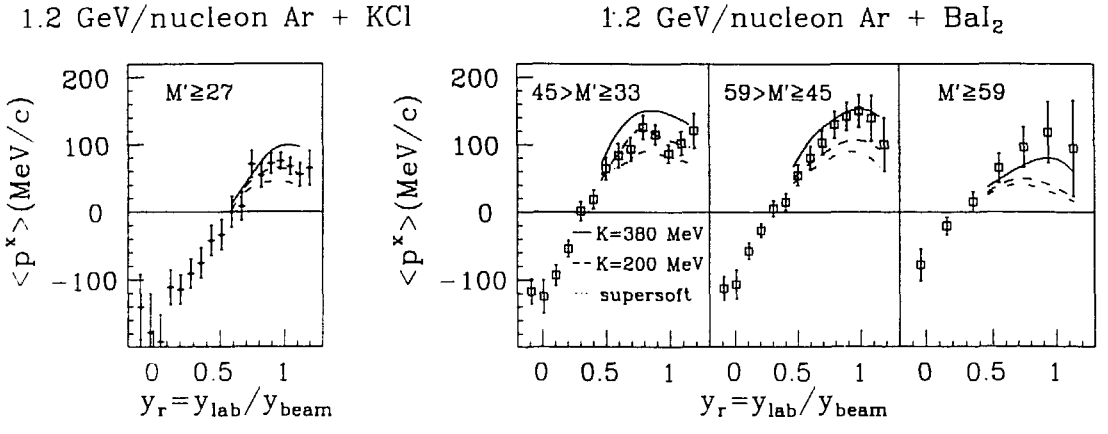

FIG. 4: Mean transverse momentum/nucleon in the reaction plane, as a function of rapidity. The VUU predictions are shown only over the rapidity region where there is useful sensitivity to the incompressibility, K (see text).

to stiff range are again favored. However, the predicted $\langle p^x \rangle$ drops off faster towards the highest multiplicities than indicated by experiment. (The last multiplicity interval, $M' \geq 59$, corresponds to the uppermost 5% of the inelastic multiplicity spectrum for Ar + BaI_2.) If it is postulated that this effect arises from a stiffening of the EOS at the higher densities associated with maximum multiplicity, then Fig. 5, which shows the M' dependence of the peak VUU nucleon density, provides an indication[24] that a very sharp increase in stiffness would be needed. It is also possible that the differing multiplicity dependence is associated with the fact that MDI[16–18] effects are neglected in the VUU model. At the very least, there are theoretical indications that a model without MDI can lead to overestimates of the incompressibility,[17,18] with the consequence that the present work may yield only upper limits on the true stiffness of the EOS.

Fig. 6 shows $\langle p^x(y) \rangle$ for 83 high multiplicity U + U events (~25% of the inelastic cross section). As in the case of 1.2 GeV/nucleon Ar + KCl, the multiplicity dependence is weak, and a medium to stiff K value is favored, but with poor statistical significance.

We emphasize that while appropriate

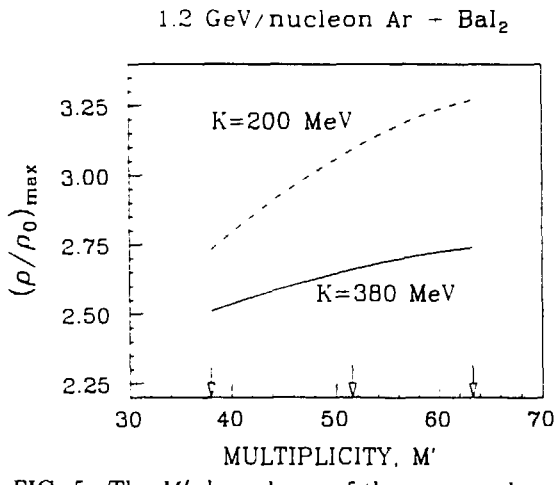

FIG. 5: The M' dependence of the mean nucleon density inside a sphere of radius 2 fm, at the time and position of maximum density in the VUU simulation of Ar + BaI_2 collisions. The three arrows along the M' axis denote the mean values for the three M' intervals for Ar + BaI_2 shown in Fig. 4. The half-maximum half-widths of the distribution of density at the peak are in the range 0.7 - 0.9 ρ_o.

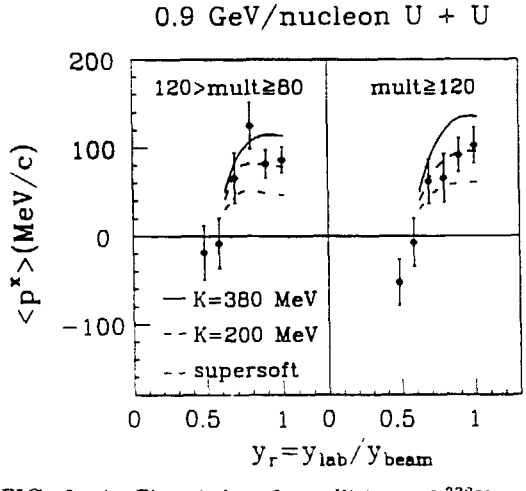

FIG. 6: As Fig. 4, but for collisions of ^{238}U + ^{238}U.

cuts can partly circumvent the need to simulate detector distortions and inefficiencies when comparing a model with experiment, there is no simple substitute for correct simulation of the impact parameter averaging associated with multiplicity and/or trigger selected subsamples. In order to illustrate this effect, we have taken VUU events for $K = 380$ MeV and plotted $\langle p^x(y)\rangle_{max}$ as a function of both impact parameter, b, and participant multiplicity, M'. Taking the peak of these plots, we define the ratio $P_{bM} = \langle p^x(y,b)\rangle_{max}/\langle p^x(y,M')\rangle_{max}$. For 1.2 GeV/nucleon Ar + KCl, we find $P_{bM} \sim 1.24$; for Ar + BaI_2 at the same energy, we find $P_{bM} \sim 1.16$. With the possible exception of the very heaviest systems, it is evident that non-trivial uncertainties arise if it is assumed[2] that $P_{bM} \sim 1$.

Table I summarizes all currently available transverse flow results from the Bevalac streamer chamber, based on a total of over 10^5 fully reconstructed events. VUU predictions have been generated for 6 systems corresponding to the boldfaced entries in Table I. As discussed above, it is not possible to conclude that one particular EOS is unambiguously favored; nevertheless, the percentage changes predicted using either the medium or hard EOS are in each case consistent with the data. Doss *et al.*[21] have reported a plateau or a decrease in the transverse flow with beam energy above 0.65 GeV/nucleon, but point out that it is

TABLE I: Transverse momentum/nucleon in the reaction plane, averaged over forward rapidities ($y_r \gtrsim 0.7$), for streamer chamber samples with a minimum bias trigger and a multiplicity cut which selects ~25% of the inelastic cross section. The Ne beam results are preliminary.

Beam energy: (GeV/nucleon)	0.4	0.8	1.2	1.8
Ne+NaF	25		**48**	**60**
Ar+KCl		50±4 §	**65±5**	**95±5** §
La+La		72±6 §		
U+U		**85±10** †		
Ne+BaI_2				160
Ar+BaI_2			**120±10**	
Ar+Pb	60±7	140±7 §		

§ Central trigger data from the GSI/LBL group; reported in refs. 6 and 23.

† These U+U collisions were at 0.9 GeV/nucleon.

well possible that this effect is influenced by the Plastic Ball response. Moreover, Doss *et al.* parametrized the flow in terms of the slope of $\langle p^x(y) \rangle$ near mid-rapidity; if the *shape* of $\langle p^x(y) \rangle$ changes with energy, then the quantity given in Table I ($\langle p^x \rangle$ at forward rapidities) need not scale in the same way. Overall, it is not clear that the balance of experimental evidence supports the view[2] that there is a softening of the EOS at the higher densities associated with beam energies at and above 1 GeV/nucleon.

We thank C. Hartnack for valuable comments, and we gratefully acknowledge the computing facilities provided by the San Diego Supercomputer Center. This work was supported in part by the U.S. Department of Energy under grant DE-FG03-86ER40271.

† Present address: Department of Physics, Harbin Institute of Technology, Harbin, PRC

‡ Present address: Department of Physics, Muhlenberg College, Allentown, PA 18104

1. H. Stöcker and W. Greiner, Phys. Rep. **137**, 277 (1986).
2. J.J. Molitoris, H. Stöcker, and B.L. Winer, Phys. Rev. C **36**, 220 (1987).
3. W. Scheid, H. Müller, and W. Greiner, Phys. Rev. Lett. **32**, 741 (1974); G. Buchwald, G. Graebner, J. Theis, J. Maruhn, W. Greiner, and H. Stöcker, Phys. Rev. Lett. **52**, 1594 (1984).
4. Y. Yariv and Z. Fraenkel, Phys. Rev. C **20**, 2227 (1979); J. Cugnon, Phys. Rev. C **22**, 1885 (1980); Y. Kitazoe, M. Sano, Y. Yamamura, H. Furutani, and K. Yamamoto, Phys. Rev. C **29**, 828 (1984).
5. D. Beavis, S.Y. Fung, W. Gorn, D. Keane, Y.M. Liu, R.T. Poe, G. VanDalen, and M. Vient, Phys. Rev. Lett. **54**, 1652 (1985).
6. P. Danielewicz and G. Odyniec, Phys. Lett. **157B**, 146 (1985).
7. J.J. Molitoris, H. Stöcker, H.-Å. Gustafsson, J. Cugnon, and D. L'Hôte, Phys. Rev. C **33**, 867 (1986); E. Braun and Z. Fraenkel, Phys. Rev. C **34**, 120 (1986).
8. D. Beavis, S.Y. Chu, S.Y. Fung, W. Gorn, D. Keane, Y.M. Liu, G. VanDalen, and M. Vient, Phys. Rev. C **33**, 1113 (1986).
9. D. Beavis, S.Y. Chu, S.Y. Fung, W. Gorn, A. Huie, D. Keane, J.J. Lu, R.T. Poe, B.C. Shen, and G. VanDalen, Phys. Rev. C **27**, 2443 (1983).
10. H.-Å. Gustafsson, H.H. Gutbrod, B. Kolb, H. Löhner, B. Ludewigt, A.M. Poskanzer, T. Renner, H. Riedesel, H.G. Ritter, A. Warwick, F. Weik, and H. Wieman, Phys. Rev. Lett. **52**, 1590 (1984); R.E. Renfordt, D. Schall, R. Bock, R. Brockmann, J.W. Harris, A. Sandoval, R. Stock, H. Ströbele, D. Bangert, W. Rauch, G. Odyniec, H.G. Pugh, and L.S. Schroeder, Phys. Rev. Lett. **53**, 763 (1984).
11. J.J. Molitoris, J.B. Hofler, H. Kruse, and H. Stöcker, Phys. Rev. Lett. **53**, 899 (1984).
12. H. Kruse, B.V. Jacak, and H. Stöcker, Phys. Rev. Lett. **54**, 289 (1985); J.J. Molitoris and H. Stöcker, Phys. Rev. C **32**, 346 (1985), and Phys. Lett. **162B**, 47 (1985).

13. D. Keane, D. Beavis, S.Y. Chu, S.Y. Fung, W. Gorn, Y.M. Liu, G. VanDalen, M. Vient, J.J. Molitoris, and H. Stöcker, in *Proceedings of the 2nd Conference on the Intersections between Particle and Nuclear Physics, Lake Louise, Alberta, 1986* (CONF-860575), p. 844.

14. M. Gyulassy, K.A. Frankel, and H. Stöcker, Phys. Lett. **110B**, 185 (1982).

15. G.F. Bertsch, W.G. Lynch, and M.B. Tsang, Phys. Lett. **189B**, 384 (1987).

16. L. Wilets, Y. Yariv, and R. Chestnut, Nucl. Phys. **A301**, 359 (1978); A.R. Bodmer, C. Panos, and A.D. MacKellar, Phys. Rev. C **22**, 1025 (1980); B. Schürmann and W. Zwermann, Phys. Lett. **158B**, 366 (1985).

17. C. Gale, G. Bertsch, and S. Das Gupta, Phys. Rev. C **35**, 1666 (1987).

18. J. Aichelin, A. Rosenhauer, G. Peilert, H. Stöcker, and W. Greiner, Phys. Rev. Lett. **58**, 1926 (1987).

19. E.A. Uehling and G.E. Uhlenbeck, Phys. Rev. **43**, 552 (1933).

20. M. Vient, thesis, U.C. Riverside, 1988 (to be published); M. Vient *et al.* (to be published).

21. K.G.R. Doss, H.-Å. Gustafsson, H.H. Gutbrod, K.H. Kampert, B. Kolb, H. Löhner, B. Ludewigt, A.M. Poskanzer, H.G. Ritter, H.R. Schmidt, and H. Wieman, Phys. Rev. Lett. **57**, 302 (1986).

22. A. Bonasera and L.P. Csernai, Phys. Rev. Lett. 59, 630 (1987).

23. P. Danielewicz, H. Ströbele, G. Odyniec, D. Bangert, R. Bock, R. Brockmann, J.W. Harris, H.G. Pugh, W. Rauch, R.E. Renfordt, A. Sandoval, D. Schall, L.S. Schroeder, and R. Stock, in *Proceedings of the International Workshop on Gross Properties of Nuclei and Nuclear Excitations XV, Hirschegg, Austria, 1987*, p. 91; H Ströbele *et al.*, these Proceedings.

24. The correct implementation of a "stiffening" of the EOS beyond a certain density requires a more elaborate functional form for the mean field potential, $U(\rho)$; however, the data in Fig. 5 imply that even a discontinuous jump from $K = 200$ MeV to $K = 380$ MeV at some critical density would not explain the differences in $\langle p^x(M') \rangle$ shown in Fig. 4.

SCALING PROPERTIES OF THE COLLECTIVE FLOW

L.P. Csernai[+]
National Superconducting Cyclotron Laboratory
Michigan State University
East Lansing, Michigan, 48824-1321 USA,

A. Bonasera[*]
Sektion Physik
University of Munich
D-8046 Garching, W.-Germany,
and

B. Schürmann
Physik-Department
Technische Universität München
D-8046 Garching, W.-Germany

Abstract: Transverse flow measurements in heavy ion collisions are analyzed in terms of the similarity properties of fluid-dynamics. The analysis of corresponding recent experimental data shows fluid-dynamical scaling behavior in a wide mass number and energy range. Deviations from perfect scaling at low beam energies are pointed out.

The energy and mass dependences of several experimentally measured inclusive quantities were discussed recently based on the scaling behavior of the fluid dynamical model [1]. The methods of analysing the collective flow developed essentially, new exclusive observables were introduced and extensively studied. Recent experiments at the Berkeley BEVALAC provided evidence of a collective sideward flow of particles emitted in collisions of two massive nuclei [2-4]. Based on these experiments there is a persistent theoretical effort [5-7] to extract information about the nuclear compressibility and the equation of state. The connection between the calculated collective flow pattern and the observed flow tensor is influenced strongly by thermal smearing [8,9], distorted by finite particle number effects [10] and composite fragment formation [11]. Additional information about the matter properties may be gained by a comparison of reactions of different beam energies and masses. By studying the scaling properties of these quantities information about transport properties of nuclear matter as well as about sudden changes in the equation of state could be gained. Such a sudden change at low beam energies was observed recently [1] by performing a first scaling study of the transverse momentum analysis.

Scaling properties of fluid dynamics are well known and in connection with nuclear reactions they were discussed first in ref. [1c]. It was shown that under some simple assumptious dimensionless variables can be introduced, and their development is governed by the same Euler or Navier-Stolus equations and continuity equation. The physical qualities are made by extracting a characteristic dimensional constant like p_1, T_1, u_1, ℓ_1, n_1 etc. For example $\vec{r} = \ell_1 \cdot \tilde{r}$, where $\tilde{r}$ is the dimensionless position vector. In the dimensionless Euler equation and continuity equation the characteristic dimensional constants appear only in one dimensionless combination: the strouhal number $st = u_1 t_1 / \ell_1$. With a proper choice of the timescale, t_1, this can always be

set to unity and on this timescale the dimensionless flow patterns are then identical. Consequently all dimensionless observables would be the same independent of beam energy and target and projectile mass [1c]. In nonperfect fluid dynamics another dimensionless combination of the characteristic dimensional constants is introduced the Reynolds number. Thus the results are identical only if the Reynolds number of the two colliding systems are the same. Similarly the Equation of state may have properties violating the scaling behaviour. This can be represented by the change of the dimensionless sound speed $\tilde{c}_1$ given by the EOS.

In perfect fluid-dynamics the flow angle θ_{cm} and the "aspect ratio" R are scale invariant quantities. If the fluid dynamical scaling were exact these quantities would not depend on A and E_0 in a given scale invariant multiplicity bin. This is, however, not the case: the flow angle decreases with increasing beam energy above E=200 MeV/nucleon and increases with increasing mass [3,12,13].

Staying within a fluid dynamical description the nonscaling behavior when comparing different beam energies has two main reasons. The most important is that the pressure in the central zone does not increase linearly with the beam energy as it should if scaling would hold. This is because the equation of state is not that of an ideal gas. The rate of pressure increase presumably stays behind the increase of the beam energy thus leading to a smaller pushing force moving the outside regions of the matter in the transverse direction. The second reason is that the dissipation (viscosity) is also energy (temperature) dependent leaving less energy in directed kinetic energy that can show up in transverse direction. The interplay of these two effects determines the non-scaling of the observed flow angles with energy.

In an infinite system the viscosity would have no effect on the flow angle. In a small system the role of dissipation is more important. The relatively larger dissipated energy leads to smaller transverse flow. Thus the flow patterns of systems at different energies and of different masses are similar only if the Reynolds numbers characterizing the flow are the same.

THE REYNOLDS NUMBER

From fluid dynamical studies we know that two fluids which have the same Reynolds, Strouhal, and Mach numbers will behave similarly. Indeed, in the derivation of the scale invariant continuity and Navier-Stokes equations [1], it has been shown that these equations depend on the Reynolds number. With the proper choice of time scale the Strouhal number can be set equal to unity. The Mach number which is defined as the ratio of the flow speed to the speed of sound is of the order of unity because of the assumption on the equation of state (EOS) we use in the scaling analysis (see eq. (14) in [1c]).

In order to calculate the Reynolds number we have to evaluate the viscosity η. The usual simple assumption is that the kinetic viscosity, $\nu=\eta/(nm)$, is constant [1]. So

$$Re = l, u, / \nu \qquad (1)$$

yields a simple energy and mass dependence. If, however, we want to have a more realistic estimate the density and temperature dependence of the viscosity should explicitly be considered. There are some theoretical estimates of the viscosity of nuclear matter [14]. Here we use the most recent calculation of Danielewicz [15] based on the Boltzmann equation. Introducing the dimensionless variables (see reg. [1]) the kinetic viscosity in this approach is given by:

$$\nu = \frac{\eta}{mn} = \frac{1}{mn_0\tilde{\tau}} \left\{ \frac{1700}{4E_0^2\tilde{T}^2/9} \left(\frac{\tilde{n}}{\tilde{n}_0}\right)^2 + \frac{22}{1+\frac{4}{9}E_0^2\tilde{T}^2/10^3} \left(\frac{\tilde{n}}{\tilde{n}_0}\right)^{0.7} + \frac{5.8\ \sqrt{2E_0/3}\ \sqrt{\tilde{T}}}{1+\frac{9\times 160}{4\ E_0^2\tilde{T}^2}} \right\}$$

$$= f(\tilde{n},\tilde{T},E_0) \ / \ n_0 \ . \qquad (2)$$

Substituting (3.2) into (3.1) gives:

$$Re = \frac{\sqrt{2mE_0}\ \ A^{1/3}\ n_0^{2/3}}{f(\tilde{n},\tilde{T},E_0)} \qquad (3)$$

In Fig. 1a the contour lines corresponding to constant Reynolds numbers are plotted in the [E_{cm}, A] plane. Since the viscosity depends on the temperature and density we assume that the temperature scales with the beam energy and that $\tilde{n}$ and $\tilde{T}$ are constants. In Fig. 1a an example is shown for $\tilde{n}$=0.2 and $\tilde{T}$=0.2, which may be a representative choice for the final stages of the collision. The largest Reynolds number within the studied energy and mass region is about Re ≈ 8. This value is obtained at A≈200 and E_{cm}≈50 MeV/nucleon. Starting from the maximum, with decreasing energy Re drops sharply to zero, while with increasing energy Re drops gradually. At asymptotically high energies Re tends to a constant depending on A only. This latter behavior can be understood since the viscosity for dilute highly excited systems increases as $\sqrt{T}\sim\sqrt{E_0}$, which cancels the energy dependence of $u_1\sim\sqrt{E_0}$.

If viscosity is important only those systems which have the same Reynolds number should yield a similar flow. Different colliding systems of given mass number A and c.m. energy E_0, that fall on the same line: Re=const., are expected to yield similar flow patterns even if the viscous flow effects are not negligible. Thus we would expect that the dimensionless parameters, like the flow angle θ_{cm} or the aspect ratio R, characterizing the final flow patterns are the same along these curves in the [A,E_0] plane. In fact in there is a slight indication of a maximum of the flow angle at about the same energy where the Reynolds number calculated at the break-up time peaks, and the flow angle decreases for this case with decreasing mass just like Re. The relatively few measured points, however, do not allow for a definite conclusion.

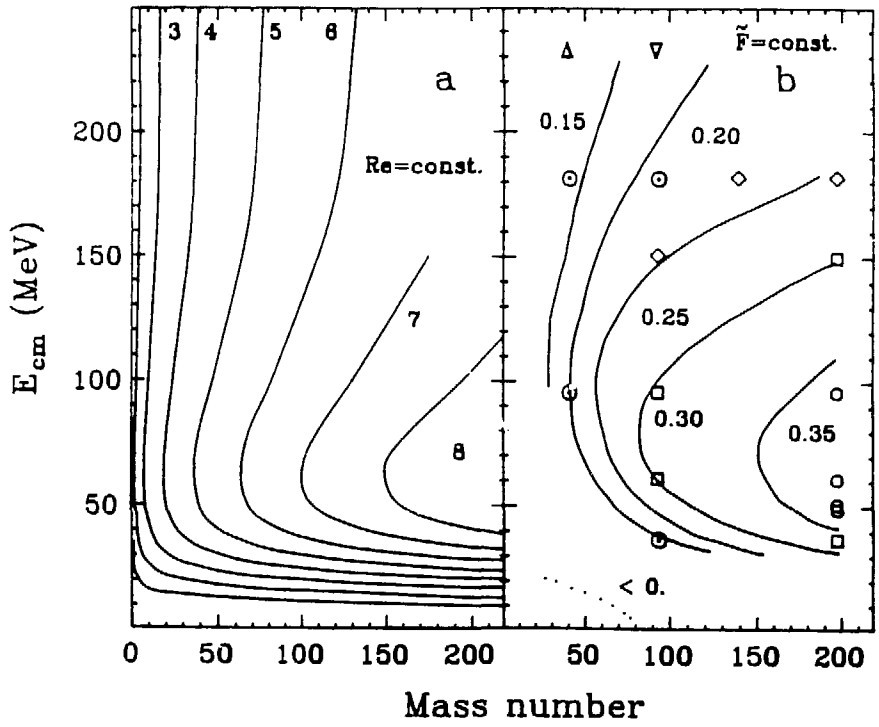

Fig. 1: (a) Contour plots in the [A, E_{cm}] plane corresponding to constant Reynolds number. The temperature and density dependence of the viscosity is taken into account by using a theoretical parametrization from ref. [15]. The dimensionless density and temperature are fixed: $\tilde{n}$=0.2, $\tilde{T}$=0.2. (b) Contour plots in the [A, E_{cm}] plane corresponding to constant scale invariant experimental flow: $\tilde{F}$. The dotted curve indicates the contour line where $\tilde{F}$ is expected to go through zero based on the experimental results of refs. [21,22]. The various symbols refer to the experimental values listed in Table 2. Symbols o, □, ◇, ⊙, ∇ and Δ, correspond to experimental $\tilde{F}$ values between 0.4, 0.325, 0.275, 0.225, 0.175, 0.125, and <0.1, respectively. From ref.[1a].

THE SOUND SPEED

The scaling assumptions about the equation of state enter via the sound speed [1]. Namely, a scale invariant flow pattern can be obtained if the pressure satisfies:

$$\nabla p = c_s^2 \nabla \rho \qquad (4)$$

with a sound speed c_s which scales with the c.m. energy as [1]:

$$c_s = \tilde{c}_s \cdot \sqrt{2.E^{CM}_{nucl.}/m} \qquad (5)$$

A sudden change in the equation of state, like a phase transition, would violate (4-5) and thus it would lead to a nonscaling behavior.

For an ideal gas $\tilde{c}_s$ = const. Using a simple EOS with a binding energy W_0=-8MeV and K=250MeV the sound speed is surprisingly constant in a wide mass and energy range. (Table 1.)

Table 1

	$\tilde{n}$ = 0.3	0.6	1.0
T [MeV]			
4.00	(0.389)	(0.778)	(1.705)
10.00	(0.535)	(0.758)	(1.216)
20.00	0.645	0.742	0.994
30.00	0.673	0.730	0.903
40.00	0.686	0.720	0.850
50.00	0.697	0.712	0.814
60.00	0.709	0.707	0.788
70.00	0.723	0.704	0.769
80.00	0.738	0.704	0.754
90.00	0.752	0.705	0.743
100.00	0.763	0.708	0.734
120.00	0.773	0.713	0.723
140.00	0.768	0.714	0.713
160.00	0.750	0.708	0.703
180.00	0.727	0.696	0.690
200.00	0.701	0.679	0.674

Adiabatic scale invariant sound speed, $\tilde{c}_s$, for three different densities and at different temperatures, $T=2E_0/3$, calculated from a simple Equation of State. The values in brackets should be considered with some caution because the EOS, includes a Maxwell-Boltzmann thermal energy term which is not realistic at low temperatures. From Ref. [1b].

Below E_0 = 40MeV the sound speed starts to be sensitive to the nuclear binding, behaving differently at different densities. At $\tilde{n}$=1 the sound speed increases with decreasing energy. On the other hand at low densities it decreases with decreasing E_0. This nonscaling behavior of the sound speed at low energies is a consequence of the nuclear binding and thus it is related to the liquid-gas phase transition. It is interesting, however, that in the Bevalac energy region the dimensionless sound speed is approximately constant. This indicates that we may expect deviations from the scaling behavior of the observables below the Bevalac energies, due to the nonscaling properties of the nuclear EOS.

TRANSVERSE MOMENTUM ANALYSIS

The transverse momentum analysis [16] is the most sensitive method to date to identify and measure collective flow effects. If we take composite fragments into account their momenta are $\vec{p}_\kappa = \vec{p}A_\kappa$, where $\vec{p}$ is the momentum per nucleon and A_κ is the fragment mass number. The transverse momentum per nucleon projected to the reaction plane, determined by the beam axis, and a unit vector $\hat{e}$ in the direction of maximum flow, can be calculated in a fluid dynamical model separately for each type of fragment κ as

$$\langle p^x/a\rangle_\kappa = 1/[A_\kappa N_\kappa(y,\Delta y)] \int F_\kappa(\vec{p},\vec{r})\ (\vec{p}\cdot\hat{e})\ d^3r\ d^3p|_{y<y(p)<y+\Delta y} \quad , \qquad (6)$$

where the momentum integral is restricted to a given rapidity bin and $A_\kappa N_\kappa(y,\Delta y)$ is the number of nucleons emitted into this bin within fragments of type κ, so that $A = \Sigma_\kappa A_\kappa N_\kappa$. The distribution $F_\kappa(\vec{p},\vec{r})$ is normalized to $A_\kappa N_\kappa$. Introducing the scale invariant variables, eq. (6) reduces to

$$\tilde{p}_{\kappa t}(\tilde{y}) = \langle p^x/a\rangle_\kappa/p_\circ = \tilde{N}_\kappa^{-1}(\tilde{y}) \int \tilde{F}_\kappa(\vec{\tilde{p}},\vec{\tilde{r}})\ (\vec{\tilde{p}}\cdot\hat{e})\ d^3\tilde{r}\ d^3\tilde{p}|_{\tilde{y}<\tilde{y}(\tilde{p})<\tilde{y}+\Delta\tilde{y}} \quad , \qquad (7)$$

where the range of the restricted momentum integral should be given in terms of the c.m. beam rapidity and $\tilde{y}=y/y_\circ=y/y_{cm}^{proj.}$. Since we are confining to the nonrelativistic regime, $y_{cm}^{proj.}=u_\circ$. Here $\tilde{F}_\kappa(\vec{\tilde{p}},\vec{\tilde{r}}) = p_\circ^3 F_\kappa$ is normalized to $\tilde{N}_\kappa = N_\kappa A_\kappa/A$, ie. $\Sigma_\kappa \tilde{N}_\kappa = 1$. The total scale invariant transverse momentum is then given by the average

$$\tilde{p}_t(\tilde{y}) = \frac{\Sigma_\kappa N_\kappa A_\kappa \tilde{p}_{\kappa t}(\tilde{y})}{\Sigma_\kappa N_\kappa A_\kappa} \ .$$

The scaling of $\tilde{p}_t(\tilde{y})$ with beam energy is not expected to be perfect due to the same reasons that were mentioned before.

BUU-VUU RESULTS

In order to investigate the validity of our scaling assumption, we express measured quantities in a scale invariant way. We introduce a scale invariant transverse momentum per nucleon

$$\tilde{p}_t = \langle p^x/a\rangle/p_\circ = \langle p^x/a\rangle / p_{proj.}^{CM} \quad , \qquad (8)$$

where $\langle p^x/a \rangle$ is the average transverse momentum per nucleon and p_{proj}^{CM} is the c.m. momentum of a nucleon in the projectile. In the same way we define the scale invariant rapidity by

$$\tilde{y} = y^{CM} / y_{proj.}^{CM} \qquad (9)$$

In ref. [17] the transverse momenta are calculated for a fixed impact parameter of 3 fm and different beam energies for Nb+Nb collisions. In ref. [6] the result of a calculation at 400 MeV/nucleon for an impact parameter average in the interval b=0-3fm is given. If we compare these results of numerical transport theoretical model calculations for transverse momenta using scale invariant variables, the calculated data follow the same basic trend above E_{beam} = 150 MeV/nucleon, the maximum of the scale invariant transverse momentum $|\tilde{p}_t|$ being about 0.07-0.1. The differences among the different beam energy curves are smaller than the statistical fluctuations. At low beam energies like 150 MeV/nucleon the maximum of the transverse momentum is observably smaller ($\approx$0.05). There are two equation of states used in the two calculations, a so called stiff one in ref. [17] and a momentum dependent one in ref. [6]. Both are in essential agreement with each other. The third equation of state used in the calculation in ref. [6], a soft one, gives about 20-30% smaller transverse momentum. It is interesting to see that the mean field present in these calculations does not lead to the destruction

of the energy scaling in the 250-1050 MeV/nucleon energy range. This is probably related to the fact that the mean field is density dependent and repulsive at higher densities, so it acts similarly to the pressure. At low energies, however, the attractive part of the mean field dominates which destroys the fluid dynamical scaling properties.

EXPERIMENTAL OBSERVABLES

The scale invariant transverse momentum $\tilde{p}_t$ as a function of scale invariant rapidity $\tilde{y}$ is shown in Fig. 2 for various experimental data. There are differences in the results which arise from different multiplicity selections (i.e. different impact parameters) and from different types of particles detected. Since these differences are not caused by scaling violations we will try to compensate for them when possible in the following analysis. For the details see ref. [1b]. In a strict way, one could only compare experiments where the multiplicity selection, the detected particles and other experimental constraints are the same. For example, as we can see in Fig. 2 the high rapidity behavior of the transverse momentum is different for Plastic Ball and Streamer Chamber data. Nevertheless, the scale invariant transverse momentum plot shows a quite constant behavior in a very wide range of energy and mass.

In Fig. 1b contour lines for $\tilde{F}$ = const. extracted from various experimental data are plotted in the $[A,E_{cm}]$-plane. Deviations from a constant $\tilde{F}$ could indicate deviations from the perfect scale invariant fluid flow. Within the fluid dynamical picture there are two main reasons for such deviations: the viscous dissipation and the nonscaling behavior of the equation of state.

Let us now in the $[A,E_{cm}]$-plane, compare the contour lines of constant $\tilde{F}$ shown in Fig. 1b with those of constant Re displayed in Fig. 1a. At medium and high energies the qualitative behavior of both contour plots are similar. The experimental $\tilde{F}$ = const. curves, however, rise somewhat sharper with increasing energy than the Re=const. curves.

The most drastic difference between the Re=const. and $\tilde{F}$=const. curves, however, appears at low energies. Below $E_{cm} \sim 50$ MeV ($E_{lab} \sim 200$ MeV) the scale invariant transverse flow $\tilde{F}$ drops suddenly. For example, taking a fixed mass number A=100 we expect $\tilde{F}$ to go through zero at about $E_{cm} \approx 20$MeV/nucleon. On the other hand the Reynolds number never becomes negative. This behavior is certainly unexplainable by minor changes in the viscosity. One may assume that either the equation of state or the reaction mechanism should change here drastically.

Table 2

lab. E (MeV) proj.	CM E (MeV) nucl.	A	F(MeV/c)	CM p (MeV/c) proj.	C	Ptcl.	$\tilde{F}$	Refs.
Symmetric systems:								
150	37	197	82± 5	265		p-α	.31±.02	[2,3]
200	50	197	120± 6	306		p-α	.39±.02	[2,3]
210	51	197	115±15	314	1.1	H	.39±.05	[4]
210	51	197	157±25	314	.78	He	.39±.06	[4]
210	51	197	220±30	314	.56	Li	.39±.06	[4]
250	61	197	132± 3	343		p-α	.39±.01	[2,3]
400	96	197	160± 4	433		p-α	.37±.01	[2,3]
650	151	197	162± 6	552		p-α	.29±.01	[2,3]
800	182	197	151± 7	613		p-α	.25±.01	[2,3]
800	182	139	170±50	613	.85	d	.24±.07	[18]
150	37	93	50± 3	265		p-α	.19±.01	[2,3]
180	44	93	50±15	291		p-	.17±.05	[23]
250	61	93	102± 3	343		p-α	.30±.01	[2,3]
400	96	93	130± 3	433		p-α	.30±.01	[2,3]
650	151	93	140± 6	552		p-α	.25±.01	[2,3]
800	182	93	136± 6	613		p-α	.22±.01	[2,3]
1050	233	93	122± 6	702		p-α	.17±.01	[2,3]
400	96	40	76± 3	433		p-α	.18±.01	[2,3]
800	182	40	140±40	613	.85	d	.19±.06	[18]
1050	233	40	72± 5	702		p-α	.10±.01	[2,3]
1200	263	40	100±40	750		p-	.13±.05	[19]
1800	375	40	140±50	919		p-	.15±.05	[13]
Asymmetric systems ($\tilde{F}$ is not evaluated):								
800	103	40+208	200±80		.85	d		[18]
734	149	197+94	104±40			He-		[20]
1059	229	132+94	69±30			He-		[20]
20	2	14+154	< 0				< 0	[21]
35	3	14+154	< 0				< 0	[21]
35	3	14+165	< 0				< 0	[22]

"Flow" F collected from different experiments and the corresponding calculated scale invariant quantity $\tilde{F}$. C is an estimated multiplicative factor used in calculating $\tilde{F}$ from different experiments in order to correct for particle type selection, multiplicity selection and experimental cuts. From [1b].

There is some experimental evidence [21,22] that at very low energies the deflection angle of the emitted particles is "negative" i.e. the projectile is deflected to the target side in non-central collisions. This means that at some given energy the attractive nuclear interaction overcomes the repulsion caused by the pressure. Such an attractive interaction is out of the scope of the fluid dynamical scaling studies, since it introduces new dimensional quantities playing an essential role in the reaction mechanism. On the other hand the mean field potential leads to a well defined equation of state if we assume thermal equilibrium in a given statistics. A strong attractive mean field may lead to a first order phase transition. Thus the two effects, the softening of the EOS by the nuclear liquid-gas phase transition, and the predominance of the nuclear interaction are, of course, the two sides of the same microscopic attractive nucleon-nucleon interaction. There are theoretical works first in a transport model [23] and later in BUU and VUU approaches [17,24,25] which predicted a "negative" deflection angle

due to the nuclear mean field. The same nuclear mean field leads to a fragmentation at a late stage of a collision representing a liquid-gas phase transition [26,27].

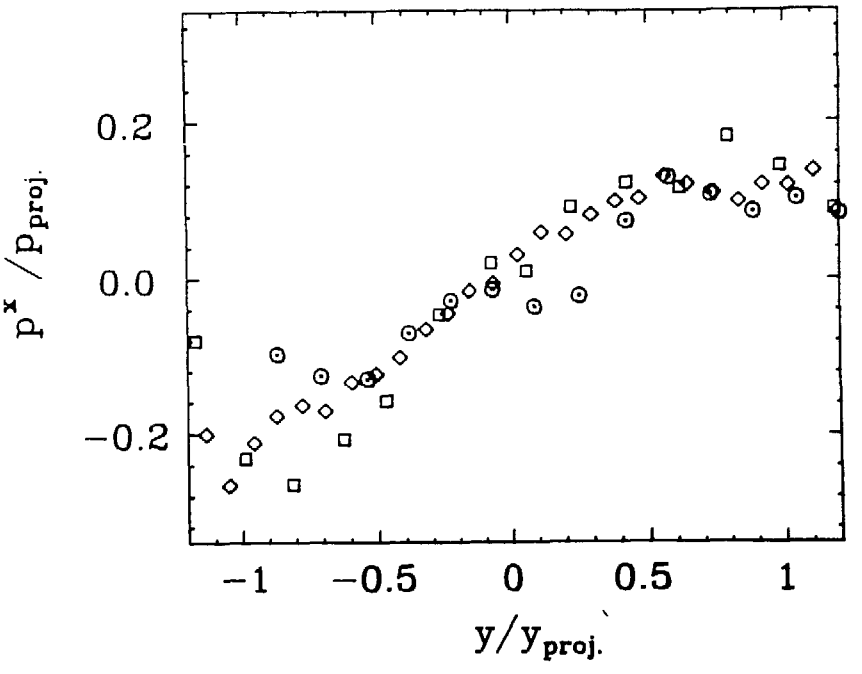

Fig. 2: Scale invariant transverse momentum from experiments versus scale invariant rapidity for three different systems. (⊙) Ar+KCl at E_{lab} = 1.8 GeV/nucleon (streamer chamber) [16], (□) La+La at E_{lab} = 0.8 GeV/nucleon (streamer chamber) [18] and (◇) Nb+Nb at E_{lab} = 0.4 GeV/nucleon (plastic ball) [2,3] . From ref. [1b].

CONCLUSIONS

Contour plots of constant Reynolds number calculated under break-up conditions at a late stage (low density and low temperature) exhibit a strong similarity with corresponding plots of the dimensionless flow $\tilde{F}$, at least for not too low energies. This indicates a buildup of the flow properties during the expansion rather than in the compression phase of heavy ion collisions.

The possibility of a negative angle scattering at low beam energies was indicated by a sudden drop of the flow for fixed mass number, at energies below $E_{cm} \approx$ 50MeV/nucleon. The possible relation to the liquid-gas phase transition is discussed. In the transition region there are very few experimental data available so far. It would be extremely important to map out this interesting region of the mass-energy plane by new experiments and transverse analysis. The first experiments are in progress just during this conference by Westfall et al.

The information about the reaction dynamics could be increased even more by detailed observables like the triple differential cross section projected into the reaction plane. This could be achieved by electronic 4π detector systems used at intermediate energy heavy ion collisions.

REFERENCES

* On leave from the INFN, Sezione di Catania, ITALY
+ On leave from the Central Res. Inst. for Physics, Budapest, HUNGARY

1 A. Bonasera and L.P. Csernai, Phys. Rev. Lett. 59 (1987) 630; A. Bonasera, L.P. Csernai, and B. Schürmann, Nucl. Phys. A in press; N. Balazs, B. Schürmann, K. Dietrich and L.P. Csernai, Nucl. Phys. A424 (1984) 605.
2 K.G.R. Doss, et al., Phys. Rev. Lett. 57 (1986) 302.
3 H.G. Ritter et al. Phys. A447 (1985)3c.
4 P. Beckmann, et al., GSI Scientific Report 1985, pg. 98.
5 G. Buchwald, et al., Phys. Rev. Lett. 52 (1984) 1594.
6 C. Gale, G. Bertsch and S. Das Gupta, Phys. Rev. C35 (1987) 1666.
7 J. Aichelin, et al., Rev. Lett. 58 (1987) 1926.
8 L.P. Csernai, H. Stöcker, P.R. Subramanian, G. Graebner, A. Rosenhauer, G. Buchwald, J.A. Maruhn and W. Greiner, Phys. Rev. C28 (1983) 2001.
9 G. Buchwald, G. Graebner, J. Theis, J.A. Maruhn, W. Greiner and H. Stöcker, Phys. Rev. C28 (1983) 1119; L.P. Csernai and H.W. Barz, Z. Phys. A296 (1980) 173.
10 P. Danielewicz and M. Gyulassy, Phys. Lett. 129B (1983) 283.
11 L.P. Csernai, G. Fai and J. Randrup, Phys. Lett. 140B (1984) 149; and L.P. Csernai, Phys. Rev. Lett. 54 (1985) 639.
12 H.A. Gustafsson, et al., Phys. Rev. Lett. 52 (1984) 1590.
13 H.G. Ritter, et al., Proc. of the 7th High Energy Heavy Ion Study, GSI Darmstadt, Oct. 8-12, 1984 (GSI) p.67.
14 V.M. Galitskij, Yu.B. Ivanov and V.A. Khangulyan, Yad. Fiz. 30 (1979) 778., Sov. J. Nucl. Phys. 30 (1980) 401.
15 P. Danielewicz, Phys. Lett. 146B (1984) 168.
16 P. Danielewicz and G. Odyniec, Phys. Lett. 157B (1985) 146.
17 J.J. Molitoris, D. Hahn and H. Stöcker, Nucl. Phys. A447 (1985) 13c.
18 A. Sandoval, et al., GSI scientific report 1985, pg. 97, and Phys. Rev. Lett. 53 (1984) 763.
19 D. Beavis, et al., Phys. Rev. C33 (1986) 1113
20 L.P. Csernai, P. Freier, J. Mevissen, H. Nguyen, and L. Waters, Phys. Rev. C34 (1986) 1270.
21 M.B. Tsang, et al., Phys. Rev. Lett. 57 (1986) 559.
22 F. Deák, et al., Nucl. Phys. in press.
23 B. Schürmann and W. Zwermann, Phys. Lett. 158B (1985) 366.
24 J.J. Molitoris, A. Bonasera, B.L. Winer, H. Stöcker, submitted for publication Phys. Rev. C (1987)
25 G.F. Bertsch, W.G. Lynch, M.B. Tsang, MSUCL-586 Preprint. 1987
26 S. Das Gupta, C. Gale, J. Gallego, H.H. Gan, and R.D.R. Raju Phys. Rev. C35 (1986) 556.
27 W. Bauer, G.F. Bertsch and S. Das Gupta, Phys. Rev. Lett. 58 (1987) 863.
28 S. Angius, private communication (1987) preliminary data from streamer chamber with CCD cameras.

Inclusive Neutron Spectra at 0° from Nb-Nb and Au-Au Collisions at 800 AMeV*

R. Madey, W.-M. Zhang, B. D. Anderson, A. R. Baldwin, B. S. Flanders,§
W. Pairsuwan,§§ J. Varga, and J. W. Watson
Kent State University
Kent, OH 44242

and

G. D. Westfall
Michigan State University
East Lansing, Michigan 44823

Introduction

Heavy-ion experiments have provided new information about nuclear structure; with increasing beam energy, these experiments offer a way to produce hotter and denser nuclear matter in the laboratory for further study. A statistical model, introduced by Feshbach and Huang[1] and extended by Goldhaber,[2] was used to interpret the projectile-fragmentation measurements of Heckman et al.[3] Our previous measurement[4] of inclusive neutron spectra at 0° from Ne-NaF and Ne-Pb collisions at 390 and 790 AMeV showed three processes of neutron emission and supported the above model and interpretation. Here we report the measurement of inclusive neutron spectra at 0° from 800 AMeV collisions of Nb ions on a Nb target and Au ions on a Au target. The experiment was performed at the Bevalac.

---

* Work was supported in part by NSF and DOE.

§ Present address: University of Maryland, College Park, MD 20742

§§ Present address: Chiang Mai University, Chiang Mai, 50002, Thailand

Inclusive Spectra

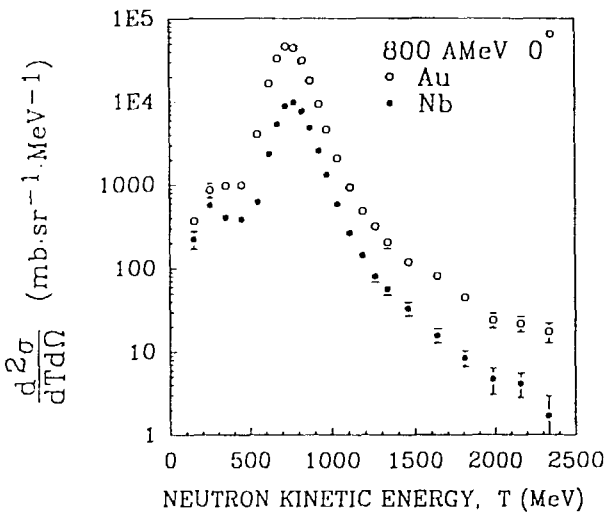

Fig. 1 The inclusive double differential cross section at 800 AMeV for neutron emission at 0° from Nb-Nb (solid circles) and Au-Au (open circles) collisions vs the neutron kinetic energy in the laboratory.

Inclusive double differential cross sections at 0° are plotted in Fig. 1 for both Nb-Nb and Au-Au collisions as a function of the neutron kinetic energy. The spectra are characterized by a high-energy tail and a strong peak at a neutron energy slightly below the beam energy per nucleon. The high-energy tail extends far beyond the kinematic limit for free nucleon-nucleon scattering and will be discussed fully later in this report. The uncertainties shown in Fig. 1 include both the statistics and the systematics. The Lorentz-invariant cross sections are plotted in Figs. 2(a) and 2(b) for Nb-Nb and Au-Au collisions, respectively, as a function of P, the momentum of the neutron in the rest frame of the projectile. Each spectrum was decomposed into three Gaussians of the form $(2\pi\sigma^2)^{-\frac{1}{2}}$ H $\exp[-(P-P_0)^2/2\sigma^2]$, which are associated with three processes of neutron emission. The decomposition was carried out by a fit that varied the

standard deviation σ, the mean momentum P_0, and the amplitude H of each Gaussian. In each of the two figures, the circles display the spectrum, the solid line represents the fit to the spectrum, and the dashed lines denote the decomposition of the spectrum into three Gaussians. The magnitude of the mean momentum P_0 shows quantitatively the downshift δP in the peak momentum of the Gaussians relative to zero momentum. After unfolding the momentum resolution of 19 ± 3 MeV/c, we extracted the standard deviations σ_1^*, σ_2^*, and σ_2^* of the three Gaussians to be 55 ± 4, 114 ± 12, and 259 ± 22 MeV/c for Nb -Nb collisions and 56 ± 4, 110 ± 10, and 279 ± 15 MeV/c for Au-Au collisions.

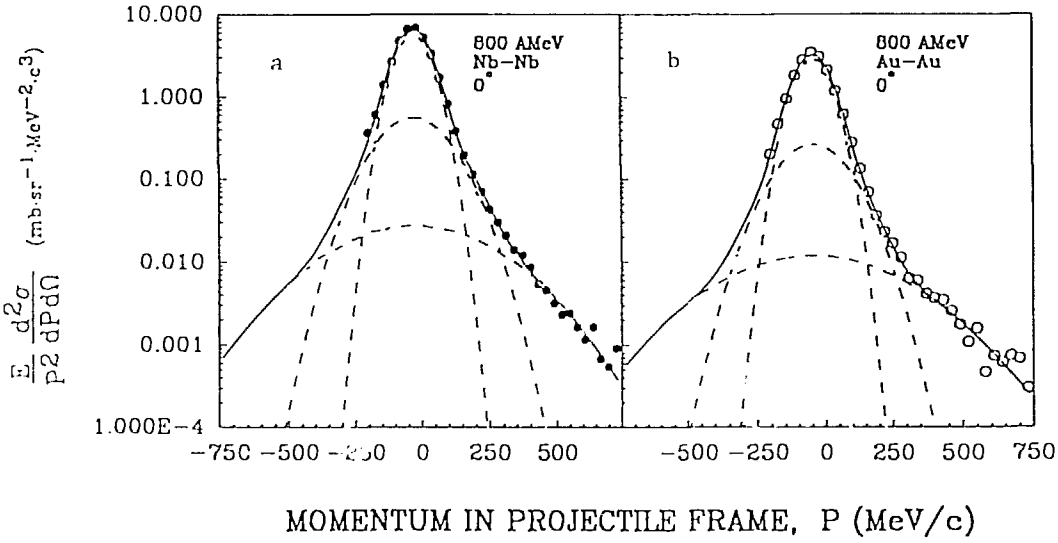

Fig. 2 The Lorentz-invariant cross section at 800 AMeV for neutron emission at 0° from a) Nb-Nb and b) Au-Au collisions vs the neutron momentum in the rest frame of the projectile, with the spectrum decomposed into three Gaussians.

The source of the first Gaussian is a thermal process of neutron evaporation after excitation of the projectile nucleus. To obtain the neutron evaporation temperature T_e, we used the formula derived by Goldhaber[2] for an equilibrated system: $\sigma^2 = MkT_eK(A-K)/A$, where σ is the standard deviation of a Gaussian, M is the mass of the nucleon, k is the Boltzmann Constant, and K and A are the mass numbers of the fragment (i.e., the neutron here) and the

projectile, respectively. Here, we extracted evaporation temperatures of 3.3 ± 0.5 MeV and 3.4 ± 0.5 MeV for Nb-Nb and Au-Au collisions, respectively, which agree with each other, and, within uncertainties, with the value of 2.7 ± 0.4 MeV obtained for Ne-NaF and Ne-Pb collisions at 390 AMeV and 790 AMeV.[4] The source of the second Gaussian is the fragmentation from the projectile. From the relation $\sigma^2 = (1/5)P_F^2$ given explicitly by Goldhaber,[2] we determined the Fermi momentum P_F, which is related to the σ_2^*, to be 255 ± 27 MeV/c and 246 ± 22 MeV/c for Nb and Au, respectively. Within uncertainties, these two values agree with the results from quasielastic electron scattering reported by Moniz el al.[5]: P_F = 254 ± 5 MeV/c for ^{89}Y and 265 ± 5 MeV/c for ^{208}Pb.

Downshift in the peak momentum

Beam energy per nucleon E (AMeV)	System	Downshift in peak momentum δP (MeV/c)
800	Nb-Nb	30 ± 5
	Au-Au	44 ± 4
790	Ne-NaF	8 ± 2
	Ne-Pb	19 ± 3
390	Ne-NaF	21 ± 4
	Ne-Pb	32 ± 5

Table I Downshift in the peak momentum for collisions of Nb-Nb and Au-Au at 800 AMeV and collisions of Ne-Pb and Ne-NaF at 790 AMeV and 390 AMeV.

The downshift in the peak momentum depends on the system and on the beam energy per nucleon. Listed in Table I are the downshifts obtained from this experiment and from our previous experiment.[4] From Table I, we see that (1) low bombarding energy causes more downshift in the peak momentum than high bombarding energy for same system; (2) for the same projectile at the same bombarding energy, the peak momentum shifts more for a heavy target than for a light target; and (3) the momentum downshift for an equal-mass

system of heavy nuclei is greater than that for an equal-mass system of light nuclei at the same bombarding energy.

High-energy tail

We interpret the third Gaussian, which is responsible for the high-energy tail, as collective backscattering of a neutron in the target from nucleon clusters in the projectile, and attribute its larger width for collisions of heavy nuclei in this experiment to a larger mean size of the nucleon cluster in heavy projectiles compared to a light Ne projectile in our previous experiment. To estimate the mean size of the nucleon cluster in the projectile, we decomposed the third Gaussian in the region above the peak momentum in Figs. 2(a) and 2(b) into three sub-Gaussians which correspond to elastic backscattering of a neutron in the target either from a nucleon in the projectile or from a nucleon cluster with a nucleon number N = 2 or 3. The centroid of each sub-Gaussian was fixed by the backscattering momentum of 0, 353, and 553 MeV/c associated with the elastic scattering from one, two, and three nucleons, respectively, minus the momentum downshift of the peak. The standard deviation of each of these three sub-Gaussians was taken to be equal to the standard deviation σ_2 of the second Gaussian. The fit yielded the amplitudes of the three sub-Gaussians. When the third Gaussian in Figs. 2(a) and 2(b) is replaced by the sub-Gaussians obtained from the fit, the envelope in the region above the momentum peak matches the data well with an insignificant difference from the match with the third Gaussian. This replacement is shown in Figs. 3(a) and 3(b) for Nb-Nb and Au- Au collisions, with the sub-Gaussians denoted by the dotted lines. From the amplitudes of the three sub-Gaussians, we estimated the mean size of the nucleon cluster in the projectile to be about 1.3 for both Nb and Au. The same fit was carried out also for our previous experiment[4] with a Ne projectile; in this case, the mean size of the nucleon clusters was estimated to be about 1.1 for 390 and 790 AMeV Ne projectiles colliding with an NaF target. From the above calculation, we see that the high-energy tail, which is represented by the third Gaussian, can be explained simply as collective backscattering of a neutron in the target from a cluster of nucleons in the projectile alone, and that the width of the third Gaussian reflects the mean size of the nucleon cluster in the

projectile. Also our interpretation appears reasonable in terms of the magnitude of the total cross section for elastic scattering of a target neutron from nucleon pairs in the projectile. We estimated that this total cross section for Au was nearly five times that for Nb; however, the cross section per target neutron from nucleon pairs was about two times larger for Au than for Nb. The magnitude of these cross sections were overestimated because of the assumption of isotropy. In comparison with the total cross section of about 12 mb for elastic scattering of an 800 MeV proton from deuterium,[6] the number of two-nucleon clusters is less than six in the Au projectile and less than three in the Nb projectile. This result is not an unreasonable expectation particularly since knowledge of the two-nucleon cluster probability is needed for more detailed interpretation.

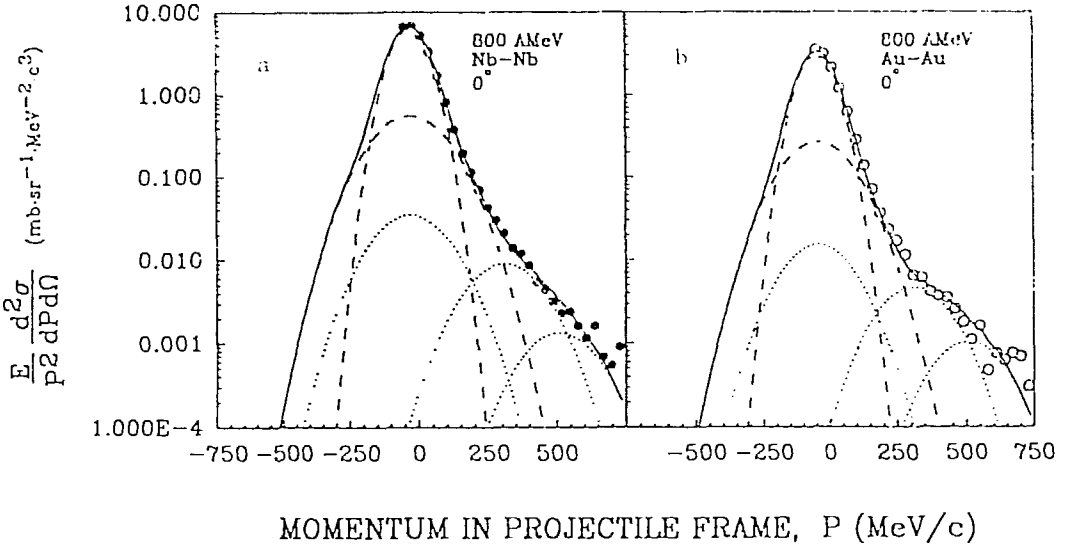

Fig. 3 The Lorentz-invariant cross section at 800 AMeV for neutron emission at 0° from a) Nb-Nb and b) Au-Au collisions vs the neutron momentum in the rest frame of the projectile, with the spectrum decomposed into the first two Gaussians and the three components of the third Gaussian.

Although this interpretation can explain the neutron observations, it does not explain the weak dependence of the width of the broad Gaussian on the mass of the target found by Geaga et al.[7] from measurements of inclusive

proton spectra at 180° from collisions of 1.05 GeV proton on targets of mass number up to 200; nor does it explain the smaller width of 200 ± 5 MeV/c for the standard deviation of this Gaussian in the proton spectra from the heaviest targets. In our experiment, the value of σ_3^* was extracted from the Lorentz-invariant cross section, whereas the value of Geaga et al. was extracted from the double differential cross section. This difference accounts for an increase of about 10 MeV/c in σ_3^* extracted from the Lorentz-invariant cross section, which is not sufficient to explain the discrepancy. Other contributions to this discrepancy might be the neglect of the downshift δP during the fit by Geaga et al. and the effect of the Coulomb interaction in the measurement of the proton spectrum. Still another possibility is that compression in heavy-ion collisions affects the neutron result.

Dependence on the impact parameter

The observed collisions were divided into two impact parameter groups which had approximately equal contributions to the total cross section. One group of non-peripheral collisions had a small average impact parameter of 0.47; The other group of peripheral collisions had a large average impact parameter of 0.86. A spectrum of the Lorentz-invariant cross section, decomposed into three Gaussians in the same manner as that in Figs. 2(a) and 2(b), was obtained for each of the two impact parameter groups. Also, each of these subspectra was fitted to three Gaussians. The standard deviations σ_1, σ_2, and σ_3, and the amplitudes H_1, H_2 and H_3 were obtained from the Gaussians fitted to the subspectra. Studying the above quantities reveals several interesting results. (1) The evaporation temperature obtained from the standard deviation σ_1^* decreases with increasing impact parameter [from 4.2 ± 0.7 to 2.3 ± 0.4 MeV for Nb-Nb collisions and from 4.6 ± 0.6 to 2.2 ± 0.5 MeV for Au-Au collisions with small and large impact parameters]; (2) the standard deviation of the second Gaussian that reflects the fragmentation process decreases with increasing impact parameter [from 126 ± 14 to 90 ± 10 MeV/c for Nb-Nb collisions and from 123 ± 12 to 87 ± 9 MeV/c for Au-Au collisions with small and large impact parameters]; (3) the standard deviation σ_3^* is independent of the impact parameter [266 ± 34 vs

249 ± 28 MeV/c for Nb-Nb collisions and 272 ± 24 vs 310 ± 17 MeV/c for Au-Au collisions with small and large impact parameters]; (4) for Au-Au collisions, the percentage contribution from the third Gaussian to the Lorentz-invariant cross section is larger for non-peripheral collisions than for peripheral collisions [viz., 2.2 ± 0.8 vs 0.9 ± 0.2 for non-peripheral and peripheral collisions]; (5) non-peripheral collisions with small impact parameters, which constitute one-half of the total, contribute about two thirds to the third Gaussian for both Nb-Nb and Au-Au collisions. This fact demonstrates that non-peripheral collisions constitute the primary source of the high- energy tail of the neutron spectrum.

Conclusions

We measured inclusive neutron spectra at 0° from collisions of 800 AMeV Nb on Nb and Au on Au. Three processes of neutron emission are distinguished by the Lorentz-invariant cross section at 0° in the rest frame of the projectile: The excitation and evaporative decay of the projectile spectator, the fragmentation of a neutron from the projectile, and the elastic backscattering of a neutron in the target from a cluster of nucleons in the projectile. The neutron evaporation temperature in the projectile is insensitive to the mass of the projectile in collisions with a target of equal mass. The extracted Fermi momentum agrees with predictions of statistical models, and (within uncertainties) with those extracted from quasielastic electron scattering. High-energy neutrons appear in both peripheral and non-peripheral collisions, but come primarily from non-peripheral collisions. Elastic backscattering of a target neutron from two- and three-nucleon clusters can account for the high-energy neutrons. The mean size of neutron cluster in the projectile is 1.3 for Au and Nb and 1.1 for Ne. The cross section for elastic backscattering of a target neutron from a two-nucleon cluster in the projectile is reasonable in comparison with the world average of the cross section for elastic scattering of a proton from the deuteron. The results also indicate that the evaporation temperature increases with decreasing impact parameter, that the width of the momentum distribution of a neutron in the projectile increases for collisions with decreasing impact parameter, and that the width of the Gaussian reflecting elastic backscattering is independent of the impact parameter.

References

1) H. Feshbach and K. Huang Phys. Lett. **47B**, 300 (1973).

2) A. S. Goldhaber, Phys. Lett. **53BB**, 306 (1974.)

3) H. H. Heckman, D. E. Greiner, P. J. Lindstrom, and F. S. Bieser, Phys. Rev. Lett. **28**, 926 (1972).

4) R. Madey et al., Phys. Rev. Lett. **55**, 1453 (1985).

5) E. J. Moniz et al., Phys. Rev. Lett. **26**, 445 (1971).

6) Particle Data Group, Phys. Lett. **170B**, 89 (1986).

7) J. Geaga et al., Phys. Rev. Lett. **45**, 1993 (1980).

Bevalac TPC*

H. Wieman, G. Odyniec, H.G. Pugh, G. Rai and P. Seidl
Lawrence Berkeley Laboratory
Berkeley, California 94720

Abstract

A time projection chamber (TPC) detector system is being proposed for use at the Bevalac where it will be used to measure central collisions with the heaviest and most energetic projectiles available.

1 Introduction

In 1986 a conceptual design report for a 4π TPC detector (EOS) was written by Howell Pugh and his collaborators.[1] The proposed TPC was a cylinder one meter long by two meters in diameter in a solenoidal magnet. The detector was designed to study central collisions with the most energetic and heaviest beams available at the Bevalac. Presented here is an alternative design which, by using the HISS dipole and other already existing HISS facilities, should greatly reduce the cost while preserving as much as possible the capabilities envisioned for the original EOS design.

A distinction should be made between two classes of experiments considered for these detectors. One class concerns flow analysis and triple differential cross sections (cross sections relative to the reaction plane). For these studies it is important to have uniform acceptance, particularly in the phi angle about the beam axis. Large beam currents are not required, however, since cross sections are large. The other class concerns study of rare events requiring large solid angles but not necessarily completely uniform coverage.

*This work was supported by the Director, Office of Energy Research, Division of Nuclear Physics of the Office of High Energy and Nuclear Physics of the U.S. Department of Energy under Contract DE-AC0376SF00098

For the first class of experiments the TPC would be operated with the beams, of $\leq 10^3$ particles per spill, passing through the active region. Elimination of the beam pipe through the chamber avoids problems with asymmetric azimuthal coverage normally associated with a dipole geometry and, actually, has an advantage over a solenoidal design in that it provides excellent momentum resolution in the forward direction. The beam current must be limited in this case to avoid excessive distortions of the drift field due to the slowly drifting positive ions created in the primary ionization. This operation will require a very effective gating grid to prevent leakage of the non interacting beam tracks into the gas amplification region where they generate additional positive ions. Another potential problem is sparking. Drift chambers have been operated with a gain of greater than 10^3 with U beams without sparking[2]. Some tests will be required, however, since in a magnetic field the electron cloud is confined to a much smaller area.

The second class of experiments, those requiring larger beam intensities, would need a beam pipe to completely isolate the heavily ionizing beam particles from the active gas volume. In this mode solid angles would still be large for studying kaons or other low cross section measurements such as momenta distributions far out on the tails.

2 Mechanical Design

The proposed HISS TPC, sketched in Figure 1, is a single rectangular box centered in the HISS dipole. The electrons will drift upward to the wire pad plane at the top of the gas volume where they will be read out. The active volume is 100 cm long in the beam direction, 60 cm wide in the bending direction and 70 cm high in the drift direction. The supporting structure will consist of aluminum box beams located at the edges of the rectangular box to minimize solid angle obstruction to detectors placed outside the TPC volume. The field cage panels will be hung from this frame and thin aluminum panels will be sealed to the outside surfaces for gas containment.

3 End Cap

The end cap is a single panel with an array of 0.5 cm $\times$ 0.5 cm pads covering a 60 cm by 100 cm rectangle (24000 pads total). The three wire planes over these pads will be essentially the same as exists in PEP4 and TOPAZ: the first plane is alternating field and anode wires, the next plane is an isolation grid, and the third plane is a gating grid which passes drifting electrons for only the accepted events in order to limit positive ion build up in the drift volume. Construction of the wire planes in the HISS TPC configuration will be simpler than other TPC's for two reasons. One, the anodes can be tied to a single bus since the signal is not read out. Second, there are no

space constraints in this design for wire termination. The termination can be located well away from the active region, thereby avoiding difficulties with gain variation. It may be preferable, however, to use more than one anode connection to permit independent gas gain adjustment for different regions of the chamber. For instance, it maybe desirable to have bands for analysis of tracks from heavier more strongly ionizing particles than α's

4 Field Cages

The field cage will be designed, like the ALEPH field cage, using kapton clad on both sides with copper strips. Four stretched kapton panels will form the cage with a minimum of material obscuring the outgoing particles. These panels will be set back ~10 cm from the active pad region thus avoiding field distortions from local imperfections in the cage. In one configuration thin entrance and exit windows will be provided for the beam. In the high beam configuration a vacuum pipe will pass through the chamber and will be surrounded with a square field cage tube of the same kapton material.

The drift field for 90% Ar plus 10% CH_4 at atmospheric pressure is 130 V/cm or total bias for the cage of 9 KV.

5 Phase Space Acceptance

The GEANT code has been used to study the phase space acceptance of possible designs for a HISS TPC. In the configuration examined (fig. 1), the active region extends from the lower pole tip to within 20 cm of the upper pole tip. Two cases were considered: one in which the beam pipe was removed, leaving the whole volume active, and a second where the vertical swath shadowed by the 12 cm beam pipe structure was inactive. The target was located 20 cm upstream from the detector and the magnet was operated with a field of 13 kG. The horizontal acceptance in $p_\perp$ versus rapidity for protons in the bending plane is shown in Figure 2. Tracks were accepted that had a minimum path length of 20 cm through the active volume. The outer acceptance boundary is set by scattering angles too large to pass through the chamber and the inner boundary shows the region where tracks are lost passing straight down the beam pipe. It is this second region that is recovered by running in the low beam current, no beam pipe mode. A mid-rapidity thermal source of protons is shown in the figure as a scatter of points, that is mid-rapidity for a 1 GeV/nucleon beam on a symmetric target. In this case the acceptance is

over 80%. For comparison, the acceptance of the plastic ball detector[3] is also shown in this figure.

The azimuthal coverage of the detector is shown in (fig. 3). The acceptance has been mapped in the $p_\perp$ plane at the mid-rapidity point. In flow analysis it is important that there are no distortions in this acceptance independent of particle type. Likewise, for particle type ratios such as those used for entropy determinations, there should be good coverage over the same phase space regions for the different particle types. For this reason the variables, $p_\perp/\sqrt{m}$ vertical versus $p_\perp/\sqrt{m}$ horizontal, have been chosen since a thermal source or coalescence model will have a population distribution in the plane that is independent of particle type. The acceptance regions are shown for both protons and tritons (to represent extremes in e/m). The cut down the center in the triton acceptance is due to tritons lost in the beam pipe. Again, as indicated by the scatter point projection of a thermal source on this plane, coverage is quite good for flow analysis if the chamber is operated without a beam pipe. In any case, there are large overlapping regions of acceptance for particle ratio studies.

6 Particle Identification by dE/dx

Identification of p,d,t, ^{3}He and ^{4}He will be possible with dE/dx and rigidity alone for a large region of phase space. This is demonstrated in Table 1 which gives dE/dx values for the particles at specified rigidities.

	p/z = 1220 MeV/c		p/z = 2780 MeV/c		p/z = 4170 MeV/c	
	K.E./A (MeV)	dE/dx (MeV $g^{-1}cm^2$)	K.E./A (MeV)	dE/dx (MeV $g^{-1}cm^2$)	K.E./A (MeV)	dE/dx (MeV $g^{-1}cm^2$)
p	597	1.84	1995.4	1.45		
d	180	3.43	738.8	1.71		
t	83.9	5.78	380.9	2.24		
^{3}He	302	10.1	1140.0	6.1	2000.7	5.81
^{4}He	181	13.7	741.4	6.8	1352.4	5.94

Table 1: dE/dx for particles of fixed rigidity in Ar

Ten percent dE/dx resolution is sufficient for identification except for the highest energy ^{3}He and ^{4}He. Monte Carlo studies are underway to determine the limits on obtaining this resolution. It was shown in the original EOS report [1] that identifying the rare kaons in the large background of protons is more difficult and will require additional detectors capable of measuring time of flight.

7 Electronics Configuration

Recent developments in analog VLSI electronics suggest a possible system for the HISS TPC that would have a number of significant advantages. The most important advantage in the VLSI approach is the ability to accomplish a high degree of multiplexing immediately on the pad plane. The resulting cabling reduction saves on valuable vertical space between the pole tips. The remainder of the electronics can be contained in one or two racks, thus avoiding the need for additional housing and greatly reducing installation and maintenance problems.

A conceptual view (see Figure 4) of the electronics is inspired by the work on SLD electronics [4] and the use of the Microplex chip [5] for pad read outs on RICH detectors [6,7]. With this system the front end electronics are arranged in blocks which plug directly into the back of the pad plane and handle a square of 11 by 11 pads. Each pad would be read, at 20 MHz, into local analog memory that is 256 samples deep. These 121 channels $\times$ 256 time samples would be multiplexed out of the analog memory on a single line at 0.5 MHz to an ADC (ie, 60 ms to digitize a complete event). Zero suppression and possible corrections would then be handled in parallel for each ADC before assembling the event data for storage.

8 Amount of Data per Event

An estimate of the data storage required for a 200 track event was made by assuming that any one plane perpendicular to the beam will have 150 track intersection points recorded. Each intersection point will consist of approximately 20 pad$\times$time pixels which contain 10% or more of the maximum pixel amplitude. At two bytes per pixel this will require 1.2 Mbytes of data per event plus an additional 0.1 Mbytes for addressing.

9 Position Resolution and Momentum Resolution

A more complete study of track reconstruction resolution is required for the proposed configuration of complete pad coverage without sense wire information. As discussed in the next section, a small test TPC is being set up to study this question. However, in the interest of learning about limitations on position resolution imposed by electronic noise, we have made the following simplified analysis.

In this exercise the position resolution of a track passing perpendicular to the pad row and parallel to the pad plane is studied. The position is obtained by a simple weighted mean of the induced signals on the pad row. The induced signal on a pad was calculated assuming that the signal is proportional to the solid angle that a pad presents to the avalanche. The geometry chosen was 5 mm square pads with anode wires 2.5 mm from the pad. With this configuration 60% of the induced charge in a pad row will be deposited in the pad centered directly beneath the track. This spreading of the charge is actually a bit more than is observed in working chambers such as the PEP-4 TPC [1]. The magnitude of the signal distributed over a pad row used in this analysis was obtained as follows:

0.5 cm minimum ionizing track	
in Ar (1 atmosphere), average	45 electrons
gas gain	$\times 10^4$
signal induced on the pad plane	$\times 0.5$
fraction in a peak time bucket	$\times 0.2$

The error in the centroid position, calculated as a function of noise in the pad signal, is shown in Figure 5. A signal threshold of $2 \times \sigma_{noise}$ was used. The position error for reasonable electronics with $\sigma_{noise} = 600e$ will be 310 μm. In actual practice a more sophisticated centroid determination should reduce the error somewhat.

The limits on momentum resolution imposed by this uncertainty in position was checked using the analysis of DELPHI [8] and EOS [1] which gives

$$(\frac{\Delta p}{p})^2 \propto \frac{\sigma^2_{position} p^2}{L^5} + \propto \frac{1}{L}$$

where L is the track length and the second term comes from multiple scattering. For tracks of a full meter length through the chamber $\frac{\Delta p}{p} = 0.4\%$, the multiple scattering limit. For shorter tracks the position error becomes significant such that a proton with momentum 0.3 GeV/c and a track length of 20 cm will have $\frac{\Delta p}{p} = 3.3\%$.

10 Prototype Test TPC

A small TPC borrowed from the PEP4 collaboration is being modified to test the proposed design which utilizes complete pad coverage with 0.5 cm square pads. The immediate goal is to demonstrate tracking and particle identification using only pad information. This test TPC, originally developed by the PEP-4 group[9] to study electrostatic field cage distortions, has a rectangular

geometry (approximately $40 \times 40 \times 40$cm) with a drift length of 30 cm. Tracks drift down to the avalanche region which consists of two wire planes and a solid ground plane. The top wire plane, which is at ground potential, is a grid of 75 μm wires on a 2 mm pitch. This grid separates the drift and amplification region. The second plane, the avalanche plane, is located 4 mm below the grid and is composed of alternate field wires (75 μm) and sense wires (20 μm) set on a 2 mm pitch. The solid ground plane, positioned another 4 mm below, completes the confinement of the avalanche cells. This structure is being modified to include a 16×16 cathode pad array which is fabricated on thin kapton printed circuit board material. The pad plane is situated beneath the field/sense wire plane next to the solid ground plane (see Figure 6). The number of usable pads were restricted in this design by the allowable trace density. The signals from the pads are conducted through vias onto the underside of the kapton and traced out to connectors mounted on the preamplifier mother board.

The electronics for this test system are 256 channels of PEP-4 electronics. Each pad signal is recorded into CCD's at 20 MHz and read out into ADC's at 10 KHz.

11 Conclusion

The proposed HISS TPC will greatly expand detector capabilities at the Bevalac. It will, for the first time, provide the ability to measure completely most of the charged particles emitted from central collisions with the heaviest and highest energy beams at the Bevalac. Three dimensional tracking makes possible the unfolding of high multiplicity events with as many as 200 charged particles. Good tracking resolution in the HISS dipole and dE/dx information provide momenta and particle identification for most of the p,d,t,^{3}He and ^{4}He ions emitted. A substantial fraction of the charged pions will also be measured. These capabilities can extend the flow and entropy studies to full energy Au on Au. This will also permit analysis of two particle correlations and measurements of triple differential cross sections to well out on the tails of the momentum distributions.

References

[1] H.G. Pugh, G. Odyniec, G. Rai and P. Seidl, **LBL-22314**, (1986).

[2] T. Kobayashi, F.S. Bieser, T.J.M. Symons and D.E. Greiner, Nucl. Instr. and Meth. in Phys. Res., **A254** (1987) 281.

[3] A. Baden, H.H. Gutbrod, H. Löhner, M.R. Maier, A.M. Poskanzer, T. Renner, H. Riedesel, H.G. Ritter, H. Spieler, A. Warwick, F. Weik and H. Wieman, Nucl. Instr. and Meth., **203** (1982) 189.

[4] D.J. Sherden, "The Data Acquisition System for SLD", IEEE Trans. Nucl. Sci., **NS-34**, 142 (1987).

[5] Analytek LTD. 845 Oak Grove Ave. #100, Menlo Park. CA 94025.

[6] S. Dhawan, "A RICH MWPC Pad Readout by Using Custom MICROPLEX I.C.", IEEE Trans. Nucl. Sci., **NS-35**, (1988) (to be published).

[7] P. Fischer, "Test of a Pad Readout uv-Detector for Ring Imaging Čerenkov Counters", IEEE Trans. Nucl. Sci., **NS-35**, (1988) (to be published).

[8] "DELPHI-TPC Handbook", CERN EF Division, **DELPHI 82-4**, (1982) 2.2.

[9] M. Iwasaki, R.J. Madaras, D.R. Nygren, G.T. Przybylski and R.R. Sauerwein, Time Projection Chamber Workshop, TRIUMPF, Vancouver, B.C., Canada, AIP Conference Proceedings **108** (1983) 214.

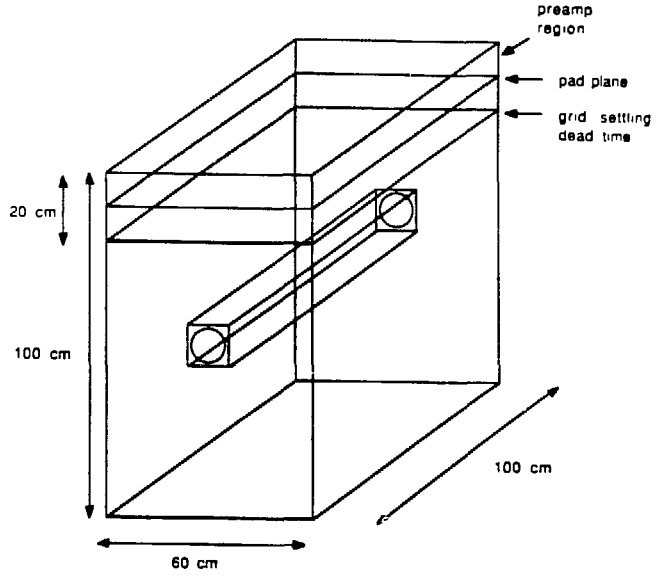

Figure 1: HISS TPC diagram. The E and B fields run vertically such that the tracks drift up to the pad plane.

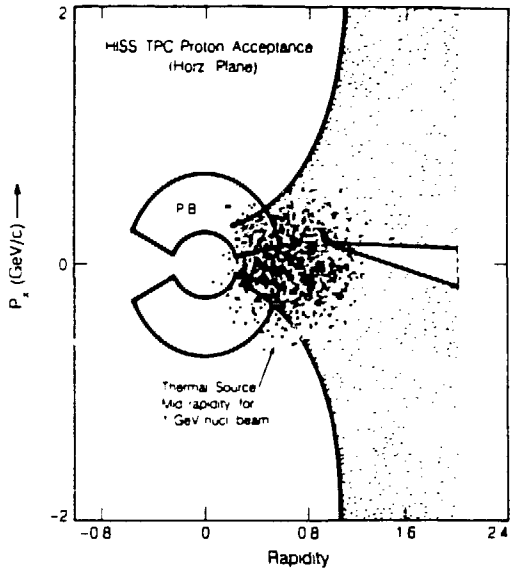

Figure 2: Acceptance in the beam bending plane for $p_\perp$ versus rapidity. The points show the projection of protons for a thermal distribution with a source rapidity of 0.68 (mid-rapidity for a 1.0 GeV/nucleon beam).

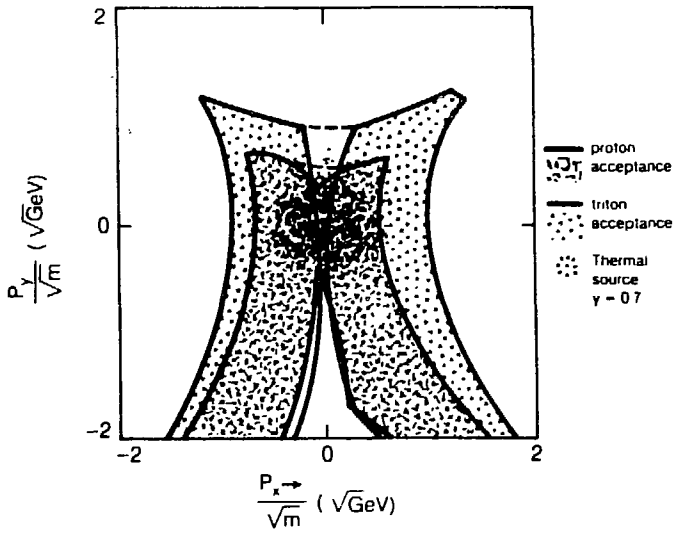

Figure 3: Acceptance for protons and tritons in the $p_\perp$ plane at rapidity = 0.68 (mid-rapidity for a 1.0 GeV/nucleon beam). The scattered dots show the projection of a mid-rapidity thermal source (T = 90 MeV) on this plane.

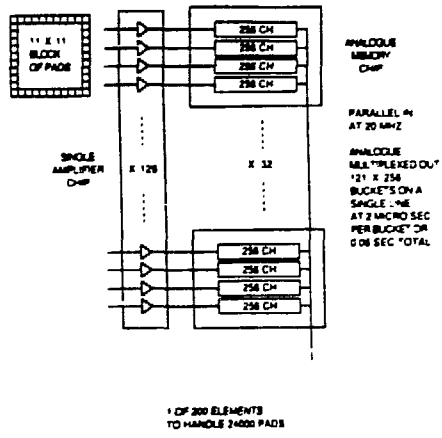

Figure 4: A conceptual view of the front end electronics which will be located on the pad plane.

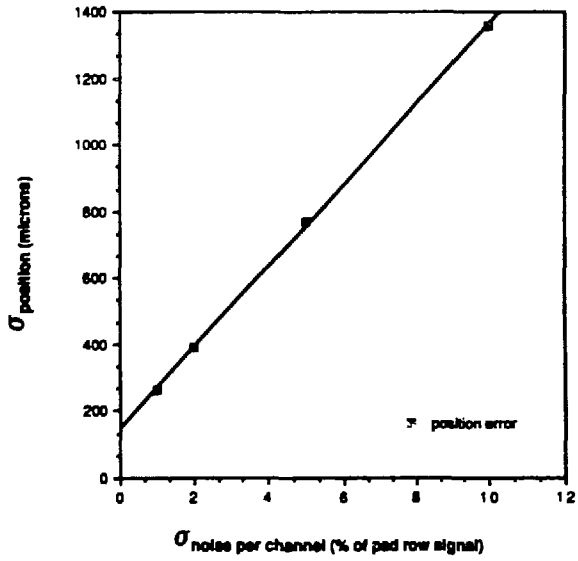

Figure 5: Error in position as a function of electronic noise where the centroid has been determined by the weighted mean.

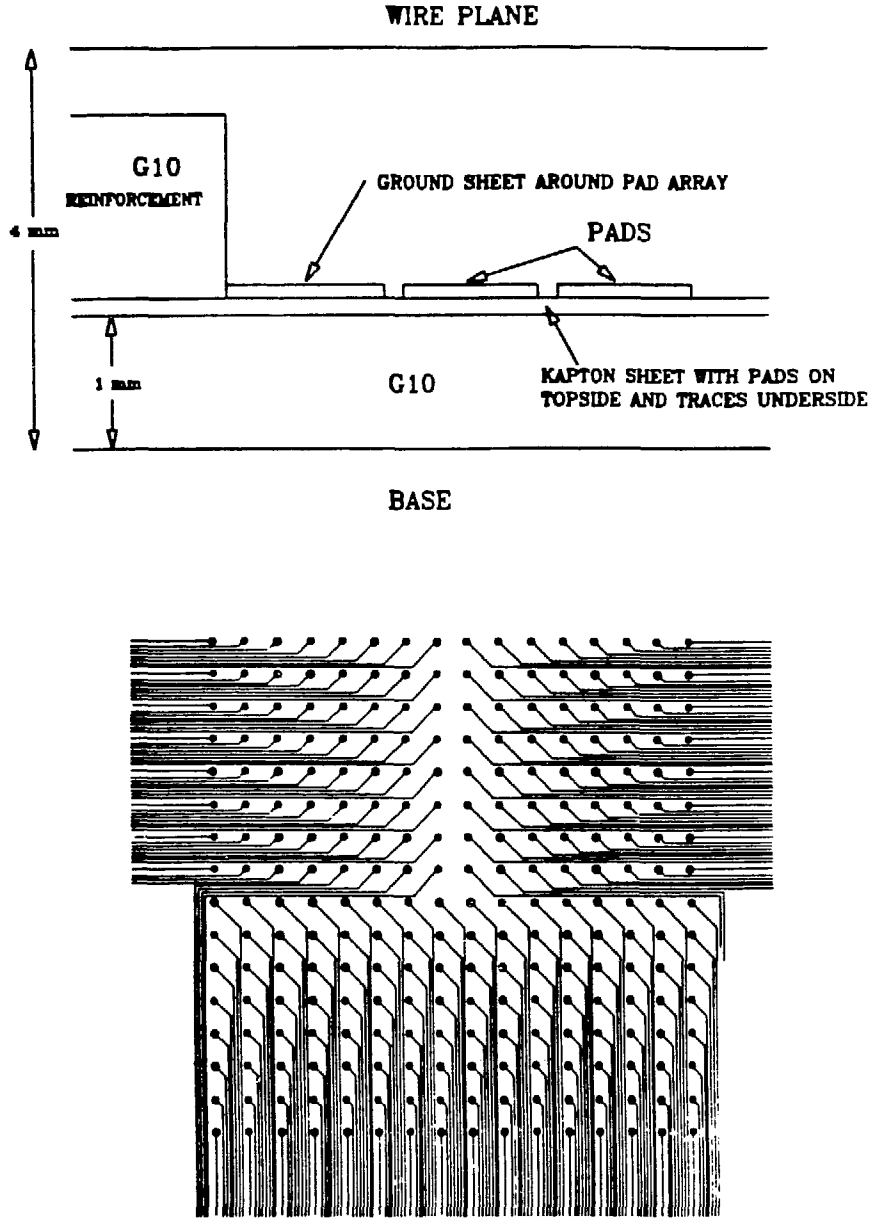

Figure 6: Sketch of the pad array layout in the test TPC. The lower portion of the figure shows the traces leading away from the pads.

Pion and High Energy Gamma Emission

STATUS OF MULTI-PION CORRELATIONS AT HISS*

D. Olson[a], W. Christie[b1], T. Abbott[a], D. Beavis[c], P. Brady[b],
H. Crawford[d], S. Fung[a], D. Keane[a], P. Lindstrom[e],
Y. Liu[f], W. Müller[e], T. J. M. Symons[e], C. Tull[b], W. Wieman[e]

[a]University of California, Riverside, CA 92521
[b]University of California, Davis, CA 95616
[c]Brookhaven National Lab., Upton, NY
[d]University of California Space Sciences Lab., Berkeley, CA 94720
[e]Lawrence Berkeley Lab., Berkeley, CA 94720
[f]Harbin Institute, People's Republic of China

1 Introduction

Bevalac experiment E684H is an investigation of multi-pion correlations at HISS. This is a continuation of the studies carried out at the LBL streamer chamber by the Riverside group.[1,2] While the streamer chamber experiments were studies of pion correlations over the entire range of mid-rapidity phase-space with modest statistics, the HISS experiment covers a large-but-limited range in phase-space with high statistics. During a run in April/May 1987 we obtained our primary data sample for 1.8 GeV/nucleon Ar+KCl and a secondary sample with 1.2 GeV/nucleon Xe+La.

*supported by DOE Contract DE-AS05-76ER04699, NSF Grant PHY81-21003, and NASA Grant NGR-05-003-513

[1]PhD thesis

2 Physics Goals

The primary objective is to obtain information about the space-time structure of the pion emitting source. The radius R and lifetime τ parameters are derived from a Hanbury-Brown Twiss analysis using a two particle correlation function from Yano and Koonin[3]

$$C(q, q_o) = K(1 + \lambda e^{-(q^2R^2/2 - q_o^2\tau^2/2)}) \quad (1)$$

where $q = |\vec{p_1} - \vec{p_2}|$, $q_o = E_1 - E_2$ and subscripts 1(2) refer to particle 1(2) of the pion pair and K is a normalization factor.

By determining R and τ with high statistics we will be able to investigate the dependence of these two parameters upon the beam/target mass (A), average pion momentum ($< \vec{p} >$), and leading fragment charge (Z_F). From the dependence upon the average pion momentum we obtain information about the expansion of the source.[2] The leading projectile fragment charge provides information about the impact parameter for the collision.

3 Experimental Layout

This experiment was performed at the HISS facility, see Fig. 1. The beam passes through beam line scintillation trigger counters (S1, V1, S2, V2), position sensitive scintillation counters (P1, P2) for beam vector measurements before striking the target in the center of the HISS vacuum tank. A beam / projectile fragment veto counter (V4) is located just outside the vacuum tank. The V4 counter is used to set a threshold on the centrality of the collision and is analogous to the streamer chamber P counter. A 15 slat wall of scintillation counter (1m by 1.5m) intercepts the particles in the projectile fragment frame. The 1.5m by 2m drift chamber is positioned to accept negative pions emitted at zero degrees. Three sections of Time-of-Flight wall are located behind the drift chamber to provide particle identification and aid in background rejection.

3.1 Position sensitive scintillation counters

The position sensitive scintillation counters (P1 and P2), see Fig. 2, consist of a 10cm by 10cm by 1mm thick plastic scintillator perpendicular to the beam line which is viewed by four photomultiplier tubes (PMT's) which are parallel to the beam line. These four PMT's provide up, down, east and west pulse height measurements from which the position is derived. A grid of scintillating fibers which are coupled to two additional PMT's are used for calibration. Figure 3 shows the position response of these counters for events in which the Xe beam hit one of the scintillating fibers before the position calibration has removed the distortions. The position resolution of each of these counters is 2mm FWHM for Xe and 6mm FWHM for Ar.

3.2 Drift chamber

The details of the HISS drift chamber are described in Ref.[4]. The main aspects of it in this experiment are the

- 1.5m by 2m aperture,
- 14 planes of sense wires evenly distributed over 1.3m of track length,
- 1 cm drift distance in each cell, and
- 100% efficiency for minimum ionizing particles.

Figure 4 shows a scatter plot of the horizontal position vs. angle of tracks from many events. Ones sees the vacant band corresponding to infinite momentum which divides the positively charged particles (upper) from the negatively charge particles (lower).

3.3 Phase space acceptance

The phase space acceptance of the drift chamber is shown in Fig. 5. Figure 5a shows a scatter plot of rapidity vs. P_X (P_X is the perpendicular component of momentum in the bending plane of the HISS magnet) for negative particle tracks. The limits

derived from the drift chamber aperture are indicated along with the software limit imposed by the momentum reconstruction. The software limit will be extended to lower momentum in future analysis of this data. Figure 5b shows a scatter plot of both perpendicular components of momentum. From this one sees the vertical acceptance of about ± 100 MeV/c for the lowest rapidity pions.

3.4 Leading projectile fragment

The charge of the largest projectile fragment is obtained from the pulse height in the fragment wall. Figure 6a shows a scatter plot of the charge of the largest fragment vs. the track multiplicity in the drift chamber. Figure 6b shows the charge distribution for events which had ≤ 3 tracks or > 3 tracks. The suppression of large fragments for events with a high multiplicity of tracks is clearly seen. After more theoretical analysis we will be able to use the leading fragment charge (or sum of projectile fragment charge) as an indicator of impact parameter in much the same way that the total multiplicity seen in the streamer chamber data is used to indicate the impact parameter.

4 Future Analysis

The main focus of the analysis will result in correlating the HBT parameters R and τ with $< p >$ and Z_F. The two primary considerations to verify the quality of the analysis are to (1) investigate the tracking efficiency for close pairs of tracks and (2) understand the effect of multiplicity on the tracking efficiency.

The cell size of 2 cm in the drift chamber sets the scale for the two track separation and this corresponds roughly to a few MeV/c momentum difference between tracks. However, the effect of crossing tracks and separations parallel to the wires must be investigated for a complete understanding of close pion pairs.

As the multiplicity of tracks increases in the drift chamber so does the number of tracks which share wires with other tracks. From a visual study of a number of events

it appears that multiplicity doesn't effect tracking efficiency for multiplicities below 10 tracks per event. This is most important for the Xe data and we will understand this effect before moving to higher mass beams, such as Au.

Another topic of investigation is a theoretical calculation for the impact parameter dependence of the leading fragment charge, Z_F. This is important for our understanding of the impact parameter dependence of the HBT parameters in addition to estimating our effective impact parameter distribution.

5 Summary

The overall status at this point is that the analysis is proceeding well and that we should have results without any prolonged delays. We obtained a good data sample with Ar+KCl and enough Xe+La data to do some HBT analysis along with investigating the effect of heavy beams on the experimental setup.

Finally, the correlation of leading fragment charge with track multiplicity in the drift chamber indicates that we do have an indicator of impact parameter which we can use to select the most central collisions.

After finishing this analysis we will be running an extension of the same experiment with Au+Au beams as a continuation to the highest masses.

References

[1] S.Y. Fung et. al., Phys. Rev. Lett. **41**, 1592 (1978); J.J. Lu et. al., Phys. Rev. Lett. **46**, 898 (1981); D. Beavis et. al., Phys. Rev. C**27**, 910 (1983); D. Beavis et. al., Phys. Rev. C**28**, 2561 (1983); Y.M. Liu et. al., Phys. Rev. C**34**, 1667 (1986).

[2] D. Beavis et. al., Phys. Rev. C**34**, 757 (1986).

[3] F. B. Yano and S. E. Koonin, Phys. Lett. **78B**, 556 (1978).

[4] T. Kobayashi et. al., NIM A**254**, 281 (1987).

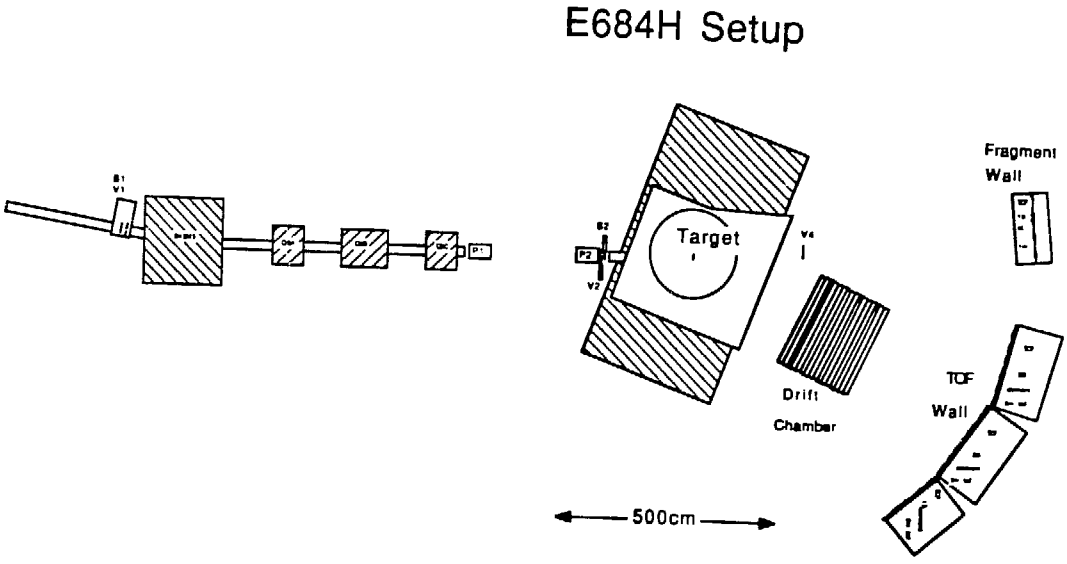

Figure 1

Schematic view of experimental hall.

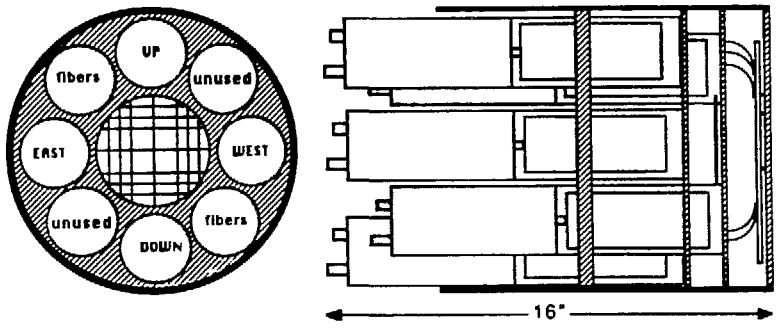

Figure 2

Position sensitive scintillation counter. Position is derived from the pulse height information from 4 PMT's which are air coupled above, below, and to each side of a scintillator which is perpendicular to the beam. A grid of scintillating fibers is used for calibration.

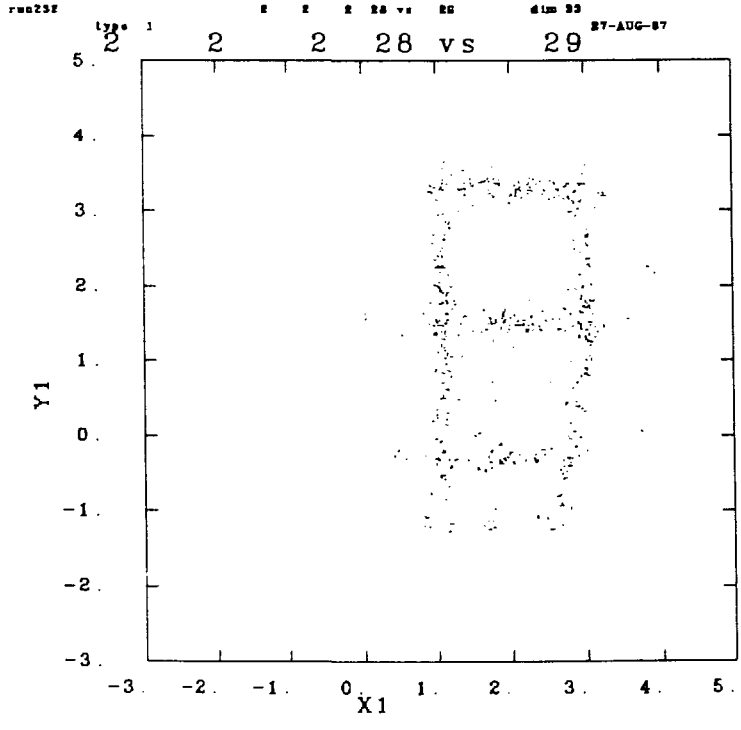

Figure 3

Response of position sensitive scintillation counters before calibration. Data points are from events in which a scintillating fiber was hit.

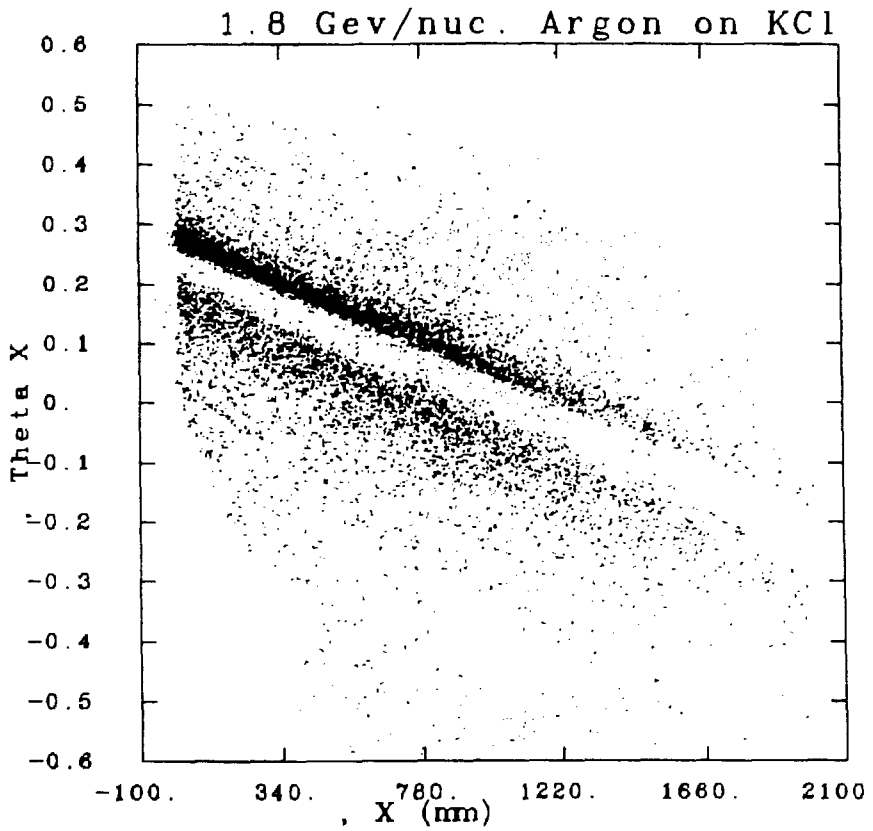

Figure 4

Plot of horizontal position (cm) vs. angle (rad) from tracks in the drift chamber. Positively charged particles are in the upper portion and negatives in the lower portion.

(a)

(b)

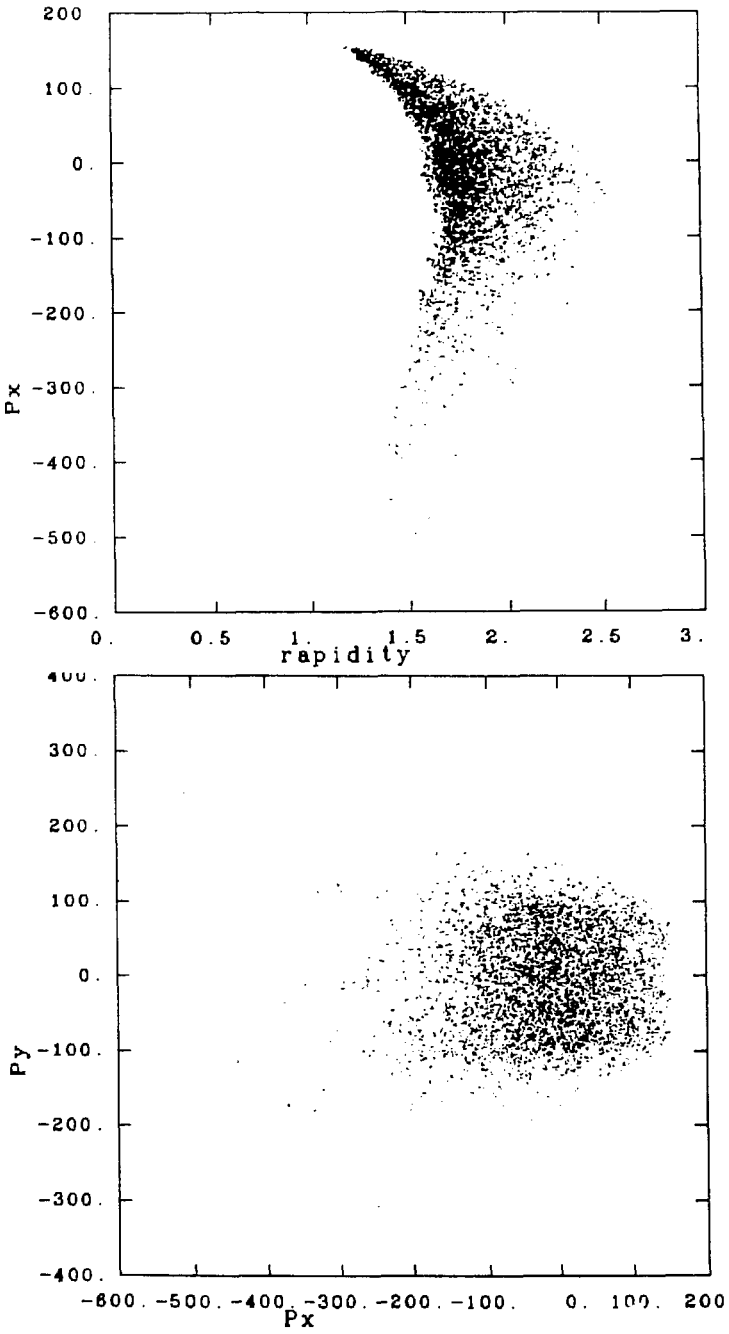

Figure 5

(a) Rapidity vs. P_X (the in bending plane momentum component) showing the preliminary phase space acceptance of the setup. The bounds resulting from the drift chamber aperture are shown along with the bound imposed by the momentum reconstruction software. (b) P_X vs. P_Y showing the vertical acceptance which is $\geq \pm 100$ MeV/c.

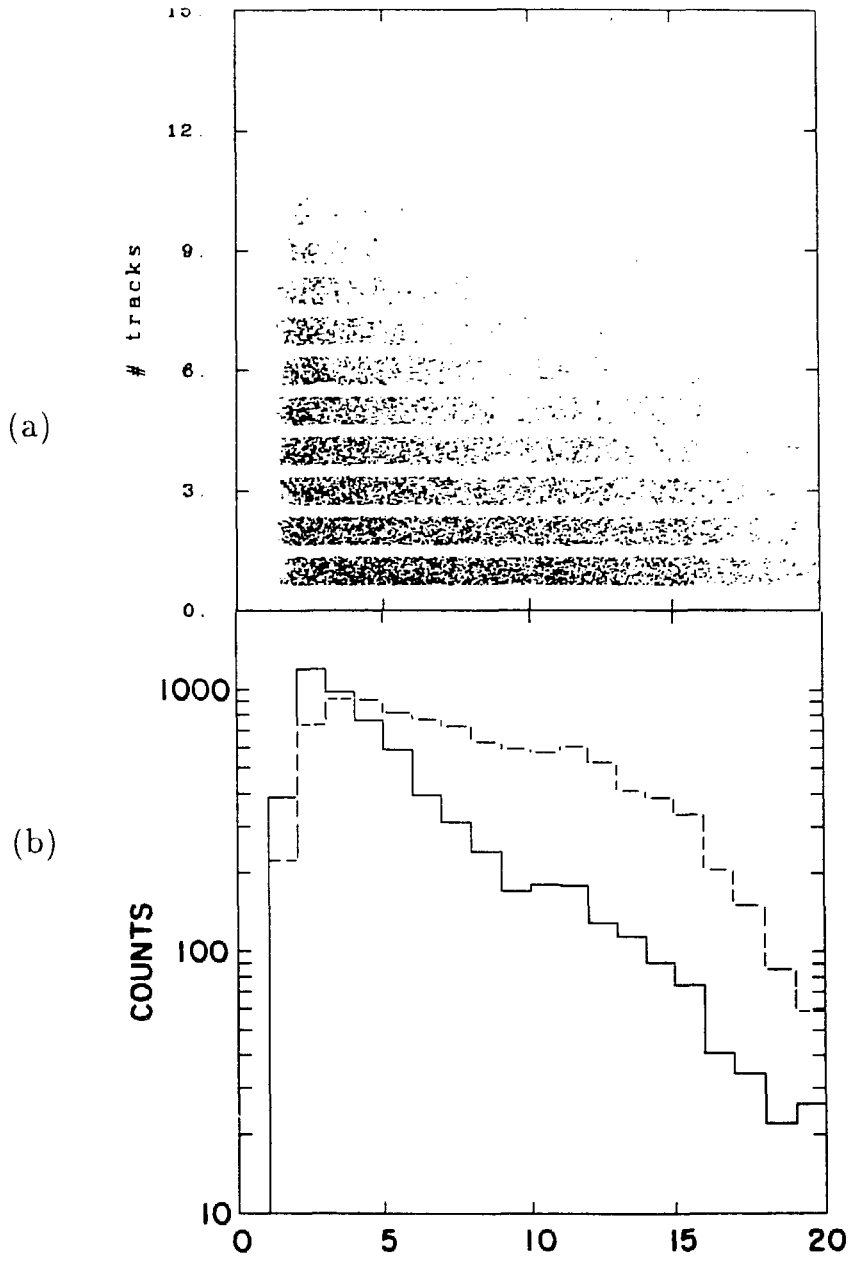

Figure 6

(a) Leading projectile fragment charge (Z_F) vs. track multiplicity in the drift chamber. (b) Z_F distributions for low ($m \leq 3$, dashed) and high ($m > 3$, solid) track multiplicity. The suppression of high Z_F with high track multiplicity is seen which indicates that Z_F is a useful parameter in estimating impact parameter.

PION SPECTRA IN CENTRAL LA + LA COLLISIONS AT 530, 740 AND 1350 MeV/A*

G. Odyniec, J. Bartke, S.I. Chase, J.W. Harris, H.G. Pugh, G. Rai, W. Rauch, L.S. Schroeder, L. Teitelbaum and M. Tincknell
Nuclear Science Division
Lawrence Berkeley Laboratory
University of California
Berkeley, California 94720

R. Stock and R. Renfordt
Fachbereich Physik
University of Frankfurt
Frankfurt, West Germany

R. Brockmann, A. Sandoval and H. Ströbele
Gesellschaft fur Schwerionenforschung
Darmstadt, West Germany

K.L. Wolf and J.P. Sullivan
Texas A&M University
College Station, Texas 77843

ABSTRACT

The negative pion spectra were measured for central La+La collisions at incident beam energies 530, 740 and 1350 MeV/A. A single exponential fit reproduces the data satisfactory at low energies, 530 and 740 MeV/N, while a two component fit is needed to adequately describe the 1350 MeV/N data. The pion spectra at 530 and 740 MeV/N and the dominant component at 1350 MeV/N can be described in term of the decay kinematics of the delta resonances in thermal equilibrium. Interpretations of the second component prevalent at 1350 MeV/N is discussed.

*This work was supported by the Director, Office of Energy Research, Division of Nuclear Physics of the Office of High Energy and Nuclear Physics of the U.S. Department of Energy under Contract DE-AC03-76SF00098.

Pion spectra in relativistic heavy-ion collisions are expected to provide information on the thermal freeze-out stage of nuclear matter believed to occur after the isotropic expansion of the hot fireball formed during the high density phase of the collision. An understanding of the reaction mechanism can provide information on the presence of collective flow effects and an insight into the nuclear equation of state. Previous experimental studies of the pion spectra have concentrated on light systems and inclusive measurements. Recently heavy ion beams became available at the Bevalac for experimentation. The collisions between two heavy nuclei are expected to be free from surface effects and provide conditions for the formation of hot fireballs.

The negative pion spectra were studied in central collisions of La + La at energies from 530 MeV/A to 1350 MeV/A. The measurements were made using the LBL 1.2 m Streamer Chamber at the Bevalac. A central collision trigger selected events with the least number of secondary charged particles passing through a scintillator located downstream from the target (in the projectile fragmentation cone). The selected events constitute about 6% of the total interaction cross section which in the geometrical model corresponds to impact parameters $b \leq 2.82$ fm or $b \leq 0.24\ b_{max}$.

The study of central collisions allows one to extract more reliable information on the temperatures reached in the collision process. The central collision trigger minimizes complications due to spectator matter in the form of quasi-free nucleon-nucleon interactions. The analysis was restricted to the 90 degree spectra in the CMS in order to study emission from the "fireball" region.

For particles in a thermal fireball distribution, the CMS energy spectrum after weighting with a $(pE)^{-1}$ factor where p is the momentum and E is the total energy of the particle, should follow a simple exponential law:

$$\frac{1}{pE}\ \frac{d^2\sigma}{dEd\Omega} = \text{const.}*\exp(-E/T) \qquad (1)$$

where T is the temperature of the fireball.
The kinetic energy spectrum $d^2\sigma/dEnd\Omega$, weighted with the same $(pE)^{-1}$ factor, should also follow an exponential behavior and provide the same temperature T.

The pion spectra at 90 degrees in the CMS are shown in Figs. 1, 2 and 3 for 530, 740 and 1350 MeV/A, respectively. All spectra were corrected for electron contamination due to π^0 decay. The procedure involved generating a pion spectrum at each beam energy using the CASCADE code and allowing pion decay using the detector simulation code GEANT3. The energy and momentum distributions of the decay products were constructed and a ratio formed with summed (π^-/π^+ contamination) spectra. The experimental spectra were corrected on a channel by channel basis. Dashed curves correspond to a single component fit (1) whereas the solid curve in Fig.3 represents a two component fit:

$$dN/dE_k = A_1 pE\exp(-E_k/T_1) + A_2 pE\exp(-E_k/T_2) \qquad (2)$$

where $A_{1,2}$ and $T_{1,2}$ are fit parameters .

A single exponential law (1) describes the data fairly well at 530 and 740 MeV/A (Figs. 1 and 2). However a slight enhancement of the high energy part of the spectrum is noticeable. Conversely, the high energy 1350 MeV/A data is poorly reproduced by a single exponential fit and extremely well fitted with the two components. The fit parameters together with values of chi**2 are listed in TABLE 1. For 1350 MeV/A the parameters describing the two components are given. R represents the fraction of the pion yield in the first exponential defined by T_1 (Fig. 3), explicitly,

$$R = A_1T_1/(A_1T_1 + A_2T_2) \qquad (3)$$

Previous magnetic spectrometer studies ([6] and references therein) have reported inclusive kinetic energy spectra in the CM system and presented evidence to support the notion that, especially at forward angles, the pion energy spectra possess a component due to the decay of delta resonances. Direct delta resonances are created in nucleon-nucleon collisions which subsequently decay with predominantly forward-backward emission in the the CM system. Nagamiya et al.[6] analyzed their spectra at 90 degrees CM where the contributions of pions from the delta decays are expected to be small. In principle their results should be compared with our analysis (Table 1) except that Nagamiya et al. "temperatures" are strictly the slope values of the invariant cross section.

TABLE 1.

Theta (CM) = 90 ± 30 degrees

La + La → π^- + X

E/A	T(T_1)	T	R	CHI**2
[MeV/A]	[MeV]	[MeV]	[%]	[N/ndf]
1350	58±1			3.4
	45±1	101±7	68±4	0.9
740	47±1			1.5
530	37±2			2.5

Pion temperatures were also determined from the transverse momentum spectrum since it is Lorentz invariant and free from frame dependent biases. It should be emphasized that the electron contamination corrections are extremely important. The electrons account for more than 50% of the contents of the first P_t bin whereas in the E_{kin} spectra at 90 degrees the electron contamination is always less then 10%.

The 1350 MeV/A P_t distribution was fitted with Hagedorn's two component formula [1]:

$$\frac{dN}{dp_\perp} = A_1 p_\perp \sqrt{p_\perp^2 + m^2} \sum_{n=1}^{\infty} (-1)^{n+1} K_1\left(\frac{n\sqrt{p_\perp^2 + m^2}}{T_1}\right) +$$

$$\frac{dN}{dp_\perp} = A_2 p_\perp \sqrt{p_\perp^2 + m^2} \sum_{n=1}^{\infty} (-1)^{n+1} K_1\left(\frac{n\sqrt{p_\perp^2 + m^2}}{T_2}\right) +$$

and the values,

T_1 = 44 + 3 MeV, T_2 = 96 + 4 MeV, R = 65% Chi**2 = 0.8/ndf.

obtained. These values are in good agreement with those obtained from the fit to the E_{kin} spectrum (see Table 1). The consistency of the results using two very different methods reflects the reliability of the corrected

experimental data. For the other two energies, 530 and 740 MeV/A, the single component Hagedorn fit reproduced the experimental spectra. However, because of low statistics at high P_t, it was not possible to draw any conclusion regarding the existence of a second component, though tentatively, the spectra shape appears to suggest the absence of, or at most, a weak second component. Again, the temperatures were in excellent agreement with those listed in Table 1.

In the Ar + KCl([2],[3]) reaction at 1.8 GeV/A there was an indication of a second component. There the main (95±1%) component with T=58±3 MeV could be understood in terms of the cascade model calculations including $\Delta \rightarrow N\pi$ decay kinematics. The observations are qualitatively consistent with thermal equilibrium in a fireball consisting primarily of protons and Δ resonances, both having a temperature of about 120 - 135 MeV; the "temperatures" extracted from the pion and proton spectra are not the true temperatures, but reflect Δ-decay kinematics. A small (5±1%) component with T = 110±10 MeV may be interpreted as a contribution of direct pions escaping from the early stages of a hot, dense nuclear matter (fireball). It is interesting to note that the thermodynamical model of Hagedorn and Rafelski [8] predicts a pion temperature of 110 MeV.

The low energy part of the La + La pion spectrum is again consistent with cascade calculations, but the higher component in the 1350 MeV/A La + La system is much more prominent than for the 1.8 GeV/A Ar + KCl. The enhanced presence of the second component in the heavier systems might signal the onset of other physics processes such as the collective (compressional) phenomena [4]. A complete understanding of these spectra must take into account all other global observations and the compressional energy of the reaction. Recently, the concave 1350 MeV/A La + La energy spectrum was conjectured to arise from an isentropic hydrodynamical expansion of hot compressed nuclear matter at freeze-out density [5].

Summarizing, our results are consistent with those of previous experiments. Comparing energy spectra one can see that the temperature clearly increases as a function of energy, and the proton temperatures (or slope parameters [6]) are systematically higher, by roughly a factor of two [7] than the pion apparent temperature in all studied reactions.

REFERENCES

[1] R. Hagedorn, TH 3684-CERN.

[2] R. Brockmann et al., Phys. Rev. Lett. 53 (1984) 2012.

[3] A. Sandoval et al., 7th High Energy Heavy Ion Study, GSI Darmstadt, October 1984, GSI-85-10 (1985) 477.

[4] J.W. Harris et al., Proceedings of XV International Workshop on "Gross Properties of Nuclei and Nuclear Excitations," Hirschegg, Austria, January 12-17, 1987.

[5] D. Hann and N. Glendenning, LBL-23864, 1987.

[6] S. Nagamiya et al., Phys. Rev. C24 (1981) 971.

[7] H. Ströbele et al., 8th High Energy Heavy Ion Study, Berkeley, November 16-20, 1987.

[8] R. Hagedorn and J. Rafelski, Phys. Lett. B97 (1980) 136.

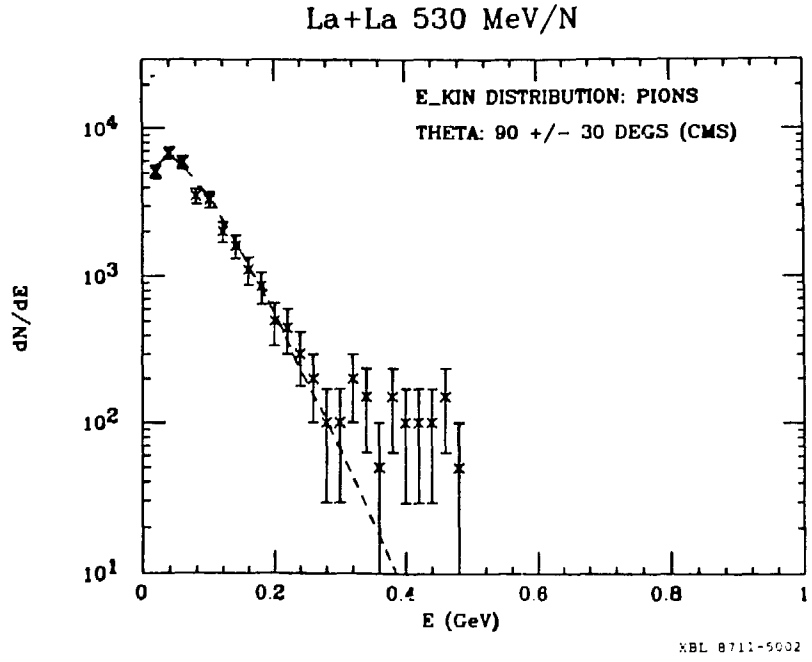

Fig. 1 Pion CMS energy spectra at 90±30 degrees for central La+La collisions at 530 MeV/A.

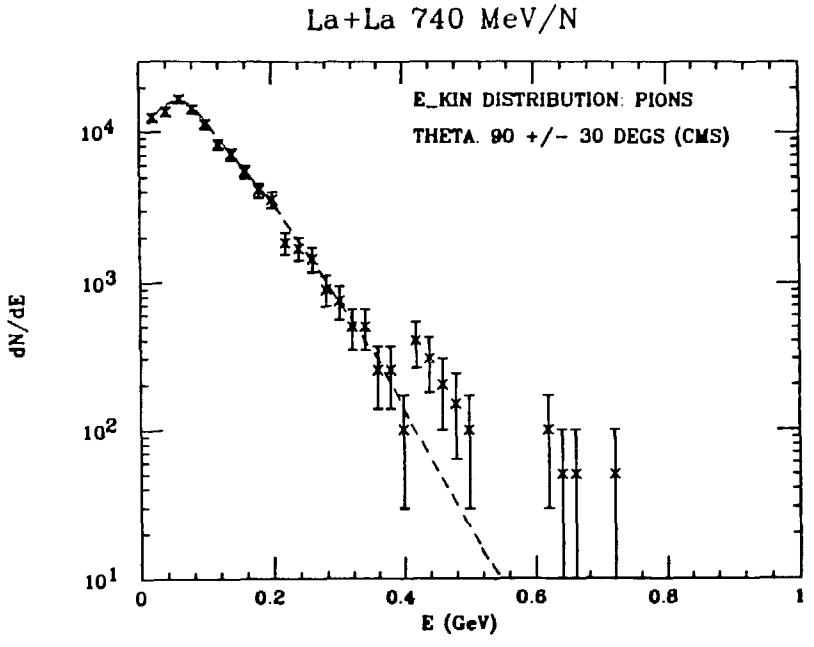

Fig. 2 Pion CMS energy spectra at 90+30 degrees for central La+La collisions at 740 MeV/A.

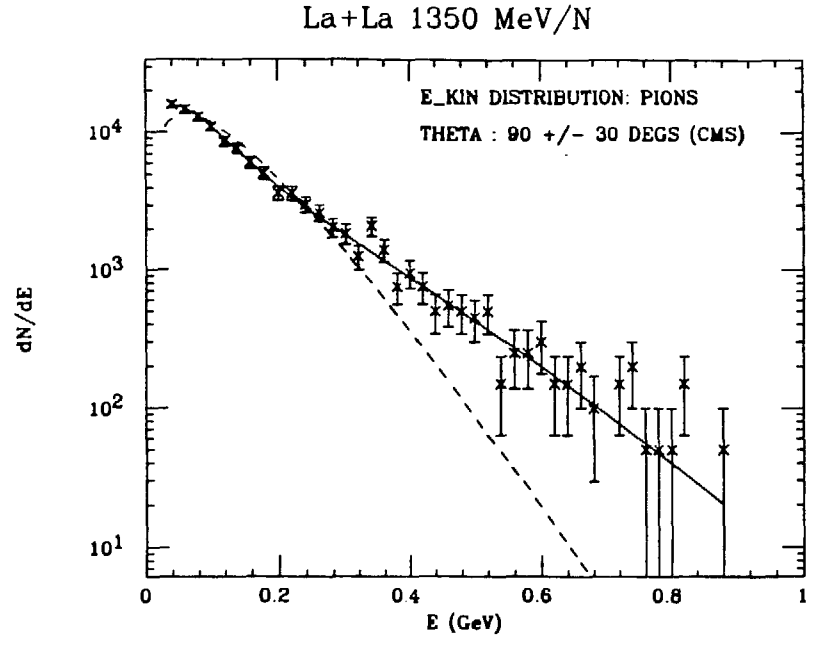

Fig. 3 Pion CMS energy spectra at 90+30 degrees for central La+La collisions at 1350 MeV/A.

HARD PHOTON AND MESON PRODUCTION IN HEAVY-ION COLLISIONS[1]

K. Niita, A.L. De Paoli[2], M. Schäfer, W. Bauer[3],
T.S. Biro, W. Cassing, U. Mosel

Institut für Theoretische Physik, Universität Giessen
D-6300 Giessen, Germany

ABSTRACT

The production of hard photons and mesons in intermediate and high energy heavy-ion collisions is discussed on the basis of incoherent nucleon-nucleon collisions. The space-time evolution of the heavy-ion reaction and the individual nucleon-nucleon collisional history is calculated within the BUU approach. The in-medium production cross section for photons is evaluated in a microscopic, covariant way while the respective quantity for mesons is adopted from experimental data. Comparisons with experimental spectra and angular distributions are presented in case of photons whereas inclusive cross sections are given for neutral pions.

1. INTRODUCTION

One of the central questions that still remain in nuclear physics is that of the equation of state of nuclear matter. Heavy-ion reactions in the intermediate energy regime between the Fermi-energy and about 1 GeV/A offer a unique tool to explore this question because sizeable densities of the order of 2-4 ρ_0 can already be reached at these energies. This is illustrated in fig. 1 where the maximum density obtained in central collisions of $^{40}Ca+^{40}Ca$ in a volume of at least 1 fm^3 is

---

[1]Supported by BMFT and GSI Darmstadt

[2]Supported by a fellowship of the Consejo Nacional de Investigaciones Cientificas y Tecnicas, Republica Argentina.

[3]Present address: California Institute of Technology, Kellogg Radiation Laboratory 106-38; Pasadena, CA 91125

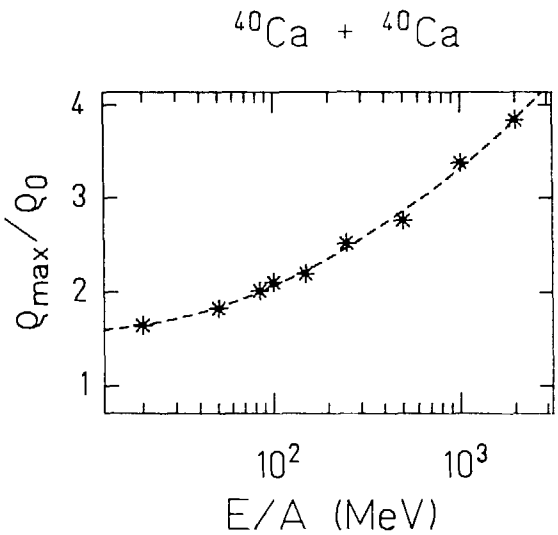

Fig. 1: The maximum density achieved in central collisions of $^{40}Ca+^{40}Ca$ as a function of bombarding energy within BUU-dynamics

shown as a function of the bombarding energy per nucleon. We note that these 'data' have been obtained by BUU simulations (cf. Section 2) and thus are model dependent, but uncertainties in the central density are limited to ± 20%. Furthermore, at these energies the reactions are not yet completely determined by cascade events such that the mean field with its density dependence still plays a considerable role.

Necessary for the determination of the equation of state are two informations, one is the density, i.e. the distributions of particles in x-space, and the second is the distribution of particles in momentum space which determines pressure and degree of thermalization in the reaction zone. In other words, the phase-space distribution of the nucleons in the reaction zone has to be known. It is, therefore, important to develop selective probes for specific regions of phase-space and for specific time-cuts during the heavy-ion reaction.

The observation of particles from the reaction zone can provide such information. Nucleons come both from the early and the late stages of the reaction. This is directly evident from their spectra that show hard preequilibrium as well as softer thermal components. Pions and hard photons, on the other hand,

are produced during the very first stages of the collision[1-4]; they contain information about the nucleonic phase-space distribution directly after contact of the two nuclei[4]. Whereas pions undergo a lot of final state interactions on their way out of the reaction volume, hard photons give a more direct picture of the phase-space distribution in the reaction zone due to the weak electromagnetic interaction. In this contribution we will, therefore, be primarily be concerned with the production of hard photons in heavy-ion collisions; more details of our studies can be found in refs. 2-4.

2. DETAILS OF THE CALCULATION

2.1 Nuclear Dynamics

A quite reliable theoretical framework for the description of intermediate-energy heavy-ion reactions is given by the Boltzmann-Uehling-Uhlenbeck (BUU) equation. This equation describes the time-evolution of the phase- space distribution $f(\vec{x},\vec{p};t)$, i.e.

$$\left[\frac{\partial}{\partial t} + \frac{\vec{p}}{m}\vec{\nabla}_x - \vec{\nabla}U\cdot\vec{\nabla}_p\right] f(\vec{x},\vec{p}) = \left[\frac{\partial f}{\partial t}\right]_{coll} \qquad (1a)$$

The r.h.s. represents the change of the Wigner-function due to collisions and is given by

$$\left[\frac{\partial f}{\partial t}\right]_{coll} = \frac{4}{(2\pi)^3}\int d^3p_2\, d^3p_3\, d\Omega\, |\vec{v}_{12}|\frac{d\sigma}{d\Omega}\,\delta\left[\vec{p}_1+\vec{p}_2-\vec{p}_3-\vec{p}_4\right] \times \left[f_3f_4(1-f_1)(1-f_2) - f_1f_2(1-f_3)(1-f_4)\right]. \qquad (1b)$$

We solve this equation by means of the test-particle method, originally proposed by Wong[5], as implemented by Bertsch and collaborators[6]. The mean field U in the calculations is given by a functional of the local density ρ:

$$U\left[\rho(r)\right] = -218\,\frac{\rho(r)}{\rho_0} + 164\,\left[\frac{\rho(r)}{\rho_0}\right]^{4/3} \qquad (2)$$

determined by a fit to nuclear saturation properties[2,3].

The collision term on the r.h.s. requires an effective nucleon-nucleon reaction cross section $d\sigma/d\Omega$. It has been customary to use an energy-dependent parametrization of the free nucleon-nucleon cross section originally provided by Cugnon et

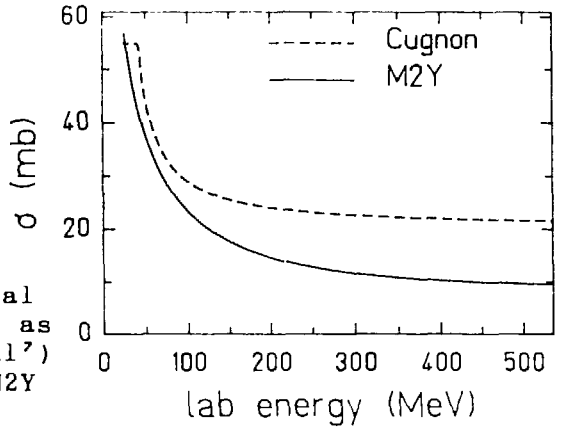

Fig. 2: Comparison of the total nucleon-nucleon cross section as parametrized by Cugnon et al[7] with that obtained from the M2Y G-matrix.

al.[7]. This may, however, quite seriously overestimate the effective in-medium cross section especially at lower bombarding energies because in the nuclear medium intermediate scattering states are Pauli-blocked. Estimates by Malfliet et al.[8] based on a selfconsistent G-matrix calculation in nuclear matter have yielded suppressions of the free cross sections by about a factor of 2.

In order to take this essential effect into account we are using a G-matrix, calculated by Bertsch et al. many years ago[9], for the calculation of the nucleon-nucleon cross section. This G-matrix, the socalled M2Y force, has been shown to be quite reliable in calculations of heavy-ion interaction potentials[10]. The nucleon-nucleon cross section obtained with it is shown in fig. 2 in comparison with the Cugnon-parametrization[7]. At higher nucleon energies above about 100 MeV (lab) the M2Y cross section drops below the free value. In the energy range of about 200-300 MeV, that will later turn out to be the most essential one for hard-photon production, the cross section has dropped by about a factor of 2 below the Cugnon value. The overall dynamics of the reaction are not changed significantly by this change of collision cross section. Single particle observables such as proton- emission from nuclei[11] are anyway reproduced only within a factor of 2 and the γ-yields are totally unaffected as shown in ref. 12.

2.2 Photon And Meson Production Cross Section

We have shown earlier that the yield of high energy photons produced by coherent, collective bremsstrahlung accounts for at most 10 % of the observed yield[13]. This conclusion is in agreement with results obtained by other authors as well[14-16]. We, therefore, alternatively assume here that the photons (or pions) originate from incoherent nucleon-nucleon (N-N) collisions. Their total yield is thus given by the probability to produce a photon (or meson) in each N-N collision summed over all collisions and then integrated over impact parameter to obtain a cross section

$$\frac{d^2\sigma}{dE_\gamma d\Omega_\gamma} = 2\pi \int bdb \sum_{N\text{-}N\ coll} \int \frac{d\Omega}{4\pi} \frac{E_\gamma}{E'_\gamma} \frac{d^2P^\gamma(|\vec{p}_1-\vec{p}_2|)}{dE'_\gamma d\Omega'_\gamma} \times \left[1-f(\vec{x},\vec{p}_3,t)\right]\left[1-f(\vec{x},\vec{p}_4,t)\right] . \quad (3)$$

Here dashed quantities are in the nucleon-nucleon c.m. system and undashed in the nucleus-nucleus c.m. system. The quantity P^γ is the in-medium γ-production probability. This probability is calculated here for the first time microscopically and consistently by using the same interaction as for the collision cross sections. The radiative correction to the M2Y G-matrix is evaluated in a covariant way, so that it properly includes all relativistic effects[3] and avoids the usual long wavelength approximation. The in-medium production probability in case of pions is approximated in the present contribution by the ratio of the experimental free cross section[17] and the free N-N cross section[7] (cf. ref. 4). The Pauli blocking in eq. (3) is handled by averaging the Wigner function f over a spherical phase-space volume $\Delta V = (2\pi\hbar)^3/4$ around $(\vec{x},\vec{p})$.

3. RESULTS

Calculations with the method described have been performed both for proton-nucleus as well as for heavy-ion collisions[3,4]. A comparison with the 140 MeV proton-nucleus data[16] is shown in ref. 3 and illustrates excellent agreement for all targets investigated.

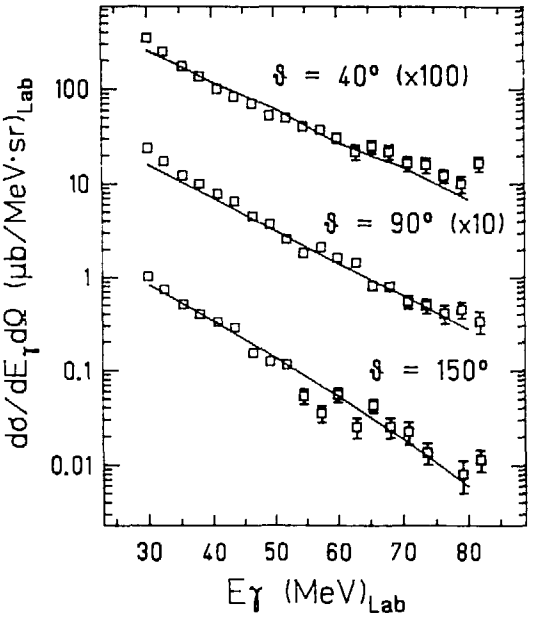

Fig. 3: Photon spectra for $^{86}Kr+^{12}C$ at 44 MeV/u at three different angles. The data are from ref. 19; the solid lines give the result of our calculations.

In fig. 3 we show the results for the γ-cross sections in case of $^{12}C+^{86}Kr$ at 44 MeV/u (ref. 19). The agreement is obviously perfect for all three angles in the laboratory system.

A comparison of photon spectra in coincidence with fusion reactions at 15 MeV/u and 24 MeV/u for $^{40}Ar + ^{70}Ge$ (ref. 20) at a laboratory angle of 160° is shown in fig. 4 by the dashed lines. The photon spectrum arizing from a statistical

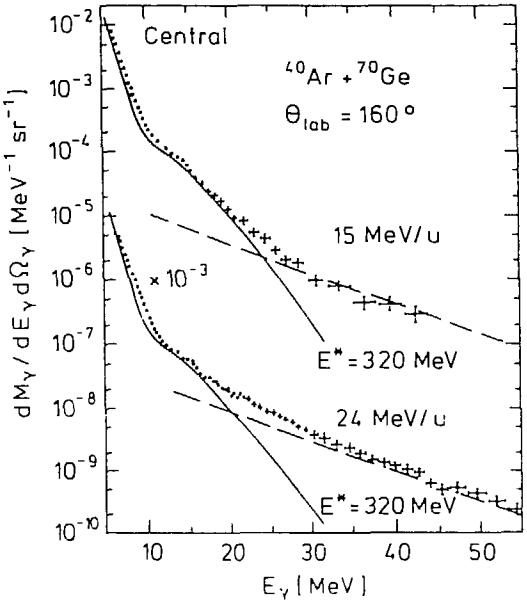

Fig. 4: Comparison of photon spectra from incoherent p-n collisions (dashed lines) with experimental data from ref.20. The photons are detected in fusion reactions of $^{40}Ar+^{70}Ge$ at 15 MeV/u and 24 MeV/u at a laboratory angle of 160°. The solid lines indicate the contribution from statistical decay of the compound nucleus[20])

deexcitation of the compound nucleus, which is evaluated within a standard evaporation code (cf. ref. 20), is given by the solid lines that underestimate the experimental yield at high photon energies substantially. Again the energetic γ-yield is consistent with the production by incoherent proton-neutron collisions.

That these photons are indeed quite selective probes for phase-space distributions is illustrated in fig. 5. The γ's of 100 MeV energy are produced in quite well defined regions of momentum space; in x-space they are originating from the spatial overlap zone of the nucleons[4]. A closer inspection of the time-history of the process shows that these photons are produced within the first ~ 15 fm/c after contact of the two nuclei[4] (cf. fig. 7) and thus provide a snapshot of the initial phase of the reaction in case of laboratory energies below 80 MeV/u.

4. FUTURE PERSPECTIVES

Since the BUU-code used in these calculations uses relativistically correct kinematics and the microscopic production process is evaluated in a covariant way we have extended our calculations to higher energies. The result is shown in fig. 6a which compares a properly scaled[3] energy- and angle-integrated γ-production cross section above ω=30MeV for heavy ions with that obtained from a p-n collision. It is nicely seen how up to bombarding energies of about 300 MeV/A the energy

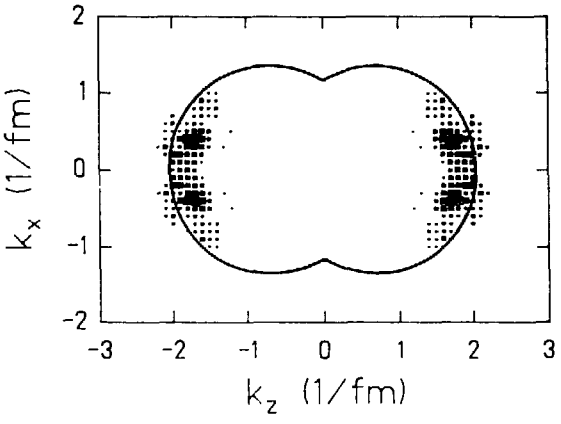

Fig. 5: Initial momentum distribution of nucleons producing 100 MeV photons under 90° in a central collision of $^{12}C+^{12}C$ at 40 MeV/u.

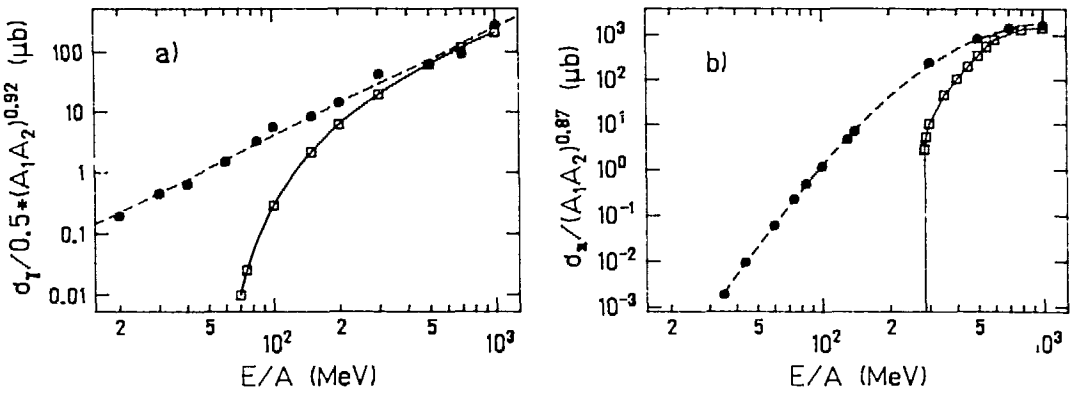

Fig. 6: (a) Comparison of the inclusive photon cross section from heavy-ion reactions properly scaled by the number of pn collisions (dashed line) (cf. ref.3) with that from free pn collisions (solid line) as a function of bombarding energy E/A. (b) The same comparison as in (a), however, performed for π^0 production.

of the Fermi-motion, that can be used in a collision to produce γ's, leads to significant increases of the γ-production per n-p collision. At the highest energies $\gtrsim$ 400 MeV/A this effect becomes negligeable and the γ's produced in a heavy-ion collision at that energy are essentially the same as those coming from free nucleon-nucleon collisions. Similar statements hold in case of pion production except for the higher threshold involved by the pion rest mass (fig. 6b). However, pions are not so well suited as selective probes for specific regions of phase space due to their strong interactions with nucleons. A qualitatively similar picture to fig. 6 arizes in case of K^+ production[21] with shifted thresholds again due to the larger rest masses involved. We propose that energetic photons might be used as triggers in the energy range up to 300-400 MeV/u while kaons (especially K^+ due to lower reabsorption) and similarly the η's are favorable from 500 MeV/u to 2 Gev/u. This is summarized in the following table

Energy	Density	Probe
$\rightarrow$0.3 GeV	$2\rho_0$	γ
$\rightarrow$0.5 GeV	$3\rho_0$	π
0.6 GeV$\rightarrow$	$4\rho_0$	η
0.7 GeV$\rightarrow$	$4\rho_0$	K

With these signals we can probe the compression stage at bombarding energies above 100 MeV/u since the maximum of the production rates roughly coincide with the maximum density achieved in the reaction zone. This is illustrated in fig. 7 for the γ-production rate in case of a central collision of $^{40}Ca+^{40}Ca$ at 250 MeV/u.

5. CONCLUSIONS

Hard photons contain information about the very first stages of a heavy-ion collision at lower energies and information about the maximum compression stage at relativistic energies. They are sensitive probes for specific phase-space regions that can be selected by putting appropriate windows on the γ-spectra. Calculations based on mean-field dynamics plus random on-shell nucleon-nucleon collisions and a microscopic calculation of $np \rightarrow np\gamma$ processes in the medium can reproduce the measured spectra and angular distributions very well up to bombarding energies of about 50 MeV/u. At higher energies the yields seem to be underestimated[2,3]; we speculate that this might be due to a change of the G-matrix at higher densities and bombarding energies.

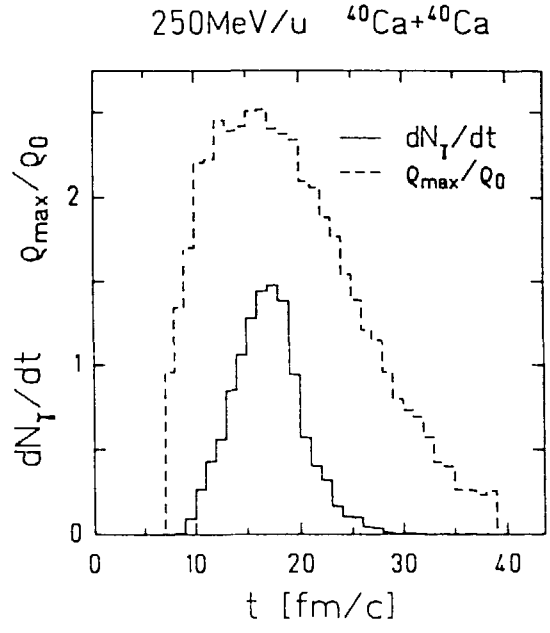

Fig. 7: Time dependence of the maximum density in the reaction zone for $^{40}Ca+^{40}Ca$ at 250 MeV/u (dashed line) in comparison with the photon production rate (solid line) for $\omega \geq 50$ MeV for the same reaction.

REFERENCES

1) M. Tohyama, R. Kaps, D. Masak and U. Mosel, Nucl. Phys. A437, 739 (1985)
2) W. Bauer, G.F. Bertsch, W. Cassing and U. Mosel, Phys. Rev. C34, 2127 (1986)
3) T.S. Biro, K. Niita, A.L. De Paoli, W. Bauer, W. Cassing and U. Mosel, Nucl. Phys. A475, 579 (1987)
4) A.L. De Paoli, K. Niita, W. Bauer, T.S. Biro, W. Cassing and U. Mosel, Nucl. Phys. A, submitted
5) C.Y. Wong, Phys. Rev. C25, 1460 (1982)
6) G.F. Bertsch, H. Kruse and S. Das Gupta, Phys. Rev. C29, 673 (1984)
7) J. Cugnon, T. Mizutani and J. Vandermeulen, Nucl. Phys. A352, 505 (1981)
8) B. Ter Haar and R. Malfliet, preprint KVI-651 (1987), submitted to Phys. Rev. C
9) G.F. Bertsch, J. Borisowicz and H. McManus, Nucl. Phys. A284, 399 (1977)
10) G.R. Satchler and W.G. Love, Phys. Rep. 55C, 183 (1979)
11) W. Bauer, Nucl. Phys. A471, 604 (1987)
12) K. Niita et al, Proc. of the Workshop on 'Physics of Intermediate and High Energy Heavy-Ion Reactions', Krakow, Poland, Sept. 28-30, 1987; to be published by World Scientific, Singapore
13) W. Bauer, W. Cassing, U. Mosel, M. Tohyama and R.Y. Cusson, Nucl. Phys. A456, 159 (1986)
14) C.M. Ko, G.F. Bertsch and J. Aichelin, Phys. Rev. C31, 2324 (1985)
15) H. Nifenecker, J.P. Bondorf, Nucl. Phys. A442, 478 (1985)
16) R. Heuer, B. Müller, H. Stöcker and W. Greiner, UFTP preprint 204/1987
17) B.J. Ver West and R.A. Arndt, Phys. Rev. C25, 1979 (1982)
18) J.A. Edgington and B. Rose, Nucl. Phys. A89, 523 (1966)
19) R. Bertholet, M. Kwato Njock, M. Maurel, E. Monnand, H. Nifenecker, P. Perrin, J.A. Pinston, F. Schussler, D. Barneoud, C. Guet and Y. Schutz, Nucl. Phys. A (1987), submitted
20) J.J. Gaardhoje, A.M. Bruce, J.D. Garrett, B. Herskind, D. Barneoud, M. Maurel, H. Nifenecker, J.A. Pinston, P. Perrin, C. Ristori, F. Schussler, A. Bracco and M. Pignanelli; Phys. Rev. Lett. 59, 1409 (1987)
21) C.M. Ko and J. Aichelin, Phys. Rev. Lett. 55, 2661 (1985)

SUBTHRESHOLD PION PRODUCTION*

Jack Miller
Lawrence Berkeley Laboratory
University of California
Berkeley, California 94720

I will begin with a very brief summary of some of the experimental and theoretical work with light projectiles, and this will serve as background for a discussion of some interesting results from our work at the Bevalac with heavy systems at beam energies near threshold.

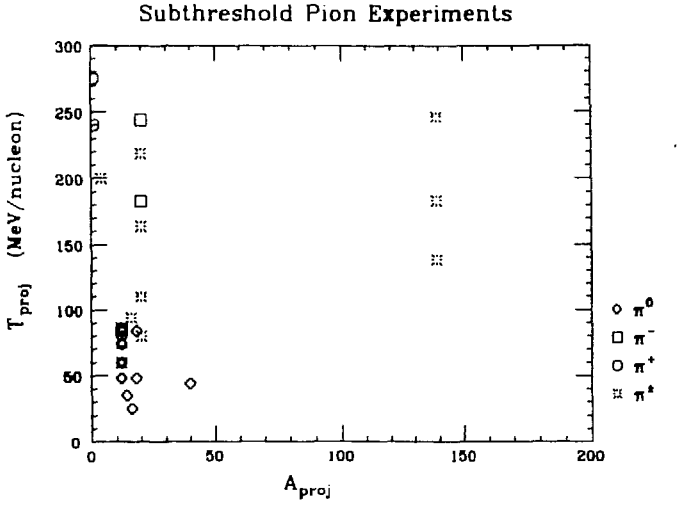

Figure 1.

Figure 1 summarizes the existing data on subthreshold pion production, according to projectile mass and energy per nucleon. (For a more extensive survey of the data, the reader is referred to two soon-to-be-published reports, Refs. 1 and 2. For additional discussions in these proceedings on the topic of subthreshold particle production, see the contributions of J. Carroll, U. Mosel and B. Schürmann.)

One of the things which makes subthreshold particle production in nucleus-nucleus collisions intriguing is that it requires the cooperation of more than two nucleons.† Probably the simplest example of this is the Fermi motion that nucleons in nuclei acquire as a consequence of being confined to a small volume in phase space. Subthreshold particle creation with the aid of Fermi momentum was predicted many years ago[3], and it is an interesting historical fact that the first pions created in the laboratory were subthreshold pions produced in 95 MeV/nucleon

*This work was supported by the Director, Office of Energy Research, Division of Nuclear Physics of the Office of High Energy and Nuclear Physics of the US Department of Energy under contracts DE-AC03-76SF00098 and DE-AS05-76ER04699 and the National Science Foundation under grant No. PHY83-12245.

†'Threshold' in this context refers to the threshold energy for particle creation in free nucleon-nucleon collisions. In nucleus-nucleus collisions, subthreshold means that the beam energy *per nucleon* is below threshold. For pions this energy is about 290 MeV/nucleon.

^{4}He +^{12}C collisions at the 184″ cyclotron[4,5]. This process is relatively well-understood, and one of the aims of subthreshold production experiments is to identify other collective effects.

Some possible signatures of collective effects are:

- Production below the 'absolute' threshold.
- Production in excess of predictions of nucleon–nucleon models.
- A change in the characteristic behavior of the pion spectra as the threshold is crossed.

I'll briefly discuss the first two cases, and devote most of my attention to the third, which is where the Bevalac data come into play.

Production below the absolute threshold. While Fermi motion makes the concept of an energy threshold in nucleus-nucleus collisions ambiguous, Bertsch has calculated in the framework of the first collision model[6] an absolute threshold value of 54 MeV, due to Pauli blocking of the final state phase space. Recent experiments at GANIL[7], and at MSU and ORNL[8] have reported non-negligible cross sections for π^0 production below this limit. These range from about 1 nb for 25 MeV/nucleon ^{16}O +^{27}Al to greater than 1μb for 44 MeV/nucleon ^{40}Ar +^{40}Ca.

Excess production. At somewhat higher energies, where binary (i.e. nucleon-nucleon) production can take place, single collision models severely underpredict the inclusive cross sections, especially when the shell model is used to calculate the initial state nucleon momenta.[8,9]

Models which incorporate collective effects do better.[8] The pion bremsstrahlung model of Vasak et al.[10,11,12] gives a good account of the 44 MeV/nucleon ^{40}Ar +^{40}Ca data and of the π^0 yield for 60–84 MeV/nucleon ^{12}C projectiles taken at the CERN SC[13], and two statistical models have been applied with some success over almost the entire range of subthreshold pion data. Bohrmann, Shyam and Knoll[9,14,15,16] have extended the Fermi statistical model[17], while Aichelin and Bertsch[18,19] and Prakash, Braun-Munzinger and Stachel[20], have made calculations based on the compound nucleus theory of Weisskopf[21].

The 'trans-threshold' region. (I define this to encompass beam energies between about 140 MeV/nucleon and threshold.) Near threshold one expects Fermi-boosted binary production to dominate, and the object is to go low enough in beam energy for other collective effects to become apparent above this incoherent background. Figure 2 shows the charged pion spectra at $\theta_{c.m.} \simeq 90°$ for three mass systems for a wide range of beam energies above and below threshold. All the spectra exhibit the well-known characteristics of inclusive pion measurements: exponential fall-off with pion energy, and slope parameters and yields monotonically decreasing with beam energy. Note that for the 246 MeV/nucleon La+La case, an intranuclear cascade simulation[22]—essentially a folding together of nucleon-nucleon collisions—reproduces the slope and *overestimates* the yield.

Figure 3 shows slope parameters extracted from exponential fits to the invariant cross section, $Ed^3\sigma/dp^3$,[‡] once again over a wide range in system mass and beam energy. There is little or no mass dependence. (This situation obtains also at beam energies down to 60 MeV/nucleon, after which the slope parameter becomes almost constant.[8]) So, at least at first glance, nothing unusual is going on.

[‡]Strictly speaking, the fits should be to the *variant* cross section, $d^3\sigma/dp^3$, but the difference is not significant in this case.

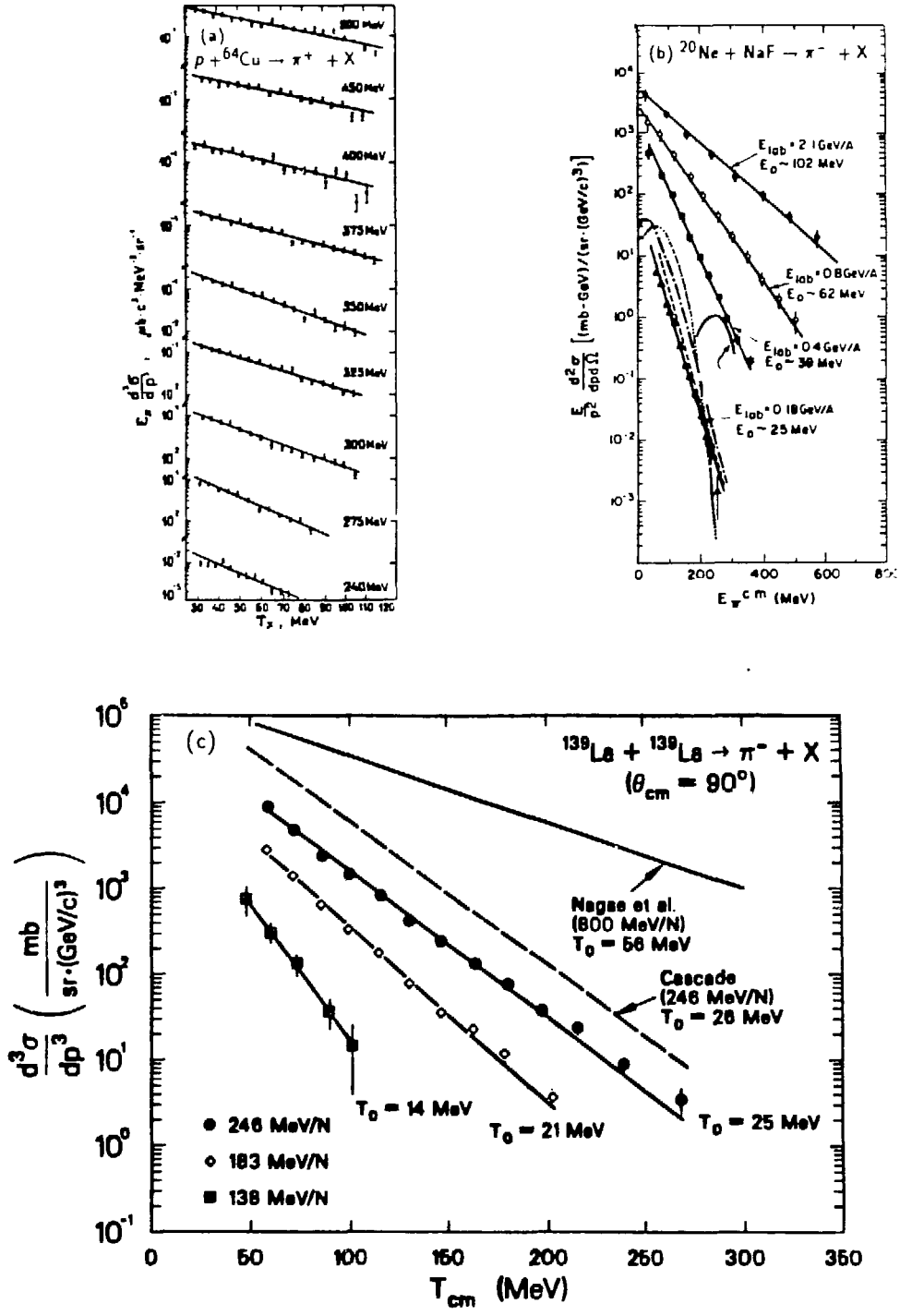

Figure 2. Inclusive cross section for charged pion production at $\theta_{c.m.} \simeq 90°$ for (a) $p + {}^{64}Cu \rightarrow \pi^+ + X$ (Ref. 23) (b) $^{20}Ne + NaF \rightarrow \pi^- + X$ (Refs. 24 and 25) (c) $^{139}La + {}^{139}La \rightarrow \pi^- + X$ (Refs. 26 and 27)

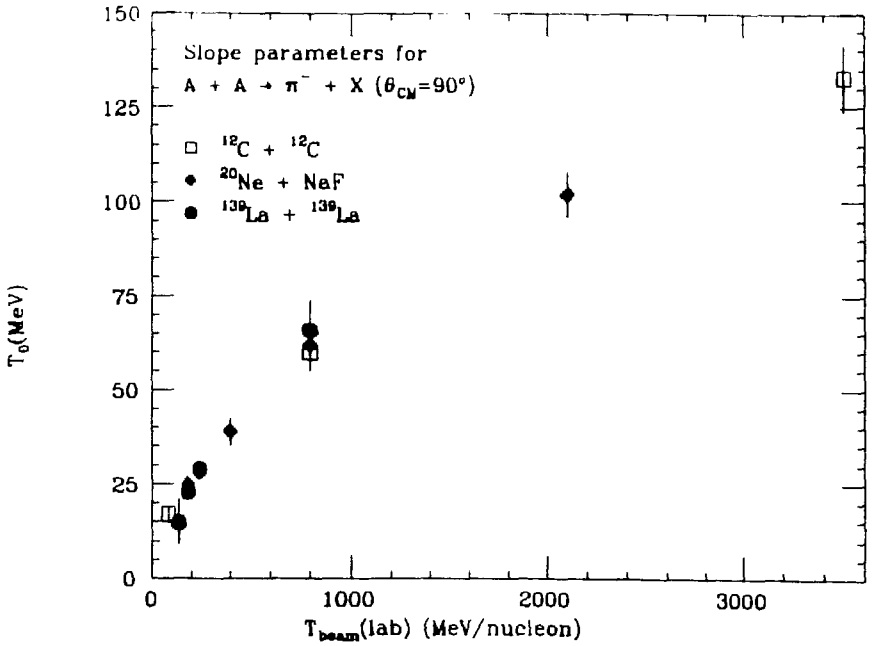

Figure 3. Slope parameter, T_0, for pion spectra at $\theta_{c.m.} = 90°$, plotted as a function of beam energy for a variety of targets and projectiles, at beam energies between 85 and 3500 MeV in the lab. T_0 is the negative inverse slope extracted from fitting the invariant cross section by a function of the form ae^{-T/T_0}. Data are from Refs. 24–29.

Mass dependence. We next consider the mass dependence of the differential yield, $d\sigma/d\Omega$, for π^- at $\theta_{c.m.} = 90°$ (Figure 4). Note that the yield has been scaled by $(A_{tgt} \cdot A_{proj})^{\frac{2}{3}}$, a form which has been found to hold for almost all of the subthreshold pion data from light systems, and we can see from the figure that it holds for both light and heavy systems above about 400 MeV/nucleon. Below threshold, however, this scaling breaks down badly. Figure 5 shows how badly. Here we limit consideration to the data for $^{20}Ne + NaF$ and $^{139}La + ^{139}La$, which were taken in several different experiments on the same spectrometer, and which have a relative normalization close to unity. The horizontal lines denote several possible scalings, including some which are weighted by neutron number. (In a collision model negative pions come predominantly from neutron-neutron collisions.) What is more important than the nature of the scaling is the fact that it varies so strongly with beam energy, below threshold. With one, possibly significant, exception, this sort of behavior has not previously been observed in the subthreshold data. The exception is in the data at 44 and 48 MeV/nucleon where the scaled cross section for π^0 from 44 MeV/nucleon $^{40}Ar + ^{40}Ca$ is three times that for 48 MeV/nucleon $^{12}C + ^{12}C$.[8]

At this point it's appropriate to note some of the other conclusions of our recent La+La experiment. From the associated charged particle multiplicities and the angular distributions we have constructed a picture of the typical subthreshold pion source as being at rest in the center of mass, and involving a large number of participants.[26] This is certainly consistent with the possibility of collective effects, but as Dr. Schürmann has pointed out in his contribution, the transition from an $A^{\frac{4}{3}}$ to an $A^{\frac{5}{3}}$ or A^2 dependence could also be characteristic of an increased

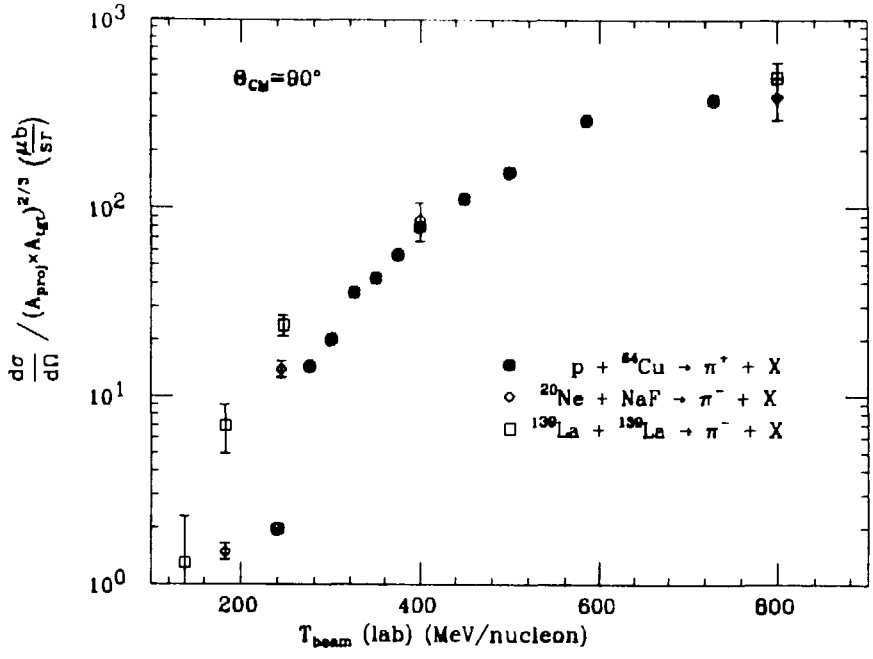

Figure 4.

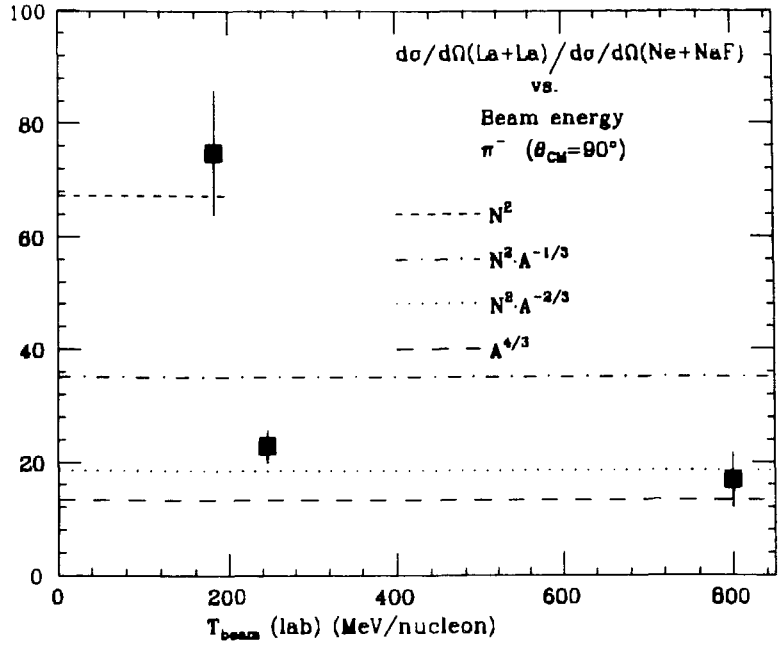

Figure 5.

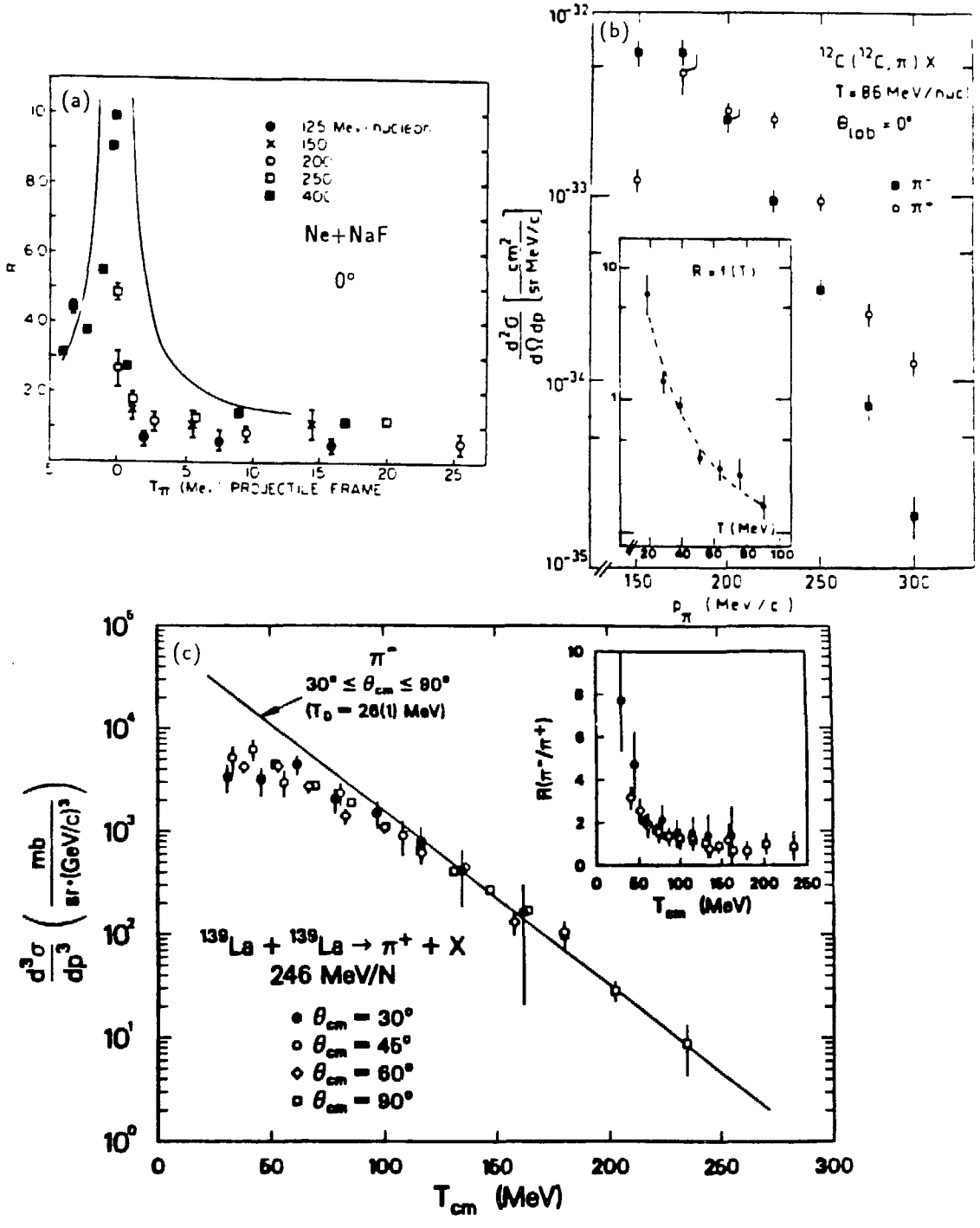

Figure 6. Charge dependence of subthreshold pion spectra from three systems:
(a) Ne+NaF at 0° (Ref. 33), (b) C+C at 0° (Ref. 34) and (c) La+La at $\theta_{c.m.} = 30° - 90°$ (Ref. 26). Note the apparent inconsistency between (a) and the inset in (b). (Both plots are in the projectile frame.) This has not yet been resolved.

incidence of multiple collisions, as might be expected in a central interaction of heavy nuclei

Charge dependence. Another interesting feature of the La+La data is the charge dependence of the pion cross sections (Figure 6). This has been previously observed in light systems at forward angles. The observation of strong charge dependence at rapidities well-separated from the beam and target probably reflects the much greater charge of the La-La system. A number of models have been put forth to account for this phenomenon. For example, Gyulassy and Kauffmann [30] and Bertsch [31] have explained some of the data in terms of Coulomb distortion. Recently, Bonasera and Bertsch [32] have combined Coulomb distortion with the compound nucleus model which has been successful in accounting for pion production at lower energies. The observed charge dependence may well turn out to be a convolution of effects acting at different stages of the pion production and emission process which, if it can be successfully unfolded, could give insight into the space-time structure of the interaction. To this end, it is probably best to study heavy, highly charged systems, where the charge dependence is strongest.

A complete understanding of the mass and charge dependence of subthreshold pion production will require additional data. Essentially, we want to fill in the gaps in Figure 1 by obtaining data for all three pion charge states for $A > 40$ at beam energies between 25 and 250 MeV/nucleon. In the near term, these experiments will continue to be done at the Bevalac. However, the low cross sections for subthreshold production make it desirable to have much higher beam intensities than presently available. Fortunately, we can look forward to these higher intensities at SIS-18 and (hopefully) at an upgraded Bevalac.

The data for pion production from La+La collisions at 138, 183 and 246 MeV/nucleon and from Ne+NaF collisions at 244 MeV/nucleon was taken at the Bevalac by an LBL/MSU/LSU/-Clermont-Ferrand collaboration. A full list of collaborators is given in Ref. 26. In particular, I'd like to acknowledge contributions to the data analysis by G. Claesson and G. Landaud, and many helpful discussions with W. Benenson, G. Roche and L.S. Schroeder. I'd also like to thank the members of the INS/LBL group for their collaboration in setting up the detector system, and for allowing us to use some of their data prior to publication.

References

[1] P. Braun-Munzinger and J. Stachel. *Ann. Rev. Nucl. Part. Sci.* **37**, (1987).

[2] J. Miller. *Subthreshold Pion Production in the Reaction* ^{139}La+^{139}La $\rightarrow \pi^{\pm}$+X. Technical Report LBL-24275, Lawrence Berkeley Laboratory, 1988.

[3] W.G. McMillan and E. Teller. *Phys. Rev.* **72**, 1 (1947).

[4] Eugene Gardner and C.M.G. Lattes. *Science* **107**, 270 (1948).

[5] John Burfening, Eugene Gardner and C.M.G. Lattes. *Phys. Rev.* **75**, 382 (1949).

[6] G.F. Bertsch. *Phys. Rev. C* **15**, 713 (1977).

[7] H. Heckwolf et al. *Z. Phys.* **A315**, 243 (1984).

[8] J. Stachel et al. *Phys. Rev.* **C33**, 1420 (1986).

[9] R. Shyam and J. Knoll. *Phys. Lett.* **136B**, 221 (1984).

[10] D. Vasak, B. Müller and W. Greiner. *Phys. Scr.* **22**, 25 (1980).

[11] D. Vasak, H. Stöcker, B. Müller and W. Greiner. *Phys. Lett.* **93B**, 243 (1980).

[12] D. Vasak, et al. *Nucl. Phys.* **A428**, 291 (1984).

[13] H. Noll et al. *Phys. Rev. Lett.* **52**, 1284 (1984).

[14] Jörn Knoll. *Phys. Rev.* **C20**, 773 (1979).

[15] Steffen Bohrmann and Jörn Knoll. *Nucl. Phys.* **A356**, 498 (1981).

[16] R. Shyam and J. Knoll. *Nucl. Phys.* **A426**, 606 (1984).

[17] E. Fermi. *Prog. Theor. Phys.* **5**, 570 (1950).

[18] J. Aichelin and G. Bertsch. *Phys. Lett.* **138B**, 350 (1984).

[19] J. Aichelin. *Phys. Rev. Lett.* **52**, 2340 (1984).

[20] M. Prakash, P. Braun-Munzinger and J. Stachel. *Phys. Rev.* **C33**, 937 (1986).

[21] V. Weisskopf. *Phys. Rev.* **52**, 295 (1937).

[22] J. Cugnon. *Nucl. Phys.* **A387**, 191 (1982).

[23] V.A. Krasnov et al. *Phys. Lett.* **108B**, 11 (1982).

[24] S. Nagamiya et al. *Phys. Rev.* **C24**, 971 (1981).

[25] S. Nagamiya et al. *Phys. Rev. Lett.* **48**, 1780 (1982).

[26] J. Miller et al. *Phys. Rev. Lett.* **58**, 2408 (1987) and **59**, 519 (1987).

[27] S. Hayashi. *Production of Pions and Light Fragments in 0.8 GeV/A La+La Collisions.* Master's thesis, University of Tokyo, 1986.

[28] V. Bernard et. al. *Nucl. Phys.* **A423**, 511 (1984).

[29] L.A. Didenko et al. Technical Report El-84-354, JINR, 1984.

[30] M. Gyulassy and S.K. Kauffmann. *Nucl. Phys.* **A362**, 403 (1981).

[31] G. Bertsch. *Nature* **283**, 280 (1980).

[32] A. Bonasera and G.F. Bertsch. Technical Report MSUCL-600, Michigan State University Cyclotron Laboratory, April 1987.

[33] W. Benenson et al. *Phys. Rev. Lett.* **43**, 683 (1979) and **44**, 54 (1980).

[34] E. Chiavassa et. al. *Nucl. Phys.* **A422**, 621 (1984).

Theory – Multifragmentation

MULTIFRAGMENTATION OF HEAVY NUCLEI — A MICROSCOPIC DESCRIPTION

Jörg Aichelin

Institut für Theoretische Physik, Universität Heidelberg
D-6900 Heidelberg, Germany
and
A. Rosenhauer, G. Peilert and H. Stöcker
Institut für Theoretische Physik, Goethe Universität
D-6000 Frankfurt am Main, Germany

We improve our microscopic approach to simulate high energy heavy ion reactions to an extent which allows detailed comparison with experimental data. We find very good agreement with experiments for the mass yield as well as for the momentum distribution. A detailed analysis shows that the system does not reach a global thermal equilibrium in the course of the reaction. This especially rules out the occurrence of a liquid gas phase transition. Large mass fragments $A \geq 40$ are evaporation residues whereas the low mass clusters measure the violence of the reaction depending strongly on the impact parameter.

Four years ago the first numerical simulations of medium and high energy heavy ion reactions were advanced[1,2]. These so called Boltzmann Uehling Uhlenbeck (BUU) or Vlasov Uehling Uhlenbeck (VUU) calculations were borne out from the high energy cascade calculations but incorporated in addition a self-consistent mean field and Pauli blocking — essential ingredients to describe clusters and medium energy reaction. In these calculations nuclei are described as a N_{target} resp. $N_{projectile}$ systems in which the single nucleons are represented as pointlike particles which move under the influence of a mean field. The theory can be viewed as a classical N body theory where the quantum corrections are only of second order in the N body correlations. The numerical method applied to solve these equations, however, requires an averaging over many simulations. By this ensemble averaging, fluctuations and correlations are washed out, and the predictive power of the model is reduced to one body observables. As a consequence one of the most exciting problems, namely how why and a nucleus breaks up in several medium mass fragments, cannot be addressed.

Recently we advanced a new microscopic model dubbed quantum molecular dynamics[3,4] (QMD). In this approach the nucleons are represented by Gaussian wave packets which interact by mutual 2 and 3 body forces. This model simulates heavy ion reactions on a event by event basis and as a consequence preserves correlations and fluctuations. Therefore, this model allows one to address the formation of clusters. The theory is a quantal theory in the sense that the nucleons are spread out in coordinate and momentum space with a Gaussian distribution. The width of the distribution, however, is kept constant. Collisions, which respect the Pauli principle, are incorporated in a similar way as in BUU or VUU. For the details of the calculations we refer to Refs. 3&4. Here we want to demonstrate that this theory reproduces the experimental results and to see which conclusions concerning the underlying process we can draw.

There is a wealth of data on the inclusive mass yield. Unfortunately it has been demonstrated that the mass yield curve is almost completely insensitive

to the underlying reaction mechanism. Data with more detailed information, however, are rather scarce. We are only aware of 2 experiments: Warwick et al.[5] measured the tripple differential cross section $d^3\sigma/dEd\Omega dZ$ of medium mass fragments, Waddington and Freier[6] have recorded the exclusive mass yield for the reaction Au + Emulsion at 1 GeV/N. The results of this experiment whose primary goal was the search for anomalons, were recently published[7] as far as they are of interest to investigate the multifragmentation of the Au nucleus.

Here we present simulations of the reaction 1050 MeV/N Ne + Au . Warwick et al.[5] measured this projectile target combination and therefore we can compare the numerical and experimental results.

Fig.1 displays the total mass yield compared with experimental data. We see the mass yield falling off with a power law $A^{-\tau}$ which corresponds to a straight line in our double logarithmic plot. For the constant τ we obtained $\tau = 2.44$. The form of the mass yield as well as the value of τ, being in the range $2 < \tau < 3$, is consistent with the assumption that the mass yield is a signal of a liquid gas phase transition[1] . The calculated slope of the mass yield curve is close to the slope of the experimental data, but we underpredict the data by roughly a factor of two. One should phrase this, however, differently: Our clusters emit 1 or two nucleons more than real nuclei.

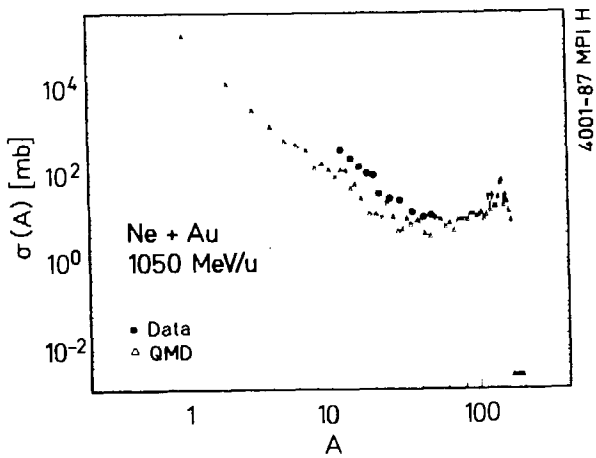

Fig.1: The inclusive mass yield compared with data[5] .

This is most probably a consequence of the instability of highly excited clusters. Whereas the cluster are stable in their ground state, the higher the excitation the less correct is our description. Also there are uncertainties how to relate the measured charges to a mass yield[5] . The mass yield has a minimum around A=50 and increases again for higher masses. In this particular experiment the mass yield of heavy fragments was not measured. Similar experiments show a U shape form of the mass yield which has a minimum around $A = A_{target}/4$. This form we reproduce and therefore we are confident that our approach also describes the large mass region properly.

Having us convinced that we reproduce experiment reasonable well we can proceed and take advantage of the fact that in a simulation much more information is accessible than in an experiment. One additional information directly

available is the impact parameter dependence of the observed quantities.

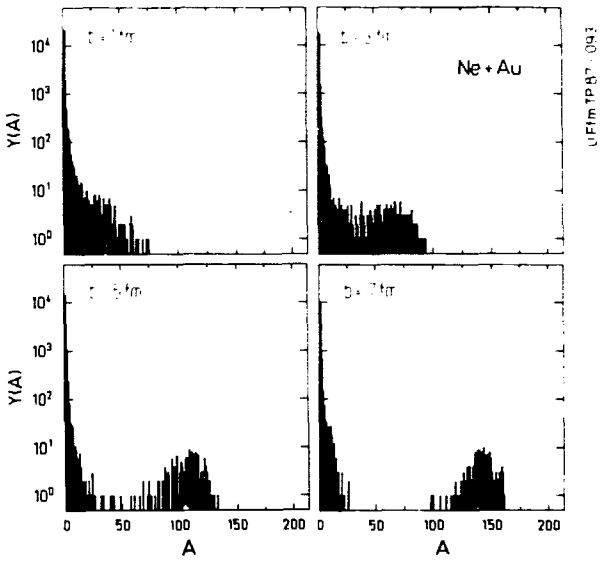

Fig.2: The mass yield for 4 different impact parameters b= 1, 3, 5, 7 fm for the reaction 1050 MeV/n Ne+Au

In Fig.2 we display the mass yield distribution at different impact parameters. We see a clear impact parameter dependence. At the lowest impact parameter no heavy target remnant survives. The gold nucleus is broken up in many pieces, none of them heavier than A = 80. The mass yield is well described by a power law. The most peripheral reactions (b= 7 fm) are not violent enough to destroy the target completely. Here less than half of the projectile volume lies in the geometrical shadow of the target. We observe a target remnant at around A=140. At the low mass side the mass yield falls of very steeply. Most of these low mass clusters are projectile remnants. There are no clusters with masses $30 \leq A \leq 90$. The intermediate impact parameters show a gradual transition from peripheral to central collisions. The mass of the heavy target remnants decreases but still there is a gap at A = 40. Also the slope of the low mass clusters steepens.

From these observations we can draw immediately several conclusions:

a) The power law form of the inclusive mass yield is accidental. In does not reflect a phase transition. A phase transition would require a mass yield independent of the impact parameter since the slope parameter τ depends on the interaction, not on the excitation energy and has therefore to be independent of the impact parameter. Also a power law form of the mass yield is only expected at the critical temperature. Below or above one expects an exponential form. Consequently, the form of the mass yield is merely a parametrization of the sum of different forms of mass yields at different impact parameters and no sign of a phase transition.

b) The transition from the power law form to a flat and ultimately increasing mass yield at masses around 40 reflects the different origin of the clusters. Fragments larger than 40 are target remnants. They are produced when the collision is not violent enough to to break up the target completely. Their creation is controlled by the impact parameter. Masses around 40 are produced in semi central

collisions by deep spallation. The ultimate increase follows from the increasing probability of peripheral reactions.

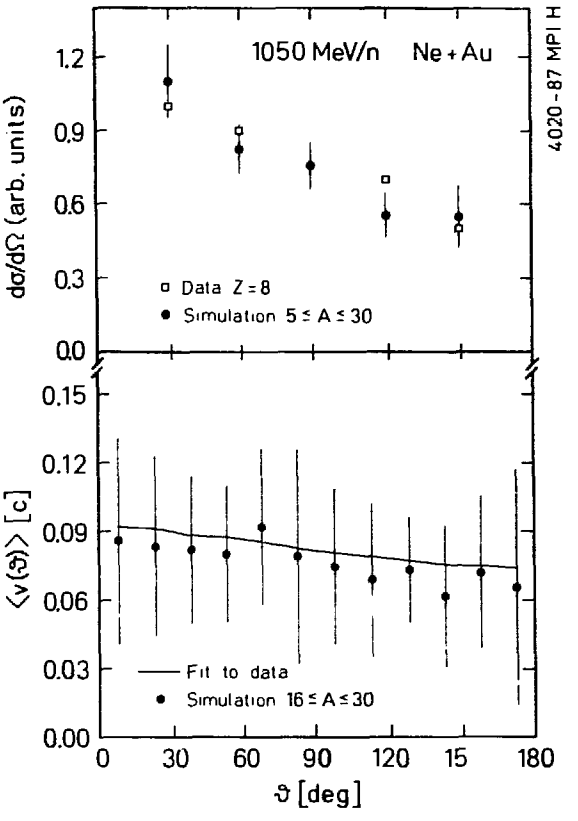

Fig.3: $d\sigma/d\Omega$ and the average velocity $v(\theta_{lab})$ for medium mass clusters produced in the reaction 1050 MeV/n Ne+Au

In principle our simulation can predict the tripple dfferential cross section $d^3\sigma/dEd\Omega dA$. However this would require several thousend hours of computing time on the fastest present computer.Therefore, we have to restrict ourselves to mean values. Here we concentrate on $d\sigma/d\Omega$ and the mean value of $v(\theta_{lab})$ of the clusters. In Fig.3 we see a quite anisotropic behaviour. The data as well as the theory show a forward enhancement. The average velocity is also quite well reproduced in our approach, as one can see from Fig 3. We see that the fragments have roughly half the center of mass velocity. The average velocity in forward direction is slightly higher theoretically as well as experimentally.

REFERENCES

1. J.Aichelin and G.Bertsch, Phys. Rev **C31** (1985) 1730:
   This paper presents an improved version of the code which was previously used to calculate the equation of state dependence of the pion cross section : G. Bertsch, S. DasGupta and H. Kruse, Phys. Rev. **C29** (1984) 673
2. H. Kruse, B.V. Jacak and H. Stöcker, Phys. Rev. Lett **54** (1985) 289
3. J. Aichelin and H. Stöcker,
   Proceedings of the International Workshop on Gross Properties of Nuclei and Nuclear Structure , Hirschegg (1986);
   Phys. Lett. **176B** (1986) 14
4. J.Aichelin, A.Rosenhauer, G.Peilert, H. Stöcker, and W. Greiner Phys. Rev. Lett. **58** (1987) 1926
5. A. I. Warwick, H. H. Wiemann, H. H. Gutbrod, M. R.Maier J. Peter, H. G. Ritter, H. Stelzer, and F. Weik, Phys. Rev. **C27** (1983) 1083
6. C. J. Waddington and P. S. Freier Phys. Rev. **C31** (1985) 888
7. J. Aichelin and X. Campi Phys. Rev. **C34** (1986) 1643
8. M. E. Fisher, Physics 3 (1967) 255

STATISTICAL TREATMENT OF NUCLEAR MULTIFRAGMENTATION

Jørgen Randrup

Nuclear Science Division, Lawrence Berkeley Laboratory,
University of California, Berkeley, California 94720

After a brief survey of statistical multifragmentation models, a unified formulation of statistical simulation incorporating interfragment forces is given. Within the hard-sphere idealization, commonly used effective-volume and Coulomb approximations are examined, and improved one-body approximations are presented. Finally, the treatment of highly excited fragments embedded in a nucleon vapor is addressed.

1. INTRODUCTION

It is of general physical interest to study hot nuclear matter at subsaturation densities. Within the general context of the "Equation of State" of matter at high energy densities, it is important to understand the phase structure of the system, its composition in terms of fragments species, and the dependence of the various thermodynamic observables on the characterizing parameters. In addition to being of direct relevance to astrophysics (*e.g.* supernova processes), this topic is also of great relevance to energetic nuclear collisions: a good understanding of the nuclear equation of state over a wide range of energies and densities is a prerequisite for making reliable predictions about the outcome of nuclear collisions and, conversely, nuclear collisions present a unique tool for probing the properties of nuclear matter away from its normal state. Moreover, a statistical calculation can provide reference results for testing the equilibrium limit of dynamical models. The formal connection between the static statistical properties of matter and the outcome of a nuclear collision is via the transition-state approximation: it is assumed that the multifragmentation degrees of freedom are effectively determined at some "freeze-out" scenario (in analogy with, for example, the transition-state treatment of nuclear fission).

The theoretical interest in nuclear multifragmentation has increased in concert with the substantial improvements in accelerator capability through the past decade. The emergence of the field was originally stimulated by the advent of the Bevalac and it has gained further momentum in recent years through the construction and planning of several modern intermediate-energy heavy-ion accelerators. Most powerful of these is the SIS-18/ESR under construction at GSI. When completed, this facility will provide beams of nuclei over the entire mass range with energies up to $\approx$1 GeV/N and with intensities exceeding those of the present Bevalac by 2-3 orders of magnitude; it will be coupled to a cooled storage ring with which a host of novel physics investigations can be made. It is noteworthy that most of the facility developments have occurred outside of the United States, and it appears that a drastic modernization of the US accelerator capabilities would be required for this country to maintain a significant role in the expanding field of medium-energy nuclear collisions.

2. BRIEF SURVEY OF STATISTICAL MULTIFRAGMENTATION MODELS

Following ideas used to describe multiparticle production in high-energy nucleon-nucleon [1] and nucleus-nucleus [2] collisions, the first formulation of a model for nuclear multifragmentation processes at intermediate energies (where there is abundant production of composite fragments) was made within the framework of a grand canonical model.[3] In that model, an assembly of non-interacting, excitable nuclear fragments was considered and the general expressions for the one-fragment observables were derived. Only particle-stable nuclear levels were included for simplicity, although it is clear that there is abundant production of unbound fragments that subsequently deexcite on a time scale long compared with that characterizing the primary disassembly.

The inclusion of such unstable nuclei, and their sequential decay by evaporation of light particles, was made subsequently in the form of the Explosion-Evaporation Model.[4] Somewhat later, the so-called Quantum Statistical Model was implemented by Stöcker [5]. The term 'quantum' refers to the fact that quantum-statistical weight factors (Fermi-Dirac for odd A and Bose-Einstein for even A) are used for the translational motion of the fragments, rather than classical (Maxwell-Boltzmann) weights. In most cases of practical interest this difference is immaterial.[6] Another difference is that in the QSM only known excited levels have been included, whereas the EEM attempts to include all relevant excited levels by extrapolating to higher-lying levels via a modulated level-density formula; this difference may be quantitatively significant. A recent thorough comparison between the EEM and the QSM has verified that the two models give similar results when the same set of excited states are employed and that, furthermore, in many cases of practical interest the subsequent "evaporation" processes to a large extent wash out the differences in primary yield ratios.[6]

The development of powerful multifragment detection systems has demanded more detailed models and established the need for addressing complete fragmentation events. For this task an approximate microcanonical procedure was developed and tested [7]; it is based on the recursive use of the grand canonical model for an ever smaller source. This convenient method was then exploited to formulate a microcanonical model for generating complete multifragment events in nuclear collisions at medium energies.[8] In conjunction with this work, a computer code, named *FREESCO*, was released;[9] it has been employed in numerous theoretical and experimental studies.

Nuclear multifragmentation has also been studied by other groups. Most relevant to the present discussion is the work of Gross *et al.* and Bondorf *et al.*: Gross *et al.* started by addressing the deexcitation process following a high-energy proton-nucleus reaction. The focus was on the fragment mass distribution and it was found that the interfragment Coulomb repulsion is instrumental in enhancing the production of heavy fragments (leading to a U-shaped yield curve), at the relatively low excitations involved.[10] After these grand-canonical studies, Monte-Carlo simulations were made within the canonical approximation.[11] Most recently, an approximate microcanonical simulation model has been developed.[12] It differs from [14] in many important respects, both as regards the physical assumptions and in the numerical implementation. For example, metastable fragments are not included.

Bondorf *et al.* have formulated a model for statistical multifragmentation of nuclei.[13]

Their focus is on the mass partition and a canonical approach is taken. The model does not incorporate any fragment interactions, although the Coulomb energy is included in the Wigner-Seitz approximation. Furthermore, there is no suppression of the level density for highly excited fragments. The numerical sampling procedure chooses evenly between all possible mass partitions and subsequently performs a weighted average of the partition-dependent observables, employing the canonical weights for the different partitions selected. Although this method is superior in certain situations, in particular when the focus is on the mass distribution in relatively small systems, it is generally less efficient than sampling the partitions according to their (strongly varying) weights, as is done in [14].

3. UNIFIED FORMULATION FOR INTERACTING FRAGMENTS

The work covered in this section was carried out in collaboration with Steve Koonin and has been reported elsewhere.[14]

Because of its link to nuclear collision dynamics, the study of subsaturation matter is often performed in the guise of multifragmentation, so that one considers an assembly of interacting, excitable nuclear fragments within a finite ("freeze-out") volume Ω; the properties of an infinite system can be found by imposing periodic boundary conditions. In the microcanonical approximation, the fundamental statistical hypothesis is that all multifragment states consistent with specified values of the total nucleon number A and energy E are equally probable. The properties of the system can then be expressed in terms of the density of states,

$$\rho_{\text{microcan}}(\Omega, A, E) = \sum_F \delta(A_F - A)\delta(E_F - E) \; . \tag{1}$$

Here $A_F = \sum_n A_n$ is the number of nucleons in the fragmentation F and E_F is its energy. The microcanonical formulation may be compared with the canonical or grand canonical approaches [3,4], where the density of states (1) is replaced by the partition functions

$$Z_{\text{canonical}}(\Omega, A, \tau) = \sum_F \delta(A_F - A)\mathrm{e}^{-E_F/\tau} \; , \tag{2}$$

$$Z_{\text{grand can}}(\Omega, \mu, \tau) = \sum_F \mathrm{e}^{(\mu A_F - E_F)/\tau} \; . \tag{3}$$

In the latter, the chemical potential μ and the temperature τ are specified and $\bar{E}$ and $\bar{A}$ follow from the appropriate derivatives of Z. While the two formulations are equivalent for large (thermodynamic) systems, there may well be differences between the two approaches for the finite systems formed in heavy-ion collisions.

For non-interacting fragments, the canonical approximation and, even more so, the grand canonical approximation lead to very simple expressions for one-body observables and an essentially analytical treatment is feasible. However, an analytical treatment is impractical

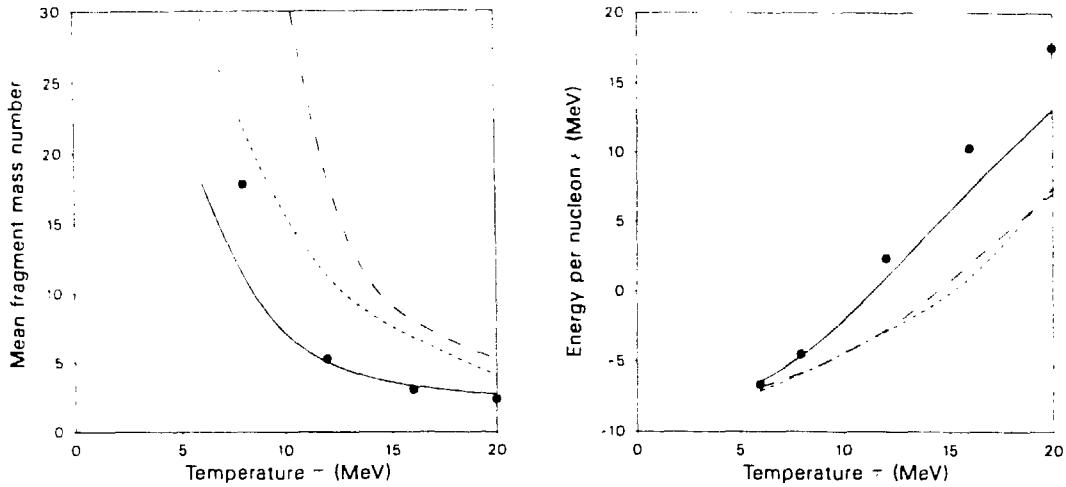

FIGURE 1: The mean fragment mass number $\bar{A}$ (left) and the mean energy per nucleon ϵ (right), as functions of the temperature τ specified in a canonical treatment of a source with $A = 100$ nucleons at a mean density of ρ=0.08 fm^{-3}. The solid curve shows the results for non-interacting fragments, using the adopted standard value τ_0=12 MeV, while the short-dashed curve corresponds to surrounding each fragment with a spherical hard repulsive potential, and the long-dashed curve arises when the mutual Coulomb repulsion between fragments are also included. The solid dots indicate the results when this latter system is expanded to ρ=0.04 fm^{-3}. (Taken from ref. [14].)

when the fragments interact and there is then a need for a more powerful formulation. Therefore, we have developed a microcanonical model.[14] In our formulation the three hierarchies of approximation described above can be given a unified treatment. Indeed, the respective statistical weights of a given multifragment configuration $C = \{A_n, \epsilon_N, \mathbf{r}_n, n = 1, ..., N_C\}$ are given by the following expressions:

$$W_{\rm microcan}(C) = \frac{1}{\Gamma(\frac{3}{2}N)} \prod_{n=1}^{N} \left[\Omega \left(\frac{mA_n}{2\pi\hbar^2} \right)^{\frac{3}{2}} \rho_n(\epsilon_n) \right] \delta(\sum_{n=1}^{N} A_n - A)\ K^{\frac{3}{2}N-1} , \qquad (4)$$

$$W_{\rm canonical}(C) = \prod_{n=1}^{N} \left[\Omega \left(\frac{mA_n\tau}{2\pi\hbar^2} \right)^{\frac{3}{2}} e^{B_n/\tau} \rho_n(\epsilon_n) e^{-\epsilon_n/\tau} \right] \delta \left(\sum_{n=1}^{N} A_n - A \right) e^{-V/\tau} , \qquad (5)$$

$$W_{\rm grand\ can}(C) = \prod_{n=1}^{N} \left[\Omega \left(\frac{mA_n\tau}{2\pi\hbar^2} \right)^{\frac{3}{2}} e^{B_n/\tau} e^{\mu A_n/\tau} \rho_n(\epsilon_n) e^{-\epsilon_n/\tau} \right] e^{-V/\tau} . \qquad (6)$$

In (4) the quantity

$$K = E - \sum_{n=1}^{N} [-B_n + \epsilon_n] - \frac{1}{2} \sum_{nn'} V_{nn'} \qquad (7)$$

is the total kinetic energy of the N fragments (B_n is the binding energy of fragment n and ϵ_n is its excitation energy). The last term in K represents the potential energy of the configuration arising from pairwise interactions between the fragments, $V = \sum_{n<n'} V_{nn'}$.

Given the appropriate statistical weights, a suitable statistical sampling procedure (*e.g.* the Metropolis method [15]) can then be employed to produce a sample of multifragment configurations, and observables can then be evaluated as ensemble averages. The significance of the interfragment forces is illustrated in figure 1.

4. THE NUCLEAR INTERACTION

The work summarized in this section was carried out with Kim Sneppen and has been reported elsewhere.[16]

The most important feature of the nuclear component in the interfragment potential arises from the high nuclear incompressibility which acts to prevent fragments from overlapping. To a rough approximation this effect can be taken into account by considering the nuclear fragments as hard spheres. The qualitative importance of this feature is illustrated in figure 1. Although relatively simple, the hard-sphere approximation is still quite demanding in terms of computation, since it requires knowledge of all the relative fragment positions. Most models developed so far do not contain this degree of detail and so it has been common to adopt some form of one-body approximation.

In intuitive terms, the presence of the other fragments limits the volume available for a given fragment. It is therefore natural to attempt to approximate the mutual fragment repulsion in terms of a reduced "effective" volume $\Omega_{\rm eff}$, within which the fragments can be considered as independent. We have examined such approximations in order to ascertain their quality and in the hope of devising more accurate approximations.

For a given mass partition $\alpha = \{A_1, ..., A_N\}$, it is convenient to define $\kappa(\alpha)$ by

$$\kappa(\alpha)^N = \prod_{n=1}^{N} \left[\int \frac{\mathrm{d}\mathbf{r}_n}{\Omega} \right] \mathrm{e}^{-V/\tau} \ . \tag{8}$$

Then, the canonical weight (5) of a particular mass partition α is equal to that associated with noninteracting fragments confined within the smaller *effective* volume $\Omega_\alpha^{\rm eff} = \kappa(\alpha)\Omega$. When the fragments are hard spheres, the interaction potential V vanishes if none of the fragments overlap and is infinite otherwise, so κ_α^N is then simply the number of allowed (*i.e.* non-overlapping) positionings divided by the total number of positionings of the N fragments. In order to achieve a simple approximation, one wishes to employ a common effective volume, $\Omega_{\rm eff} = \kappa_{\rm eff}\Omega$, for all the different mass partitions α. A number of effective-volume approximations have been devised and employed in studies of nuclear disassembly. In the simplest one the effective volume is taken as the total volume minus the volume occupied by all the fragments combined, $\Omega_{\rm eff} = \Omega - \Omega_0$, where $\Omega_0 = \sum_n \Omega_n = A/\rho_0$ is the volume of the N hard spheres. This approximation has been employed in particular by Kapusta and

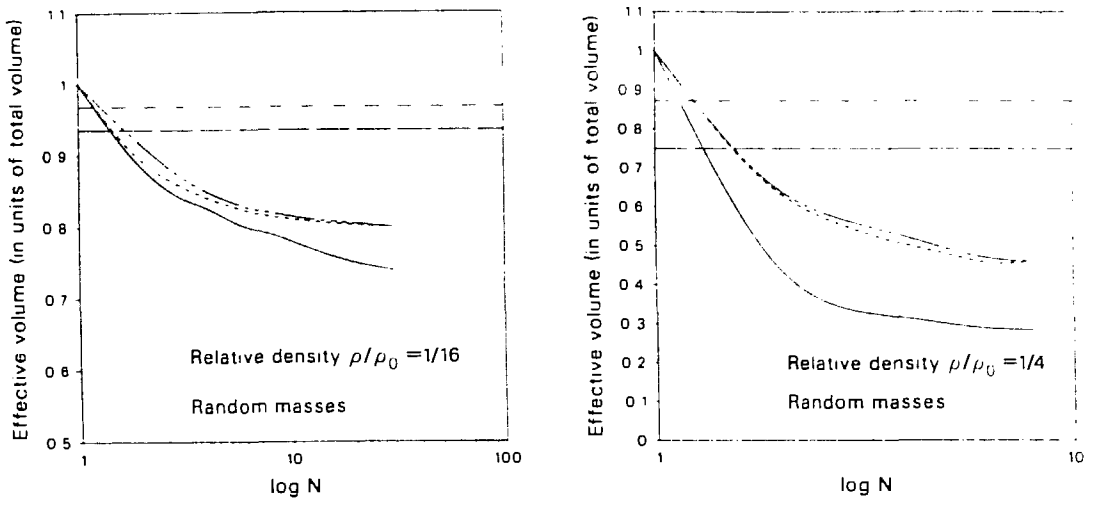

FIGURE 2: The effective κ-values as functions of the fragment multiplicity N, in either a dilute system ($\rho = \rho_0/16$) or a dense one ($\rho = \rho_0/2$). The fragments are sharp spheres with a random mass. The solid curve is the "exact" value $\kappa_{\rm eff}^N$. Also shown are κ_K (— —) and κ_{FR} (– –), and the Virial approximation $\kappa_{\rm V}$ (- - -) and its one-body approximation $\bar{\kappa_{\rm V}}$ (— - - -).

coworkers.[17] It follows that $\kappa_{\rm K} = 1 - \Omega_0/\Omega = 1 - \rho/\rho_0$. A more refined approach was taken by Fai and Randrup,[4] based on the recognition that the (anti)correlated positioning of the N fragments can be viewed as a sequential process, so that progressively less volume is available as the fragments are placed. These considerations led to $\kappa_{\rm FR} = (1/e)(1 - \rho/\rho_0)^{1-\rho_0/\rho}$.

These two approximations depend only on the relative density, ρ/ρ_0, and thus employ the same value of κ for all multiplicities N. Moreover, the considerations employed do not take account of the fact that the volume blocked by a given fragment exceeds its own volume by a layer of thickness equal to the radius the next fragment placed. Therefore such approximations are expected to typically underestimate the effect of blocking, and hence to overestimate the value of κ. This feature is most significant effect for dilute systems, for which the average excluded volume is typically underestimated by a factor of four or eight, respectively.

We have developed a more reliable approximation, based on the assumption independent pairwise correlations between the fragments. We denote it the Virial approximation, because of the similarity with the Virial treatment of interacting particles. For a given mass partition α, each fragment pair ij contributes a factor $P_{ij} = \exp(-\omega_{ij})$ to $\kappa_{\rm V}(\alpha)^N$. The exponent is the relative amount of volume that one fragment excludes from the other, $\omega_{ij} = (4\pi/3)(R_i + R_j)^3/\Omega$. The Virial approximation is amenable to a one-body treatment, leading to $\bar{\kappa_{\rm V}}$. Writing $\bar{\kappa_{\rm V}}^N = \prod_i \bar{\kappa_i}$, we find $\ln \bar{\kappa_i}(\alpha) \approx -(\sum_A \bar{\nu_A}\omega_{iA} - \omega_{ii})/2$, where $\bar{\nu_A}$ is the ensemble mean multiplicity of fragments with mass number A. This one-body approximation yields a κ-value for any given mass partition α, provided that the one-fragment distribution is known for the system. An overall effective value for the entire system can then be obtained by averaging over the mass partitions α.

An impression of the quality of the various approximations can be gained by considering

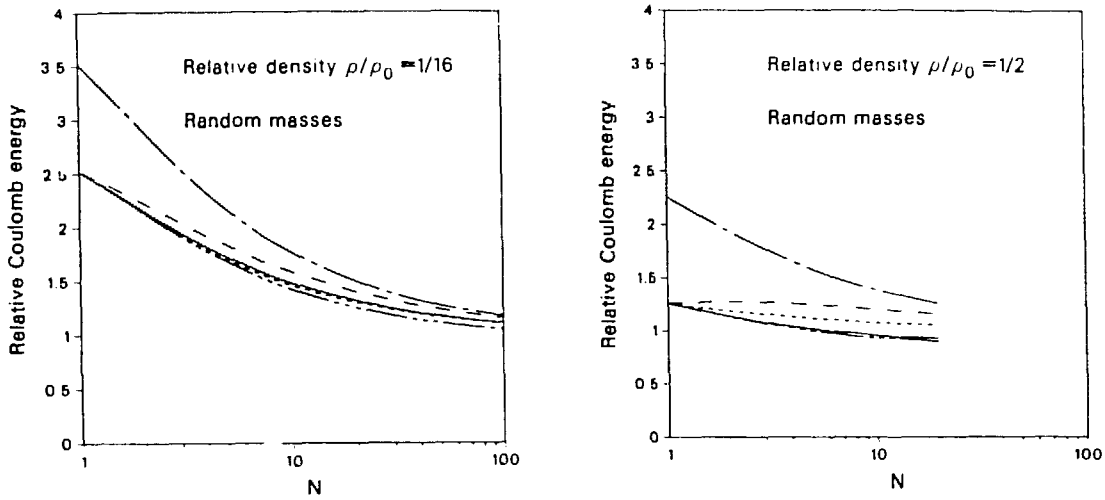

FIGURE 3: This figure shows the Coulomb energy of N uniformly charged spheres of random size. The solid curve is the exact result. Also shown are the mean-field approximation (— -), the refined mean-field approximation (– –), the Wigner-Seitz approximation (- - -), and our improved one-body approximation (— - - -).

idealized systems consisting of N uncharged hard spheres. Figure 2 displays typical results. It is seen that the simple effective-volume approximations are very crude, whereas the Virial approximation is rather good. Studies with more realistic scenarios have verified that this latter approximation is generally quantitatively superior and does in fact lead to reasonably accurate results.[16]

5. THE COULOMB ENERGY

The work summarized in this section was carried out with Michael Robinson and has been reported elsewhere.[16]

The calculation of the exact Coulomb energy of N non-overlapping uniformly charged spherical fragments requires the knowledge of all the fragment positions $\mathbf{r}_n$ and the evaluation of a double sum in the fragments. So it is desirable to approximate the electrostatic energy in a manner that only involves a single sum over the fragments and makes no reference to their specific positions.

The simplest such approximation, the *mean-field approximation*, replaces the interaction of a given fragment with the residual fragments by its interaction with the electrostatic field arising if the charge Z of the entire multifragment system were distributed uniformly throughout the confining volume Ω. The mean-field approximation was first formulated for nuclear disassembly in [3] and has been employed in most of the subsequent work along that line.

It was first noted by Gross [10] that the above mean-field approximation is relatively inaccurate for configurations having only a few fragments, because the mean field ϕ is calculated on the basis of *all* the charge, rather than only the charge associated with the residual $N-1$

fragments. Therefore, we shall also consider the *refined mean-field approximation*, in which this shortcoming is remedied by using only the residual charge $Z - Z_n$ when calculating the mean field. The incorporation of the last term leads to a substantial lowering of the Coulomb energy of configurations with a low fragment multiplicity. This effect has been discussed in detail by Gross.[10]

A commonly employed approximation in condensed-matter problems was introduced in 1934 by Wigner and Seitz.[18] It is based on the fact that the Coulomb energy can be considered as composed of two terms, one associated with a primordial uniform charge distribution and another associated with the condensation of the individual fragments. This redistribution process is considered as the shrinking of a uniform sphere from an original radius of R_n^0 to the actual fragment radius R_n. Although the Wigner-Seitz approximation is formally very similar to the refined mean-field approximation, the Wigner-Seitz energy is always lower.

It is instructive to consider the Coulomb energy of N spheres with equal or random masses. Typical results are shown in figure 3.

We have sought to develop simple improved formulas for the Coulomb energy. A particularly simple, but often quantitatively superior approximation consists of replacing the denominator $\frac{5}{6}R$ in the refined mean-field by $\frac{5}{6}R + R_n$, which is the sum of the mean separation between two random points within a sphere and the minimum separation between the considered fragment n and any other fragment. The results of this approximation are also shown above. For relatively high densities, it is more accurate than any of the other approximations mentioned and may thus offer a quantitative improvement of available statistical one-body models, essentially without any increase in computational effort.

6. UNBOUND FRAGMENTS

The work reported in this section is being carried out in collaboration with George Fai and will be reported in more detail elsewhere.[19]

When the total excitation energy of the system is comparable to its total binding energy, as is typically the case at medium-energy nuclear collisions, it is important to take account of unbound levels in the (pre)fragments. This was first attempted in [4] by a modulated level-density formula. Based on the intuition that only sufficiently long-lived states should be included as potential "final" states, the Fermi-gas level density was suppressed by a Gaussian cut-off factor, so that highly excited (hence, supposedly, very short-lived) levels were suppressed. A similar method was employed in [14], using an expoential modulation ($\exp(-\epsilon_n/\tau_0)$) which is formally more convenient since it leads directly to an effective temperature, $\tau_{\text{eff}} = 1/(1/\tau + 1/\tau_0)$, in qualitative accodance with finite-temperature mean-field studies.[20]

Although such treatments have some intuitative appeal, they have not yet been formally derived. One problem is that the relevance of the life-time criterion is unclear in a static, equilibrium situation. Another is that particle-unstable fragments must be considered embedded in a vapor of their ejectiles, such as is customary in astrophysical studies at lower energies and densities where neutron-rich fragments are embedded in a neutron vapor.

Since the treatment of this ingredient in the model is important, both qualitatively and quantitatively, we have recently undertaken to reexamine the problem, in the hope of arriving at a better-based formulation. Space limitations restrain us to make only the following brief remarks.

By invoking Levinson's theorem, [21] it can be shown that the mass distribution is affected only little by the precise nature of the criterion used to tell whether a given nucleon should be considered as part of the particular fragment within which it happens to be situated, or as part of the surrounding vapor. However, since this primary fragment distribution is modified by subsequent decays, the final (observed) mass distribution *is* sensitive to how that separation is made.

The insensitivity of the mass distribution appplies only to an idealized independent-particle system. Since subsaturation matter tends to cluster, many-body effects are present and the analysis of the idealized situation should only be a guide. (Recall that the Fermi gas has a level-density parameter $a \approx A/16$ MeV, whereas real nuclei have about twice that.)

We are currently exploring a particularly promising criterion: A given nucleon, situated within the domain of a fragment, should be considered as part of that fragment if it is deflected back when reaching the nuclear surface. Accordingly, the nuclear level density should be modulated by the average reflection coefficient for nucleons at the particular energy, $\bar{R}(\epsilon_n)$. As it turns out, this model appears to yield reasonable results in that it produces a "limiting" nuclear temperature decreasing from 12-15 MeV for $A \approx$ 100-200 to 6-8 MeV for $A \approx$ 10-20. These studies are still in progress and our conclusions will be reported elsewhere.[19]

7. CONCLUDING REMARKS

Recently, we have formulated a practical and well-founded method for an exact description of the statistical mechanics of the type of finite, interacting system of nucleons and nuclei likely to be formed in an energetic nuclear collision.[14] In the present note, we have discussed some important theoretical aspects of any microcanonical model for nuclear multifragmentation. In particular, recent studies of interfragment forces and unbound fragment states have been summarized.

There are many interesting applications of the type of model discussed here, especially in astrophysics and nuclear collision dynamics. However, and this is particularly true of simulation studies which often lack the transparency of more analytical studies, the utility of massive calculations depends entirely on the soundness of the physical assumptions and the formal basis of the model. Therefore, it is important to solidify the ingredients before detailed confrontation with experimental data is attempted.

This work was supported in part by the Director, Office of Energy Research, Division of Nuclear Physics of the Office of High Energy and Nuclear Physics of the U.S. Department of Energy under Contract No. DE-AC03-76SF00098.

REFERENCES

1. E. Fermi, Prog. Theor. Phys. 5 (1950) 570
2. A.Z. Mekjian, Phys. Rev. C17 (1978) 1051; R. Bond, P.J. Johansen, S.E. Koonin, and S.I. Garpman, Phys. Lett. 71B (1977) 43; J. Gosset, J.I. Kapusta, and G.D. Westfall, Phys. Rev. C18 (1978) 844
3. S.E. Koonin and J. Randrup, Nucl. Phys. A356 (1981) 223
4. G. Fai and J. Randrup, Nucl. Phys. 381 (1982) 557
5. H. Stöcker, G. Buchwald, G. Gräbner, P. Subramanian, J.A. Maruhn, W. Greiner, B.V. Jacak, and G.D. Westfall, Nucl. Phys. A400 (1983) 63c
6. L.P. Csernai, J.I. Kapusta, G. Fai, D. Hahn, J. Randrup, H. Stöcker, Phys. Rev. C35 (1987) 1297
7. G. Fai and J. Randrup, Phys. Lett. 115B (1982) 281
8. G. Fai and J. Randrup, Nucl. Phys. A404 (1983) 551
9. G. Fai and J. Randrup, Comp. Phys. Comm. 42 (1986) 385
10. D.H.E. Gross, L. Satpathy, Meng Ta-chung, and M. Satpathy, Z. Phys. A309 (1982) 41; D.H.E. Gross, Phys. Scripta T5 (1983) 213
11. Sa Ban-hao and D.H.E. Gross, Nucl. Phys. A437 (1985) 643; D.H.E. Gross and Xiao-ze Zhang, Phys. Lett. 161B (1985) 47
12. D.H.E. Gross, Zhang Xiao-ze, and Xu Shu-yan, Phys. Rev. Lett. 56 (1986) 1544; A.Y. Abul-Magd, D.H.E. Gross, Xu Shu-yan, and Zheng Yu-ming, Z. Phys. A325 (1986) 373
13. J.P. Bondorf, R. Donangelo, I.N. Mishustin, C.J. Pethick, and K. Sneppen, Phys. Lett. 150B (1985) 57; J.P. Bondorf, R. Donangelo, I.N. Mishustin, C.J. Pethick, H. Schulz, and K. Sneppen, Nucl. Phys. A443 (1985) 321; J.P. Bondorf, R. Donangelo, I.N. Mishustin, and H. Schulz, Nucl. Phys. A444 (1985) 460; J.P. Bondorf, R. Donangelo, H. Schulz, and K. Sneppen, Phys. Lett. 162B(1985) 30
14. S.E. Koonin and J. Randrup, Nucl. Phys. Axxx (1987) in press
15. N. Metropolis, A.W. Rosenblut, M.N. Rosenblut, A.H. Teller, and E. Teller, J. Chem. Phys. 21 (1953) 1087
16. J. Randrup, M.M. Robinson, and K. Sneppen, LBL-24333 (1987), Phys. Lett. B
17. J.I. Kapusta and K. Olive, Nucl. Phys. A408 (1983) 478
18. E. Wigner and F. Seitz, Phys. Rev. 46 (1934) 509
19. G. Fai and J. Randrup, LBL-24368 (1987), in preparation
20. P. Bonche, S. Levit, and D. Vauterin, Nucl. Phys. A427 (1984) 278; A436 (1985) 265; S. Levit and P. Bonche, Nucl. Phys. A437 (1985) 426
21. D.L. Tubbs and S.E. Koonin, Ap. J. (Letters) 232 (1979) L59; D.R. Dean and U. Mosel, Z. Phys. A322 (1985) 647

Relativistic Vlasov-Uehling-Uhlenbeck Model for Heavy-Ion Collisions

Che Ming Ko and Qi Li
Cyclotron Institute and Center for Theoretical Physics
Texas A&M University
College Station, Texas 77843

To construct a theory for heavy-ion collisions at high energies when particles move with a velocity not negligible with respect to the velocity of light, it is important to take into account the relativistic effects. This includes the explicit mesonic-exchange nature of the interaction, the small component of the nucleon wave function, and the existance of the negative energy states. Also at very high density and/or temperature, the restoration of the chiral symmetry is expected to play an importnat role in high-energy heavy-ion collisions. As a first step towards the development of a relativistic transport theory for heavy-ion collisions which incorporates the above effects, we have recently derived a relativistic Vlasov equation from the Walecka model in the local-density and the semiclassical approximation[1]. In the Walecka model[2], the interaction between the nucleons are mediated by a scalar meson ϕ with mass m_s and a vector meson V_μ with mass m_v. Introducing the phase space distribution function $f(\mathbf{r},\mathbf{p})$ for the nucleons, then the following relativistic Vlasov equation has been obtained in ref.1),

$$\partial_t f + \dot{\mathbf{r}}\cdot\nabla_{\mathbf{r}} f + \dot{\mathbf{p}}\cdot\nabla_{\mathbf{p}} f = 0, \tag{1a}$$

where

$$\dot{\mathbf{r}} = \mathbf{p}^*/\epsilon^*, \tag{1b}$$

and

$$\dot{\mathbf{p}} = -\nabla_{\mathbf{r}} U = -\nabla_{\mathbf{r}}(\epsilon^* + g_v V_0). \tag{1c}$$

The coupling constants of the mesons to the nucleon are denoted by g_s and g_v for the scalar and the vector meson, respectively. In the above, $\mathbf{p}^* = \mathbf{p} - g_v\mathbf{V}$ and $\epsilon^* = (\mathbf{p}^{*2} + M^{*2})^{1/2}$ with $M^* = M - g_s\phi$. The nucleon mass is denoted by M. In the mean-field approximation, the meson fields are treated as classical fields and are thus related to the nuclear densities via

$$\phi = (g_s/m_s^2)\rho_s, \quad V_0 = (g_v/m_v^2)\rho_B, \quad \mathbf{V} = (g_v/m_v^2)\rho_{\mathbf{v}}. \tag{2}$$

In the above, the baryon density ρ_B, the scalar density ρ_s, and the current density $\rho_{\mathbf{v}}$ can be expressed in terms of the phase space distribution function as follows,

$$\rho_B(\mathbf{r}) = \int d^3\mathbf{p}\, f(\mathbf{r},\mathbf{p}), \tag{3a}$$

It has to be noted here that no real discontinuity is expected between the yields of light particles and that of the lighter fragments. For this reason, and also because the intrinsic efficiency of the parallel plate detectors is expected to decrease gradually for lighter fragments, only fragments with mass $A > 20$ will be considered.

The background-subtracted and efficiency-corrected 2–body and 3–body TKE spectra obtained for the system ^{100}Mo + ^{100}Mo at 12, 14.7, 18.7 and 23.4 MeV/u are shown in fig.4. One can observe that:

— 3–body events are concentrated at low TKE-values (high energy-loss);

— the yield of 3–body events increases with increasing bombarding energy and becomes comparable or even higher than the 2–body yield.

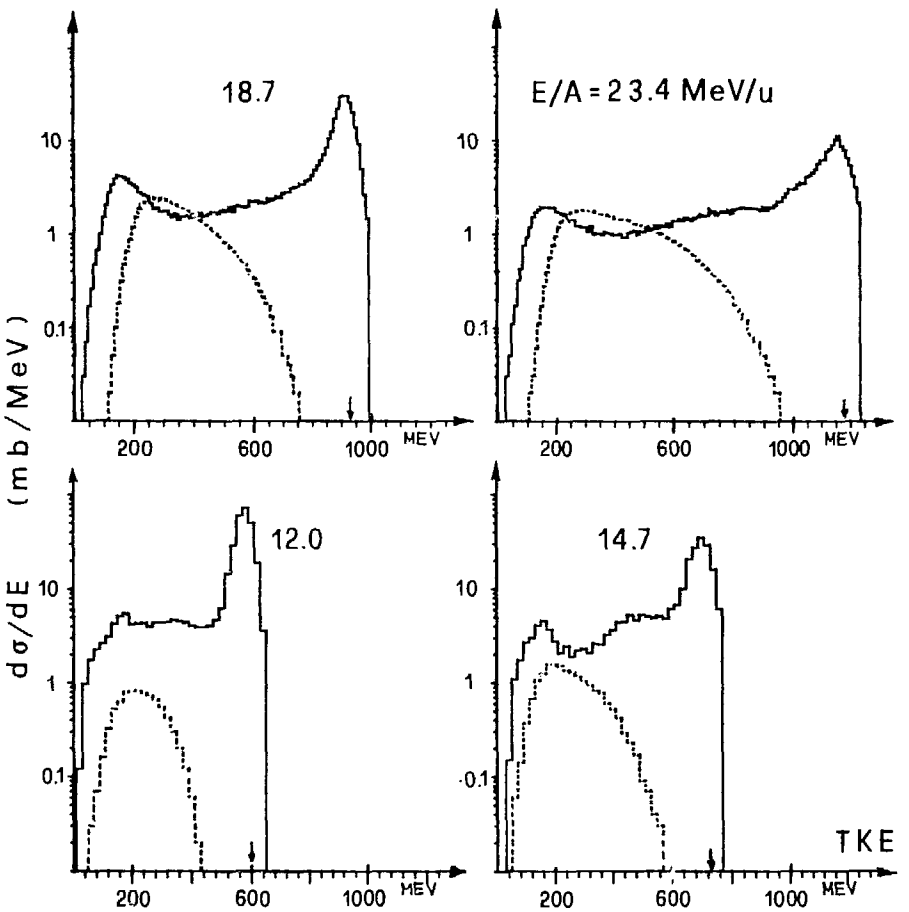

Fig.4: Total kinetic energy spectra for 2–body (solid curve) and 3–body events (dashed curve) in the collision ^{100}Mo + ^{100}Mo at four bombarding energies. The data are integrated over angle θ_{cm} and mass $A > 20$, after background subtraction and geometry correction.

The two parameters b and c make it possible to obtain different values of the compressibility and the effective nucleon mass as shown in ref.10) . With the self-interaction of the scalar meson, the relation between the value of the scalar meson and the nuclear scalar density in eq.(2) becomes

$$m_s^2\sigma + b\sigma^2 + c\sigma^3 = g_s\rho_s. \tag{6}$$

We shall apply the relativistic model to study the high-energy heavy-ion collisions. At such high energies, pion production plays an important role. To include such effects, we allow the nucleon to be excited to the delta resonance in the collision. However, we neglect the decay of the delta resonance into the pion as we do not know yet how to include properly pions in the relativistic theory. From the cascade model[11], it has been shown that pions appear mostly in the later stage of the collision and will probably not affect appreciably the initial dynamics which is what we are mainly interested in. To treat the delta resonance in the relativistic model, we need to know its couplings to the scalar and the vector mesons which we take to be the same as those of the nucleon.

We have studied the reaction $^{40}Ca + ^{40}Ca$ at an incident energy of 1.8 GeV/nucleon[12]. The nucleon transverse momentum distribution after the collision has been measured. An earlier study of this reaction with the normal VUU model has led to the conclusion that the nuclear equation of state is rather stiff with a compressibility of 380 MeV[13]. This equation of state, expressed as the binding energy per nucleon as a function of the nuclear density, is shown in Fig.1 by the long-dashed curve. We have calculated the transverse momentum distribution for this reaction with the same compressibility but with an effective nucleon mass of 0.83 M which is suggested by the latest determination by Johnson *et al.* from the optical model analysis of nucleon-nucleus scattering[9]. To obtain these values of the compressibility and the nucleon effective mass, we use the following values for the parameters in the generalized Walecka model,

$$C_v = (g_v/m_v)M = 9.04, \quad C_s = (g_s/m_s)M = 11.78.$$

$$B = b/(g_s{}^3M) = 2.59\cdot 10^{-2}, \quad C = c/g_s{}^4 = 0.169, \tag{7}$$

if a binding energy of 15.96 MeV at a saturation density 0.145 fm^{-3} is required. The corresponding equation of state is given by the solid curve in Fig.1 and is seen to be much softer than the previous one at high densities. The transverse momentum distribution as a function of the rapidity calculated from the relativistic model with the parameters given by eq.(7) is shown in Fig.2 by the solid curve. It agrees reasonably with the experimental data as shown by the open diamonds. When a momentum-dependent potential is included in the normal VUU model, a similar result can be obtained for the transverse momentum

distribution with a compressibility of about 200 MeV[14,15]. We have also carried out calculations with this value of the compressibility and an effective nucleon mass 0.83 M. This equation of sate is shown by the dashed curve in Fig.1. The resulting transverse momentum distribution is shown in Fig.2 by the dashed curve and is similar to the previous one obtained with a compressibility of 380 MeV. We therefore conclude that in the relativistic model the transverse momentum distribution in high-energy heavy-ion collisions is not sensitive to the value of the compressibility. To understand this result, we note that the final transverse momentum distribution is essentially reached at the highest compression in the collision. The pressure responsible for the particles to move sideways is determined by the density dependence of the nuclear part of the single-particle energy as shown in eq.(1c). For heavy-ion collisions at high energies, the density dependence of the nucleon kinetic energy through the nucleon effective mass is small in comparison with the density dependence of the potential energy due to the interaction with the vector meson. Since the vector meson coupling constant is fixed by the value of the nucleon effective mass, the pressure on the nucleons is similar for the two values of compressibility. The apparent stiffness of the nuclear equation of stae at high densities for a larger value of compressibility has thus no direct effect on the transverse momentum distribution for high-energy heavy-ion collisions. At lower incident energies, the density dependence of the nucleon kinetic energy will be appreciable and the transverse momentum distribution is therefore expected to be sensitive to the value of the compressibility. On the other hand, the transverse momentum distribution changes drastically if a different value of the nucleon effective mass is used as shown by the dotted curve in Fig.2 which corresponds to an effective mass of 0.7 and a compressibility of 380 MeV. The corresponding equation of state is given by the dotted curve in Fig.1. The reason for this is because a smaller effective mass implies a larger value of the vector meson coupling constant which leads thus to a stronger sideways pressure on the particles.

In summary, we have applied the relativistic transport model to study the transverse momentum distribution in heavy-ion collisions. From comparing with the available experimental data, it is concluded that a relatively soft equation of state is required. This result is similar to that from previous studies with a momentum-dependent potential.

We are grateful to Norman Glendenning for bringing to our attention the recent work of Mahaux *et al.* on the nucleon effective mass. This work is supported in part by the National Science Foundation under Grant No. 8608149 and the Robert A. Welch Foundation under Grant No. A-1110.

References

1. C. M. Ko, Q. Li, and R. Wang, Phys. Rev. Lett. **59**, 1084 (1987).
2. J. D. Walecka, Ann. Phys. **83**, 491 (1974).
3. H. Elze *et al.*, Mod. Phys. Lett. **2**, 451 (1987).
4. Q. Li and C. M. Ko, Mod. Phys. Lett., in press.
5. R. Y. Cusson *et al.*, phys. Rev. Lett. **55**,2786 (1985).
6. G. F. Bertsch, H. Kruse, and S. Das Gupta, Phys.Rev. **C29**, 673 (1984).
7. B. ter Haar and R. Malfliet, Phys. Rep. **149** (1987).
8. G. E. Brown, Proc. of the 8th High Energy Heavy Ion Study, Berkeley (1987).
9. C. H. Johnson, D. J. Horen, and C. Mahaux, preprint (1987).
10. J. Boguta and H. Stöcker, Phys. Lett. **120B**, 289 (1983).
11. J. Cugnon, D. Kinet, and J. Vandermeulen, Nucl. Phys. **A379** 553 (1982).
12. H. Ströbele *et al.*, Phys. Rev. **C27**, 1349 (1983).
13. J. J. Molitoris and H. Stöcker, Phys. Rev. **C32**, 346 (1985).
14. J. Aichelin *et al.*, Phys. Rev. Lett. **58**, 1926 (1987).
15. C. Gale, G. Bertsch, and S. Das Gupta, Phys. Rev. **C35**, 1666 (1987).

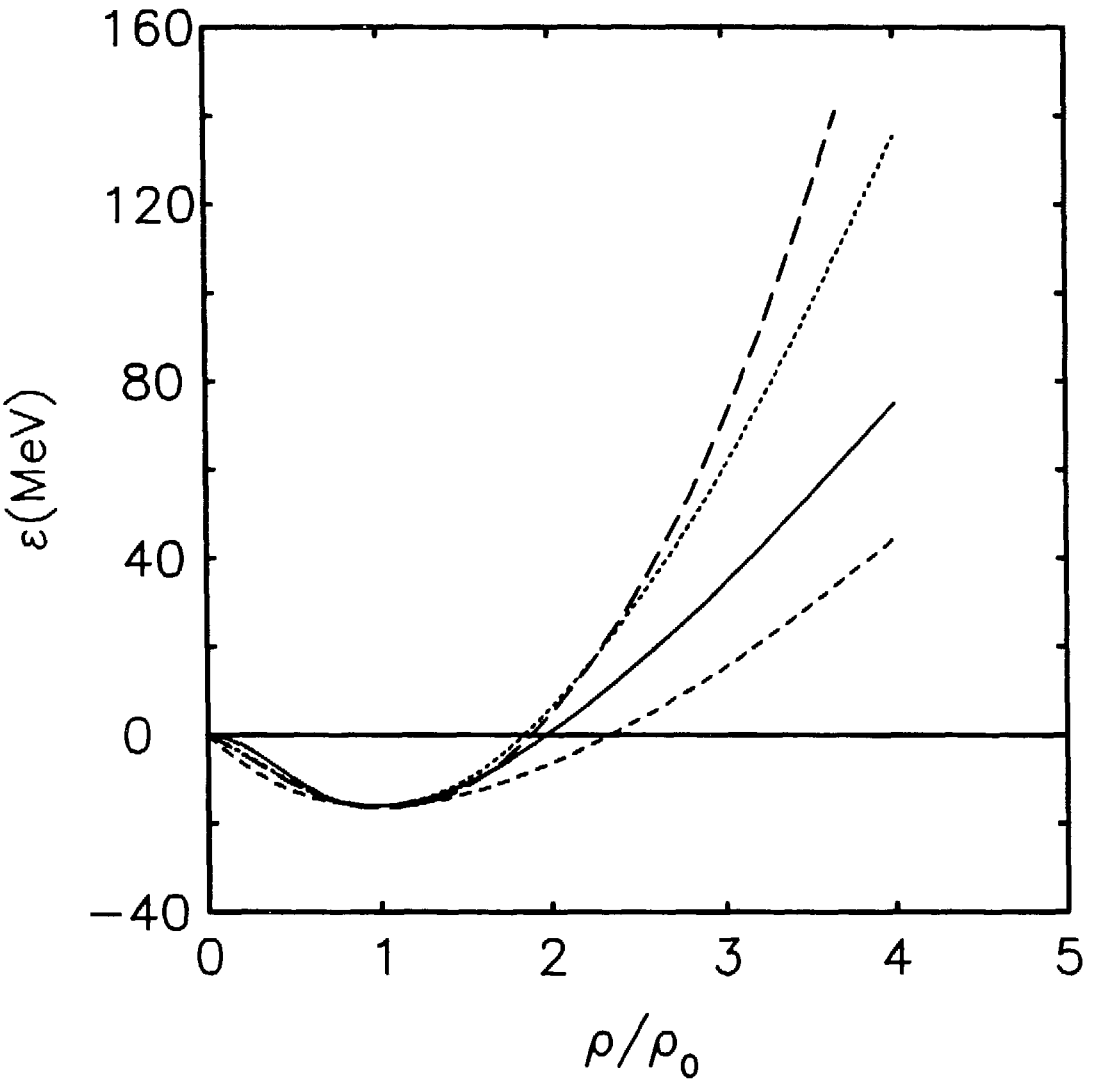

Fig.1 The binding energy per nucleon ϵ as a function of the ratio of the density to the saturation density ρ/ρ_0 for the three cases: solid curve ($M^*=0.83$ M, K=380 MeV), dashed curve (0.83 M, 200 MeV), and dotted curve (0.7 M, 380 MeV). The long-dashed curve corresponds to a stiff equation of state used in the normal VUU model[13].

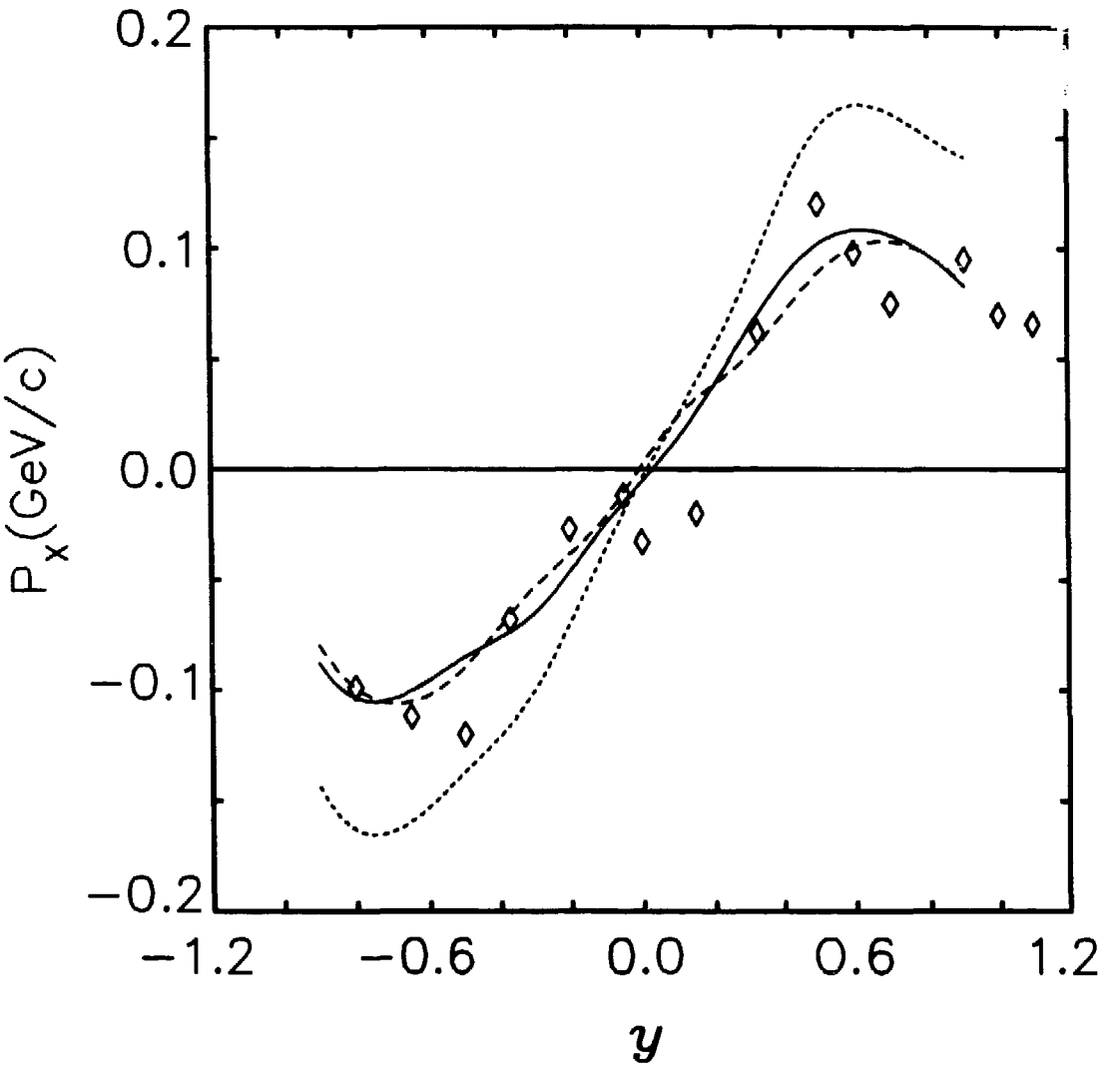

Fig.2 The transverse momentum projected onto the reaction plane and averaged over all perpendicular momentum P_τ, as a function of the rapidity y for the reaction $^{40}Ca+^{40}Ca$ at 1.8 GeV/nucleon. The open diamonds are the experimental data from ref.12). The solid curve and the dashed curve are from the theoretical calculations with the same effective mass $M^*=0.83$ M but different values of the compressibility K=380 MeV and K=200 MeV, respectively. The dotted curve corresponds to $M^*=0.7$ M and K=380 MeV.

COLLECTIVE FLOW AND PION PRODUCTION IN A HYDRODYNAMIC MODEL*

J. Zingman, T. McAbee, J. Wilson and C. Alonso
Lawrence Livermore National Laboratory,
PO Box 808
Livermore, Ca. 94550

Abstract

A new heavy-ion collision model which couples ideal, relativistic hydrodynamics with dynamical pions is described. The collective flow predicted by the model is shown to compare favorably to results obtained by earlier workers using quite different numerical methods. Discrepancies with experimental data are discussed, as are possible resolutions of the differences. Pion distribution functions resulting from the model are presented along with their experimental implications. Extensions to the model are discussed as well.

Since there is as yet no complete quantum description of relativistic heavy-ion collisions, we must use macroscopic phenomenology to model the events that occur in these reactions. Many models have been proposed and investigated over the past decade, ranging from single particle models which attempt to mock up quantum effects, such as quantum molecular dynamics[1] and VUU theories,[2] to collective models such as hydrodynamics.[3,4] Different models have been developed depending on the phenomena being investigated. As experiments have been performed at the BEVALAC and at CERN, the theories have had to be refined in order to reproduce the data.

We present here a hydrodynamical model designed to address two types of data that have appeared from these experiments. The first of these is the collective flow of matter in the collisions. The collective flow was first predicted in a hydrodynamical model,[5] and the observation of the flow[6] was one of the earliest major results from

* This work was performed under the auspices of the U. S. Department of Energy at Lawrence Livermore National Laboratory under contract No. W-7405-Eng-48.

this experimental program. This flow has been described in terms of the flow angle,[5] the perpendicular momentum per particle against rapidity[7] and the slope of this momentum at zero rapidity.[8] The second class of data deals with light meson production, mostly pions at the BEVALAC, which had heretofore only been investigated statically in fluid models. Chemical production[9,10] has been the major method of coupling fluid dynamics to mesons so far, but in this work we present a model in which the pions are dynamical particles interacting with a baryonic fluid. One of our objectives was thus to determine whether or not a dynamic pion model could be developed within the framework of hydrodynamics.

The basis of our model is fully three-dimensional, relativistic, ideal fluid dynamics.[4] Ideal hydrodynamics results from the conservation of energy, momentum and density in a fluid without viscosity or heat conduction. These conservation laws may be formulated covariantly by considering the ideal stress-energy tensor,

$$T^{\mu\nu} = (\rho + \varepsilon + p)\, u^{\mu} u^{\nu} + g^{\mu\nu} p \qquad (1)$$

where ρ is the proper density, ε the proper energy density, p the proper pressure, u^{ν} the 4-velocity, and $g^{\mu\nu}$ the metric tensor. The divergence of the (0v) and (iv) rows of the tensor yield conservation of energy and momentum, respectively. The conservation of baryon number arises from conservation of the baryon current, ρu^{ν}. We solve the equations numerically through finite differencing with a second-order van Leer scheme used for the advection terms.[11] Further details on our numerical methods, along with tests of the numerical procedures can be found in ref 4.

Nuclear physics enters our hydrodynamical model through the compressional equation of state, or the amount of compressional energy at zero temperature. Many models for this have been proposed,[12] but we use one that preserves the known facts about ground state nuclear matter (binding energy ~-16 MeV, no pressure, incompressibility ~210 MeV) while allowing us to vary its properties away from normal nuclear density. It has the form

$$E_0(u) = \frac{K_1}{u} + K_2 + \frac{3}{5}\frac{k_f^2}{2m^*} + \frac{1}{9}(K_3 - K_4)\ln u + \frac{1}{9}\left(\frac{u-1}{u}\right)\left(\frac{1}{2}K_4(u+1) - K_3\right). \qquad (2)$$

We set $u=\frac{\rho}{\rho_0}$, and K_1, K_2, and K_3 are constrained to fit the above data, while K_4 is varied to adjust the high density properties. Note that we have included an effective mass m^* as well. Sample plots of this EOS are shown in Fig. 1, along with a Skyrme[13] EOS for comparison. Nuclear physics also plays a role in defining the finite temperature EOS. We assume that the baryonic matter behaves as a relativistic Fermi gas, either as a single component gas composed of nucleons or as a two-component gas with both nucleons and deltas.[10] Since it is believed that nucleons and possibly deltas behave dynamically with an effective mass different from their free mass,[14] we have included this effect. Note that if we include an effective mass for the deltas, we must modify the Fermi energy term in Eq. (2).

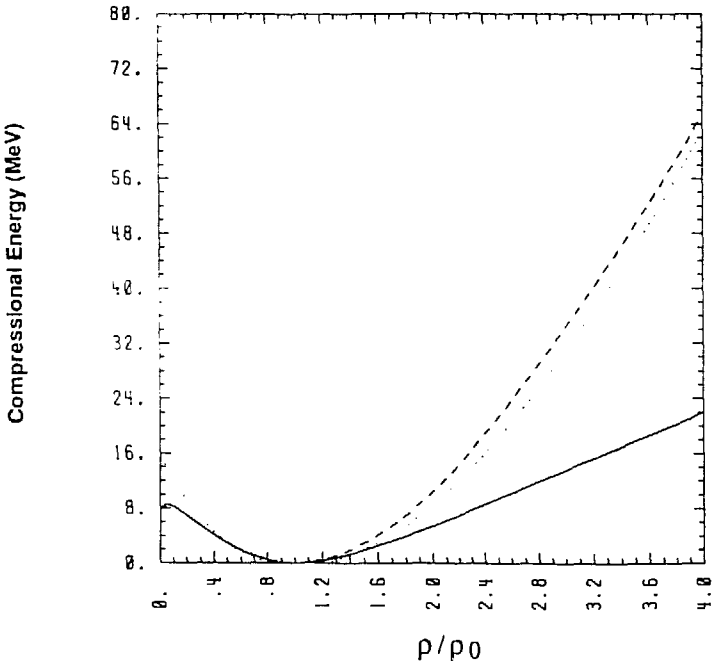

Figure 1. EOS from Eq (2). Shown are $K_4 = 0$ (solid) and 800 (dashed) MeV, and a Skyrme (dotted) EOS for comparison.

To this we couple a dynamical pion model.[15] We can define a master equation for the pion momentum distribution function,

$$\frac{dN_\pi}{dt}(p_\pi) = v_\pi \rho\, \sigma_A(\rho, p_\pi)\, f_{BE}(p_\pi, T) - v_\pi \rho\, \sigma_A(\rho, p_\pi)\, N_\pi(p_\pi)$$

$$- \rho N_\pi(p_\pi) \int v_{\pi N} \sigma_S(\rho, p_{\pi N})\, D_B(r_N, T)\, d^3p_N + \rho \int \langle v_\pi \sigma_S N_\pi' \rangle\, d^3p_\pi' \qquad (3)$$

Here N(p) is the distribution function, σ_A and σ_S the absorption and scattering cross-sections for pions from nucleons, respectively, and <> indicates a thermal average over the nucleon velocity in the fluid rest frame. Subscripts π denote pion quantities, while N indicates a nucleon. ρ is the nucleon density, f_{BE} is the Bose-Einstein distribution, which we take to be the equilibrium solution for the model, and D_B is a relativistic Boltzmann distribution for the nucleons. The first term in the equation represents the production of pions by the thermal motion of the baryonic fluid. The second represents absorption of pions on pairs of nucleons. Note that these terms are taken so that detailed balance is guaranteed. The third term describes pion-nucleon scattering out of a given momentum state; the last term describes the scattering of pions with momentum p'_π into the state p_π from a thermalized baryon distribution. We use cross-sections such that when we scatter pions from cold nuclei, we reproduce the experimental data.

We do not solve this equation explicitly. Instead, we generate fractional marker particles that behave dynamically as pions but carry proportionately less mass and momentum. These particles interact with the baryonic fluid by exchanging momentum and energy density during production, scattering, and absorption. We enforce local conservation of the exchanged quantities through relativistic kinematics. Since in BEVALAC experiments, only a few tens of pions at most are detected, we use particles significantly smaller than pions in order to generate higher statistics in our collisions. Details of the solution of eq (3) and how we couple the two components of the model together may be found in ref. 15.

In order to investigate the flow characteristics of the baryons with minimal influence from the pions, we first consider a low-energy system. We calculate as a test case Au+Au collisions at 200 MeV in the laboratory frame. We use a quadratic ground-state EOS, rather than eq(2), and only nucleons in the finite temperature EOS, so that these calculations may be compared with the work of other groups. The first way that collective flow was described was in terms of the flow tensor,[5] which may in general be written

$$F^{\mu\nu} = \sum_i P_i^{\mu} P_i^{\nu} w_i \quad . \qquad (4)$$

The sum is over all particles, or in our case cells, and the superscripts refer to the direction of the momentum. With the choice of the weighting function w_i as the inverse of twice the mass of the particles, diagonalizing this tensor yields the direction of the principal axis of the momentum ellipsoid, and hence gives an indication of the flow. We can study the angle of this principal axis with respect to the collision axis. In Fig. 2 we present the time history of this quantity for the above collision at an impact parameter of b=3 fm. We find that the calculations of ref. 16 yield very similar results in spite of very different numerical methods used.

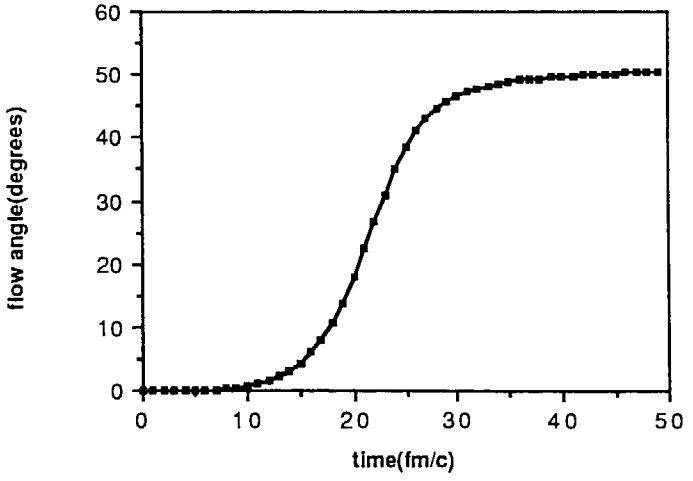

Figure 2. Flow angle versus time for Au+Au at 200 MeV and impact parameter b=3.

Other methods which are less sensitive to experimental cuts than the flow tensor[8] have also been developed to describe the flow. One such measure is the transverse momentum as a function of rapidity.[7] We have analyzed our fluid flow in this way, as shown in Fig. 3. As above, we agree rather well with other hydrodynamic calculations,[16] both in absolute scale and in the slope at zero rapidity.[8] Both results, however, overpredict the experimental value by approximately a factor of two.[17] Viscous non-relativistic calculations have been performed [16] which indicate that by including non-ideal terms of the order predicted by a phenomenological QCD analysis,[18] flow of the experimental magnitude may be obtained.

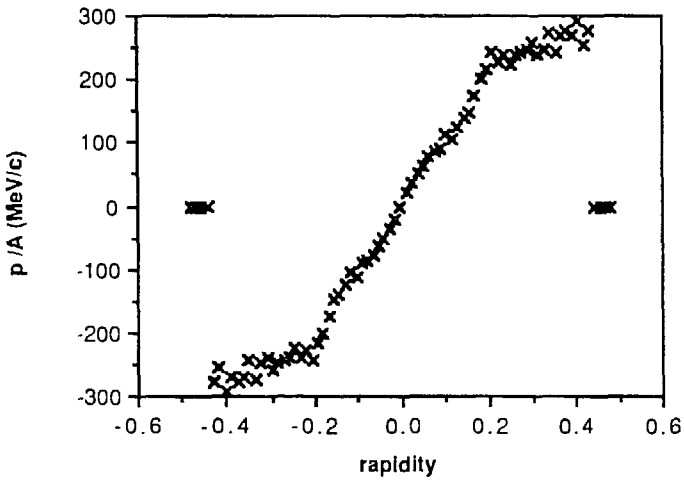

Figure 3. In-plane transverse momentum versus rapidity for 200 MeV Au+Au.

To demonstrate the pion part of the model, we consider La+La at 1350 MeV, an experiment that has been performed at the BEVALAC.[19] We use the EOS of eq. 1, generally with K_4=800 MeV. We will vary the ground state and finite temperature EOS to show their effect on pion production. Even though we perform all calculations with marker particles of mass much less than the pion mass, our results are scaled to real pions.

The first result is that the stiffness of the zero temperature EOS affects the pion production much less than does varying the thermal part of the EOS. In fig. 4, we see final pion production as a function of K_4 while using an effective mass in the thermal EOS and note that the number of pions produced varies by approximately 10 %. Setting K_4=800 MeV and varying the finite temperature part of the EOS, however, yields larger differences. In fig. 5, we show the time history of the pions for three different finite temperature EOS's; with only nucleons in the thermal EOS, with both nucleons and deltas in the EOS, and with nucleons having an effective mass of the form $m^* = \frac{m}{1+\beta\rho}$, β=1.673. Note that even in the most favorable case, we produce only 60% of the ~51 pions actually observed.[19]

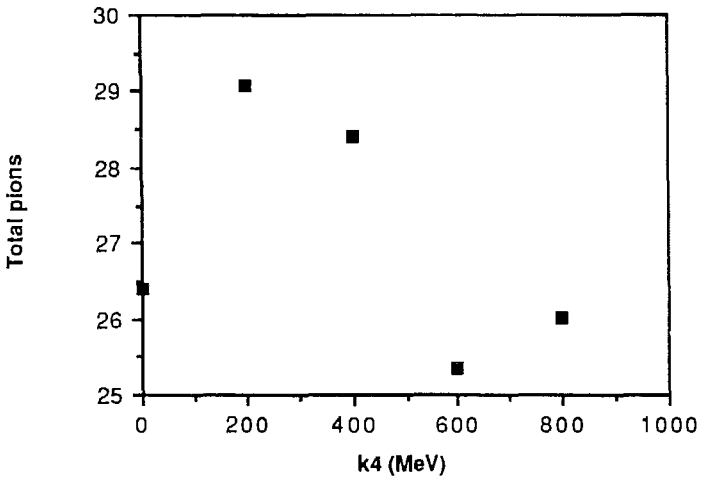

Figure 4 Total pions produced versus the stiffness parameter K_4.

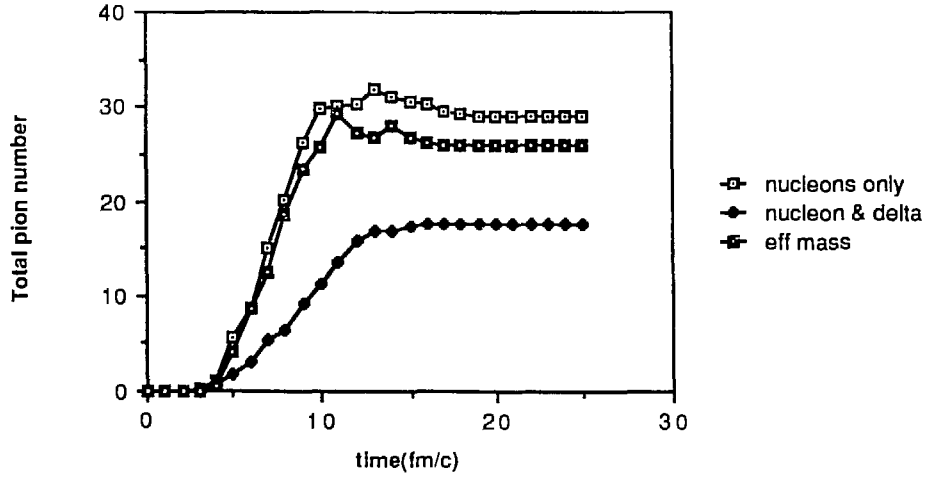

Figure 5. Pion production histories with nucleons only in the thermal EOS (open squares), nucleons and deltas in thermal EOS (filled diamonds) and with an effective mass in both thermal and ground state EOS (filled squares).

In fig. 6, we see a clue as to where the missing pions may come from. We present here a time history of our pion production along with a static chemical model calculation.[10] In the chemical calculation, the equilibrium number of pions was

calculated in each cell and summed over the grid, but no pions from resonances were included. This differs from the usual implementation of the model, in which the pion number is only calculated at the time of maximum compression. Two important observations may now be made. The first is that even though we do not force our system to assume an equilibrium solution, the number of pions we observe at late times is very nearly that from the chemical model taken at maximum compression. We observe a drop in the number of pions chemically produced at late times, as the system expands and cools. The second observation is that we do appear to reach a rough equilibrium for a short time in the calculation. Hence we be may underpredicting with respect to the observed pion number [19] because we do not have a channel for pion production from resonance decay.

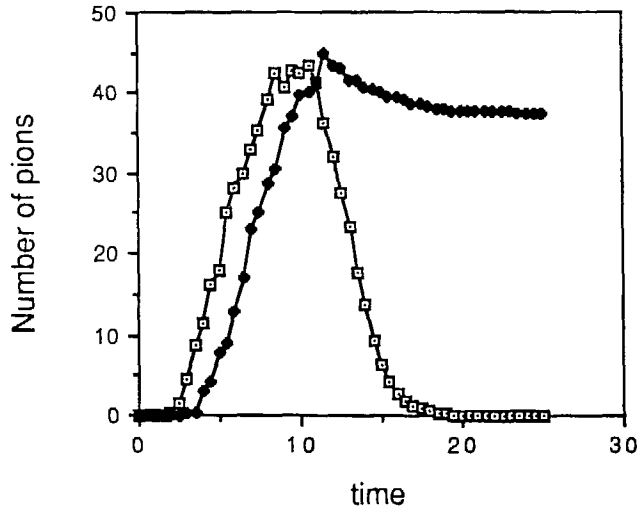

Figure 6. Total active pion number for the dynamical(solid diamonds) and an instantaneous pion number for the thermal(open squares) pion models as a function of time.

In summary, we have presented a new coupled hydrodynamical-pion production model for relativistic heavy-ion collisions. We have shown that its flow predictions are consistent with those of previous workers, in spite of a very different approach to the numerics. As with other hydrodynamical calculations,we overpredict the magnitude of collective flow of matter in the collisions. The introduction of viscosity, however, has been shown to allow fluid dynamical models to reproduce ex-

perimental flow results. We have two ways that we can introduce this effect. The first is to include conventional transport terms into our equations. The other is to note that our pions can serve the same purpose as a viscosity term; they can dissipate energy and momentum from regions where it is concentrated. Hence by increasing the number of marker particles, we may be able to simulate the viscosity. We have also shown results from dynamic pion production. In this case, there is some discrepancy with respect to the experimentally observed pion multiplicity, but we believe that by explicitly adding deltas to the model and allowing them to have a pion decay channel, we may be able to reproduce the observed number.

We wish to thank Horst Stöcker for making available to us the results from ref. 16. We also wish to thank Jim LeBlanc and Randy Christensen for valuable assistance in developing numerical procedures.

References

1. J. Aichelin, H. Stöcker, Phys. Lett. **B176** , 14 (1986).
2. H. Kruse, B.V. Jacak, J.J. Molitoris, G.D. Westfall, H. Stöcker, Phys. Rev.C **31** , 1770 (1985) ; H. Kruse, B.V. Jacak, H. Stöcker, Phys. Rev. Lett. **54** , 289 (1985); J.J. Molitoris, H. Stöcker, Phys. Rev. C **32** , 346 (1985).
3. A. A. Amsden, G.F. Bertsch, F.H. Harlow, J.R. Nix, Phys. Rev. Lett. **35** , 905 (1975); G. Buchwald, G. Graebner, J. Theis, J. Maruhn, W Greiner, H. Stöcker, Phys. Rev. Lett. **52** , 1594 (1984).
4. J. Zingman, T. McAbee, J. Wilson, C. Alonso, Lawrence Livermore National Laboratory UCRL-97153 (1987); J. Zingman, T. McAbee, J. Wilson, C. Alonso, Lawrence Livermore National Laboratory UCID-21126 (1987).
5. W. Scheid, H. Müller, W. Greiner, Phys. Rev. Lett. **32**, 741 (1974); H. Stöcker, J. Maruhn, W. Greiner, Z. Phys. **A290**, 297 (1978).
6. H.A. Gustafsson, *et al.*, Phys. Rev. Lett. **52** , 1590 (1984).
7. P. Danielewicz, G. Odyniec, Phys. Lett. **157B**, 146 (1985) .
8. K.G.R. Doss*et al.*, Phys. Rev. Lett. **57**, 302 (1986).
9. H. Stöcker, W. Greiner, W. Scheid, Z. Phys. **A286**, 121 (1978); P. Danielewicz, Nucl. Phys. **A314**, 465 (1979).
10. D. Hahn, H. Stöcker, Nucl. Phys. **A452**, 723 (1986).
11. J. Hawley, L. Smarr, J. Wilson, Ap. J. **277**, 296 (1984); Ap. J. Supp. **55**, 211 (1984).

12. B. Freedman, V.R. Pandharipande, Nucl. Phys. **A361**, 502 (1981); E. Baron, J. Cooperstein, S. Kahana, Nucl. Phys. **A440**, 744 (1985).
13. H. Stöcker, W. Greiner, Phys. Rep. **137**, 277 (1986).
14. G.E. Brown, W. Weise, G. Baym, J. Speth, Comm. in Nucl. and Part. Phys., 39 (1987).
15. T. McAbee, J. Zingman, J. Wilson, C. Alonso, in preparation.
16. H. Stöcker, private communication.
17. J.W. Harris*et al.*, Lawrence Berkeley Laboratory LBL-23476 (1987).
18. P. Danielewicz, M. Gyulassy, Phys. Rev. D**31**, 53 (1985).
19. J.W. Harris*et al.*, Phys. Rev. Lett. **58**, 463 (1987).

Intermediate Energies

Role of Compound Nuclei in Intermediate Energy Heavy Ion Reactions

Luciano G. Moretto, Michael Ashworth and Gordon J. Wozniak

Nuclear Science Division, Lawrence Berkeley Laboratory, University of California, Berkeley, California, 94720, USA

Abstract: The presence of compound nuclei in the exit channels of many intermediate energy reactions is reviewed. The statistical decay of such compound nuclei may be responsible for many of the observed features. The role of compound nuclei in complex fragment production, multifragmentation and high energy gamma-ray emission is illustrated.

Introduction

Present attempts to clarify the reaction mechanisms prevailing at intermediate energies seem to suffer from two prejudices both associated with the jump in energy that the field has forced upon some of us. The first prejudice stems from the legacy of our low energy experience. We are very familiar with the standard mode of formation of compound nuclei through complete fusion, and with their decay by the dominant channels, like light particle evaporation and fission. However, the fact that at higher energies compound nuclei may be formed in less conventional ways, or that they may decay by unusual channels does not seem to occur immediately to our attention.

The second prejudice is due to our excessive expectations. We are so attuned to searching for new mechanisms which we expect to be prompt, or fast, or dynamically controlled, that we tend to forget about "conventional mechanisms" which dominate at low energies but may be quite alive and well even at higher energies. These mechanisms, insofar as we know, may be responsible for all that we have observed so far or, at the very least, may provide a substantial background on top of which the "novel" effects must ride.

The consequences of this state of affairs is similar to that resulting from "weak" interactions with new and exotic lands. As exemplified in the "Bestiaria" of the Middle Ages or in the "Natural History" of Pliny the Elder:

1) Everything is anecdotal; one experiment and we are off to a new land.
2) Everything is new and different; otherwise we do not feel justified in our "modus operandi".
3) A rigid and restricted view of what is normal is held; this is to insure point 2.
4) Complexity is confused with novelty; the fact that we do not understand immediately what is

going on means that it must be new. The more complicated, of course, the better.

In order to illustrate the generalities presented above, let us consider, as examples the following topics which are of some relevance today:

1) Complex particle production
2) Multifragmentation and nuclear comminution
3) γ-ray emission

In what follows you may be reminded at times of Don Quixote who saw liquid-vapor equilibrium, multifragmentation, n-p bremsstrahlung and other marvels every day, and of Sancho Panza, who in his simplicity could only see compound nucleus decay. Despite your inclinations and sympathies, you should try and decide which of the two, the hero or the antihero, is right.

About Compound Nuclei And New Ways of Forming Them

At low energies we are used to preparing compound nuclei by means of fusion reactions; after all, it is not an accident that compound nuclei are called compound. However, what Bohr had in mind when he introduced this new concept was not the particular way in which the compound nucleus was formed. To the contrary he insisted that, due to total relaxation of the system, all the dynamical information associated with the entrance channel was forgotten, and that the decay could only depend upon the statistical features of the available exit channels. In order to prove that it does not matter how the compound nucleus is formed, the early and not so early literature is rich with examples of different "fusion" channels leading to the same compound nucleus - which does indeed decay always in the same way. So, the essence of the compound nucleus is **not** in the fusion of target and projectile but in the **decoupling** of Entrance and Exit Channels.

Having accepted that, we realize that compound nuclei may be more common than previously thought. For instance:

1) The residue product after a compound nucleus evaporates a particle is still a compound nucleus.
2) The two fragments produced in fission do relax and eventually evaporate neutrons as compound nuclei.
3) Quasi elastic and Deep Inelastic heavy ion reactions produce fragments which also relax into compound nuclei and decay as such.
4) In the process of incomplete fusion both the incomplete fusion product and the spectator do eventually relax into compound nuclei.
5) In the fireball production mechanism, the two spectator fragments are expected to relax into compound nuclei, and even the fireball may not be far from a compound nucleus, either.

As a conclusion, it seems advisable to inspect exit channels for the possible presence of compound nuclei. A lot of the particles observed may well be coming from them!

Complex Fragment Production

In view of the many fragments observed in intermediate energy reactions and of the many authors studying them, we would like to present the following comprehensive classification.[1)]

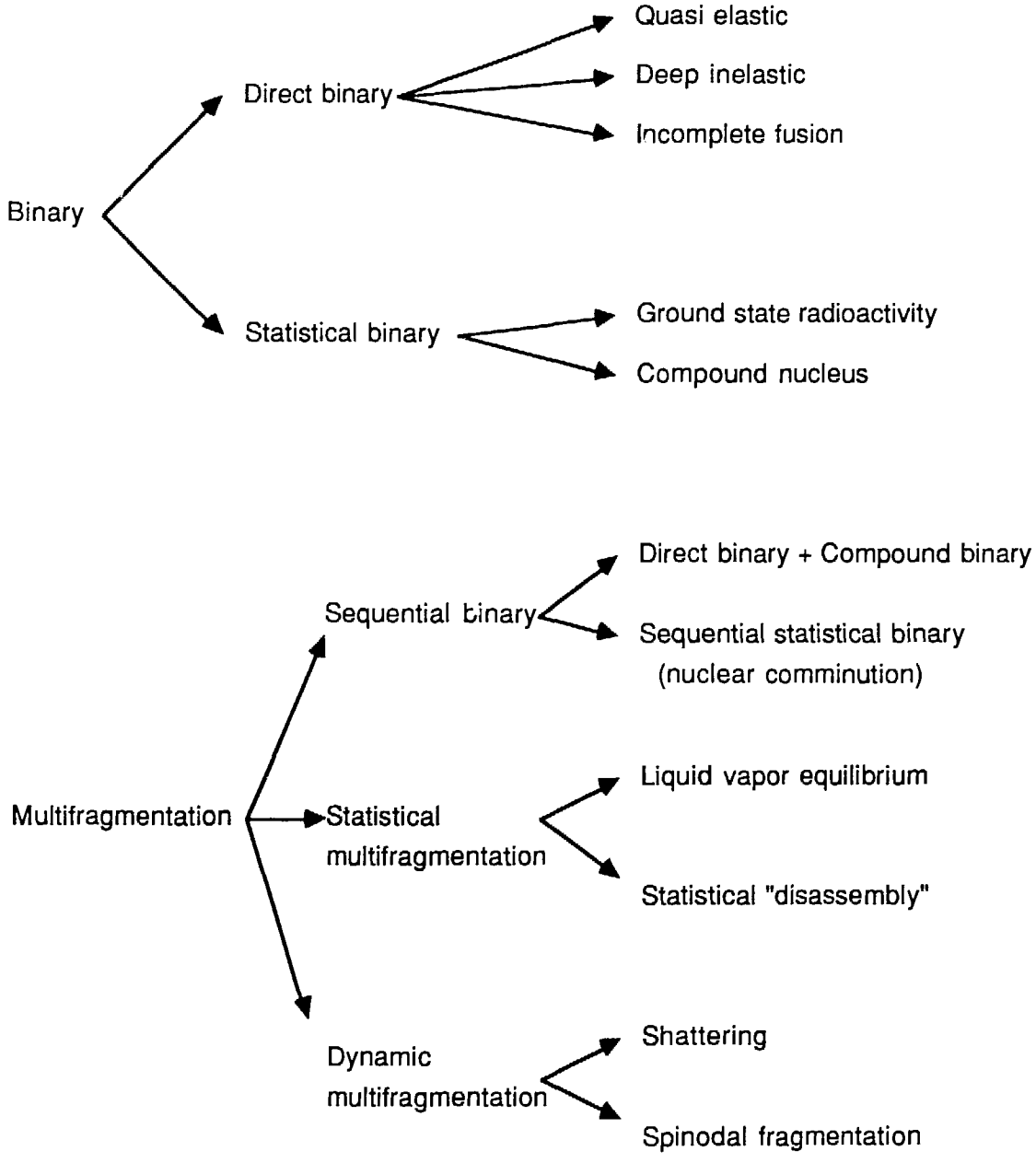

We shall see which of the above ways Nature decided to choose in order to produce complex fragments.

With the advent of intermediate energies, complex fragments have become a very pervasive presence. Where could they possibly come from? Conventional wisdom held that compound nuclei decay either by n, p, and α emission or by fission. As a consequence, complex fragments could only come from some other novel mechanism, like liquid vapor equilibrium, multifragmentation, etc.[1] However, it has been shown that compound nuclei at low energy can emit complex fragments.[2] In fact, it is possible to consider light fragment emission and fission as the two extremes of a single mode of decay, connected by the mass asymmetry degree of freedom.[3] This process allows for the decay by emission of complex fragments and the rarity of its occurence is due to the important but accidental fact that the barrier associated with such an emission is quite high.

Let us consider the potential energy surface of a nucleus as a function of a suitable set of deformation coordinates. This surface is characterized by the ground state minimum and by the fission saddle point. We can cut this surface with a line passing through the fission saddle point along the mass asymmetry coordinate in such a way that each of its points is a saddle point if one freezes the mass asymmetry coordinate. The locus of all these conditional saddle points we call the "ridge line".[3] Fig. 1 shows two examples of this line, one for a light system below the Businaro-Gallone point and the other for a heavier system above the Businaro-Gallone point. The same figure shows the expected particle yield following the statistical prediction:

$$Y(Z) \propto \exp[-V(Z)/T].$$

One can make three observations:

1) The systems below the Businaro-Gallone point give rise to a U-shaped mass or charge distribution with a minimum at symmetry.
2) The systems above the Businaro-Gallone point give rise to a similar distribution but with a maximum (fission peak) growing in at symmetry.
3) The yield increases with temperature and the yield associated with the highest barriers increases the fastest.

Consequently complex fragments, although very rare at low energy, become rapidly abundant at high energies. The existence of this compound nucleus mechanism at low energies has been proven in detail.[2] Could the fragments observed at higher energies arise from the same mechanism?

In experiments up to 50 MeV/u,[4] we have been able to identify three kinds of sources of complex fragments, which turn out to be rather conventional. The three sources are:

1) Quasi elastic/deep inelastic scattering.
2) Spectators in incomplete fusion processes.

3) Compound nucleus.

The first two sources produce fragments which are target and/or projectile related. The third is just the high energy version of the low energy compound nucleus decay. How can these three sources be distinguished? We have found that reverse kinematics and very asymmetric target-projectile combinations are particularly useful for a series of reasons. The principal reasons are: 1) the quasi elastic/deep inelastic processes and the incomplete fusion spectators are confined to very low atomic numbers leaving the remaining Z-range for compound nucleus products; 2) The associated limited range of impact parameters leads to a corresponding narrow range of momentum transfers and consequently to a small range of source velocities; 3) Reverse kinematics brings all the fragments into a relatively narrow forward cone and boosts their energy, thus greatly simplifying their detection and identification.

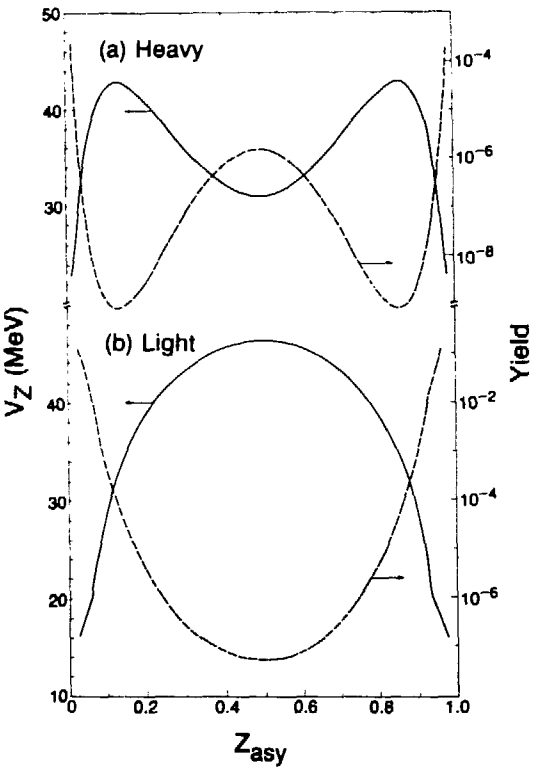

Fig. 1 Schematic ridge line potentials (solid curve) and calculated yields (dashed curve) for: a) a heavy CN above the Businaro-Gallone point; and b) a light CN below the Businaro-Gallone point as a function of the mass asymmetry coordinate (Z_{asy}).

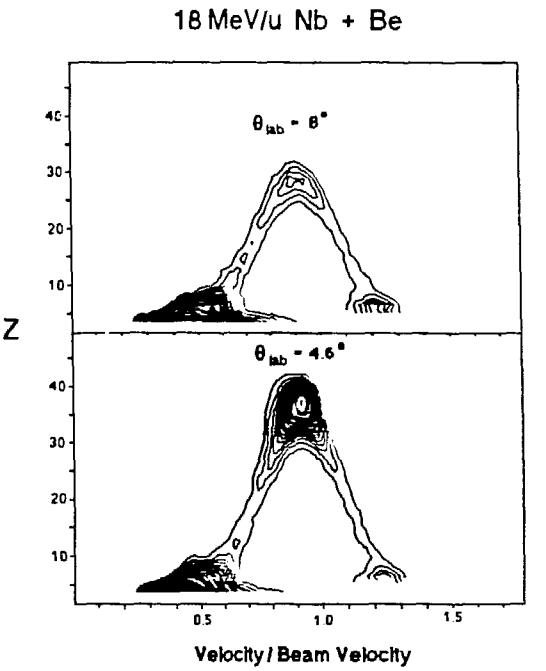

Fig. 2 Contours of the invariant cross section in the Z - velocity plane for complex fragments emitted from the 18 MeV/u ^{93}Nb + ^{9}Be reaction at θ_{lab} = 4.6° and 8°. The "big foot" visible at low velocities for Z < 10 is attributed to quasi elastic and deep inelastic products.

The evidence of the compound nucleus origin of these fragments can be seen in the plots of the cross section in the velocity - atomic number plane like that shown in Fig. 2. The two legs of the lambda pattern represent the upper and lower solutions in reverse kinematics associated with the binary decay of the source, and correspond to the Coulomb circles visible in the $v_{||}$ - $v_{\perp}$ plane for each Z value.[1] The telltale signature of a binary decay is not only the presence of a sharp Coulomb circle, but the fact that its radius decreases with increasing Z value as required by momentum conservation. The large cross sections observed at low Z values and attached to the low velocity branch (big foot) are associated with quasi and deep inelastic products. The choice of very asymmetric target projectile combinations shows here its wisdom. The more symmetric the

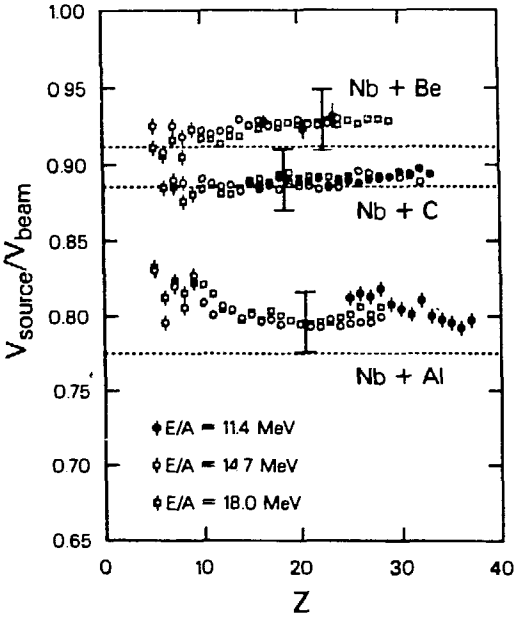

Fig. 3 Source velocities extracted from the Coulomb ring of each Z-species produced in the reactions 11.4, 14.7 and 18.0 MeV/u ^{93}Nb + ^{9}Be,^{12}C & ^{27}Al reactions. The small error on each point represents the statistical error associated with the extraction process. The large squared error bars indicate the possible systematic error. Note the suppressed zero on the abscissa. Although there is a small systematic deviation of the measured velocities above the complete fusion velociy, the lack of energy dependence of this effect suggests that complete fusion has taken place.

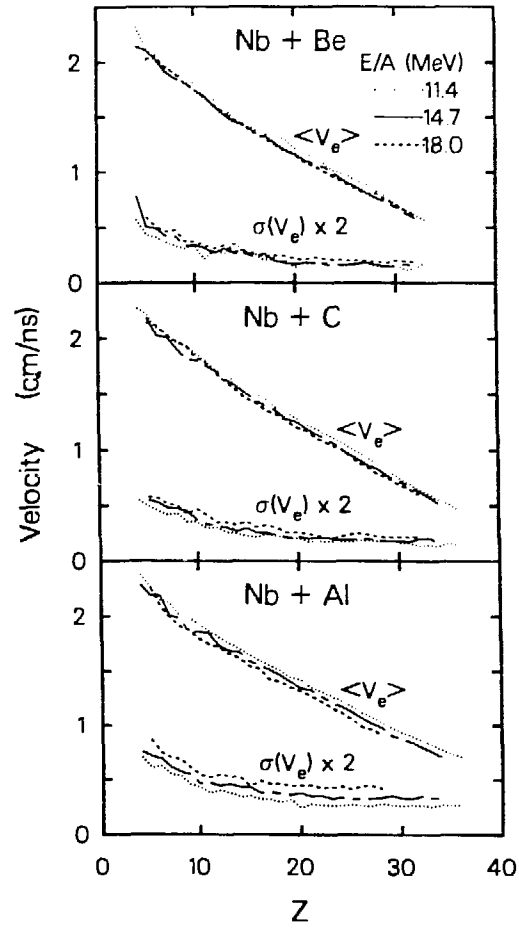

Fig. 4 First and second moments of the velocity spectra for each Z-species produced in the 11.4, 14.7 and 18.0 MeV/u ^{93}Nb + ^{9}Be,^{12}C & ^{27}Al reactions. To show the three bombarding energies on the same plot, lines are used rather than the data points.

target-projectile combination is, the more extensive the obscuration of the compound nucleus component by quasi - deep inelastic fragments is expected to be.

The centers of the circles give the source velocities which, as shown in Fig. 3 are remarkably independent of the fragment Z value and correspond to either complete or incomplete fusion of the light target with the heavy projectile.

The radii of the circles, plotted vs fragment atomic number demonstrate with their nearly linear dependence vs Z their Coulomb origin as shown in Fig. 4.

The cross sections and their dependence upon energy and fragment atomic number are of particular importance to demonstrate their compound nucleus origin. When a compound nucleus is about to decay, it is offered many channels which will be choosen proportionally to their associated phase space. In particular, neutron, proton, and alpha decay, because of their small associated barriers are the dominant decay channels with which complex fragments must compete. Thus the cross section associated with the emission of any given fragment reflects this competition. In Fig. 5 an example of absolute charge distributions is given, together with a calculation performed with a compound nucleus decay code (GEMINI)[4] which follows the decay of the compound nucleus through all the channels including complex fragment emission. The code reproduces the absolute cross sections and their charge and energy dependence very accurately, thus confirming compound nucleus decay as the dominant mechanism in this energy range.

Coincidence data confirm the binary nature of the decay. The Z_1 - Z_2 scatter plots (see Fig. 6) show the diagonal band characteristic of binary decay. The hatched area is the predicted locus of events after correcting for sequential evaporation from the primary fragments. The spectra associated with the sum $Z_1 + Z_2$ show a rather sharp peak very near the value of Z_{total} indicating again that there is only a small charge loss and that most of the total charge available in the entrance channel is to be found in the two exit channel partners.

All the evidence produced above is but a small sample of the evidence available for compound nucleus emission of complex fragments at bombarding energies up to 50 MeV/u. So far binary decay has dominated the scene while multifragmentation has been conspicuously absent. Yet it is not unreasonable to envision at even higher energies exit channels presenting more than two main fragments. Does that mean, automatically, that the role of the compound nucleus is over? Most likely not.

Multifragmentation and Nuclear Comminution

The evidence presented so far illustrates the emission of complex fragments through binary compound nucleus decay. If there is enough excitation energy available, the primary fragments are also very excited and can have a significant probability of decaying in turn into two more fragments. In this way, which is a very conventional way, one can foresee one possible

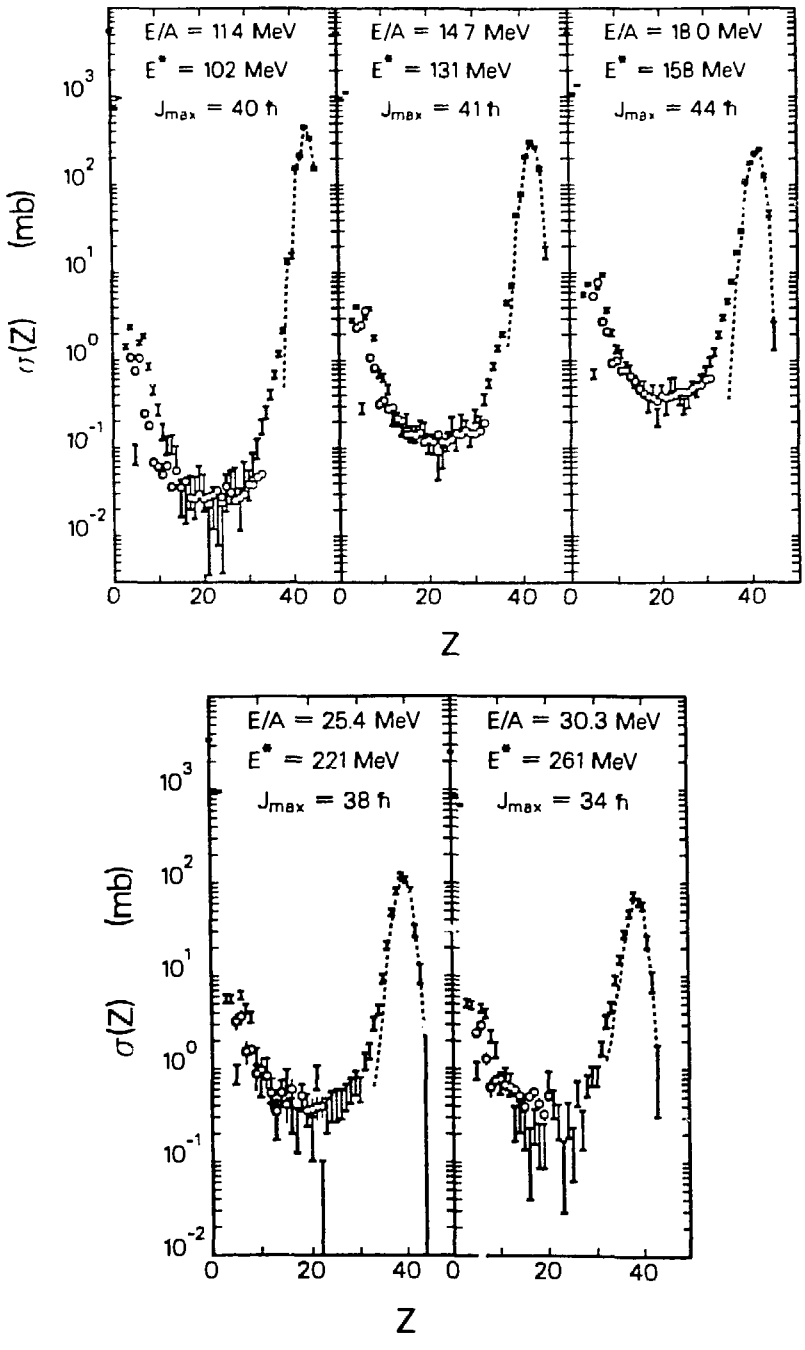

Fig. 5 Comparison of experimental and calculated charge distributions for the $^{93}Nb + ^{9}Be$ reaction at E/A = 11.4, 14.7, 18.0, 25.4 and 30.3. The experimental data are indicated by the hollow circles and the values calculated with the code GEMINI are shown by the error bars. The dashed curve indicates the cross sections associated with classical evaporation residues which decay only by the emission of light particles ($Z \leq 2$). Note the value of the excitation energy (E^*) corresponding to complete fusion and the value of J_{max} assumed to fit the data.

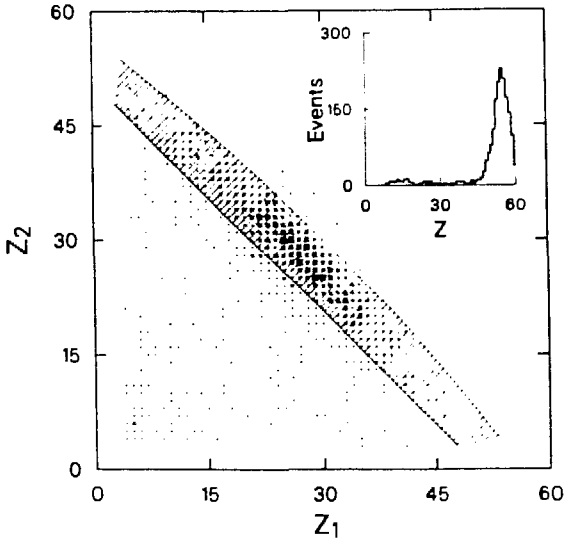

Fig. 6 Scatter plots of the coincidence events, Z_1 - Z_2, detected in the two telescopes on opposite sides of the beam, for the ^{139}La + ^{12}C reaction at 50 MeV/u. The hatched area is the predicted locus of events after correcting for sequential evaporation from the primary fragments. The distributions of the sum of the charges (Z_1 + Z_2) is shown in the inset.

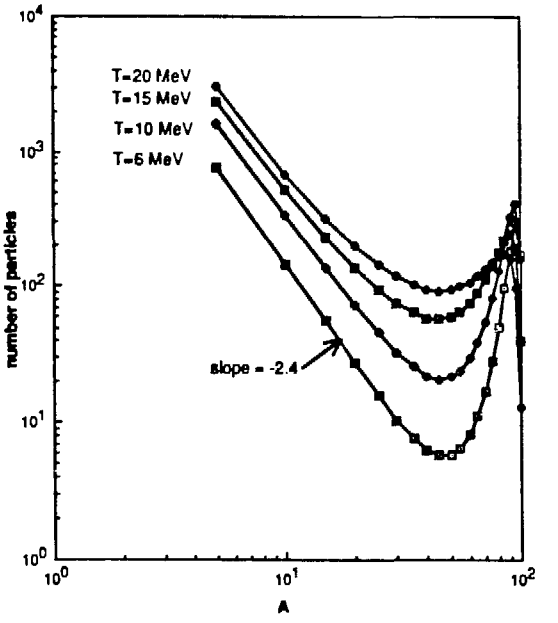

Fig. 7 Theoretical mass distributions from comminution calculations of the dexcitation of a mass 100 compound nucleus at several temperatures. Notice the beautiful power law behavior at small masses.

explanation for multifragmentation, namely that arising from sequential binary decay. We can expect that this mode will be responsible for a predictable and substantial background to other multifragmentation mechanisms if any.

This process of sequential binary decay, controlled at any stage by the compound nucleus branching ratios, we call "nuclear comminution".[1] The calculations of the resulting mass distributions are trivial although tedius and time consuming. We have tried to simulate the process by assuming a potential energy curve vs mass asymmetry (ridge line) with a maximum at symmetry of 40 MeV and with the value of 8 MeV for the extreme asymmetries. The primary yield curve is taken to be of the form:

$$Y(A) = K \exp\left[- V(A)/T(A) \right] . \qquad (1)$$

Each of the resulting fragments is assumed to have a similar ridge line and a properly scaled temperature and is allowed to decay accordingly, until all the excitation energy is exhausted. The resulting mass distributions for a series of initial temperatures are shown in Fig. 7. The log-log plots show an exquisite power law dependence for the low masses with exponents around 2.3 - 2.4 which, incidentally, are very close to the exponent expected for the liquid vapor phase transition at

the critical temperature. This result shows that a power law dependence is not a unique diagnostic feature of liquid vapor equilibrium, but rather is an apparently "generic" property arising even from sequential binay decay or comminution. A more realistic calculation with the statistical code GEMINI is shown in Fig. 8. Even in this calculation, the power law is evident. With this code it is possible to calculate the excitation energy dependence of the binary, ternary, quaternary decays, etc. as shown Fig. 9. These kinds of excitation functions should be of help in verifying the mechanism of nuclear comminution in the experimental data.

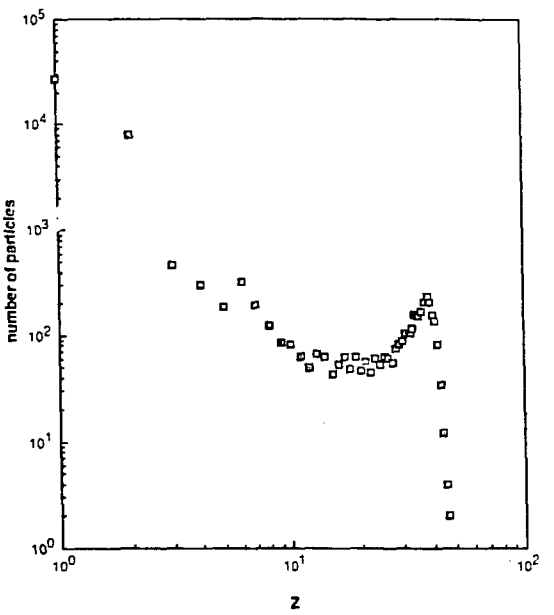

Fig. 8 A plot of the predicted charge distribution associated with the fragments produced in the deexcitation of a ^{139}La compound nucleus at 1100 MeV and J = 50ħ. The calculations were done with the statistical model code GEMINI.

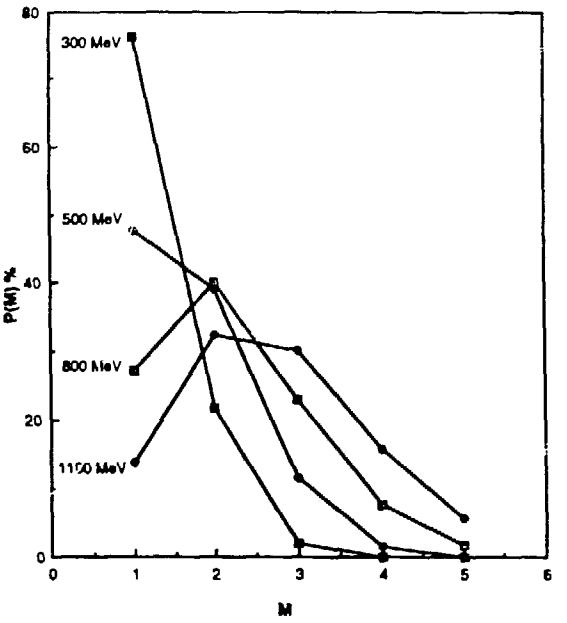

Fig. 9 A plot of the predicted multiplicity distribution of fragments with A > 4 associated with the deexcitation of a ^{139}La compound nucleus at four different excitation energies. The calculations were done with the statistical model code GEMINI.

Statistical γ-ray Emission

High energy γ rays associated with intermediate energy ion reactions were studied initially in order to observe the theoretically predicted "coherent bremsstrahlung"[5,6] associated with the collective deceleration of the two partners in the collision. Nature's lack of cooperation forced the interpretation of the data back to the less exalted "incoherent nucleon-nucleon bremsstrahlung"[5,6]

which had at least the glamour of being associated with the entrance channel. This interpretation is probably correct in many cases. However, in reviewing the data available in the literature, we were struck by the possibility that some of the high energy γ rays could come from some excited compound nuclei present in the exit channel. Unfortunately in all of these experiments the exit channels were too poorly characterized to permit any serious analysis of this sort.

Eventually we found an experiment, ^{100}Mo + ^{100}Mo at 20 MeV/u,[7] where the exit channel was very well characterized. In this reaction the two nuclei undergo a deep inelastic collision. The dissipated energy which may amount to as much as 800 MeV (400 MeV for each fragment!) is disposed of mainly by sequential light particle emission. This emission is a true evaporation from the two deep inelastic fragments and has been studied in detail as a function of exit channel kinetic energy.[8] At times these excited fragments emit complex fragments giving rise to a 3-body and a 4-body exit channel.[9] This emission is also statistical and is in competition with the main decay channels like n, p, and a particle emission. This can be inferred from the probability of 3-body decay as a function of dissipated energy. From this dependence, we can see whether we are dealing with a statistical process. A plot of the log of the probability vs fragment excitation to the -1/2 power should give a linear dependence. This is very clearly visible in Fig. 10, where the data were taken from three different bombarding energies for the same reaction. All this is to prove that

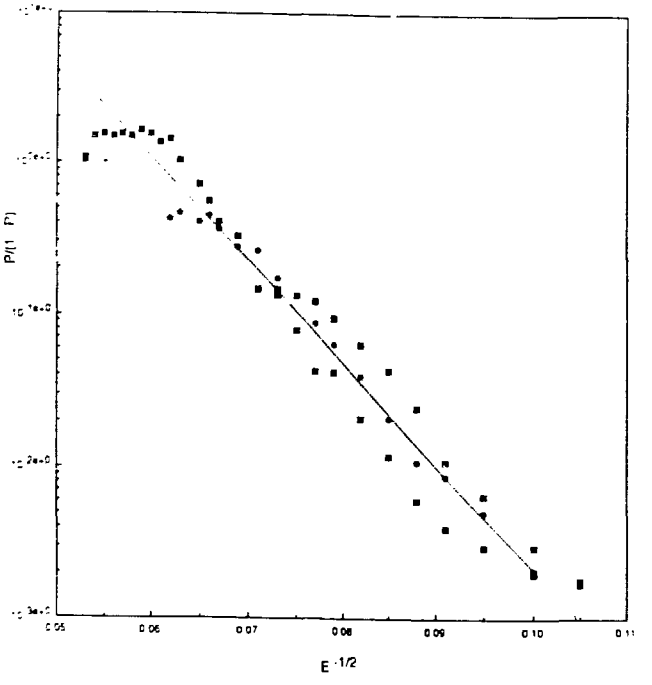

Fig. 10 Dependence of the relative three body emission probability P upon excitation energy for the reaction ^{100}Mo + ^{100}Mo at various bombarding energies.[9] The linearity of this particular plot indicates statistical emission.

there are honest-to-goodness compound nuclei in the exit channel which decay as such, not only insofar as the common n, p, and α particle channels are concerned, but also with respect to the more exotic complex fragment emission as well.

Coming back to γ rays, the experiment measured them up to 60 MeV of energy and for 10 bins of total kinetic energy loss. The ungated γ rays look very much like those measured in other reactions and interpreted in terms of nucleon-nucleon bremsstrahlung. However, when these spectra are gated with different bins of total kinetic energy loss (TKEL), a very surprising picture emerges, suggesting an exit channel rather than an entrance channel origin.

In Fig. 11 three spectra are shown covering the total kinetic energy loss range of the experiment. Notice how the high excitation energy bin is associated with the stiffest γ-ray tail while the low excitation energy bin is associated with the softest. In Fig. 12a this is shown better by plotting the slope parameters vs the TKEL. The square root-like dependence is very suggestive and one is tempted (and should be!) to interpret the slope parameter as a temperature. Similarly, the integrated multiplicites with two different lower bounds of 15 and 30 MeV γ-ray energies shown in Fig. 12b, when plotted vs the fragment excitation energy, reveal a dependence typical of compound nucleus decay.

This evidence does not come totally unexpected. We <u>know</u> that there are two compound nuclei in the exit channel. We know that they decay as such by light particle emission and by complex fragment emission. Why should they not decay by γ-ray emission? <u>Perhaps</u> there are additional sources for the γ rays, like incoherent bremsstrahlung, etc., but we know <u>for sure</u> that <u>those compound nuclei must emit γ rays.</u> So let us calculate this emission. We can calculate the γ decay width in an "almost" model independent way from detailed balance and the inverse cross section:

$$P(\varepsilon_\gamma) = \frac{\Gamma(\varepsilon_\gamma)}{\hbar} = \frac{8\pi}{c^2 h^3 \rho(E)} \sigma(\varepsilon_\gamma)\, \rho(E-\varepsilon_\gamma)\, \varepsilon_\gamma^2 \qquad (2)$$

$$\cong \frac{8\pi}{c^2 h^3} \sigma(\varepsilon_\gamma)\, \varepsilon_\gamma^2\, e^{-\varepsilon_\gamma/T} \qquad (3)$$

The inverse cross section is fairly well known experimentally. In the low energy region between 6 - 20 MeV, it is dominated by the giant dipole resonance, while above that the quasi deuteron mechanism prevails. The temperature T can be calculated from the excitation energy as $E_x = aT^2$.

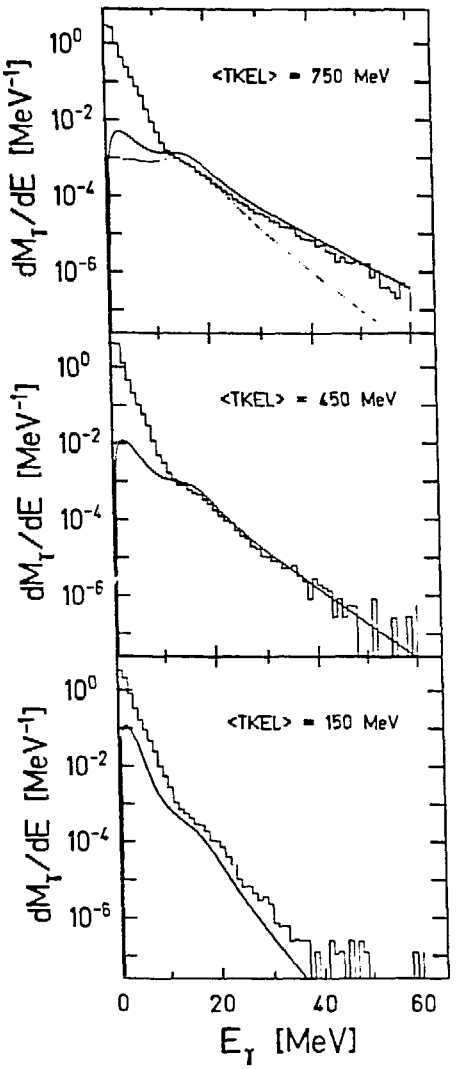

Fig. 11 Gamma ray spectra for three different bins in total kinetic enegy loss. The solid curves represent statistical model calculations. The dotted curve curve is obtained in the same way as the solid curve except for the elimination of the quasideuteron component in the γ-cross section.

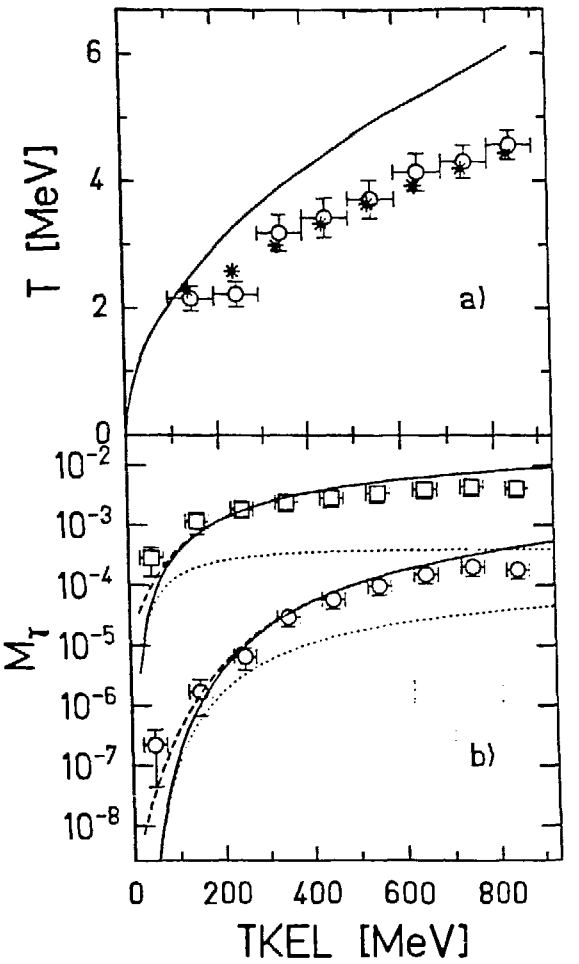

Fig. 12 a) "Temperatures" of Boltzman fits to measured (open circles) and calculated (stars) γ spectra. The solid line denotes the primary temperature of the fragments which has been calculated from the energy loss. b) Experimental and theoretical multiplicities of hard photons with energies ≥ 15 (squares) and 30 McV (circles), respectively. The different lines are the result of a statistical model calculation and show the first chance contribution (dotted line), the sum over all generations (solid line) and the effect of the experimental binning of the excitation energy (dashed line).

In the actual decay, γ emission competes with n, p and α particle emissions which can be calculated in a similar fashion. In this way we can generate the "first chance" γ ray emission probability vs excitation energy:

$$P_{\gamma}(\varepsilon_{\gamma}) = \frac{\Gamma(\varepsilon_{\gamma})}{\Gamma_{T}} \cong \frac{\Gamma(\varepsilon_{\gamma})}{\Gamma_{n} + \Gamma_{p} + \Gamma_{\alpha} + \ldots.} \qquad (4)$$

At this point one proceeds trivially to calculate the 2nd, 3rd etc. chance emission probability. The overall sum can be compared with experiment. In Fig. 11 we see that this calculation reproduces the spectra from 15 MeV γ-ray energy up to 60 MeV almost perfectly for all the energy bins, both qualitatively and quantitatively. The slope parameters can also be compared with the data. This is shown in Fig. 12a and again the fit is essentially perfect. The solid line in the figure represents the initial calculated temperature. The actual slope parameter is somewhat smaller due to the substantial presence of higher chance emission at the highest energies. Similarly the integrated γ-ray multiplicities are equally well reproduced by the calculation, as can be seen in Fig. 12b. The unescapable conclusion is that all of the γ rays observed experimentally actually come from the statistical emission of the fragments. No room is left here for any other mechanism!

Somebody might object by saying, and perhaps by showing, that "other" theories fit the data almost as well and that there is no reason to choose one "theory" over another. The point is that our calculation is really no theory to speak about. We know that there are two compound nuclei in the exit channel, emitting light particles and complex fragments, because their decay products have been measured and their statistical properties verified. Therefore, we know that these compound nuclei must also emit γ rays. All we have done is to calculate, as it were, the "background" γ rays coming from compound nucleus decay. Any other "theory" can be tested only after this "background" has been substracted. In this case nothing is left and the matter is settled.

It would be interesting to check how much of the π^{o},$\pi^{\pm}$ production in intermediate heavy ion reactions can be explained in terms of emission from the compound nuclei present in the exit channel. Unfortunately, this will have to wait for more complete experiments, although it is an easy guess that, in certain low energy reactions, the compound nucleus contribution may not be negligible and must be evaluated.

Conclusions

There is one thing worse then not discovering a new process or mechanism, and that is of discovering it when it is not there!

Acknowledgements

This work was supported by the Director, Office of Energy Research, Division of Nuclear Physics of the Office of High Energy and Nuclear Physics of the U. S. Department of Energy under Contract DE-AC03076SF00098.

References

1) L. G. Moretto and Gordon J. Wozniak, to be published in Progress in Particle and Nuclear Physics, LBL- 24558, and references therein.
2) L. G. Sobotka et al., Phys. Rev. Lett. **51**, 2187 (1983).
M.A. McMahan et al., Phys. Rev. Lett. **54**, 1995 (1985).
3) L. G. Moretto, Nucl. Phys. **A247**, 211 (1975).
4) R. J. Charity et al., Phys. Rev. Lett. **56**, 1354 (1986).
R. J. Charity et al., Nucl. Phys. A, in press, LBL-22447 (1988).
R. J. Charity et al., LBL-22448 (1988).
D. R. Bowman et al., Phys. Lett. **B189**, 282.
5) W. Cassing et al. Phys. Lett. **181B**, 217 (1986).
6. H. Nifenecker et al. Nucl. Phys. **A442**, 478 (1985).
7) N. Herrmann et al. to be published in Phys. Rev. Lett.
8) K. D. Hildenbrand et al. Proc. Int. Workshop on Gross Properties of Nuclei and Nuclear ReactionsXIII, Hirschegg, 111 (1985).
9) A. Olmi et al. to be published Europhys. Lett. (1988). Also see contribution by A. Olmi in these proceedings (1988).

ENERGY DEPENDENCE OF TERNARY PROCESSES IN DISSIPATIVE COLLISIONS

Alessandro OLMI
Istituto Nazionale di Fisica Nucleare
Sezione di Firenze
c/o Dipartimento di Fisica dell'Università
50125 Florence, Italy

Abstract: In symmetric systems at bombarding energies between 12 and 24 MeV/u an increasing yield of ternary processes has been observed. They are however related more to the total excitation of the system than to the bombarding energy itself, thus suggesting that in this energy range the ternary processes reflect a property of the decay of highly excited nuclei, rather than the dynamics of the reaction.

1. Introduction

In heavy ion reactions the high energy regime (E_{lab} >>100 MeV/u) is dominated by the 2–body collisions among nucleons and characterized by complicated events with high multiplicities of light particles and light nuclei.

On the contrary, the low energy regime (E_{lab} <10 MeV/u) is best described in terms of mean field and characterized by such reaction mechanisms as the complete fusion, leading to one single piece of excited nuclear matter, and the socalled deeply inelastic (or dissipative) collisions, which are essentially of binary nature.

At intermediate energies, aspects from both extremes can merge together, leading to a rather complex transition. For these reasons, a proper understanding of the intermediate energies still represents a hard task both for theories and for experiments. Indeed, when the bombarding energy of nucleus–nucleus collisions is raised from the low energy domain (<10 MeV/u) of deeply inelastic collisions towards the higher energy regime, it becomes increasingly difficult to isolate the signatures of the deexcitation of the system from those of the preceeding interaction. The time scales of the two processes become comparable and little is generally known about the decay of nuclei at large excitation energies (E^*/A >2 MeV/u), besides that heavier and heavier clusters can be emitted with increasing probability. Nevertheless, the disentanglement of dynamical aspects of the collision from the decay patterns of the products remains a very important piece of information.

High excitation energies can be easily reached in dissipative collisions. For example, the energy above the barrier available in the collision of a symmetric system with $A_1 = A_2 \approx 100$ at 24 MeV/u amounts to about 1 GeV. If this energy is completely dissi-

pated, excitation energies per nucleon of $E^*/A \approx 5$ MeV/u can be reached, corresponding to temperatures of 6 MeV or higher. That such high excitations can be actually obtained in dissipative collisions will be shown later.

The present contribution focuses on the study of the heavy fragment multiplicity, as the bombarding energy is raised step by step from 12 to 24 MeV/u. An evolution is found from a pure binary mechanism to processes with three or four heavy reaction products, which may eventually lead to the higher and higher multiplicities observed at high energies. Nonetheless, the reseparation of the system into two massive fragments is still the dominant part of the total cross section. The main result is that the measured probability P_3 (defined as the ratio of the 3–body to the sum of the 3– plus 2–body cross section) is found to scale with excitation energy rather than with bombarding energy.

2. Set–up and analysis

In order to obtain reliable and quantitative results, extensive Monte Carlo simulations with realistic parametrisation of the reaction mechanisms have to be performed. However, even more important is the use of an optimized experimental set-up covering a very large solid angle.

The experimental set-up used in the experiments reported here is sketched in fig. 1a). It consists of twelve identical large–area position–sensitive parallel plate avalanche detectors (PPAD), mounted in an axially symmetric configuration around the beam axis [1]. The scatter plot of fig. 1b) is a projection of the set–up onto a unit sphere: the distance from the origin represents the scattering angle θ_{lab} and the polar angle represents the angle ϕ. It can be seen that the detectors cover $\approx$ 75 % of the forward hemisphere, where almost all reaction products of a symmetric system are emitted.

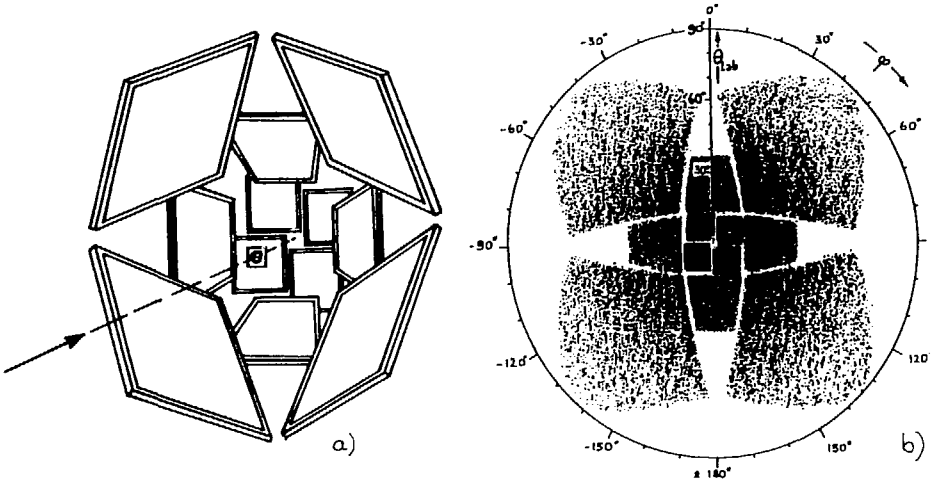

Fig.1: Schematic view a) and polar projection b) of the experimental set–up.

Behind the PPAD, 24 gas plastic telescopes were used for the identification of light charged particles and of heavier clusters. However the present report will concentrate on the results obtained only from the PPAD.

The investigated systems are: ^{100}Mo + ^{100}Mo at the four bombarding energies of 12, 14.7, 18.7 and 23.4 MeV/u and ^{120}Sn + ^{120}Sn at 18.4 MeV/u. The first two energies of the Mo+Mo system had been measured in a previous experiment with a somewhat different set-up [2].

In all cases an exclusive measurement of 2, 3 and 4 heavy fragments was performed, and from the measured velocity vectors of all fragments triple differential cross sections $d^3\sigma/dE.dA.d\theta$ could be deduced by means of the kinematic coincidence method.

It has to be noticed that the measured velocity vectors differ from the original primary ones because of perturbations, caused primarily by the emission of light particles, but also by the passage of the fragments through the target matter and by the experimental resolution. The hypothesis on which the kinematic coincidence method is based, is that the direction and length of the velocity vectors are not changed, *on the average*, although they are certainly changed on an event-by-event basis. Therefore, if the light particles are emitted, within a good approximation, isotropically by the fragments and a correction for the mean energy loss in the target is applied, this method allows the direct reconstruction of primary quantities, again *on the average*.

The measurement of all (perturbed) velocity vectors gives a two-fold and one-fold overdetermination of the events with two and three outgoing heavy fragments respectively. A new approach has then been developed to take into account the whole experimental information in a selfconsistent and statistically meaningful way. Remembering that in each event the measured velocities $\vec{v}_i^{\,exp}$ do not coincide with the primary velocities $\vec{v}'_i$, but are only (in the jargon of statistics) their unbiased estimators, one can consider both the primary masses m'_i and the primary momenta $\vec{p}'_i = m'_i \times \vec{v}'_i$ as unknowns. The best estimate of these unknowns is then obtained by minimizing the expression $\Delta^2 = \Sigma_i\ \alpha_i \times |(m'_i \times \vec{v}_i^{\,exp} - \vec{p}'_i)|^2$ under the constraints of conservation of mass and linear momentum (α_i are statistical weights and are here set to 1). Practically, one has to solve the linear system resulting from:

$\Sigma_i\ \vec{p}'_i = \vec{p}_{beam}$ i = 1,2 for 2-body events

$\Sigma_i\ m'_i = M_{tot}$ 1,2,3 " 3-body "

$\Delta^2(m'_i, \vec{p}'_i)$ is a minimum

This version of the kinematic coincidence method has the following advantages:

- it gives fully selfconsistent solutions m'_i and $\vec{p}'_i$, which satisfy conservation laws;
- it allows the treatment of 2- and 3-body events on an equal footing;
- the quantity Δ^2 has a clear statistical interpretation.

In fact, if Δ^2 is the sum of squares of normally distributed random variables with zero mean values and comparable variances, then Δ^2 is expected to have a χ^2–shaped distribution, with two and one degree of freedom for the 2- and 3-body kinematics respectively (as many degrees of freedom as redundancies).

The solid histograms of fig.2 show the distributions of Δ obtained for the 2–body events measured in the reaction ^{100}Mo + ^{100}Mo at 18.7 MeV/u. The four sections of fig.2 correspond to four different windows on the total kinetic energy loss (TKEL) of the system, from the quasi–elastic region down to the fully relaxed one. One can notice that:

- the curves have indeed the shape expected for a χ–distribution with two degrees of freedom;

- the widths of the peaks increase with increasing energy-loss, thus indicating that the main source of perturbation is the light particle emission;

- there are flat tails of increasing intensity at high energy-losses.

These high-Δ tails have to be attributed to the background of 3–body events, in which only two fragments have been detected; this is an unavoidable source of background for any set-up covering a limited solid angle. Indeed, the random exclusion of one fragment in the measured 3–body events and the analysis of the remaining two fragments with the binary kinematics yields the dotted distributions of fig. 2. They have been normalized with one single factor. A reduction of the solid angle coverage has the effect of increasing the importance of these tails, thus justifying the need for an experimental set–up with large acceptance.

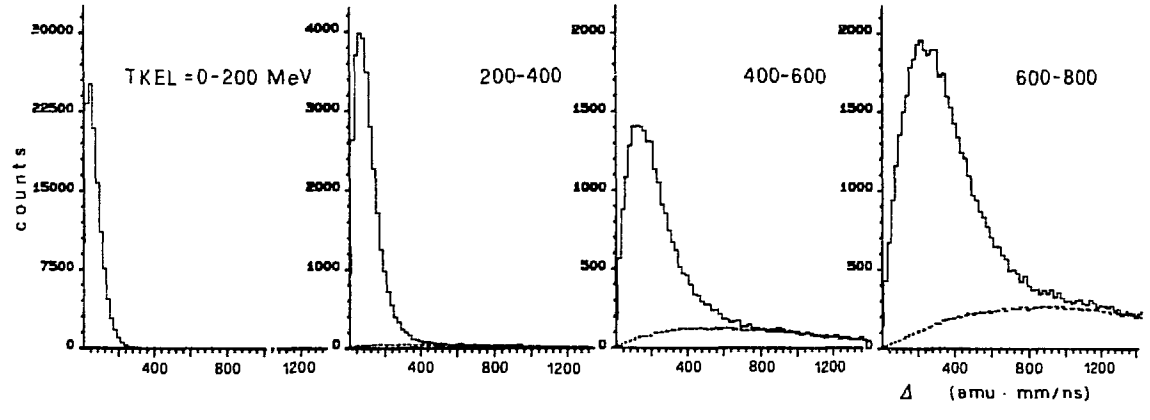

Fig.2: Distributions of Δ (see text) for binary events in different energy–loss bins from the reaction $^{100}Mo + ^{100}Mo$ at 18.7 MeV/u. The dashed lines represent the estimated background of (incompletely measured) 3–body events as explained in the text.

With this procedure, the background of (incompletely measured) 3–body events has been subtracted from all distributions of binary events shown in the next pictures.

In a similar way also the 3–body data have been corrected for the background of 4–body events. Finally, all experimental data have been corrected for the experimental geometry by means of Monte Carlo simulations.

3. Results

Fig.3 shows, as an example, the preliminary results of the double differential cross section $d^2\sigma/dE.dA$ for the binary events measured in the reaction ^{100}Mo + ^{100}Mo at 23.4 MeV/u. One can recognize the typical behaviour of the "diffusion–plot" in dissipative collisions, with the increasing large broadening of the mass distribution with increasing energy–loss.

The data presented in fig.3 show that binary events are found even at energy losses as large as 1 GeV, corresponding to very high excitation of the system.

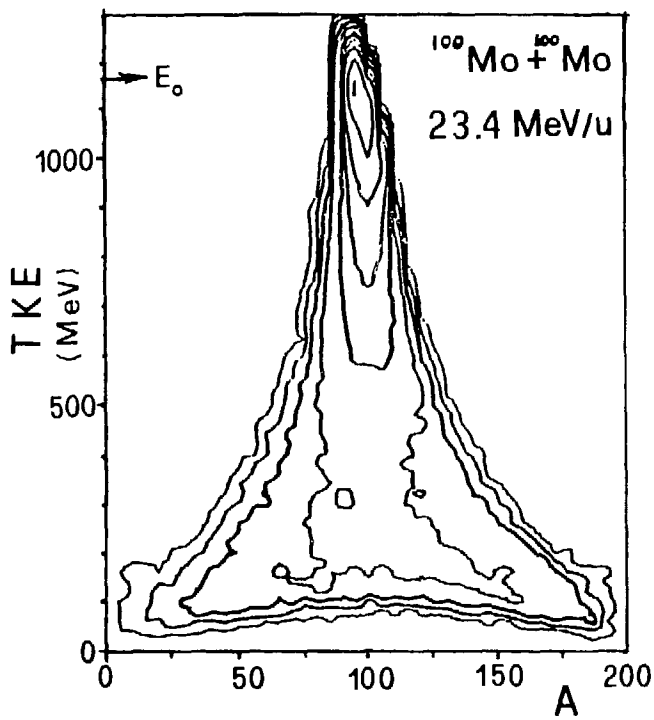

Fig.3: Preliminary correlation of TKE vs. A for the binary events of the system $^{100}Mo+^{100}Mo$ at 23.4 MeV/u after subtraction of 3–body background and correction for geometric efficiency. The contour lines are calibrated in absolute units and correspond to .4, 1, 2, 4, 10, 20, 40, 100 and 200 $mb/(MeV \times amu)$.

It has to be noted here that no real discontinuity is expected between the yields of light particles and that of the lighter fragments. For this reason, and also because the intrinsic efficiency of the parallel plate detectors is expected to decrease gradually for lighter fragments, only fragments with mass $A > 20$ will be considered.

The background-subtracted and efficiency-corrected 2–body and 3–body TKE spectra obtained for the system ^{100}Mo + ^{100}Mo at 12, 14.7, 18.7 and 23.4 MeV/u are shown in fig.4. One can observe that:

— 3–body events are concentrated at low TKE-values (high energy-loss);

— the yield of 3–body events increases with increasing bombarding energy and becomes comparable or even higher than the 2–body yield.

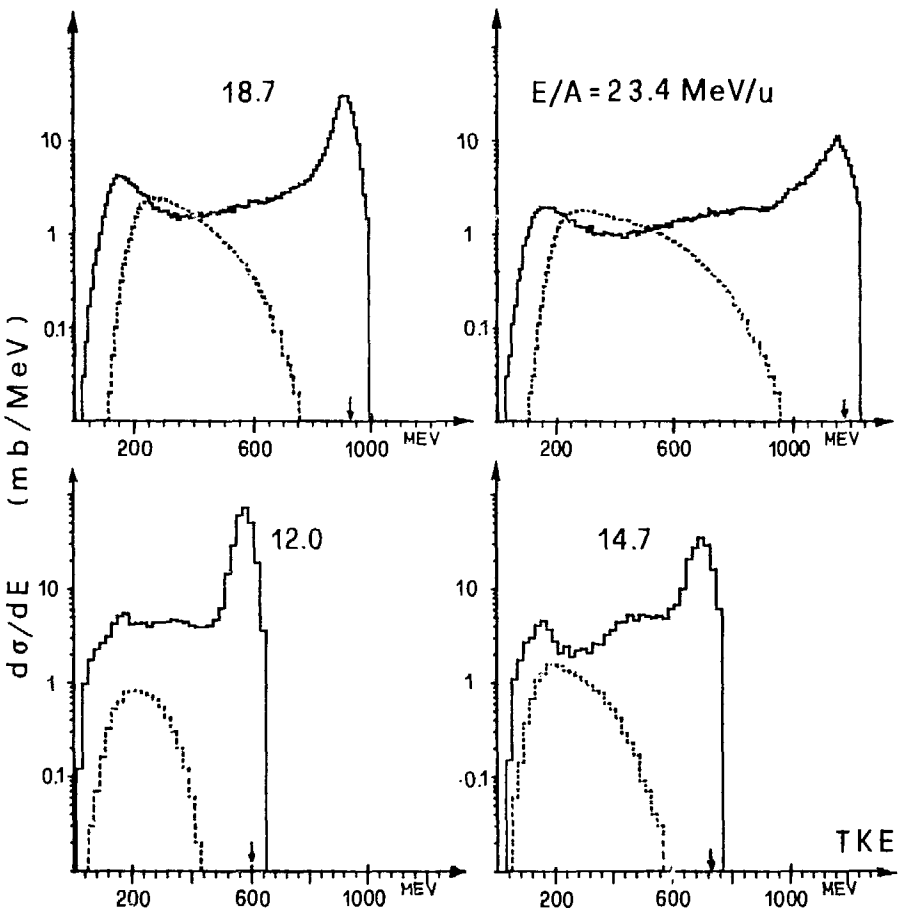

Fig.4: Total kinetic energy spectra for 2–body (solid curve) and 3–body events (dashed curve) in the collision ^{100}Mo + ^{100}Mo at four bombarding energies. The data are integrated over angle θ_{cm} and mass $A > 20$, after background subtraction and geometry correction.

The binary channel is still the dominant one and even at 18.7 and 23.4 MeV/u it seems to account for a large part of the reaction cross section. However, a reliable and quantitative estimation of the binary yield is difficult, as it requires a good separation of elastic and inelastic events near the grazing angle.

The mass-, energy- and angle-integrated yields of 3–body events amount to about 4, 9 and 14% of the estimated total reaction cross sections σ_R at 12, 14.7 and 18.8 MeV/u respectively. Preliminary data indicate that the 3–body yield still amounts to about 14% of σ_R in the reaction ^{100}Mo + ^{100}Mo at 23.4 MeV/u, whereas it reaches about 22% of σ_R in the reaction ^{120}Sn + ^{120}Sn at 18.4 MeV/u; 4–body events seem to account for only 2 or 3% of σ_R at the highest bombarding energies of the present investigation.

The reaction mechanism leading to a 3–body channel could be of two types, either an "instantaneous" division of the total system into three pieces (which should probably reflect the dynamics of the interaction), or a sequential process with a first binary division followed by the scission into two pieces of one excited fragment (this case should be related more to the decay of the system). However, one can distinguish between different reaction mechanisms only from their different population of the phase space and not on an event–by–event basis.

In the present work, the 3–body events seem to be mainly produced in a two-step process. In fact it was found that in many cases two of the three fragments present some degree of correlation in their relative velocity and relative center-of-mass angle, suggesting a fission-like second scission, as already observed at lower energy [3]. A Monte Carlo simulation showed that this hypothesis is compatible with the data. However, it showed also that, at high energy losses, it becomes increasingly difficult to determine which two fragments, out of the three produced, belonged to the second step, and that a reliable decision is therefore possible only for a subset of the data.

In order to compare the 2– and 3–body yields on the basis of the energy loss TKEL in the first reaction step, it is necessary to subtract from the measured total kinetic energy of the three fragments, the additional kinetic energy released in the second step E_{rel}. For those 3–body events in which it was possible to assign unambiguously two out of the three measured fragments to a fission–like process in the second step, a broad distribution of E_{rel} with a mean value in agreement with the Viola–systematics was found. In order to treat the totality of the events, including those in which a unique assignement was not possible, an average value of E_{rel} of 60 MeV was subtracted from the measured total kinetic energy value.

The ratio P_3 of the 3–body yield divided by the sum of the 2– and 3–body yields is shown in fig. 5 for all the measured systems. P_3, which represents the probability of having a (second) scission of one of the two fragments produced in the first reaction step, can reach the rather high values of 50 % at the highest energy–losses.

However, the most important fact displayed in fig.5 is that the curves obtained at the three lowest bombarding energies coincide within the experimental uncertainties (the experimental resolution, the analysis method and the efficiency corrections are estimated to result in systematic errors of the order of 50%). Therefore, the relevant quantity for the abundance of these processes seems to be not the relative velocity of the collision, but rather the dissipated kinetic energy, which is transformed into excitation energy of the reaction products. P_3 appears to be related more to the decay properties of the excited primary products than to the dynamics of the reaction. This result is practically independent of the applied subtraction of 60 MeV from the 3-body TKE spectra, as a different value (or no subtraction at all) would mainly result in a shift of the abscissa of fig.5, the same for all three curves.

The preliminary data at 23.4 MeV/u seem to indicate that the 3-body probability P_3 is somewhat lower, and this fact, if confirmed by the final evaluation, could be an indication that dynamic effects begin to play a role at these higher bombarding energies.

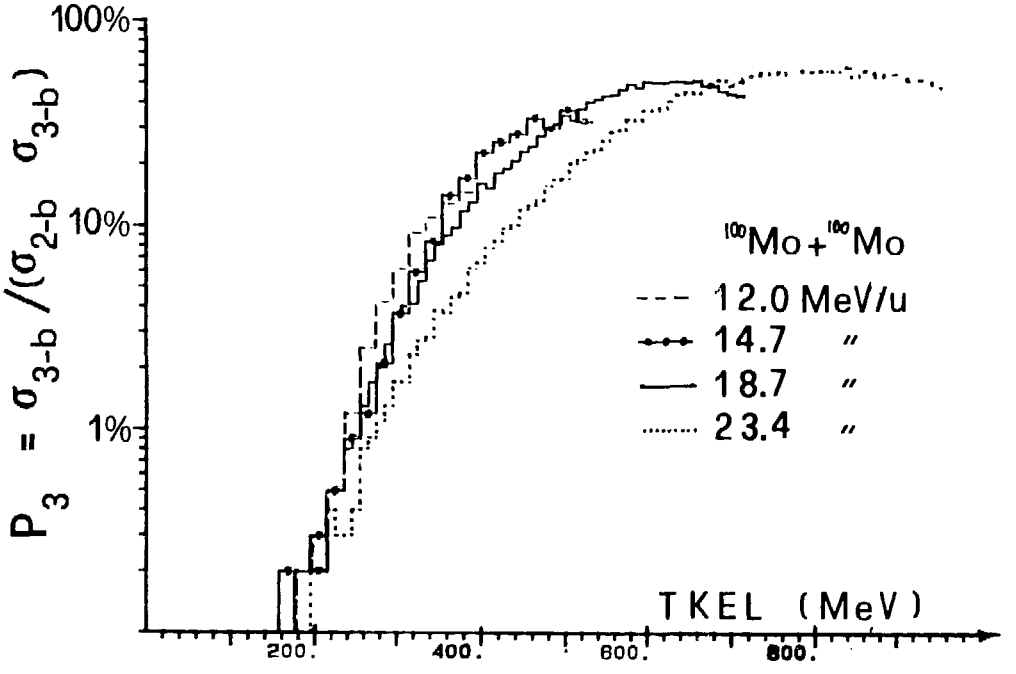

Fig.5: Ratio P_3 of 3-body to the sum of 2- and 3-body yields measured as a function of the total kinetic energy-loss TKEL released in the first reaction step, for the system ^{100}Mo + ^{100}Mo at four incident energies (the data at 23.4 MeV/u are still preliminary).

4. Conclusions

Non–binary exit channels in the collision of symmetric systems between 12 and 24 MeV/u have been studied.

Binary events still account for the larger part of the reaction cross section. However, with increasing excitation energy deposited into the system, an increase of the yield for ternary massive products has been observed, whereas 4–body events still represent a minor channel.

The similar rise of the relative yield of ternary events (as a function of excitation energy) for different beam energies indicates that their production mechanism reflects more a property of the decay of the excited system than of the dynamics of the interaction.

The slower rise of P_3 deduced from still preliminary data at 23.4 MeV/u could point to the appearence of some dynamical effects. The evaluation of the data measured with the gas–plastic telescopes will add an important piece of complementary information.

An extension of the present quantitative and systematic study toward still higher bombarding energies would be desirable to understand the development of low–energy reaction mechanisms into the multifragmentation region.

Aknowledgement: The results shown in this paper were obtained in several experiments performed in collaboration with P.R. Maurenzig and A.A. Stefanini of the University of Florence, and with J. Albinski, R. Bock, R. Freifelder, A. Gobbi, S. Gralla, N. Herrmann, K.D. Hildenbrand, J. Kuzminski, W.F.J. Müller, M. Petrovici, H. Stelzer and J. Toke of the Gesellschaft für Schwerionenforschung (GSI) of Darmstadt. The recent experiment at the UNILAC and at GANIL were performed in collaboration with J. Galin, D. Guerreau, U. Jahnke (GANIL) as well as J.C. Adloff, B. Bilwes, R. Bilwes, G. Rudolf (CRN Strasbourg) and M. Gnirs, D. Pelte and J. Wessels (University Heidelberg). Thanks are also due to P.G. Bizzeti, M. Bini (University of Florence) for many helpful discussions and suggestions.

References

[1] R. Freifelder et al., GSI Annual Report 1986, p.51

[2] A. Olmi et al., Europhysics Letters 4 (1987) 1121
A. Olmi, Nuclear Physics **A471** (1987) 97c

[3] P. Glässel et al, Zeit. f. Phys. A310(1983)189

CO-EXISTENCE OF EQUILIBRATED AND NON-EQUILIBRATED SOURCES OF COMPLEX FRAGMENTS AT INTERMEDIATE ENERGIES*

V.E. Viola
Department of Chemistry and IUCF
Indiana University
Bloomington, IN 47405

Understanding the formation and decay of hot nuclear matter at low-to-intermediate energies presents many complex challenges to both theorists and experimentalists.[1] From the point of view of reaction dynamics this effort is complicated by the interplay between mean field and nucleon-nucleon collision degrees of freedom as the projectile velocity transcends the Fermi velocity in nuclear matter. The possibility of particle and fragment emission from the colliding composite system prior to full mass and energy equilibration leads to final states characterized by a broad distribution of excitation energy and angular momentum, as well as Z and A. This situation demands that inclusive data be interpreted with caution and imposes the need for well-focussed exclusive studies in order to define the emitting source and associated reaction mechanism. A knowledge of the source properties is equally vital to description of the statistical decay of fully equilibrated residual nuclei produced in the collision stage - which involves the emission of species ranging for nucleons to intermediate-mass fragments (IMFs) to fission fragments. Of great current interest is the possibility of multifragmentation from highly excited systems.[1] Describing these phenomena places further demands on our understanding of both single-particle and collective properties of nuclei under extreme conditions.

The emission of intermediate-mass fragments provides a particularly valuable probe of highly excited nuclear matter. In this paper a systematic set of measurements is described for IMF formation across the E/A ≈ 20-100 MeV range. First, inclusive excitation function data for the ^{14}N + ^{nat}Ag system are examined to illustrate the general features of these reactions.[2] Similar results exist for the ^{3}He + ^{nat}Ag system.[3,4] With this information as a guide, the linear momentum balance associated with IMF formation in the

*Research supported by the U.S. Department of Energy Contract and the National Science Foundation.

E/A = 35 MeV ^{14}N + ^{232}Th and E/A = 90 MeV ^{3}He + ^{232}Th reactions is investigated via coincidence studies with angle-correlated fission fragments. Specific goals of this analysis are: 1) to establish the existence and relative strength of equilibrated and non-equilibrated emission mechanisms and 2) to search for evidence of multifragmentation in this region of excitation energy.

1. Inclusive Studies

The ^{14}N + ^{nat}Ag excitation function measurements were performed at the National Superconducting Cyclotron Laboratory at Michigan State University using beams of E/A = 20, 30, 40 and 50 MeV.[2] Telescopes for detection of Z = 3-14 fragments consisted of gas-ionization chamber/silicon surface barrier/Si(Li) detectors fixed at angles of θ = 60°, 90°, 120° and 165° and a four-element silicon telescope which was rotated from 20° to 40° at each energy. A high purity silver target was employed and all experimental variables were kept constant throughout the experiment, except the forward detector and the beam energy, in order to insure highly systematic data. The results presented here are in good agreement with more limited data sets for this system.[5,6]

The energy spectra obtained in these studies exhibit characteristic IMF features as a function of angle and atomic number; i.e. the spectra evolve from rather flat pre-compound-like behavior at forward angles to steep compound-nucleus-like character at extreme backward angles for all Z values (except near the grazing angle). The most striking feature of the energy spectra is that for energies from E/A $\approx$ 30 to 50 MeV, the spectral slopes for a given IMF and angle are essentially constant - implying that on the average there is a temperature saturation across this energy range.[7] The only other systematic feature of the spectra is a broadening of the Coulomb peak at forward angles for each fragment type as the energy increases, suggestive of enhanced contributions from sequential decay processes.

In Fig. 1 representative angular distributions for Z = 8 fragments provide some initial indication of the relative importance of equilibrated and non-equilibrated emission mechanisms in these reactions. At all energies a strong enhnancement of the fragment yields is observed at forward angles. This pre-compound-like component grows in importance with increasing projectile energy. In contrast, the backward-angle data ($\theta > 90°$) exhibit a behavior reminiscent of fission following complete fusion at E/A = 20 MeV.

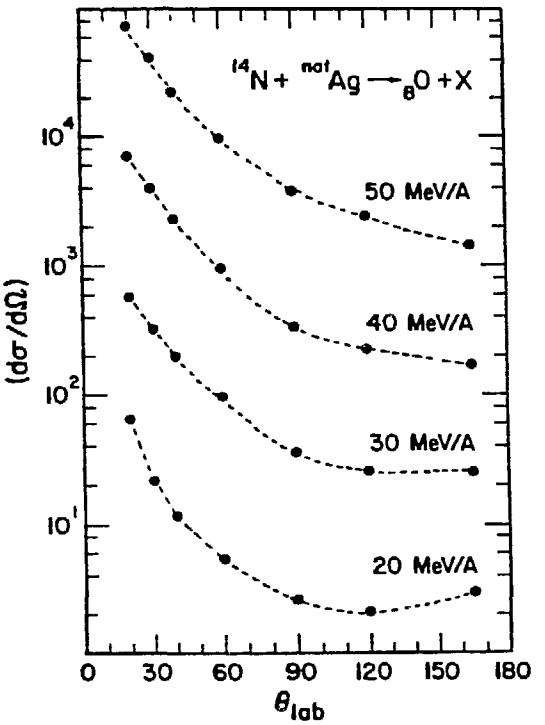

Fig. 1. Angular distributions of oxygen fragments.

This component decreases in relative strength as the bombarding energy increases. Table I presents results of a decomposition of these two components into what we shall define as equilibrated (σ_{eq}) and non-equilibrated (σ_{neq}) sources. The basic assumptions of this decomposition are: 1) the differential cross section at 165° arises only from a fully equilibrated source which follows a 1/sin θ angular distribution and 2) the remainder of the cross section arises from non-equilibrium mechanisms. It is apparent in Table I that the non-equilibrated component becomes increasingly dominant at higher bombarding energies, but that nonetheless some equilibrated species persist, even at the highest energies. These same trends are observed for all IMF Z-values, with σ_{neq} being enhanced for the lightest fragments, whereas σ_{eq} is enhanced for the heaviest fragments.

The elemental cross sections also exhibit nearly identical behavior at each energy. When fit with a power-law function,

$$\sigma(Z) \propto Z^{-\tau} \qquad (1)$$

the values of τ (listed in Table I) show little energy dependence. Only at E/A = 20 MeV is there a meaningful difference. The origin of this difference can be traced to the forward-and backward-angle data; the former yield τ = 2.9 and the latter τ = 2.1. Thus at all energies the values of τ for the σ_{neq}

Table I

E/A =	20 MeV	30 MeV	40 MeV	50 MeV
σ_{eq}/σ_{eq} <	1.0	0.45	0.27	0.17
τ	2.6	2.9	3.1	3.2

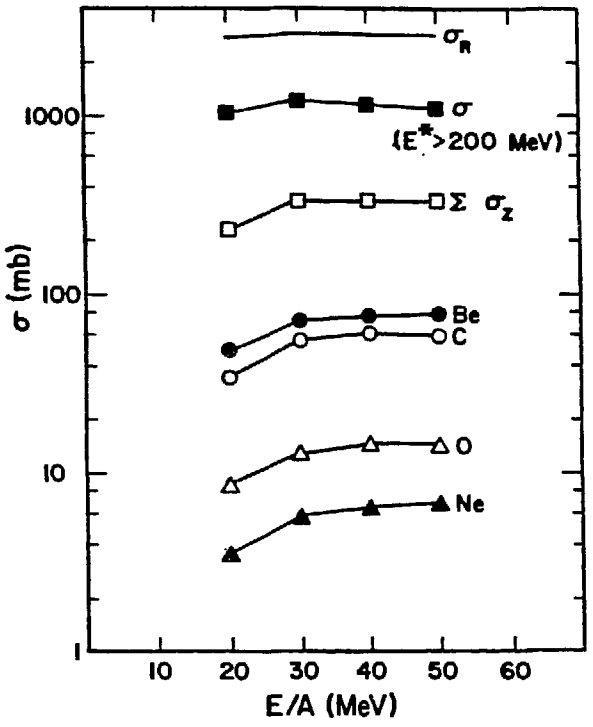

Fig. 2. Cross sections for IMF production for the ^{14}N + ^{nat}Ag reaction; σ_{IMF} is the total IMF value, σ_R is the calculated reaction cross section from Ref. 9, and $\sigma(E^*>200$ MeV) is derived from data of Ref. 10.

component are essentially identical. The significantly lower value of τ for the σ_{eq} component supports the suggestion that the τ parameter may provide a useful test for changes in reaction mechanisms leading to IMF formation.[8]

In Fig. 2 the excitation functions for emission of Z = 4, 6, 8 and 10 fragments from the target-like source are presented with the total IMF cross sections. In deducing these values, the influence of projectile fragmentation contributions was excluded from the energy spectra to the extent possible (primarily Be and C at small angles). For reference, Fig. 2 also shows calculated values for the total reaction cross section,[9] σ_R, and an estimate of the cross section for events which deposit greater than 200 MeV of excitation energy, $\sigma(E^*>200$ MeV), which is the approximate threshold for IMF formation in this reaction. The latter were derived from linear momentum transfer distributions for a ^{238}U target;[10] this procedure sets an upper limit for $\sigma(E^*>200$ Mev) since the average momentum transfer is known to decrease with decreasing target mass.[11] The most pronounced feature of Fig. 2 is the relative insensitivity of the inclusive cross sections to bombarding energy, once the threshold energy is exceeded. This behavior is consistent with the relative constancy of the average linear momentum transfer as a function of energy in this same domain.[12] Thus, while increasing E/A of the incoming projectile may broaden the distribution of excitation energy and angular momentum, on the average mass and energy dissipation processes change little. This is most readily understood in terms of the rapid growth in pre-compound nucleon emission in the vicinity of the Fermi energy - which appears to be paralleled by a similar enhancement of IMF emission from non-equilibrated sources relative to fully equilibrated ones

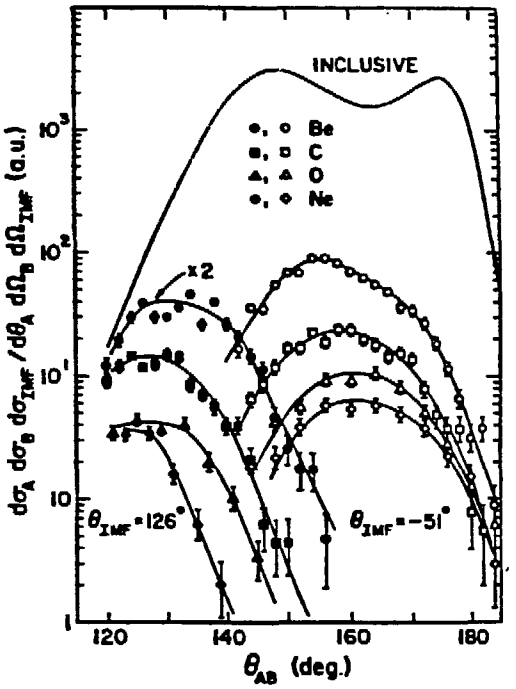

Fig. 3. Fission folding-angle distributions in coincidence with Be, C, O and Ne fragments at $\theta_{IMF} = -51°$ (open points) and $\theta_{IMF} = \pm 126°$ (closed points).

(Table I). It can also be deduced from Fig. 2 that multifragmentation probably does not contribute significantly to IMF production for these systems, since the multiplicities are much less than unity ($\sigma_{IMF}/\sigma_R \lesssim 0.15$).

2. Exclusive Measurements

In order to investigate whether or not equilibrium and non-equilibrium IMF sources can be differentiated, as suggested by the preceding inclusive data, triple coincidence experiments were performed between IMFs and angle-correlated fission fragments, thereby tagging each event according to the linear momentum transfer to the residual target-like nucleus. Measurements were carried out as a function of IMF emission angle for the E/A = 35 MeV ^{14}N + ^{232}Th system, where a finite probability for complete fusion exists (≈ 300-400 mb), and for the E/A = 90 MeV ^{3}He + ^{232}Th system, where complete fusion should be negligible.

The E/A = 35 MeV ^{14}N + ^{232}Th studies were carried out at the Michigan State NSCL; experimental details have been described elsewhere.[13,14] In Fig. 3 the measured fission-fragment folding-angle distributions gated on various Z-values are shown for IMF detection angles of 51° and 126°. Also shown is the inclusive folding-angle distribution for this system (unnormlized). These results demonstrate the strong kinematic dependence of the fission folding-angle on IMF emission angle and charge. In a context separate from the immediate concerns of this paper, the influence of IMF emission on inclusive folding-angle distributions should be stressed. Because σ_{IMF}/σ_R is small for the present systems, the inclusive results are only slightly affected. However, for much heavier projectiles such as ^{40}Ar, where IMF multiplicities approach unity, a major perturbation of the folding-angle distribution should be expected on the basis of Fig. 3. Because the cross-section for forward-angle IMFs dominates, this effect will strongly

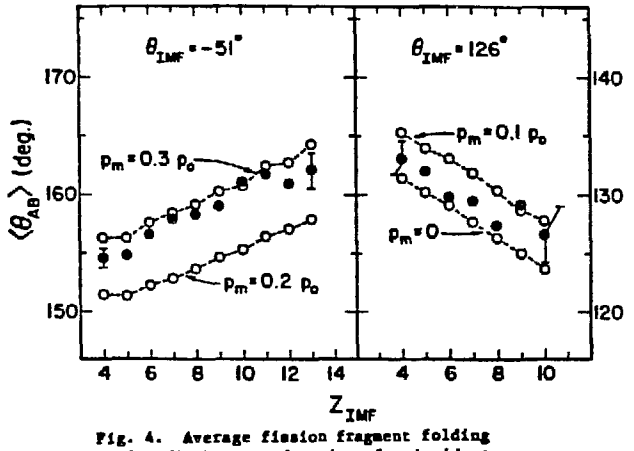

Fig. 4. Average fission fragment folding angle, $\langle\theta_{AB}\rangle$, as a function of coincident ejectile Z. Closed points are experimental values. Open points are calculations based on various values of missing momentum, p_m.

shift the inclusive folding angle distribution to angles nearer 180°. The disappearance of fusion-like events for E/A > 40 MeV ^{40}Ar ions, as reported in recent work from GANIL,[15] must be at least partially due to this effect.

In Fig. 4 the average fission-fragment folding-angle, θ_{AB}, is plotted as a function of coincident IMF Z-value. These data show the expected kinematic behavior and are analyzed in terms of the missing longitudinal momentum, p_m, defined by

$$p_m = p_o - p_R - p_{IMF}\cos\theta_{IMF} \quad , \quad (2)$$

where p_o is the beam momentum, p_R is the momentum of the fissioning nucleus and p_{IMF} is that of the IMF. Calculations for various values of p_m are shown on the figure. For forward-emitted fragments, considerable missing momentum is observed, corresponding to $p_m = 28 \pm 3\%$ (compared with 42% for the inclusive data) and an average excitation energy of $\langle E^* \rangle \approx 320$ MeV.[16] In Fig. 5 energy spectra for the corresponding IMFs are shown. A two-component fit to these forward-angle spectra describes the data well with a slope temperature of T ≈ 13 MeV, well in excess of the fully equilibrated value, and source velocity $v \approx 4\ v_{CF}$, where CF refers to the velocity expected for complete fusion of target and projectile. Coupled with the strongly forward-peaked angular distributions, these results provide strong evidence for a non-equilibrium emission mechanism in which pre-compound nucleon emission occurs prior to or simultaneous with IMF formation.

In contrast, at backward angles the momentum balance is nearly complete, $p_m = 5 \pm 5\%$, suggesting emission from a nearly fully equilibrated, complete-fusion (CF) source with $E^* \approx 420$ MeV. Correspondingly, the coincidence IMF energy spectra in Fig. 5 are consistent with such an interpretation, being well described by a slope temperature of $T \approx T_{CF} = 4$ MeV and source velocity $v \approx v_{CF}$. Hence, these results indicate the presence of an additional fully-

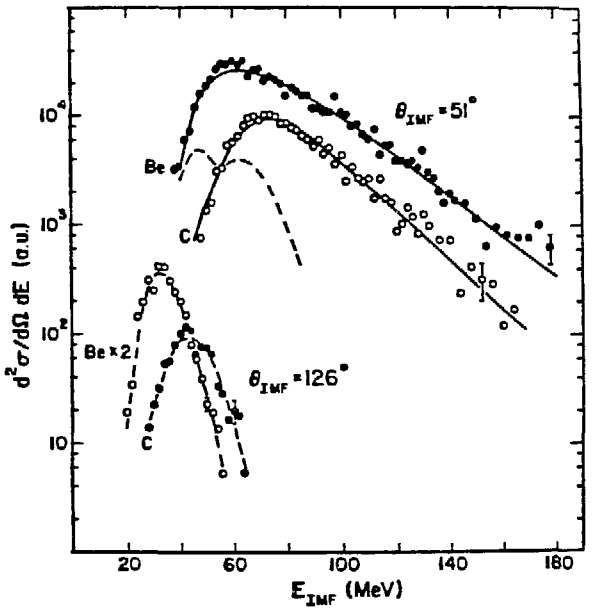

Fig. 5. Energy spectra of Be and C fragments in coincidence with angle-correlated fission fragments for $\theta_{IMF} = -51°$ and $\theta_{IMF} = \pm 126°$. Dashed lines give the results of statistical calculations assuming emission from a fully equilibrated complete fusion event. Solid line adds a Maxwellian component with T = 13 MeV and $v = 4v_{CN}$.

equilibrated complete-fusion-like source for IMF's, although with significantly reduced yield at this energy.

The effect of increasing the projectile E/A was investigated via similar measurements on the E/A = 90 MeV ^{3}He + ^{232}Th system. In this experiment a detector configuration was employed which determined both the magnitude and at direction of the missing momentum.[14,17] In Fig. 6 the missing momentum is shown for IMFs measured at 15° for two energy bins (55-75 and 75-200 MeV) and 75° and 160° for the entire spectrum. On the average one finds that 20-25% of the beam momentum is unaccounted for by the longitudinal component of p_m and that there is little sensitivity to ejectile kinetic energy. Also, the transverse component of p_m is near zero for all angles. Based on charged-particle conicidence measurements with fission fragments,[18] this missing momentum is attributed to precompound nucleon emission prior to or during IMF emission.

The relationship between the target-like recoil angle and the direction of the missing momentum is shown in Fig. 7. The missing momentum appears to be directed primarily along the beam direction. This supports the concept of precompound nucleon emission is the primary source of missing momentum[19] and argues for an emission sequence in which precompound nucleons precede or accompany IMFs, followed by fission of the residual excited nucleus. The absence of missing momentum in the direction of the IMF indicates that sequential decay is not a major mechanism of momentum less for this system.

Finally, it is found that while the probability for IMF emission accompanied by fission is nearly unity for all IMF charges observed at forward angles, this probability decreases strongly at more backward angles. This behavior implies that the backward-angle fragments are associated with a less fissionable source than those at forward angles; i.e. the average source

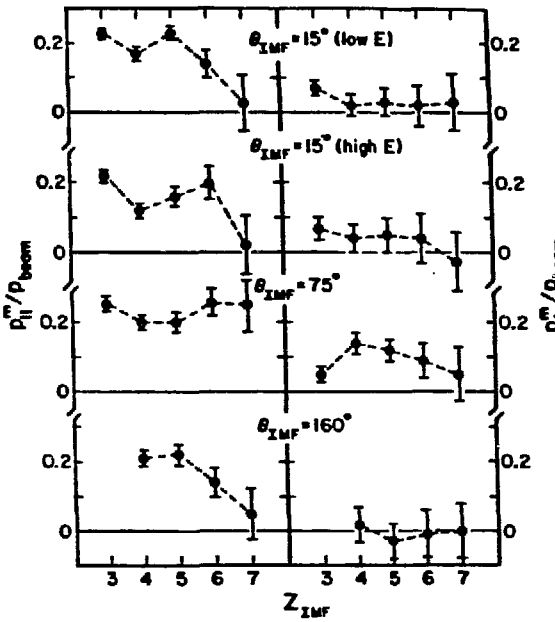

Fig. 6. Two components of missing linear momentum (longitudinal, $p_{\parallel}$, and transverse, $p_{\perp}$) plotted as a function of the ejectile atomic number. Low E corresponds to a gate on IMF energy E_{IMF} = 55–75 MeV, while high E corresponds to E_{IMF} = 75–200 MeV.

charge and/or angular momentum is smaller for the back-angle events. This can be understood in terms of a picture in which the forward-angle spectra arise from more peripheral collisions, while the backward-emitted IMFs originate in more central collisions, accompanied by a relatively isotropic emission of precompound nucleons (leading to $p_{m\perp} \approx 0$ as in Fig. 6).

3. Summary

From examination of both inclusive and exclusive data for IMF emission in intermediate-energy collisions, convincing evidence can be found for the coexistence of both fully equilibrated and non-equilibrated target-like sources. At near-barrier energies, the principal mechanism appears to be statistical decay from a system which possesses most of the excitation energy of the incoming beam. With increasing projectile E/A, IMF formation becomes increasingly dominated by pre-compound processes. In this respect there appears to be a strong parallel between the emission of IMFs and nucleons in the intermediate energy regime.

Systematic inclusive excitation function data for the ^{14}N + ^{nat}Ag system exhibit remarkably energy-independent behavior, consistent with the previously observed saturation in linear momentum transfer and high excitation-energy events in this E/A region. The fragment angular distributions support a two-component decomposition in terms of compound and pre-compound mechanisms. This interpretation is reinforced by the corresponding spectral slope temperatures and τ parameters associated with a power-law fit to the elemental cross sections. Exclusive studies of these two components in the E/A = 35 MeV ^{14}N + ^{232}Th system demonstrate that: 1) the strongly-forward peaked component exhibits significant missing momentum and is characterized by large slope temperatures and velocities (T ≈ 13 MeV; v ≈ 4 v_{CF}), and 2) the backward

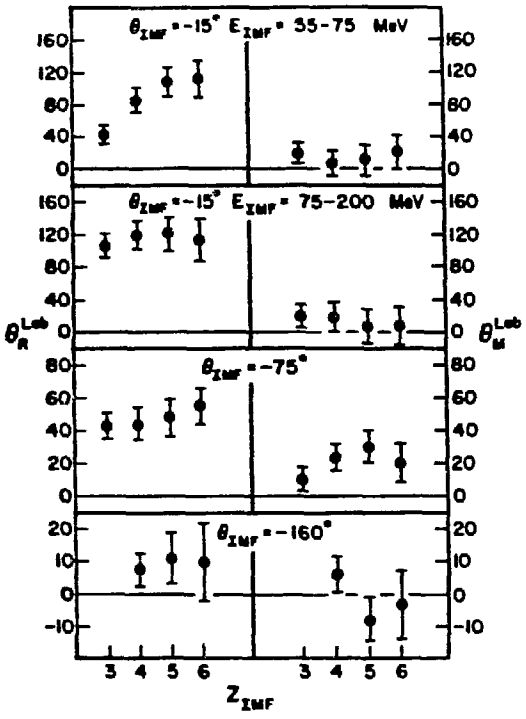

Fig. 7. Recoil direction (left column) and missing-momentum direction (right column) plotted as a function of IMF atomic number for E/A = 90 MeV ^{3}He + ^{232}Th reaction.

component is essentially consistent with decay of a fully-equilibrated complete fusion event.

Studies of the E/A = 90 MeV ^{3}He + ^{nat}Ag system show that at higher E/A values IMF emission at all angles is accompanied by signficiant missing momentum and that the direction of the missing momentum is strongly correlated with the beam direction. This is consistent with the emission of fast nucleons prior to or during the IMF formation process. The relative probability of IMF events accompanied by fission compared to the inclusive IMF yields in this reaction further suggest that the forward-angle fragments are formed predominantly in peripheral reactions, while those occurring at back angles are more clearly associated with central collisions.

Finally, no evidence for multifragmentation processes was observed in these studies.

The author is greatly indebted to his many colleagues who have been responsible for these results. Most significantly, Kris Kwiatkowski has taken a major role in the conduct of all of the work discussed here; Mirek Fatyga had primary responsibility for the exclusive experiments and Doug Fields undertook the data analysis of the inclusive work. Among many other Indiana University collaborators were Doug Bonser, Roger Byrd, Randy Viola, Warren Wilson and Lai-Wan Woo. The vital collaboration of our Michigan State colleagues in the ^{14}N measurements is also gratefully acknowledged; these include Sam Austin, Ziping Chen, Charles Chitwood, David Fields, Konrad Gelbke, Bill Lynch, Tappan Nayak, Josef Pochodzalla and Betty Tsang. We also acknowledge the participation of Hugon Karwowski of the University of North Carolina and Wojtech Skulski and Jerzy Jastrbski of Warsaw University in the ^{3}He work. The dedicated efforts of the operating crews and technical staffs

(in particular Keith Solberg, Dick Yoder, Derek DuPlantis, Bill Lozowski, and Bryan Cox at IUCF) and at NSCL (especially John Yurkon and Reg Ronningen) should also be recognized as critical to the success of this program. Finally, we are grateful to both the U.S. Department of Energy and the National Science Foundation for their support of various aspects of these measurements.

References

1. Proc. Symp. on Central Collisions and Fragmentation Processes (editor: C.K. Gelbke), Nucl. Phys. A471, p.1-451 (1987).
2. D.E. Fields, et al., Bull. Am. Phys. Soc. 32, 1551 (1987).
3. L.G. Sobotka et al., Phys. Rev. Lett. 51, 2187 (1983).
4. K. Kwiatkowski et al., Phys. Lett. B171, 41 (1986).
5. T. Murakami, private communication.
6. C. Bloch, Ph.D. thesis, Michigan State University, 1987.
7. D. Fabris et al., Nucl. Phys. A471, 351 (1987); G. Nebbia et al., Phys. Lett. B176, 20 (1986).
8. N.T. Porile et al., Nucl. Phys. A471, 351 (1987).
9. S. Kox et al., Nucl. Phys. A420, 162 (1984).
10. M. Fatyga et al., Phys. Rev. Let. 55, 1376 (1985); M.B. Tsang et al., Phys. Lett. 134B, 109 (1984).
11. T. Batsch et al., Phys. Lett. B189, 287 (1987).
12. V.E. Viola, Nucl. Phys. A471, 53 (1987).
13. M. Fatyga et al., Phys. Rev. Lett. 58, 2527 (1987); Ph.D. thesis, Indiana University, 1986.
14. K. Kwiatkowski, Nucl. Phys. A471, 271 (1987).
15. S. Harar, Nucl. Phys. A471, 205 (1987); E.C. Pollacco et al., Phys. Lett. 146B, 29 (1984).
16. D. Jacquet et al., Nucl. Phys. A445, 140 (1985).
17. M. Fatyga, Phys. Lett. 185B, 321 (1987).
18. T.C. Awes et al., Phys. C24, 89 (1981); B.B. Back et al., Phys. Rev. C22, 1927 (1980).
19. C.K. Gelbke and D.H. Boal, MSU Report CL-584, to be published in Prog. Part. Nucl. Phys.

PROJECTILE BREAKUP AND LINEAR MOMENTUM TRANSFER INDUCED BY 32.5 MeV/A ^{16}O-IONS‡

Y. Chan, E. Chavez[a], A. Dacal[a], S.B. Gazes[b], A. Harmon, M.E. Ortiz[a], E. Plagnol[c], J. Pouliot and R.G. Stokstad

Nuclear Science Division, Lawrence Berkeley Laboratory,
University of California, Berkeley, Ca.94720.

1. Introduction

Although it appears inappropriate to talk about such low energy experiments in front of this audience, there are, nevertheless, certain well known aspects about the 30-50 MeV/nucleon region that makes it distinct and worthwhile exploring. First of all, the relative velocity of the reactants is comparable to the intrinsic velocity of the individual nucleons inside the nucleus. One therefore expects the nucleonic degrees of freedom to play important roles *dynamically*, in addition to the effective two-body potential between the two nuclei. Secondly, being the onset region, the available phase space for these nucleonic degrees of freedoms are relatively confined so that one hopes to be able to address more detailed dynamical questions about these processes that are otherwise treated statistically at higher bombarding energies. With fully striped ion-beams (such as $^{16}O^{8+}$) available from the ECR source at the LBL 88-Inch Cyclotron, we have performed a series of measurements to study reaction mechanisms responsible for projectile breakup, as well as their relationship to massive-transfer processes induced by a 32.5 MeV/nucleon ^{16}O beam.

2. Instrumentation

The major equipment involved in these measurements is a close-packed plastic phoswich array which comprises a 48-element hodoscope (Fig.1) and several position-sensitive phoswich detectors (the *slice* detectors, Fig.2). The modular hodoscope typically covers an angular

‡ Work supported under DOE contracts DE-AC03-76SF00098 and DE-AM03-76SF000326. Presented at the VIIIth LBL-GSI Physics Meeting, Berkeley, California, Nov., 1987.

a) permanent address: Instituto de Fisica, UNAM, 01000 DF Mexico.

b) present address Department of Physics, University of Rochester,Rochester, NY 14627

c) present address : Institut de Physique Nucleaire, B.P. No 1, 91406, Orsay, France.

region of $\pm 2.5^\circ$ to $\pm 17.5^\circ$ around the beam axis. These detectors were chosen because of their relatively low manufacturing and electronics cost, excellent packaging factor, ruggedness, as well as adequate Z-resolution. The hodoscope has a geometrical close-pack factor of 95% such that one can operate it in veto-mode for studying certain kinds of processes. The phoswich detectors could resolve fragments with Z up to 12 and p,d,t particles in case of Z=1 (Fig.1).

The plastic array is triggered either by high resolution Si-telescopes (identifying both the mass and charge of the fragment) or by pairs of multi-wire proportional counters. The latter is mainly used to detect fission products of the target-like fragment (TLF) to measure the linear momentum transfer and correlations with the projectile-like fragments (PLF).

3. Projectile Breakup and Pickup-Breakup Reactions

In order for the projectile to breakup into one or more pieces, a certain amount of excitation energy has to be transferred. Undoubtedly the acceptance of nucleonic masses from a donor (e.g. pickup reaction) is one of the most efficient way to heat up the projectile. At low bombarding energies, this mechanism is well understood in terms of DWBA theories which depends critically on structural properties of the projectile and target nuclei at low excitation. The cross sections are, in general, quite small. The behavior of the pickup cross section at higher bombarding energies is not well known, however. One reason for this is probably experimental, as most of the intermediate products (projectile plus transferred mass) are populated at excitation energies above particle emission thresholds. Consequently, elaborate reconstruction procedures have to be employed in order to deduce the initial yield.

Experimentally, we have studied the generic process

$$P + T \rightarrow 1 + 2 + X_T \qquad (T = \text{Ni, Nb, Au, Pb and Th})$$

where 1 denotes a projectile-like fragment with mass and charge identified by a Si-telescope and 2 is a light charged particle detected by the phoswich array. By assuming 3-body final-state kinematics, quantities of interest $E_{TOT} \equiv E_1+E_2+E_{X_T}$ and $E_{REL}(1,2)$ are generated. Here E_{X_T} is the calculated kinetic energy of the undetected target-like nucleus (or group of particles) X_T. By examining the PLF excitation energy spectrum $E^*(1,2)$ which is directly related to $E_{REL}(1,2)$, and the $Q_3(\equiv E_{TOT} - E_{Beam})$ spectrum, we have arrived at the following conclusions :

(1) The predominant contribution to the breakup of the ^{16}O projectile is sequential rather than direct at 32.5 MeV/nucleon. There is no evidence for the presence of direct-breakup mechanisms such as those observed for ^7Li[1]

(2) High excitation energy is generated by the acceptance of nucleons from the target donor.

(3) The *pickup-breakup* (or transfer-reemission[2]) cross section is significant at this energy. FiC.3 shows the Q_3 spectrum for $^{12}C\alpha$ events observed in the $^{16}O+^{197}Au$ reaction at $E_{c.m.}$ = 481 MeV. It can be seen that besides a sharp sequential breakup peak, there is a conspicuous broad bump sitting to the left. From the energetics and bombarding energy dependence of the centroid of this broad structure, it was established that the $^{12}C\alpha$ yield in this region results from the neutron pickup breakup process : $^{16}O+n \rightarrow {}^{17}O^{*} \rightarrow {}^{12}C\alpha n$, where the neutron is not detected. By summing the yield from this bump to that of the observed ^{17}O (bound ^{17}O, $^{13}C\alpha$) yield, one finds that the relative cross section for this process (pickup-breakup) is comparable to that of inelastic ^{16}O breakup (by a ratio of approximately 1 to 1, after averaging over the Nb, Au, and Th targets). The pursuit of the pickup-breakup process at even higher bombarding energies will be very interesting, as it may turn out to be an important mechanism for injecting a sufficient amount of excitation energy into the PLF to lead to multifragmentation.

4. Projectile Breakup, Incomplete Fusion and Mechanisms for Incomplete LMT in Central Collisions

There have been suggestions that the major mechanism for incomplete fusion is nucleon-nucleon scattering, where particles with local velocity larger than the characteristic fermi velocity of the composite nucleus are emitted prior to thermalization. This process is predicted by several theoretical models such as the precompound emission model and the promptly-emitted-particle (PEP) mechanism and its variations. On the other hand, it is also possible that after the breaking-up of the projectile in the vicinity of the target nucleus, part of the remnants could be captured by the target to form a highly excited nucleus, i.e., $P+T \rightarrow 1+(2+X_T)$, instead of $P+T \rightarrow 1+2+X_T$. In particular, when the mass of the captured remnant is comparable to the projectile mass, this will lead to processes very similar to incomplete fusion.

In such cases, the parent nucleus does not carry the full linear momentum brought in by the projectile. The missing linear momentum transfer can either be due to partial capture of the projectile in a binary reaction (e.g. breakup-fusion) as described above, or, even though capture is complete and an intermediate mono-nucleus system is formed, precompound emission occurs before all degrees of freedom of the composite system are equilibrated. Which of these apparently different mechanisms are responsible or more important for incomplete fusion ? One possible way to differentiate between them is by looking at the detailed properties of the emitted energetic fragments and their correlation with the fusion-like products.

Specifically, in the breakup-fusion picture one expects to see a wide spectrum (masses may range from 1 to A_{PROJ}) of energetic (~beam velocity) projectile remnants emerging from the reaction with their momenta strongly correlated to the decay products of the parent nuclei (residues or fission fragments). The missing linear momentum is mostly carried away by a *single* nuclear cluster in this case, due to the binary nature of this mechanism. On the other hand, if PEP is the dominating process, the energetic particles in coincidence with central fission products will mostly be nucleons and the missing linear momentum would be shared among them.

Using the same phoswich array and multiwire proportional counters we have investigated the problem of mechanisms for missing LMT for the $^{16}O+^{238}U$ reaction at $E_{c.m.}$=487 MeV. For heavy and fissile systems, the most probable initial LMT could be deduced empirically from the relative opening angle Θ_{12} between the two emerging fission fragments (the folding-angle method). Our inclusive Θ_{12} data indicates that the average momentum of the fissioning parent nuclei is only about 75% of the beam for this reaction. This is consistent with the systematics of LMT for heavy systems.

A plot of the charge of the detected energetic fragment (Z_{FRAG}) versus the fission opening angle Θ_{12} is shown in Fig.4. There are three noticeable regions in this plot :

(A) Binary transfer, the strongly correlated region (Z=5,6,7).

There is a very strong and almost linear correlation between heavy fragment and Θ_{12} in this region. This is consistent with the interpretation that these fragments are results of binary transfer processes. The heavier the observed beam velocity fragment, the smaller the transferred mass Ξm should be, resulting in a smaller LMT (larger Θ_{12}).

(B) Preequilibrium emission and/or massive transfer (Z=1,2 fragments).

Generally speaking, the distributions in Θ_{12} corresponding to Z=1 and 2 particles are very broad, implying that the emission of energetic Z=1 and 2 particles are possible in almost all ranges of impact parameters. According to our previous studies most of the energetic particles with large Θ_{12} (small LMT) originate from the sequential-breakup of the projectile (region B). The portion corresponding to smaller Θ_{12} (large LMT) are presumably due to either massive transfer or pre-compound emission.

(C) Projectile breakup and target decay.

In this case, the excitation energy sharing between the projectile and target nuclei is such that the former is excited above its particle decay threshold and the target also receives sufficient excitation to undergo fission. It differs from (A) in that both remnants of the projectile are not captured by the target, resulting in small LMT. The strong yield of energetic α-particles observed in this region suggests the importance of projectile breakup in heavy-ion

peripheral collisions. These α-particles are probably coming from the $^{16}O \rightarrow {}^{16}O^{*} \rightarrow {}^{12}C+\alpha$ breakup process. They are not likely to be produced in binary transfer because in that case the capture of a ^{12}C cluster will introduce a significant LMT.

The correlation between the estimated average initial linear momentum of the fissioning parent nucleus, $P_{fission}$ and the longitudinal momentum, P_{FRAG}, of a *single* detected energetic fragments is shown in Fig.5. The linear momentum of the fissioning nucleus is obtained from Θ_{12} by assuming that the missing linear momentum is carried away by particles travelling along the beam direction. Also indicated in the figure is the corresponding beam momentum. The dash-dotted trend curve connects regions where the yield is more concentrated. One can see that in region (I), the summed momentum approaches the limiting value of the beam. However, the deviation between the trend curve and the beam momentum limit becomes larger and larger with increasing LMT to the target. This would indicate that the missing momentum must have been shared by more than one single energetic particle in the large LMT region, in contrast to the simple binary assumption of the massive-transfer mechanism. This would also suggest, in the preequilibrium emission interpretation, that more than one fast particles are emitted prior to the thermalization of the target-like nucleus.

5. Comparison with precompound emission models

All the observed light particle (p, d, t, α) spectra are peaked at energies slightly below the beam velocity and contain relatively high energy components extending close to the fermi velocity limit. Fig.6 shows a proton spectrum observed by a phoswich detector at 6° in the laboratory. One can see that the spectrum peaks at ~30 MeV and has a high energy cutoff at about 120 MeV. This latter number corresponds to a proton fermi energy ϵ_F~23 MeV in the projectile frame. To see whether the preequilibrium emission mechanism is responsible for incomplete fusion one can compare the observed nucleon spectra at forward angles with model predictions. Such a comparison has been made for the $^{16}O+^{238}U$ reaction using the master-equation/exciton-model code of Blann *et al.*.[3] (Fig.6). The number of excitons used in the calculation is set equal to 16, the same as the projectile mass. The calculated curve represents time integrated proton yield up to 1.6×10^{-22}s (~7 interaction steps for the excitons). Generally speaking, the observed proton spectrum is softer than what the model predicts. It should be noted that the model also predicts a much larger cross section for preequilibrium neutron emission than for proton emission. Consequently a better test of the role of nucleon-nucleon scattering mechanism at these energies is by detecting neutrons instead of charged particles.

In conclusion, the binary massive transfer mechanism appears to be able to account for many of the observed features of the reaction. Even though there are indications that a higher

fast particle multiplicity is required to account for the missing momentum in case of large LMT, favoring the interpretation of prompt nucleon emission, the observed experimental proton spectra are softer than those predicted by preequilibrium emission codes.

References

(1) Shotter *et al.*, Phys. Rev. lett. 46, 12 (1981).

(2) K. Siwek-Wilczynska *et al.*,Phys. Rev. C35, 1316 (1987).

(3) M. Blann, Phys. Rev. C31, 1245 (1985) and private communications.

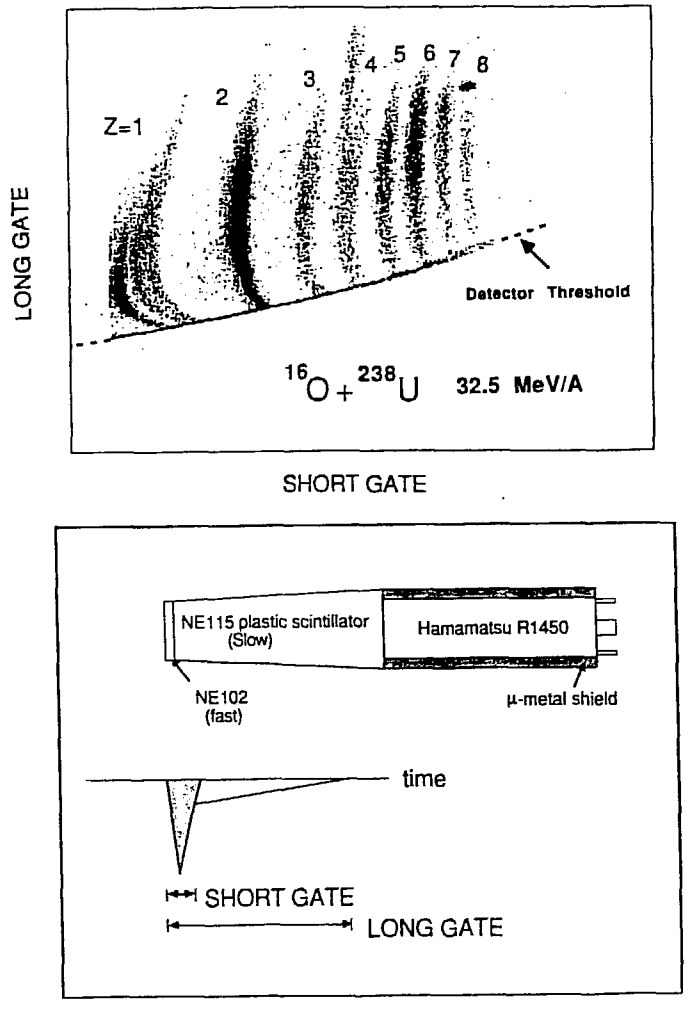

Fig. 1 Schematic drawing and performance of a single hodoscope element of the phoswich array.

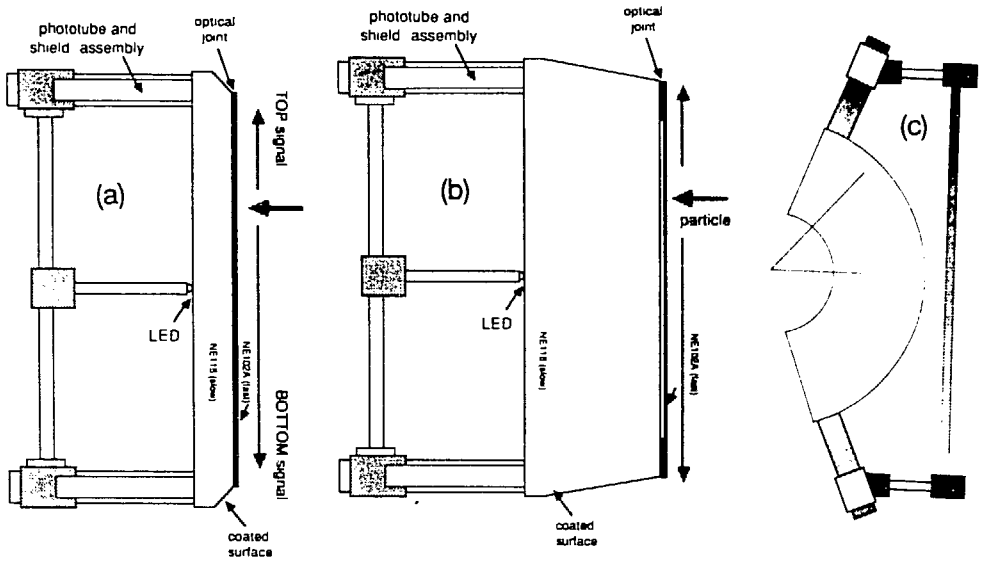

position-sensitive phoswich detectors

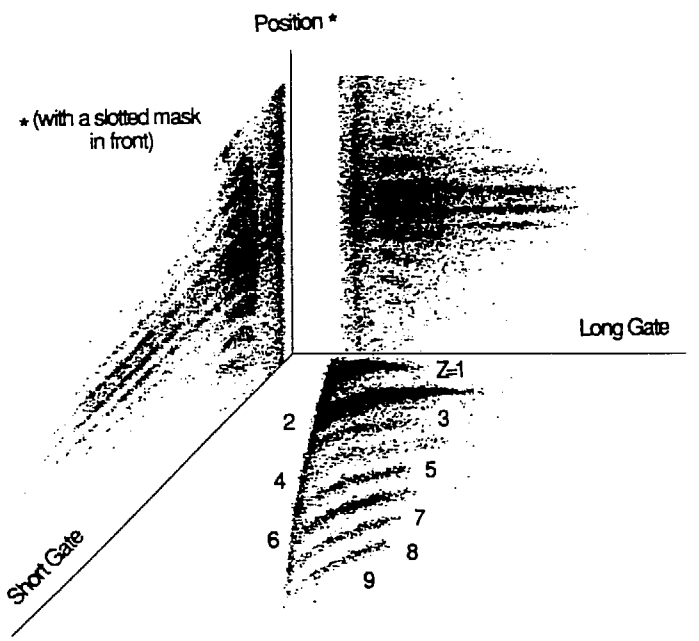

Fig. 2 Different versions of position-sensitive phoswich detectors used in the experiment.

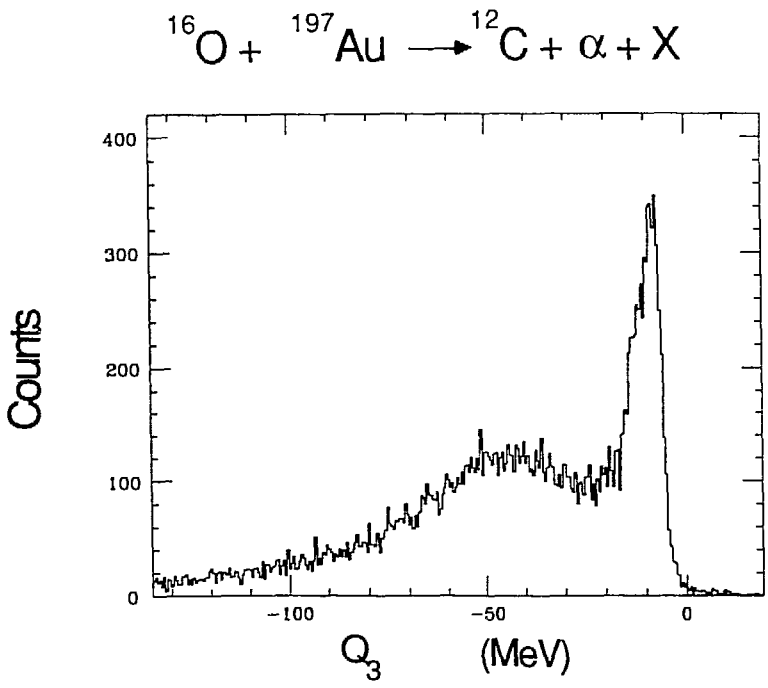

Fig.3 Reconstructed Q_3 spectrum for $^{12}C\alpha$ events.
(See text for the interpretation of the broad bump.)

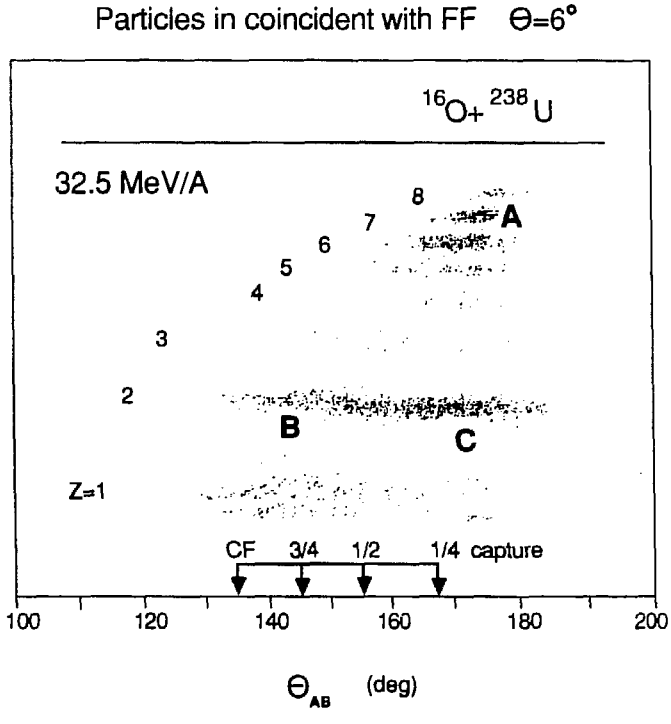

Fig.4 Correlation between the Z of the detected energetic fragment and fission fragment folding angles.

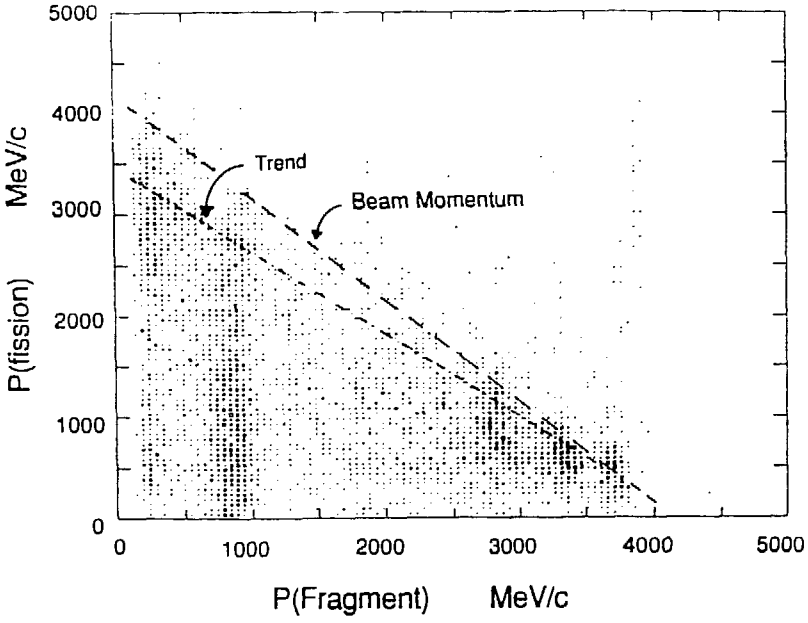

Fig.5 Momentum correlation between the fissioning nucleus and a single detected fragment.

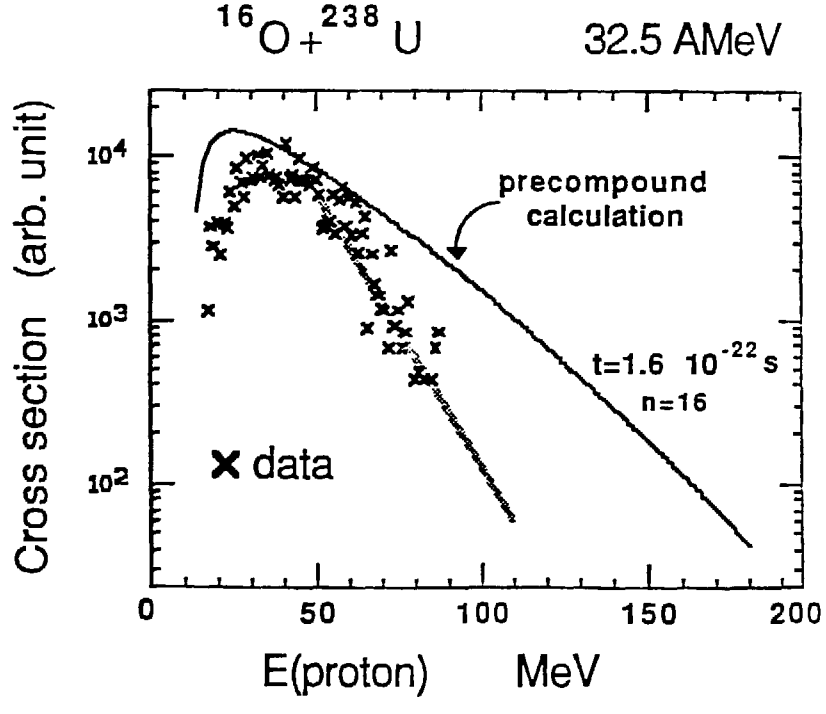

Fig.6 Comparison of the observed proton energy spectrum to precompound model calculations.

COMPLEX FRAGMENTS FROM THE La INDUCED REACTIONS AT 46.8 MeV/u*

Walter L. Kehoe†
Department of Chemistry
University of Maryland
College Park, Maryland 20742

What is the source or sources of complex fragments emitted during intermediate energy heavy-ion reactions? To help guide them in their understanding of the experimental observables in this energy regime, investigators studying these reactions have available to them a large wealth of experimental and theoretical information, from the studies of low energy reactions (E/A ≤ 10 MeV) and high energy or "Bevalac energy" reactions (100 MeV ≤ E/A ≤ 2000 MeV). At low bombarding energies the target and projectile may form a compound nucleus, which may then deexcite by a number of statistical processes, including: evaporation, complex fragment emission ($2 < Z < 1/2Z_{CN}$) or fission [1,2]. Interactions of nuclei at high energies may undergo dynamical multifragmentation, as observed in the 200 MeV/u Au + Au reaction [3]. In of both these energy regimes complex fragments are produced, but from two distinctly different reaction mechanisms, namely, statistical emission and multifragmentation. Is there a smooth or an abrupt transition between the mechanisms responsible for complex fragment emission? Where is the onset of multifragmentation?

Previous work by the LBL/Maryland/Milano collaboration [4,5] has shown that complex fragments can come from the statistical emission of equillibrated compound nuclei produced in either complete or incomplete fusion reactions. In these studies the advantages of reverse kinematics were exploited to allow for the easier detection of the complex fragments. In reverse kinematics a high mass projectile impinges on a low mass target, and the reaction products are emitted at near beam velocity and focused in a forward cone about the beam in the laboratory. The binary nature of the 50 MeV/u La + C reaction is shown in Fig. 1 from the charge coincidence data of two ΔE-E telescopes symmetrically placed about the beam [5]. The narrow band about $Z_1 + Z_2 = 55$ virtually excludes any multifragmentation events.

A new 48 element Si-Si-plastic wall array has been designed by our collaboration to measure the charge, energy and position of high multiplicity complex fragment events from reverse kinematic reactions [6]. During February, 1987, the first experiment using a ten element prototype of the Si-Si-plastic wall array to detect

complex fragments was performed. Using the Bevalac of the Lawrence Berkeley Laboratory, beams of E/A = 46.8-MeV ^{139}La incident on targets of ^{27}Al, $^{nat.}$Cu and ^{139}La were used to investigate the dominate decay channels in intermediate energy heavy-ion reactions, as a function of excitation energy.

The experimental set-up, shown in Fig. 2, consisted of ten telescopes close packed about the beam. Each telescope was composed of three detectors: a 300-μm Si, a 5-mm Si(Li), and a 7.6-cm BC400 plastic detector. The array was placed 40 cm from the target and mounted so that the center of each telescope was perpendicular to the target. The front face of each telescope was 55 mm x 57 mm, covering 8.2 degrees in the laboratory, however the active area of each telescope was 44.8 mm x 44.8 mm, covering 6.4 degrees in the laboratory. The array was mounted on two arms in the 60 inch scattering chamber of Beam 44. On one arm eight telescopes were mounted: A1, A4 and A7 were positioned with their centers +9.5 degrees out-of-plane; A5 and A8 were positioned in-plane and A3, A6 and A9 were centered -9.5 degrees out-of-plane. Telescopes A2 and A10 were mounted on the other arm and positioned in-plane. The two arms could be moved independently to minimize the opening through which the beam passed between A2 and A5. Throughout this experiment A2 and A5 were positioned symmetrically about the beam with opening angles between the beam and the detector centers of ±6.8 degrees. This put the inner edges of the active areas of A2 and A5 at +3.4 and -3.4 degrees, respectively.

The data analysis is still at an early stage and is concentrated on the calibration of the 300-μm Si - 5-mm Si(Li) ΔE-E telescopes. Most of the complex fragments produced in these reactions should be stopped in these detectors. Presently, only A2, A5, A8 and A10 are satisfactorily calibrated. The superb Z resolution and large dynamic range of the ΔE-E telescope is shown in a plot of the A5 telescope particle identification function (PIF) distribution in Fig. 3 for the La + Al reaction. The completely separated peaks in the PIF distribution correspond to charged particles with Z=1 to Z=48. Punch through of light charged particles through the detectors was responsible for the decreased yield for products with Z<6. The Si and Si(Li) detectors were divided into 15 charge resistive strips to determine the position of the charged particle traversing the telescope. The 300-μm Si and 5-mm Si(Li) were rotated 90 degrees relative to each other to determine both the X and Y positions. Fig. 4 shows a sample position spectrum from the 5-mm SiL(i) detector of the A5 telescope, again for the La + Al reaction. The fifteen strips are clearly resolved, each strip corresponding to about 0.4 deg in the laboratory. Based upon these results the

collaboration is satisfied that the project design goals have been achieved and completion of the 48 element array is under way.

While all the detectors are not yet calibrated, a great deal of insight into the reaction mechanism(s) responsible for the production of complex fragments can be gained by looking at the coincidence data between the four in-plane telescopes. A summary of the coincident heavy fragment data between A2, A5, A8 and A10 is shown is Table 1. The event yields have been normalized to the number of four-fold multiplicity events detected from the La + La system and gated on $Z > 2$ for A2, A5 and A8, and $Z > 3$ for A10.

The number of two-fold coincidences is larger for the La + Al than the La + Cu and La + La reactions. Figs. 5, 6 and 7 show the Z_1 vs Z_2 plots for these reactions, where the atomic charges of the particles detected in A2 were plotted as a function of the atomic charges detected in A5. The Z_1 vs Z_2 plot for the 46.8 MeV/u La + Al reaction is strikingly similiar to that of the 50 MeV/u La + C shown in Fig. 1, strongly suggesting the binary nature of this reaction. Most of the events fall in a band corresponding to about a constant $Z_1 + Z_2 = 50$ (see inset in Fig. 5). For this system, Viola systematics [7] predicts a 56% momentum transfer, corresponding to an excitation energy up to 600 MeV. The Z_1 vs Z_2 plots for the La + Cu and La reactions are dramatically different than that for the La + Al reaction, showing a filling in of the Z_1-Z_2 space. The multibody nature of these reactions is shown by the lack of a band of correlated Z_1-Z_2 products and the broad sum Z distribution shown in the insets of Figs. 6 and 7. The interpretation of the Z_1 vs Z_2 plots for the La + Cu and La reactions is not immediately clear. This range of products may arise from either the sequential binary breakup or multifragmentation of a very hot system.

The La + Cu and La, and to a lesser degree the La + Al, systems should have high multiplicity events of $Z>2$. Three-fold coincidence events for the three systems are shown in Fig. 8 as Z_1(A2) vs Z_2 (A5 and A8) plots. The line in these plots is to guide the eye and represents $Z_1 + Z_2 = 50$. For the La + Al reaction the three-fold multiplicities fall along the binary ridge of the two-fold multiplicities, suggesting that these products could come from the sequential binary breakup of the primary reaction products. The three-fold events for the La + Cu and La reactions show a filling in of the allowed Z_1-Z_2 space, but again, unfortunately, the Z_1 vs Z_2 plots do not aid in distinguishing the reaction mechanism(s) responsible for these reaction products.

The qualitative results from the study of 46.8 MeV/u La induced reactions incident on Al, Cu and La targets are straight forward. Coincidence data, plotted as

Z_1 vs Z_2 correlations, for the La + Al reaction clearly show the binary ridge characteristic of the emission of complex fragments from compound nucleus-like systems. This ridge disappears when the target mass and the available excitation energy of the system are increased. The Z_1 vs Z_2 correlations for the La + Cu and La reactions show evidence for the onset of multi-fragment final states by the filling in of the Z_1-Z_2 space. Continued analysis of the data will focus on distinguishing the relative importance of sequential binary decay of the primary products and multifragmentation for the emission of complex fragments. Further experiments using the complete 48 element Si-Si-plastic array are planned to study the same and other systems at still higher bombarding energies to map out the excitation energy functions for n-fold reaction products (n = 2,3,4,...).

References

* This work was supported by the Director, Office of Energy Research, Division of Nuclear Physics of the Office of High Energy and Nuclear Physics of the US Department of Energy under contracts DE-AC03-76SF00098 and DE-FG05-87ER40321.

† The author wishes to acknowledge the effort and support given by his colleagues toward the success of this experiment: D.R. Bowman, S. Bradley, R.J. Charity, H. Han, I. Iori, K. Jing, A. Marchetti, R.J. McDonald, M.A. McMahan, A.C. Mignerey, L.G. Moretto, A. Moroni, L. Vinet and G.J. Wozniak.

1. R. Vandenbosch and J.R. Huizenga, Nuclear Fission (Academic Press, New York, 1973).

2. L.G. Sobotka, *et al.*, Phys. Rev. Lett. **51** (1983) 2787.

3. B.V. Jacak, et al., Los Alamos National Laboratory preprint LA-UR-86-2273.

4. R.J. Charity, *et al.*, Lawrence Berkeley Laboratory preprint LBL-22447 and accepted to Nuclear Physics A.

5. D.R. Bowman, *et al.*, Physics Letters **189B** (1987) 282.

6. W.L. Kehoe, *et al.*, NSD Annual Report 1985-1986, LBL-22820.

7. V.E. Viola Jr. *et al.*, Phys. Rev. **C 26** (1982) 178.

Table 1. Coincidence heavy fragment data between the four in-plane telescopes. The yields have been normalized to the number four-fold multiplicity events detected in the La + La reaction.

n-fold	Telescope Coincidence*	La + Al	La + Cu	La + La
n = 2	A2 vs A5	2377	883	761
	A2 + A10 vs A5 + A8	3499	1639	1468
n = 3	A2 vs A5 and A8	38.0	38.6	21.0
n = 4	A2 and A10 vs A5 and A8	0	1.80	1.00

* All coincidences gated on low gain events, Z>2 for A2, A5 and A8, and Z>3 for A10

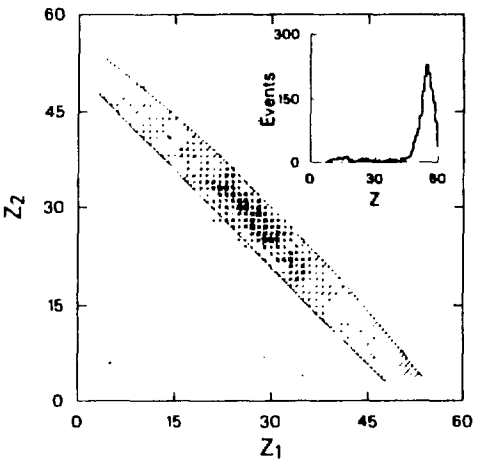

Fig. 1. Z2 vs Z1 coincidence plot for the 50 MeV/u La + C reaction. The distribution of the sum charges (Z1 + Z2) is shown in the inset.

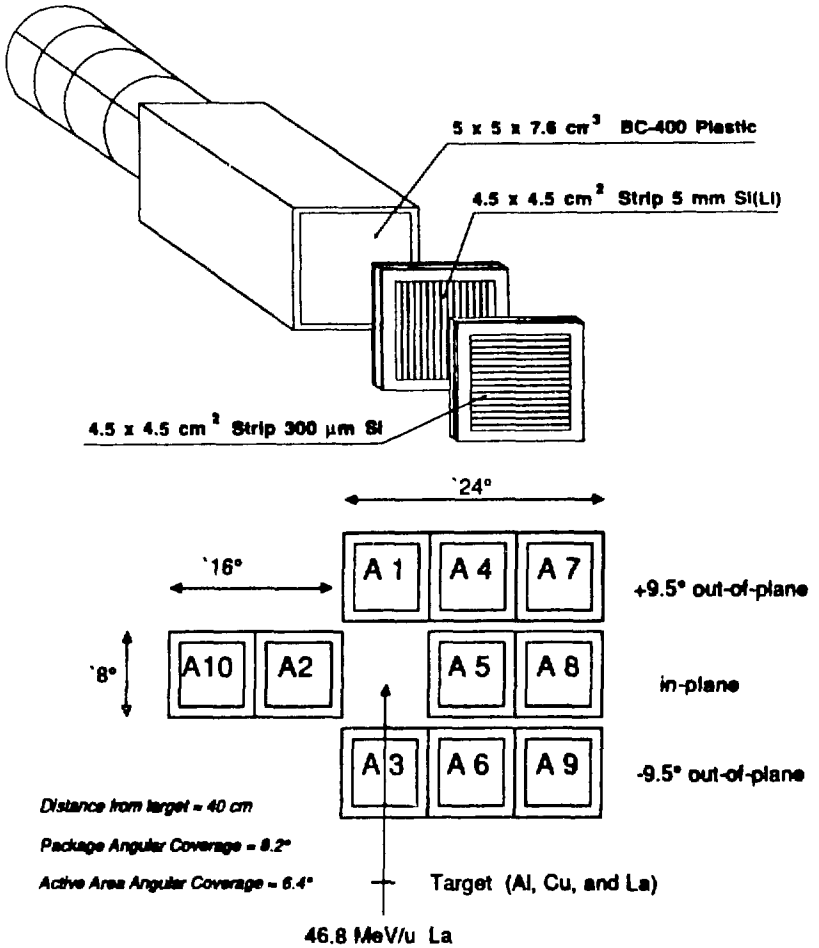

Fig. 2. Detail of Si-Si-plastic array telescope and experimental setup.

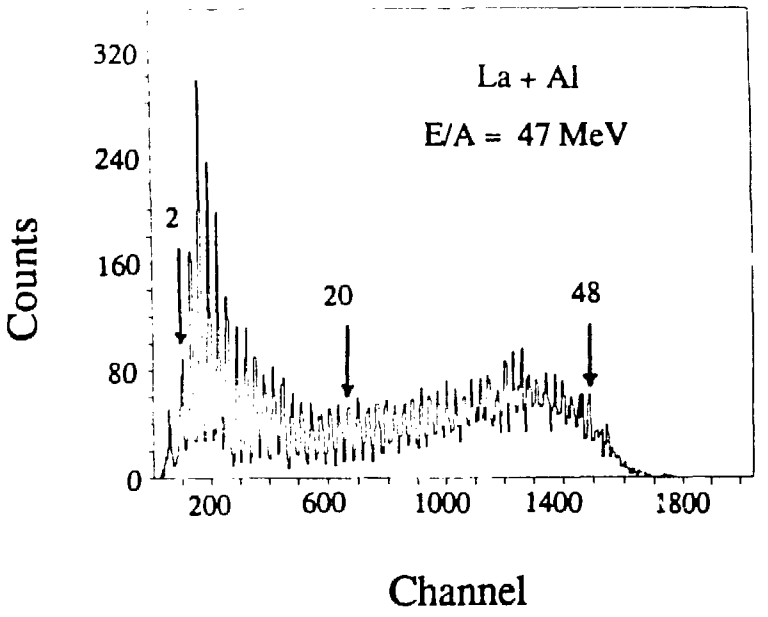

Fig. 3. Particle identification function distribution for the La + Al reaction, showing charged particle identification from Z = 1 to Z = 48. This spectrum is from the 300 μm Si -5mm Si(Li) detectors of the A5 telescope.

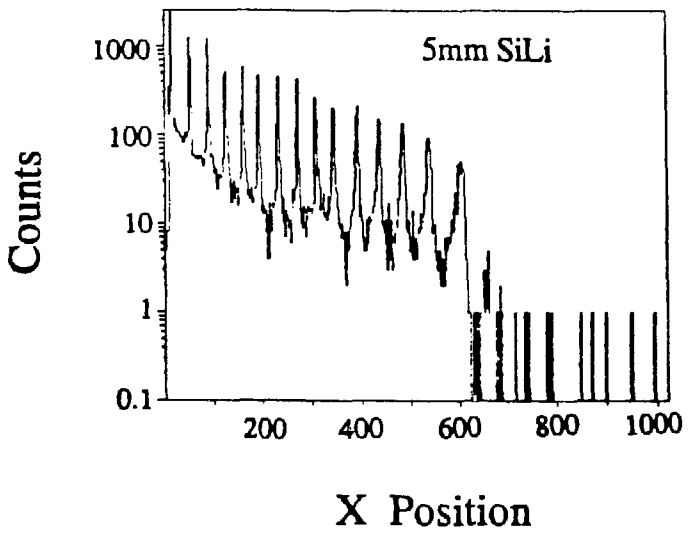

Fig. 4. Example of the position spectrum from the resistive chain strips on front of the 5-mm Si(Li) detector of the A5 telescope from the La + Al reaction.

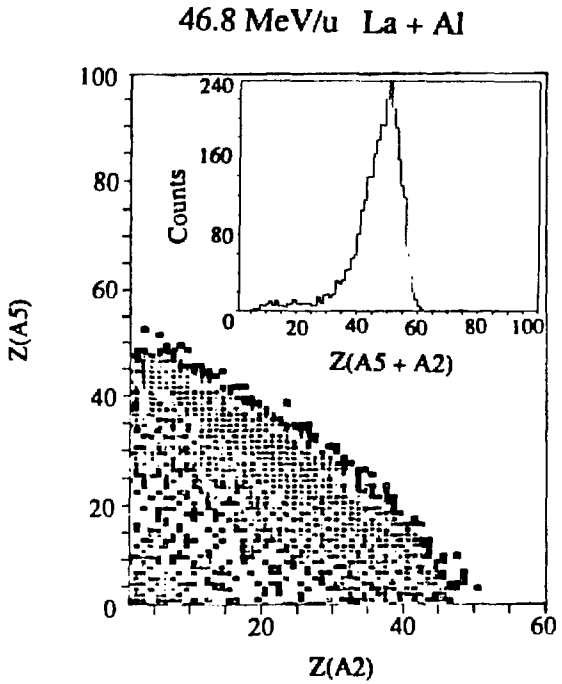

Fig. 5. Z1 vs Z2 coincidence plot between telescopes A2 and A5 for the 46.8 MeV/u La + Al reaction. The distribution of the sum charges (Z1 + Z2) is shown in the inset.

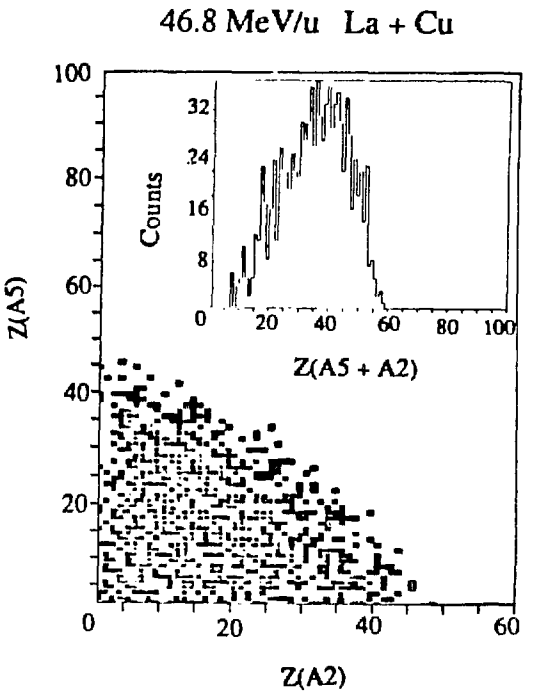

Fig. 6. Z1 vs Z2 coincidence plot between telescopes A2 and A5 for the 46.8 MeV/u La + Cu reaction. The distribution of the sum charges (Z1 + Z2) is shown in the inset.

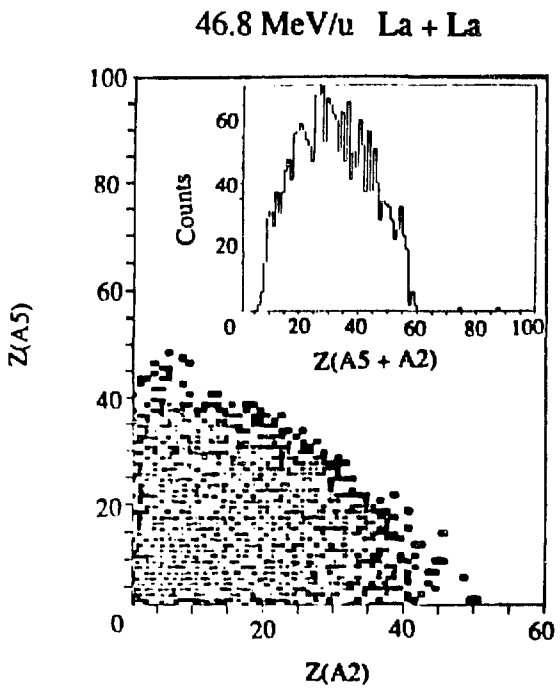

Fig. 7. Z1 vs Z2 coincidence plot between telescopes A2 and A5 for the 46.8 MeV/u La + La reaction. The distribution of the sum charges (Z1 + Z2) is shown in the inset.

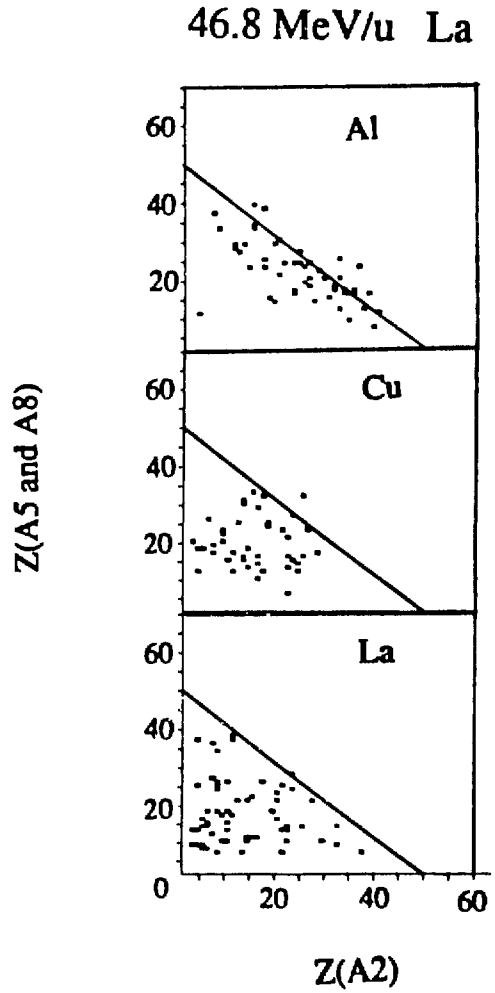

Fig. 8. Three-fold coincidence events plotted as Z1(A2) vs Z2(A5 and A8) for the reactions 46.8 MeV/u La + Al, Cu and La reactions. The line is to guide the eye and corresponds to Z1 + Z2 = 50.

CONDITIONS OF FRAGMENT EMISSION IN LIGHT HEAVY-ION INDUCED REACTIONS

W. Trautmann
GSI Darmstadt
D-6100 Darmstadt, West Germany

The widespread interest in intermediate mass fragment (IMF) emission at large angles in intermediate and high energy heavy ion collisions is fuelled by the prospects to discover new properties of nuclear matter at extreme densities and excitation. However, as shown by the present debate, many of the basic features of the inclusive data, e.g. the mass yield distributions, can be reproduced within a variety of approaches with rather different starting points. So far, it has not been ruled out that we may be looking at a process well known from the low energy regime and appearing moderately disguised in the high energy environment. Detailed studies with refined techniques are needed and, in fact, are under way in many laboratories.[1)]

In this talk some new results concerning IMF emission in light heavy-ion induced reactions (projectiles ranging from ^{12}C to ^{20}Ne) on heavy targets at intermediate bombarding energies (30 MeV $\leq$ E/A $\leq$ 84 MeV) will be summarized. Both dynamical and statistical conditions favouring IMF emission, as appearing from these data, will be discussed. Particular emphasis will be given to the time scales involved. They follow from the dynamical evolution of the reaction process and determine the scale on which equilibration may proceed. The time scales thus represent a natural link between dynamics and statistics.

In the energy range under consideration, E/A < 100 MeV, the nuclear mean field governing the reaction is expected to be mainly attractive.[2)] This has been confirmed in experiments determining the sign of the scattering angle, i.e. the direction of the transverse momentum imparted to particles and fragments, from the circular polarization of gamma rays emitted by the residual composite nuclei.[3)] The polarizations measured with beams from the MSU cyclotron in the ^{14}N on ^{154}Sm reaction at E/A = 35 MeV are positive both for the preequilibrium light particles and for the IMFs (Fig. 1), indicating that these reaction products are preferentially emitted to negative angles. The magnitude of the polarizations was found to be sensitive to the interplay of nucleon nucleon collisions and mean field dynamics.[3)] The observation of polarizations significantly different from zero for IMFs (Fig. 1) also indicates that IMFs are emitted before full dynamical equilibrium is reached.

The multiplicity of gamma rays emitted, in coincidence with IMFs, by the heavy residues in the ^{14}N on ^{154}Sm reaction is of the order of 15 and nearly independent of the fragment atomic number Z. This value, although still prelim-

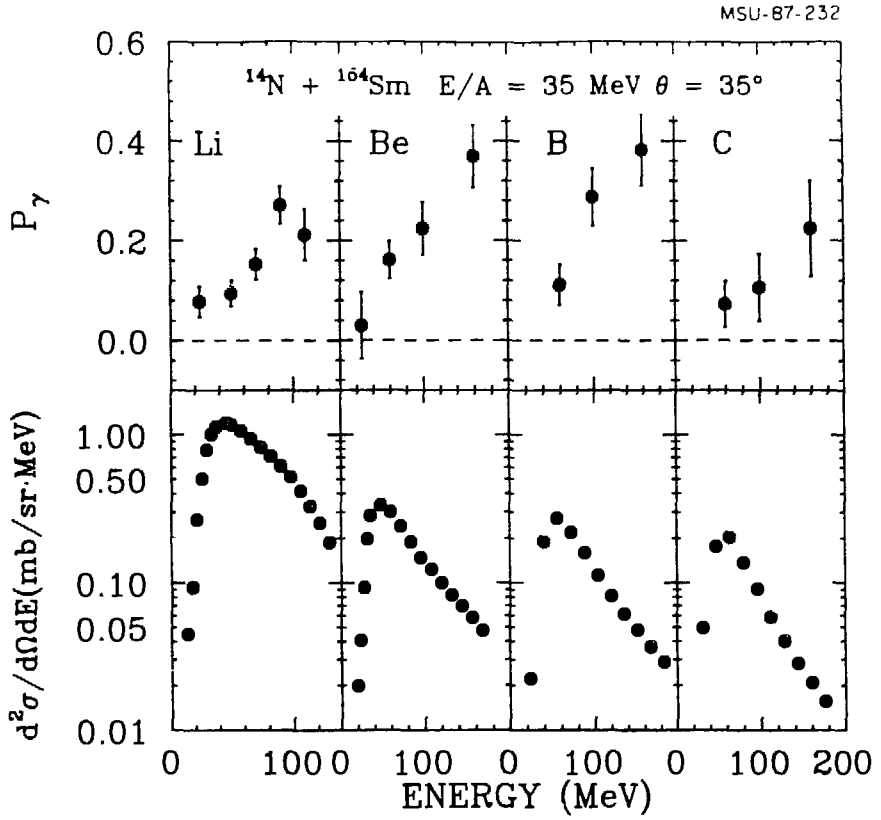

FIGURE 1
Average circular polarization of coincident gamma rays (upper part) and cross sections (lower part) for IMFs of $3 \leq Z \leq 6$ detected at θ(lab) = 35° in the reaction ^{14}N on ^{154}Sm at E/A = 35 MeV (from Ref. 3).

inary, is conspicuously close to multiplicities measured in a similar reaction ,^{20}Ne on ^{168}Er, but at the considerably lower energy E/A = 13.5 MeV.[4] The picture developed for the interpretation of these multiplicities and of the angular momenta deduced thereof is based on a concept of dynamical equilibrium in the exit channel.[4] It relies on (i) a decoupling of the entrance and exit channel energies and angular momenta via the emission of preequilibrium light particles and (ii) on the balance of the nuclear, Coulomb and centrifugal forces in the exit channel as the most favourable condition for IMF emission. The similarities of the absolute magnitude and of the Z dependence of the gamma ray multiplicities and hence of the angular momenta residing in the system suggest that these conditions may still be the same at the higher energy E/A = 35 MeV. This not only demonstrates that angular momentum continues to play an important role in the intermediate energy regime, as noted by other authors[5-7], but also allows the derivation of a time scale from the speed of rotation of the intermediate dinu-

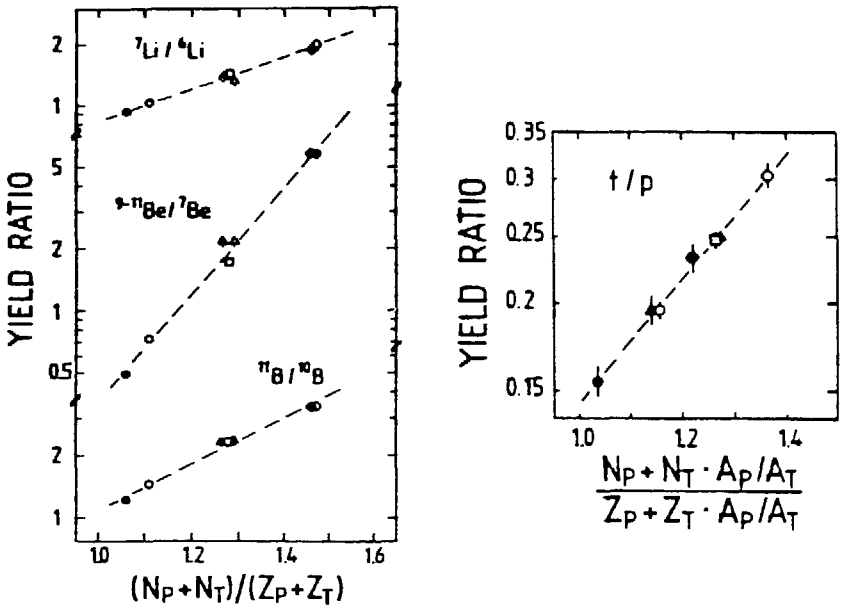

FIGURE 2
Left hand side: Ratios of energy integrated isotope yields, measured at E/A = 84 MeV and the laboratory angle $\theta = 41°$, as a function of the N/Z ratio of the combined system of projectile and target. Full and open symbols denote ^{12}C and ^{18}O projectiles; circles, squares, triangles, and diamonds stand for ^{58}Ni, ^{64}Ni, Ag, and ^{197}Au targets, respectively. The dashed lines are meant to guide the eye. Right hand side: Ratios of triton over proton yields from the same reactions but plotted as a function of the N/Z ratio of a source consisting of equal numbers of nucleons from the projectile and from the target (from Ref. 9).

clear complex. For critical angular momenta as given by the Wilczynski prescription[8] times of the order of 500 fm/c are necessary for a rotation of the complex by about 90 degrees.

An independent measure of the time scales governing IMF emission is provided by the observation of N/Z equilibration prior to IMF emission in these reactions.[9] Fig. 2 (left hand side) gives ratios of energy integrated isotope yields measured in seven reactions at E/A = 84 MeV at the CERN synchrocyclotron. The isotope yield ratios follow a monotonically increasing curve if plotted as a function of the neutron to proton ratio of the combined system of projectile and target, indicating that equilibration of the N/Z degree of freedom is attained throughout the whole system. Estimates of the actual times needed to reach N/Z equilibrium differ somewhat but are in the range of one to several 10^{-22}s or about 100 fm/c (Ref. 10). This might be considered a lower limit for the time elapsing prior to IMF emission and as such is consistent with the time scale derived above.

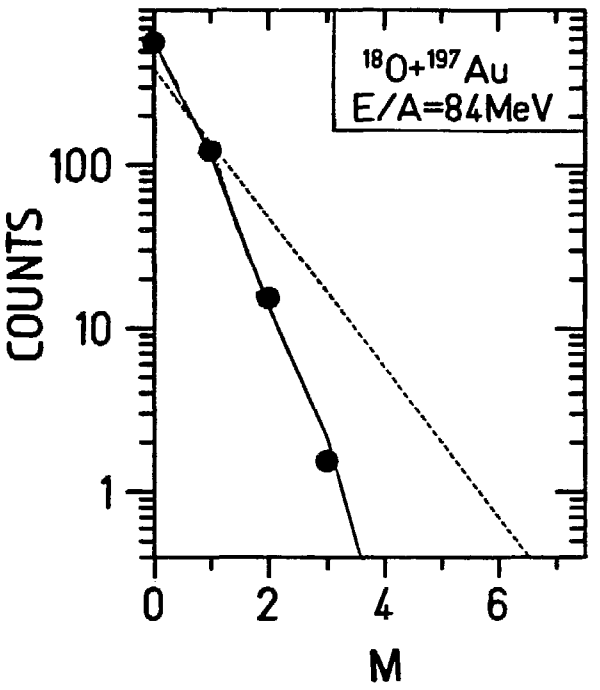

FIGURE 3
Relative probability to detect M additional fragments of $Z \geq 5$ with a large area parallel plate detector ($\Delta\Omega = 2.6\ \pi$ sr, $\theta \geq 22°$) in coincidence with a fragment of $Z \geq 6$ for the reaction ^{18}O on ^{197}Au at E/A = 84 MeV (full points). The fit curve (full line) was obtained by assuming an exponential primary multiplicity distribution (dashed line) and by applying a Monte Carlo model to account for the efficiency gap in solid angle and in the element range $Z < 5$ (from Ref. 12).

It is a characteristic of the intermediate energy regime that more than one IMF may be emitted simultaneously. This has been first observed in emulsion studies[11] and, more recently, also in electronic counter experiments.[12] Fig. 3 gives the measured and the reconstructed primary distributions of the multiplicities of IMFs in coincidence with one trigger fragment of $Z \geq 6$ for the reaction ^{18}O on ^{197}Au at E/A = 84 MeV. Additional IMFs are detected with the employed large area parallel plate detectors with about 20% probability. The deduced mean primary IMF multiplicity under this trigger condition is about 1.5 which includes the triggering fragment.[12] In order to test whether multifragment events are associated with a time scale different from that of the more conventional binary events, as might be expected for true multifragmentation conceived

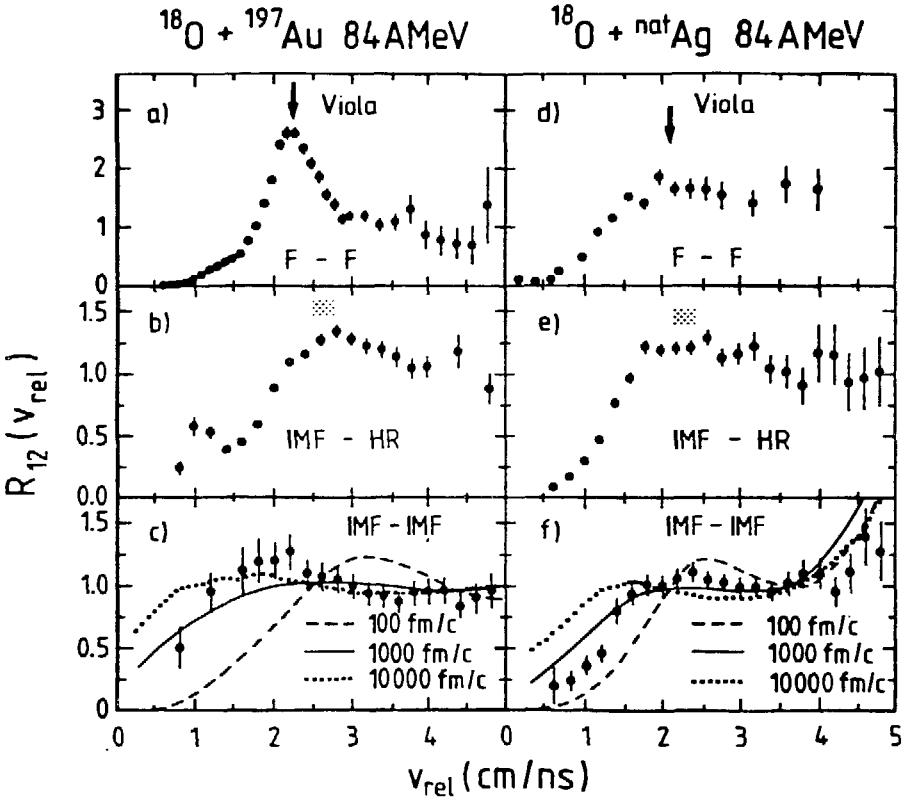

FIGURE 4
Correlation functions for fission-fission (parts a,d), IMF-heavy recoil (parts b,e), and IMF-IMF coincidences (parts c,f) for the reactions ^{18}O on Au (left panels) and Ag targets (right panels) at E/A = 84 MeV (from Ref. 13).

as a simultaneous multi-body breakup, the velocity correlations of coincident IMFs were analyzed.[13] Fig. 4 shows two-fragment correlation functions, defined as the normalized ratio of the true over random coincidences, as a function of the relative velocity for ^{18}O induced reactions on Au and Ag targets at E/A = 84 MeV. The IMF-IMF correlations are given in the bottom panels. The lines represent the results of classical Coulomb trajectory calculations based on the assumption that the second IMF is emitted with the indicated half life after the first one from the residual nucleus. The agreement with the data is best for half lifes of 500 fm/c (Ag target) up to 1000 fm/c (Au target). These times are similar to those associated with inclusive IMF emission as given above or as derived from the degree of forward peaking of the cross section angular distributions.[13] Multifragment events at these reactions and energies thus seem to be of a multi-sequential nature.

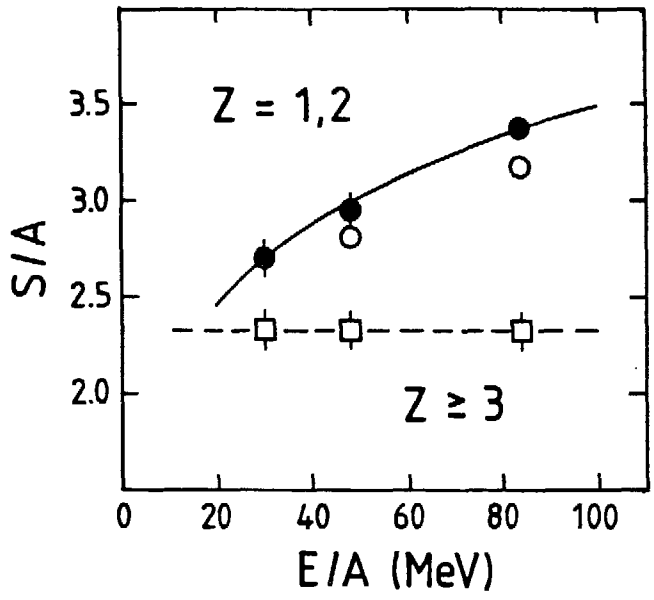

FIGURE 5
Entropy per nucleon, S/A, versus bombarding energy for preequilibrium light particles (Z = 1,2), inclusive (full circles) and with IMF trigger (open circles), and for IMFs (Z ≥ 3, open squares) from the reaction ^{12}C on ^{197}Au (from Ref. 15).

The measured isotope yield ratios may be used to establish a hierarchy of time scales for these reactions. If the ratios of the preequilibrium yields of tritons over protons are plotted as a function of the N/Z ratio of the combined system a strong projectile dependence remains.[9] N/Z equilibration over the whole system has not yet been achieved. However, the t/p ratios actually fall on a monotonically increasing curve if they are plotted as a function of the N/Z ratio of a system consisting of equal numbers of nucleons from the projectile and from the target, chosen according to their individual N/Z ratios (Fig. 2, right hand side). Apparently, preequilibrium light particles are emitted on a faster time scale from a system considerably smaller than the combined system. Even shorter reaction times are associated with projectile fragmentation. For ^{12}C induced reactions at E/A = 86 MeV the measured isotope yield ratios are virtually independent of the chosen target.[14]

The differences of the emission times for preequilibrium light particles and for IMFs are reflected in other observables as well. For example, the temperature and velocity parameters obtained from moving source fits to the measured cross sections are different not only in magnitude but also in their variation with bombarding energy. The temperature parameters of the preequilibrium light particle source increase with bombarding energy, as e.g. expected in

a thermal model, whereas those of the IMF sources remain practically the same.[12] The IMF dynamics seem to be fairly well decoupled from the entrance channel, in accordance with the ideas presented in the beginning.

The isotope yield ratios of preequilibrium light particles and of IMFs also vary in a different way with the bombarding energy.[15] Fig. 5 shows values of the specific entropy S/A which were derived from the isotope yield ratios with the help of a quantum statistical model[16] and which reflect this behaviour. Interpreted as the disorder generated in the heavy ion collision, the derived entropies fit into the picture that has emerged from the above discussion. In particular, it is worth mentioning that the fact that smaller entropies are associated with the IMFs (Fig. 5, open squares) than with the preequilibrium light particles (open points) under identical trigger conditions does not represent a puzzle. At the time of IMF emission the equilibration process may have spread the disorder generated in the primary collision over a larger part of the system and the entropy per nucleon S/A may thus be smaller. The value S/A ≈ 2 for the sources of IMFs is in the same realm as the entropies that for several reactions and with the same model were derived from measured mass yield distributions.[17,18] S/A ≈ 2 seems to be quite generally characteristic of IMF emission, and one may speculate that the attainment of the associated degree of disorder is a (statistical) condition necessary for IMF emission. This may be connected to the observed invariance of the breakup temperatures T ≈ 5 MeV (Refs. 19-21) and, together with it, implies that also the breakup density in IMF emission, $\rho/\rho_0 \approx 0.1$ (Ref. 9), is virtually independent of the reaction parameters.

In conclusion, the presented experimental results show that IMF emission occurs on a time scale slow enough so that some of the faster degrees of freedom (N/Z ratio) have reached equilibrium but before full dynamical equilibrium is attained. In particular, it proceeds slower than the emission of preequilibrium light particles which, conceptually, supports a two-step picture[22] in which the disorder generated by the primary nucleon-nucleon collisions spreads over the major part of the combined system, thereby creating conditions favourable for the emission of major nuclear fragments.

The experimental data discussed in this talk were obtained in collaboration with M.B. Tsang, W.G. Lynch, R.M. Ronningen, Z. Chen, C.K. Gelbke, T. Nayak, F. Zhu, M. Tohyama, and W. Dünnweber (experiments at the MSU-NSCL cyclotron), and with K.D. Hildenbrand, U. Lynen, W.F.J. Müller, H.J. Rabe, H. Sann, H. Stelzer, R. Trockel, R. Wada, N. Brummund, R. Glasow, K.H. Kampert, R. Santo, E.M. Eckert, J. Pochodzalla, I. Bock, and D. Pelte (experiments at the CERN synchrocyclotron).

REFERENCES

1) for references see, e.g., Proceedings of the Symposium on Central Collisions and Fragmentation Processes, Denver, Colorado, edited by C.K. Gelbke, Nuclear Physics A471 (1987) Nos. 1,2; see also the numerous topical contributions presented at this conference and references given therein.
2) G.F. Bertsch et al., Phys. Lett. 189B, 384 (1987).
3) M.B. Tsang et al. Phys. Rev. Lett. 57, 559 (1986); M.B. Tsang, Nucl. Phys. A471, 253c (1987).
4) W. Dünnweber et al., Phys. Rev. Lett. 52, 1405 (1984).
5) L. Sobotka et al., Phys. Rev. Lett. 53, 2004 (1984).
6) W. Mittig et al., Phys. Lett. 154B, 259 (1985).
7) K. Kwiatkowski et al., Phys. Lett. 171B, 41 (1986).
8) K. Siwek-Wilczynska et al., Nucl. Phys. A330, 150 (1979).
9) R. Wada et al., Phys. Rev. Lett. 58, 1829 (1987).
10) H. Freiesleben and J.V. Kratz, Physics Reports 106, 1 (1984).
11) B. Jakobsson et al., Z. Phys. A307, 293 (1982).
12) R. Trockel, thesis (1987), report GSI-87-17.
13) R. Trockel et al., preprint (1987), GSI-87-36.
14) J. Mougey et al., Phys. Lett. 105B, 25 (1981).
15) R. Trockel et al., preprint (1987), GSI-87-52.
16) H. Stöcker et al., Nucl. Phys. A400, 63c (1983); D. Hahn and H. Stöcker, preprint 1986.
17) B.V. Jacak et al., Phys. Rev. C29, 1744 (1984).
18) B.V. Jacak et al., Phys. Rev. C35, 1751 (1987).
19) J. Pochodzalla et al., Phys. Rev. Lett. 55, 177 (1985).
20) C.B. Chitwood et al., Phys. Lett. 172B, 27 (1986).
21) Z. Chen et al., preprint (1987), MSUCL-620.
22) J. Aichelin et al., Phys. Rev. C30, 107 (1984).

FISSION INDUCED BY PERIPHERAL REACTIONS WITH $^{56}Fe + {}^{197}Au$ AT 100 MeV/u*

F. Videbaek, B. Dichter, S. Kaufman
Physics Division, Argonne National Laboratory, Argonne, IL 60439-4843
O. Hansen, M. J. Levine, C. E. Thorn, W. Trautman
Brookhaven National Laboratory, Upton, NY 11937-9999
J. Boissevain, T. Blaich, M. Fowler, A. Gavron, B. Jacak,
P. Lysaght, J. Wilhelmy
Los Alamos National Laboratory, Los Alamos, NM 87545-0001
H. C. Britt
Lawrence Livermore National Laboratory, Livermore, CA 94550-0008
R. L. Ferguson
Oak Ridge National Laboratory, Oak Ridge, TN 37831-2008
G. Westfall, D. Cobra
Michigan State University, East Lansing, MI 48824-1116
G. Mamane, Z. Frankel
Weizmann Institute of Science, 76100 Rehovot, Israel

As part of a study of heavy ion reactions at intermediate energies carried out at the Bevalac we report the observation of fission-like processes induced by peripheral reactions. Studies of this kind have been carried out earlier with lighter heavy ions in the energy range 250-5000 MeV/u [1,2] and at lower energies with many different projectiles ranging form ^{12}C to ^{40}Ar (see ref. [3] and references therein). Via a study of the linear momentum transfer it is of interest to observe the limits on excitation energy which can be held by the nuclear system and to study the transition to multi-fragmentation, which is an important reaction channel at these energies. Theoretical studies [4] indicate that one of the important factors for this transition is the excitation energy in the residual target fragment.

The analysis will show that the features of the observed correlation between momentum transfer and mass in the fission process can be understood with simple models involving momentum and energy conservation. The results are

*This work supported by the U. S. Department of Energy, Nuclear Physics Division, under contract W-31-109-ENG-38; LANL; LLNL; Brookhaven National Laboratory under contract DE-AC02-76-CH00016; and Oak Ridge National Laboratory under contract DE-AC05-84OR21400.

consistent with little mass transfer taking place to the target for reactions involving fission decay. This indicates that the mechanism for transfer of momentum at these energies may be by inherent multiple nucleon-nucleon collisions, and not the result of massive incomplete fusion processes as at lower bombarding energies. The conclusions are supported by comparisons to Intranuclear Cascade (INC) calculations for the reaction.

The PAGODA system is designed to measure fragments from reactions over a broad range of energies and masses. The initial design focused on detection of heavy masses with the aim of studying the fission process induced by heavy projectiles at intermediate energies. More recently the detector modules have been redesigned to push towards the detection of lighter masses. A detailed description can be found in the paper following [5]. The setup consists of an array of 6 gas detectors, each with two position sensitive multiwire detectors and a high pressure ion chamber. Several of the gas modules were backed by a 3*3 array CaF2 phoswich detectors to measure and identify light particles in coincidence with heavy fragments. The mass identification for the present experiment was obtained from the time of flight information between the MWPC's combined with the energy measurement in the ion chamber. The calibrations were performed using a Cf fission source and beams from the LBL 88 inch cyclotron. Corrections to the measured energies due to energy loss in the target, foils and gas were made. For this dataset we estimate a mass resolution of 30 u, with the centroid being determined to better than 5 u. The efficiency in the present dataset for detecting masses A > 60 and determining their angular positions is close to 100%, but dropping rapidly for lighter masses. Absolute cross sections were obtained using the integrated beam current and the known target thickness. It is estimated that the singles cross sections are determined to better than 20%, and the binary cross sections to about 40%.

The data for heavy fragments were divided into mass bins of 10 units and into angular bins of 8°. Typical results are displayed in fig. 1 for the mass bin centered around 90 u. The double differential cross section is displayed as function of energy for emission angles from 24-120°. It can be inferred from these data that the mass 90 products come from at least two sources: one with a higher velocity ($\beta \sim 0.08$ v/c) giving rise to the forward peaked angular distribution, and with a Coulomb peak in the energy distribution and another with low velocity which dominates at back angles. The distributions have been integrated over all energies and angles yielding the inclusive fragment cross section shown in fig. 2. It should be pointed out that the differential cross sections are quite similar to those seen in Ne- and proton-induced reactions on

Au with similar total energies (around 5 GeV) (ref [2]). As will be shown later, part of the mass yield around mass 90 is due to a fission process which constitutes about 20% of the total cross section in this mass range. The remaining part has often been named deep spallation, and is correlated with more violent processes, but is not well understood and studied.

The binary mass correlations are shown for different opening angles in fig 3. For the 180° opening angle a typical fission distribution with an mass sum of 200 is observed. At the smaller opening angle of 144°, a distribution with a mass sum of 150 is observed, but with a broader mass distribution. At the other angles little indication for fission is seen. The total kinetic energy observed for the heavy coincidence partners is consistent with the kinetic energies from fission of a target-like mass 197. At all angles we observe (but with reduced efficiency) a significant coincidence yield between medium mass fragments.

The parallel and perpendicular momentum transfer was calculated on an event by event basis. Distributions of these quantities for pairs of opening angles were made under the requirement that the sum of the masses was greater than 120. The values of P_{ll} and P_t for 3 opening angles combinations averaged over the individual gas detector acceptances, and summing all detectors pairs with the same opening angle are summarized in the table.

θ_{12}	P_{ll} (GeV/c)	P_t (GeV/c)
180	.54	.35
144	1.97	.4
108	3.70	.4

Note that for these opening angles p_t is quite small confirming the essential binary nature of these events.

The yields for each value of P_{ll} were corrected for efficiency evaluated from a Monte Carlo simulation assuming isotropic emission of fission fragments in a moving frame. The cross section is shown in fig 4. We observe that the most likely momentum transfer is 2 GeV/c, a value typical for heavy ion induced reaction above 20 MeV/u. From this we can extract the total fission yield of 40-60 mb, to be compared with the total yield for the mass range 120 > A > 70 of 250 mb.

There are several models which attempt to describe the peripheral fission process and associated momentum transfer. One class is based on simple concepts of of energy and momentum conservation coupled with assumptions on the mass transfer from projectile to target. Analysis of higher energy reactions with projectiles of protons and neon have been presented in [6] and demonstrated that the process leading to fission has little or no mass transfer to the target. The experimentally derived parameters $<P_{ll}>$ can be expressed as function of the observed mass loss

$$P_{ll} = P_{ll}^{0} \cdot \Delta M$$

where ΔM is the mass loss of the fissioning system and where one assumes that no transfer takes place to the Au target. The data for different systems are consistent with a linear expression

$$\beta \cdot P_{ll}^{0} = \Delta E$$

with ΔE being a constant representative of the loss of excitation energy per nucleon due to evaporation from the fissioning system. The current set of data have been analyzed following these guide lines. The binary data were sorted according to their mass sum. The results for the opening angle distributions are given in fig 5 for mass bins with centroids 195, 175, and 145. The most probable fission angle is indicated by an arrow. The momentum transfer is calculated according to

$$P_{ll} = M_t \cdot <v_{ll}> \cdot \cos(\theta_{12}/2)$$

where M_t is the mass of the fissioning system, $<v_{ll}>$ is the most probable velocity for the fission fragments, and θ_{12} the observed opening angle. Figure 6 shows the data for 100 MeV/u ^{56}Fe + ^{197}Au together with the data for ^{20}Ne + ^{197}Au from ref [6]. The lines are least square fits to the data. The value of the slope parameter $\Delta E/\beta$ is the same for the two systems, 13 MeV. This shows the similarity between the reactions for different projectiles at the same energy, and confirms the peripheral nature of the reaction. It should be remarked that the fission-like nature of the decay is observed for momentum transfers of up to 2 GeV/c, corresponding to excitations energies up to 600 MeV as estimated either from the simple model,or the INC calculations described below.

At lower energies such data are often analyzed using an incomplete fusion picture in which the momentum transfer is obtained by an initial massive transfer from the projectile to the target. Such an analysis was carried out for 60 MeV and 84 MeV/u C + Au [7] and seems to work quite well. Following this scheme for the present system would result in the curve given by the dashed line in figure 6 which seems inconsistent with the present data.

Conversely, if these data are analyzed in terms of the peripheral model we extract a slope parameter $\Delta E/\beta$ of 22 MeV which is unrealistic considering that this parameter is normally identified with the excitation energy carried away by each evaporated nucleon. Thus these results appear consistent with a change of reaction mechanism at these projectile energies.

An approach which may be applicable to this energy regime is that of the Intranuclear Cascade. This has been applied previously to the study of the energy dependence of linear momentum transfer [8,9]. To gain insight into the reaction mechanism we have started a study of the reaction using the INC code ISABEL by Yariv and Frankel [10]. At the present time we have just started these calculations so the results are preliminary and are included to show what may be learned. A feature which has been added to the code is that the effect of evaporation and fission of the residual heavy fragments produced in the collision, is included by following these decay modes by addition of the program PACE [11]. This will enable us to make a realistic comparison between the prediction of the model and the data measured here and in upcoming experiments.

The start basis for PACE is the list of the residues with the calculated physical quantities. Nuclei with excitation energies above 1000 MeV are discarded. The program begins with the nuclei above 300 MeV excitation energy and cools them by fast particle emission. At this stage, only protons and neutrons are considered. The choice is made according to the Z/A ratio and the energy is picked from a Maxwellian distribution with a slope of 15 MeV. As soon as the nuclei have been cooled to below 300 MeV a standard statistical calculations takes place where competition between p,n, alpha, gamma emission and fission is considered. The kinematics of the final products are followed before making distributions of the observable physical quantities. The standard options in ISABEL have been employed and calculations have been averaged over impact parameter. Here two qualitative results will be shown. The distributions of residue mass vs. parallel momentum and excitation energy are shown in figs. 7 and 8. One result is that the initially formed residues have masses slightly lower than the target. The excitation energies range to above 1000 MeV, and that the momentum transfer is induced by the underlying nucleon-nucleon collisons. The decay mode of most highly excited fragments cannot be described with standard codes, so more refined theoretical methods has to be employed. It is likely [4] that the decays for these excitation energies result in breakup into several medium mass fragments. Another result is that some excitation of the projectile is predicted, a feature which has been ignored in most of the earlier

work with simple models. An analysis of the momentum transfer show that for a value for $<P_{||}>$ = 2 GeV/c where we did see binary fission as much as 600 MeV of excitation energy has been transferred to the target. We seem to have a fair agreement between the calculations and the momentum transfer vs. observed mass. The detailed comparison of the $P_{||}$ distributions will be done later.

Results of peripheral fission at 100 MeV/u ^{56}Fe + ^{197}Au have been presented. The data follows the trends observed in reactions at higher incident energies, but not those with lighter projectiles at lower energies. The average momentum transfer follow the trend in the systematics as collected by Viola [9] with $<P_{||}>/A$ ~ 40 MeV/c and show a momentum transfer (~ 2GeV/c) to the target residue system that subsequently decays to binary fission. An analysis in terms of INC calculations shows promise in being able to describe the data, and a detailed comparison will tell us more about the limits to conventional compound nucleus formation and statistical evaporation in heavy ion reactions at intermediate energies. The well known fission process again is used as a tool to understand more complicated reaction mechanisms.

REFERENCES

[1] S. Kaufman, Nucl. Phys. **A471** (1987) 163c.

[2] A. I. Warrick et al., Phys. Rev. **C 27** (1983) 1083.

[3] C.-K. Gelbke and D. H. Boal, Michigan State University Report, 584.

[4] D. H. E. Gross, Zhang Xiao-ze and Xu Shu-yan, Phys. Rev. Lett. **56** (1986) 1544.

[5] D. Fields, contribution this conference.

[6] S. Kaufman et al., Phys. Rev. **C 26** (1982) 2694.

[7] D. Jacquet et al., Nucl. Phys. **A445** (1985) 140.

[8] L. W. Woo et al., Phys. Lett. **132B** (1983) 283.

[9] V. E. Viola, Nucl. Phys. **A471** (1987) 53c.

[10] Y. Yariv and Z. Frankel, Phys. Rev. **C 20** (1979) 2227.

[11] A. Gavron, Phys. Rev. **C 21** (1980) 230.

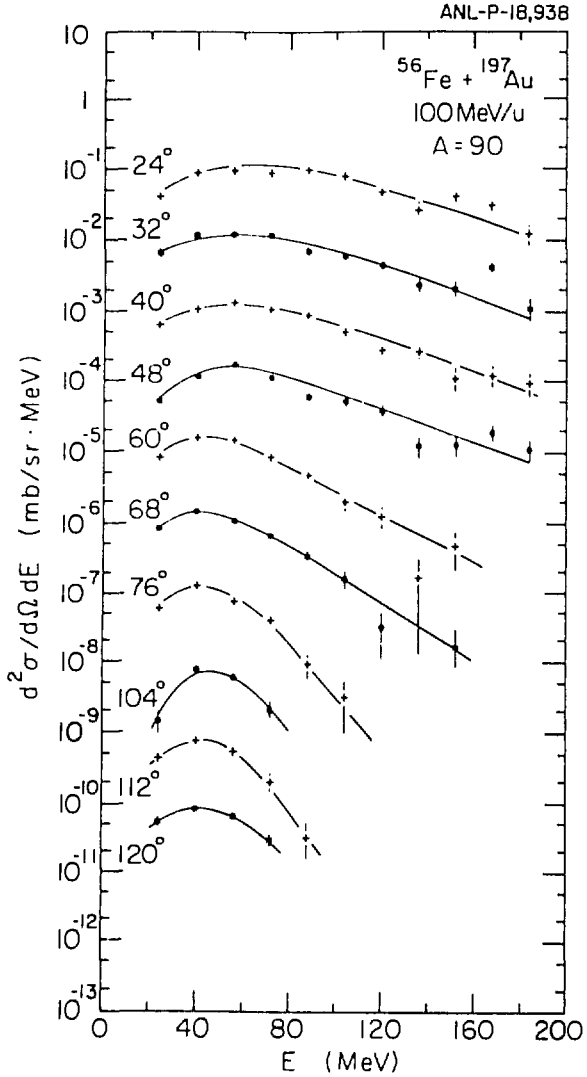

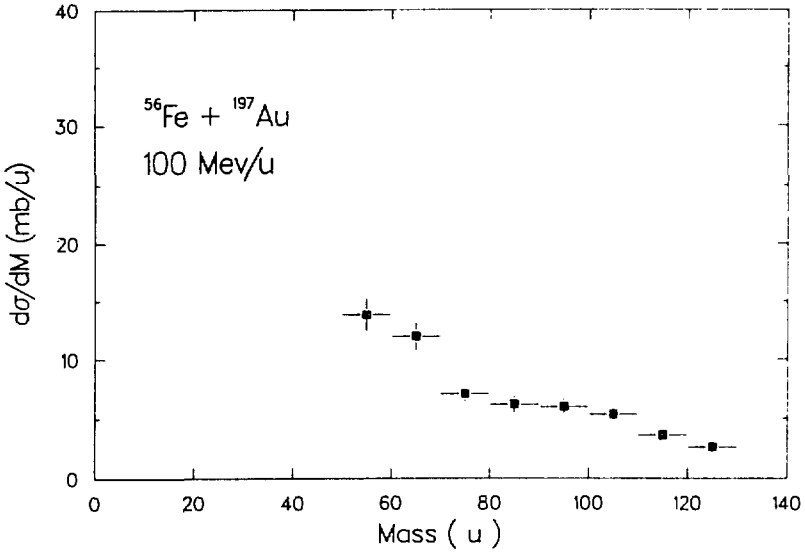

Figure 1. Energy spectra of mass 90 fragments for different laboratory angles. For each increment in angle the data have been divided by 10 before plotting.

Figure 2. Integrated yields for A › 50.

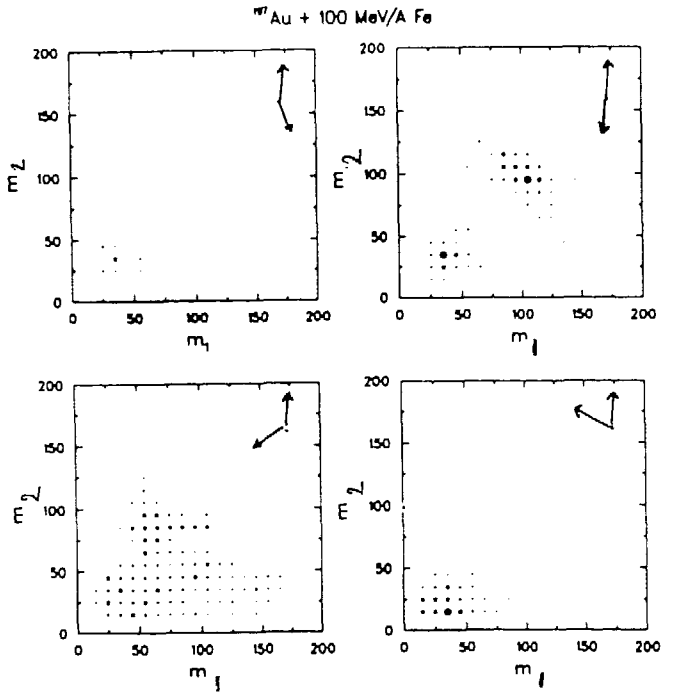

Figure 3. Mass correlations between 4 different sets of Pagoda modules. The arrows indicates the detector position with the beam going towards the left.

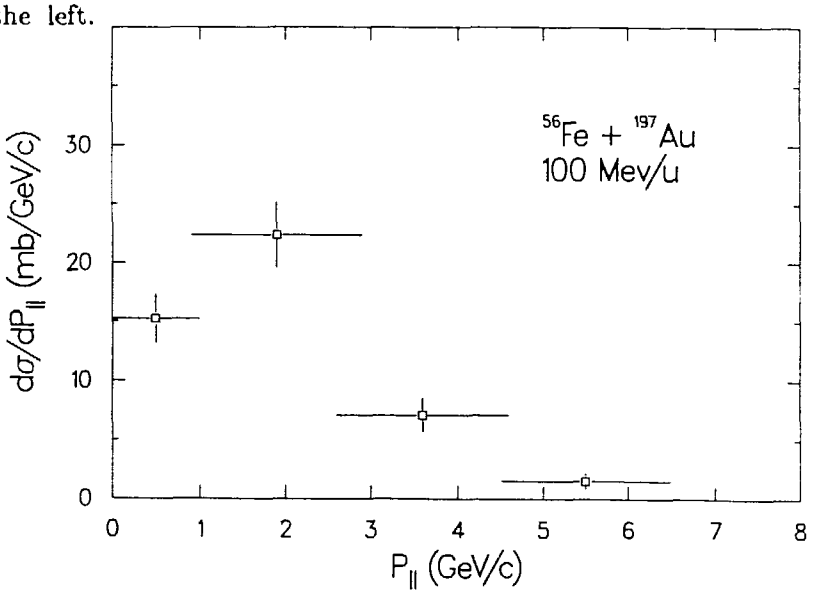

Figure 4. Parallel momentum distribution for binary events with total mass > 120.

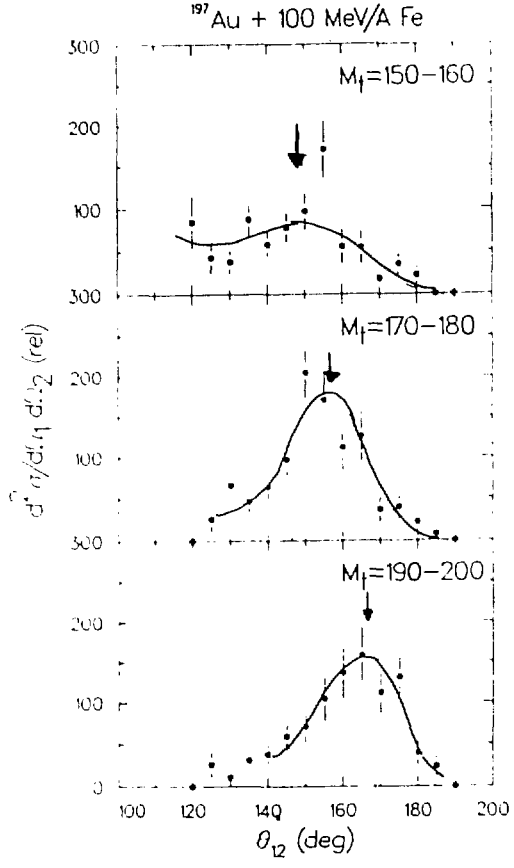

Figure 5.

Double differential coincidence angular distributions for a total mass in the range given on the figure.

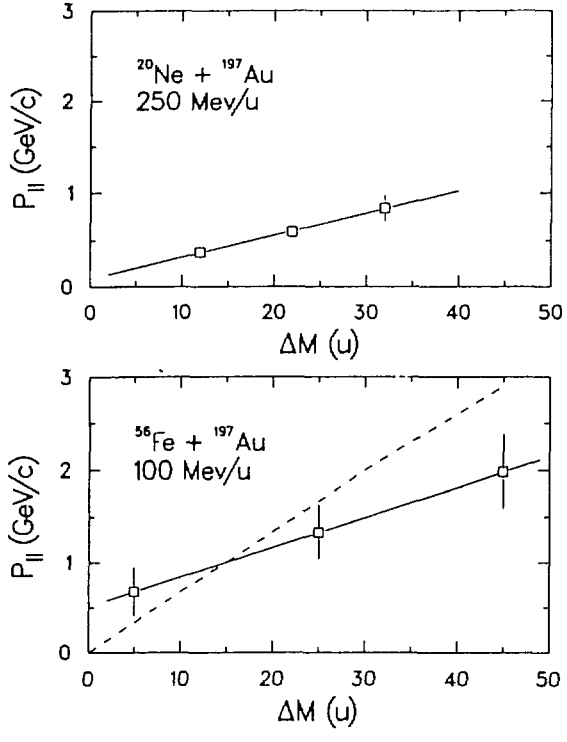

Figure 6. P_{II} vs mass loss for Fe, Ne induced reactions.

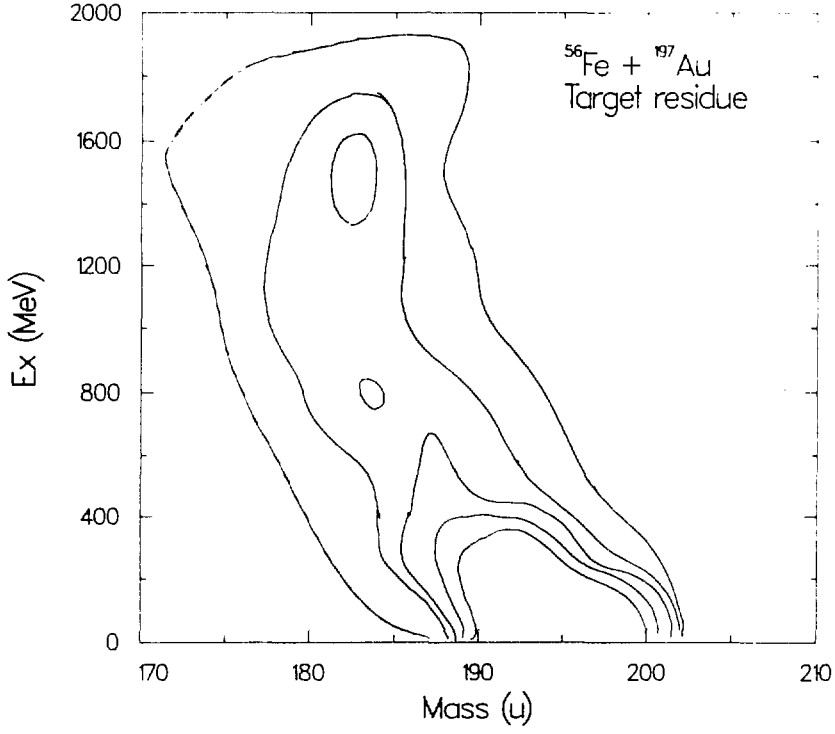

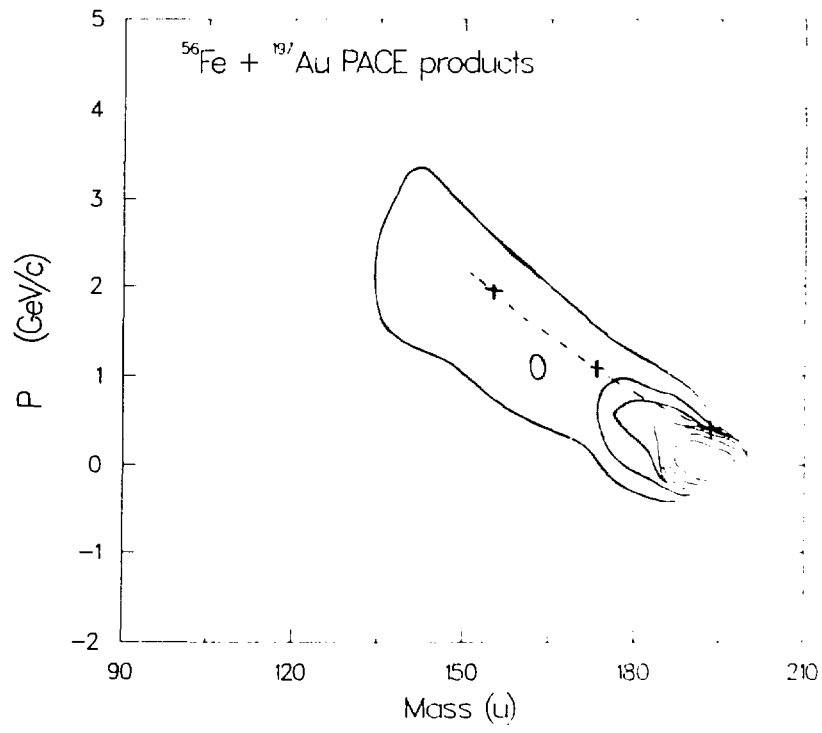

Figure 7. Result of combined INC and PACE calculation. P_{II} vs. M_t. The crosses show the experimentally observed values for binary fission events.

Figure 8. INC calculation Ex vs. M_t for ^{56}Fe + ^{197}Au.

STUDIES OF FRAGMENTATION AT 100 MEV/A AT THE BEVALAC LOW ENERGY BEAM LINE

H.C. Britt, D.J. Fields, L. Hansen, R.G. Lanier, R.R. Marquardt,
D. Massoletti, N. Namboodiri, B. Remington, T.C. Sangster,
G. Struble, M.L. Webb
Lawrence Livermore National Laboratory
Livermore, California

T. Blaich, M. Fowler, J. Wilhelmy
Los Alamos National Laboratory
Los Alamos, New Mexico

B. Dichter, S. Kaufman, F. Vidabaek
Argonne National Laboratory
Argonne, Illinois

Y.D. Chan, A. Ducal, A. Harmon, J. Pouliot, R. Stokstad
Lawrence Berkeley Laboratory
Berkeley, California

Abstract

The detector system currently operating at the Bevalac Low Energy Beam Line is discussed. This system consists of a 34 element forward angle hodoscope and an 8 element array of gas-phoswich modules which has both a wide dynamic range and a large geometrical solid angle. This latter array is arranged at large angles to detect intermediate mass fragments, fission products, and slow, heavy target residues. Applications of this system to studies of reaction mechanisms at intermediate energies are discussed.

Studies of reaction mechanisms in intermediate energy nuclear collisions are motivated by reasonably general questions about the behavior of nuclear systems. The static properties of bulk nuclear matter, including its equation of state and phase properties, are of particular interest. Except for the

rather indirect and scarce evidence provided by astrophysics and the behavior of nuclei near or in their ground states, most of our information is derived from the rather small, transient systems created in nuclear collisions. Because of this, both the dynamical properties of these systems and the mechanisms by which they decay are essential elements of these studies.

Added to the complexity of the questions posed are the difficulties in identifying and executing appropriate measurements. The energetic reactions used in these studies lead to rather chaotic final states, with large particle multiplicities and broad distributions. This fast has led to the desire for increasingly complicated, complete measurements, and for detector arrays designed to detect as many of the reaction products as possible. Because the reaction products cover a very large dynamic range, from light particles with energies of several hundred MeV/A to heavy reaction residues with masses greater than 100 and energies of a few tens of keV/A, an ideal detector should not only cover a large geometrical solid angle, but also possess a large acceptance in both particle energy and mass.

At the Bevalac Low Energy Beam Line, we have developed a detector array with both a large geometrical solid angle and a wide dynamic range. The previous paper (Videbaek, et. al.) reports on data taken with an earlier version of this array, which was optimized for fission studies. Improvements to the system have extended its range to include nearly the entire range of reaction product energies and masses. The addition of an array of phoswich telescopes at forward angles which can detect projectile remnants and other fast particles allows for an increase in the exclusivity of the measurements. I will discuss this new system and its anticipated performance. In addition, I will present an example of the data which the array will provide and will discuss measurements which we expect to make in upcoming experiments.

The Pagoda detector system, which is depicted in Figure 1, consists of two major subsystems. At forward angles is a 7x5 array of 34 fast/slow plastic telescopes. This array is designed to detect the forward focussed energetic fragments associated with the projectile and the intermediate rapidity source. It extends horizontally from 2° to 10° on either side of the beam, and vertically from 2° to 14° on either side of the beam. Using the standard phoswich technique it can identify light particles by charge above 10 MeV/A, carbon ions above 16 MeV/A, neon ions above 22 MeV/A, and niobium above 40 MeV/A. Figure 2 is a scatter plot of data taken at the Bevalac Low Energy Beam Line with a Ne beam incident on a Au target at E/A = 100 MeV using a single

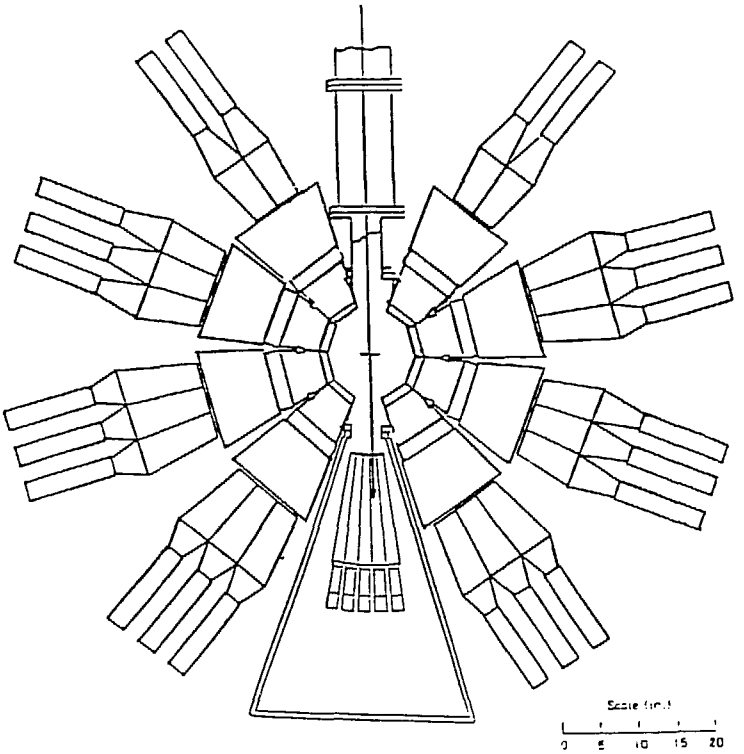

Figure 1. A schematic diagram of the Pagoda array. The eight gas-phoswich telescopes are positioned about the target at large angles. The 34 element fast/slow plastic array is located at forward angles.

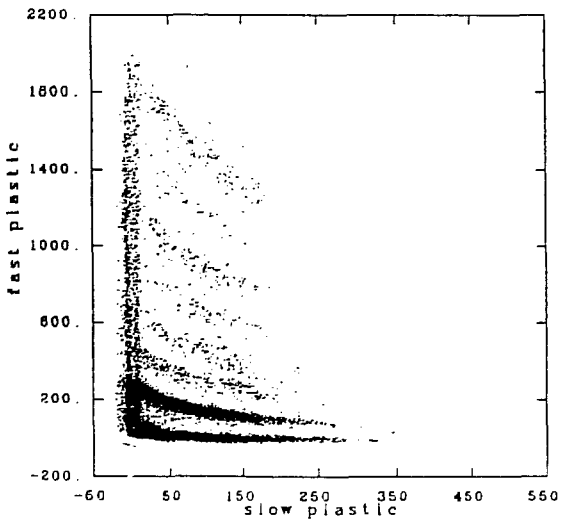

Figure 2. A scatter plot of data taken with a fast/slow plastic hodoscope element at about 12° from Ne + Au at E/A= 100 MeV. In this plot the fast (ΔE) and slow (E) components of the scintillator output have been separated.

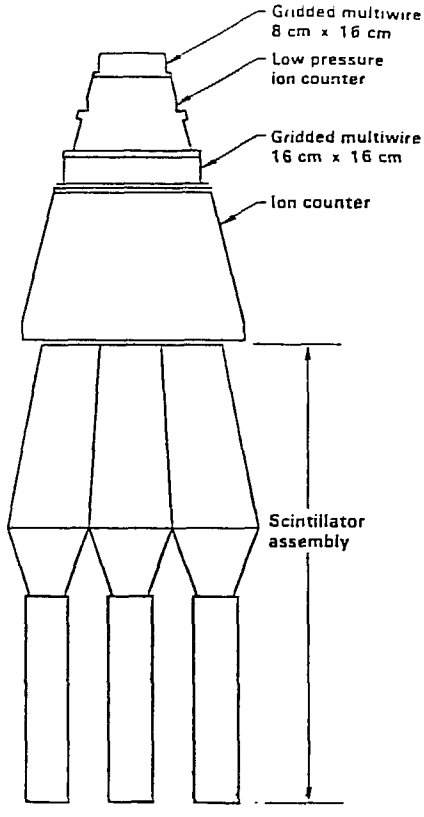

Figure 3. A schematic diagram of a gas-phoswich telescope module.

element of the array. In addition, the time of flight and total energy measurements can be used to identify products below these thresholds with somewhat lower resolution. The scintillators can stop protons with energies of 200 MeV and exhibit an energy resolution of about 3% FWHM.

The second major subsystem consists of eight gas-phoswich telescope modules. A diagram of a module is shown in Figure 3. Each module consists of a series of six elements. In the front are two position sensitive multiwire counters separated by 18 cm of gas where a low pressure proportional counter is operated. The detectors are operated at about 2 torr of isobutane. The time of flight of fragments between the two multiwires is an important tool in fragment identification, as will be shown later. The resolution of the time of flight of 5 MeV α particles between these detectors has been measured to be 650 ps, FWHM. An important operating characteristic of these counters is their gain. The counters are a two step amplifier design[1] using a foil cathode, with gains sufficient to provide a reliable trigger for C ions with energies up to ≈33 MeV/A, Li ions up to 6 MeV/A, Be ions up to 12 MeV/A, and B ions up to 25 MeV/A. Thus the multiwire counters provide a nearly full range trigger for fragments of mass greater than 10. In addition to time of flight, all three elements measure energy loss. The proportional counter possess the highest resolution of about 10% FWHM. The multiwire counters measure position with a resolution of about 2 mm. Because there are two detectors, the location of the interaction in the target can be determined, mitigating the effect of a large beam spot.

Behind this three element assembly is a longitudinal field Frisch grid ion chamber, which is operated with between 50 and 100 torr of CF_4. It

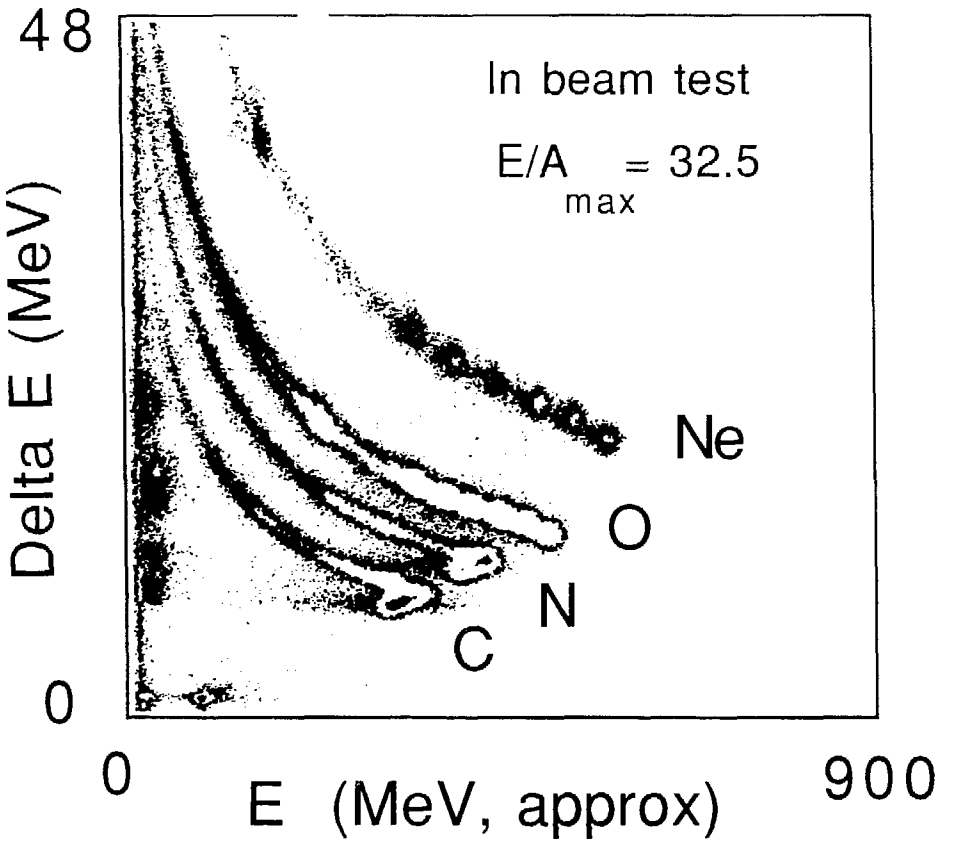

Figure 4. Plot of ΔE, as measured in the ion chamber, against E, as measured by the CaF_2 scintillator showing Z resolution for A/Z=2 isotopes of C, N, O, and Ne.

provides an energy loss measurement with a resolution of about 5% FWHM. At these pressures, fragments with energies less than 3-5 MeV/A will either stop in the ion chamber or in its anode foil.

Fragments with energies greater than about 3-5 MeV/A reach the scintillation assembly, comprised of a two element phoswich scintillation telescope which measures residual energies and can identify energetic fragments and light particles. The energy resolution of these scintillators is about 3% FWHM. The telescopes are presently made of a 1 mm thick CaF_2 crystal backed by a thick "fast" plastic scintillator. This construction results in a very high energy threshold for identification and triggering. A new set of telescopes, made with "fast" and "slow" plastic scintillators, are under construction. These new telescopes will complete the dynamic range of the gas-

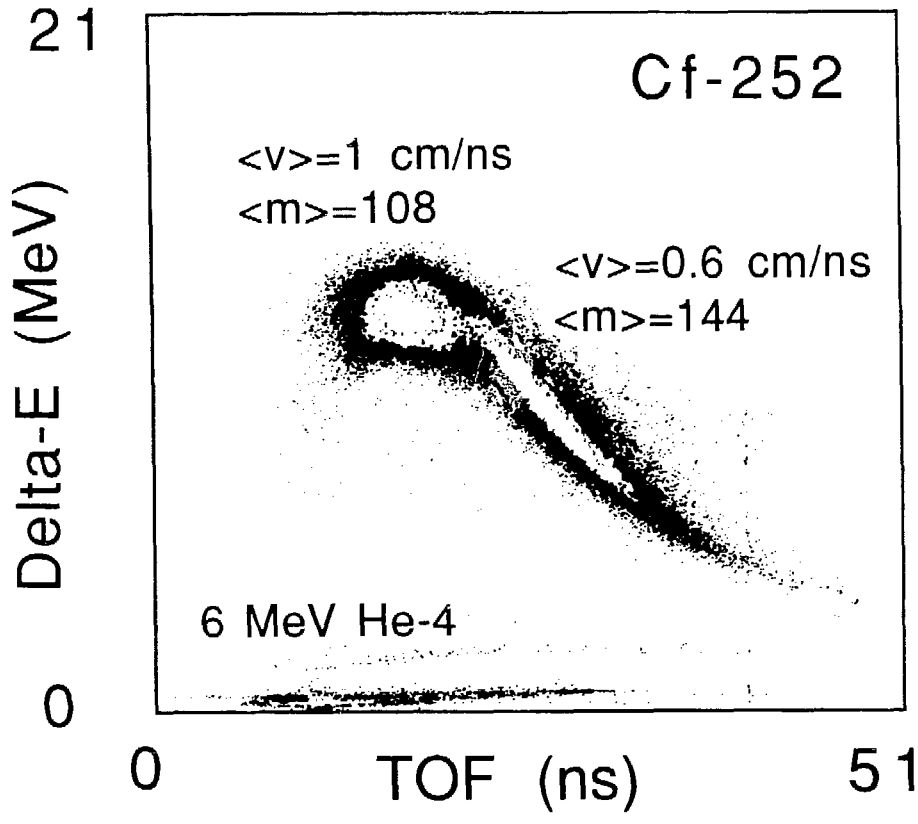

Figure 5. Plot of time-of-flight between multiwire counters against the energy loss in the low pressure proportional counter for ^{252}Cf fission fragments and alpha particles.

phoswich telescope for energetic light fragments to which the front multiwire counters are not currently sensitive.

The eight gas-phoswich telescopes are centered at 36°, 72°, 108° and 144° on either side of the beam in a cylindrically symmetric arrangement, as indicated[2] in Figure 1. The front multiwire counter of each module has an active solid angle of 290 msr, providing a position, time and energy loss measurement. The remainder of the elements are active over a solid angle of about 150 msr. This provides a coverage of about 20% of 4π for coincident fission fragments and heavy residues, for which the front multiwire can provide reasonable identification. Approximately 10% of 4π is covered with the complete dynamic range of the module.

The performance of the system is demonstrated in Figures 4 and 5. In Figure 4, the charge identification of ^{12}C, ^{14}N, ^{16}O, and ^{20}Ne is demonstrated

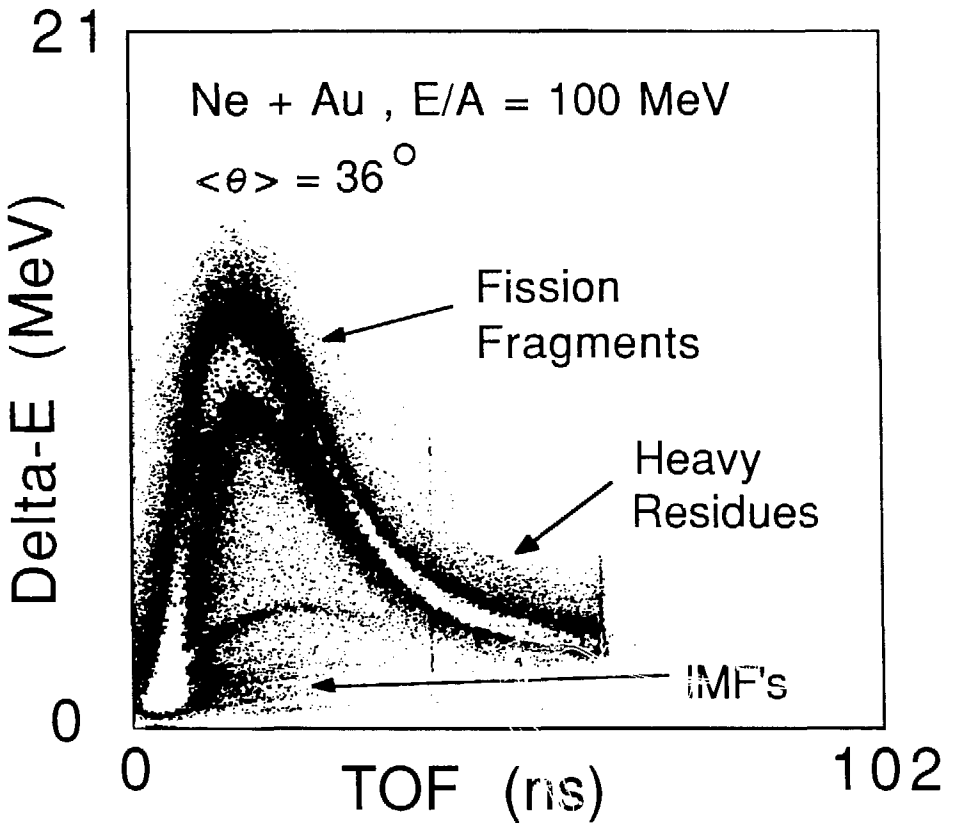

Figure 6. Plot of time-of-flight between multiwire counters against the energy loss in the low pressure proportional counter for products from the Ne + Au reaction at E/A = 100 MeV, as measured at 36°.

in the plot of energy loss in the ion chamber vs residual energy in a CaF_2 scintillator. The beams, provided by the 88" cyclotron at LBL, had a maximum energy of E/A=32.5 MeV, with less energetic ions being provided by foil degraders. (The irregularities along the charge lines are due to the different degraders.) This data was taken requiring a coincidence between the front and back multiwire detectors, demonstrating their sensitivity. In fact, data was taken with 120 MeV α particles using the same triggering requirements but with reduced efficiency.

Figure 5 shows the capabilities of the detector for low energy particles. The plot is of energy loss in the low pressure proportional counter versus time of flight between the multiwires for products of a ^{252}Cf source . The peak from the 6 MeV α particles is clearly present at the lower left. There are two mass groups of fission fragments, one with an average mass about 107

and an average energy of 1 MeV/A, and other with an average mass of 142 and an energy of about .6 MeV/A. These groups are clearly distinguished.

While the first experiment with this new system is not scheduled till December, 1987, we have run sections of these detectors at the Bevalac during beam development time with Ne beams of E/A=100 MeV on a Au target. Figure 6 shows a plot of time of flight against energy loss, as in Figure 5, taken during this run. The detector subtends the lab angles $20°<\theta<44°$. We can identify three groups of reaction products in this plot. The first group, close to the origin, represents intermediate mass fragments of Z<20. In fact, one can see lines corresponding to charge identified low energy fragments from Z=2 to 10 extending into this group of events. Events with somewhat larger flight times and the largest energy losses are fission fragments with Z≈30-40. At much larger flight times one finds another group of events which correspond to relatively slow, heavy target-like fragments with energies of 0.2 to 0.3 MeV/A.

The Pagoda array is clearly suited to studies of fission products in these reactions. Approximately a quarter of the events in this plot are fission products. With its co-planar arrangement, the array is very likely to catch both fragments of such a binary decay. Such studies provide inclusive information on momentum and energy transfer in reactions leading to fission. Because of the high efficiency for detecting intermediate mass fragments, more exclusive studies of the fission mechanism, such as those described in a previous report (Viola, et al and reference 3) are also possible.

The very slow heavy reaction products are also of interest in studies of reaction mechanisms. Their energies (.2 to .3 MeV/A) suggest that they are products of large (50%) momentum transfer events. Since about a third of the events in this plot are of this type, there may be a significant cross section for such violent events. However, because their energies are rather low, few studies have been made of these products.

Multifragmentation is a topic of particular interest. The large acceptance of this detector array will allow studies of high multiplicity events. Roughly a third of the inclusive events represent intermediate mass fragments, and the fragment-fragment coincidence rate appears to be high. The large dynamic range of the system will yield data which is not significantly troubled by energy thresholds.

Finally, all of these studies can be done in conjunction with measurements in the forward angle hodoscope. Measurements of forward going

projectile remnants may help to specify the energy and momentum transfer in peripheral collisions. This system will provide information on the energy sharing between the projectile and target, on the multiplicities in central collisions, and on the overall momentum and energy balance in the reactions.

In summary, we have constructed an array of detectors to study heavy ion collisions at intermediate energies. It provides both a large geometrical coverage and an extended dynamical range, making it possible to study, simultaneously fast light fragments and slow, heavy reaction residues.

This work was performed under the auspices of the U.S. Department of Energy by the Lawrence Livermore National Laboratory under contract number W-7405-ENG-48.

1) A. Breskin, Nucl. Instrum. Methods 196 (1982) 11, and B.D. Wilkins, Argonne National Laboratory, Private communications.

2) The entire detector has been rotated 4° from the original position, depicted in Figure 1, so that the array is presently symmetric about the beam axis.

3) M. Fatyga, K. Kwiatkowski, V.E. Viola, W.G. Wilson, M.B. Tsang, J. Pochodzalla, W.G. Lynch, C.K. Gelbke, D.J. Fields, C.B. Chitwood, Z. Chen, and T. Nayak, Phys. Rev. Lett. 58 , 2527 (1987).

COMPLEX FRAGMENT EMISSION IN THE REACTION 250 MeV/u $^{20}Ne + ^{197}Au^*$

D. R. Bowman, R. J. Charity, H. Han, K. Jing, M. A. McMahan, R. J. McDonald,
L. G. Moretto, and G. J. Wozniak
Lawrence Berkeley Laboratory
University of California
Berkeley, California 94720

W. L. Kehoe, B. Libby, and A. C. Mignerey
University of Maryland
College Park, Maryland 20742

In the past few years we have performed a number of experiments directed at elucidating the mechanism of complex fragment (CF) emission in reactions with beam energies ≤ 50 MeV/u. We have concluded that for asymmetric systems all of the CF emission originates from three catagories: 1) an isotropic component which is consistent with the binary decay of compound nuclei following either complete or incomplete fusion reactions, 2) An anisotropic component characterized by target-like and projectile-like species resulting from spectator fragments, and quasi-elastic and deep inelastic processes, and 3) a possible additional fast-fission mechanism for the $^{93}Nb + ^{27}Al$ reactions at E/A ≤ 18 MeV.[1-4]

The nature of the former process is shown by the invariant cross sections in velocity space for emission of various complex fragments following $^{93}Nb + ^{27}Al$ reactions at E/A = 18 MeV (Fig. 1). These distributions are characterized by Coulomb rings typical of isotropic emission from a source with a well defined velocity. It has been verified that the extracted source velocities, emission velocities, angular distributions, and coincident events are all consistent with the compound nucleus mechanism. To verify the compound nucleus nature of the cross sections, which demonstrate the statistical competition of the various exit channels, we have recently written a generalized statistical decay code that incorporates complex fragment emission in the manner prescribed by Moretto.[5] The theoretical results and the experimental data are in very good agreement for the $^{93}Nb + ^{9}Be$, and ^{12}C reactions between 8 and 30 MeV/u.[4]

The above experimental program has the dual goals of mapping the binary decay process until it (presumably) vanishes above a given energy, and detecting the onset of multifragmentation --

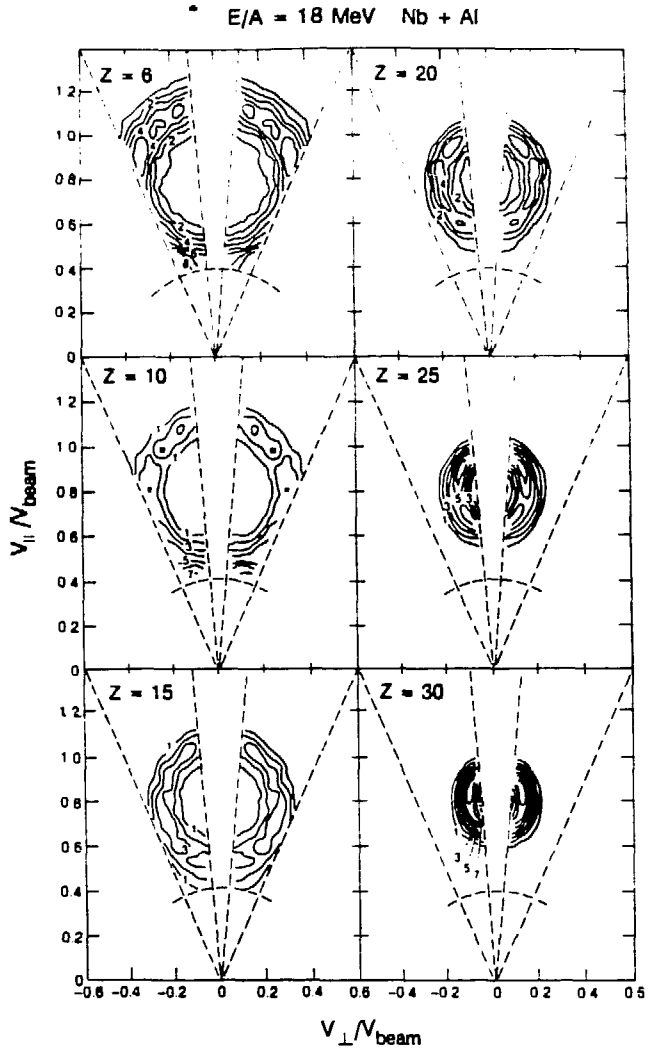

Fig. 1. Invariant contours of the experimental cross section $\partial^2\sigma/\partial V_{\parallel}\partial V_{\perp}$ in the $V_{\parallel}$ - $V_{\perp}$ plane for representative fragment Z-values detected in the reaction E/A = 18.0 MeV ^{93}Nb + ^{27}Al. The beam direction is vertical. The dashed lines show the maximum and minimum angular thresholds and the low velocity threshold of the detectors. The magnitudes of the contour levels are relative.

defined here as the production of 3 or more fragments significantly more massive than alpha particles. The reverse kinematic technique that has been so successfully employed in clarifying the experimental picture is limited to E/A below approximately 100 MeV due to the increased kinematic focusing of the reaction products to smaller and smaller angles. To study asymmetric reactions at larger incident energies one must use light ion beams impinging upon heavy targets.

Recent developments in this field have produced results similar to our work at lower energy. We are therefore interested in developing a complementary experimental program using light projectiles of E/A ≥ 100 MeV. To this end, we have performed a preliminary experiment of 250 MeV/u ^{20}Ne + ^{197}Au to study the emission of the slow, target-like complex fragments, and to compare the results to our earlier systematics.

To review the long history of light ion - nucleus collisions one must begin with the radiochemical studies of the 1950's in which the emission of complex fragments was first observed in high energy proton (0.6 - 3.0 GeV) induced reactions.[6] The initial counter experiments of this type were done at the Bevalac with 5.5 GeV proton beams in the early 1970's.[7,8] A large amount of similar work followed, peaking in the middle of the decade and then tailing off with the availability of heavier beams in the 1980's. The general results of these experiments using a variety of beams (p, d, ^{4}He, ^{20}Ne), targets (C, Al, Ag, Au, U), and energies (total beam energy > 1 GeV), can be summarized as follows:[9-13] 1) The bulk of the complex fragments could be explained as originating from a single slow-moving source with a laboratory velocity < 1 cm/ns which emitted fragments nearly isotropically in its center-of-mass. 2) The kinetic energy spectra for all Z-values was "Coulomb-like" with peaks corresponding either to emitting sources lighter than the target, or to more extended sources. 3) The slope parameters or apparent temperatures of the kinetic energy spectra were in the range of 10 - 30 MeV. 4) The cross sections for complex fragment production were on the order of tens of millibarns for Z < 20, decreasing with increasing Z-value. 5) The presence of a binary fission component similar to low energy thermal fission was observed.

Perhaps the magnum opus of this body of work was that of Warwick et al[14]. To study the target decay mechanism, they measured inclusive and coincident slow fragment yields up to A ~ 140 along with the associated fast charged particle multiplicity for p, He, Ne induced reactions on Au targets with total incident energies of 5-40 GeV. In addition to their inclusive data which was consistent with the above results, they detected very few complementary heavy fragments with in plane correlation angles of 150° - 210° in coincidence with complex fragments of A ~ 30 detected at 90° in the lab. The associated fast charged particle multiplicity was also found to be a function of the mass of the trigger particle, decreasing with increasing fragment mass up to masses approximately one-half of the target residue. These two results were taken as evidence

for the multifragment (non-binary) nature of the target breakup process, giving rise to virtually all of the fragments of A ~ 30 and approximately 50 % of those of A ~ 90.

It should be noted that even the miniscule source velocity of 0.54 cm/ns measured by Warwick et al. for the 5 GeV ^{20}Ne + ^{197}Au reaction has a profound effect on the kinematics of the target decay process. It appears that the detection system they employed was particularly sensitive to these kinematics. Detecting a fragment of any mass at 90° in the lab following a binary decay requires that the complementary fragment be emitted forward of 60°, the forward angular threshold of their coincidence detector. It is suggestive that for the symmetric decays the recoil will be emitted furthest backward, and that it is this class of events in which there are a reasonable number of coincidences detected. In a similar manner the Coulomb velocities for the heavy recoils are so small that they will be focused forward into a limited angular region about the beam. The slower the source is moving, the smaller will be the kinematic focusing effect. Perhaps this effect can explain the dependence of the associated fast charged particle multiplicity upon the complex fragment mass. The efficiency for detecting the heavier fragments is greater when they are emitted from a slower source, presumably after a more peripheral, less violent reaction, and with a smaller associated multiplicity. These kinematic effects may explain some of the discrepancies between the results of Warwick et al. and those of more recent work.

In the new generation of light ion - nucleus experiments it has been found necessary to invoke a binary decay mechanism to account for much of the experimental data. In particular, results with ^{3}He projectiles[15-17] at lower energy have shown similar (isotropic and non-isotropic) components as observed in our own complex fragment studies.[1-4,18] Sangster et al.[19] found it necessary to include gaussian (presumably binary) components in their fits to the kinetic energy spectra of CF in 1 - 6 GeV proton induced reactions on Xe. In addition, evidence for the binary thermal fission of heavy targets (Ho, Au) following reactions with ^{4}He of up to 800 MeV/u has been presented.[20] In this study, contrary to the results of Warwick et al. at a somewhat larger energy, binary coincidences were detected with trigger fragments of mass $10 \leq A \leq 140$.

It is possible that following the initial collision between target and projectile the spectator portion of the target might manage to relax as in lower energy reactions. If this is true then some or all of the isotropic portion of the complex fragment cross section could be due to statistical emission from this source. As we have shown in our earlier work, the presence of a thermal fission component requires that the statistical emission of complex fragments must compete. For highly excited target residues with large excitation energies and temperatures, statistical CF emission could compete rather strongly even in very fissile systems. An interesting question to answer is the degree to which the equilibrated target residue is excited in high energy reactions. Additionally if the emission of complex fragments can be described in this manner, then the

knowledge of the characteristics of the emitting system can give information relating to the primary interaction between target and projectile, and to the nonequilibrium emission of prompt fragments.

A simple geometrical-kinematic model may provide some insight into the energy deposition/momentum transfer process. This model is based on the fireball models of the 1970's where the reaction products are assumed to partition into spectator and participant regions in a "clean-cut" fashion. The velocity of the target spectator can be determined analytically from the impulse associated with the projectile traversing the target and creating nuclear surface[21]

$$V_{source} = V_{beam} \frac{B}{B+\alpha} \frac{m^*_\alpha}{A-\alpha} \left(1 - \sqrt{1 - \frac{2\Delta_\alpha}{m^*_\alpha v_0}} \right) \qquad (1)$$

with

$$m^*_\alpha = \frac{(B+\alpha)(A-\alpha)}{A+B} \qquad v_0 = \frac{B}{B+\alpha} V_{beam} .$$

Here A is the initial target mass, B the projectile mass, and α is the mass of target material swept out by the projectile. The separation energy of the piece α is Δ_α.

The excitation energy of this fragment is then the difference in (liquid-drop) energies of the fragment immediately following the interaction and at equilibrim (spherical shape), and can be approximated in the manner presented by Gosset et al.[22] Interestingly, the excitation energy of the target residue depends only upon the impact parameter (and the masses of the target and projectile), and is completely independent of the E/A of the projectile. The excitation energies of the target remnant are not particularly high at any impact parameter, even in central collisions $E^* \leq 200$ MeV for the 250 MeV/u $^{20}Ne + {}^{197}Au$ system.

This model can be used to predict the systematic properties of the excited target residue. In the limit of large incident energy

$$V_{source} \xrightarrow[\left(\lim 1/v_{beam} \to 0\right)]{} \frac{B}{(B+\alpha)(A-\alpha)} \frac{\Delta_\alpha}{V_{beam}} \qquad (2)$$

the source velocity should become inversely proportional to the beam velocity, whereas the cross

sections, which depend upon the excitation energy and transferred angular momentum, should to first order remain constant. The 5 - 40 GeV ^{20}Ne + ^{197}Au results of Warwick et al. show exactly this type of behavior.

As a first step in investigating the dependence of the source velocities and cross sections on incident energy we have performed the 250 MeV/u ^{20}Ne + ^{197}Au experiment mentioned above incorporating very low threshold (< 400 keV deposited energy) ΔE-E telescopes with excellent angular (~ 0.2°) and charge resolution ($Z \leq 17$). We have measured energy, charge, and angular distributions for complex fragments from 25° - 110° in the lab, along with the associated charged particle multiplicity and sum energy in a 17 element Si array covering approximately 40 % of 4π.

The preliminary results are similar to the previous studies in that the fragments of $4 \leq Z \leq 14$ appear to be emitted with Coulomb energies, but a representation of the invariant cross-section in the $v_{\parallel}$ - $v_{\perp}$ plane (Fig. 2) for Z = 6 fragments shows the striking circular distribution similar to that seen at E/A ≤ 50 MeV, suggestive of the presence of a very slowly moving source emitting fragments isotropically in its own center-of-mass, along with a forward-peaked non-isotropic component. From spectra such as this, the emission velocities as a function of Z-value and the source velocity can be determined.

In Fig. 3(a) the extracted emission velocities as a function of fragment Z-value are shown. The solid line is a qualitative estimate of emission velocities following the binary decay of a ^{197}Au nucleus with a separation at emission of $R = 1.22\ (A_{frag}^{1/3} + (197\text{-}A_{frag})^{1/3}) + 2$ fm. As would be expected from the large body of earlier work, the emission velocities are Coulombic. Figure 3(b) shows, as a function of impact parameter, the source velocities predicted by the model introduced above. For comparison the mean experimental source velocity (arrow) with error bars (solid lines) is also shown. The experimental value of 0.6 ± 0.2 cm/ns is consistent with the model predictions for the smaller impact parameters which have the largest excitation energies, and hence give rise to the bulk of the complex fragment emission. This source velocity is also consistent with the value measured earlier by Warwick et al. for the same system.

The Z_1 - Z_2 correlation data from coincidence events at a 90° - 90° (Fig. 4a) detector setting show the correlated fission fragments from the Au target residue which have been seen in earlier experiments. At an asymmetric detector setting of 35° - 75° there are a number of coincidence events that do not add up to the total Z-value of the target (Fig. 4b). Perhaps this indicates the beginning of target multifragmentation, but it is interesting to speculate whether some of these nonbinary events may be due to the onset of sequential statistical complex fragment emission which we have recently predicted theoretically.[4, 23]

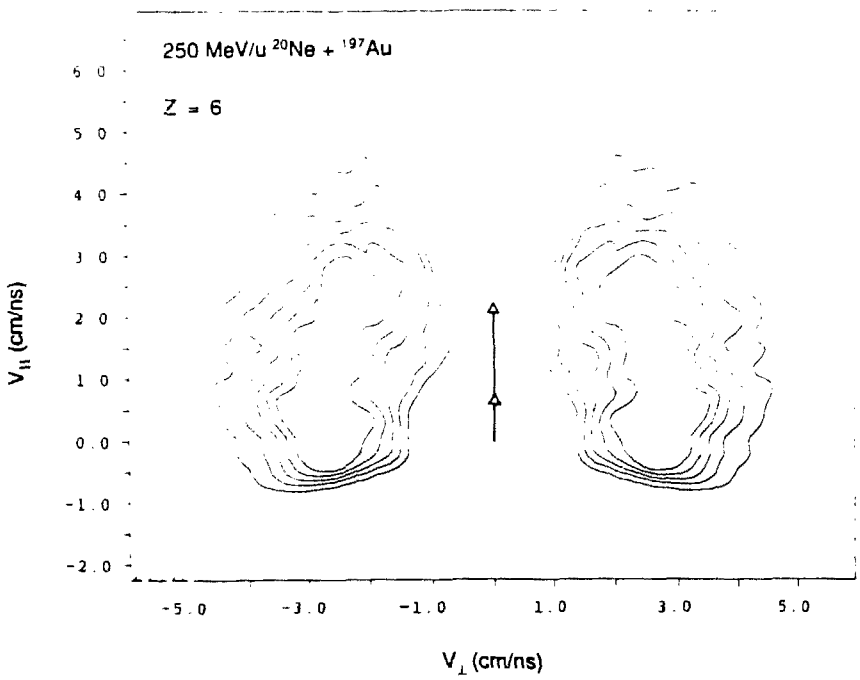

Fig. 2. Invariant contours of the experimental cross section $\partial^2\sigma/\partial V_{\parallel}\partial V_{\perp}$ in the $V_{\parallel}$ - $V_{\perp}$ plane for Z = 6 fragments detected in the reaction E/A = 250 MeV ^{20}Ne + ^{197}Au. The beam direction is again vertical. The experimentally determined source velocity (short arrow) and the velocity corresponding to full momentum transfer (long arrow) are shown for comparison.

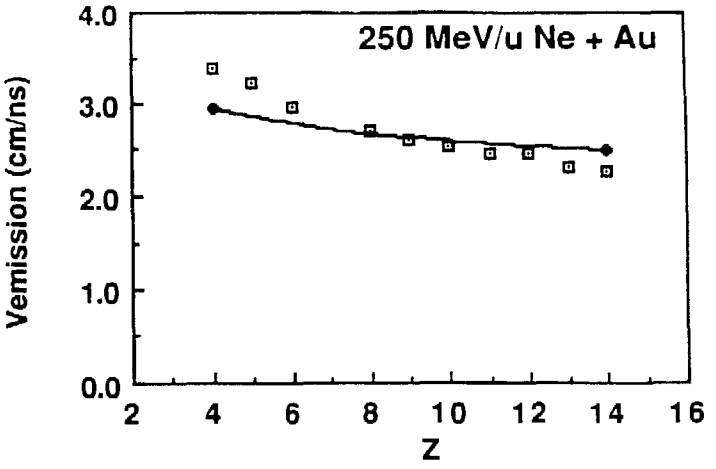

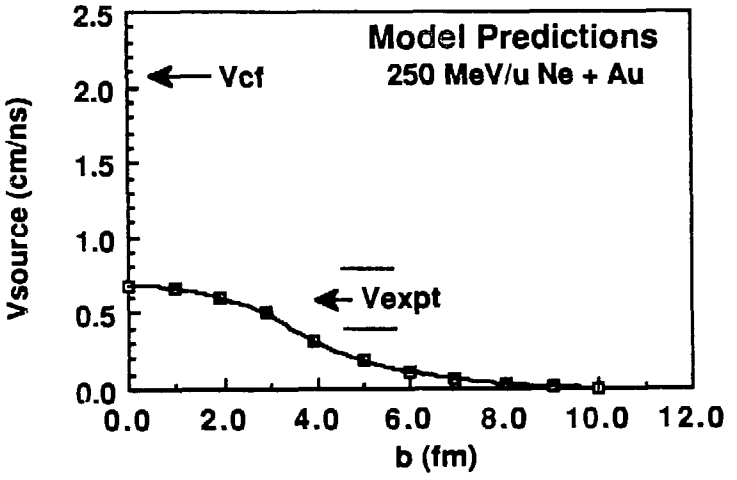

Fig. 3. (a) The emission velocities vs. Z-value for slow complex fragments following the Ne + Au reaction. The solid line is a calculation of the Coulomb velocity for fragments emitted from a Z = 79, A = 197 system with a radius at scission given by R = 1.225 $(A_{frag}^{1/3} + (197-A_{frag})^{1/3}) + 2$ fm. (b) The source velocity calculated as a function of impact parameter in the geometric-kinematic model (see text). The measured source velocity (lower arrow) is shown, along with experimental error bars (solid lines). For reference, the source velocity for complete momentum transfer is also indicated.

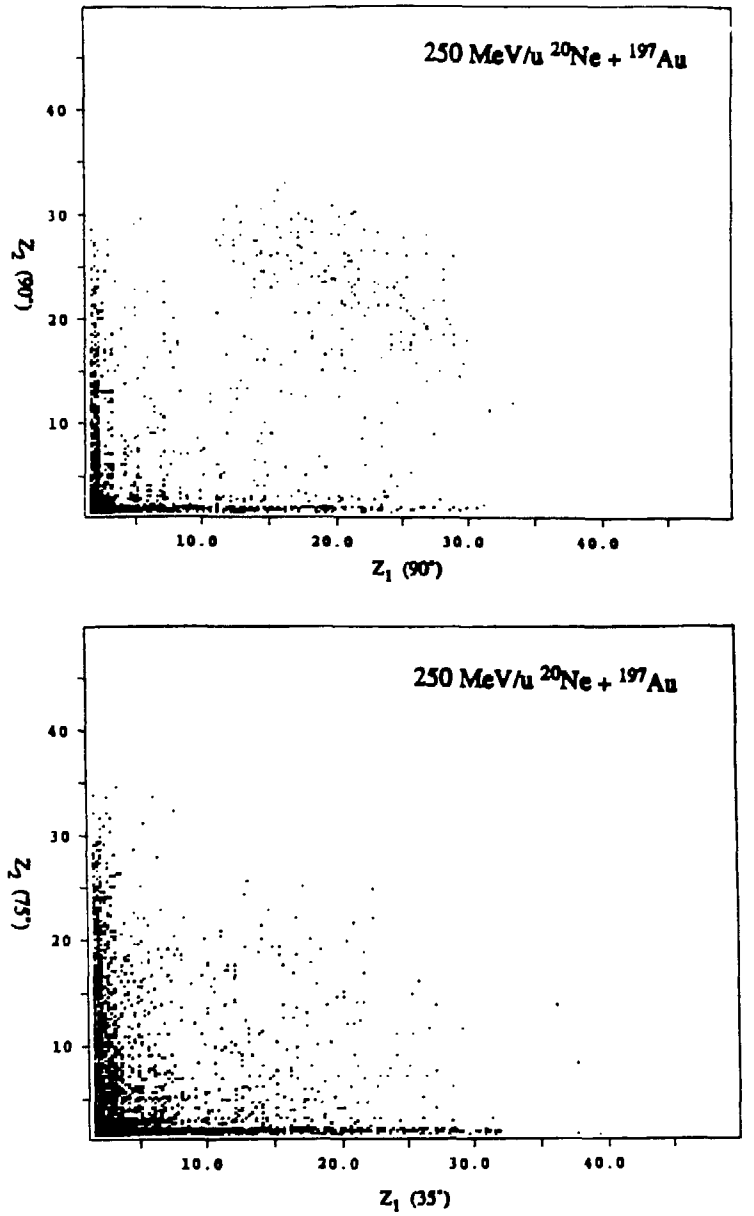

Fig. 4. (a) Z_1 - Z_2 correlation diagram of the coincidence events with the detector boxes centered at 90°-90° in the lab. The binary fission component is clearly visible. (b) Similar plot for a 35°-75° detector setting. For both (a) and (b), the Z-values > 17 are extrapolated and should be taken as approximate lower limits to the true Z-value.

The charged particle multiplicities, and a sum energy in the 17 element Si box, associated with complex fragments have also been detected. Although the multiplicity information is cruder than has been measured in earlier experiments, the element thresholds are much lower. Initial analysis has not shown strong correlations between the Z-value of the emitted complex fragment and either the multiplicity or the sum energy in the Si box.

At this stage of data analysis the preliminary results reported upon here are not much different from the results of earlier work. The difference is in the interpretation made of both the old and new data. The palpable changes to the statistical emission process brought on by the introduction of large amounts of excitation energy and angular momentum can generate effects that previously could be attributed only to new, exotic mechanisms. In the final analysis the absolute cross sections, and the presence or absence of coincidence events consistent with binary decay, should indicate the degree to which the statistical process can account for the above experimental results.

Although the field of E/A >100 MeV/u light ion + nucleus reactions is not new, there is ample opportunity for the reevaluation of previous results and the undertaking of new experimental programs based on the recent understanding of some long observed phenomenon. Specifically, the statistical emission of complex fragments, whether regarded as a entity for study in of itself or just as a nuisance obscuring more interesting processes, is the only theory of complex fragment emission (in a sea of phase transitions, statistical multifragmentations, and nuclear shattering) that has been proven to produce complex fragments. It is important to probe the limits of its existence at higher energies to carefully delineate under what conditions other mechanisms must be invoked to explain the emission of complex fragments. Only in this way can the newer, more exotic processes be properly studied.

Footnotes and References

* This work was supported by the Director, Office of Energy Research, Division of Nuclear Physics of the Office of High Energy and Nuclear Physics of the US Department of Energy under contract DE - AC03 - 76SF00098.

1) R. J. Charity et al., Phys. Rev. Lett. **56**, 1354 (1986).
2) D. R. Bowman et al., Phys. Lett. **189B**, 282 (1987).
3) R. J. Charity et al., LBL-22447, and accepted by Nucl. Phys.
4) R. J. Charity et al., LBL-22448.
5) L. G. Moretto, Nucl. Phys. **A247**, 211 (1975).
6) R. Wolfgang et al., Phys. Rev. **103**, 394 (1956).
7) A. M. Poskanzer et al., Phys. Rev. C **3**, 882 (1971).

8) E. K. Hyde et al., Phys. Rev. C **4**, 1759 (1971).
9) R. G. Korteling et al., Phys. Rev. C **7**, 1611 (1973).
10) A. M. Zebelman et al., Phys. Rev. C **11**, 1280 (1975).
11) H. H. Gutbrod et al., Phys. Rev. Lett. **37**, 667 (1976).
12) G. D. Westfall et al., Phys. Rev. C **17**, 1368 (1978).
13) W. G. Meyer et al., Phys. Rev. C **22**, 179 (1980).
14) A. I. Warwick et al., Phys. Rev. C **27**, 1083 (1983).
15) K. Kwiatkowski et al., Phys. Lett. **171B**, 41 (1986).
16) K. Kwiatkowski, Indiana Nuclear Chemistry Report INC-40007-40 (1986).
17) M. Fatyga et al., Phys. Lett. **185B**, 321 (1987).
18) L. G. Sobotka et al., Phys. Rev. Lett. **51**, 2187 (1983).
19) T. C. Sangster et al., Phys. Lett. **188B**, 29 (1987).
20) G. Klotz-Engmann et al., Phys. Lett. **187B**, 245 (1987).
21) L. G. Moretto and D. R. Bowman, XXIV International Winter Meeting on Nuclear Physics, Bormio 1986, Ricerca Scientifica ed Educazione Permanente, suppl. 49, 1986, p. 126, Ed. I. Iori.
22) J. Gosset et al., Phys. Rev. C **16**, 629 (1977).
23) L. G. Moretto and M. Ashworth, to be published.

FRAGMENT PRODUCTION FROM 1 TO 20 GEV p + Xe REACTIONS

T. C. Sangster

Lawrence Livermore National Laboratory
University of California
PO Box 808, L-397
Livermore, CA 94550

A. Bujak, D. D. Carmony, Y. H. Chung, L. J. Gutay, A. S. Hirsch,
M. Mahi, G. L. Paderewski, N. T. Porile,
R. P. Scharenberg and B. C. Stringfellow

Department of Physics and Department of Chemistry,
Purdue University, W. Lafayette, IN 47907

Abstract

The kinetic energy spectra of fragments ($2 \leq Z \leq 14$) from the interaction of 1 to 19 GeV protons and xenon nuclei have been measured using an internal gas jet target in the AGS main ring. It is observed that the shape of the energy spectra change radically as the incident proton energy decreases from about 10 GeV while at energies between 10 and 19 GeV, the shape of the spectra are identical to those measured using much higher proton energies. The evolution of the lower energy spectra can be viewed as the superposition of two components. One component is identical to the higher energy spectra; the second component is symmetrical and consistent with the fragment spectra emitted from a binary or asymmetric fission process.

We have recently reported the results of an inclusive measurement of intermediate mass fragment production from the interaction of 80 to 350 GeV protons with Kr and Xe nuclei [1-5]. These reports indicate that this range of proton energies is well within the limiting fragmentation region, where the observed fragment production systematics are no longer dependent on the incident proton energy. In an effort to further understand the p + nucleus reaction, we proposed to study intermediate mass fragment production in the threshold region where production cross sections are known to vary.

The experiment was conducted at the AGS where we installed an internal gas jet target in one of the straight sections of the main ring [6]. The jet could typically be fired for about 50 ms during each AGS acceleration cycle, sampling a 2 to 3 GeV wide beam energy interval. By adjusting the start of the jet pulse relative to beam injection, we were able to study fragment production over a nearly continuous range of incident energies between 1 and 19 GeV. Fragment charge (2/Z/14) and kinetic energy (5 to 120 MeV) were measured at scattering angles of 48.5° and 131.5° using identical hybrid gas ionization delta-E, Si E telescopes. The gas jet target consisted of a 1% or 3% xenon-hydrogen mixture which provided a xenon thickness of about 3 ng/cm^2. Elastically scattered protons from the hydrogen component were measured using two delta-E-E-Veto Si stacks located at 84.4° to the beam. The p-p elastic data were used to provide an absolute normalization for the fragment differential cross sections.

Figure 1 shows the differential production cross sections as a function of the incident proton energy for Li through Si at 48.5°. The data have been binned into eleven beam energy intervals and span the range 1.3 to 19.1 GeV. The points at 80 GeV are from our previous Fermilab experiment [3,7]. The differential cross sections between 10 and 20 GeV agree remarkably well with this earlier data. Clearly the limiting fragmentation region is reached by about 10 GeV. It is also evident from the figure that there is a well-defined threshold for significant fragment production near 1 GeV. Interestingly, this threshold coincides with the rapid increase in the p-p inelastic cross section between 1 and 2 GeV. It should also be noted that the differential cross sections for Li through Si at 131.5° show a similar energy dependence but are somewhat reduced from the forward values.

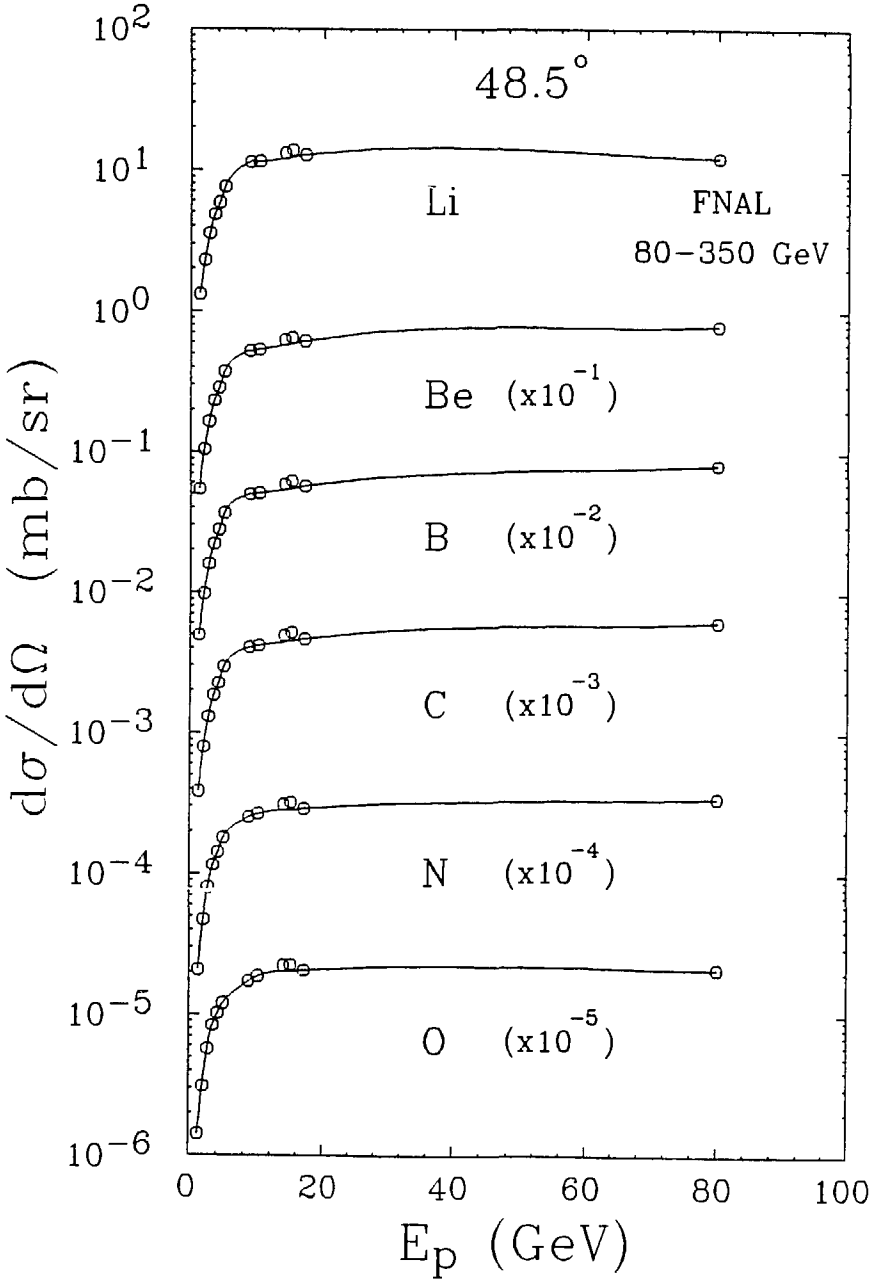

Figure 1. Excitation functions for Li thru Si at 48.5°. The statistical errors in $d\sigma/d\Omega$ are generally 10% to 14% while the systematic errors are estimated to be as much as 30% to 40% for the points at 14.5 and 15.6 GeV due to uncertainty in the AGS beam intensity at these energies.

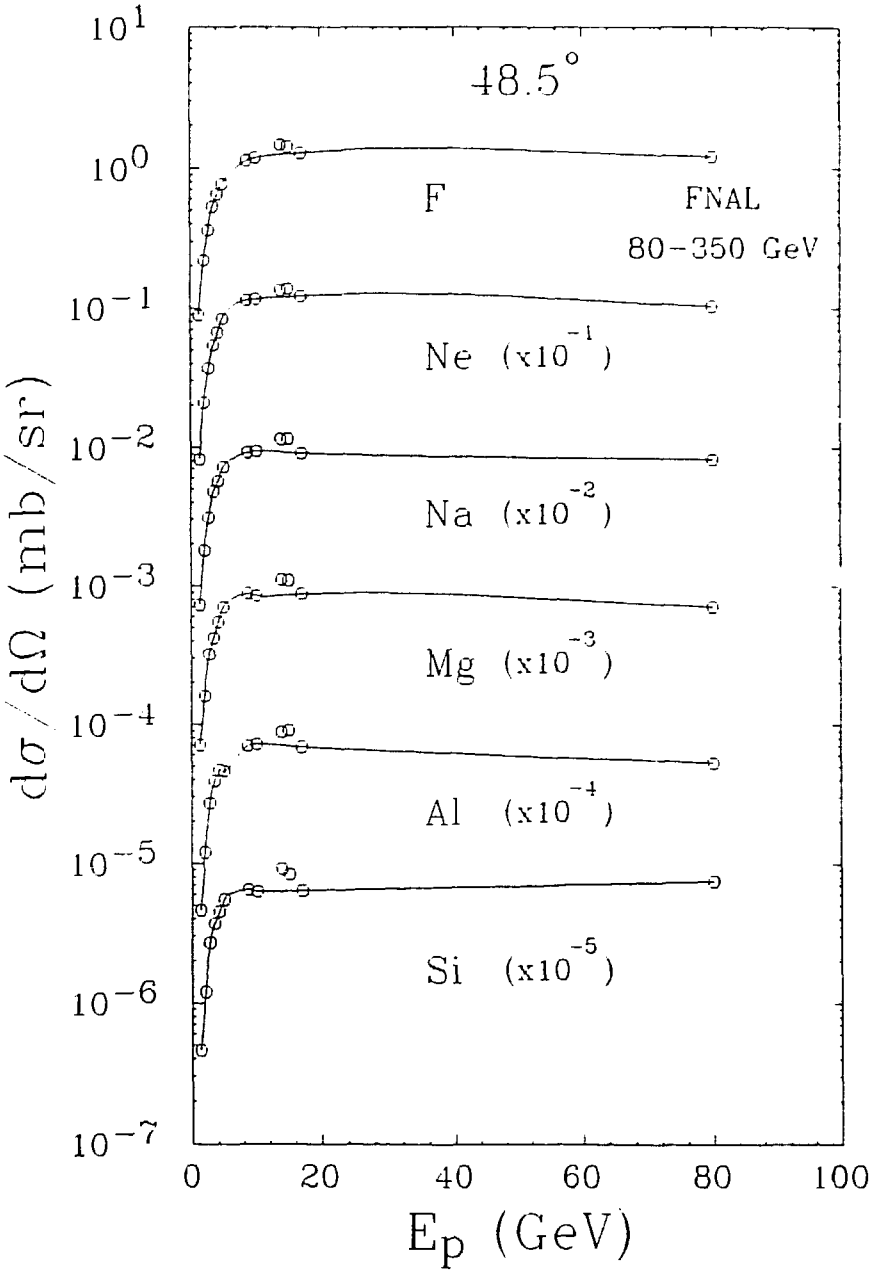

Figure 1 continued.

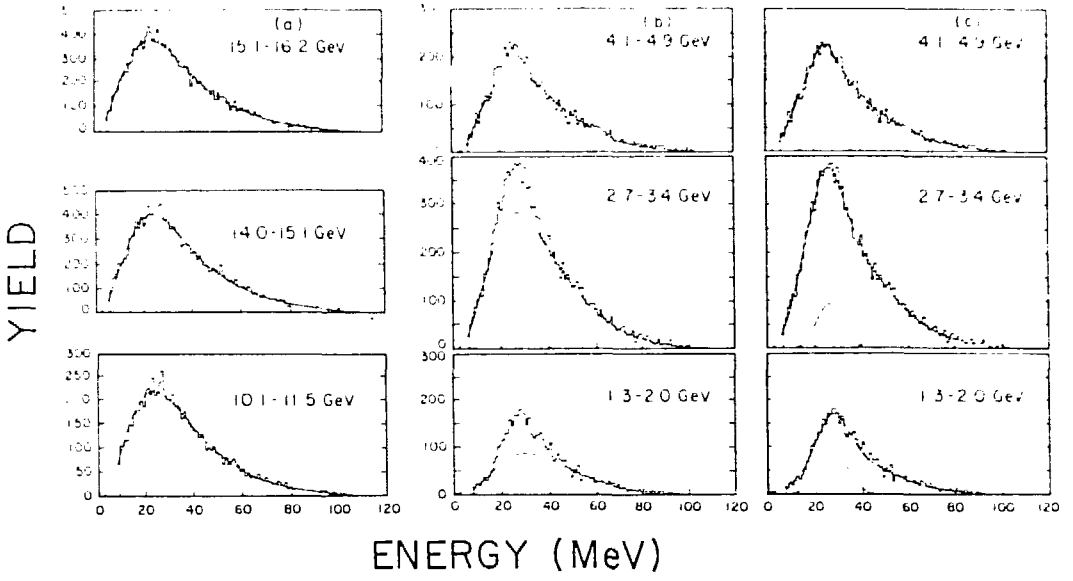

Figure 2. Kinetic energy spectra of Be fragments emitted at 48.5°. The width of the proton energy interval is indicated in the figure. (a) These spectra are for proton energies between 9 and 19 GeV. The functional form for the curves is described in the text. (b) These spectra are for proton energies below 6 GeV. The functional form used in (a) provides an increasingly poor fit. (c) The addition of a gaussian component to the curves in (b) restores the fit to the data.

In order to calculate the fragment differential cross sections, the total yield of each element in every proton energy interval had to be reliably estimated. The measured yields obtained from the kinetic energy spectra were not an accurate estimate of the total yield due to the low energy cutoffs in the measured laboratory kinetic energy imposed by a number of absorbers (foils and windows) along the length of the fragment telescopes. To reliably estimate a total elemental yield from a measured kinetic energy spectrum, a functional form was developed to describe the spectrum shape. Each spectrum is described as a convolution of two Maxwell-Boltzmann distributions. One distribution is characterized by a slope parameter T1, which we associate with the mean square nucleon momentum in the fragment emitting system. The second distribution is characterized by a slope parameter T2, which we interpret as the temperature of the emitting system. The Coulomb energy, which, in this model, is characterized by the radial position of the fragment within an assumed spherical emitting system, must be explicitly removed from the energy used in the convoluted

Maxwellian. This energy (the available center-of-mass energy) is essentially fixed by the thermal and non-thermal Maxwell-Boltzmann distributions before the system disintegrates.

To allow for a continuum of Coulomb energies, a probability distribution is chosen for the radial position of a fragment at freeze-out. By arguing (or assuming) that the probability to form a fragment at a particular location within the emitting system is directly related to the density distribution just prior to freeze-out, and that the density distribution is radially symmetric with a maximum at the center of the emitting system, a gaussian radial probability distribution with mean zero is chosen. The convoluted Maxwellian is then weighted by the radial probability distribution and integrated over all possible Coulomb energies. The shape of the kinetic energy spectra are then described by only four parameters, i.e., an overall normalization, T1, T2 and σ, the width of the gaussian probability distribution. The parallel component of the center-of-mass velocity, β, is determined separately for each element from the shift in the kinetic energy spectra peaks at 48.5° and 131.5°. Because the emitting system is essentially at rest in the laboratory frame, β has very little influence on the shape of the kinetic energy spectra.

Figure 2 shows the kinetic energy spectra of Be fragments emitted at 48.5° for various proton energy intervals. The curves in Figure 2a were produced by the functional form described above with T1=16 MeV, T2=2.3 MeV, and σ approximately 1.5 fm. The quality of the fits for all of the other elements and for every beam energy interval above 9 GeV is comparable. However, below 6 GeV [8], the shape of the kinetic energy spectra begin to change radically as a function of the incident proton energy. In Figure 2b, the functional form used to describe the spectra above 9 GeV provides an increasingly poor fit to the data as the beam energy decreases. Within the framework of the above parameterization, we were unable to restore the fits by allowing the values of the model parameters to vary. We did find, however, that the addition of a gaussian component to the curves in Figure 2b was able to restore the fit to the data (Figure 2c).

The key to the fits in Figure 2c is that the values of the parameters T1, T2 and σ were fixed at their average values from the higher energy (>9 GeV) fits. The only fitted parameters for all of the spectra below 6 GeV were the normalization for the Maxwellian component, and the

normalization, peak and width of the gaussian component. The peak of the gaussian component at 48.5° increases monotonically from about 22 MeV for the Li spectra to about 40 MeV for the Ne spectra, and is independent of the proton energy. The width of the distribution is approximately 30% of the peak value for all beam energy intervals and elements. The gaussian component was not included for the fits to the Na, Mg, Al and Si spectra because the low energy cut-offs in these spectra were comparable to the peak energy. Notice that the relative contribution of the symmetric component increases with decreasing proton energy and becomes comparable to the Maxwellian component at the lowest energy interval; this behavior was evident for the other elements as well. The inclusion of the gaussian above 9 GeV does not improve the fits; typically the gaussian was only one or two percent of the total integrated yield.

The evolution in the kinetic energy spectra seen below 6 GeV may indicate the appearance of an additional fragment producing mechanism [9]. In intermediate-energy heavy ion collisions, fragment production is the result of a binary process [10-13] and can be understood as part of a continuum of statistical break-up processes ranging from evaporation to fission [14]. The observation of the symmetric component in the kinetic energy spectra below 6 GeV may simply be the result of the rapidly decreasing cross section for the Maxwellian component which is reflected in the excitation functions in Figure 1. This symmetric component is likely due to a statistical binary process (asymmetric fission) which has been proposed by Moretto [14]. This viewpoint is consistent with the observed spectra since the statistical model [14] predicts symmetric kinetic energy distributions for all but the lightest fragments. Furthermore, the mean energy of the gaussian component is consistent with tangent-spheres Coulomb energies for the breakup of the emitting system. It is interesting to note as well that the differential cross sections for the asymmetric fission component are approximately constant as a function of the incident proton energy, and decrease slightly with increasing fragment charge (although within the estimated error bars, the cross section is also constant as a function of Z). At 48.5°, the average differential cross section for the symmetric component is about 210 microbarns and at 131.5°, the average is about 190 microbarns. At 5 GeV, the symmetric component is only about 5% of the total differential cross section.

In summary, there is a distinct threshold for significant fragment production in p + nucleus reactions at a proton energy of about 1 GeV. This threshold corresponds with the rapid increase in the p-p inelastic cross section between 1 and 2 GeV. The fragment kinetic energy spectra measured using 9 to 19 GeV protons on xenon are identical to those obtained at Fermilab energies (80 to 350 GeV) [3]. Fragments are most likely produced in this limiting fragmentation region by a multi-fragmentation process. Perhaps the most distinctive feature of this mechanism is the Maxwellian shape of the kinetic energy spectra and the observation that this shape does not change as a function of the incident proton energy from the threshold up to 350 GeV. The spectra obtained at energies below 6 GeV, however, clearly indicate a contribution from a fragment producing mechanism whose systematics are completely different from the multi-fragmentation component dominant at the higher energies. This second component is consistent with a statistical binary process and appears to have a relatively stable cross section as a function of the proton energy between 1 and 6 GeV, and as a function of observation angle and fragment charge.

This work was performed under the auspices of the U.S. Department of Energy by the Lawrence Livermore National Laboratory under contract number W-7405-ENG-48.

REFERENCES

[1] J. E. Finn, et al., Phys. Rev. Lett. 49 (1982) 1321.

[2] R. W. Minich, et al., Phys. Lett. B 118 (1982) 458.

[3] A. S. Hirsch, et al., Phys. Rev. C 29 (1984) 508.

[4] A. S. Hirsch, et al., Nucl. Phys. A 418 (1984) 267c.

[5] N. T. Porile, et al., Phys. Lett B 156 (1985) 188.

[6] B. C. Stringfellow, et al., NIM A251 (1986) 242.

[7] The FNAL data were obtained at a lab angle of 34°.

[8] We were unable to obtain data between 6 and 9 GeV due to instabilities in the AGS proton beam at these energies.

[9] T. C. Sangster, et al., Phys. Lett. B 188 (1987) 29.

[10] R. J. Charity, et al., Phys. Rev. Lett. 56 (1986) 1354.

[11] B. Grabez, et al., Phys. Rev. C 34 (1986) 170.

[12] W. Mittig, et al., Phys. Lett. B 154 (1985) 259.

[13] L. G. Sobotka, et al., Phys. Rev. Lett. 53 (1984) 2004.

[14] L. Moretto, Nucl. Phys. A 247 (1975) 211.

EXPERIMENTAL OVERVIEW OF TEMPERATURE MEASUREMENTS AT INTERMEDIATE ENERGIES*

C.K. Gelbke
Department of Physics and Astronomy
National Superconducting Cyclotron Laboratory
Michigan State University, East Lansing, MI 48824-1321, USA

Introduction

Present microscopic descriptions of intermediate energy nucleus-nucleus collisions include the effects of individual nucleon-nucleon collisions, the Pauli exclusion principle, and the mean nuclear field in a semiclassical approximation [1-4]. Even though promising approaches have been made to describe the growth of density fluctuations which lead to the emission of complex particles during the final disintegration stages of the reaction [5-7], dynamical descriptions do not yet exist which properly include relevant aspects of cluster formation such as nuclear binding energies and individual nuclear states. At present, such considerations are only contained in models based on the assumption of statistical emission from highly excited nuclear subsystems characterized in terms of their average velocity, space-time extent, and excitation energy [8-14]. It is clearly important to test the validity of such approximations. In this talk I will discuss methods aimed at measuring the average excitation energy per nucleon or "temperature" of the reaction zone.

Noncompound Particle Emission

Most attempts to obtain experimental information about the temperature of highly excited nuclear systems were based on analyses of the kinetic energy spectra of the emitted particles [15-17]. As an example, Fig. 1 shows measurements [18] for ^{16}O induced reactions on ^{197}Au at E/A=25 MeV. At intermcdiate angles the cross sections can be rather well described in terms

* This work was supported by the National Science Foundation under Grants No. PHY 8401845 and PHY 8611210.

of simple Maxwellian energy distributions ("moving source" parametrization) centered at velocities slightly less than half the beam velocity, see dot-dashed curves. Temperature parameters of 7.2, 8.7, and 9.9 MeV are extracted from the proton, deuteron and triton energy spectra, respectively. These values are considerably larger than the compound nucleus temperature ($T_0 \approx 3.6$ MeV using a level density parameter of A/8MeV), possibly indicating emission from a highly excited subset of nucleons in the processes of cooling with the surrounding cold nuclear matter.

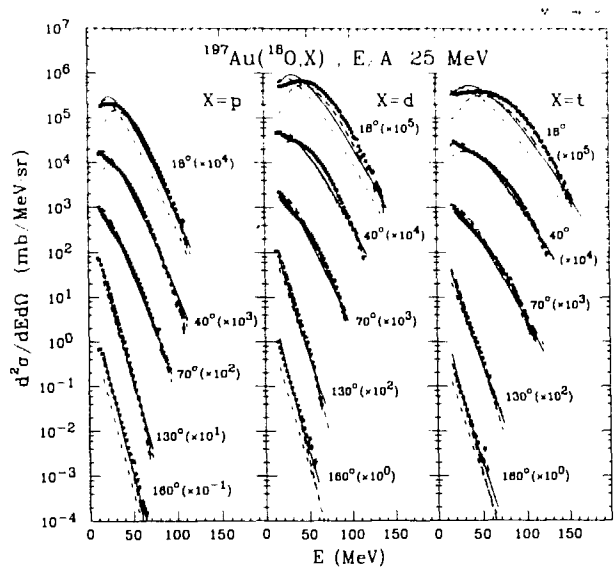

Fig. 1. Single particle inclusive proton, deuteron, and triton cross sections for ^{16}O induced reactions on ^{197}Au at E/A=25 MeV. The curves are explained in the text. [18]

The description of the inclusive spectra in terms of simple Maxwellian distributions is neither ideal nor unique. Somewhat improved fits with similar temperature parameters can be obtained by assuming $1/\sin\Theta$ angular distributions in the "rest frame" of the emitting source, see solid curves in Fig. 1. In contrast, the dashed curves show distributions expected for the simple case of particle emission from a rotating ideal gas of temperature T. For that parametrization, temperature parameters of 4.2, 4.7, and 5.6 MeV are extracted [18] for protons, deuterons, and tritons, respectively. They are considerably lower than those extracted from Maxwellian distributions (but still higher than the temperature of the equilibrated compound nucleus). To a large extent these lower temperatures can be traced back to the assumption of collective rotation which tends to make the slopes of the energy spectra less

steep [18]. The rotating gas calculations illustrate the difficulties of extracting unambiguous temperature parameters from the kinetic energy spectra of the emitted particles when the effects of collective motion are unknown [19].

For a fixed choice of parametrization, the "kinetic" temperature parameters extracted from the slopes of the kinetic energy spectra of the emitted particles exhibit a systematic dependence [15-18,20,21] on the incident energy per nucleon, see Fig. 2. However, considerable ambiguities concerning the temperature of the emitting system exist in the presence of appreciable collective velocity components [18,19]. The existence of collective velocity components in intermediate energy heavy ion collisions was established by a number of experiments [18,22,23]; the extent to which they modify temperature parameters extracted from kinetic energy spectra is, however, difficult to infer.

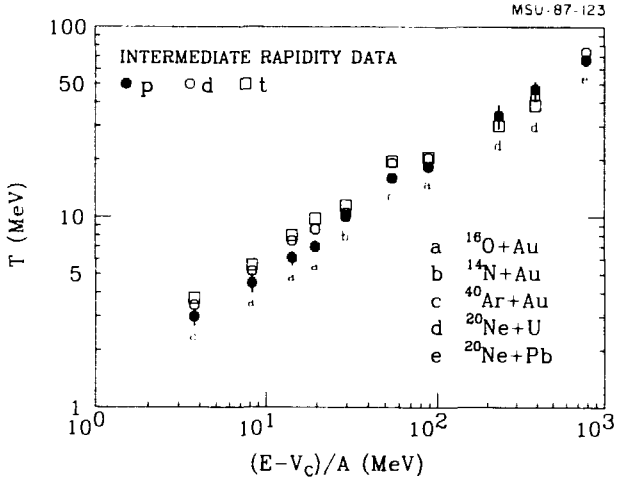

Fig. 2. Temperature parameters extracted from fits of single particle inclusive cross sections with Maxwellian distributions ("moving source" parametrizations).

Population of Particle Unbound States

If chemical equilibrium is attained during the final disintegration stages of the reaction, information about the excitation energy per nucleon or "temperature" of the emitting (sub)system can be obtained from the relative populations of nuclear states [20,21, 24-28]. In most calculations, in-medium corrections [12-14] are neglected and the asymptotic nuclear states (bound and unbound) are used to specify the available decay configurations.

As an example, Fig. 3 shows the α-d correlation function (left hand side) and the coincidence yields (right hand side) resulting from the decay $^{6}Li^{*}\rightarrow\alpha+d$ for the $^{16}O+^{197}Au$ reaction at E/A=94 MeV [21]. Here, the two-particle correlation function, R(q), is defined in terms of the coincidence yield, $Y_{12}(\vec{p}_1,\vec{p}_2)$, and single particle yields, $Y_1(\vec{p}_1)$ and $Y_2(\vec{p}_2)$:

$$\sum Y_{12}(\vec{p}_1,\vec{p}_2) = C_{12}\cdot\{1+R(q)\}\cdot\sum Y_1(\vec{p}_1)\cdot Y_2(\vec{p}_2) \ , \qquad (1)$$

where $\vec{p}_1$ and $\vec{p}_2$ are the laboratory momenta of particles 1 and 2, and q is the momentum of relative motion. The normalization constant, C_{12}, is determined by the requirement that R(q)=0 for large relative momenta. The coincidence yield, Y_c, from the decay of particle unstable states was extracted by assuming that the total coincidence yield, Y_{12}, can be expressed as:

$$Y_{12} = Y_c + C_{12}\cdot Y_1 Y_2[1+R_b(q)], \qquad (2)$$

where $R_b(q)$ denotes the "background" correlation function shown by the solid curve on the left hand side of the figure. For a thermal population of states, the yield $Y_c(E^*)$ can be written as:

$$Y_c(E^*) = N\cdot\int \varepsilon_c(E^*,E)\cdot e^{-E/T}\cdot\sum_i \frac{(2J_i+1)\Gamma_i/2\pi}{(E-E_i)^2+\Gamma_i^2/4}\cdot\frac{\Gamma_{c,i}}{\Gamma_i}\cdot dE. \qquad (3)$$

In Eq. 3, N is a normalization constant; $\Gamma_{c,i}/\Gamma_i$ denotes the branching ratio for the decay into the channel c; $\varepsilon_c(E^*,E)$ is the efficiency function of the experimental apparatus for the detection of particle pairs resulting from the decay of particle unstable nuclei; E and E* denote the actual and measured excitation energies, respectively. The efficiency function can be determined from Monte Carlo calculations. Equation 2 serves as an operational definition of the "apparent emission temperature", T, which characterizes the relative populations of states. Apparent emission temperatures extracted in terms of this equation differ from the temperatures of the emitting systems if the primary populations of states are altered after emission and before detection, for example by feeding from higher lying states.

Calculations based on Eq. 2 are shown on the right hand side of Fig. 3. The spectral shapes are sensitive to temperatures smaller than the level separation; higher emission temperatures are more difficult to distinguish.

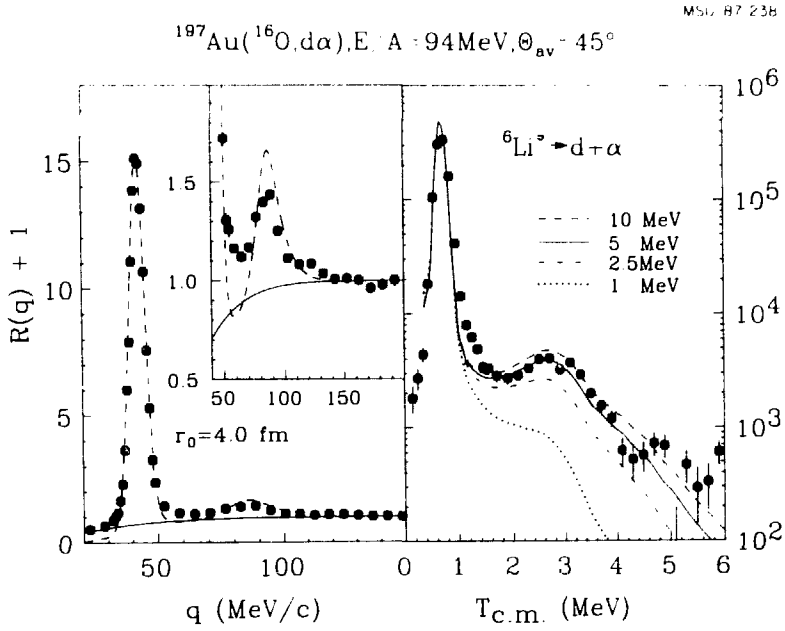

Fig. 3. Left hand side: α-d correlation function measured for the $^{16}O+^{197}Au$ reaction at E/A=94 MeV. The solid curve shows the background correlation function. The dashed curve shows a calculation with the model of refs. 29,30 assuming negligible lifetime for the emitting system. Right hand side: Energy spectrum resulting from the decay of particle-unstable states in ^{6}Li. The curves correspond to thermal distributions, Eq. 3, with T=1, 2.5, 5, 10, and 20 MeV. (Ref. 21)

The experimental yields are consistent with an emission temperature of about 5 MeV. This value is lower than typical temperature parameters, T ≈ 17-20 MeV, which characterize the energy spectra of light particles (p, ..., Li) emitted in this reaction [21].

Figure 4 gives a comparison of the apparent emission temperatures measured [20,21,26] for ^{14}N, ^{16}O, and ^{40}Ar induced reactions on ^{197}Au at E/A = 35, 94, and 60 MeV, respectively. Very similar values are extracted for the three reactions. The measurements are consistent with a slight increase of about 20% over the energy range considered; this increase is of comparable magnitude as the systematic uncertainty and, therefore, not established beyond doubt. The surprising insensitivity of the relative populations of states stands in marked contrast to the systematic energy dependence of the kinetic temperature parameters which characterize the slopes of the kinetic energy spectra of the emitted particles. As shown in Fig. 2, the kinetic temperatures increase by nearly a factor of two as the incident energy is increased from E/A≈35 to 96 MeV.

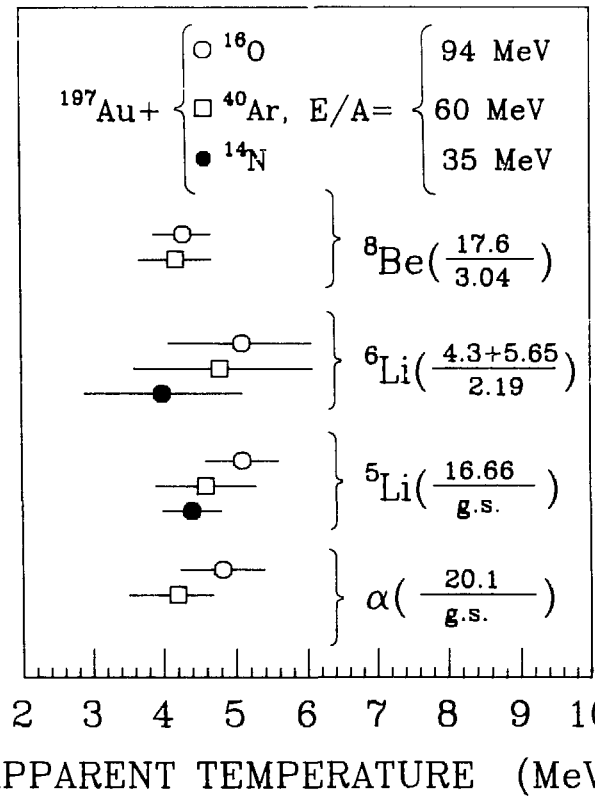

Fig. 4: Apparent emission temperatures extracted from the relative populations of states in ^{4}He, ^{5}Li, ^{6}Li, and ^{8}Be nuclei emitted in the reactions: ^{14}N+^{197}Au at E/A=35 MeV (ref. 26, solid points), ^{40}Ar+^{197}Au at E/A=60 MeV (ref. 20, open squares), and ^{16}O+^{197}Au at E/A=94 MeV (ref. 21, open circles).

Because of possible feeding from the sequential decay of higher lying particle unstable states, the apparent emission temperatures extracted from Eq. 3 could be smaller than the true emission temperatures of the emitting systems. The extent of feeding to particle unbound states is not known experimentally. In order to assess the importance of feeding from higher lying particle unstable states one has to rely on calculations. The results of two recent calculations [31,32] are shown in Fig. 5. The figure shows the temperature dependence of the normalized population ratio of states, R_p/R_∞, where R_∞ is the high temperature limit of the primary population ratio. The solid curves show the primary population ratios. The dashed and dotted-dashed curves show the results of quantum statistical calculations [31] for densities of ρ/ρ_0=0.05 and 0.9, respectively, where ρ_0 denotes the density of normal

nuclear matter. The dotted curves show the result of ref. 32 in which the primary isotopic distributions were parametrized by a simple analytical function of the ground state masses and Coulomb barriers of the emitted nuclei. The shaded horizontal bands indicate the population ratios which are consistent with our measurements. The calculations indicate significant perturbations for all cases except for the decays of ^{5}Li. The predicted perturbations are very sensitive to the detailed assumptions on the primary nuclide distributions. Without more detailed knowledge of the primary distributions, the measured populations of states in ^{4}He, ^{6}Li, and ^{8}Be nuclei cannot provide reliable upper bounds for the true emission temperatures. From the relative populations of states in ^{5}Li, the best estimate for the emission temperature, T=4.6-6.0 MeV, is extracted. This value is significantly lower than the kinetic temperature parameters, T≈17-20 MeV, which characterize the slopes of the kinetic energy spectra of the emitted particles.

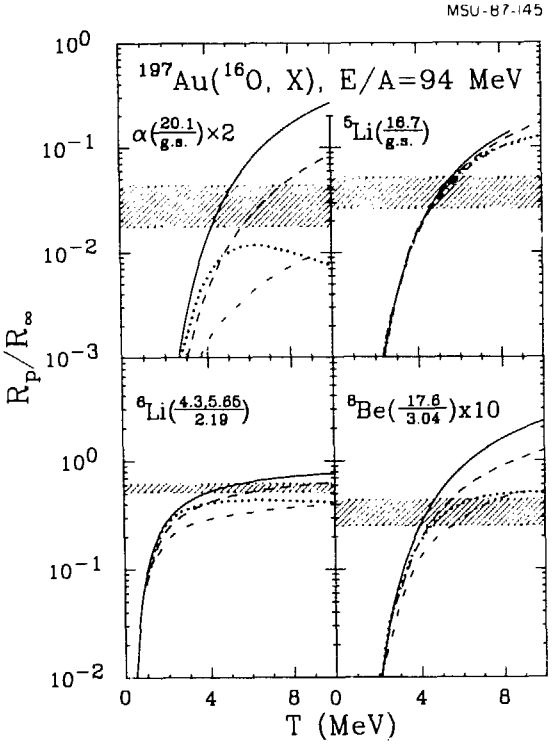

Fig. 5. Temperature dependence of population ratios, R_p/R_∞, for specific states in ^{4}He, ^{5}Li, ^{6}Li, ^{8}Be nuclei. Ratios measured for the ^{16}O+^{197}Au reaction at E/A=94 MeV are shown by hatched regions. Solid curves: temperature dependence of primary population ratios; dashed and dashed-dotted curves: final ratios predicted by quantum statistical calculations [31] for densities of ρ/ρ_0= 0.05 and 0.9, respectively; dotted curves: calculations from ref. 32.

Distributions of Relative Kinetic Energies

The large discrepancy between the relatively small temperatures which characterize the populations of particle unbound states and the relatively large kinetic temperature parameters which characterize the slopes of the kinetic energy spectra is not understood quantitatively. In principle, the large kinetic temperature parameters extracted from the slopes of the kinetic energy spectra could arise from the superposition of a large collective velocity component onto smaller thermal velocity components [18,19]. While collective velocity components can strongly affect single particle inclusive energy distributions, they should be less visible in the distributions of relative kinetic energy spectra between two coincident particles, provided that the two coincident particles are emitted from the same source. For the extreme case of purely collective motion, all particles have the same velocity; the relative velocity of two coincident particles is zero. One might, therefore, expect that a superposition of small thermal and large collective velocity components could be detected in the distributions of relative kinetic energies, $T_{c.m.} = q^2/2\mu$, between coincident particles detected at small relative angles.

Figure 6 shows the experimental α-d coincidence yield as a function of the relative kinetic energy; decays of particle unstable states in ^{6}Li contribute only for E≦5 MeV. The curves correspond to yields predicted in terms of Maxwellian distributions folded by the detection efficiency of the experimental apparatus. Clearly temperatures below 10 MeV are excluded by the data which are most consistent with values of the order of 30 MeV. Since final state Coulomb interactions and momentum conservation effects can modify the detailed shape of the relative kinetic energy spectra, we feel that temperatures of 20 or 40 MeV cannot be ruled out with absolute certainty.

It is clear that the relative kinetic energy spectra between coincident light particles and the relative populations of particle unbound states cannot be described in terms of similar temperatures. Discrepancies between temperatures characterizing relative kinetic energy spectra and relative populations of states can arise from an expansion of the emitting system. Yet, it is rather surprising that the relative populations of states indicate rather similar emission temperatures over the range of incident energies of E/A≈35-94 MeV, while the kinetic energy spectra indicate temperatures which increase by about a factor of two.

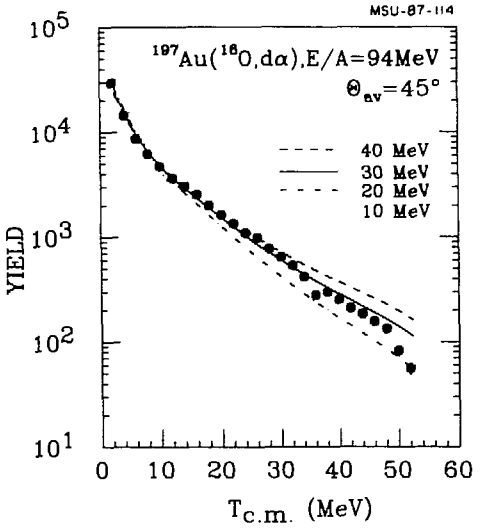

Fig. 6: Experimental α-d coincidence yield as a function of the relative kinetic energy, $T_{c.m.}$, of the two coincident particles. The curves represent Maxwellian distributions of different temperatures folded by the detection efficiency.

It is tempting to speculate about a possible relation of our experimental findings to recent theoretical investigations of multifragmentation reactions which have predicted a plateau in the temperature versus excitation energy curve [33]. These calculations nearly predict constant temperatures of T≈5 MeV over a range of excitation energies per nucleon of ε^*≈2-8 MeV. Over this range of excitation energies, additional excitation energy is consumed to create new fragments, increasing the volume without significantly raising the temperature of the reaction zone. Unfortunately, there are considerable ambiguities in estimating the excitation energy per nucleon of the emitting system. If one neglects reaction Q-values, one estimates the limits of ε^*≈6.5 MeV for an equilibrated compound nucleus (this is clearly a lower and unrealistic bound) and ε^*=23.5 MeV for a reaction zone formed by equal number of projectile and target nucleons (this represents an upper bound for the initial reaction zone, approximated as a free fireball). If one were to approximate the fragmentation process by a grand canonical treatment, characterized by a freeze-out density and temperature, the insensitivity of the relative populations of states to the incident energy requires that complex fragment freeze-out occurs at nearly constant temperature rather than at constant density as is commonly assumed. Our observations could, instead, also indicate that complete thermal and chemical equilibrium is not achieved during the final stages of the reaction.

Questions such as these can only be addressed by dynamical calculations which treat the temporal evolution of the reaction in a more realistic framework than present equilibrium statistical approaches. Clearly, a better understanding of the populations of states is of fundamental importance for realistic descriptions of nuclear fragmentation reactions.

References

1. G. Bertsch, et al., Phys. Rev. C29, 637 (1984).
2. J. Aichelin and G. Bertsch, Phys. Rev. C31, 1730 (1985).
3. H. Kruse, et al., Phys. Rev. C31, 1770 (1985).
4. C. Grégoire, et al., Nucl. Phys. A465, 317 (1987).
5. B. Strack and J. Knoll, Z. Phys. A315, 249 (1984); J. Knoll and B. Strack, Phys. Lett. B149, 45 (1984).
6. G.E. Beauvais, et al., Phys. Rev. C35, 545 (1987).
7. W. Bauer, et al., Phys. Rev. Lett. 58, 863 (1987).
8. G.D. Westfall, et al., Phys. Rev. Lett. 37, 1202 (1976).
9. J. Gosset, et al., Phys. Rev. C18, 844 (1978).
10. J. Knoll, Phys. Rev. C30, 773 (1979).
11. D.J. Fields, et al., Phys. Rev. C30, 1912 (1984).
12. L. Münchow, et al., J. Phys. G8, L135 (1982).
13. H. Schulz, et al., Phys. Lett. B124, 458 (1983).
14. G. Röpke, Phys. Lett. B121, 223 (1983).
15. T.C. Awes, et al., Phys. Lett. B103, 417 (1981); Phys. Rev. C24, 89 (1981); Phys. Rev. C25, 2361 (1982).
16. G.D. Westfall, et al., Phys. Lett. B116, 118 (1982).
17. B.V. Jacak, et al., Phys. Rev. Lett. 51, 1846 (1983); Phys. Rev. 35, 1751 (1987).
18. C.B. Chitwood, et al., Phys. Rev. C34, 858 (1986).
19. P. J. Siemens and J.O. Rasmussen, Phys. Rev. Lett. 42, 880 (1979).
20. J. Pochodzalla, et al., Phys. Rev. C35, 1695 (1987).
21. Z. Chen, et al., Phys. Rev. (in press).
22. M.B. Tsang, et al., Phys. Rev. Lett. 52, 1967 (1984); Phys. Lett. B148, 265 (1984); Phys. Rev. Lett. 57, 559 (1986).
23. D.J. Fields, et al., Phys. Rev. C34, 536 (1986).
24. D.J. Morrissey, et al., Phys. Lett. 148B, 423 (1984); Phys. Rev. C32, 877 (1985); Phys. Rev. C34, 761 (1986).
25. J. Pochodzalla, et al., Phys. Rev. Lett. 55, 177 (1985); Phys. Lett. B161, 275 (1985).
26. C.B. Chitwood, et al., Phys. Lett. 172B, 27 (1986).
27. H.M. Xu, et al., Phys. Lett. B182, 155 (1986).
28. C. Bloch, et al., Phys. Rev. C36, 203 (1987); Phys. Rev. C36, 855 (1987).
29. S.E. Koonin, Phys. Lett. B70, 43 (1977).
30. D.H. Boal, and J.C. Shillcock, Phys. Rev. C33, 549 (1986).
31. D. Hahn and H. Stöcker, Phys. Rev. C35, 1311 (1987).
32. D.J. Fields et al., Phys. Lett. B187, 257 (1987).
33. J.P. Bondorf, et al., Nucl. Phys. A444, 460 (1985).

INCLUSIVE STUDIES OF INTERMEDIATE MASS FRAGMENT PRODUCTION IN ULTRA-RELATIVISTIC NUCLEAR COLLISIONS

W. Loveland[a] and K. Aleklett[b]
[a]Oregon State University, Corvallis, OR 97331
[b]Studsvik Neutron Research Lab. S-61182 Nykoping, Sweden

In this paper we[1] present the results of a recent set of inclusive measurements of the production of intermediate mass fragments (A<60) in ultrarelativistic nuclear collisions. The reactions studied were the interaction of 14.5 GeV/nucleon ^{16}O and ^{32}S with ^{197}Au and the interaction of 60 and 200 GeV/nucleon ^{16}O with ^{238}U. The former measurements were made at the AGS at BNL while the latter measurements were made at CERN. The quantities measured were the yields of the intermediate mass fragments (CERN, BNL) and their kinematic properties (BNL). Detailed descriptions of the experimental procedures can be found elsewhere.[2,3]

A. Cross Sections

In Figure 1, we show a fragment isobaric yield distribution for the reaction of 14.5 GeV/nucleon ^{28}Si with ^{197}Au. In this distribution, one notes evidence for possibly three reaction mechanisms. They are: (a) multifragmentation which is responsible for the production of intermediate mass fragments ($A < 60$). (b) spallation which is responsible for the production of the heavier fragments and (c) fission, which contributes to the yields near $A \sim 100$. Multifragmentation requires large deposition energies and therefore it was of interest to us to measure how the probability of this mechanism would change as the projectile energy increased from 25 GeV to the newly accessible projectile energies of 0.96 and 3.2 TeV.

The measured production cross sections for four typical multifragmentation products are shown in Figure 2 along with similar data from p-nucleus[4-7] and nucleus-nucleus collisions[5,8,9]. For both the heavy ion and proton induced reactions, limiting fragmentation behavior, (i.e., the cross sections become roughly independent of beam energy above some minimum energy) occurs. The onset of limiting fragmentation appears to be at ~10 GeV for proton induced reactions and ~2.1 GeV/nucleon for the heavy ion reactions. The lower threshold for multifragmentation (expressed in units of E/A) in heavy ion reactions compared to proton induced reactions is consistent

with models[10] in which multifragmentation is due to mechanical instability of nuclear matter.

In these models, the incident heavy ion or proton compresses the nuclear matter of the target, increasing its density (Fig. 3). The nucleus then expands insentropically to a region of lower density. If the nucleus expands to the point where its compressibility is negative, it will be dynamically unstable and fragment. The regions of low density where the nucleus is dynamically unstable ("fragmentation zone") and the regions of initial energy-density (the "overstressed zone") that will expand to the "fragmentation zone" are shown in Figure 3. When an incident proton strikes the nucleus, very little compression occurs ($n \approx n_0$) and it takes a large amount of deposited energy ($\sim$10 MeV/nucleon) to raise the system from its ground state to the overstressed zone, from which it can expand and fragment. In a heavy ion reaction, the incident heavy ion will compress the nucleus to $\sim 1.4 n_0$ with a deposited energy of only $\sim$3.5 MeV/nucleon thus reaching the overstressed zone and ultimately, the unstable zone, at a lower projectile energy.

For p-U collisions, the excitation energy, E^*, of the multifragmenting nucleus can be estimated from the relation[11]

$$E^* = 0.80\ E_p\ M_R\ V_{11}/P_p \qquad (1)$$

where v_{11} is the average impact velocity of the struck nucleus, P_p and E_p the momentum and kinetic energy of the incident proton and M_R the mass of the residual nucleus following the fast intranuclear cascade ($\approx$235amu). If the threshold for multifragmentation is defined as the proton energy at which the production cross section for the multifragmentation product is 1/2 its limiting value, one might estimate the threshold for multifragmentation in p-U collisions to be $\sim$3-4 GeV (Fig. 2). Using measured values[4] for v_{11} for multifragmentation products, one deduces $E^* \gtrsim 1681$ MeV, i.e., $E^*/A \gtrsim 7.2$ MeV in fair agreement with Fig. 3.

For O-U collisions, one might estimate the threshold for multifragmentation to be $\sim$250-400 MeV/A. If we assume that multifragmentation events are the result of collisions with impact parameters < 2.5 fm (which is roughly consistent[9] with the relative fraction of the product yields for A<50 events), then we can use intranuclear cascade calculations[12] to deduce the average excitation energyof the residual nuclei that multifragmented. This average E^* for the collision of 400 A MeV ^{16}O + ^{238}U is 1000 MeV,

or ∿4.3 MeV/nucleon. This estimate is also consistent with the model shown in Figure 3.

B. Fragment Kinematic Properties

In studies of the reaction of 14.5 GeV/nucleon ^{16}O with ^{197}Au, we measured the number of target fragments that recoiled out of a target of thickness W (mg/cm^2) in the forward (F) and backward (B) directions. The values of the F/B ratio for various products are shown in Figure 4. Surprisingly, the values of F/B for the intermediate mass fragments (A<60) are less than one. (The F/B values for the heavier fragments are in good agreement with previous observations of energetic p-nucleus[14] and nucleus-nucleus collisions.[15]) The intermediate mass fragments are thought to be formed by multifragmentation.[16] While slightly backward-enhanced, sideward-peaked angular distributions have been observed previously for such multifragmentation products from p-nucleus[17] and nucleus-nucleus collisions,[18] this is the first instance in which the F/B ratios are so much less than one. This phenomenon of a preferential backward emission in the laboratory system of multifragmentation products in ultrarelativistic nuclear collisions has been termed "backsplash."

This "backsplash" phenomenon appears to be related to the size and mass of the target nucleus. For example, for a typical multifragmentation product such as ^{24}Na, the F/B ratios for the interaction of 14.5 GeV/nucleon ^{16}O with V, Cu, Ag and Au are[3] 2.83±0.09, 1.90±0.07, 1.39±0.05 and 0.81±0.05, respectively.

It would be of obvious interest to directly measure the angular distribution and energy spectra of these multifragmentation products or their correlations with each other and other emitted particles. Hopefully our data will serve to stimulate more sophisticated experiments to investigate these fragments. We also hope that these measurements can serve as a testing point for our understanding of multifragmentation at ultrarelativistic energies.

References

1. The CERN work was done in collaboration with L. Sihver. The BNL work was done in collaboration with M. Dronikowski, Y.Y. Chu, J.B. Cumming, P.E. Haustein, M. Hellström, S. Katcoff, N.T. Porile and L. Sihver.
2. K. Aleklett, L. Sihver and W. Loveland, Phys. Lett. B197, 34 (1987)

3. W. Loveland, K. Aleklett, M. Bronikowski, Y.Y. Chu, J.B. Cumming, P.E. Haustein, S. Katcoff, N.T. Porile, and L. Sihver, Phys. Rev. C. (submitted for publication).
4. O. Scheidemann and N.T. Porile, Phys. Rev. C14 (1976) 1534.
5. G.D. Cole and N.T. Porile, Phys. Rev. C24, (1981) 2038.
6. I. Haldorsen, et al., J. inorg. nucl. chem 43 (1981) 2197.
7. J. Hudis in Nuclear Chemistry, Vol I, L. Yaffe, Ed. (Academic, New York, 1968).
8. E. Hagebø, private communication, 1987.
9. P.L. McGaughey et al., Phys. Rev. C31, (1985) 896.
10. G. Bertsch and P.J. Siemens, Phys. Lett. 126B (1983) 9.
11. N. Metropolis et al., Phys. Rev. 110 (1958) 204.
12. Y. Yariv and Z. Fraenkel, Phys. Rev. C20 (1979) 2227.
13. P.J. Karol, Phys. Rev. C11, (1975) 1203.
14. S.B. Kaufman, E.P. Steinberg, B.D. Wilkins, and D.J. Henderson, Phys. Rev. C 22, 1897 (1980).
15. S.B. Kaufman, E.P. Steinberg, and M.W. Weisfield, Phys. Rev. C 18, 1349 (1978).
16. A.I. Warwick, H.H. Wieman, H.H. Gutbrod, M.R. Maier, J. Perer, H.G. Ritter, H. Stelzer, F. Weik, M. Freedman, D.J. Henderson, S. B. Kaufman, E.P. Steinberg, and B.D. Wilkins, Phys. Rev. C 27, 1083 (1983).
17. N.T. Porile, D.R. Fortney, S. Pandian, R.A. Johns, T. Kaiser, K. Weilgoz, T.S.K. Chang, N. Sugarman, J.A. Urbon, D.J. Henderson, S.B. Kaufman, and E.P. Steinberg, Phys. Rev. Lett. 43, 918 (1979).
18. J.B. Cumming, P.E. Haustein, and R.W. Stoenner, Phys. Rev. C 33, 926 (1986).

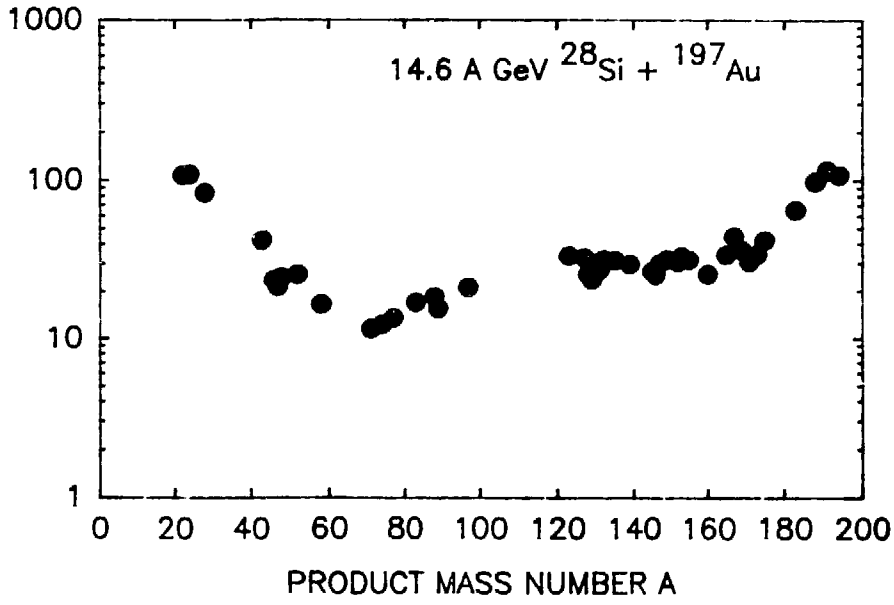

Figure 1. Fragment isobaric yield distribution for the reaction of 14.6 GeV/nucleon ^{28}Si with ^{197}Au.

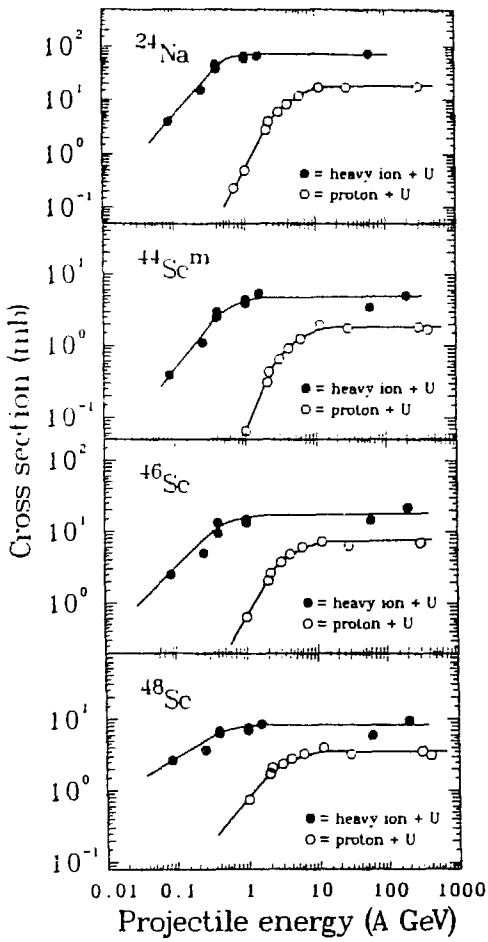

Figure 2. Excitation functions for the production of multifragmentation products in p-nucleus and nucleus-nucleus collisions. Ordinate is projectile energy/nucleon. The cross sections for the ^{12}C and ^{20}Ne induced reactions have been scaled by the ratio of the "soft spheres" total reaction cross sections[13] for ^{12}C and ^{20}Ne induced reactions to the soft spheres cross sections for ^{16}O induced reactions.

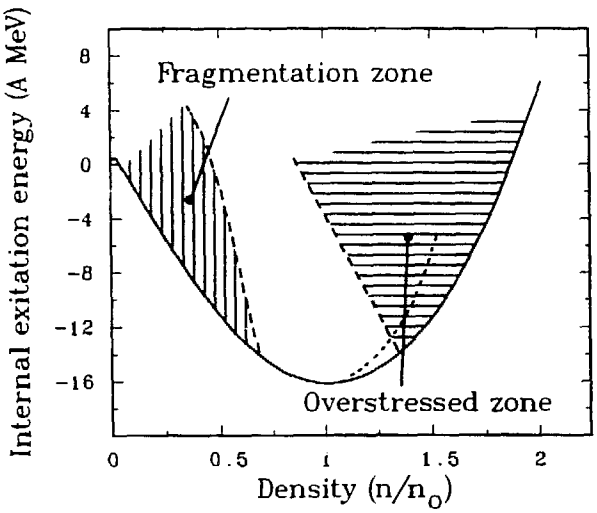

Figure 3. An energy-density diagram for nuclear matter showing the fragmentation and overstressed zones. The densities are expressed in terms of the number density $n_0 \sim 0.16/fm^3$. From Ref. 10.

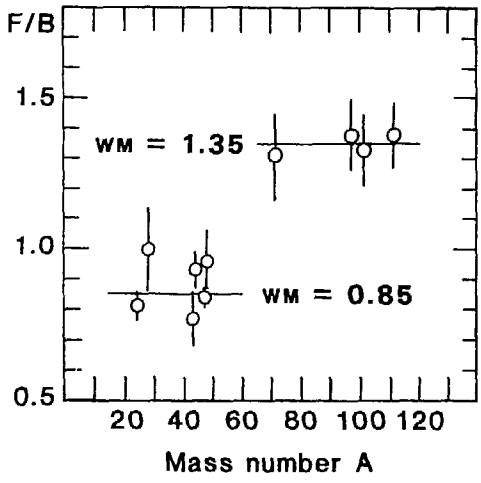

Figure 4. Fragment F/B ratios for the reaction of 14.5 GeV/nucleon ^{16}O with ^{197}Au.

STATUS OF THE MUSIC II DETECTOR*

Walter F.J. Müller and F. Bieser
Lawrence Berkeley Laboratory, University of California
Berkeley, California 94720

W. Christie and C. Tull
Crocker Nuclear Laboratory, University of California
Davis, CA 95616

and

G. Bauer, H. Beeskov, U. Lynen and H. Sann
Gesellschaft für Schwerionenforschung, Darmstadt, West Germany

Abstract

A new tracking detector for LBL's Heavy Ion Superconducting Spectrometer (HISS) was designed, built and tested. The new device is a second generation *MU*ltiple *S*ampling *I*onization *C*hamber and employs concepts from classical ionization chambers and time projection chambers. *MUSIC* II provides a unique charge identification and a precise determination of track position and angle for up to 10 particles in a wide range from carbon to uranium. The system is optimized for the detection of intermediate mass ($Z \geq 6$) and heavy projectile rapidity fragments and complements the existing HISS drift chamber system which will be mainly used for lighter fragments and mid rapidity coverage.

1 Introduction

The Heavy Ion Superconducting Spectrometer (HISS) facility [1] at the BEVALAC was designed to study multiparticle correlations in relativistic heavy ion collisions. The central part is a large aperture dipole magnet with a large dispersion but practically no focusing. The determination of the momentum vector $\vec{P}$ of a particle requires the measurement of the magnetic deflection (or rigidity $\vec{R} = \vec{P}/Z$) and the charge Z. This is currently being accomplished by using a drift chamber [2] for particle tracking and either scintillators or Čerenkov counters for the charge identification.

The main design goal for *MUSIC* II was to combine the measurement of position, angle and charge of fragments in a single gas detector without gas amplification. This minimizes the total detector thickness and thus the amount of secondary interactions.

*This work was supported by the Director, Office of Energy Research, Division of Nuclear Physics of the Office of High Energy and Nuclear Physics of the U.S. Department of Energy under Contract DE-AC03-76SF00098 and by the Bundesminister für Forschung und Technologie (West Germany).

2 The Detector

The *MUSIC* II design is summarized in Fig. 1. The detector consists mainly of three field cage structures which are aligned in a cylindrical vessel filled with an Ar-CH_4 gas mixture at atmospheric pressure. The field cages have an active area of 100 by 60 cm and a depth of 48 cm each, the vessel (not shown in Fig. 1) has an inner diameter of 124 cm and length of 250 cm. Two cages generate a horizonal drift field with a cathode plane in the middle and two anodes planes on the sides. The central cage generates a vertical drift field in which the cathode is at the top and the anodes are at the bottom.

A heavy ion traversing the active gas volume creates an ionization track of about $70 \cdot Z^2$ ion pairs per cm. The uniform drift field separates the electrons and positive ions. The electrons drift with a constant velocity through the active volume and a grounded frisch grid and arrive at the anode with a time delay proportional to their drift distance. The anode planes are subdivided along the main axis into 16 anode strips 3 cm wide. The signals are processed by charge sensitive preamplifiers and shaping amplifiers with 150 ns peaking time. The signal shape is finally digitized every 60 ns with a sampling ADC system and recorded by the data acquisition system.

The offline data analysis starts with a simple peak finding algorithm to find hits for each anode and than uses a reference pulse fit technique to extract the amplitude and the position within a fraction of a time bin. Fig. 2 shows the signal generated by an Iron ion for a single anode. The crosses represent the data values, the closed line the fitted reference pulse. This combination of a sampling ADC with digital signal processing as in a TPC allows us to handle many simultaneous tracks without physically subdividing the detector volume into cells. The reference pulse fitting can deconvolute even overlapping hits and yields a double pulse resolution better than the pulse width. The lower part of Fig. 3 shows such a resolved double hit of two fragments with charges 27 and 14 and with a 20 mm separation.

The next analysis step is to reconstruct the tracks from the set of amplitudes and positions for all the anodes. A track traverses two horizontal and one vertical field cage with 16 anodes each, giving a total of 32 (16) position measurements in the horizontal (vertical) plane and 48 energy deposition measurements. The pattern recognition is considerably simplified by the good single anode charge resolution of about 1 unit FWHM.

3 The Electronics

The performance of *MUSIC* II is to a large degree determined by the electronics. The requirements of low noise and large dynamic range led to a redesign of almost all components of the electronic chain, compared to the *MUSIC* I detector [3].

The detection threshold depends only on the noise level of the preamplifiers. We use charge sensitive preamplifiers developed at GSI and tailored for our environment. They are built in surface mount technology and are mounted right on the anode plane inside the gas vessel to minimize the wiring capacitance. We have achieved an rms noise level of 1300 electrons with the relatively large capacitance of a 150 cm^2 anode and 150 ns peaking time of the shaper. This corresponds to a signal to noise ratio of 1:4 for Boron, which is currently the lowest detectable charge.

The Z^2 proportionality of the signals results in a very large dynamic range, a Gold signal is 250 times larger than a Boron signal. This prompted the development of a dedicated sampling ADC system at LBL. The main features are: a 10.3 bit effective dynamic range, up to 20 MHz sampling rate, 256 samples buffer depth, hardware assistance for an effective data compression, a readout time of 1ms/track and a density of 128 channels in a single VME crate. Each channel will use two 8 bit FADC to form a bilinear characteristic.

The double pulse resolution for pulse pairs with very different amplitudes is mainly determined by the precision of the pole zero cancelation and baseline restoration of the shaping amplifier. Specially adapted shapers with four channels in a single width NIM chassis were built by a contractor and are now in use.

4 Test Results

The *MUSIC* II field cages and the vacuum tight gas vessel were constructed at GSI and tested there with a 20 A Mev Bismuth beam in December 1986. The detector was then shipped to LBL and staged at the BEVALAC in early spring 1987. We performed the first beam tests with about 1 A GeV Neon, Argon and Xenon in May 1987 and recently with 1.05 A GeV Nitrogen and Iron. The dedicated FADC for *MUSIC* II is still under construction and will be available in February 1988. All the tests so far were performed by instrumenting one side of a horizontal field cage with LRS 2261 sampling ADCs.

The fragment charge spectra for Iron and Nitrogen interactions with a 1 inch CH_2 target are shown in Fig. 4. The charge resolution is 0.28 and 0.35 units FWHM respectively. The charge was determined as the square root of the sum of amplitudes in 14 anodes of one field cage. It is *not* necessary to use truncated means because the distribution of energy deposition for a 3 cm gas layer is approximately gaussian for ions heavier than Carbon [4]. The total charge resolution improves almost inversely proportional to the square root of the number of averaged anodes (Fig. 5) and can be parameterized by $\Delta Z = 0.926 \cdot n^{-0.459}$ (n = number of anodes).

The position resolution of a single anode was determined from the fit residue for this anode after a track was fitted through all the other anodes. We achieved an rms resolution of 1.3 mm for Nitrogen and 130 μm for Iron (Fig. 6). The position resolution is proportional to $1/Z^2$ or to

the noise to signal ratio for Iron and Nitrogen fragments. This can be described with the simple relation

$$\sigma_{\text{position}} \sim v_{\text{drift}} \cdot t_{\text{rise}} \cdot \frac{\sigma_{\text{noise}}}{\text{Signal}}$$

A resolution of 110 μm for Xenon was determined in an earlier test with a relatively poor quality of the counter gas. It is currently not clear whether the single anode resolution is limited to about 100 μm or whether the Xenon point mainly reflects the poor gas conditions.

The contribution of multiple scattering to the single anode position resolution is only of the order of 10 μm and is negligible compared to intrinsic detector resolution. The angle resolution, however, is dominated by multiple scattering when the single anode position resolution is better than 1.5 mm [5]. This limits the rms angle resolution to about 0.6 mrad.

The detection threshold was at about Z=5. The setup had a limited efficiency for Boron fragments but Carbon fragments were detected with 100% efficiency. Further improvements of the preamplifiers will probably yield full efficiency for Boron fragments.

5 Summary

We have demonstrated that the *MUSIC* II system can be used as a tracking detector, gives an outstanding charge resolution for heavy ions and detects all fragments from Carbon and heavier.

The full system will be ready in February 1988 after the FADC system is operational. It will be used in a BEVALAC experiment to study the multifragmentation of heavy beams, Niobium, Lanthanum and Gold, on light targets in summer 1988. This experiment will use the strong forward focusing in reverse kinematics collisions to achieve a large acceptance for intermediate mass projectile rapidity fragments with a single planar detector like *MUSIC* II.

References

[1] D. Greiner, LBL Report, LBL-15701(1982)

[2] T. Kobayashi et al., NIM, A254, 281(1987)

[3] W. Christie et al., NIM A255, 466(1987)

[4] K. Nagata et al., NIM A196, 217(1981)

[5] P. Billoir, NIM A225, 352(1984)

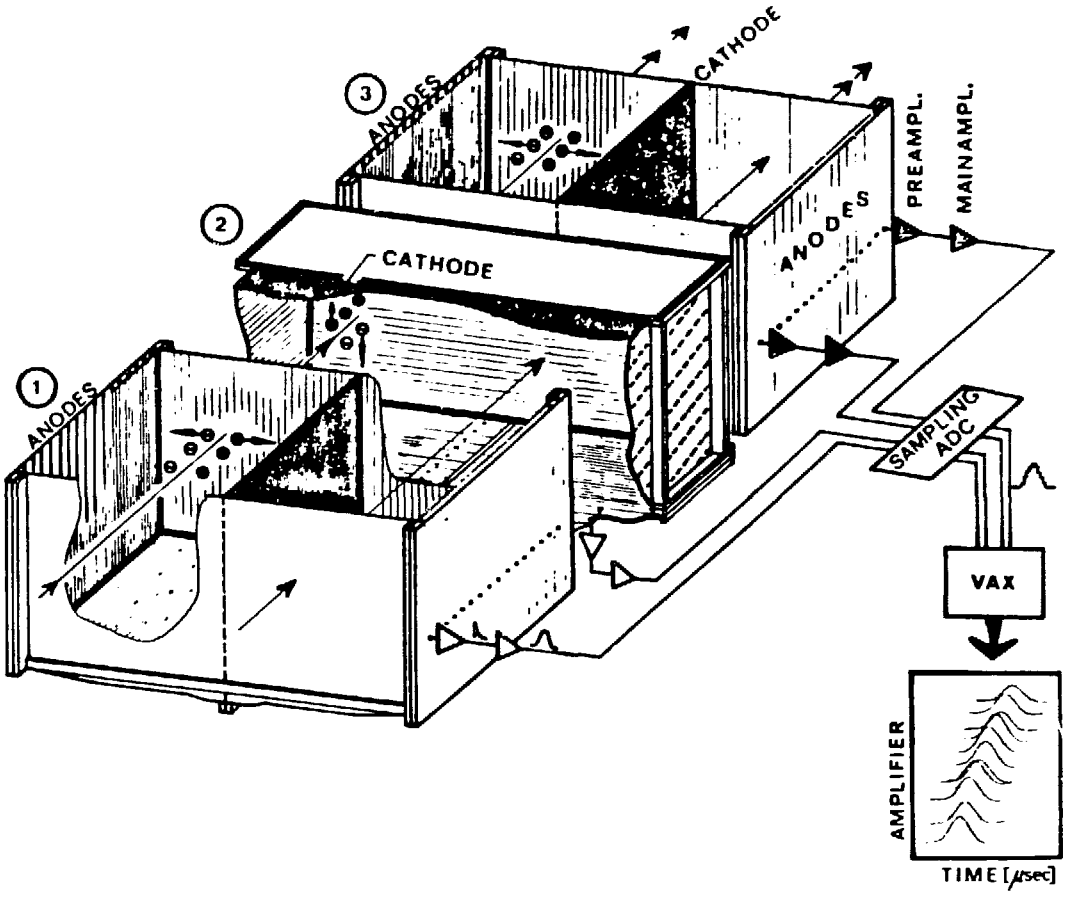

Figure 1: Schematic view of the *MUSIC* II detector

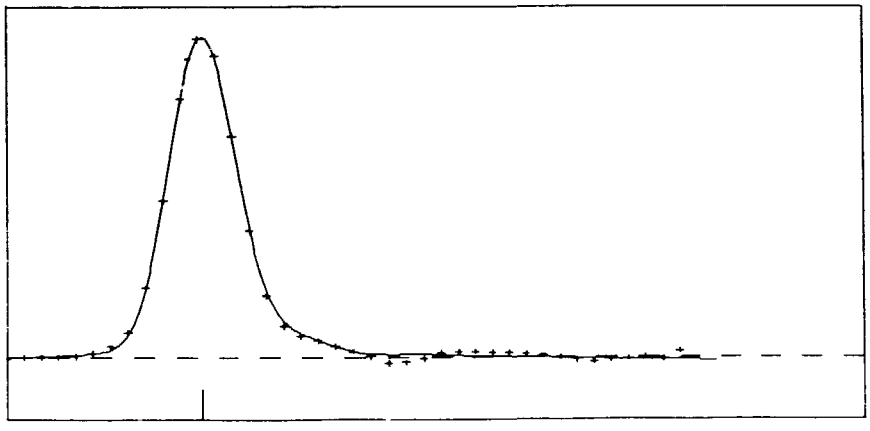

Figure 2: A typical signal generated by an Iron ion on a single anode

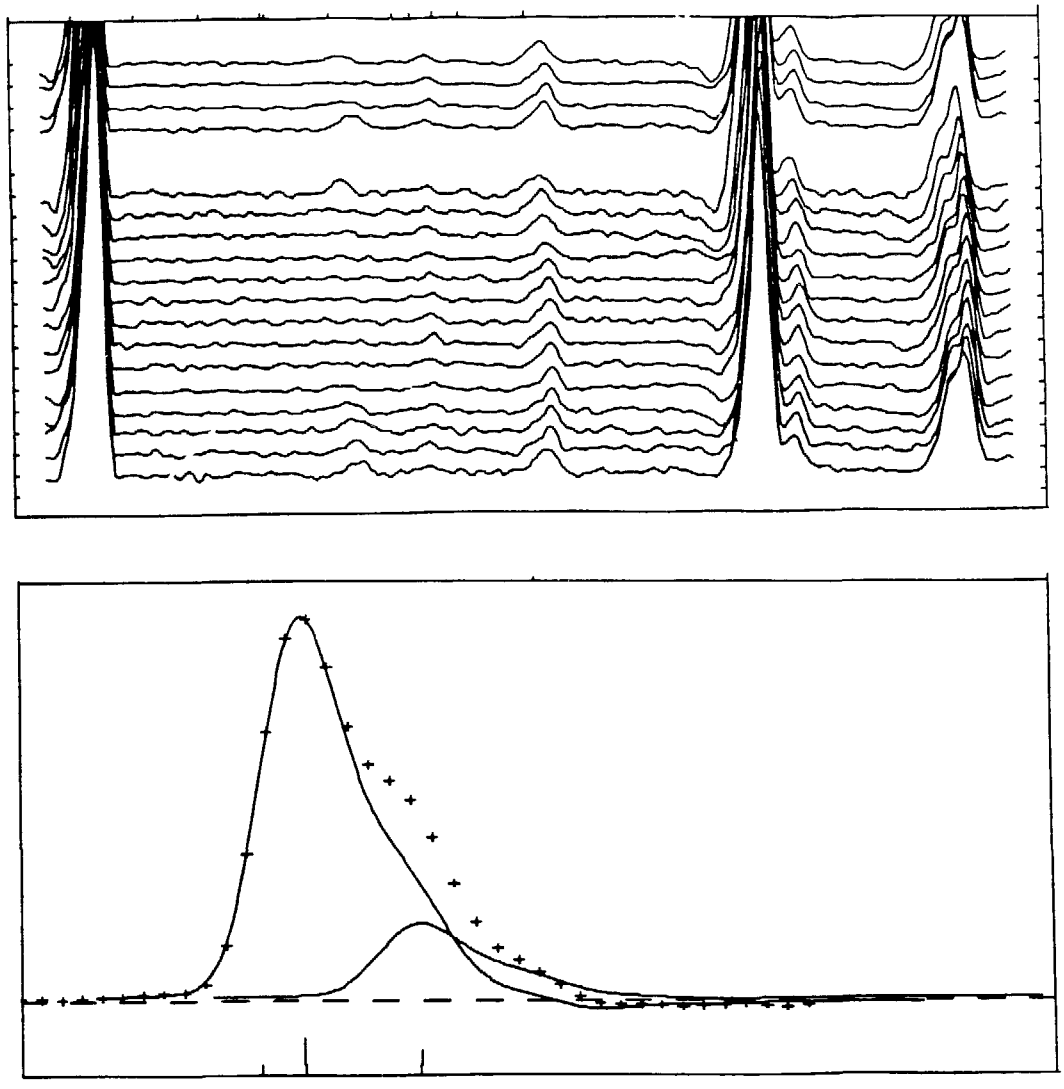

Figure 3: Event display for one field cage.

This event has been taken with a Xenon beam in May '87. The upper half shows the signals of the 14 instrumented anodes with at least 6 tracks (with charge 27,14,15,50,12 and 7 from right to left) and a reference pulser at the left. The double hit at the right is separated by about 20 mm, the one in the middle by about 35 mm. The charge sum is larger than the beam charge of 54 because more than one beam particle interacted during the 12 μs drift time. The top four traces are sums of four anode signals.

The lower half shows a close hit in one anode. The crosses represent the detector signal, the lines the components after deconvolution.

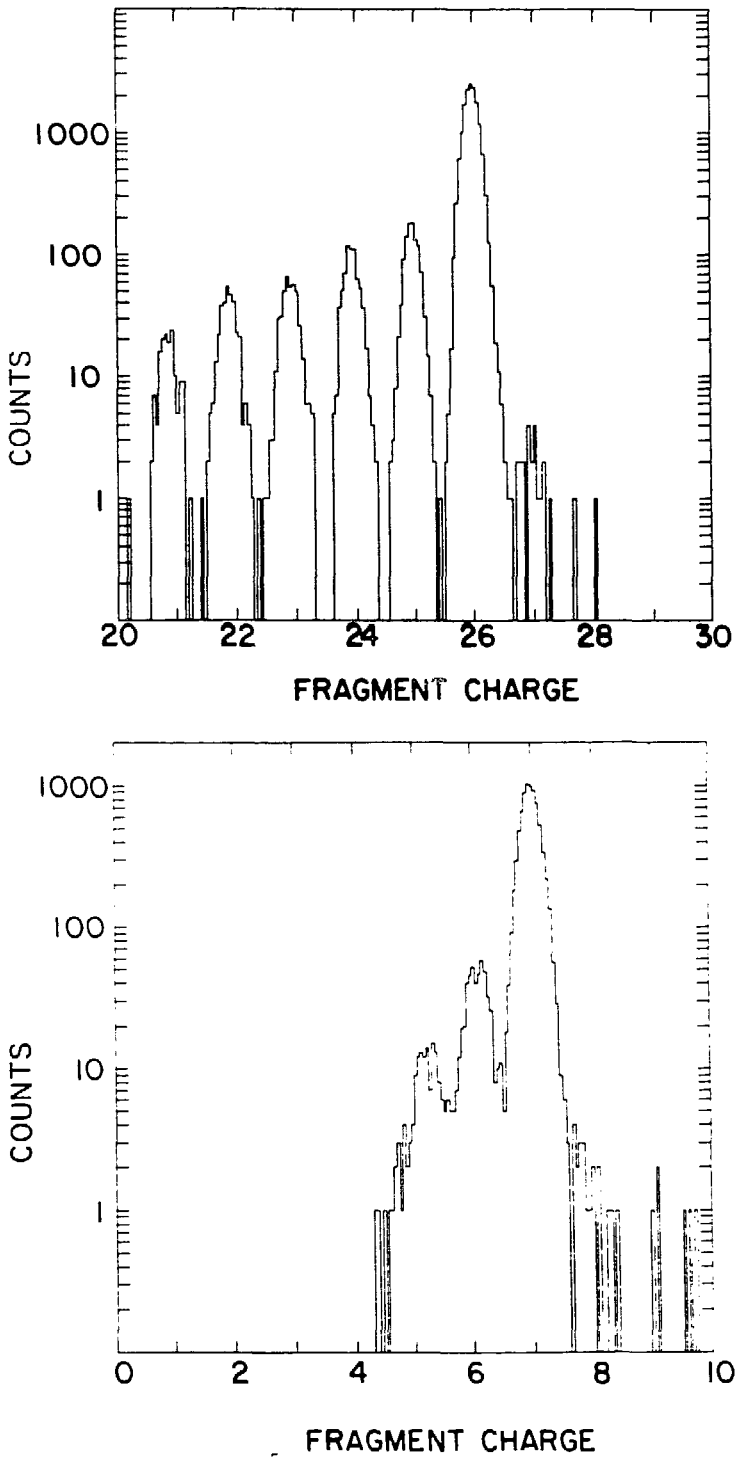

Figure 4: Charge distributions for Iron (top) and Nitrogen (bottom) fragmentation at 1.05 A GeV on a CH_2 target.

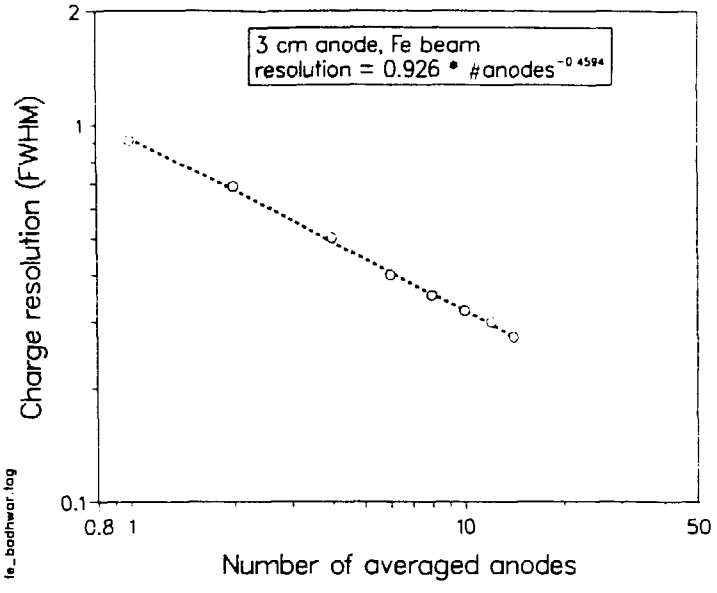

Figure 5: The total charge resolution as the function of the number of averaged anodes.

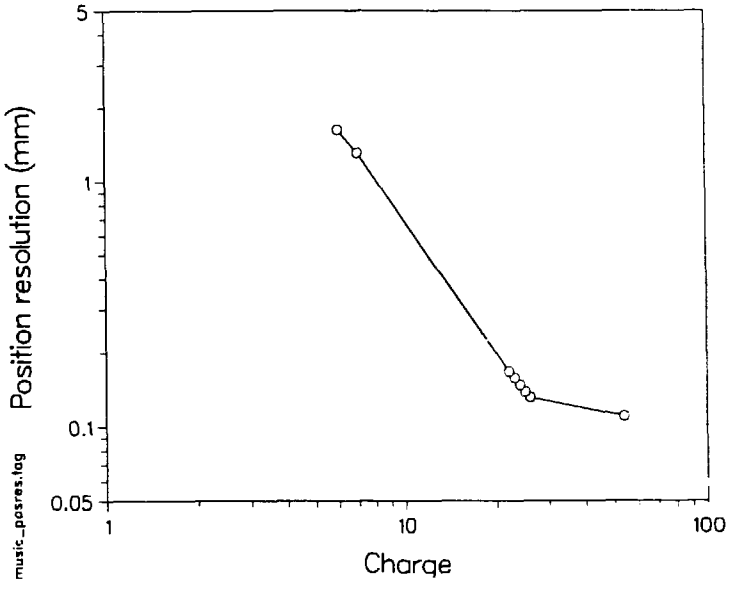

Figure 6: Position resolution as a function of fragment charge

Fragmentation

Role of the Δ in ^{12}C Projectile Fragmentation

P.J. Lindstrom[a], M.E. Baumgartner[b], H.J. Crawford[c], J. Engelage[d], D.E. Greiner[a], D. L. Olson[e], R. Wada[f], M.L. Webb[d]

[a] Lawrence Berkeley Laboratory, University of California,Berkeley, CA 94720
[b] Hoffman-LaRoche, Basel, Switzerland
[c] Space Science Laboratory, University of California, Berkeley, CA 94720
[d] Lawrence Livermore Laboratory, Livermore, CA 94550
[e] Heavy Ion Physics, University of California, Riverside, CA 92521
[f] Texas A and M University

Abstract

We show the effect of one or two inelastic N-N collisions causing the fragmentation of ^{12}C at 2.1 GeV/n. At this energy the dominant inelastic channel is Δ(1232) production. The signature we use to isolate these events is the change in nuclear charge of the ^{12}C fragments.

Most models of projectile fragmentation view the process as two step - an abrasion (prompt) stage followed by an ablasion (slow-evaporation) stage. The prompt stage of fragmentation is generally considered at relativistic energies to be some form of inter-nucleon cascade. The initial interactions are just a superposition of free nucleon-nucleon collisions. In single particle inclusive measurements, the final products are relatively insensitive to the prompt stage of fragmentation, thus, rendering speculation of its nature inconclusive. Our experiment was designed to measure exclusive channels of ^{12}C fragmentation, allowing us to directly address questions of initial interactions.

In this presentation we focus on a subset of the data where 1) all twelve nucleons of the projectile are observed and 2) where evidence of an inelastic collision are strong. At 2.1 GeV/n the dominant ($\approx$90%) inelastic channel is via Δ(1232) production. Questions which we will address are: What is the role of the delta in ^{12}C fragmentation? Can we see delta signature? How does the delta affect the final state(s)? Can we see multiple delta production?

This experiment was run on the HISS facility at the Bevalac. The detector arrangement is diagrammed in Figure 1. Using a combination of beam defining scintillators, up stream and downstream drift chambers and a large time of flight wall, we were able to reconstruct the mass, charge, and vector momentum of all charge fragments with rigidity greater than one sixth of the beam rigidity.[1] Figure 2 shows the system acceptance of secondary protons from the target. The cross indicates beam rapidity (a proton at rest in the projectile rest frame). This plot shows we can measure protons

down to approximately 1/2 of beam rapidity (nucleon-nucleon center of mass). Projectile fragments of mass two and greater are completely contained within our acceptance. With this system we can study a wide variety of multi-particle final state systems.

It would be unreasonable to expect the final state fragment correlation to be insensitive to whether the initiating collision was a nucleon-nucleon elastic or inelastic collision. Figure 3 shows simply the difference in a nucleus-nucleus collision. The nucleon-nucleon (quasi) elastic collision is basically transverse and has a high probability of driving the nucleons into the parent nucleus thus further exciting the nuclei. In contrast, the nucleon-nucleon inelastic collision is basically parallel to the beam direction. In case of delta production the delta is moved approximately 3 fermis away from the parent nucleus before decaying. The expected signatures should be 1) a cold nuclear residue, 2) a high relative momentum associated nucleon and 3) a good chance for nuclear charge exchange in the associated nucleon.[2]

Since the nucleon-nucleon elastic to inelastic collision ratio is changing rapidly as a function of energy in the range of a few 10's of MeV/n to 2-4 GeV/n (Figure 4).[3] We would expect this difference to be reflected in the final state products. This expected difference is not observed to be strong in single particle exclusive fragmentation experiments. The reason for the insensitivity of single particle final state products to the initial (prompt) stage of fragmentation was shown by Morrissey, et al.[4] As shown in Figure 5 the de-excitation of the projectile fragments yield final state cross sections which are independent of the initial collision process. This is why multi-particle correlations are needed to reconstruct the early stages of the fragmentation process.

We have selected a small number of ^{12}C fragmentation channels to study the role of nucleon-nucleon inelastic collisions initiating the fragmentation. These channels are shown in Table 1. All of these channels have a mass sum of 12 nucleons within our acceptance. All but one of these channels has a charge sum greater than 6, providing a tag for inelastic collisions. Since the dominant inelastic channel at 2.1 GeV/n is nucleon- nucleon goes to nucleon-delta, this tag extracts events initiated by delta production. The channel with charge sum 6 ($^{12}C \rightarrow {}^{11}B+p$) was studied in depth by Webb, et al.[2]

We show in Figure 6 the proton momentum distribution from the reaction $^{12}C \rightarrow {}^{11}B+p$. There are three major features in this distribution: 1) a peak at beam rapidity, 2) a ridge along the elastic scattering line, and 3) a plateau at low rapidity. Webb has shown that the plateau is well described by a single nucleon-nucleon collision producing a delta. The ^{11}B in this computation behaves as a spectator. We have a direct check on this assumption. A companion channel to $^{11}B+p$ is $^{11}C+n$. If the reaction $^{12}C \rightarrow {}^{11}C+n$ is initiated by an inelastic collision then the nucleon accompanying the ^{11}C can easily be a proton by $NN \rightarrow N\Delta$ combinations. We can examine $^{12}C \rightarrow {}^{11}C+p$ for confirming signatures of delta production.

We show in Figure 7 the proton distribution from $^{12}C \rightarrow {}^{11}C+p$. The features on this plot can be directly compared with $^{12}C \rightarrow {}^{11}B+p$ (Figure 6). The proton distribution in Figure 7 shows no signs of an elastic scattering ridge, as expected from a reaction proceeding from a single nucleon-nucleon inelastic collision. The broad plateau expected

from delta production is now prominent. The small peak at small transverse momentum and near beam rapidity requires further study.

The low energy proton peak (in the projectile rest frame) can be isolated by looking at the invariant mass minus the rest mass of the ^{11}C+p system. (Figure 8a). We see in Figure 8a a strong peak at $\approx$6 MeV excitation, consistent with a ^{12}N decay. The unexcited ^{12}N contribution to this plot is miniscule. Our first thoughts on this peak were that it was a result of a massless charge exchange reaction (NP$\rightarrow$PN). Figure 8b shows that massless charge exchange is not the explanation for the peak. This Figure shows the excitation energy for the ^{11}C+p system vs. the parallel momentum shift. Note the low excitation system is shifted by approximately 150 MeV/c. We show in Figure 9a the total momentum (in the projectile rest frame) of the ^{11}C+p system where the internal excitation is less than 12 MeV. This momentum distribution is directly compared with predicted positions for massless charge exchange and delta production.[5] The dominant feature of Figure 9a is consistent with delta production, followed by reabsorption of the free nucleon, followed by ^{12}N$\rightarrow^{11}$C+p decay. The missing mass indicated by the momentum shift is in the escaped pion,

Given the observations of the ^{11}C+p final state system, we can now examine the other mass sum 12, charge sum 7 systems. In Figure 10 we look at the momentum of the protons from ^{12}C$\rightarrow^{10}$B+p+p. Roughly half of the protons are in the delta plateau region and half at low momentum. Figure 11a shows the excitation energy in the ^{10}B+p+p system. Note the lack of a low energy peak, indicating that there is at least one high momentum proton in the system. This momentum feature is further illustrated in Figure 11b where the parallel momentum of one proton vs. the other proton in ^{10}B+p+p is plotted. Note the trend of one large p parallel and one small p parallel. The data indicate that one or both protons in ^{10}B+p+p come from delta production and often the second proton from ^{11}C decay (^{11}C+p$\rightarrow^{10}$B+p+p). In Figures 12a and 12b we see the ^{12}C$\rightarrow$p+^{3}He+α+α system. Both the excitation energies in Figure 12a and the proton momentum distribution show this channel to result a mix of ^{11}C+p decay and proton reabsorption leading to ^{12}N$\rightarrow$p+^{3}He+α+α. On the other hand, Figures 13a and 13b show that the ^{10}C+d channel is dominated by the ^{12}C$\rightarrow^{11}$C+p$\rightarrow^{12}$N$\rightarrow^{10}$C+d chain. Note the similarity to the low energy peak in ^{12}C$\rightarrow^{11}$C+p as shown in Figures 8 and 9.

As further verification of delta production populating these charge exchange channels the proton momentum characteristics should persist into the mass sum 12, charge sum 8 channels. In Figure 14a we see the protons from ^{12}C$\rightarrow^{10}$C+p+p and in Figure 14b we see the momentum of the protons from ^{12}C$\rightarrow^{7}$Be+^{3}He+p+p. In the examples in Figure 14 both protons are consistent with direct delta production and no reabsorption. Examination of the momentum correlations of the two protons show no sign of coherent delta decay. On the other hand, of the protons from the channel ^{12}C$\rightarrow$p+p+p+p+α+α only half can come from charge exchange via delta production. Figure 15 shows that half of the protons appear to be from deltas and the other protons from subsequent decay.

This dissection of events containing nuclear charge exchange show the power of multi-particle correlation experiments. From the ^{12}C$\rightarrow^{11}$B+p study, delta production is

consistent with inter-nucleon cascade computations. Charge exchange in ^{12}C fragmentation is from delta production and by tagging an interaction by charge exchange we can study the excitation and decay of the remaining nuclear system.

REFERENCES

1. J. Engelage et.al.,LBL Report LBL-23867 (1988)
2. M.L. Webb et.al,Phys Rev C,36 (1987) 193
3. Particle Data Group,UCRL report UCRL20000 NN (1970)
4. D.J.Morrissey et. al.,Phys. Rev. Lett. 43 (1979) 1139
5. Celenza et. al.,Nuc. Phys. A276 (1977) 509

^{12}C TARGET

CHANNEL	σ (mb)	ΣZ
$^{11}B+p$	36	6
$^{11}C+p$	9	7
$^{10}B+p+p$	2	7
$^{7}Be+\alpha+p$	1	7
$^{3}He+\alpha+\alpha+p$	.6	7
$^{10}C+d$	.1	7
$^{10}C+p+p$	.05	8
$^{7}Be+^{3}He+p+p$	.04	8
$\alpha+\alpha+p+p+p+p$	.07	8

Table 1. Final state products of ^{12}C fragmentation chosen to study delta production. The charge sum for most channels are greater than 6, providing a tag for inelastic processes. The cross sections have $\approx$20-30% errors.

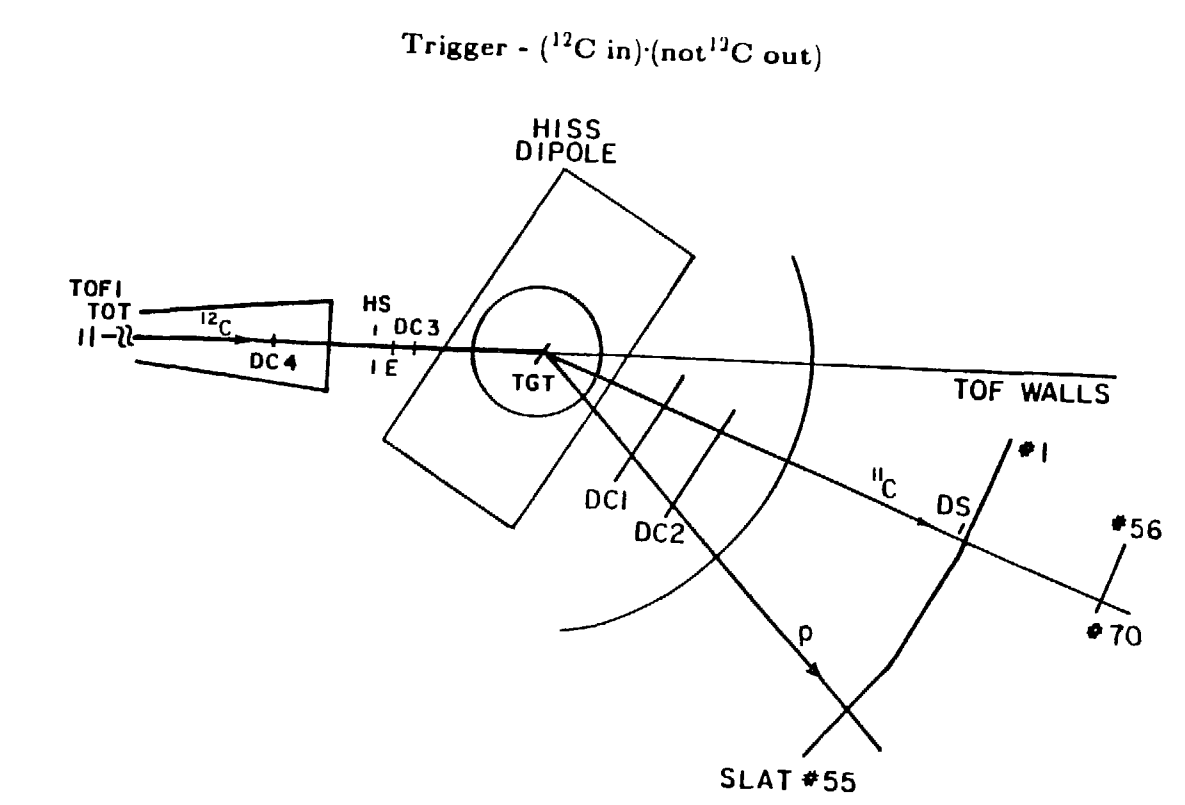

Figure 1. Detector setup for this experiment. Scintillators TOF1, TOT, HS, E, and DS provided a fast trigger consisting of a Z = 6 particle upstream within the beam envelope and not proceeded or followed by another particle within 300 ns and no Z = 6 particle hits DS, where the uninteracted beam hits. Drift chambers DC 3 and 4 measure the incoming beam vector and chambers DC 1 and 2 measure the outgoing fragments. The TOF wall measures the charge and flight time of the outgoing fragments.

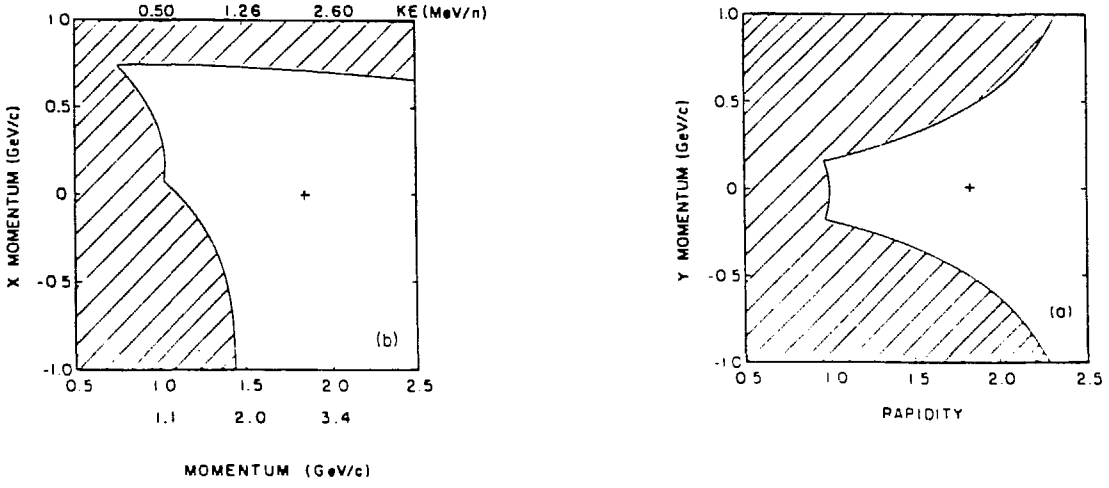

Figure 2. System acceptance of protons from the target. The cross shows beam rapidity.

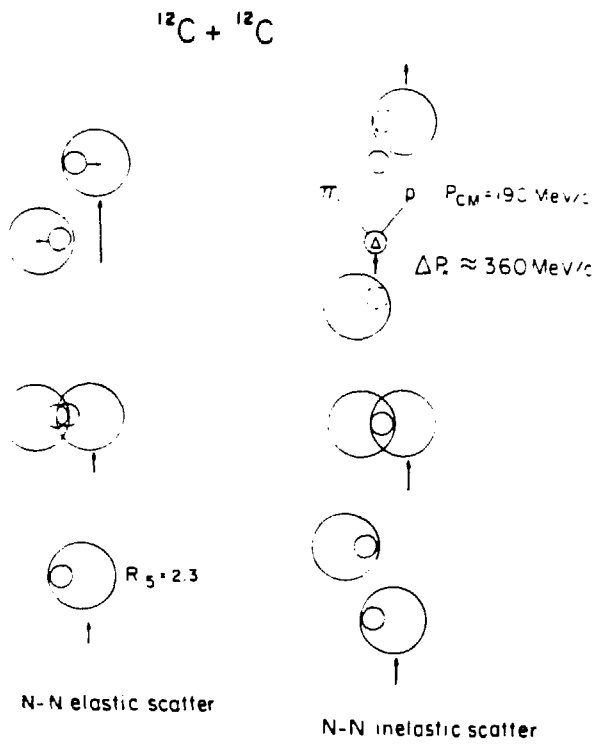

Figure 3. Nucleus-nucleus collisions. The left column shows an elastic nucleon-nucleon collision. Note the transverse nature of the process. The right column shows an inelastic collision via delta production. This process is parallel to the beam direction and the delta generally decays outside the projectile (or target).

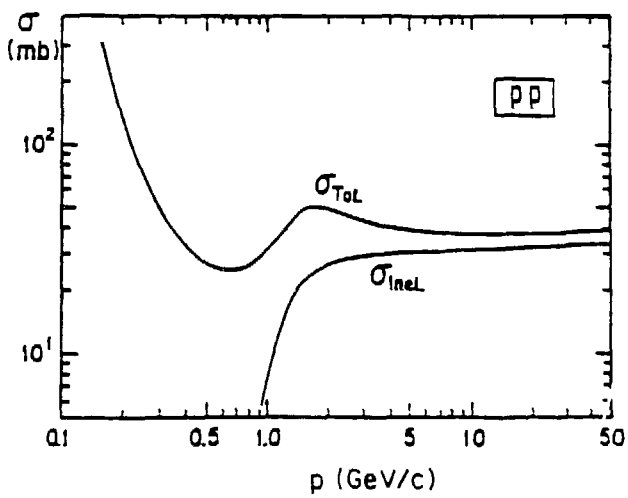

Figure 4. Proton-proton total and inelastic cross sections vs. momentum. The x axis was mislabeled energy at the time of the presentation.

Isotope Production Cross Sections for ^{40}Ar[1]

- **Comparison of abrasion-ablation (a-b) and Monte Carlo (c-d) models**

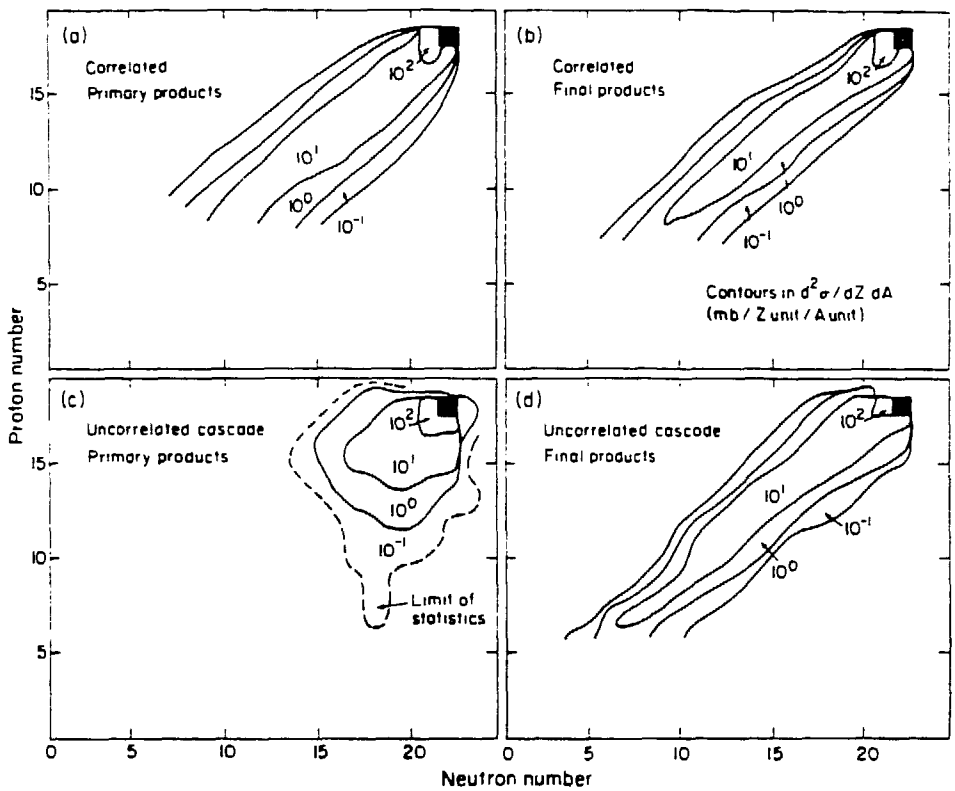

Figure 5. Two fragmentation models are compared for the isotope production cross sections for ^{40}Ar.[4] The left hand column shows the mass charge distributions after the prompt stage of the collision. The right hand column shows the final products after de-excitation. Note the final products are insensitive to the initial process.

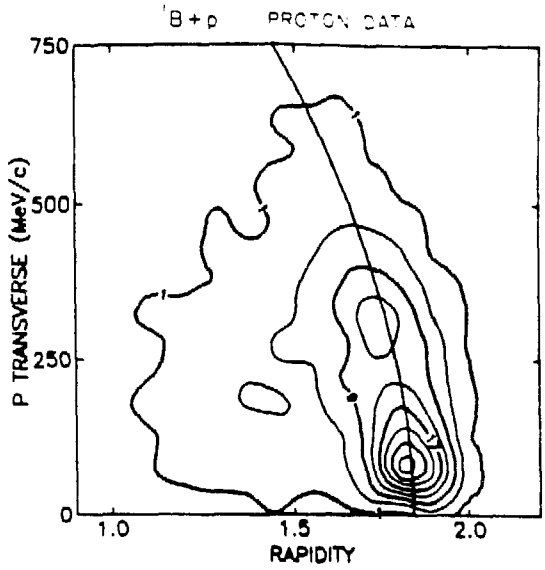

Figure 6. Proton momentum distribution in the reaction $^{12}C \rightarrow ^{11}B+p$. The line starting at $p_T=0$ and rapidity ≈ 1.8 is the nucleon-nucleon elastic scattering line.

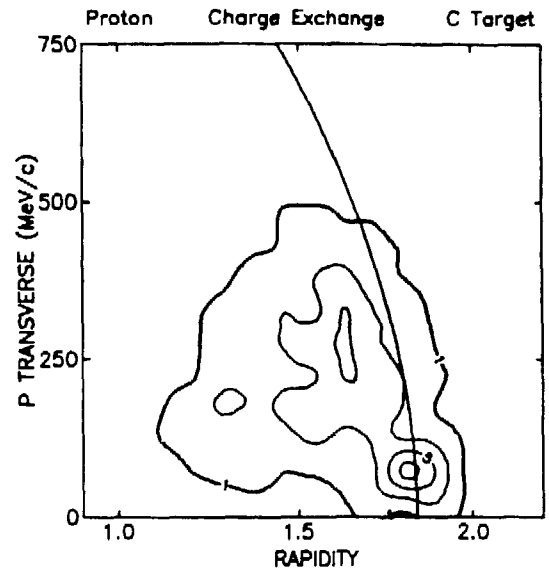

Figure 7. Proton momentum distribution in the reaction $^{12}C \rightarrow ^{11}C+p$. Note the loss of the elastic scattering ridge as seen in Figure 6.

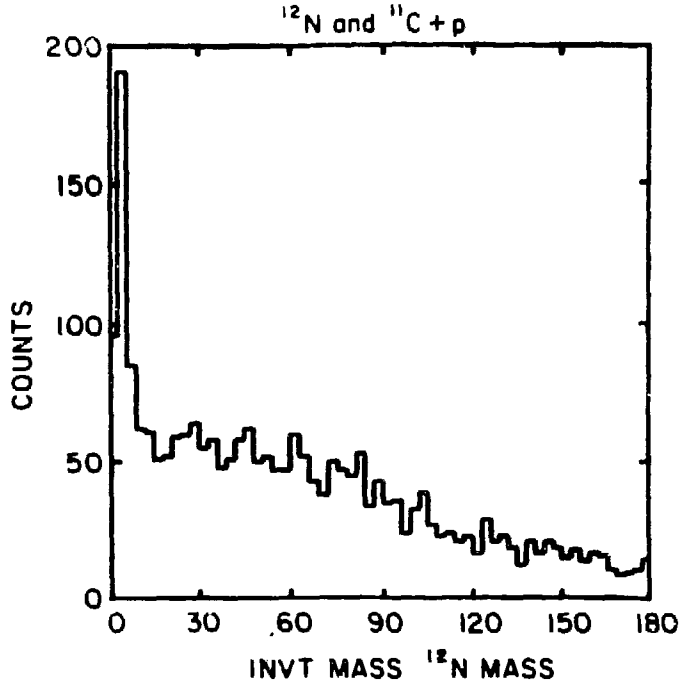

Figure 8a. Invariant mass-^{12}N rest mass for the ^{11}C+p system. The low energy peak corresponds to the peak in Figure 7.

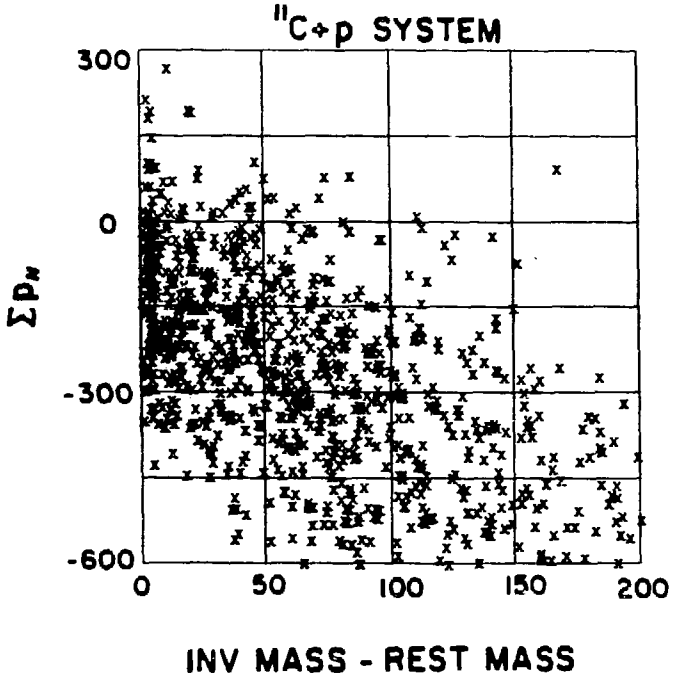

Figure 8b. Invariant mass-rest mass for ^{11}C+p system vs. total parallel momentum shift. A negative momentum shift even at the lowest excitation energies indicate missing mass.

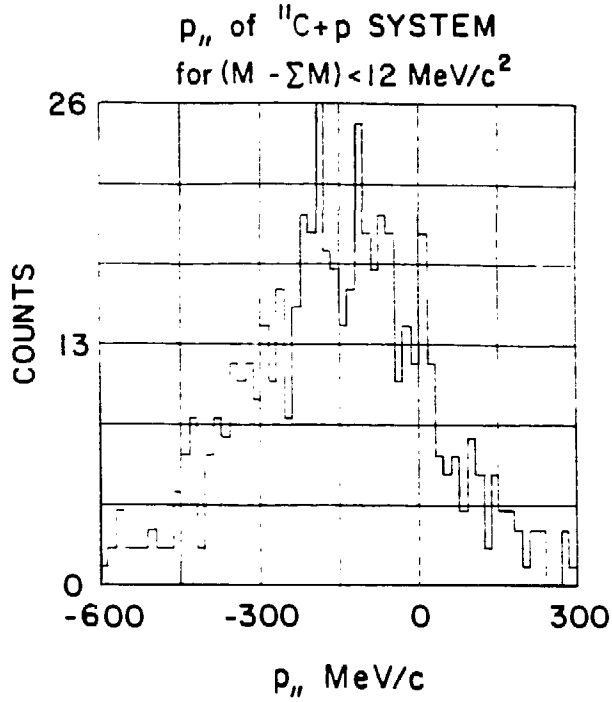

Figure 9a. Parallel momentum shift of the $^{11}C+p$ system where the excitation of the system is less than 12 MeV.

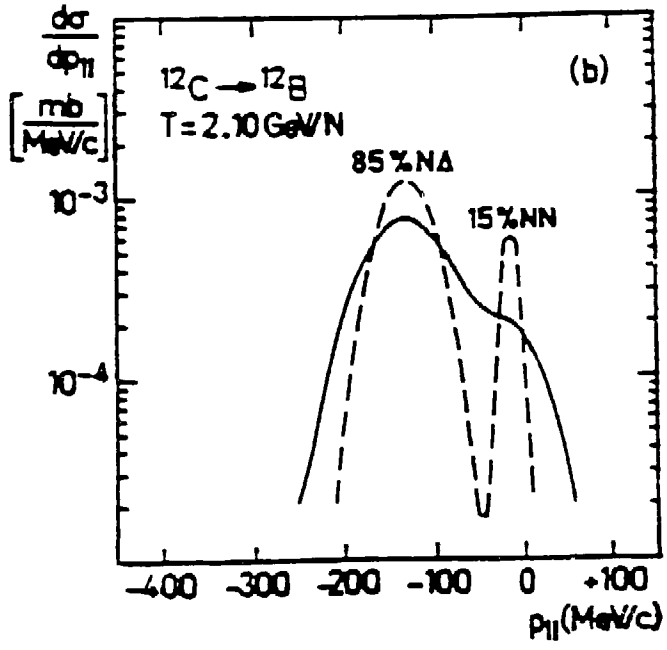

Figure 9b. Predicted momentum shifts for NN→NN and NN→NΔ for ^{12}C system within charge exchange.

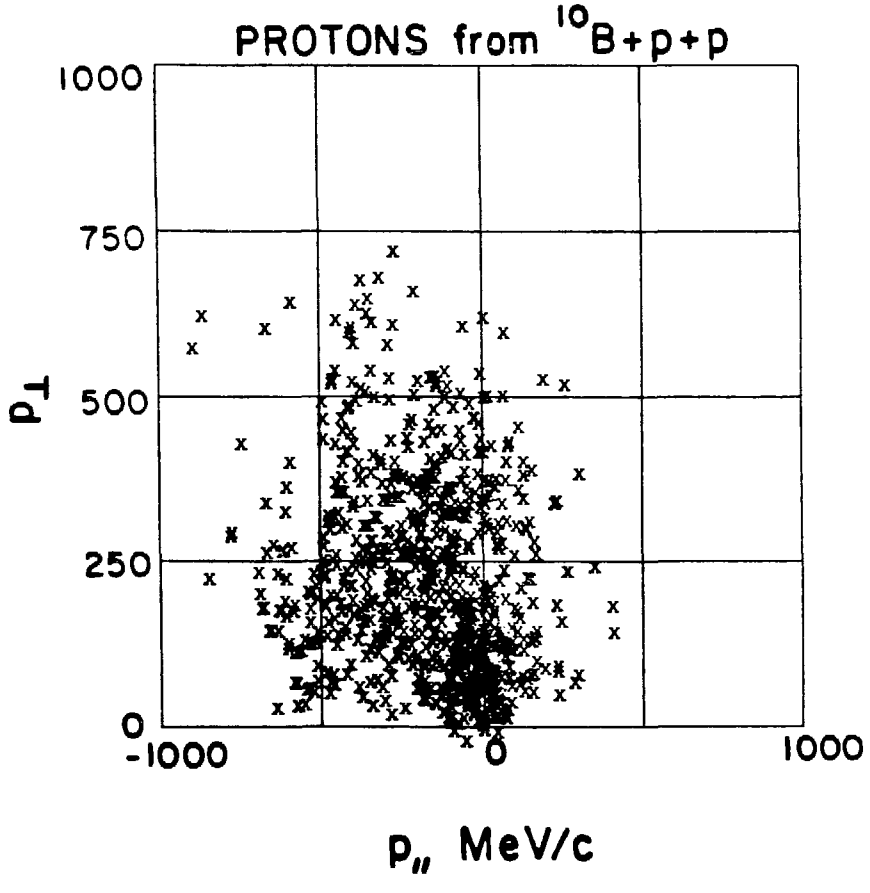

Figure 10. Parallel momentum vs. perpendicular momentum of protons from $^{12}C \rightarrow ^{10}B+p+p$.

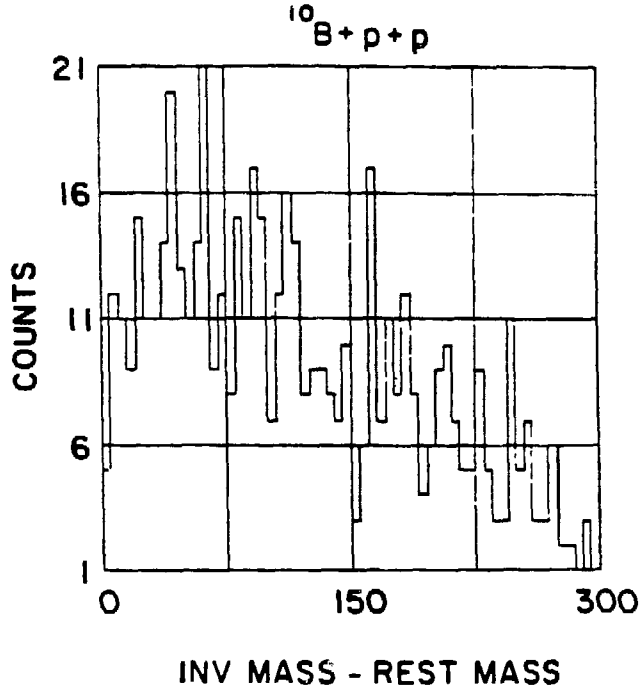

Figure 11a. Invariant mass-rest mass of the ^{10}B+p+p system. Note the lack of a low excitation energy peak.

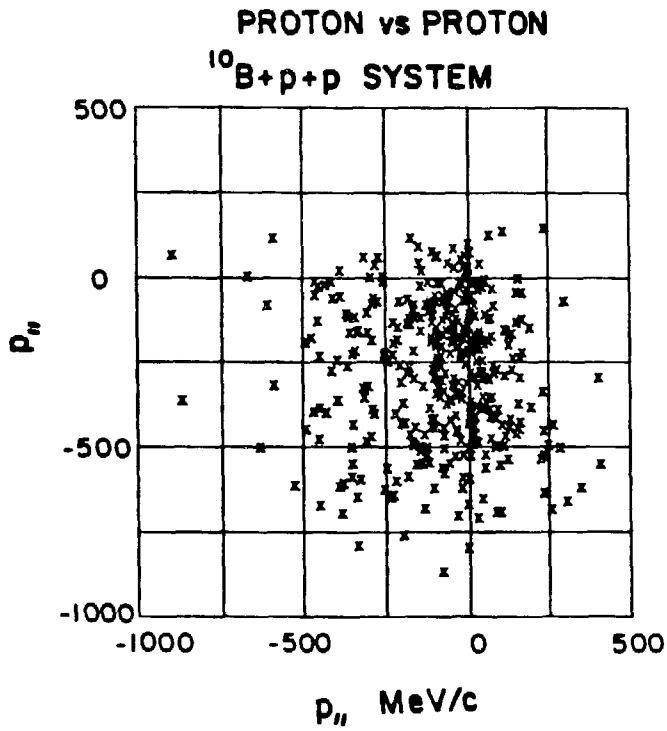

Figure 11b. Parallel momentum of one proton us. the other in the ^{10}B+p+p system.

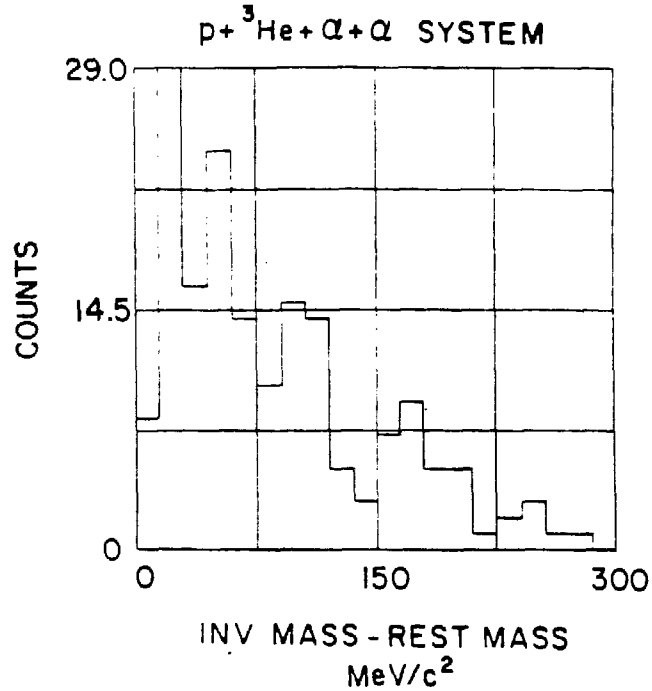

Figure 12a. Invariant mass-rest mass of the p+^{3}He+α+α system. Comparison to Figure 11a shows a low energy peaking.

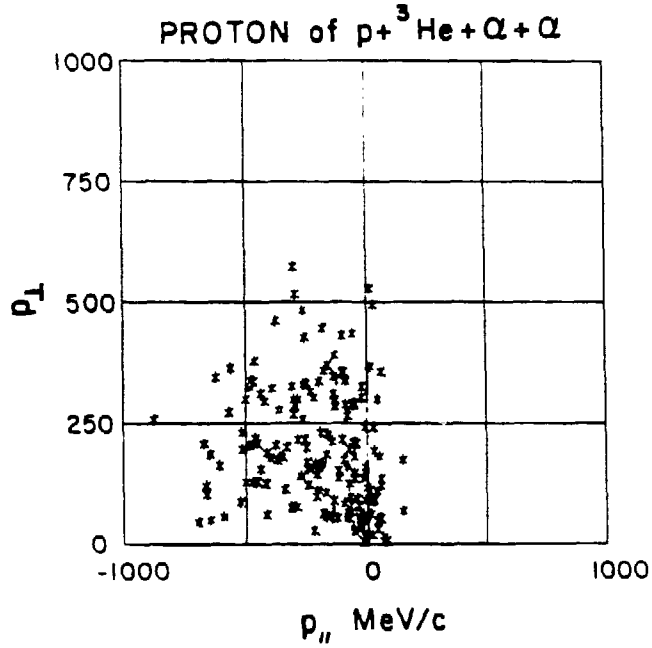

Figure 12b. Parallel momentum vs. ^{12}C$\rightarrow$p+^{3}He+α+α. The low energy proton peak indicate proton reabsorption before subsequent decay.

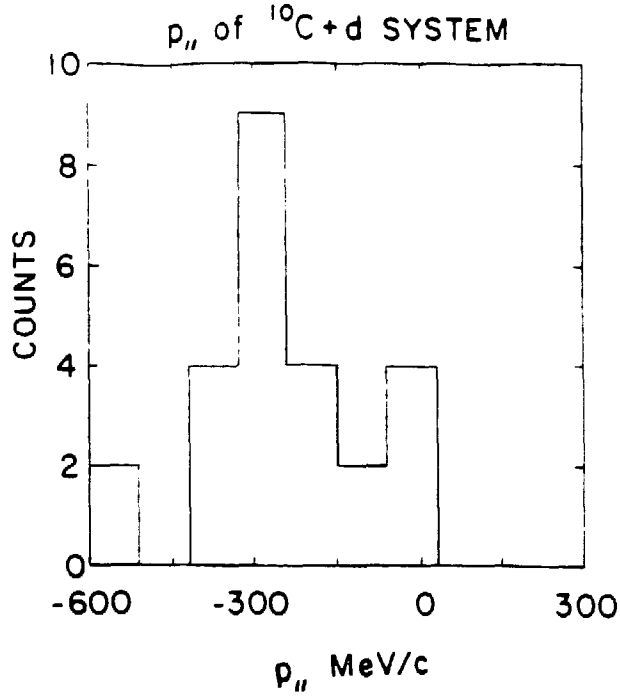

Figure 13a. Parallel momentum of the $^{10}C+d$ system. The parallel momentum shift is indicative of absorption of a proton from delta production followed by subsequent decay.

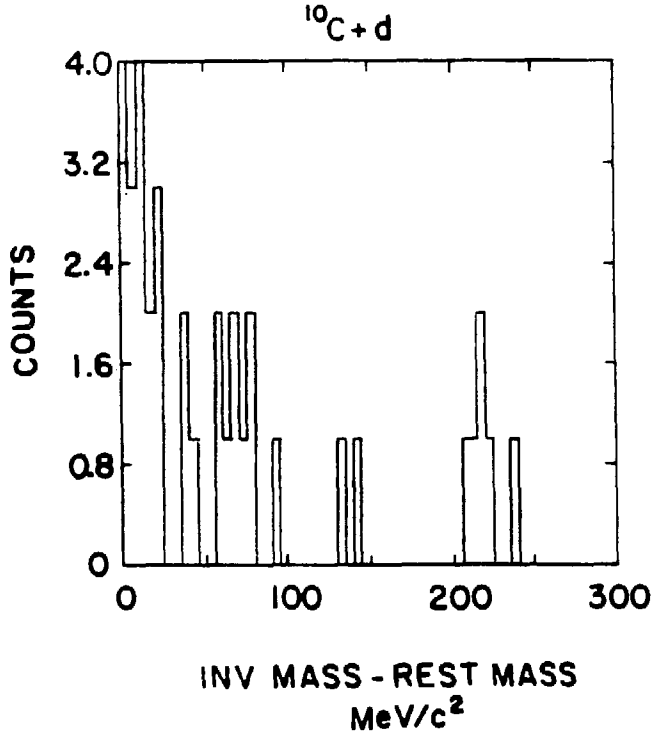

Figure 13b. Invariant mass-rest mass of the $^{10}C+d$ system. The low energy peak implies $^{12}N \rightarrow {}^{10}C+d$ as the decay scene.

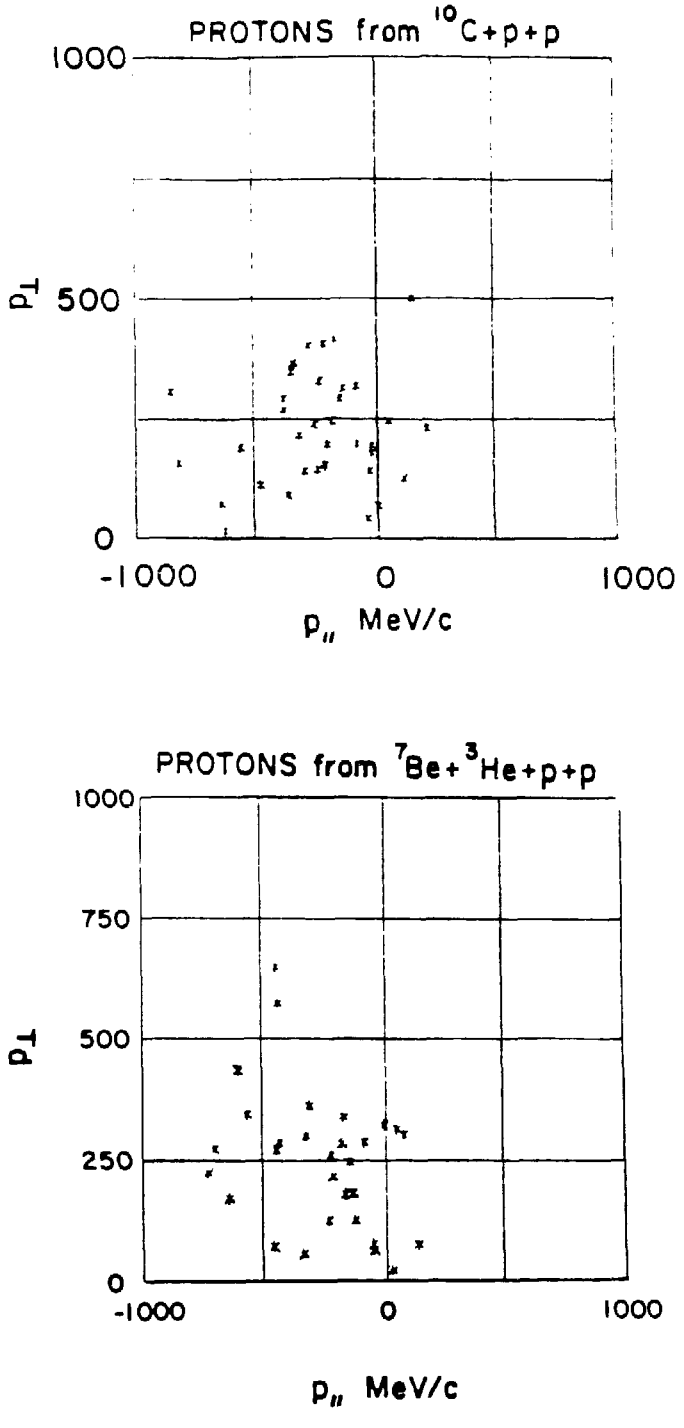

Figure 14. Proton parallel vs. perpendicular momentum for a) $^{12}C \rightarrow ^{10}C+p+p$ and b) $^{12}C \rightarrow ^{7}Be+^{3}He+p+p$.

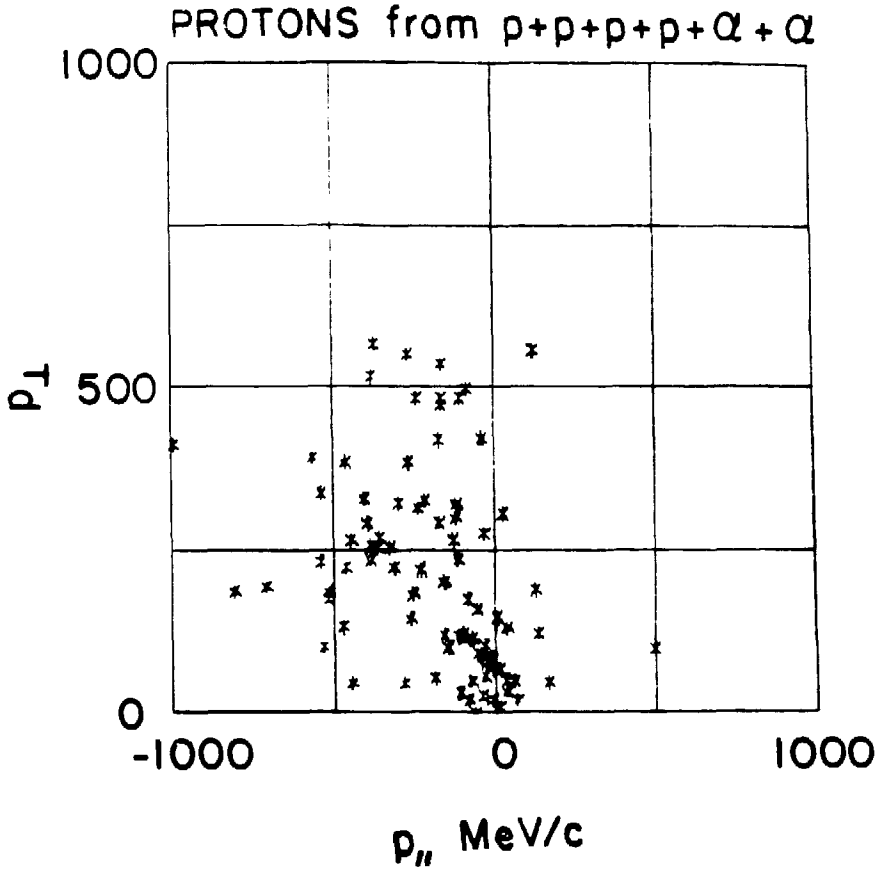

Figure 15. Protons from $^{12}C \rightarrow p+p+p+p+\alpha+\alpha$. Note half of the protons are in the delta production region and half are at low energy indicative of decay products.

MASS OF Δ IN NUCLEI — QUASIFREE Δ PRODUCTION —

Junsei Chiba

National Laboratory for High Energy Physics (KEK)
Oho 1-1, Tsukuba, Ibaraki, 305 Japan

Abstract

Recent measurements of the $(^3\mathbf{He}, \mathbf{t})$ reactions at SATURNE have been received attention because of the peak shift in triton momentum distributions which may corresponds to mass shift of Δ in nuclei. On the contrary, our experiments at KEK measuring $(\mathbf{p}, \mathbf{p'\Delta})$ reactions shows no shift of the resonance energy. I think, however, only from those experiments, it is premature to make any firm conclusion, and it is necessary to carry out both inclusive and coincident measurements in the same reaction channel. I introduce our new experiment planned at KEK to answer parts of this problem.

1. Introduction

It is widely believed that the (3,3) resonance ($\Delta(1232)$) plays an important role in nuclear reactions at the incident energy of around 1 GeV. However we have not yet understood how the Δ behaves in a nuclear medium.

Recently, a shift of the peak position in the momentum spectra of outgoing particles (or in the excitation energy of the Δ produced in nuclei) in the $(^3\mathbf{He}, \mathbf{t})$ reactions were reported [1]. It is very interesting and exciting if the shift attributes to a change of the resonance energy of the Δ, because it would become first evidence that particles are modified in nuclear medium and different from those in free space.

We have measured multiple particles produced in hadron-nucleus collisions in coincidence with scattered projectile hadrons, aiming at searching for a new kind of baryonic excitations [2]. Though the main purpose of the experiment seems not to be successful, we have obtained plenty of semi-exclusive data for hadron-nucleus collisions, which are, unfortunately, not fully understood since no standard theory to calculate complicated processes in nuclear reactions exist yet. While quasifree processes may be rather simple to understand. Therefore we concentrate our analysis on the quasifree reactions for a while.

We have studied the strength of $\Delta\mathbf{N}$ interactions, namely the annihilation of Δ in nuclei ($\sigma_{\Delta\mathrm{N}-\mathrm{NN}}$), through a Monte Carlo calculation based on a intranuclear cascade model [3]. However we discuss, in this paper, only the resonance energy of Δ measured in our KEK experiment in relation to the other corresponding inclusive measurements.

FANCY

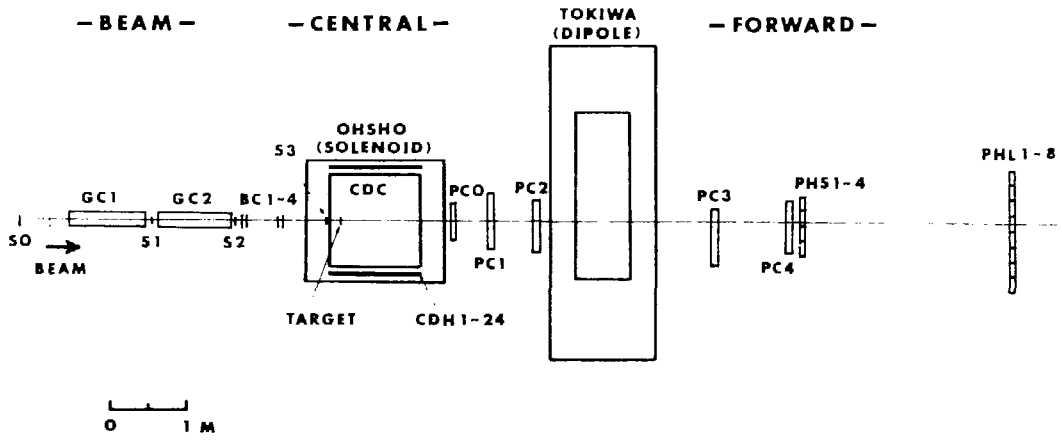

Figure 1: A schematic plan view of the FANCY detector system.

2. Experiments and Results

Experiments were carried out at the $\pi 2$ beam line of the 12-GeV Proton Synchrotron at KEK using a large-acceptance spectrometer called FANCY. Fig. 1 shows a schematic plan view of our detector system. It consists of a forward spectrometer and a cylindrical spectrometer. (FANCY is an abbreviation of Forward ANd CYlindrical). I will not mention the details of the spectrometer, but describe briefly the essence of the system. The forward spectrometer covered 0.5 ~5.5 degrees in polar angle. The momentum resolution was about 1 % at 4 GeV/c and protons were well separated from pions by the time-of-flight (TOF) measurements. The cylindrical spectrometer was composed of a solenoid (3kG magnetic field), a cylindrical drift chamber (jet-chamber type) and a cylindrical hodoscope. It covered polar angles between 25 ~105 degrees in full azimuth. By measuring pulse heights from both ends of resistive sense wires, we are able to reconstruct tracks in three dimensional space. The momentum resolution of $\sigma_p/p \sim 0.1 \cdot p$ (in GeV/c) was achieved. Particles with momenta up to 800 MeV/c were well identified using the energy loss (dE/dx) in the chamber and the TOF measurement by the hodoscope. Events were taken when at least one charged particle entered the cylindrical spectrometer in coincidence with the forward spectrometer. The target materials used were CH, CD_2, C, Al and Cu.

For the analysis of quasifree Δ production in proton-nucleus reactions, events containing only one proton and one charged pion in the cylindrical spectrometer were selected. Since we required a scattered proton in the forward spectrometer, the "quasifree" condition is

satisfied only for part of the $p\pi^-$ events. All $p\pi^+$ events resulted from intranuclear multiple collisions. Fig. 2 shows the momentum distribution of scattered protons and the $p\pi^\pm$-invariant mass distributions for events with different cuts on the momentum of scattered protons. Quasifree N^* productions are clearly seen as well as quasifree Δ productions.

Then we tried to deduce the quasifree component in $p\pi^-$ tagged spectra. Setting a cut on the invariant mass between 1080 and 1400 MeV, a significant peak corresponding to quasifree Δ production was observed in the momentum distribution of scattered protons for $p\pi^-$ events but not at all for $p\pi^+$ events as expected. Since the momentum distributions for $p\pi^+$ events and $p\pi^-$ events were almost identical in the region lower than the quasi-free kinematics, the $p\pi^+$ tagged distribution was subtracted from that tagged by $p\pi^-$ to obtain the quasifree component in the $p\pi^-$ tagged distribution, assuming the non-quasifree component in the $p\pi^-$ tagged distribution is equal to the $p\pi^+$ tagged distribution. However, this assumption may be too naive. In order to select "quasifree" events, we applied a kinematical constraint which essentially required small missing energy and momentum in an event. Momentum distributions of scattered protons in "quasifree" Δ productions deduced by two methods agreed well. The peak location in the distribution shifted toward the low momentum side compared with the kinematics of free pp collision. The direction of the shift was opposite to that of the inclusive $(^3He, t)$ and (p, n) measurements.

For quasifree processes, nuclear binding effects and the Fermi motion of nucleons must be taken into account. We have parameterized those effects and obtained reasonable values from the difference between pp elastic scatterings and quasielastic scatterings. From the shift of peak positions, the averaged separation energy was determined to be 25 MeV, and from the change of peak widths the r.m.s. width of 120 MeV/c was obtained for the Fermi motion assuming a Gaussian shape of the distribution. Taking into account the binding effect and the Fermi motion, the measured momentum spectra were well reproduced with the mass and width of the Δ being the same as those in free space as shown in Fig. 3. We'd like to mention that an extension of a model proposed by Gugelot [4] well reproduces the peak position. In this model the binding effect is naturally included and no free parameter is necessary.

3. Discussions

As mentioned in the previous section, neither mass shift nor broadening of the Δ was observed in our experiment, while significant shift was measured in the $(^3He, t)$ [1] and (p, n) [5] reactions. What do these experimental results tell us about the nature? The peak positions of the Δ mass calculated from the peak of the momentum distribution of scattered particles or the ω (the energy transfer) distributions are listed in Table 1. In this calculation, only two-body kinematics is considered. I'd like to stress the following points about the inclusive measurements; (1) the peak position of the Δ mass tends to be restored to its free-space

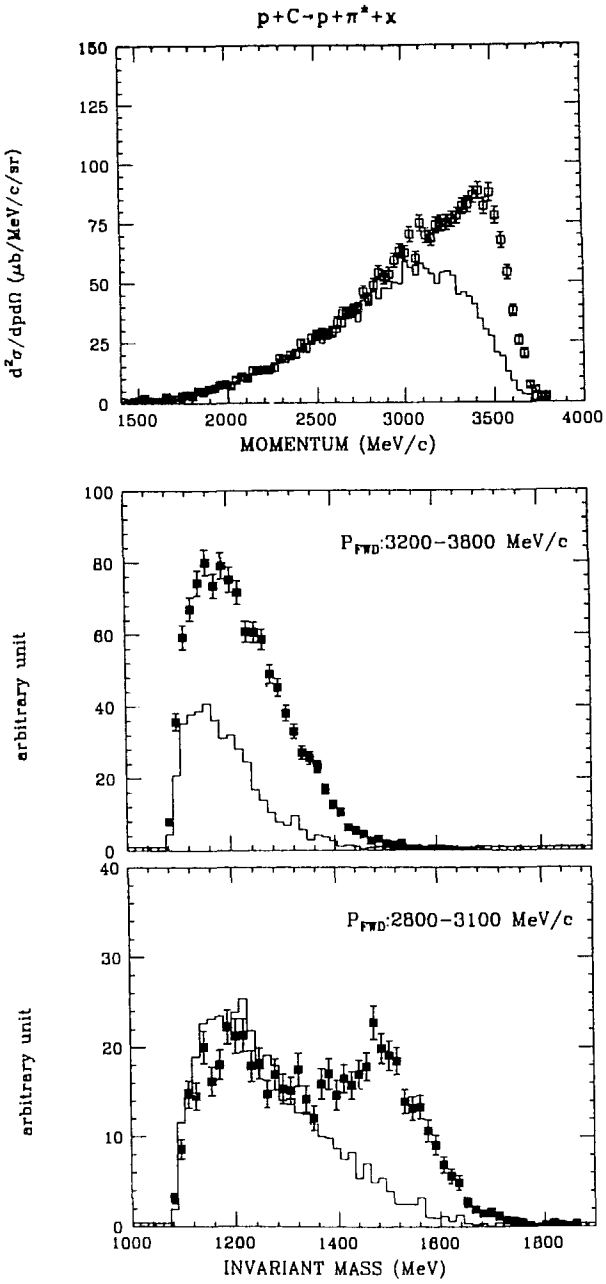

Figure 2: Momentum distribution of scattered protons from the carbon target for events in which only a proton and a pion were detected in the cylindrical spectrometer (upper). Invariant mass distributions for $p\pi$ pairs are shown in lower two figures with different cuts on the momentum of scattered protons. In all the figures, squares indicate data for $p\pi^-$ events and histograms for $p\pi^+$ events.

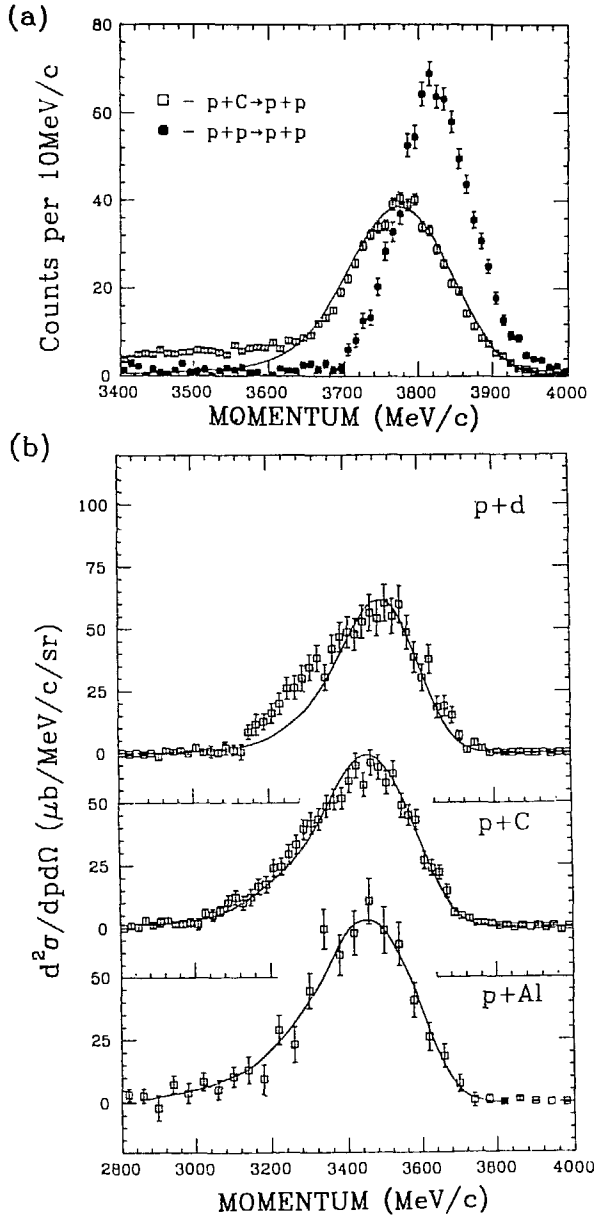

Figure 3: (a) Momentum distribution of scattered protons from the (quasi) elastic scattering on hydrogen (circle) and carbon (square). Solid curve shows a calculation with the averaged separation energy of 25 MeV and the Fermi motion of σ_F=120MeV/c. (b) Momentum distributions from the quasifree Δ production. Solid lines show results of a calculation.

value as the incident energy increases in the $(^3\mathbf{He},\mathbf{t})$ reactions, (2) there were significant shifts observed even for the elementary processes (in other words, for hydrogen targets), and (3) the shift was seen not only the $(^3\mathbf{He},\mathbf{t})$ reactions but also the $(\mathbf{p},\mathbf{n})$ reaction.

Table 1

Peak positions of $\mathbf{m_\Delta}$ calculated from the peak in the momentum distribution of scattered particles.

Reaction	Incident	Peak (m_Δ) (MeV)	
	Momentum (GeV/c)	H target	Nuclear target
$(^3\mathbf{He},\mathbf{t})$	3.90	~1190[8]	~1120[1]
$(^3\mathbf{He},\mathbf{t})$	4.37	~1185[6]	~1120[6]
$(^3\mathbf{He},\mathbf{t})$	6.78	~1200[6]	~1140[6]
$(^3\mathbf{He},\mathbf{t})$	10.78	~1220[6]	~1170[6]
$(\mathbf{p},\mathbf{n})$	1.46	~1210[7]	~1160[5]
$(\mathbf{p},\mathbf{p'\Delta})$	3.88		~1230[3]

When we consider all of these experimental results including ours, it is most likely that the inclusive spectra contain at least two components; one due to the process of real quasifree Δ production and the other due to the process of non-resonance associated pion production. The latter may not be such a simple process but a more exotic one which we don't know yet. It seems to me that any theoretical models trying to fit the inclusive spectra in a framework of any single process are not appropriate. By carrying out inclusive and coincidence measurements for the same reaction, the above statement will be easily proved (or disproved). Though we have measured inclusive spectra of scattered protons, there was no bump observed in the region of quasifree Δ production because of huge background.

We have planned to carry out such an experiment at KEK using $(\mathbf{p},\mathbf{n})$ reactions at 1.5 GeV/c [9]. The reaction channel was selected because of (1) lower background in $(\mathbf{p},\mathbf{n})$ reactions than in $(\mathbf{p},\mathbf{p'})$, (2) lower background at lower incident momentum, and (3) inclusive data (at 0 degree) exist at 1.46 GeV/c [5]. Neutron counter is made of a stack of plastic scintillators with a total thickness of 15cm and its dimensions are 2 meters in width and 1 meter in height. Detection efficiency of about 15 % is expected. The experiment has been approved and will start in spring or summer of 1988. In this experiment, we expect that (1) shift will be seen in inclusive measurements as in LAMPF data, but (2) no shift might be observed in Δ tagged spectra as in our $(\mathbf{p},\mathbf{p'\Delta})$ coincidence experiments at 4 GeV/c. Most important outcome will be obtained in π tagged and $\mathbf{2p}$ tagged spectra, since the contribution

of non-resonant π productions can be determined from the former one and the effect of mass shift of Δ in nuclei, if exists, can be observed in the latter distribution. In 2p tagged events with an appropriate kinematics, we may be able to identify events in which Δ is produced deeply inside a nucleus.

4. Summary

We have measured quasifree Δ production in proton-nucleus collisions at 4 GeV/c, for the first time, detecting both decay products of the Δ and scattered protons. Taking into account the nuclear binding effect (the averaged separation energy of 25 MeV was derived from the quasielastic scattering), the momentum distributions of scattered protons in the quasifree Δ production were well reproduced with the mass and width of the Δ being the same as those of the Δ in free space.

Combining our results with the other inclusive measurement, I come to a conclusion that the inclusive spectra are composed of two component (the quasifree Δ production is only a part) which of course need to be proved experimentally. We are going to carry out an experiment at KEK to answer the question.

I would like to thank all collaborators of the KEK PS experiment E133 and E173; K. Nakai, T. Kobayashi, T. Nagae, K. Tokushuku, H. Sano, M. Sekimoto, I. Arai, H. Sakamoto, A. Manabe, K. Aoki, H. Nunokawa, M. Tanaka, M. Nimomiya and M. Tomizawa.

References

[1] D. Contardo et al., Phys. Lett. **168B**(1986) 331.
[2] KEK PS proposal E133 (in Japanese)
J. Chiba, KEK Report 84-20 "Nuclear Physics in GeV Region"
(ed. K. Nakai) p231.
[3] T. Nagae et al., Phys. Lett. **191B**(1987) 31
[4] P.C. Gugelot, Phys. Rev. C **30**(1984) 654
P.C. Gugelot and R.D. Ransome, Phys. Rev. C **35**(1987) 1353.
[5] B.E. Bonner et al., Phys. Rev. C **18**(1978) 1418.
[6] V.G. Ableev et al., JETP Lett. **40**(1984) 763.
[7] C.W. Bjork et al., Phys. Lett. **63B**(1976) 31.
[8] C. Ellegaard et al., Phys. Lett. **154B**(1985) 110.
[9] KEK PS proposal E173.

FRAGMENTATION OF MEDIUM-HEAVY BEAMS AT HISS

C. Tull[a b †], T. Kobayashi[c], M. Baumgartner[a], F.P. Brady[b], W. Christie[a b †], H.J. Crawford[d], J.P. Dufor[e], D.E. Greiner[a], P.J. Lindstrom[a], W. Mueller[a], D.L. Olson[f], J. Romero[b], T.J.M. Symons[a], I. Tanihata[g], M. Webb[h], and H. Wieman[a]

a Lawrence Berkeley Laboratory, University of California, Berkeley, CA 94720.
b Crocker Nuclear Laboratory, University of California, Davis, CA 95616.
c National Laboratory for High Energy Physics (KEK), JAPAN.
d Space Science Laboratory, University of California, Berkeley, CA 94720.
e Centre d'Etudes Nucleaires de Bordeaux-Gradignan, FRANCE.
f Heavy Ion Physics, University of California, Riverside, CA 92521.
g Institute for Nuclear Study, University of Tokyo, Tokyo, JAPAN.
h Lawrence Livermore Laboratory, Livermore, CA 94550.

ABSTRACT

Preliminary results from experiment E772H -- *Inclusive Measurement of Projectile Fragments using Medium-Heavy Beams* are presented.

1. INTRODUCTION AND EXPERIMENTAL SETUP

Experiment E772H is an inclusive measurement of projectile fragmentation at relativistic energies using the Heavy Ion Spectrometer System (HISS) at the LBL Bevalac. The experiment is a collaborative effort by the HISS group at the Lawrence Berkeley Laboratory, and the Nuclear Physics group at the University of California, Davis.

E772H used the full HISS facility as it existed before the development of the new 1.5 X 2.0 meter drift chambers. Figure 1 is a schematic diagram of the HISS cave and the experimental setup used. More detailed treatment of this setup, and two of the main detectors used can be found in references 1-3.

Upstream of the target are four scintillators (V1, S1, V2, S2) for timing reference and for beam definition. A good beam particle is one which falls within the beam envelope defined by the veto scintillators V1 and V2, has appropriate pulse height in S1 and S2, and is not preceeded by another particle within the time window of

detector system. Also upstream of the target are two multi-wire proportional counters (W1, W2) with 1 mm pitch used to measure the incident vector of the beam particle on the target.

The target is located three meters from the center of the superconducting HISS dipole magnet, which for the argon run provided a bending power of approximately 3 Tesla-meters. The target is surrounded by a 120 element Multiplicity Array (MA) used to measure the mid-rapidity charged particle multiplicity between θ=9°-66° from the beam in the laboratory frame.

The beam-rapidity heavy fragments are bent through the 1 meter gap of the dipole and into the prototype drift chamber (DC) which is placed at an angle of $\approx$18°. The prototype drift chamber has an active area of 30 X 40 cm and is flanked front and back by multi-wire proportional counters (W3, W4) to aid in calibration. Behind the drift chamber is a trigger scintillator (S3) used to reject beam particles on-line, and to flag interactions in the quartz hodoscope radiators off-line.

The final detector in the fragment path is the Cerenkov Hodoscope (VMD). The VMD consists of two planes of radiators. The front plane (Q) is composed of fused silica (quartz) and is used to measure the fragment velocity. The back plane (G) is composed of BK7W glass and is used to measure the charge of the fragment.

Combining the upstream vectoring of W1 and W2, the downstream vectoring of the drift chamber, and the field map of the dipole we are able to determine the rigidity (R = p/Z) of the fragment to within $\Delta R/R \approx 2X10^{-3}$. In addition, since the drift chamber measures the fragment trajectory *vector*, we can extract the momentum perpendicular to the beam direction (both horizontal and vertical) as well as the longitudinal momentum.

2. MOTIVATION AND PREVIOUS WORK

Experiment E772H was designed to identify projectile fragments and to measure their momentum vector relative to the incoming beam particle. This data set enables us to measure isotopic production cross sections, mass and charge distributions, and fragment momentum distributions; and to correlate these quantities with each other and with the associated multiplicity of mid-rapidity charged particles. In addition to being important tests of theory, these properties are of practical importance for

designing future heavy-ion experiments.

One important motivation to do this experiment is the paucity of data for projectile fragmentation of heavy beams at high energies. Though some work has been done with ^{40}Ar at 213·A MeV[4], very little work has been done for beams larger than ^{12}C and ^{16}O[5].

We wanted to extend the work of Viyogi, et al.[4] to higher energy and larger masses where the assumptions made in their analysis are more valid. Also, we wanted to measure the transverse momentum of the fragments and associate a multiplicity with each event as a measure of the impact parameter of the collision; data that were missing in the previous study.

One question to be addressed by this experimental data set concerns the exact nature of the fragmentation mechanism. Is projectile fragmentation dominated by excitation and decay of the projectile, which would mean that the injected excitation spectrum is the important feature? Or is it better described by an abrasion-ablation argument where the collision geometry is the most important parameter?

We have measured the fragmentation of three medium-heavy beams (^{40}Ar, ^{56}Fe, and ^{93}Nb) at 1.65·A GeV and one beam (^{139}La) at 0.85·A GeV. For each beam we took data for a carbon target, a lead target, and a target of the same size as the beam (ie. KCl, Fe, Nb, or La). This provides us with data for both types of asymmetric systems and a symmetric system for each beam. Our statistics are quite good for ^{40}Ar and ^{93}Nb ($\approx 10^6$ events for each beam, all targets), about a factor of 2-4 lower for ^{56}Fe, and another factor of 2-4 lower for ^{139}La.

Of the three major detectors in our setup, the multiplicity array is the most conventional. It consists of 120 scintillators and photo-multiplier tubes arranged in three sections. Each section is axially symmetric about the beam direction and covers a different region of opening angle from θ=9°–66° in the laboratory frame. This detector allows us to make an independent measurement of the impact parameter of the collision and hence, the excitation energy of the prefragment.

The drift chamber used consists of twelve 30 X 40 cm planes, distributed over 110 cm to facilitate tracking of heavy ions with minimum contamination from delta rays. The per plane resolution of the drift chamber for the high-voltage used in the ^{40}Ar experiment ranged from 250 μm at Z=18 to $<$ 400 μm at Z=4. Though the drift

chamber has a rather small active area, the strong kinematic focusing of the projectile rapidity fragments allows us to detect almost all beam-rapidity fragments of $A \geq 10$.

The newest detector in the system was the Cerenkov hodoscope. We know that the index of refraction of a material determines both the opening angle of Cerenkov radiation from a charged particle traversing the material ($\cos(\Theta_{Cer})=(1/\beta \cdot n)$) and the angle of total internal reflection for light in the material ($\sin(\Phi_{TIR})=(1/n)$). For measurement of fragment charge we chose glass with n=1.52 where $\Theta_{Cer} > \Phi_{TIR}$ and all visible wavelengths are internally reflected providing a PMT response which goes as Z^2. However, for measurement of velocity we use fused silica with n=1.46 where $\Theta_{Cer} \approx \Phi_{TIR}$. When this condition is met, the dispersion of the radiator medium causes a sharp linear dependence of the PMT response on the velocity of the particle.

Using the charge measured by the glass Cerenkov radiators, the rigidity from the vectoring detectors and dipole magnet, and the velocity from the quartz radiators we can identify the fragment isotope. The resolutions of the system for mass and charge are $\Delta Z_{FWHM}=0.5e$ and $\Delta A_{FWHM}=0.7u$. Figure 2 shows the resultant isotope resolution for charges from Z=10 to Z=15 from the fragmentation of ^{40}Ar on a carbon target at 1.65·A GeV.

3. DATA AND RESULTS

Since we identify both mass and charge for each particle, we can investigate isotopic production cross sections. Figure 3 shows the yield of isotopes of even charged fragments for carbon to silicon from 1.65·A GeV ^{40}Ar + C. The distribution of isotopes for each element appears gaussian in shape with widths of $\sigma_A \approx 1u$.

Figures 4a and 4b show the raw distributions of mass and charge, respectively, from the reaction ^{40}Ar + C at 1.65·A GeV for what we call our interaction trigger. These distributions are distorted by two major effects. First, the upper end of both distributions are affected by the threshold set on the trigger scintillator (S3). This threshold was intended to ensure that a reaction had taken place before S3 (ie. $Z(S3) < Z_{Beam}$). However, for the ^{40}Ar runs, the threshold was set low enough to affect charges down to Z=15. The second effect has to do with the acceptance of the detector system. The constraining detector is the VMD. In the vertical direction, the VMD begins to cut off the tails of the distribution of light fragments (the lighter fragments

have wider spatial distributions) for masses A$\leq$14.

For the mass distribution I have included a simple abrasion calculation normalized to have the same number of counts between A=20 and A=30. This is more for reference than as a serious comparison with theory. About all one can conclude from this comparison is that the slope of the distribution from A=18 to A=31 is similar to that for prefragments predicted by simple geometric overlap.

The momentum distribution for fragments of ^{40}Ar + C at 1.65·A GeV are gaussian in all three spatial directions. Though individual widths for different isotopes are comparable to those predicted from random sampling of the Fermi momentum (as formulated by Goldhaber[6]), there seems to be a systematic dependence of the reduced momentum width (σ_0) on the mass of the fragment at this stage of the analysis. We are currently investigating this effect to determine what significance this dependence may have.

To confirm that the multiplicity array provides an independent measurement of the impact parameter of the collision, we examine the correlation between the charge of the leading fragment as measured by the glass VMD radiators, and the MA multiplicity. Figures 5a and 5b show the relation between leading fragment charge and midrapidity multiplicity. Requiring few hits in the MA ($<$5) results in a charge distribution in the VMD which is peaked at high Z (trigger bias still depresses the high Z end of the distribution). A requirement of more hits in the MA gives a Z distribution peaked at low Z (VMD acceptance reduces the low Z end of the distribution). Contrapositively, looking at events with high or low leading fragment charge gives multiplicity distributions which are shifted towards lower or higher multiplicities.

4. CONCLUSION AND FUTURE WORK

In conclusion, we have measured and partially analyzed the fragmentation of ^{40}Ar + C at 1.65·A GeV. We have also measured and are beginning analysis of data from ^{40}Ar on lead and KCl targets, as well as three other beams on a similar collection of targets.

From the analysis of ^{40}Ar + C we can extract isotope production cross sections, mass and charge distributions, and fragment momentum distributions with an independent measurement of the impact parameter of the collision from the multiplicity of

mid-rapidity charged particles.

We see that the isotopic production "cross sections" appear gaussian with widths of $\sigma_A \approx 1u$. Also, the mass and charge distributions (within the region unaffected by either trigger bias or detector acceptance) have minima at values approximately half that of the beam.

The momentum distributions of projectile fragments are well described by gaussians in all three dimensions, as predicted by statistical models such as Goldhaber's. The average width of these distributions is consistent with a Fermi momentum of $\approx 241 MeV/c$, though there is some question about the dependence of the widths on fragment mass.

We are currently extracting absolute cross sections from the yields measured, and correcting for the biases introduced by the trigger threshold and detector acceptance. Now that the detector system is well understood, and the software debugged, we hope to extend this same analysis to the other beams early next year.

† Associated Western University Graduate Fellow

REFERENCES

[1] A Detector System for Heavy Projectile Fragments in a Few GeV/nucleon Energy Region, T. Kobayashi, et al., to be submitted to Nucl. Instr. and Meth., (1987).

[2] A Drift Chamber for High-Energy Heavy-Ions, T. Kobayashi, et al., Nucl. Inst. and Meth., **A254,** 281, (1987).

[3] A Cerenkov Particle Identifier for Relativistic Heavy Ions, J.P. Dufour, et al., LBL-18643 Preprint, (1985).

[4] Fragmentations of ^{40}Ar at 213 MeV/Nucleon, Y.P. Viyogi, et al., Phys. Rev. Lett. **42,** 33 (1979).

[5] Momentum Distributions of Isotopes Produced by Fragmentation of Relativistic ^{12}C and ^{16}O Projectiles, D.E. Greiner, et al., Phys. Rev. Lett., **35,** 152, (1975).

[6] Statistical Models of Fragmentation Processes, A.S. Goldhaber, Phys. Lett., **53B,** 306, (1974).

Figure 1

Top view of the HISS cave showing the detector setup used in experiment E772H.

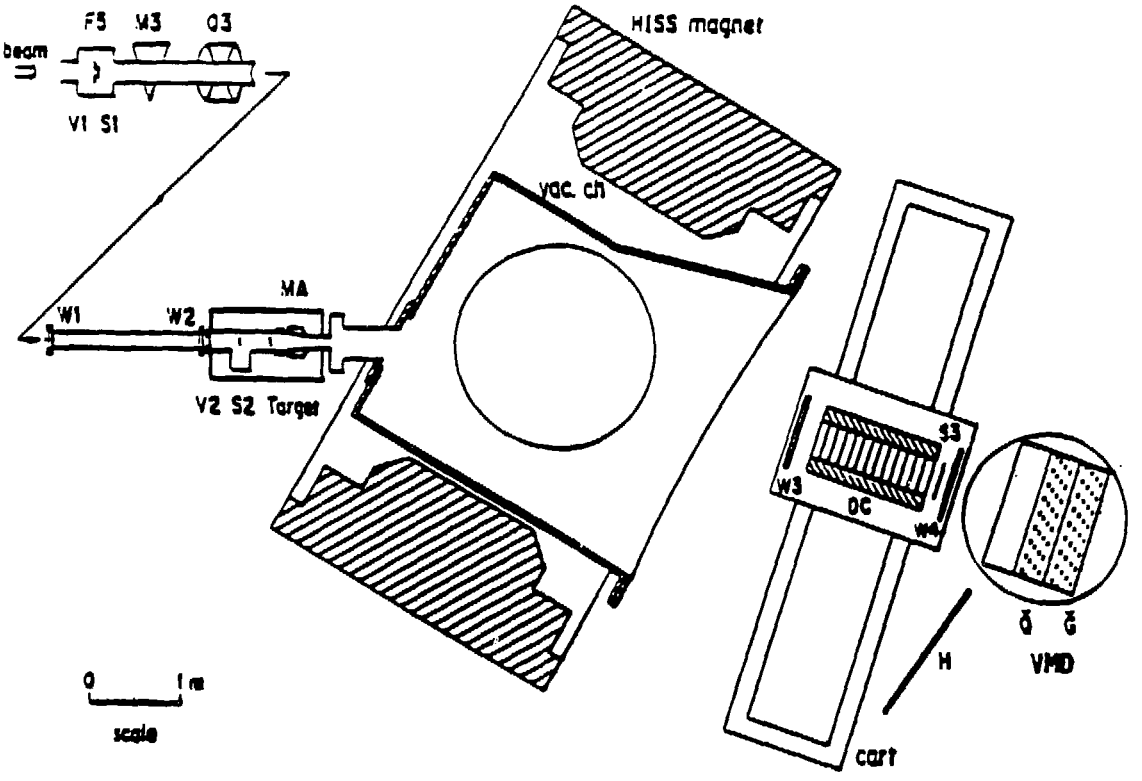

Figure 2

Isotope separation for charges from Z=10 to Z=15 from the fragmentation of ^{40}Ar on a carbon target at 1.65·A GeV.

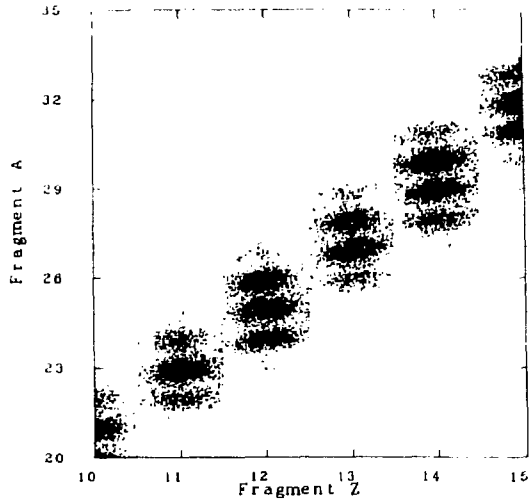

Figure 3

Isotope yields for even charged elements from Z=6 to Z=16 from fragmentation of 1.65·A GeV ^{40}Ar + C. Trigger bias and detector acceptance are not corrected for.

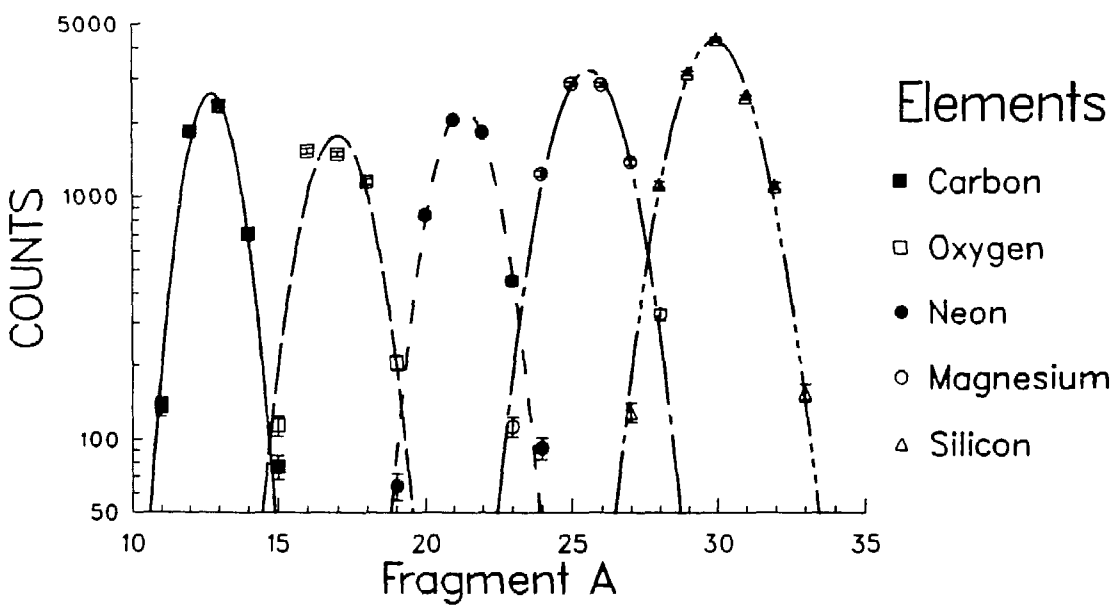

Figure 4a

Raw mass distribution from the reaction of ^{40}Ar + C at 1.65·A GeV. Trigger bias and detector acceptance are not corrected for.

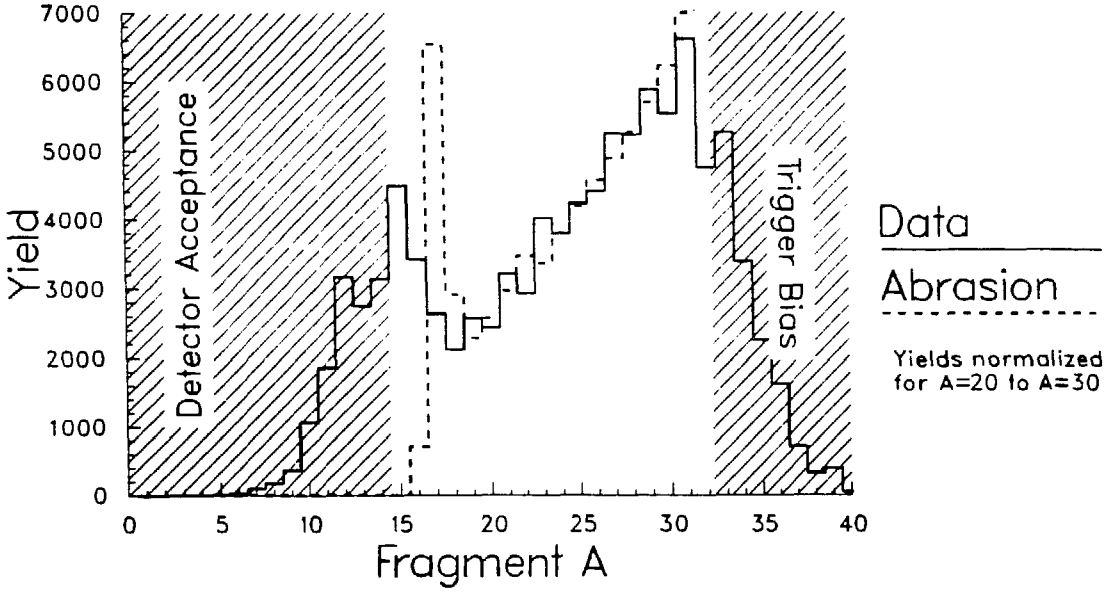

Figure 4b

Raw charge distribution from the reaction of ^{40}Ar + C at 1.65·A GeV. Trigger bias and detector acceptance are not corrected for.

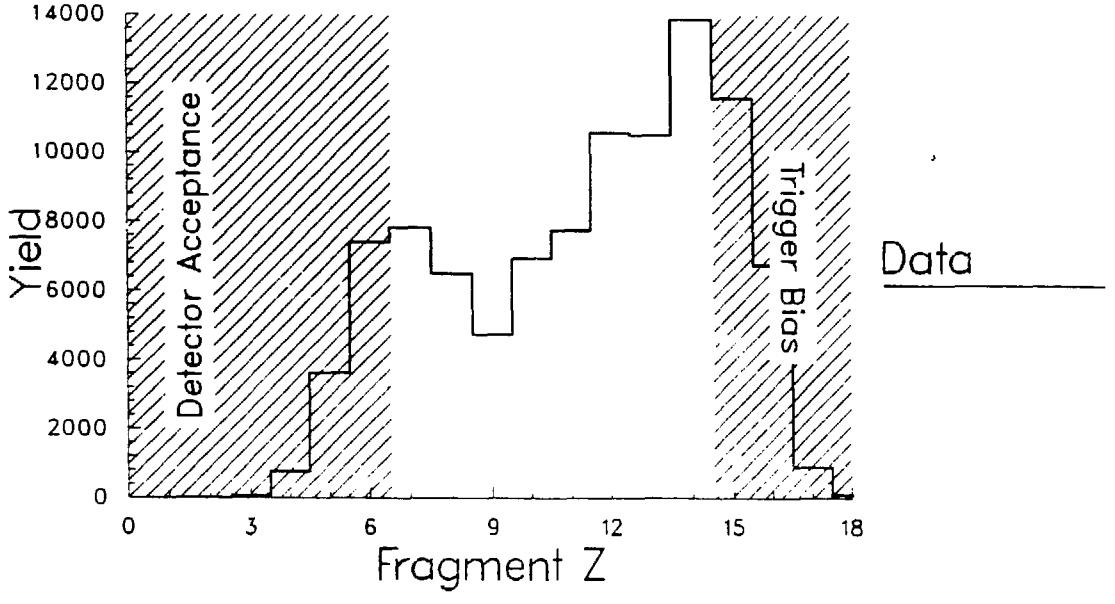

Figure 5a

Leading fragment charge distribution with requirements on the multiplicity seen in the MA.

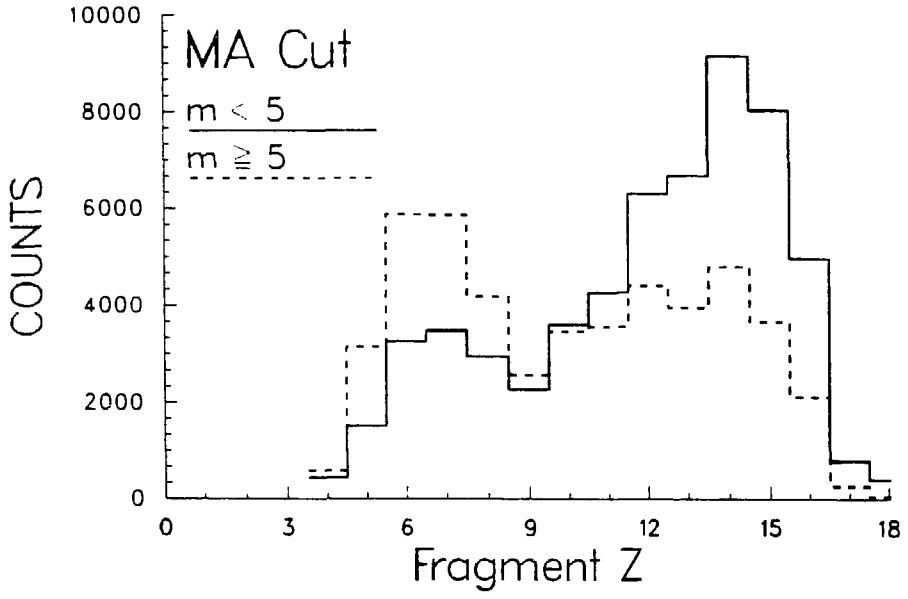

Figure 5b

Multiplicity distribution seen in the MA with requirements on the leading fragment charge in the VMD.

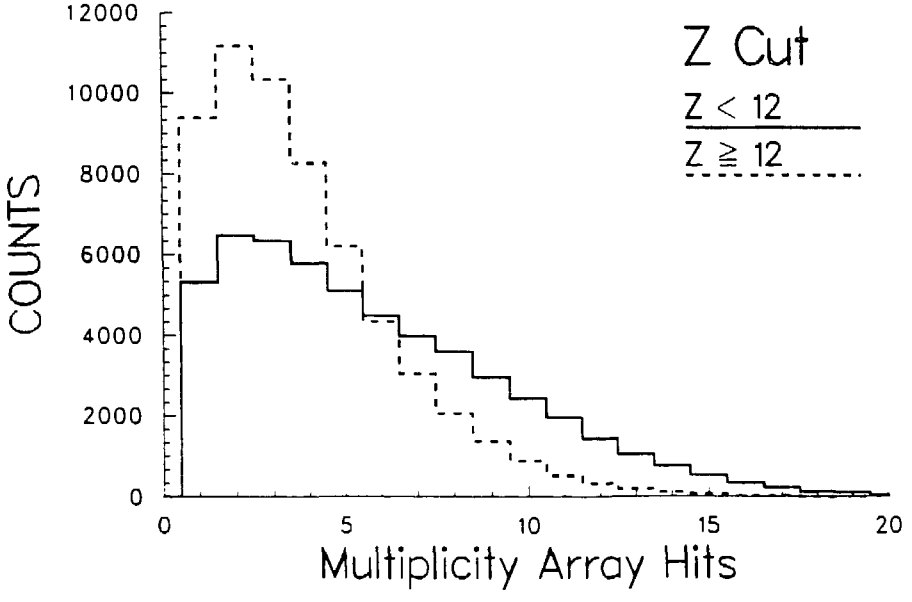

A parametric representation of the energy and charge dependence of fragmentation cross-sections.

C. Jake Waddington
School of Physics and Astronomy
University of Minnesota, Minneapolis, Mn. 55455

Abstract: The fragmentation of various heavy ions in several different targets has been studied at the Bevalac during a series of calibrations of the cosmic ray detectors used on the Third High Energy Astronomy Observatory (HEAO - 3). While these results have been mainly of interest to us because of their relevance to understanding the processes of cosmic ray propagation, they have also allowed us to study the physics of the production of nuclear fragments in high energy nucleus - nucleus collisions. In the course of this work we have determined the total charge changing cross-sections, and the partial cross-sections for the production of heavy fragments by the various beams, as functions of the beam charge, the target charge, and the beam energy. Examination of these partial cross-sections has shown that their variation with the charge of the fragment produced can be represented by simple exponential or power law expressions, whose coefficients are functions of the charges and the energy. While the experimental data is currently inadequate to fully determine these functional dependencies, they will, eventually, allow the prediction of cross-sections that have not yet been measured.

Introduction: The detectors on the HEAO - 3 Ultra Heavy Nuclei experiment consisted of parallel plate ion chambers, plastic radiator Cherenkov counters and multi-wire ion chamber hodoscopes[1]. They were designed to measure the abundances of the "Ultra Heavy" nuclei in the cosmic radiation, those with $Z \geq 30$. The response of these detectors to high energy very highly charged nuclei could not be calibrated prior to the launch in 1979 but has since been determined from three calibration runs to heavy ion beams from the Bevalac. The non Z^2 and velocity dependent terms found in the signals from the different detectors have been discussed elsewhere[2,3].

As we anticipated from the begining, the data on fragmentation that we obtained during these runs was very relevant to the long standing problem of how to use the observed elemental abundances of the cosmic ray nuclei to calculate the abundances present at the cosmic ray sources. Since the cosmic ray nuclei propagate through the interstellar medium, which is predominantly (90%) hydrogen, and then through the material surrounding the detectors, which is predominantly aluminum, the observed abundances have to be corrected for the effects of interactions in this matter. These corrections demand a knowledge of the cross-sections for production of fragments, $\sigma(Z_B,Z_T,E)$, as a function of the charge, Z_B, and energy, E, of the cosmic ray nucleus and the charge of the target nucleus, Z_T. In general the cross-sections in hydrogen have not been measured for these heavy nuclei, but have, instead, to be calculated from semi-empirical expressions derived from the sparse p - A data available[4]. The uncertainties in these cross sections reflect directly into uncertainties in the source abundances.

In our initial calibration run in 1982 we[5] determined the partial cross-sections for gold nuclei of 990 MeV/nucleon incident on carbon and polyethylene targets, for fragments with Z between 78 and 65, i.e. for charge changes, ΔZ, of 1 - 14. The charge resolution was only fair, being characterised by a s.d. of about 0.3 charge units, but was sufficient to allow us to determine values of $\sigma(79,Z_T,990)$ for both carbon and polyethylene targets, and hence, by subtraction, for hydrogen, which then could be compared with the predictions of the semi-empirical models. This comparison showed that the measured values differed by as much as a factor of two from those predicted.

During the same run we[6] also produced a number of interactions of individual gold nuclei in nuclear emulsions. The results from the analysis of these emulsions showed that for

Beams and targets for first two runs

All energies in MeV/nucleon

Targets / Beams	blank <E>	polyethylene <E>	polyethylene dE	carbon <E>	carbon dE	aluminum <E>	aluminum dE
krypton	1474					1419	110
xenon	1237	1190	54	1175	82	1155	124
holmium	1100	1067	68	1048	104	1022	156
gold, I	990	960	60	940	100		
II	1016	982	68	961	110	932	166

Beams and targets for third run

Targets / Beams	blank <E>	polyethylene <E>	polyethylene dE	carbon <E>	carbon dE	aluminum <E>	aluminum dE	copper <E>	copper dE
lanthanum	1251	1203	96	1203	96	1201	101	1201	101
	1150	1100	100	1100	100	1100	100	1100	100
	989	937	104	937	104	937	104	940	99
	850	795	110	795	110	794	112	798	105
	705	644	112	645	110	643	115	645	110
	577	549	57	555	44	549	57	551	53
holmium	1007	957	100	959	97	957	100	954	107
	850	798	105	800	100	798	105		
	603	543	121	553	101				
gold	1033	978	105	985	90	984	92	980	100
	850	795	110	800	100	796	108	798	105
	750	694	113	695	110	695	110	695	110
	650	589	122	593	115	593	115	593	115

interactions where $\Delta Z \leq 0.4\ (Z_B)$, the overwhelming majority of the residual charge was carried on just one fragment. Hence, our electronic detectors, which measure the total energy loss of all the fragments that pass through them, see signals that are determined mostly by the single high charge fragment. The only exception to this is when the projectile is massive enough to have a significant probability of undergoing high energy fission, when a background of signals due to the two fission fragments is seen superimposed on the individual charge peaks of single fragments

Our second calibration run[7,8], in 1984, used improved detectors and examined interactions of krypton, xenon, holmium, gold and uranium nuclei in targets of aluminum, carbon and polyethylene. In each case these nuclei were accelerated to maximum Bevalac rigidity. The improved charge resolution, characterised by a s.d. of about 0.16 to 0.25 charge units, depending on Z_B, allowed a wider range of ΔZ to be examined, and this, combined with the range of Z_B available, allowed a more detailed comparison with the results of the semi-empirical models. For each beam there were differences from the calculated cross-sections of up to a factor of two. At the same time it became possible to begin to examine the systematics of the dependence of $\sigma(Z_B,Z_T,E)$ on the charge and energy parameters[9,10]. This analysis, which is summarized below, made it clear that we could not separate these dependencies without further data at several different energies for a single beam.

Our third calibration run, in 1986, the results from which are only preliminary, allowed us to examine beams of iron, lanthanum, holmium and gold with up to six different energies falling on targets of lead, copper, aluminum, carbon and polyethylene. In this run we used a still further improved detector array, with better ion chambers and two separate Cherenkov counters, characterised by a s.d. of about 0.11 to 0.20 charge units, depending on Z_B and E. The resolution for both high and low energy nuclei is illustrated in Fig. 1 for lathanum on carbon.

In all three runs the peaks due to the individual fragments are clearly separated, although the separation improves markedly for the later runs, and the numbers of fragments of each value of the charge change can be readily obtained. Also it is seen, at least in runs 2 and 3, that not only are there fragments of reduced charge, but there is also a well defined population of nuclei whose charge has increased by one unit. Presumably these are due to charge pickup, via pion exchange, or nucleon pickup.

The beams and targets used in these runs are listed in the table, which gives the energy of each beam at the middle of the target, <E>, and the spread in energy, dE, due to the energy loss in each target. Target thicknesses were chosen as a compromise between maximizing the number of interactions produced and minimizing the corrections introduced due to secondary interactions of fragments in the targets. In general this led to target thicknesses of about 0.2 of an interaction mean free path, with energy spreads of about 100 MeV/nucleon.

Total Charge Changing Cross-Sections: Earlier measurements with lighter beam nuclei ($Z \leq 26$) by Westfall et al.[11] led them and Hagen[12] to derive expressions for the total charge changing cross-section, σ_{tot}, as a function of beam and target nuclei mass numbers (A_B, A_T). Neither of these relations extrapolates well to fit the data in the mass region covered in this work. Instead we have fit our data to a relation of the form:

$$\sigma_K = 10\ \pi\ (1.35)^2\ \{ A_T^{1/3} + A_B^{1/3} - p[A_T + A_B]^q \}^2 \text{ mb} \quad \text{.....Eq. 1}$$

where p and q are related constants determined from the data to be 0.209 and 0.332 respectively. If q is assigned the value of 1/3 then $p = 0.209 \pm 0.002$. This relation also gives a good fit to the data of Westfall et al. on Fe nuclei for our light targets where $A_T << A_B$, but does not match their data for still lower beam charges. Fig. 2 plots our measured cross-sections and those predicted by Eq. 1 and the Westfall et al equation, as a function of the size of the nucleus-nucleus "core", $(A_T^{1/3} + A_B^{1/3})$. Each of our measurements was made with beams having different

Fig. 1 Plot of the Cherenkov signal versus the ion chamber signal for 1251 and 577 MeV/nucleon lanthanum nuclei incident on a carbon target as observed in run 3.

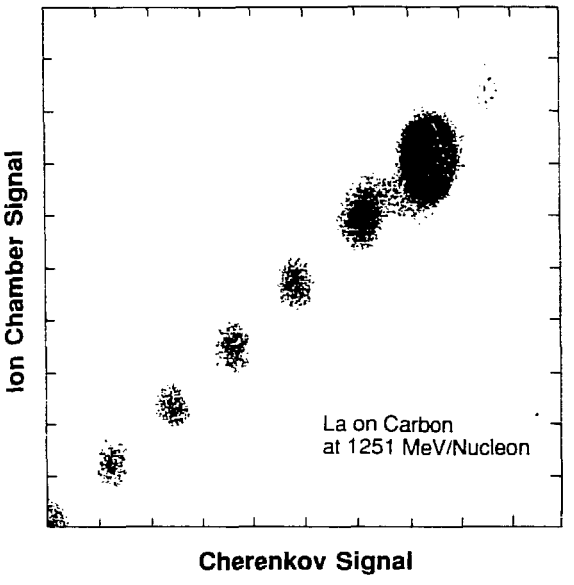

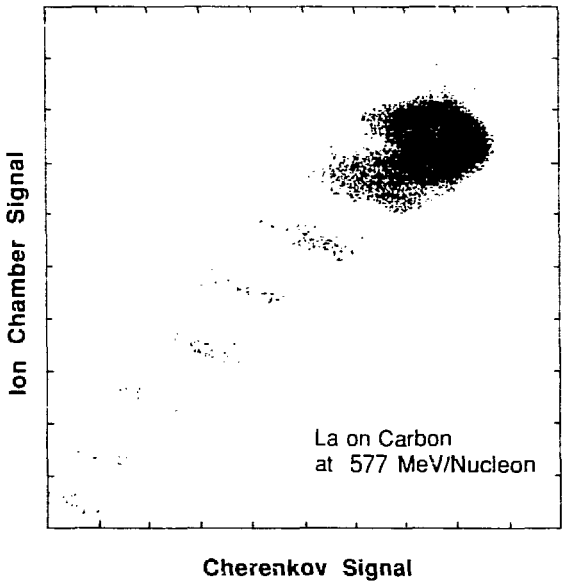

Fig. 2 The measured total cross sections, sigma, in mb, plotted as a function of the "core" size, ($A_T^{1/3} + A_B^{1/3}$), compared with those calculated from Eq. 1 and the predictions of Westfall et al[11].

Fig. 3 The mean free path, in g/cm^2 as a function of the energy, of lanthanum nuclei in the material of the detector. The value predicted by Eq 1 is also shown.

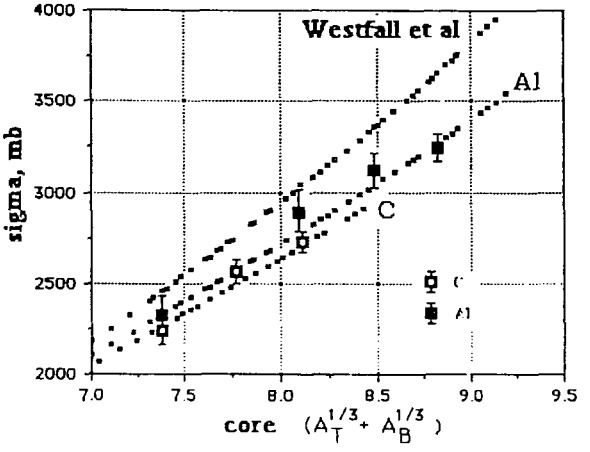

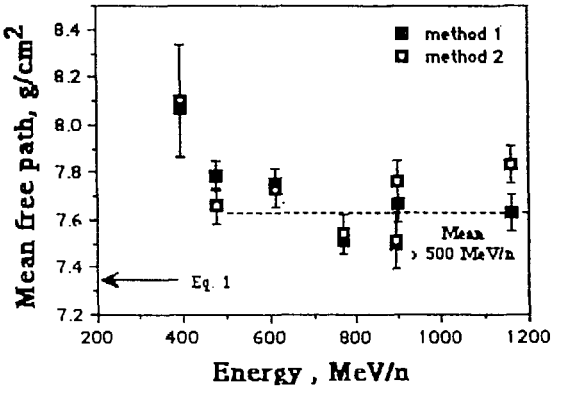

energies per nucleon and hence it was necessary to make the implicit assumption that σ_K was independent of energy between some 1200 and 900 Mev/nucleon.

The energy dependence of the total cross-sections could be studied in the third run. We could not determine the total charge changing cross-sections in the various targets because of the coincidence requirements that were imposed in the detector. However, using those blank runs where there was no target in the array, we can investigate the energy dependence of the total charge changing mean free path, λ_t, in the material of the detectors. For these runs we can determine λ_t for the material between two pairs of ion chambers, one on each side of the Cherenkov counters. The material involved by mass consists of 45.7% carbon, 25.1% oxygen, 14.2% aluminum, 6.1% hydrogen, 4.5% nitrogen and 4.4% argon Those particles that interact do so mainly in the lucite of the Cherenkov counters and hence fragments have to be resolved using the ion chambers signals alone. This means that the interactions with a charge change of one are not cleanly resolved from the incident beam but have to be deconvolved assuming that the experimental distributions are Gaussian in shape. Two separate techniques for this deconvolution gives results that are generally similar to within the statistical errors and are shown in Fig. 3 for our lanthanum data.

Above 500 MeV/nucleon these measurements give a mean value of $\lambda_t = 7.65$ g/cm^2, which can be compared with the value of 7.35 g/cm^2 calculated from Eq. 1. More significantly, examination of these results allows us to conclude that, over this range of energies, the mean free path, and thus the total cross-section, is independent of energy to within 2 or 3 percent.

Partial Cross-sections: In every run the partial cross-sections were determined from the numbers of nuclei that are fragments of a given charge and were produced by identified beam nuclei in the target and survive through the detectors. These observed numbers have been corrected for the effects of secondary interactions in the target, interactions in the detector, and resolution smearing, by using the results from a "blank" run with no target and by calculation based on the total mean free paths. The details of these corrections are given elsewhere[8,10], and have been shown to leave residual errors that are much less than the statistical uncertainties.

These corrected values of $\sigma(Z_B,Z_T,E)$ have been determined for a wide range of Z_B,Z_T and E, listed in the table. In every case the majority of the individual values of σ are found to regularly decrease as the charge change, ΔZ, increases. As an example fig. 4 gives the variation of $\sigma(\Delta Z)$ with ΔZ for 1.05 GeV/nucleon holmium nuclei on carbon and hydrogen targets, showing smooth and regular decreases in each case, although with quite different forms for each target. In fact, we find that the variation of $\sigma(\Delta Z)$ can, for all targets, be quite well represented by either a power law or exponential law relation between $\sigma(\Delta Z)$ and ΔZ. Examples are given in Figs. 5 to 7, which show several representative examples of such fits to the data. The only major exception to this behavior is for the gold beam at large charge changes, Fig. 7, where the occurrence of fission causes a peak to appear in the $\sigma(\Delta Z)$ distributions. In addition, the values of $\sigma(\Delta Z)$ for $\Delta Z = 1$ nearly always appear to be anomalously high, probably due to the additional process of electromagnetic dissociation causing proton stripping, These excess cross-sections, while poorly defined due to the considerable errors, are in reasonable agreement with those reported by Mercier et al.[13] for one neutron removal from heavy targets by light projectiles.

For the targets with heavy nuclei, copper, aluminum and carbon, the variation in the cross-sections, for $2 \le \Delta Z \le 20$, can be fitted with acceptable values of reduced χ^2, by simple power law expressions of the form:

$$\sigma(\Delta Z) = \Sigma_O (\Delta Z)^{-\alpha} \text{ mb} \qquad \text{.....Eq.2}$$

where $\Sigma_O(Z_B, Z_T)$ and $\alpha(Z_B, Z_T)$ are constants for each beam and target.

Fig. 4 The variation of the partial cross sections, $\sigma(\Delta Z)$, for holmium nuclei in carbon and hydrogen targets, plotted on linear scales, Also shown are the best power and exponential fits for $2 \leq \Delta Z \leq 20$.

Fig. 5 $\sigma(\Delta Z)$ for xenon nuclei in a carbon target as a function of ΔZ, plotted on log-log scales. Also shown is the best power law fit for $2 \leq \Delta Z \leq 20$

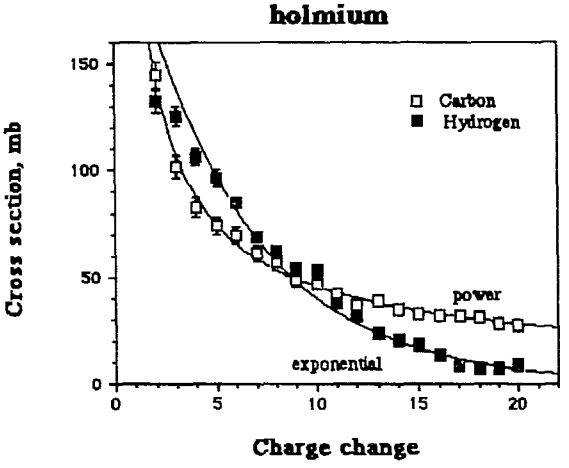

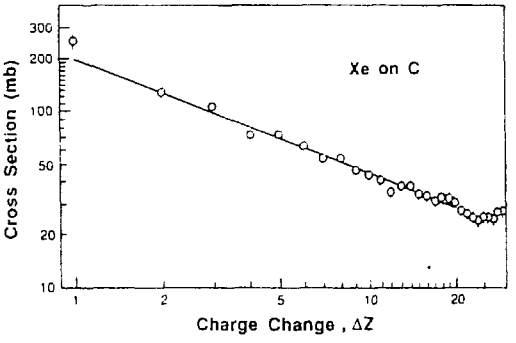

Fig. 6 $\sigma(\Delta Z)$ for holmium nuclei in a polyethylene target as a function of ΔZ, plotted on log - linear scales Also shown is the best exponential fit for $2 \leq \Delta Z \leq 20$

Fig. 7 $\sigma(\Delta Z)$ for gold nuclei in a hydrogen target as a function of ΔZ, plotted on log-linear scales, showing the fission peak at high ΔZ, The values that have an appreciable fission component are shown as filled in circles. The exponential fit for $2 \leq \Delta Z \leq 20$ has been extended into the fission region as a dotted line.

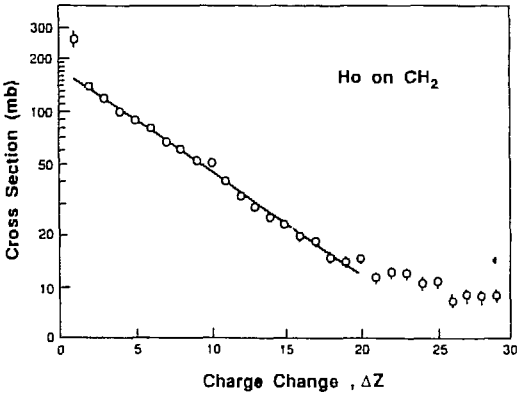

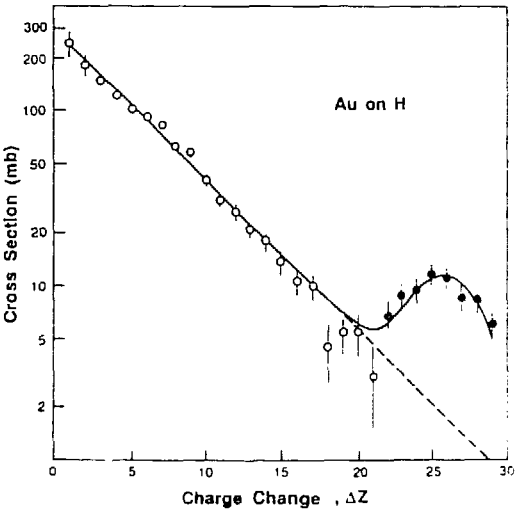

For the targets which contain hydrogen, i.e. polyethylene (CH_2) and hydrogen, the cross-sections are not well fitted by this power law form, e.g. for holmium nuclei on a hydrogen target an attempted power law fit has a reduced χ^2 of 26, but instead can be reasonably well represented by exponential expressions of the form:

$$\sigma(\Delta Z) = \sigma_0 \exp(-(\Delta Z) / \Delta_0) \text{ mb} \quad \text{.....Eq.3}$$

where $\sigma_0(Z_B, Z_T)$ and $\Delta_0(Z_B, Z_T)$ are constants for each beam and target.

These fitting parameters were initially determined from the results of the first two runs, where each beam was at a different energy. As a consequence it was impossible to distinguish between a charge and an energy dependence from these data. As an example,Figs.9 and 10 show the values of the fitting parameters for the aluminum target expressed as functions of beam charge or beam energy. However, by taking the results obtained by Webber[14] for the fragmentation of an iron beam at several different energies, also measured during a cosmic ray calibration run, it was possible to verify that there was a significant energy dependence for these heavier beams, at least in light targets such as carbon and polyethylene. By fitting the iron data to relations of the type above, it was possible to obtain fitting parameters for the iron data set which could be compared with those for the heavier beams at the same energy. This comparison established that the parameters were strongly dependent on the beam charge, but also showed a dependence on energy[10].

This energy dependence was addressed directly in our third run. Even though the results are not yet fully analyzed there is a clear determination of the energy dependence from the present analysis. The partial cross-sections have been determined for Lanthanum nuclei incident on carbon and polyethylene targets at six different energies.

For $_{57}$La nuclei on Carbon the partial cross-sections show a very good fit at all energies to the power law dependence on the charge change found before. When fitted to Eq. 2 over the range $2 \le \Delta Z \le 25$ all the values of reduced χ^2 are between 1.09 and 2.20. The energy dependence of the resulting fitting parameters are shown in Fig. 10 . At high energy these parameters are in excellent agreement with those found in run 2 for xenon on carbon. The values found for the fitting parameters from Webber's data[14], although of less accuracy due to the limited range of ΔZ available, also follow the same trends but show an appreciable charge dependence.Fig. 10 suggests that although $\alpha(57,6)$ shows some signs of a reduced energy dependence at high energies there is a clear indication that $\Sigma_0(57,6)$ continues to decrease with increasing energy beyond the energies accessible with the Bevalac. The iron data on the other hand suggests that both parameters level off at the highest energies. Whether the same behaviour will occur for the heavier beams must await the commissioning of the AGS Booster at Brookhaven.

For $_{57}$La nuclei on hydrogen the cross-sections have to be deduced from the values found in carbon and polyethylene by subtraction. The deduced partial cross-sections are not well fit by the power law expression, Eq. 2, giving reduced χ^2 values of > 40, but relatively well fit over the range $2 \le \Delta Z \le$ largest value with a positive $\sigma(\Delta Z)$, by the exponential expression, Eq. 3 with reduced χ^2 values of between 2.8 and 7.8. As can be seen, with such values of reduced χ^2, these are not "excellent" fits. However, they do provide a reasonable representation of the data. The energy dependence of the fitting parameters obtained are shown in Fig 11. Both parameters show a strong energy dependence over this range of energies and cannot be reliably extrapolated to higher energies.

For $_{57}$La nuclei on polyethylene the cross-sections fit neither of these relations well, although at high energies the best fit is to the exponential, while at the lowest energy the best fit is to the power law. That neither relation is a good fit in general, is not surprising when account

Fig. 8 Fitting parameters $\Sigma_0(Z_B, Z_T)$ and $\alpha(Z_B, Z_T)$ as functions of beam charge, Z_B, for an aluminum target.

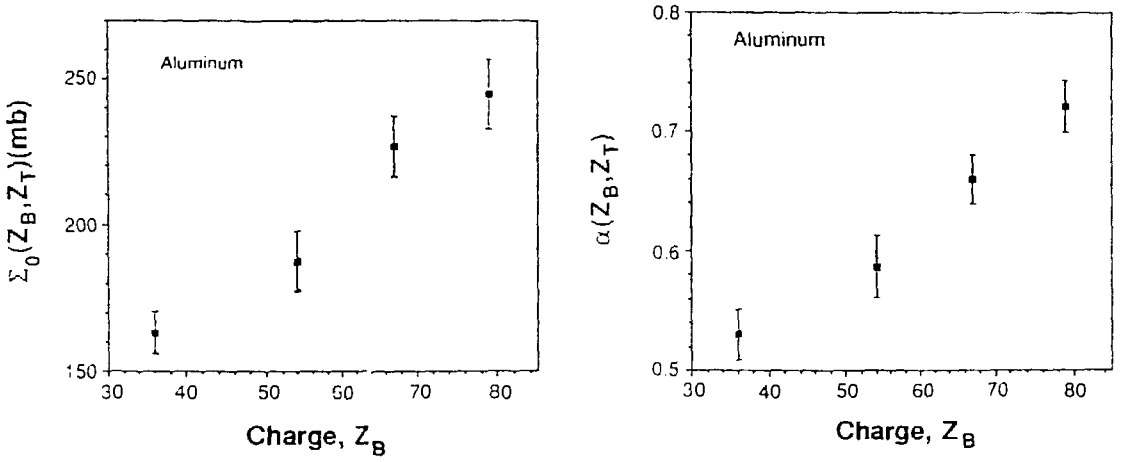

Fig. 9 Fitting parameters $\Sigma_0(Z_B, Z_T)$ and $\alpha(Z_B, Z_T)$ as functions of beam energy, E_B, for an aluminum target and a number of different beams.

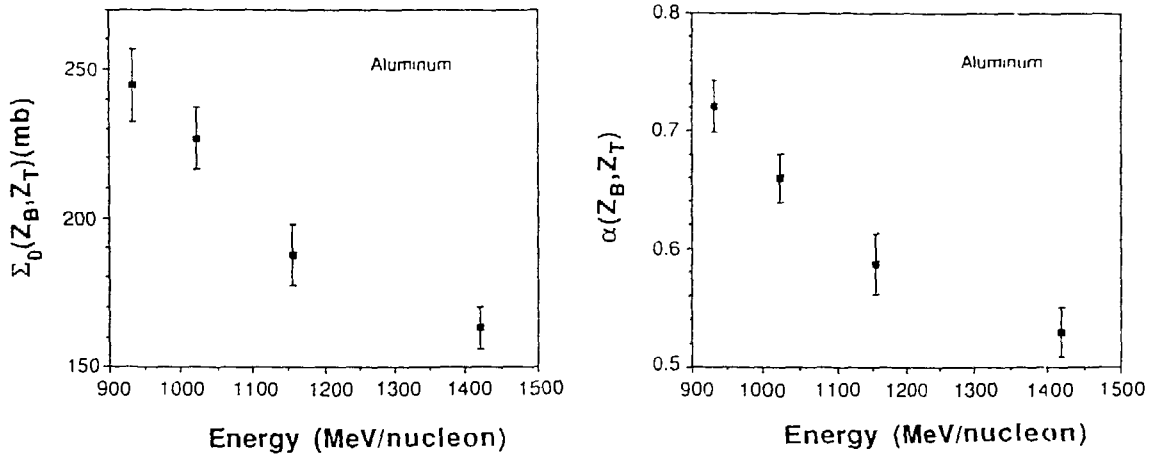

Fig.10 Fitting parameters $\Sigma_0(Z_B, Z_T)$ and $\alpha(Z_B, Z_T)$ as functions of beam energy, E_B, for lanthanum, $_{57}La$ (solid squares) and iron, $_{26}Fe$ (open squares) nuclei in a carbon target. The energy spreads at each mean energy are indicated by horizontal bars. The values obtained in run 2 for xenon, $_{54}Xe$, nuclei in a carbon target are shown by rectangles.

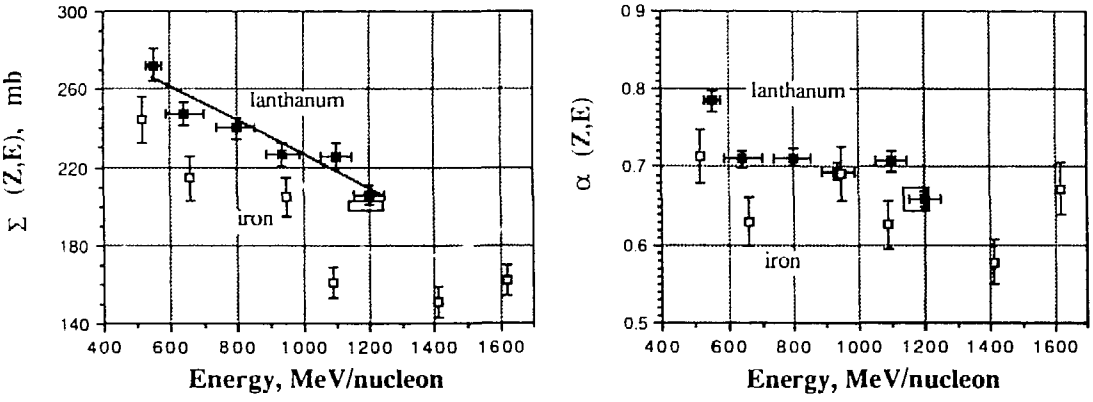

Fig. 11 Fitting parameters $\sigma_0(Z_B, Z_T)$ and $\Delta_0(Z_B, Z_T)$ as functions of beam energy, E_B, for lanthanum, $_{57}La$, nuclei in a hydrogen target. The energy spreads at each mean energy are indicated by horizontal bars. The values obtained in run 2 for xenon, $_{54}Xe$, nuclei in a hydrogen target are shown by rectangles.

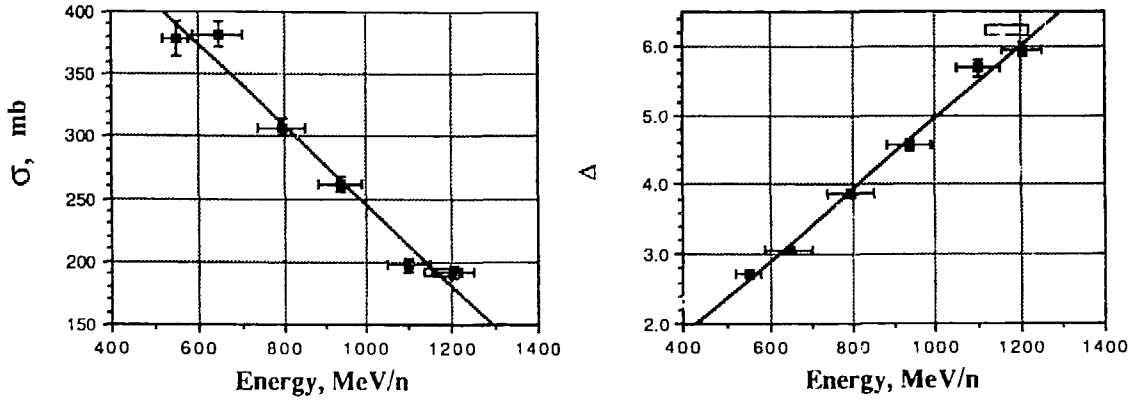

is taken of the composite nature of the target. Presumably the best fit would be provided by the appropriate mixture of the hydrogen and carbon representations.

Conclusions The production of fragments in nucleus - nucleus collisions can be very well represented by a simple power law relation. In addition, the production of fragments in nucleus - nucleon collisions can be fairly well represented by a simple exponential relation. In both cases these representations are described by two parameters which are both charge and energy dependent. Our data, combined with those obtained by other workers at lower charges, has examined the dependence on the beam charge over essentially all the periodic table, but the dependence on the target charge only that up to that of copper, $_{29}$Cu. A strong energy dependence has been observed but the energies currently available are inadequate to allow us to determine at what energy these parameters reach their asymptotic high energy values, or even if such asymptotic values do exist. It will not be possible to make reliable predictions of these cross sections at energies higher than those typical of the Bevalac until the AGS Booster becomes available.

Acknowledgements: This work was performed with my colleagues at Washington University, St. Louis and CalTech., who are listed in the references , and without whose aid these results would never have been obtained. I am also indebted to a succession of graduate students, N.R.Brewster,M.P.Kertzman and J.R.Cummings, who have had the responsibility of the data analysis on each run. Finally none of this would be possible without the cooperation of the staff of the LBL Bevalac and in particular of H. Crawford, who worked long and hard to get us the beams and energies that we needed. My work on this project was partially supported by NASA under Grant NAG 8-500

[1] W.R.Binns, M.H.Israel, J.Klarmann, W.R.Scarlett, E.C.Stone and C.J.Waddington (1981) Nucl. Instr. Meth. **185**, 415

[2] J.Klarmann, C.J.Waddington, W.R.Binns, T.L.Garrard, P.S.Gibner and M.H.Israel (1987) Proc. Moscow Cosmic Ray Conf. **Vol 2**, p.390

[3] B.N.Newport, E.C.Stone, C.J.Waddington, W.R.Binns, D.J.Fixsen, T.L.Garrard, G.Grimm, M.H.Israel and J.Klarmann (1985) Proc SanDiego Cosmic Ray Conf. **Vol.3**, p. 287

[4] R.Silberberg and C.H.Tsao,(1973) Ap.J. Suppl, **25**, 315 and (1973) Ibid **25**, 335 (see also R.Silberberg, C.H.Tsao and J.R.Letaw, "Composition and Origin of Cosmic Rays" ed. M.M.Shapiro, Reidel, p 321 (1983)

[5] N.R.Brewster, 1984, PhD Thesis, University of Minnesota

[6] C.J.Waddington and P.S.Freier (1985) Phys.Rev. C ,**31**, 888

[7] M.P.Kertzman, J.Klarmann, B.J.Newport, E.C.Stone, C.J.Waddington, W.R.Binns, T.L.Garrard and M.H.Israel (1985) Proc SanDiego Cosmic Ray Conf. **Vol 3**, p.95

8 M.P.Kertzman (1987) PhD Thesis, University of Minnesota

[9] C.J.Waddington, W.R.Binns, T.L.Garrard, M.H.Israel, M.P.Kertzman, J.Klarmann and E.C.Stone (1987) Proc. Moscow Cosmic Ray Conf. **Vol 2**, p.152

[10] W.R.Binns, T.L.Garrard, M.H.Israel, M.P.Kertzman, J.Klarmann, E.C.Stone and C.J.Waddington (1987) Phys.Rev. C, to be published.Nov.1987

[11] G.D.Westfall, L.W.Wilson, P.J.Lindstrom, H.J.Crawford, D.E.Greiner and H.H.Heckman (1979) Phys Rev C **19**, 1309

[12] F. Hagen(1976) Ph.D. Thesis, University of Maryland

[13] M.T.Mercier, J.C.Hill, F.K.Wohn, C.M.McCullough, M.E.Nieland, J.A.Winger, C.B.Howard, S. Renwick and D.K.Matheis (1986) Phys Rev C **33**, 1655

14 W.R. Webber (1985) Proc. Baton Rouge Conf, "*Cosmic Ray and High Energy Gamma Ray Experiments for the Space Station Era*" Ed W. V. Jones and J.P.Wefel, p.283; (1987) Proc. Moscow Cosmic Ray Conf. **Vol 2**, p.125, and private communication

EXCITATION DECAY CONTRIBUTION OF PROJECTILE AND PROJECTILE FRAGMENTS TO (^{12}C,$^{11}B+P$) CROSS SECTION AT 2.1 A GEV WITH ^{12}C TARGETS

Ferdous Khan and Govind S. Khandelwal

Old Dominion University

Norfolk, VA 23508

John W. Wilson and Lawrence W. Townsend

NASA Langley Research Center

Hampton, VA 23665

John W. Norbury

Washington State University

Pullman, WA 99164

The recent measurement[1] of the direct step of the relativistic heavy ion reaction (^{12}C, $^{11}B+P$) at 2.1 GeV/Nucleon with C and CH_2 targets tests various theoretical models. These measurements, exclusive in projectile fragments, supersede and refine the previous quasi-exclusive[2,3] measurements and identify the direct step as contributing 39.7 ± 4.5 mb and 19.7 ± 3.4 mb to the total inclusive cross sections[4] of 53.8 ± 2.7 mb and 30.9 ± 3.4 mb for ^{12}C target and Hydrogen targets respectively. In this paper we show that excitation-decay of projectile fragments (^{11}B,^{12}B) in the nuclear field of the target gives rise to additional intensity which brings these measurements in agreement with the inclusive cross sections. We postulate two different sources of cross section: the direct step (^{12}C, $^{11}B+P$) and the excitation-decay of projectile fragments (^{11}B, ^{12}B). Also, the 'new' feature observed in the direct step, i.e., the low momentum transfer and excitation energy peak can be explained as the excitation-decay of the projectile in the nuclear field of the target. Finally, we calculate cross sections for these processes and compare them with experiment.

Heavy-ion fragmentation theory has been described in terms of an abrasion-ablation model where the ablation process is usually analyzed using Glauber theory[5] or classical geometrical overlap models.[6,7] Wilson, Townsend and co-workers[8,9,10] have developed an optical potential model to the nucleus-nucleus multiple scattering series. This has been successfully utilized to calculate total and reaction cross sections[11,12] and projectile abrasion cross sections.[13,14] We continue to use this formalism in the present work.

The cross-section for abrading m projectile nucleons in this model is given by

$$\sigma_m = \binom{A_p}{m} \int d^2\vec{b}\, [1-P(\vec{b})]^m\, [P(\vec{b})]^{A_p-m} \qquad (1)$$

where $P(\vec{b})$ is the probability, as a function of impact parameter, for not removing a nucleon in the collision, and the residual mass number, A_F is $A_F = (A_p - m)$.

Within the context of eikonal scattering theory, the optical model potential approximation to the exact nucleus-nucleus multiple scattering series yields

$$P(\vec{b}) = \exp(-A_t \sigma(e) I(\vec{b}))$$

with

$$I(\vec{b}) = [2\pi B(e)]^{-3/2} \int dz \int d^3\vec{\xi}_t \rho_t(\vec{\xi}_t) \int d^3\vec{y}_p \rho_p(\vec{b} + \vec{z} + \vec{y}_p + \vec{\xi}_t) \qquad (2)$$

$$\exp(-y^2/2B(e))$$

The total reaction cross section is obtained by summing over all values of m according to

$$\sigma_{abs} = \sum_m \sigma_m \qquad (3)$$

The projectile and target densities ρ_p, ρ_t respectively used in (2) are ground state single particle matter densities, which are extracted from nuclear charge distributions according to the procedure outlined in ref. 11. Whenever such information is not available, Gaussian or Woods-Saxon distributions were used, depending on the species involved. Average values for the energy dependent nucleon-nucleon cross sections, $\sigma(e)$, slope parameters, $B(e)$, and the ratio of real to imaginary part of the NN forward scattering amplitude,

$\alpha(e)$ (for future use) were taken from compilations in ref. 15. Figure 1 displays the single nucleon removal cross section σ_1 (m=1)in (1) for ^{12}C at 2.1 GeV/nucleon on ^{12}C target. Note that σ_1 peaks at a certain impact parameter $b=b_{max}$. Also note the range of impact parameters that contribute to the cross section σ_1.

Excitation energy and momentum transfer to the projectile and projectile fragments (^{11}B,^{12}B) are calculated using the formula [5,16,17]

$$E^* = \frac{1}{2m} \int d^3 \vec{\xi}_T \rho_T(\vec{\xi}_T) \int d^3 \vec{\xi}_p \rho_p(\vec{\xi}_p) \left[\vec{\nabla}_{\xi p} \int_{-\infty}^{\infty} V_{opt}(b,\vec{\xi}_p, \vec{\xi}_T, Vt\,\hat{z})\, dt\right]^2 - E_{cm} \quad (4a)$$

where

$E_{cm} = \frac{\vec{p}_t^{\,2}}{2m_n A_{pF}}$ and A_{PF} = mass number of the projectile or projectile fragment

and

$$\vec{p}_t = -\int d^3\vec{\xi}_T\, \rho_T(\vec{\xi}_T) \int d^3\vec{\xi}_p \rho_p(\vec{\xi}_p) \left[\vec{\nabla}_{\xi p} \int_{-\infty}^{\infty} V_{opt}(b,\vec{\xi}_p, \vec{\xi}_T, Vt\,\hat{z})dt\right] \quad (4b)$$

The geometry of the collision process is displayed in Figure 1 where various symbols are explained. The complex Optical Potential was taken to be, as in ref. 10,

$$V_{opt}(\vec{r}) = -A_p A_T \cdot \sqrt{e/m}\, \sigma(e) \left[\alpha(e) + i\right] (3/2\pi a_v^{\,2})^{3/2} \exp\left(-\frac{\vec{3r}^{\,2}}{2a_v^2}\right) \quad (5)$$

where

$$a_v^2 = a_p^2 + a_T^2 + 3 \cdot B(e) \tag{6}$$

a_p, a_T being the matter rms radii for the projectile and target, B(e) is the slope parameter (fm^2) introduced previously, and e is the constituent energy in the two body CM frame, given in terms of relative velocity by

$$e = \frac{1}{2} \mu \vec{v}^2 \tag{7}$$

where $\mu = m/2$ is the two body reduced mass and the relative velocity is

$$\vec{v} = \frac{(A_p + A_T)\vec{K}}{m_N A_p A_T} . \tag{8}$$

Gaussian forms were chosen for matter densities mainly for ease of computation of the bracketed terms in Eq. (4). These have been tested by comparing with Woods-Saxon and Harmonic Well distributions and should be quite reliable for the light nuclei considered in this paper. Since we are dealing with a complex optical potential, absolute value is implied in (4a). In (4b) the physics is determined mainly by the attractive part of the optical potential since $|\alpha| \cong .3$ at 2.1 GeV/N. The repulsive real part was retained, however, and a nonzero net momentum transfer was calculated which is the vector sum of the two contributions from V_R and V_{IM}, respectively. Excitation energy values are displayed as a function of impact parameter for ^{12}C, ^{12}B, ^{11}B projectiles with a ^{12}C target in figure 2.

Next, we calculate the cross section arising from excitation and decay of ^{11}B fragments to the inclusive cross section. By superposing the E^* curve to σ_1 we note that the lowest particle unstable threshold in ^{11}B is at 8.665 MeV ($^{11}B \rightarrow Li + \alpha$). Thus, the intensity due to stable ^{11}B is found

from σ_1 by integrating from b outwards where $E^*(b) = 8.665$ MeV. For ^{12}B one integrates between b_1 and b_2 where $E^*(b_1) = 10.001$ MeV ($^{12}B \rightarrow {}^{8}Li + \alpha$) and $E^*(b_2) = 3.369$ MeV ($^{12}B \rightarrow {}^{11}B + P$). Notice that there is a distribution of E^* values which contribute to the cross section and not a single excitation energy. The cross section results are displayed in Table 1. Since these two projectile fragments exhaust the sources of ^{11}B intensity due to excitation-decay, then $\sigma_{inclusive} = \sigma_{exclusive} + \sigma_{excitation\text{-}decay}$ The agreement is quite satisfactory.

Next, we calculate the excitation-decay contribution of the projectile itself to the exclusive cross section (4.5 ± 0.67 mb for ^{12}C target and 0.81 ± 0.45 mb for CH_2 target). The E^* curve for ^{12}C is shown in figure 2; by matching the E^* curve to σ_1 we again determine two impact parameter values b_1, b_2 where $E^*(b_1) = 18.721$ MeV ($^{12}C \rightarrow {}^{11}C+n$) and $E^*(b_2) = 15.956$ MeV $^{12}C \rightarrow {}^{11}B + P$). The cross section contribution is associated with the area between these two impact parameters. The results are also shown in table 1. The agreement is again quite satisfactory.

Thus, we have shown that the excitation-decay mechanism proposed here is able to explain the inclusive cross section for ^{11}B fragments. The energy transfers involved (under 20 MeV) are consistent with conclusions drawn in ref. 1 and distinguish this model from the nuclear Weizsacker-Williams model of Feshbach and Zabek.[18] It is also possible to predict[17] the momentum distributions (transverse and longitudinal) of these fragments; this could constitute a momentum signature that may distinguish between different sources of intensity.

Fruitful discussions, at the beginning of this work with Dr. Scott Fricke and Dr. Khin Maung, are gratefully acknowledged. The work was funded by the National Aeronautics and Space Administration Grant # NCCI-42.

Table 1a: Excitation-Decay Cross Section Contribution of Projectile Fragments to the Inclusive Cross Section of ^{11}B

Projectile Fragment	σ excitation decay Cross Section (mb)	$\sigma_{inclusive} - \sigma_{exclusive} = \sigma_{excitation-decay}$ (mb)
^{11}B	6.79	
^{12}B	8.77	
TOTAL	15.56	14.1

Table 1b: Excitation Decay Cross Section Contribution of Projectile to (^{12}C, $^{11}B+P$) Direct Step with C Target

Target	Theory (mb)	Exp. (Ref 1)(mb)
^{12}C	5.90	4.5 ± 2.5

References

1. M. L. Webb et al., Phys. Rev. C, 36, 193 (1987).

2. G. M. Chernov et al., Nucl. Phys. A280 , 478 (1977); H. H. Heckman et al., Phys. Rev. C 17, 1651 (1978); H. H. Heckman et al.; ibid. 17, 1735 (1978).

3. A. Sandoval et al., Nucl. Phys. A400, 365 (1983).

4. D. E. Greiner et al., et al., Phys. Rev Lett. 35, 152 (1974).

5. J. Hufner et al., Phys. Rev. C, 12, 1888 (1975); M Bleszynski and C. Sander, Nucl. Phys. A, 326, 525 (1979).

6. J. D. Bowman et al., LBL-2908 (1973).

7. L. Oliveira et al., Phys. Rev. C, 19, 826 (1979).

8. J. W. Wilson, Phys. Lett., 52B, 149 (1974).

9. L. W. Townsend, Bulletin Am. Phys. Soc., 26, 540 (1981).

10. J. W. Wilson, Ph.D. Dissertation, College of William and Mary (1975), unpublished.

11. L. W. Townsend et al., Can. Jour. of Phys., 63 (1985), 135.

12. L. W. Townsend, NASA TP 1893 (1981).

13. L. W. Townsend et al., NASA TP 2305 (1984).

14. L. W. Townsend et al., Phys. Rev. C., 34 (1986), 1491.

15. K. H. Hellwege, Scattering of Elementary Particles, Landolt-Bornstein series, vol. 7, (1973); Particle Data Group, NN and NP Interactions (above 0.5 GeV/C), ICR;-2000 NN (1970).

16. S. H. Fricke, Ph.D. Dissertation, University of Minnesota (1984), unpublished.

17. F. Khan et al, to be submitted.

18. H. Feshbach and M. Zabek, Ann. Phys. (NY) 107, 110 (1977).

Figure 1:
ABRASION-ABLATION FRAGMENTATION MODEL

Before Collision

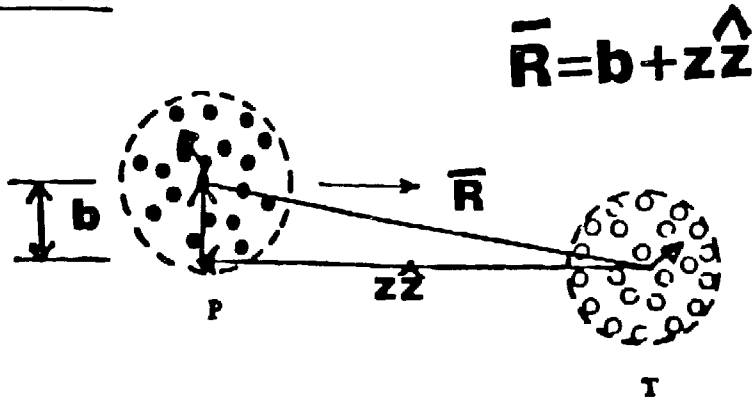

Abrasion

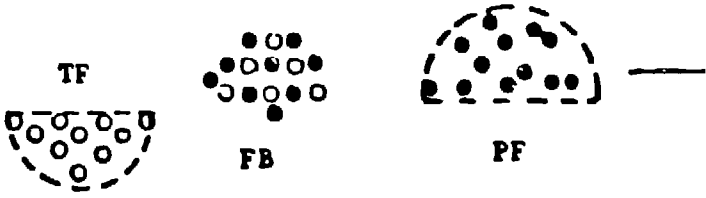

Ablation

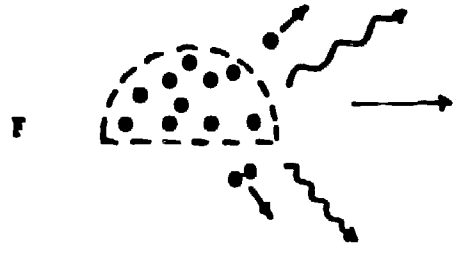

Figure 2:

EXCITATION ENERGY(MEV) vs. IMPACT PARAMETER(fm

FOR BORON FRAGMENTS IN C12 ON C12

AT 2.1 GEV PER NUCLEON (Also shown is the single nucleon removal cross section)

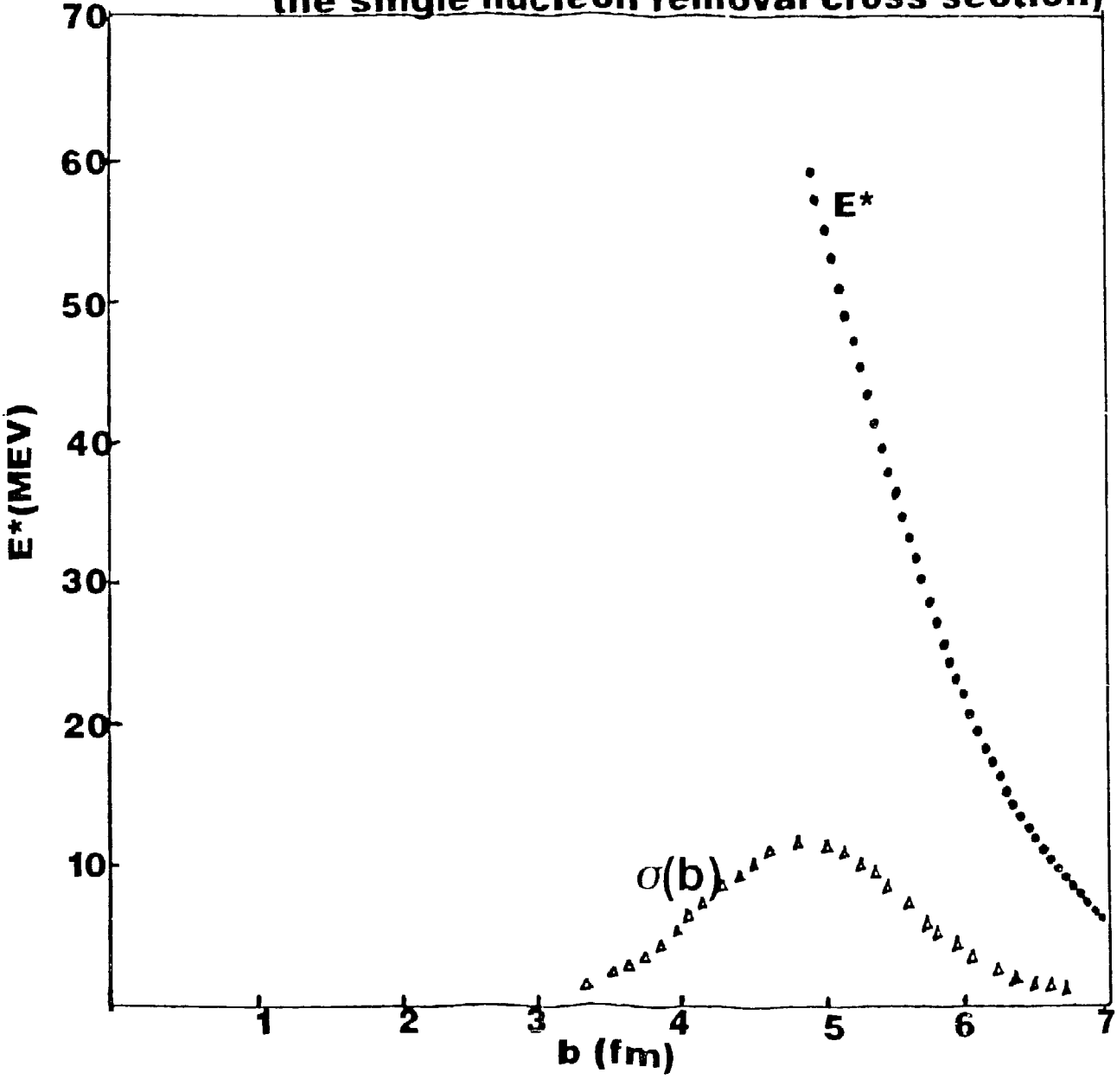

STUDIES OF EXOTIC AND NON-EXOTIC PROCESSES IN RELATIVISTIC PROJECTILE FRAGMENTATION

P. B. Price, G. Gerbier, Ren Guoxiao and W. T. Williams
Physics Department, University of California
Berkeley, CA 84720

1. Introduction

We present a progress report on our recent studies -- both published and unpublished -- of projectile fragments in relativistic nucleus-nucleus collisions. For about a year we have been using a fully automated track scanning and measuring system that measures about 20,000 etchpits per day at the surface of a track-recording solid such as CR-39 plastic or VG-13 glass. The characteristics and performance of these two types of detectors are:

Minimum separation of tracks for non-interference: 0.01 μm
Sampling thickness: ~30 μm
Detector thickness: ~1 mm
Charge resolution: $\sigma_Z = \sigma_1/\sqrt{n}$; n = no. of etchpits
Measurement rate: 1 sec/etchpit if ≳4 etchpits per field of view
Ang. resolution: σ_θ = 30 μrad for a 1 cm portion of trajectory
Detector sensitivity: $5.5 \lesssim Z/\beta \lesssim 70$ for CR-39
$65 \lesssim Z/\beta \lesssim 110$ for VG-13

Table 1. Resolution Achieved at Bevalac or at CERN ($\beta \gtrsim 0.87$)

Detector	Z	σ_Z (1) (1 surface)	σ_Z (n) (n surfaces)
CR-39	8	0.2	0.065 (n = 10)
	16	0.16	0.06 (n = 12)
	26	0.26	0.11 (n = 6)
	57	0.42	0.16 (n = 6)
VG-13	57	0.2	in progress
	70-79	0.16	0.05 (n = 10)
	92	0.2	in progress

2. Search for Fractionally Charged Projectile Fragments

The feature of projectile fragmentation that makes such a search feasible, even simple, is the persistence of velocity. Because projectile fragments are usually formed with almost exactly the same velocity as that of the projectile, only one parameter is needed in order to measure Z.

The procedure is to pass the beam through a target and a stack of track-recording sheets, then to etch the sheets and automatically measure the distribution of etchpit diameters (or areas) at top and bottom of each sheet. In all but one of our experiments, the distribution of average values of etchpit diameters (or areas) has shown sharp peaks at integral charges, with no evidence for subsidiary peaks at non-integral charges. In the most recent experiment, in which 800 MeV/nucleon Au interacted in an Al target, we found a peak at a non-integral charge, ~80.33, if we assumed no shift of velocity. In section 4 we discuss the experiment and show that the apparent nonintegral charge is due to a substantial velocity downshift.

In Table 2, σ_Z gives the charge resolution and σ_r gives the spatial resolution at a single surface. By tracking an event through many surfaces, its angle to the beam can be determined with high precision, permitting an accurate measurement of transverse momentum to be made, on the assumption of a velocity equal to the beam velocity.

Table 2. Summary of Null Results of In-flight Fractional Charge Searches

Beam	Target	Events	σ_Z	σ_r	ref.
1.8 GeV/N ^{40}Ar	CR-39	1100	0.06	---	1
1.0 GeV/N ^{197}Au	Al	5000	0.06	<2μm	2
200 GeV/N ^{16}O	Pb	9400	0.065	0.6μm	3
200 GeV/N ^{32}S	Al	15000	0.05	<1μm	unpub.

Figure 1 shows the distribution of mean values of charge for fragments of 200 GeV/N ^{32}S interactions in Al.

3. Transverse momenta of projectile fragments

The extraordinarily high resolution of centroids of tracks in glass

and plastic detectors makes it possible to determine small deflections

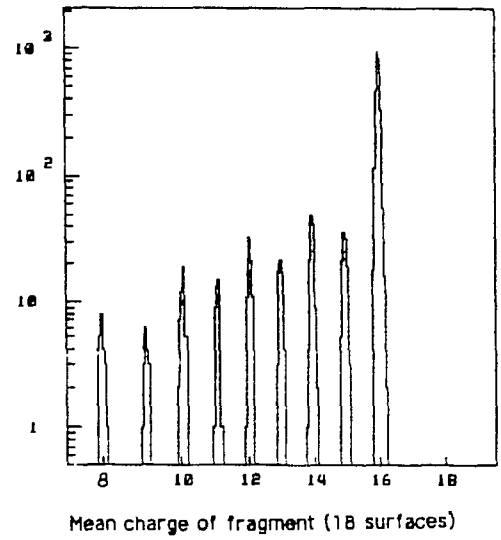

Fig.1. Distribution of charges of projectile fragments of 6.4 TeV ^{32}S interactions in Al.

from the beam direction very precisely. Figure 2 gives an example of the angular distribution of the oxygen beam and of nitrogen and carbon projectile fragments from interactions of 3.2 TeV ^{16}O nuclei in a 10-cm thick Pb target at CERN (ref. 3).

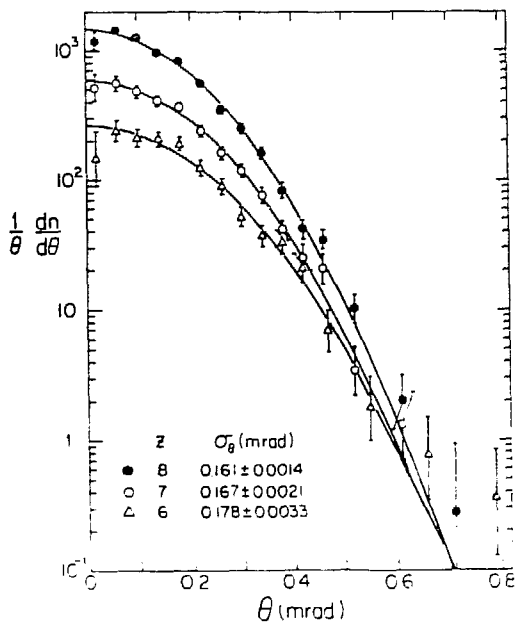

Fig.2. Angular distributions of projectile fragments of 3.2 TeV ^{16}O interactions in Pb, fitted with Gaussians.

The Gaussian angular distribution of oxygen beam nuclei emerging from the Pb is due to multiple Coulomb scattering. Deconvolution of the three Gaussians -- resolution function, multiple Coulomb scattering in Pb, and transverse momentum incurred in projectile fragmentation -- gives the results summarized in Table 3. Our results for $\sigma_{p\perp}$ in projectile fragmentation at 200 GeV/N, inferred from the angular deflections, are consistent with measurements of $\sigma_{p\parallel}$ for projectile fragmentation at a factor 10^2 lower energy, obtained with a magnetic spectrometer at LBL (ref. 4), and with values calculated with Goldhaber's model[5], which assumes that the momentum dispersion of the fragment reflects the momentum distribution of the equivalent cluster inside the original nucleus.

Table 3. Transverse Momenta of Projectile Fragments

Beam	Z	σ_θ (mrad)	$\sigma_{p\perp}$(MeV/c) (this work)	$\sigma_{p\parallel}$(MeV/c) (ref. 4)	calc. $\sigma_{p\parallel}$
3.2 TeV	8	$\equiv 0$	$\equiv 0$	----------	$\equiv 0$
^{16}O	7	0.044	123	----------	134
	6	0.070	168	----------	176
34 GeV	7	-----	---	~ 110	134
^{16}O	6	-----	---	~ 150	176
160 GeV	79	$\equiv 0$	$\equiv 0$	----------	---
^{197}Au	73-78	1.37	387	----------	350
	80	-- in progress --		----------	N.A.

These results support the concept of limiting fragmentation -- no new physics appearing in charge and momentum distributions at bombarding energies as high as 200 GeV/N and for projectiles as heavy as gold.

3. Cross sections for charge pickup of the projectile

Some years ago Greiner et al.[4] and Olson et al.[6] observed interactions at the sub-millibarn level in which the projectile increased in charge by one unit with very small momentum transfer. The most

likely mechanism for such charge pickup would be through pion exchange, converting a neutron in the projectile into a proton and a proton in the target nucleus into a neutron. We have used plastic and glass detectors to measure cross sections for charge pickup for several projectiles and bombarding energies. Our results are shown in Fig. 3, along with results of other workers. Two trends are apparent: (1) For a given projectile, the pickup cross section decreases with bombarding energy per nucleon. (2) At a given energy per nucleon, the pickup cross section increases dramatically with projectile mass, reaching values of 25 to 35 millibarns for La and Au projectiles.

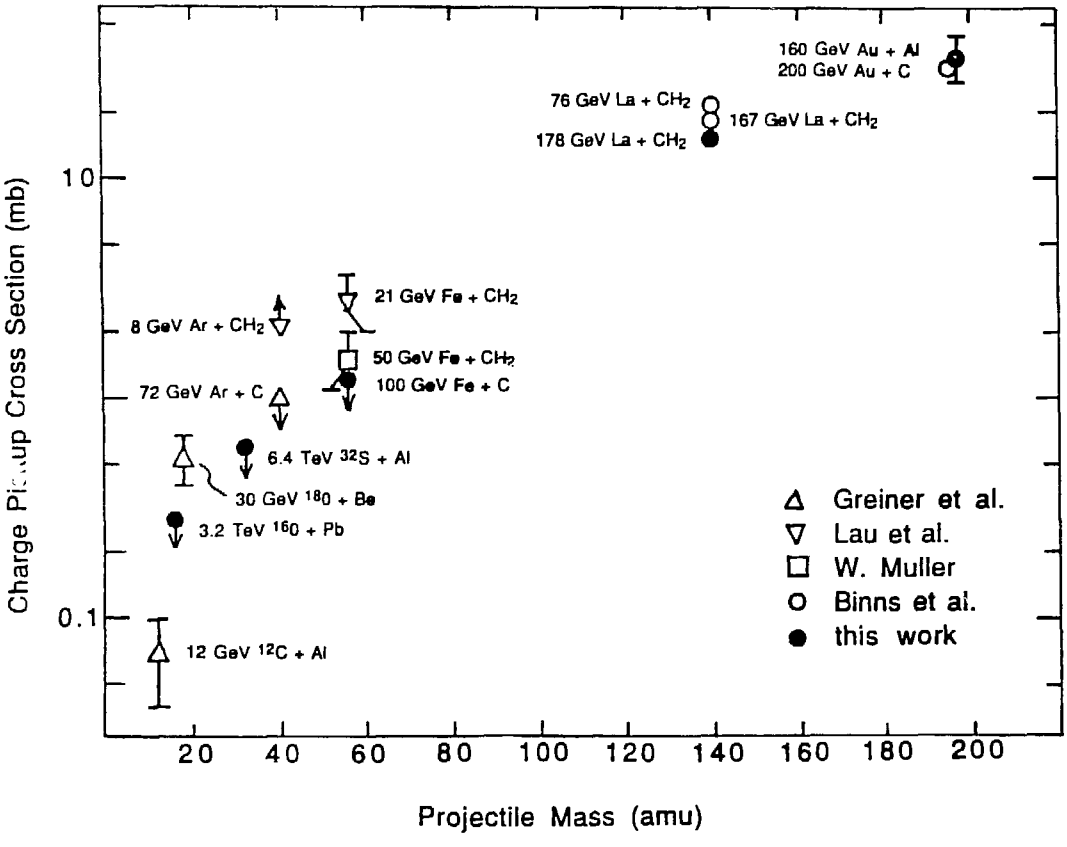

Fig.3. Charge pickup cross sections as a function of projectile mass.

4. Large, nondestructive momentum loss in charge pickup by heavy nuclei

The most startling result to come out of our studies of projectile fragmentation is the discovery that charge pickup reactions of heavy nuclei are accompanied by an extraordinarily large momentum downshift,

as much as 6 GeV/c, corresponding to a loss of kinetic energy of $\gtrsim$ 20 MeV/nucleon. We observed the effect while searching for production of fractionally charged projectile fragments in interactions of 900 MeV/N ^{197}Au in an Al target. In that experiment we used a stack of five sheets of VG-13 glass to identify the particles. A detailed account of the work will appear elsewhere[2]. Analysis of Au and its fragments is complicated by the fact that, in steady state, more than 10% of the nuclei have a K-electron attached, which makes their instantaneous ionization rate look like that of the next lower nucleus in charge. (For La and lighter nuclei at Bevalac energies the fraction of incompletely stripped nuclei is so small that it presents no problem.)

For a mean energy of 730 MeV/N for Au in VG-13, we estimate that the mean free paths for capture and stripping of a K-electron are λ_c ~ 460 μm and λ_s ~ 80 μm, to be compared with the ~30 μm sampling thickness. Thus, a single etchpit usually samples a single charge state. By sampling the charge state of each particle at all ten surfaces of the five glass sheets, we were able to distinguish atomic from nuclear charge. Figure 4 gives examples of sequences of ten measurements in which one can detect single electron capture and stripping (in a and b)

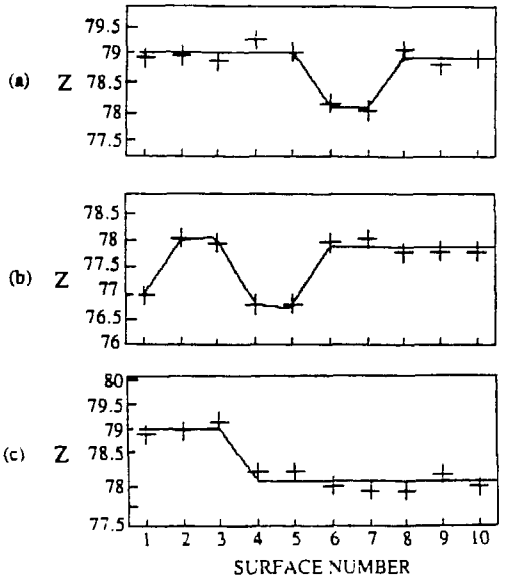

Fig.4. Examples of measurements of ionic charge states at 10 surfaces of glass for (a) a Au nucleus, (b) a Pt nucleus, and (c) a Au nucleus undergoing fragmentation.

and fragmentation with loss of one unit of nuclear charge (in c). The frequency of occurrence of correlated pairs such as appear in Fig. 4a and b is related to the relative sizes of λ_s and sampling thickness, and offers a direct way of measuring λ_s. We then get λ_c by measuring the ratio n(+78)/n(+79) for particles identified as Au nuclei. Our results agreed well with the calculated values.

Figure 5 shows the charge distribution of projectile fragments of interactions in the Al target and an upstream scintillator paddle, after correction for ionic charge states.

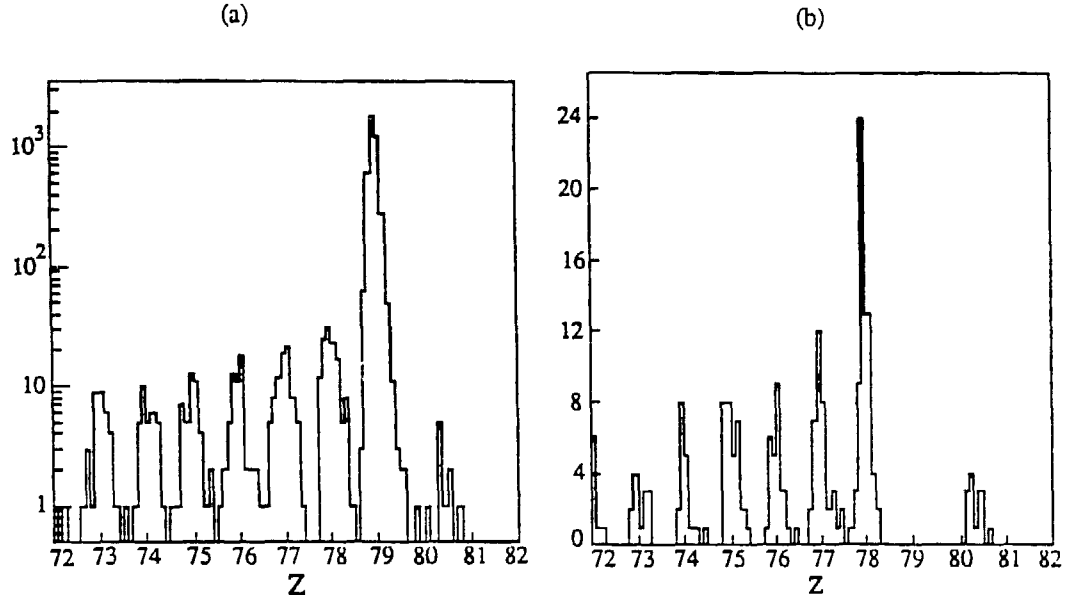

Fig.5. (a) Distribution of nuclear charges for particles emerging from the Al target; (b) nuclear charges of fragments of Au nuclei that interacted in the glass.

From these data we have computed cross sections for production of fragments with $70 \leq Z \leq 80$. The results are shown in Table 4, along with results of Binns et al.[7], supplemented with their new result for production of Z = 80, presented by C. J. Waddington at the Heavy Ion Study. These authors used a combination of two ion chambers and a Cerenkov detector. The results obtained by the two different techniques agree well.

Table 4. Interactions of 800 MeV/N Au in Al and Upstream Plastic

Fragment	no. of events	σ (mb) this work	σ (mb) Binns et al.[7]
≥80	27	33 ± 6	32 ± 3
77	148	182 ± 15	162 ± 16
76	94	115 ± 12	112 ± 5
75	78	96 ± 11	86 ± 4
74	50	61 ± 9	83 ± 4
73	61	75 ± 10	60 ± 3.5
72	41	50 ± 8	59 ± 3.2
71	33	41 ± 7	53 ± 3
70	44	54 ± 8	51 ± 3

Focussing on the events in which Au interacted to produce nuclei with $Z \geq 80$, in Fig. 5 we see that the Z inferred *assuming no change of* β is an integer for $Z \leq 79$ but is displaced for $Z \geq 80$. For the interactions in Al + upstream matter (Fig. 5a) there are ten events with a mean apparent charge $\langle Z \rangle \equiv Z(\beta_i/\beta_f) = 80.41 \pm 0.05$, with an additional systematic error of at most 0.1 arising in the conversion from etchpit radius to Z. By studying interactions of the surviving Au in the VG-13 detectors (Fig. 5b), we obtained an additional 12 events with $\langle Z \rangle = 80.32 \pm 0.04$, with a systematic error of at most 0.1.

With only five glass plates, we could not determine Z and β separately. From our data alone, we could not rule out the possibility that fractionally charged nuclei had been created. However, from Table 4 we see that our events with $Z \geq 80$ almost certainly correspond to those identified by Binns et al. as $Z = 80$. We are then led to attribute the increase in Z/β to a decrease in β. Drawing on the result of calibrations[8] of VG-13 with fragments of U, Au and La, which have shown that $s \sim f(Z/\beta)$ for relativistic particles with $\beta \gtrsim 0.7$, we infer that $\delta\beta/\beta_i = (80-\langle Z \rangle)/80 = -0.4/80$ for $\langle Z \rangle = 80.4$, and $\delta\beta = -0.0044$, for $\beta_i = 0.86$. Such a large velocity downshift was completely unexpected and demands an explanation.

At our suggestion Waddington examined the data of Binns et al.[7] for charge pickup, to look for large velocity downshifts. Their plastic Cerenkov detector is sensitive to velocity downshifts of the magnitude required by our data only for beams at energies $\lesssim$ 500 MeV/N. He reported at the Heavy Ion Study that their data for charge pickup of 500 MeV/N La are consistent with a downshift of β of magnitude similar to ours. In previous studies of charge pickup, the momentum/nucleon downshifts for light ions were two orders of magnitude smaller than ours.

Since the Heavy Ion Study we have studied charge pickup by 1.28 GeV/N La ions using CR-39 track-recording plastics as both target and detector. Figure 6 shows the charge distribution of the fragments with $39 \leq Z \leq 58$. The cross section calculated for charge pickup, ~20 mb, agrees well with that reported by Waddington at the Study. Our data show no evidence for a velocity downshift in this experiment. For charge pickup we measure a mean charge $\langle Z \rangle = 58.03 \pm 0.02$. The resulting upper limit for the velocity downshift is 0.0008 at 84% confidence level. (Waddington's Cerenkov detector could not have seen a velocity downshift at 1.28 GeV/N.)

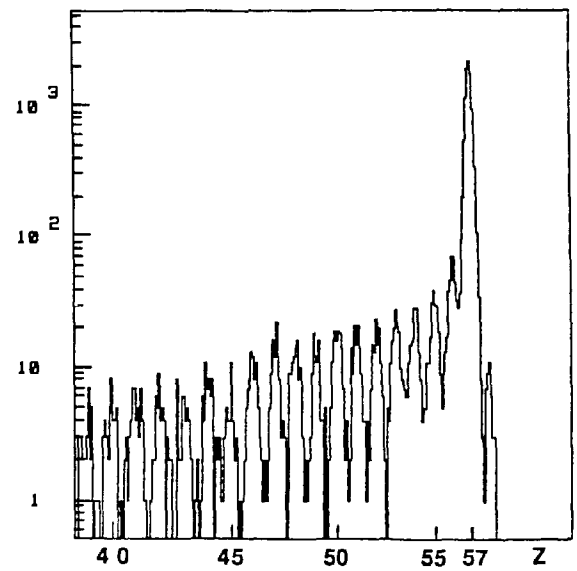

Fig.6. Distribution of charges of projectile fragments of 178 GeV ^{139}La interactions in CR-39.

From the data just discussed, it appears that in charge pickup reactions of Au at maximum Bevalac energy/nucleon and of La at a lower energy/nucleon, the resulting fragments undergo a coherent momentum downshift of 20 to 30 MeV/c *per nucleon* without destruction. A coherent process involving the strong interaction and extending through the volume of a nucleus as large as Au is hard to understand. One can formally reduce the momentum of a Au nucleus by the required amount either by sweeping up two nucleons from rest or by the nucleus undergoing a headon elastic collision with one nucleon at rest. We are planning further studies, using thick stacks of VG-13 plates to measure not only $\delta\beta$ but also the range of the Hg nuclei (and therefore their mass) and their interaction cross section (or lifetime).

This work was supported in part by NSF Grant INT-8611276 and by DOE.

References

1. P. B. Price et al., Phys. Rev. Lett. 50, 566 (1983).
2. G. Gerbier, Ren Guoxiao and P. B. Price, submitted to Phys. Rev. Lett.
3. G. Gerbier et al., Phys. Rev. Lett. 59, 2535 (1987).
4. D. E. Greiner et al., Phys. Rev. Lett. 35, 152 (1975).
5. A. S. Goldhaber, Phys. Lett. 53B, 306 (1974).
6. D. L. Olson et al., Phys. Rev. C 24, 1529 (1981).
7. W. R. Binns et al., Phys. Rev. C 36, 1870 (1987).
8. P. B. Price et al., Nucl. Instr. Meth. B21, 60 (1987).
9. K. H. Lau et al., Proc. 19th Inter. Cosmic Ray Conf., LaJolla, 3, 91 (1985).
10. K. H. Lau et al., Proc. 18th Inter. Cosmic Ray Conf., Bangalore, 9, 255 (1983).

THE GSI SEPARATOR FOR PROJECTILE FRAGMENTS

H. Geissel, P. Armbruster, H.-G. Clerc[1], J.P. Dufour[2], B. Franczak, E. Hanelt[1], O. Klepper, B. Langenbeck, G. Münzenberg, F. Nickel, K. Poppensieker, M.S. Pravikoff[2], E. Roeckl, D. Schardt, K.-H. Schmidt, D. Schüll, T. Schwab[4], B. Sherrill[3], K. Sümmerer and H. Wollnik[4]

GSI Darmstadt, TH Darmstadt[1], C.E.N Bordeaux[2], Michigan State Univ.[3], Univ. Giessen[4]

THE SIS-FRS-ESR CONCEPT

The heavy-ion synchrotron SIS can accelerate all ions up to a maximum magnetic rigidity of 18 Tm, i.e., depending on their ionic-charge-to-mass ratio the energy of the ions will be up to 1-2 GeV/u.
New frontiers in the investigation of exotic nuclei and their applications will be reached with the projectile fragment separator /1/ now under construction at GSI as a part of the SIS-ESR accelerator and storage ring facility. The separator will provide isotopically separated nuclei, produced by the fragmentation of relativistic heavy ions.
The in-flight separated projectile fragments can be studied at various experimental areas, see Fig. 1 . The radioactive isotopes can be most efficiently separated (highest transmission, shortest separation times) at the final focus of the separator (exp. area 2), where studies of nuclear properties and exotic decays can be made. In combination with the ESR storage ring, experiments with circulating radioactive beams are possible. The ESR has the capability of beam cooling, deceleration, and internal targets (exp. area 3). Beams extracted from the ESR, with high phase space density, after cooling or deceleration, can be delivered to the experimental areas in the target hall. The possibility to transfer the full-energy beam directly into the target hall is under discussion (area 4).
The separator is designed as a high resolution achromatic system with $p / \Delta p > 10^3$ at the dispersive focal plane. It can also be used as an energy-loss spectrometer /1/, by placing the target into the symmetry plane, where space for detectors for prompt reaction products is provided (exp. area 1).

THE PRODUCTION OF RADIOACTIVE NUCLEI

The fragmentation of relativistic heavy ions has been proven to be a suitable tool for the production of exotic nuclei /2/ and led to the discovery of new isotopes near the neutron- as well as the proton drip-lines /3/. Up to now it has been mainly applied to medium mass $A \lesssim 80$ nuclei and intermediate energies of (10 - 200) MeV/u.
The heavy fragments are produced in peripheral collisions, At SIS-energies the total nuclear cross-section is determined by the geometric dimension of the colliding nuclei /4/, and a contribution from electromagnetic dissociation. This contribution is significant at higher energies and heavy target material, as demonstrated in Figure 2 for the systems U + U and U + Be /5/.

	SIS PARAMETER
ENERGY	(1 – 2) GeV/u $[B\varrho_{max} = 18\ T_m]$
INTENSITY	$5 \cdot 10^{11}$ s^{-1} (all ions)
MOMENTUM SPREAD	10^{-3}
TIME SPREAD	50 ns
EMITTANCE	20 π mm mr

	ESR PARAMETER
ENERGY	(3 – 800) MeV/u $[0.5\ T_m \leq B\varrho < 10\ T_m]$
INTENSITY	space charge limit
MOMENTUM SPREAD	10^{-3}
TIME SPREAD	
EMITTANCE	(2 – 0.05) π mm mr

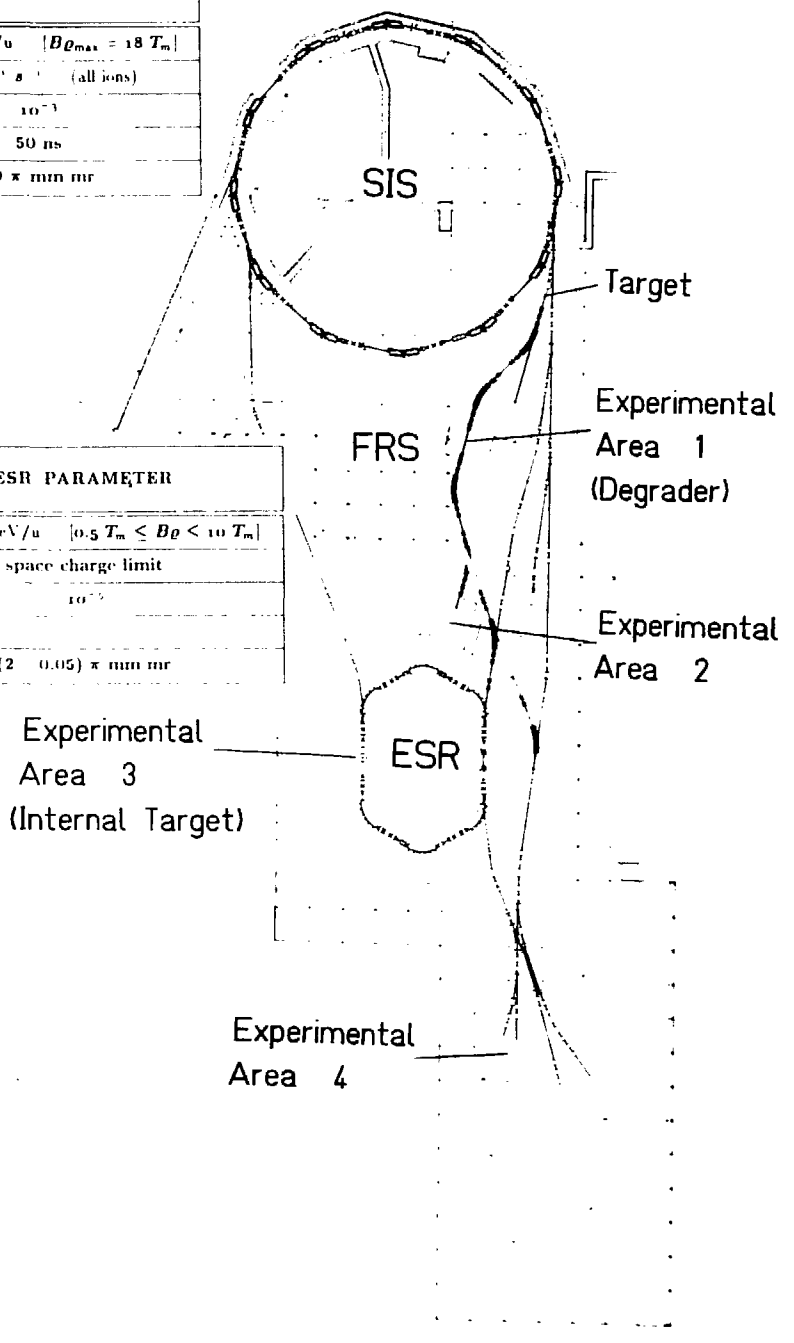

Fig. 1:

Layout of the heavy-ion synchrotron SIS, the fragment separator FRS, the cooler- and storage-ring ESR and the experimental areas. Isotopically separated radioactive beams can be delivered to the areas 2-4.

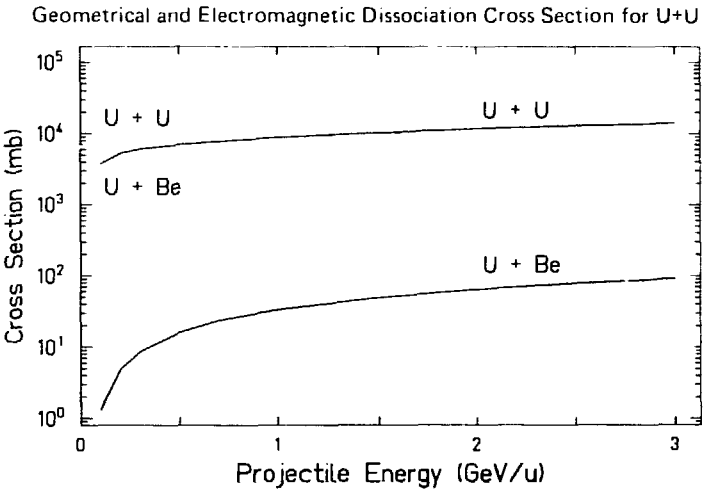

Fig. 2: Electromagnetic dissociation and geometrical (dashed lines) cross sections for U + U and U + Be as a function of the incident energy.

Projectile fragmentation and target fragmentation have similar isotopic yield distributions. Hence the parametrization of Rudstam /6/ can be used as a basis for an estimate of isotopic yields. This formula has been refined for our application on the basis of more recent experimental data /7/.

Figure 3 shows the chart of nuclides with the estimated region of new isotopes which can be produced via projectile fragmentation at a rate exceeding 1/s. Within the corresponding full lines, about 700 new isotopes are waiting to be discovered. For radioactive nuclides close to stability, production rates up to 5×10^6/s are expected.

The kinematic properties of the projectile fragments are determined by the nuclear reactions and the atomic interactions in the production target. If a comparatively small number of nucleons is abraded from the projectile, the velocity of the fragments is close to that of the projectile. The momentum distributions are Gaussians, which are determined by the intrinsic Fermi-motion of the nucleons in the projectile and the number of abraded nucleons /8/. The resulting angular spread is shown in Figure 4 for different fragments of 1 GeV/u U projectiles. The angular acceptance of the fragment separator is also indicated.

In addition, in collisions with heavy nuclei the Coulomb interaction can have an important contribution /9/.

The momentum spread due to the target thickness is determined by the difference in the energy-loss of projectile and fragment. In Figure 5 calculated energy spread is presented for different fragments produced by 1 GeV/u U projectiles in 1 g/cm² Be. It is obvious that this energy spread is the more pronounced the more the atomic number differs from that of the projectile. Therefore the transmission of the fragment separator is best used, if the projectile is chosen to be close in A and Z to the desired fragment.

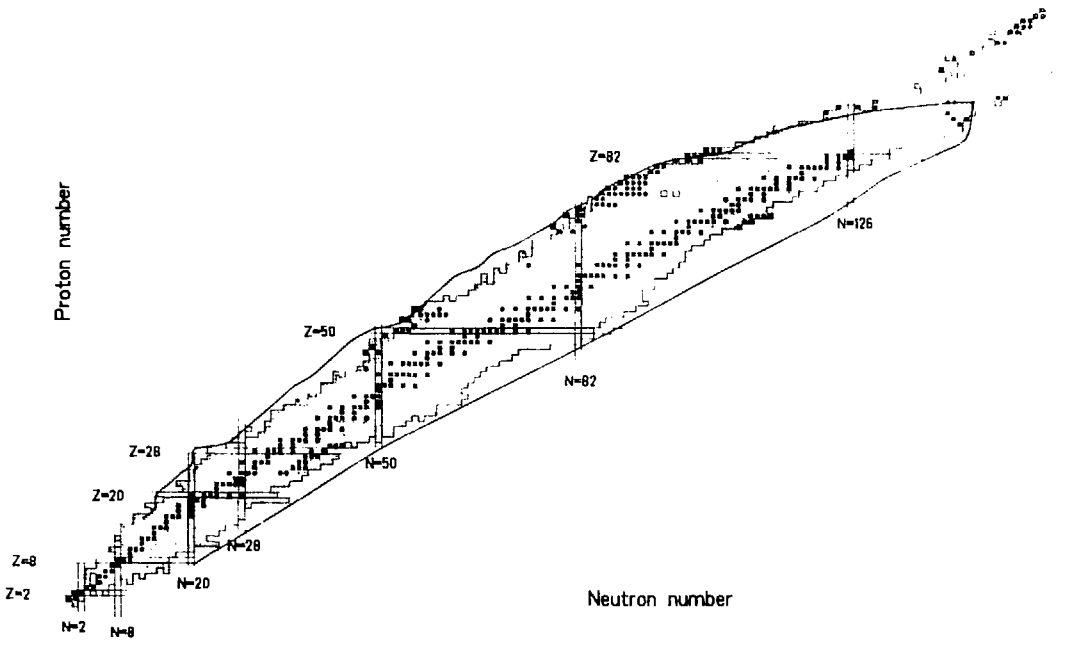

Fig. 3: Chart of nuclides, with the new isotopes for which production rates > $1s^{-1}$ are expected.

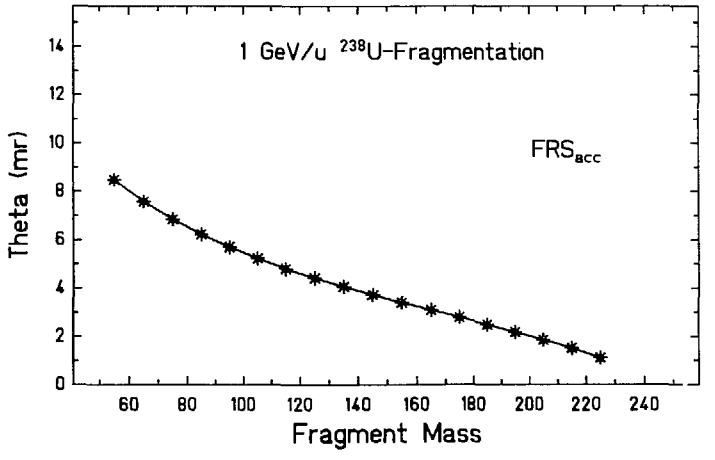

Fig. 4: Angular spread of fragments of 1 GeV/u ^{238}U projectiles /8/.

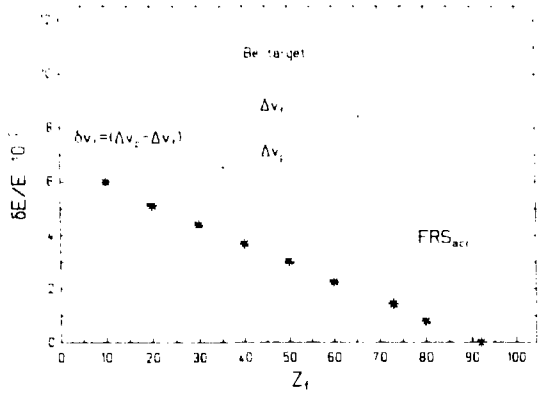

Fig. 5: Energy spread of fragments of 1 GeV/u ^{238}U projectiles. The fragments are produced in 1 g cm^{-2} Be.

The contribution due to energy-loss straggling at relativistic energies is negligible /1/. For thin targets the atomic angular scattering is small compared to that from the nuclear reaction.

IN-FLIGHT SEPARATION OF RELATIVISTIC PROJECTILE FRAGMENTS

It has been shown that the isotopic separation of relativistic ions using conventional ion-optical methods is not possible /1/. A solution for this problem is to use the different stopping powers of particles in matter, and to combine with a magnetic analysis. This method has been used for particle detection , e.g. $\bar{\pi}$, K and $\bar{p}$ or fission fragments /10,11/. Recently the method has been applied to the separation of light and medium (A < 50) nuclei with the LISE-Separator at GANIL /12,13/. The keys to this separation are an achromatic magnetic analyzer, with high resolving power and a profiled degrader at the dispersive focal plane, providing a separation in A and Z independent of the initial velocity spread of the fragments.
The separation principle is demonstrated in figure 6. Due to the reaction kinematics the first stage of the achromat separates ions of a selected A/Z-ratio. All fragments with the same magnetic rigidity are focused on the same position of the degrader. The electronic energy-loss of the ions penetrating the degrader provides a different A- and Z- dependent isotopic selection in the second stage. By matching the velocity dispersions of the two stages with an appropriately shaped degrader, this separation can be made velocity-independent /13,14/. This second separation makes a different cut in the A/Z-plane and, as shown in figure 6 for the example of the separation of ^{212}Pb produced by fragmentation of 1 GeV/u ^{238}U in a 0.5 g/cm^2 Be-target and using a 5.8 g/cm^2 Be degrader.
The optimum energy range of the separation method is determined by two conditions: For efficient isotope separation, it is necessary, that all the fragments are fully ionized to avoid ambiguities due to different charges states. However if the energy is too high, secondary reactions will severely reduce the intensity, and may cause also significant background /see contribution of Schmidt et al. in these proceedings/.

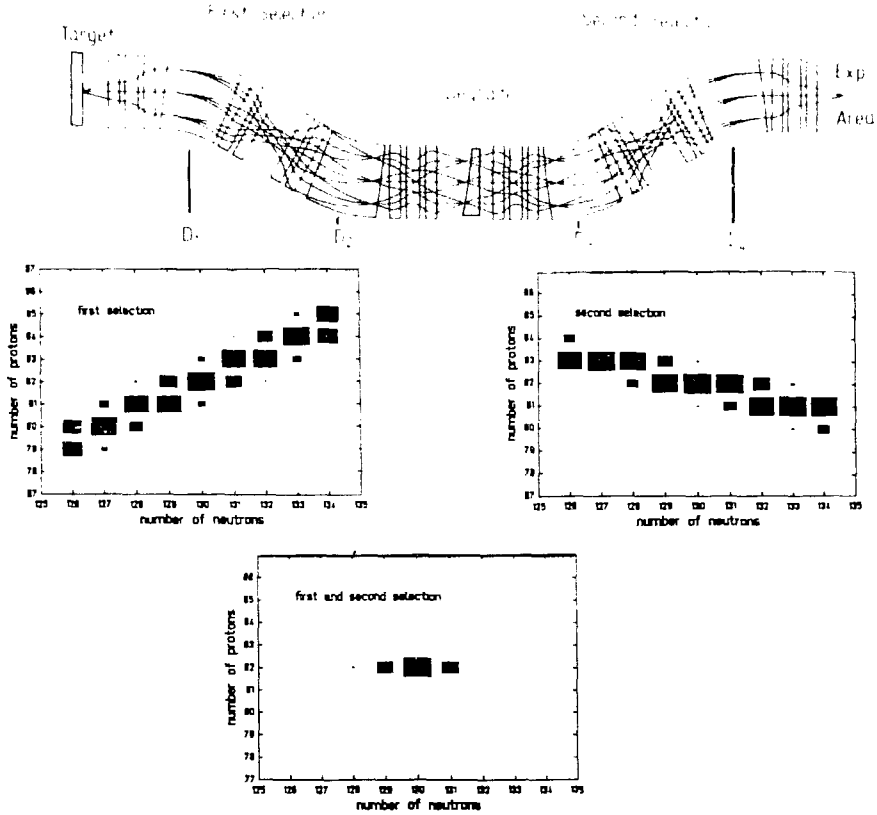

1 GeV/u ^{238}U-fragmentation, selection-criteria in PFS

Fig. 6: The separation principle of the fragment separator, demonstrated for a difficult test case of a heavy fragment (^{212}Pb), produced by fragmentation of ^{238}U.

THE LAYOUT OF THE GSI PROJECTILE FRAGMENT SEPARATOR

The fragment separator has been designed to include dedicated experimental areas, as well as to inject into the ESR (Fig. 7a). The separator has been designed as an achromat, optically corrected to the second order. It is possible to operate the fragment separator in different dispersive modes. The system has four stages, each consisting of a 30°- dipole magnet and quadrupole magnetic focusing (Fig. 7b).

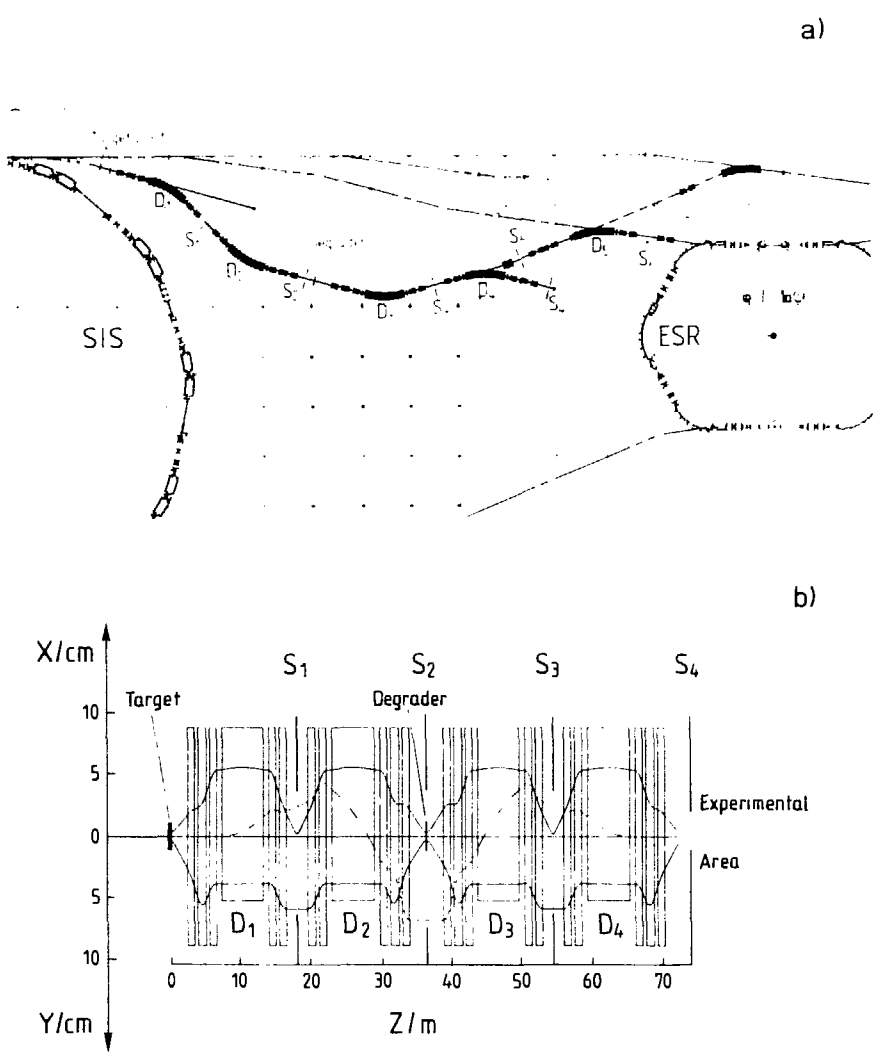

Fig. 7: Ion-optical layout of the fragment separator. The 30°-dipole magnets and the slits at the different focal planes are indicated by D_1-D_5 and S_1-S_6 respectively.

The first two stages of the achromat consist of the dipoles D_1 and D_2. The resolving powers of the two dipole stages are equal and add. The dispersion for $\Delta p / p = 1$ % (dashed line in Fig. 7b) reaches a maximum at the central focal plane. The last two stages consist of the dipoles D_3, D_4 for the experimental area and alternatively D_3, D_5 for injection into the ESR. These magnets cancel the dispersion generated by the first stages, so that the separator is doubly achromatic at S_4, or adjusted for dispersion matching into the ESR. The hexapoles for correction to second order have been positioned, where they show the strongest coupling to the aberrations to be corrected /15/. By virtue of the symmetry of the separator, the induced higher order aberrations are small. The efficiency of the correction has been checked with the 3rd-order programs GIOS, TRANSPORT, and the raytracing program RAYTRACE. Table 1 shows the parameters of the fragment separator.

Table 1:Parameters of the Fragment Separator

ENERGY RANGE	0.1–1.4	GeV/u
BEAM RIGIDITY, maximum	18	Tm
LENGTH	75	m
TARGET THICKNESS	.1–10	g/cm^2
SOLID ANGLE	0.42–0.80	msr
MOMENTUM ACCEPTANCE	2	%
TRANSMISSION (approx.)	60	%
MOMENTUM RESOLUTION	1500	
FOCAL PLANE TILT	90	degrees
FINAL FOCUS	ACHROMATIC	
$\Delta\ell/\ell$	$< 10^{-3}$	

To calculate the beam profiles in the ion optical system, and to optimize phase-space matching for the injection into the ESR, a Monte-Carlo-Programme has been developed /16,17/. This program combines higher order ion-optics (presently up to 3rd order) with nuclear reaction kinematics and the interaction of the heavy ions with matter. Results for the fragmentation of ^{20}Ne (670 MeV/u) into ^{19}Ne in a 4.5 g/cm^2 Be-target are shown in Figure 8. Without a degrader, the isotopes ^{19}Ne, ^{17}F, ^{15}O etc. cannot be spatially separated with a magnetic system. Even if the target would be very thin, it would not help since the energy spread is dominated by the reaction mechanism . Figure 8 shows the isotopic distributions for ^{19}Ne separation, calculated with various degrader shapes. The homogeneous degrader already gives sufficient spatial resolution for light isotopes. The resolution is significantly improved, by almost a factor of ten by using an achromatic degrader. The monoenergetic degrader again reduces the isotope resolution, but bunches the energy spread of the fragments by about a factor of 10. Figure 8 also shows fragment energy-position correlations for the same calculations .

The separation of ^{212}Pb-fragments from the fragmentation of ^{238}U has been calculated (see Fig. 6). The results are in agreement with the convolution method of Schmidt et al. /18/. It shows the excellent separation quality of the set-up, which suppresses the other elements by more than one order of magnitude, and also supresses neighbouring isotopes by at least a factor of two. Further improvements may be possible by optimization of the system parameters, e.g. degrader thickness, incident energy and accepted momentum range. This is an improvement in separation, compared to other systems used for heavy-ion separation. For example, ISOL separators generally have contaminations from isobars, velocity filters from similar velocity fusion-evaporation products and recoil separators from A/q- ambiguities.

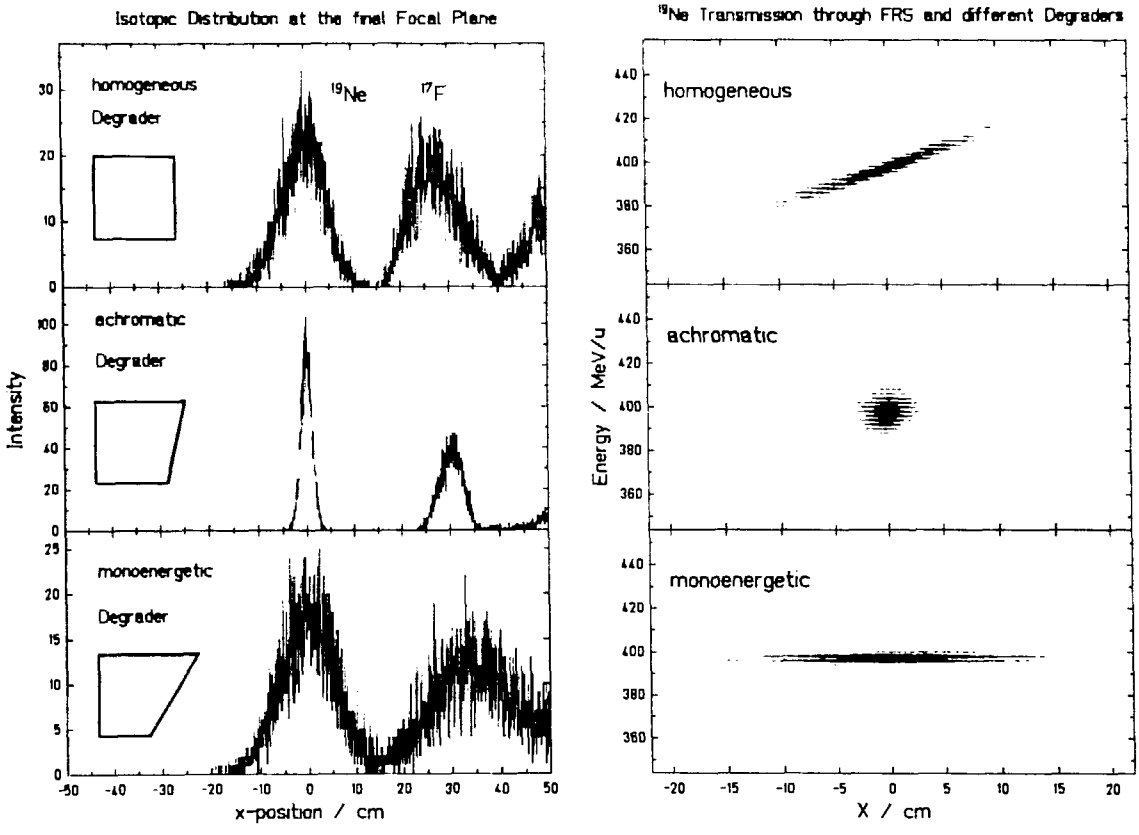

Fig. 8: The influence of various degrader shapes on the isotopic resolution.

The separator can also be operated as a high resolution energy-loss spectrometer. Independent of the relatively large momentum spread of the incident beam, precise measurement of energy transfers in nuclear or atomic reactions become possible. In this mode of operation, the target is placed at the central dispersive focal plane. In Figure 9 computer simulations for the energy-loss mode of the separator show results for an energy difference of $1.5 \cdot 10^{-3}$, which demonstrates the feasibility of high-resolution experiments.

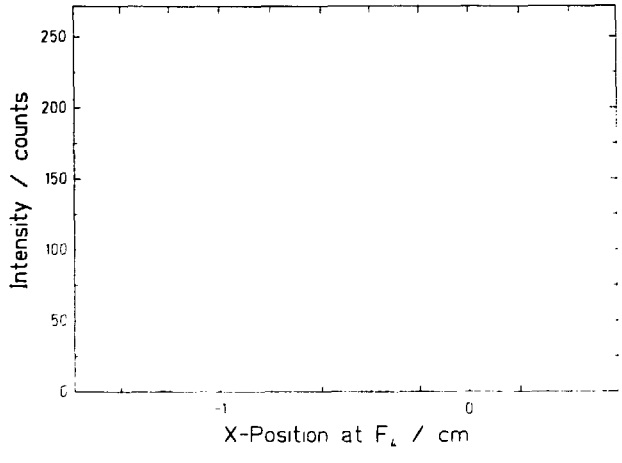

Fig. 9:
Monte-Carlo simulation for the energy-loss mode of the separator for two energies, separated by $1.5 \cdot 10^{-3}$.

If a cooled beam from the ESR is reinjected into SIS, the beam energy spread may be as low as 10^{-5}. Then it is advantageous to add the resolution of the four dipole stages of the fragment separator, resulting in a total resolution of $> 3 \cdot 10^3$.

PLANNED EXPERIMENTS

Proposals for experiments with the separator cover nuclear physcis, atomic physics, and applications of radioactive beams /19/. Included are: The investigation of ground-state properties of exotic nuclei up to uranium, decay-spectroscopy of exotic nuclei, atomic spectroscopy of few-electron systems, direct-mass measurements in the ESR, the measurement of nuclear radii, and high resolution nuclear reaction spectroscopy in quasi-elastic reactions carried out with circulating beams in the ESR and an internal target consisting of light nuclei.
The energy-loss mode will be used for the study of nuclear interactions, for example the study of Δ-resonances, as well as for the investigation of atomic collisions with few-electron ions, slowing down or charge-exchange of relativistic heavy ions in matter.
The application of radioactive beams which may be a developing field for the future is also planned in first experiments.

For helpful discussions we are indebted to K.L. Brown (SLAC) and K. Halbach (LBL), the technical layout is made in collaboration with the GSI engineering groups.

REFERENCES

1. H. Geissel et al., Projectile-Fragment Separator, a proposal for the SIS-ESR experimental program (1987)

2. T.J. Symons et al., Phys. Rev. C **42** (1979) 40
   G.D. Westfall et al., Phys. Rev. C **43** (1979) 1859

3. J.P. Dufour, 5th Int. Cont. on Nuclei far from Stability, Rosseau Lake, Canada (1987)
   D. Guillemaud - Mueller, ibid.
   J.C. Jacmart et al., ibid.

4. S. Kox et al., Phys. Lett. **159P** (1985) 15

5. C. Bertulani et al., Phys. Rev. **C34** (1986) 1654

6. G. Rudstam, Z. Naturforsch. **21a** (1966) 1027

7. K. Sümmerer , GSI Nachrichten 7-87 (1987)

8. I. Hüfner, Phys. Rep. **125** (1985)
   D.C. Scott, Nucl. Phys. A **354** (1981) 394

9. R. Matzdorf and G. Soff Z. Phys D 6, 5 (1987)

10. S. Marcowicz et al., Rev. Sci. Instr. **33** (1962) 552

11. P. Armbruster, Journal de Physique **C5** (1976) 161 (1976) 129

12. R. Anne et al., Nucl. Instr. and Meth. **A257** (1987) 215

13. I.P. Dufour et al., Nucl. Instr. and Meth. **A248** (1986) 267

14. L.H. Harwood et al., Workshop on Phase II Apparatus NSCL (1982)

15. K.L. Brown et al., SLAC 75, Stanford (1982)

16. Th. Schwab, PhD. thesis, University Giessen, in preparation

17. Th. Schwab et al., Contribution to the Spring Meeting of DPG (1988)

18. K.H. Schmidt et al., Nucl. Instr. Meth. **A260** (1987), 287

19. Workshop on Experiments and Experimental Facilities at SIS/ESR GSI Report 7-87 (1987)

POSSIBILITIES AND LIMITS OF THE MOMENTUM-LOSS ACHROMAT

K.-H. Schmidt, P. Armbruster, H. Geissel, G. Münzenberg, K. Sümmerer
GSI Darmstadt, FRG

H.-G. Clerc, E. Hanelt
Institut für Kernphysik, TH Darmstadt, FRG

J.P. Dufour, R. Del Moral, F. Hubert, D. Jean, M.S. Pravikoff, A. Fleury
C.E.N Bordeaux, Gradignan, France

H. Delagrange, A.C. Mueller, Y. Schutz
CANIL, Caen, France

J. Fréhaut, M. Beau, G. Giraudet
Commissariat à l'Energie Atomique
Centre d'Etudes de Bruyères-le-Chatel, France

Recently, an impressing number of nuclei became for the first time accessible to observation or to investigations as secondary beams from projectile-fragmentation reactions. Fig. 1 shows part of those as taken from refs. [1-20] on a chart of nuclides.

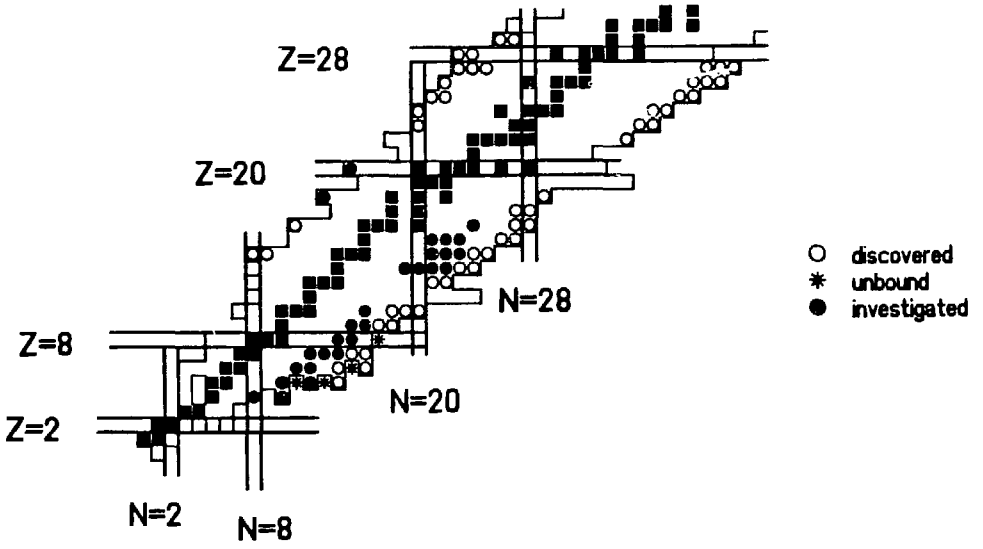

Fig. 1: Some isotopes which were observed (open symbols) or spectroscopically investigated (full symbols) for the first time as secondary beams [1-20].

As demonstrated in fig. 1, the investigation of secondary beams is not limited by their chemical properties. In contrast to Isolde-type mass separators, each nucleus is accessible, if its production rate is sufficiently high. For several of those investigations an isotopical separation was necessary. Until now, the work on secondary beams concentrates on light nuclei.

While planning the Darmstadt fragment separator [21] at SIS-ESR, we tried to understand better the isotopical separation of projectile fragments. For this purpose, we made some model calculations [22,23] and several experiments [19,20] at GANIL by using the magnetic spectrometer LISE [24] as a momentum-loss achromat with a profiled intermediate degrader.

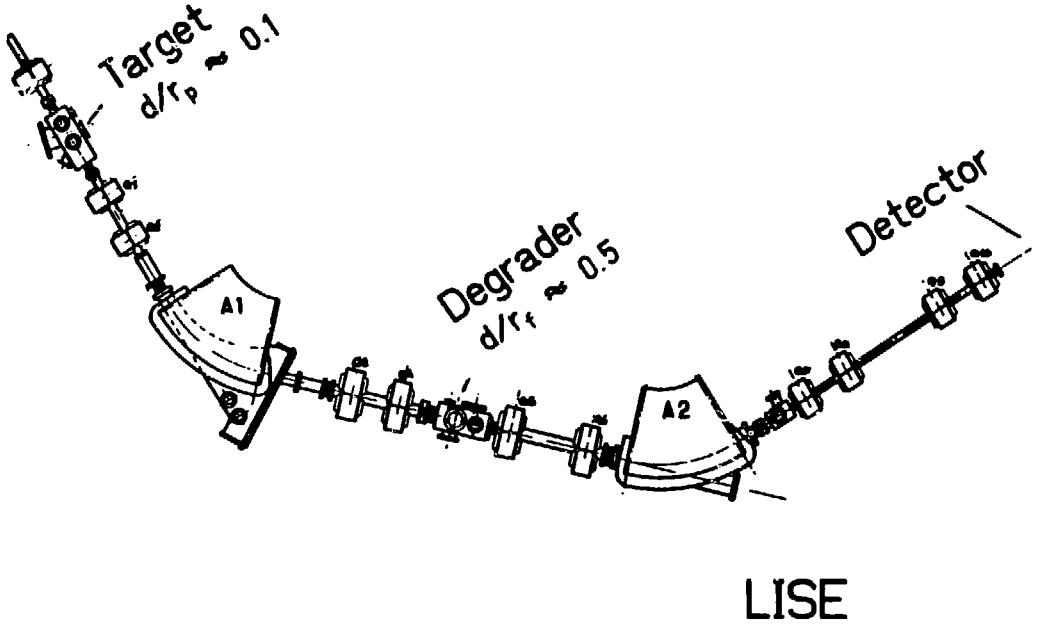

Fig. 2: The magnetic spectrometer LISE, operated as a momentum loss achromat for isotopic separation of projectile fragments.

Although the energy of GANIL is limited to about 60 MeV/u, the experiments with LISE were very important for our understanding of the separation method. Moreover, we extended our knowledge on the techniques of spectroscopic investigations on nuclei at the exit of in-flight separators.

The separation quality achieved with LISE is illustrated in the following figures. Fig. 3 shows the intensities of the nuclei at the exit of the separator in a typical case. This result has been obtained by recording a ΔE-TOF spectrum at the exit of LISE by use of a silicon surface-barrier

detector and the micro structure of the beam. For comparison, the result of a model calculation is shown. Althoug in the calculation some quantities as the specific energy loss are not known experimentally with sufficient accuracy, the two patterns are very similar. This encourages us to give some confidence on our model calculations also for nuclei of higher energy and mass.

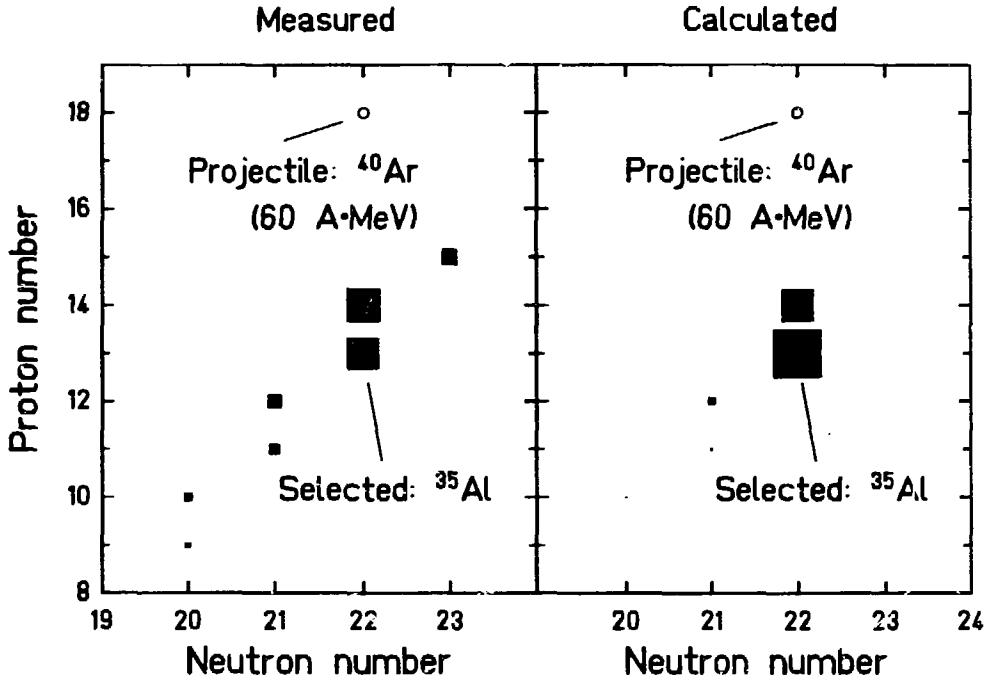

Fig. 3: Intensities of nuclei at the exit of LISE which was operated as a high-resolution in-flight isotopic separator. a) Experimental result. b) Prediction of a model calculation [23]. The calculation is performed on an absolute scale. The model was not able to predict the cross section of ^{38}P [25]. The area of the symbols is proportional to the intensity.

In order to illustrate the quality of the separation and the kind of spectroscopic investigations which have been achieved at LISE, fig. 4 shows a γ spectrum of ^{30}Mg. Note that the γ lines of ^{30}Mg and ^{30}Al dominate the spectrum. ^{30}Al is produced by β decay of the chosen fragment ^{30}Mg in the catcher. Any γ lines of cross contaminants hardly exceed the level of the background. γ-spectroscopic studies were made for the first time on about 15 neutron-rich nuclei from ^{17}C to ^{40}S [20].

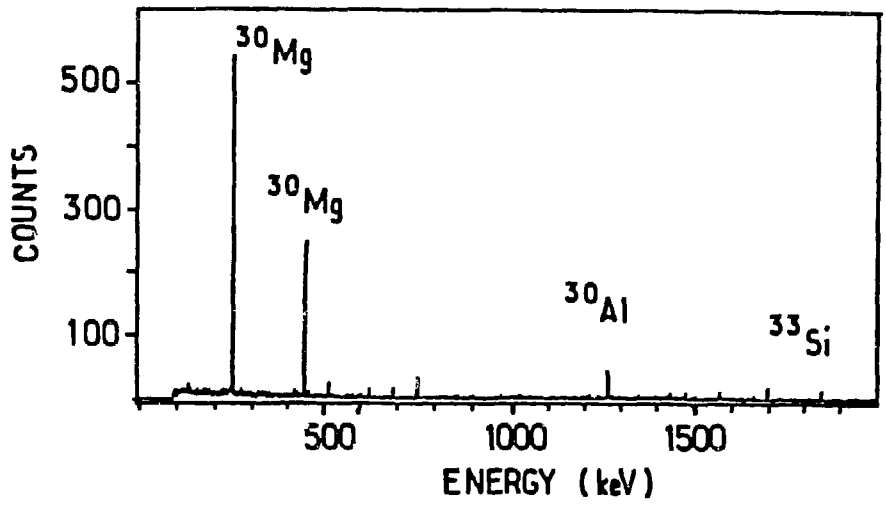

Fig. 4: γ spectrum recorded at the exit of LISE. The separator was tuned to select ^{30}Mg. From ref. [22].

In a recent experiment at LISE, the β-delayed neutron emission of ^{17}B has been investigated. For the first time, there is evidence for a β-4n process [20]. In these rather sophisticated spectroscopic investigations a high degree of isotopic separation is required.

At the new accelerator SIS at GSI heavy ions up to uranium will be available with energies of 1 to 2 GeV•A. In our model calculations [23] we tried to estimate the separation properties of a momentum-loss achromat under these conditions.

Fig. 5 shows that the operation domain is limited. The lower energy limit is given by the condition that the ions are fully stripped. Below this energy a high level of cross contaminants with other ionic charge states is present. The upper energy limit is given by the increasing amount of secondary reactions in the intermediate degrader. For a sufficient isotopic-separation quality, a degrader thickness of about half the range of the projectile fragments is required. If the fragments are stopped in a catcher behind the separator, once again about the same amount of fragments undergoes a secondary reaction. Obviously, the energies available at SIS are well adapted to this separation method.

In our calculations, the total nuclear reaction cross section according to ref. [26] was included. In addition, the total cross section for

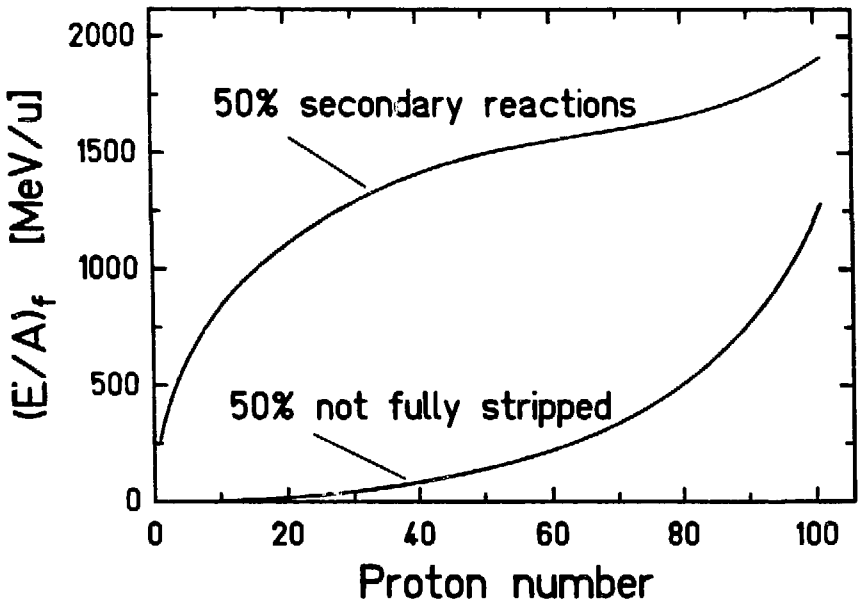

Fig. 5: Operation domain of the momentum-loss achromat.

electromagnetic dissociation was considered as described in [23]. Each reaction type which changes the nuclear composition of the fragment leads to a loss of the selected fragment. E.g. there is no difference between the loss of one neutron and fission.

The cross contaminants due to different charge states and secondary reactions are suppressed to a high degree by the second magnetic selection and an additional range selection. In addition, several high-resolution detectors at the exit of the separator may serve to detect the contaminations.

Another important feature is the selection quality. The fig. 6 shows the calculated transmission values in a medium-mass and a heavy-mass region. The separation quality decreases slightly with increasing mass. Due to the sufficiently high beam energy of SIS and the high magnetic resolving power of the fragment separator, our calculation yields even in the most unfavorable case a relative transmission of the selected fragment of more than 50% at the exit of the separator.

Some kinds of cross contaminants are not considered explicitely in fig. 6: those produced by secondary reactions in the degrader or in the stopper material and those originated by ionic-charge changing processes in the target and in the intermediate degrader. These processes are discussed in more detail

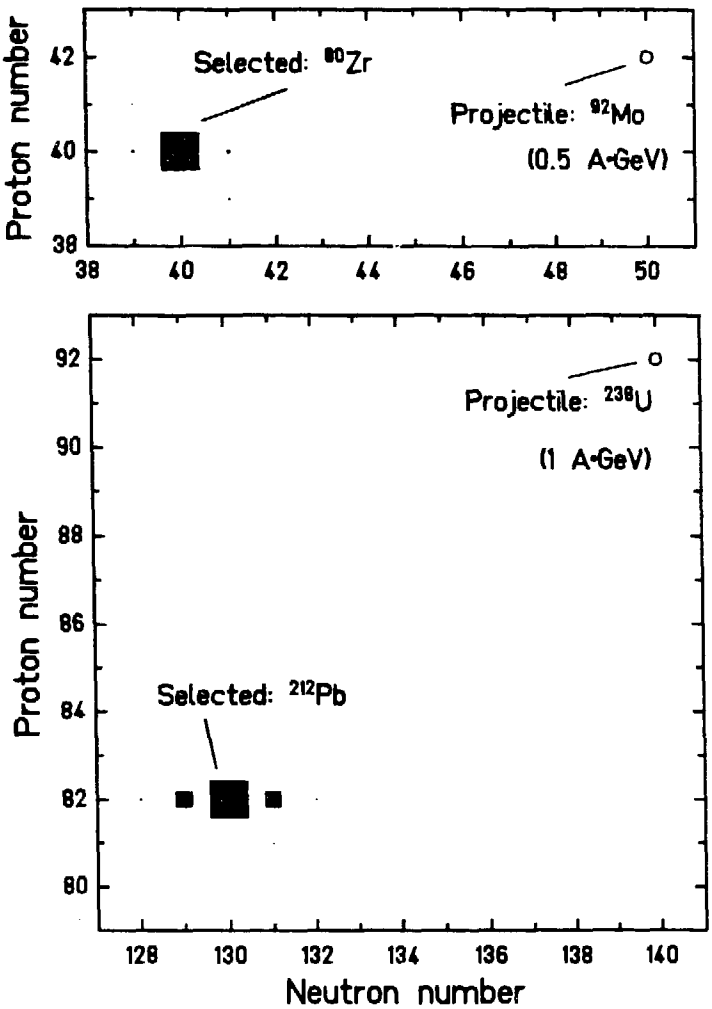

Fig. 6: Transmission values on a chart of nuclides a) when ^{80}Zr is selected, b) when ^{218}Pb is selected.
Operation conditions: Magnetic resolution at the intermediate dispersive focal plane: $p/\Delta p = 1500$.
a) Beam: ^{92}Mo, 500 MeV•A.
Be target ($d/r_p = 0.2$).
Pb degrader ($d/r_f = 0.4$).
Loss due to secondary reactions of the fragments in target, degrader and stopper: 31 %.
b) Beam: ^{238}U, 1 GeV•A.
Be tartet ($d/r_p = 0.05$).
Pb degrader ($d/r_f = 0.4$).
Loss due to secondary reactions of the fragments in target, degrader and stopper: 54 %.

in the following. In addition to the magnetic deflection we will discuss an additional range selection which can be realized by implanting the fragments in a catcher foil just covering the range distribution of the selected isotope at the exit of the separator. Most of the energy is degraded in an homogenious predegrader just in front of the catcher foil. By use of special detectors still other selection criteria may be important.

Secondary nuclear reactions in the target act on the production rates of different isotopes and on their momentum distributions. The influence on the selection quality is expected to be weak. There is no influence at all on the second selection criterium.

All nuclei with an A/Z ratio close to that of the selected fragment reach the intermediate degrader and may undergo secondary reactions. However, most of them are suppressed by the second magnetic selection; either they are not transported at all to the final detector position or they are spread over a large range of deflection angles and their intensity at the detector position is reduced because the achromaticity condition is generally not met. An additional suppression especially for light nuclei with their long ranges is achieved by the range selection.

If the fragments are to be stopped in a catcher, the highly separated secondary beam may produce additional secondary reaction products in the predegrader. The beam energy can always be chosen to ensure that not more than 50 % of the seperated beam undergoes secondary reactions (see fig. 5). Therefore, the total amount of secondary reaction products is limited to this fraction. A great part of those may be suppressed by the range selection. The most important contaminants of this kind are those with a few nucleons less than the selected fragment.

The beam energy should be chosen high enough, that most part of the secondary reaction products leaving the target are fully ionized. If charge-changing effects occur in the intermediate degrader, the spectrometer will separate reaction products with different nuclear composition. However, these cross contaminants are nearly totally suppressed by an additional range selection.

We intend to test our calculations as soon as possible at the magnetic spectrometer SPES 4 at the SATURNE accelerator with high-energetic Ar and Kr projectiles.

We hope that in the future the fragment separator will be a standard and versatile instrument for the production und separation of radioactive isotopes. We are presently witnessing the first period of this developement at the LISE magnetic spectrometer at GANIL and at other places.

REFERENCES

[1] T. J. M. Symoms, Y.P. Viyogi, G. D. Westfall, P. Doll, D. E. Greiner, H. Faraggi, P. J. Lindstrom, D. K. Scott, H. J. Crawford, C. McParland, Phys. Rev. Lett. 42 (1979) 40

[2] G. D. Westfall, T. J. M. Symons, D. E. Greiner, H. H. Heckmann, P. J. Lindstrom, J. Mahoney, A. C. Shotter, D. K. Scott, H. J. Crawford, C. McParland, T. C. Gelbke, J. M. Kidd, Phys. Rev. Lett. 43 (1979) 1859

[3] J. D. Stevenson, P. B. Price, Phys. Rev. C24 (1981) 2102

[4] J. A. Musser, J. D. Stevenson, Phys. Rev. Lett. 53 (1984) 2544

[5] J. P. Dufour, S. Beraud-Sudreau, R. Del Moral, H. Emmermann, A. Fleury, F. Hubert, C. Poinot, M. Pravikoff, J. Frehaut, M. Beau, A. Bertin, G. Giraudet, A. Huck, G. Klotz, C. Miehe, C. Richard-Serre, H. Delagrange, Z. Phys. A319 (1984) 237

[6] J. Äysto, D. M. Moltz, X. J. Xu, R. E. Reiff, Joseph Cerny, Phys. Rev. Lett. 55 (1985) 1384

[7] M. Langevin, E. Quiniou, M. Bernas, J. Galin, J. C. Jacmart, F. Naulin, F. Pougheon, R. Anne, C. Detraz, D. Guerreau, D. Guillemaud-Mueller, A. C. Mueller, Phys. Lett. 150B (1985) 71

[8] D. Guillemaud-Mueller, A. C. Mueller,D. Guerreau, F. Pougheon, R. Anne, M. Bernas, J. Galin, J. C. Jacmart, M. Langevin, F. Nolin, E. Quiniou, C. Detraz, Z. Phys. A322 (1985) 415

[9] M. Langevin, D. Guillemaud-Mueller, M. G. Saint-Laurent, R. Anne, M. Bernas, J. Galin, D. Guerreau, J. C. Jacmart, S. D. Hoath, F. Naulin, F. Pougheon, E. Quiniou, C. Detraz, Nucl. Phys. A455 (1986) 149

[10] M. S. Curtin, L. H. Harwood, J. A. Nolen, B. Sherrill, Z. Q. Xie, B. A. Brown, Phys. Rev. Letters 56 (1986) 34

[11] A. Gillibert, L. Bianchi, A. Cunsolo, B. Fernandez, A. Foti, J. Gastebois, Ch. Gregoire, W. Mittig, A. Peghaire, Y. Schutz, C. Stephan, Phys. Lett. B176 (1986) 317

[12] C. Detraz, Proc. Int. Nuclear Physics Conf., Harrogate 1986, Preprint GANIL P.86-20

[13] D. Guillemaud-Mueller, Int. School-Seminar on Heavy Ion Physics, Dubna 1986, Preprint GANIL P.86-25 and to be published

[14] A. C. Mueller, 25. Winter Meeting on Nuclear Physics, Bormio 1987, Preprint GANIL P.87-06

[15] M. G. Saint Laurent, J. P. Dufour, R. Anne, D. Bazin, V. Borrel, H. Delagrange, C. Detraz, D. Guillemaud-Mueller, F. Hubert, J. C. Jacmart, A. C. Mueller, F. Pougheon, M. S. Pravikoff, E. Roeckl, Phys. Rev. Lett. 59 (1987) 33

[16] W. Mittig, J. M. Chouvel, Zhan Wen Long, L. Bianchi, A. Cunsolo, B. Fernandez, A. Foti, J. Gastebois, A. Gillibert, C. Gregoire, Y. Schutz, C. Stephan, Phys. Rev. Lett. 59 (1987) 1889

[17] V. Borrel et al., Preprint ORSAY/GANIL (1987)

[18] D. Guerreau, J. Phys. C-4, 47 (1986) 207

[19] J. P. Dufour, R. Del Moral, A. Fleury, F. Hubert, D. Jean, M. S. Pravikoff, H. Delagrange, H. Geissel, K.-H. Schmidt, Z. Phys. A324 (1986) 487

[20] J. P. Dufour, R. Del Moral, F. Hubert, D. Jean, M. S. Pravikoff, A. Fleury, H. Delagrange, A. C. Mueller, K.-H. Schmidt, E. Hanelt, K. Sümmerer, J. Frehaut, M. Beau, G. Giraudet, Contrib. to the 5th Conf. Nuclei far from Stability, Rosseau Lake (Canada), Sept. 1987

[21] H. Geissel, P. Armbruster, B. Franczak, B. Langenbeck, O. Klepper, F. Nickel, E. Roeckl, D. Schardt, K.-H. Schmidt, D. Schüll, K. Sümmerer, G. Münzenberg, J. P. Dufour, M. S. Pravikoff, H.-G. Clerc, E. Hanelt, T. Schwab, H. Wollnik, B. Sherrill, Projectile-Fragment Separator, Proposal for the SIS-ESR Experimental Programme 1987 and contribution to this conference

[22] J. P. Dufour, R. Del Moral, H. Emmermann, F. Hubert, D. Jean, C. Poinot, M. S. Pravikoff, A. Fleury, H. Delagrange, K.-H. Schmidt, Nucl. Instr. and Methods A248 (1986) 267

[23] K.-H. Schmidt, E. Hanelt, H. Geissel G. Münzenberg, J. P. Dufour, Nucl. Instr. and Methods A260 (1987) 287

[24] R. Anne, D. Bazin, A. C. Mueller, J. C. Jacmart, M. Langevin, Nucl. Instr. and Methods A257 (1987) 215

[25] K. Sümmerer, in: GSI annual report 1986 (GSI, Darmstadt, 1987)

[26] S. Kox, A. Gamp, C. Perrin, J. Arvieux, R. Bertholet, J. F. Bruandet, M. Buenerd, Y. El Masri, N. Longequeue, F. Merchez, Phys. Lett. 159B (1985) 15

Atomic Physics, Nuclear Structure, and Electromagnetic Processes

CHANNELING OF RELATIVISTIC URANIUM*

Nelson Claytor†
Materials and Chemical Sciences Division
Lawrence Berkeley Laboratory
University of California
Berkeley, California 94720

This paper describes the channeling of relativistic uranium ions in silicon single crystals, and some interesting physics which we investigated using this technique. In particular, we investigated the electron impact ionization of highly stripped, high–Z ions, which it has not previously been possible to investigate. Electron impact ionization is important in understanding the high temperature plasmas encountered in magnetic fusion.

I. Channeling

Channeling takes advantage of the fact that when one "looks through" a single crystal along one particular direction, one can "see" all the way through the crystal. In other words, since the atoms are arranged in a particular periodic structure, there are "channels" along which there are no nuclei. This is shown in Figure 1 for the <110> axis of silicon, which was used in this experiment. In the figure, the ion is coming out of the page at the viewer, and the hexagonal channel extends back into the page. If an incident ion is to channel, its trajectory must be such that it makes only large impact parameter collisions with the atoms of the crystal, and thus is scattered by the atoms only through very small angles. We may see this if we note that for positive ions, the channel potential is very nearly parabolic[1]. Thus if the incident particle has a sufficiently small transverse

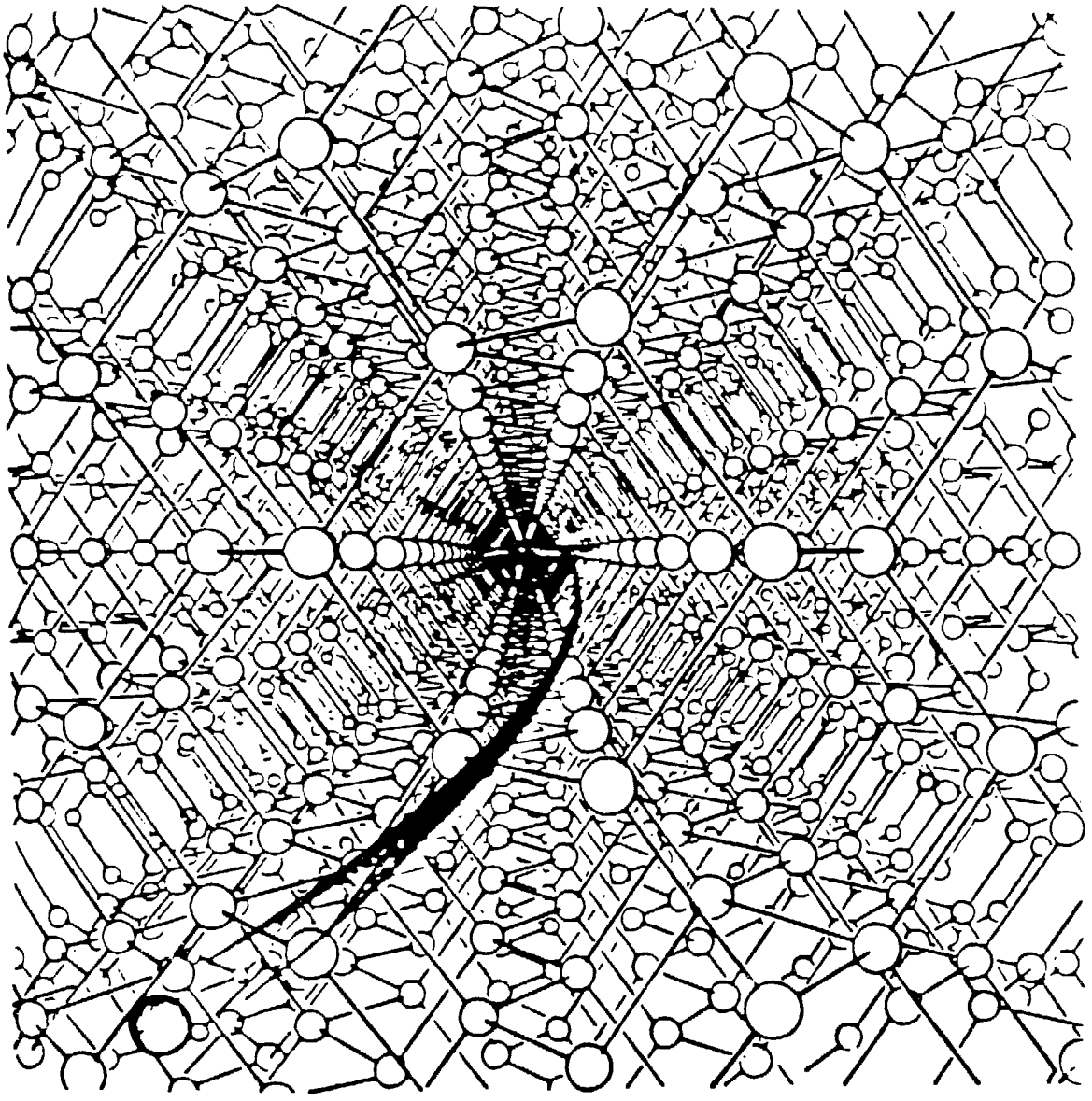

Figure 1. Artist's conception of channeling at the microscopic level. The computer–generated image is of an ion traveling toward the viewer in the <110> axis of silicon. (From W. Brandt, "Channeling in Crystals," ©1968 Scientific American.)

energy, it tends to make only small oscillations about the center of this well. If, however, a large transverse energy is imparted to the particle by a small impact parameter Coulomb collision with an atom in the crystal, the particle is removed from the channel potential well and assumes a random trajectory through the crystal.

We determine whether channeling has taken place as follows. It is clear from Figure 1 and the explanation above that if an ion channels, it can only undergo collisions with the electrons of the target. In the Bethe formula for the ionization cross section of a heavy ion in matter[2], there are terms in Z_t and in Z_t^2, where Z_t is the atomic number of the target. The term in Z_t is the term corresponding to electron impact ionization, while the term in Z_t^2 corresponds to Coulomb collisions with the nuclei of the crystal. In silicon (Z=14), the contribution to the cross section from electron impact ionization is 14 times smaller than the contribution from Coulomb collisions with the nuclei. Thus we would expect that the fraction of incident ions which are ionized in the crystal would be much smaller when the ions follow a channeling trajectory than when the ions follow a random trajectory. This expectation is borne out rather nicely by experiment, as is shown in Figure 2. The two graphs in the figure show the fraction of each charge state which emerged from the crystal when the crystal was at a random orientation to the incident beam (a) and when the <110> axis was aligned with the beam (b). In each case the incident charge state was lithium–like U^{89+}. When the crystal was aligned with the beam, a much larger fraction of U^{89+} survived than when the crystal was in a random orientation to the beam. Furthermore, when the crystal was aligned with the beam, the peak corresponding to U^{89+} was much narrower than when the crystal was aligned randomly. This indicates that there was a smaller

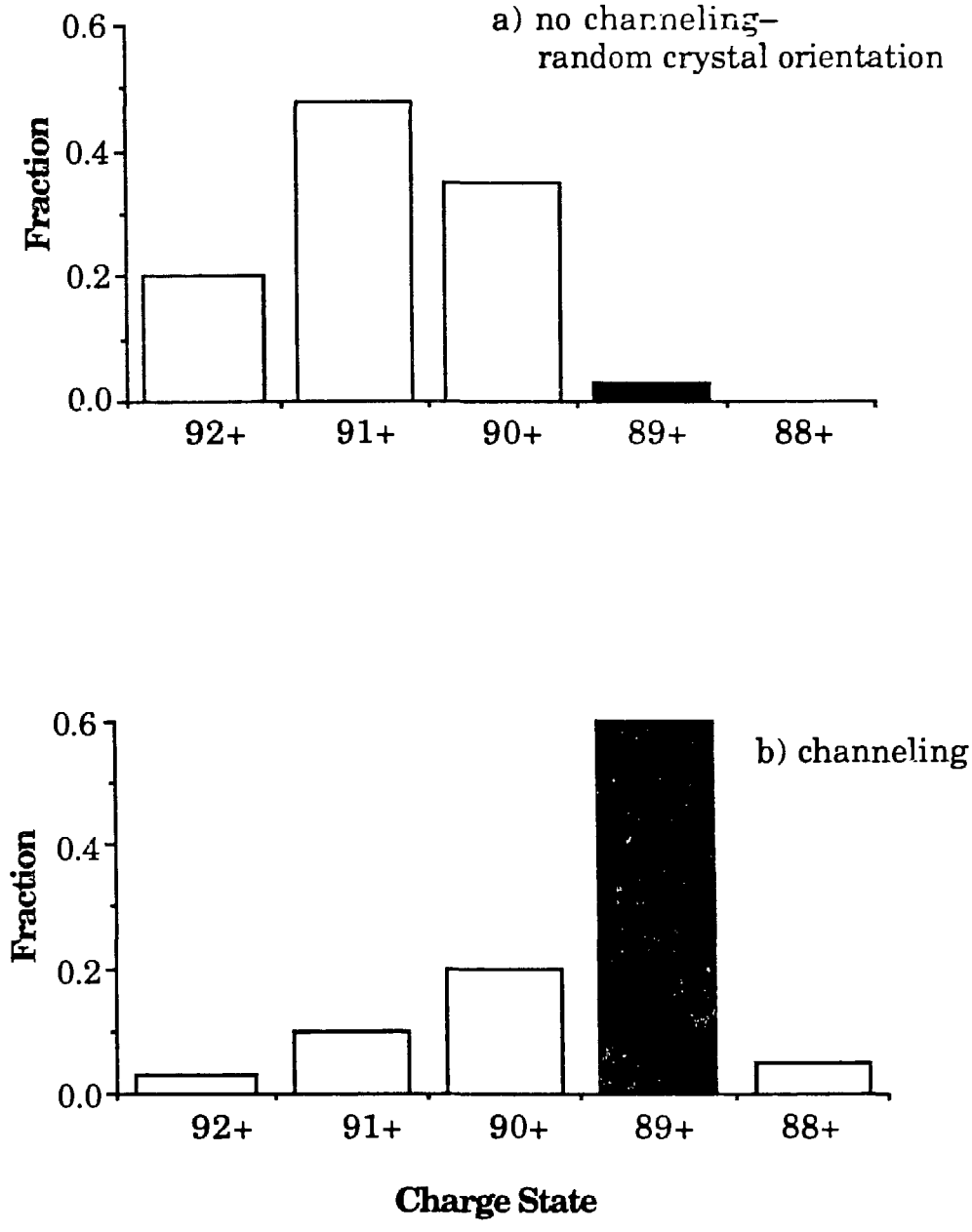

Figure 2. Charge state distributions measured for U^{89+} incident on a 370μ Si crystal. Note that in a), for a crystal oriented randomly to the incident beam, the fraction of U^{89+} is very small, while in b), for a crystal oriented with its <110> axis along the incident beam, the fraction of U^{89+} is quite large. This provides a graphic demonstration of channeling.

degree of multiple small–angle Coulomb scattering from the nuclei of the crystal when the crystal was aligned with the beam, as we would expect from the discussion above.

II. Electron impact ionization

Previous measurements of electron impact ionization have used the technique of crossed ion–electron beams[3]. This technique, however, is incapable of performing measurements on high–Z, highly stripped ions such as few–electron Fe, which is seen in magnetic fusion reactors. (We used few–electron Fe ions in the initial tests of our apparatus.)

Channeling is useful for electron impact ionization measurements because an ion which channels is only able to have collisions with the nearly–free valence electrons of the crystal in which it channels; small–impact–parameter Coulomb collisions with the target nuclei are suppressed. Thus to the incident projectile ion, the crystal appears as a gas of free electrons moving toward it with a velocity equal to that of the projectile (in this case v=0.72c, so that the electrons have an energy E=224keV).

III. Experiment

The experimental apparatus is shown schematically in Figure 3. The salient features are the collimators, which allowed us to achieve an emittance of 0.75π mm–mr; the goniometer, which allowed angular positioning about two axes to $1.25 * 10^{-4}$ degrees; and the dipole spectrometer magnet, which separated the charge states in space for viewing on our position–sensitive detector. Operationally, the experiment involved first finding the <110> axis of each silicon crystal used, and then measuring charge–state distributions for various incident charge states in

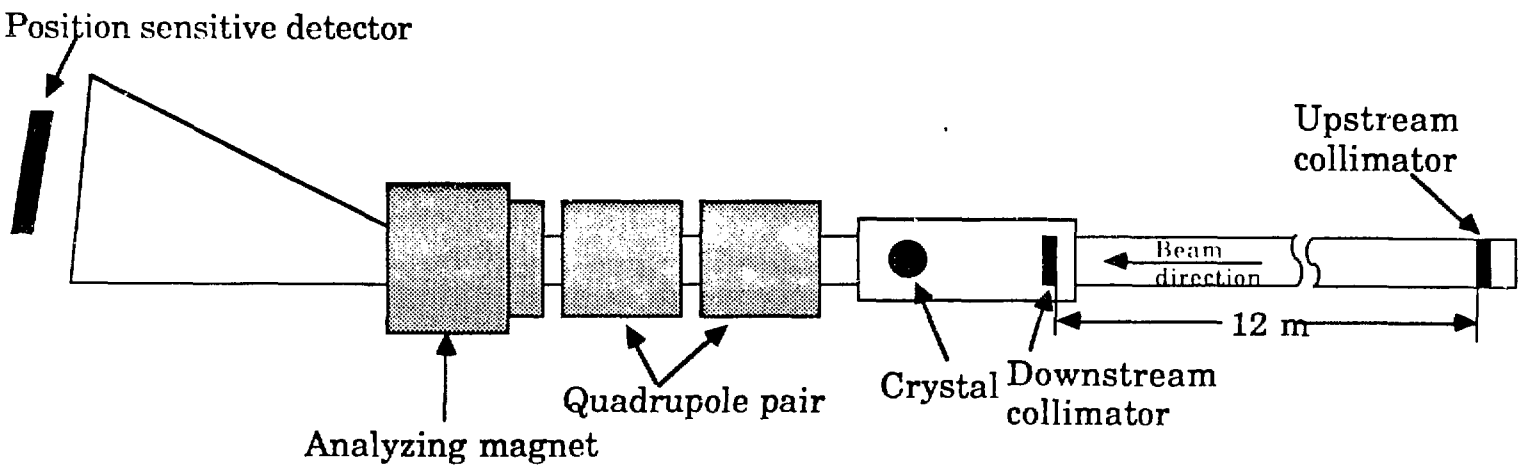

Figure 3. Configuration of the Bevalac experimental area for channeling. Main features are noted in the text.

both on– and off–axis crystal orientations. Finding the axis of the crystal presented some difficulty, since the channeling peak was only 0.017° wide. The criterion used for finding the axis of the crystal was that the observed fraction of the incident charge state rose dramatically when the channeling peak was reached. Measurements were performed using incident charge states from 88+ (Be–like) to 91+ (H–like).

The data were analyzed to give electron impact ionization cross sections for K and L1 shell electrons in U. A computer program employing the method of least squares (due to Betz[4]) was used to fit cross sections to the charge–state spectra. This yielded cross sections in units of barns/target atom; we needed to obtain the effective number of electrons per target atom order to compare with theories of electron impact ionization.

We measured the effective number of electrons per target atom as follows. It is necessary that the only electron capture mechanism employed by ions which channel is radiative electron capture, since nonradiative capture is a three–body mechanism involving the target nucleus. We took the ratio of our measured radiative electron capture cross sections for channeled ions to those measured for ions traveling in bulk material (random trajectories) by Anholt et al.[5] to obtain a value for the electron density in the channel relative to that in bulk material. We then divided the original cross sections (in barns/target atom) by (14 * relative electron density) to obtain cross sections in barns/electron.

IV. Experimental results

The results obtained are shown in Table 1. Several theoretical values are listed for comparison. We can see that the theories are not in complete accord with the experimental results, even given the large uncertainties in

the experimental cross sections. The better agreement of theory with the experimental results for the L shell electrons than for the K shell electrons suggests that the theories may not take fully into account the relativistic nature of the inner–shell electrons in high–Z ions.

Table 1.

Charge	Experimental result	Theories		
		Scofield[6]	scaled from Lotz[7]	Younger[8]
88+	42	60	25.4	21.5
89+	27	32	13.4	11.1
90+	11	3	1.4	1.7
91+	3.9	1.5	0.7	0.8

All cross sections are in barns/electron. Margin of error in experimental results is approximately a factor of two.

*) We thank Joe Jaklevic, Lynette Levy, Paul Luke, and Jack Walton. We especially thank the operators, staff, and management of the Bevalac for making experiments with few–electron uranium possible. This work was supported by the Director, Office of Energy Research, Office of Basic Energy Sciences, Chemical Sciences Division of the U.S. Department of Energy under Contract No. DE–AC–03–76SF00098 (LBL) and by the Office of High Energy and Nuclear Physics, Nuclear Science Division of the U.S. Department of Energy under Contract No. DE–AC05–84R21400 with Martin Marietta Energy Systems Inc. (ORNL).

†) This work was performed in collaboration with B. Feinberg and H. Gould from Lawrence Berkeley Laboratory and C.E. Bemis Jr., J. Gomez del Campo, C.A. Ludemann, and R. Vane from Oak Ridge National Laboratory.

References:

1. M.W. Thompson, in **Channeling** (ed. D.V. Morgan), p.18ff. (1973)

2. H.A. Bethe, Ann. Phys. (Leipzig) **5**, 325. (1930)

3. D.H. Crandall, R.A. Phaneuf, D.C. Gregory, A.M. Howard, D.W. Mueller, T.J. Morgan, G.H. Dunn, D.C. Griffin, and R.J.W. Henry, Phys. Rev. A **34**, 1757. (1986)

4. S. Datz, H.O. Lutz, L.B. Bridwell, C.D. Moak, H.D. Betz, and L.D. Ellsworth, Phys. Rev. A **2**, 430. (1970)

5. R. Anholt, W.E. Meyerhof, X.-Y. Xu, H. Gould, B. Feinberg, R.J. McDonald, H.E. Wegner, and P. Thieberger, Phys. Rev. A **36**, 1586. (1987)

6. J. Scofield, Phys. Rev. A **18**, 963. (1978)

7. W. Lotz, Report IPP 1/50, Institut für Plasmaphysik, Garching bei München. (1967)

8. S.M. Younger, Phys. Rev. A **22**, 111 (1980); S.M. Younger, Phys. Rev. A **22**, 1425 (1980); S.M. Younger, Phys. Rev. A **24**, 1278 (1981); private communication, S.M. Younger to H. Gould, 1987.

STUDY OF NUCLEAR STRUCTURE USING RADIOACTIVE BEAMS*

Susumu Shimoura
Department of Physics
Kyoto University
Kyoto 606, Japan

1. Introduction

Projectile fragmentation process in high-energy heavy-ion reaction provides us a possibility of using beams of radioactive nuclei, because of two useful properties. One is large production cross sections of radioactive nuclei over a wide range in the nuclear chart. The other is the kinematical focusing of produced nuclei; i.e. almost all fragments are emitted into a very narrow cone with almost same velocities as that of the projectile. Thus, high-energy radioactive beams can be produced by simple separation technique.

Since particle-stable nuclei in a wide range of nuclear chart can be produced and used as beams for nuclear reaction, we can investigate nuclear structures of various beam nuclei by regarding a target nucleus as a probe. It is possible not only to find new phenomena but also to expand our knowledge of nuclear structures systematically by changing various parameters such as neutron numbers, isospin, mass excess and so on.

Here I present two topics resulting from the experiments performed at HISS beam line at Bevalac. One is the systematic study of the nuclear radii of light unstable nuclei determined by the measurements of interaction cross sections. The isospin dependence of the matter radii of isobars has been investigated. The other is the fragmentation of the ^{11}Li nucleus which shows a different feature from the fragmentation of the stable nuclei.

2. Interaction Cross Section and Nuclear Radii

The interaction cross sections were systematically measured for light (*p*-shell) nuclei at 0.8 GeV/nucleon at the BEVALAC[1,2]. The interaction cross section (σ_I) is defined by the total cross section of nucleon(s) removal from the projectile nucleus. This can be measured very precisely (within 1 %) by attenuation method.[1] At high energy, the

interaction cross sections are known to reflect the geometrical size of nucleus. The data[1] of Be and Li isotopes at 0.8 GeV/nucleon with different target nuclei shows the interaction cross section (σ_I) can be described by a sum of nuclear interaction radii (R_I) of a projectile (P) and target (T) as

$$\sigma_I(P,T) = \pi\,[R_I(P) + R_I(T)]^2\ , \qquad (1)$$

which shows separability of radii of projectile and target nuclei.

Although the nuclear interaction radius is a well defined quantity at 0.8 GeV/nucleon, the relation to the nucleon distribution is not clear without a help of model calculation. In addition, the nuclear interaction radius may be energy dependent at lower energy because of energy dependence of the nucleon-nucleon cross sections. As a nuclear size directly related to the nucleon distributions, root mean square (*rms*) radii are derived by fitting the interaction radii with a Glauber-type calculation. In this calculation, assumptions of three kinds of nucleon distributions give equal *rms* radii. As shown in Fig. 1, the charge *rms* radii for stable nuclei derived from the calculation are also consistent with those by electron scattering data. These results imply that the *rms* radii can be determined precisely from the nuclear interaction cross sections.

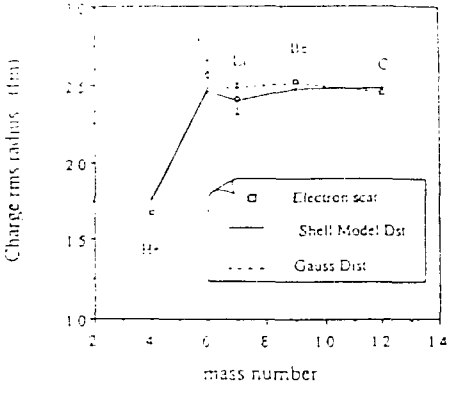

Fig. 1. Comparison of charge *rms* radii

The *rms* radii for light *p*-shell nuclei have been discussed in terms of isospin dependence.[2] The matter *rms* radii obtained for A = 6,7,8,9,11, and 12 isobars are shown in Fig. 2. A pair of nuclei with the same isospin show equal radii. This suggests the Coulomb force is not important for the nuclear radii in the light mass region. On the other hand, a nuclei with

a larger isospin shows a larger radius except for $A = 9$ isobars. A simple droplet model (dotted line) predicts *rms* radii are independent of isospin, *i.e.* data shows a stronger isospin dependence than this prediction. Such a strong isospin dependence can be explained by a Hartree-Fock calculation with a strong density-dependent effective interaction (SIII; dash-dotted line), whereas that with a density-independent interaction predicts weaker isospin dependence (SV; dashed line). This indicates an importance of density dependence of interaction to understand the radii of light nuclei.

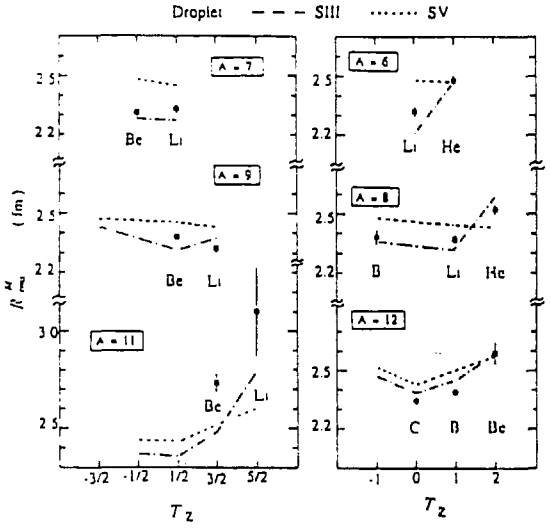

Fig. 2. Isospin dependence of the *rms* radii.

The abnormal behavior of $A = 9$ isobars, namely a larger radius of ^{9}Be than that of ^{9}Li, can be understood by a specific 2α+n cluster structure of ^{9}Be nucleus. The Hartree-Fock calculation does not take into account such a cluster correlation which is important to understand the structure of light ($N \sim Z$) nuclei. It is also interesting to study the cluster correlation in exotic nuclei. Recently, Hansen and Jonson[3] have proposed a model with weakly bound di-neutron cluster in the nuclei near neutron drip line. They predict the very large radius for ^{11}Li nucleus due to very weak binding of di-neutron with this model.

3. Fragmentation of Exotic Nuclei

Projectile fragmentation was extensively studied using beams of stable nuclei. One of the important findings is the regularity of the momentum distribution of the projectile fragments.[4] In high energy around 1 GeV/nucleon, the fragments have an isotropic Gaussian

momentum distributions in the projectile frame, and the width (σ) of the Gaussian is depend only on the mass numbers of the projectile (A_B) and the fragment (A_F). The dependence of A_B and A_F can be expressed as[5]

$$\sigma = \sigma_0 \sqrt{\frac{A_F (A_B - A_F)}{A_B - 1}} \qquad (2)$$

where σ_0 = 80 - 100 MeV/c. The normalized width σ_0 has been related to Fermi momentum (P_f) assuming a fast process:

$$\sigma_0 = P_f / \sqrt{5} , \qquad (3)$$

or temperature (T) assuming a slow process:

$$\sigma_0 = \sqrt{mkT \frac{A_B - 1}{A_B}} \qquad (4)$$

The assumption of the fast process can be extend to a finite nucleus. For one-nucleon removal fragments, the momentum distribution of the fragments reflects the momentum distribution of the removed nucleon at a surface region in the projectile nucleus.[6] The wave function of a nucleon at the surface region can be approximated to $\exp(-\kappa r)/r$, where κ is expressed by the reduced mass (μ) and the binding energy (ε) of a nucleon as $\kappa^2 = 2\mu\varepsilon$. This implies the momentum distribution of the fragments relates to the binding energy of the removed nucleon:

$$\sigma^2(A_F = A_B - 1) = f(\mu\varepsilon) \qquad (5)$$

$$\sim m\,\varepsilon\,(A_F / A_B) . \qquad (6)$$

The expression (6) is derived by approximating the Fourier transform of $\exp(-\kappa r)/r$ (Lorentzian) to a Gaussian. To extend this idea to a many-nucleons removal fragment (F), we assume the beam nucleus (B) can be expressed as :

$$B = (...((F + 1) + 2) +...+ n) , \qquad (7)$$

where removed nucleons are labeled as 1, 2, ..., n ($=A_B - A_F$) and i-th nucleon is bound by (F + 1 + ... + (i-1)) core with an average separation energy (<ε>) of the removed nucleons. Under this assumption we obtain momentum distributions of n-body nucleons. By integrating all the momentum coordinates of the n-body distributions except for the relative momentum between F and the center of mass of n nucleons, the momentum distribution of the fragment can be determined. If we use eq. (6), the width parameter (σ) of the Gaussian distribution is described as[7]

$$\sigma = \sqrt{m<\varepsilon>\frac{A_F(A_B - A_F)}{A_B}} \qquad (8)$$

This expression is equivalent with eq. (4) by changing temperature (kT) with the average separation energy of the removed nucleon (<ε>). This idea is applicable for a certain case such as weakly bound nuclei or nuclei with cluster correlation.

For stable nuclei, the expressions (4), (5), and (8) give consistent parameters (P_f = 180 - 220 MeV/c , temperature $kT \sim$ 8 MeV, or average separation energy <ε> ~ 8 MeV), although they are different standing points. How about radioactive (exotic) nuclei? Now we come to the fragmentation of ^{11}Li nuclei at 0.8 GeV/nucleon.[8]

Figure 4 shows the transverse momentum distribution of ^{9}Li fragment with a carbon target. A striking difference from the fragmentation of stable nuclei is the momentum distribution has two components Gaussian structure. One component has a wide width σ = 95 ± 12 MeV/c (σ_0 = 71 ± 9 MeV/c), and the other has a narrow width σ = 23 ± 5 MeV/c (σ_0 = 17 ± 4 MeV/c). Although the wide component is rather consistent with the systematic of the fragmentation of stable nuclei, it is difficult to consider two Fermi momenta or two temperatures in simple Fermi gas model or temperature description. The expression (7) predicts very narrow momentum distribution for ^{9}Li fragments because of a very low separation energy (150 ± 100) keV for two neutrons. Although this

expression gives too narrow width ($\sigma \sim$ 10 MeV/c), other corrections such as a neutron evaporation of particle-unstable ^{10}Li fragments and effect of di-neutron cluster could give a reasonable description.

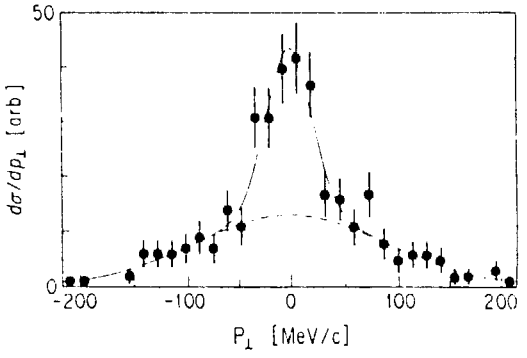

Fig. 3. Transverse momentum distributions of ^{9}Li fragment from ^{11}Li + C reaction at 0.8 GeV/nucleon

A narrow width of momentum distribution of ^{9}Li is equivalent to a small momentum fluctuation of the center of mass of two neutrons (di-neutron). This implies a longer decay constant of space wave function of di-neutron and gives a large *rms* radius of the di-neutron in the ^{11}Li nucleus. It also can be suggested that the large matter *rms* radius of ^{11}Li is mainly due to large tail of di-neutron wave function, *i.e.* neutron skin.

As a consequence of large tail of di-neutron wave function, Hansen and Jonson predict a large cross section of the electromagnetic dissociation (EMD) for high-Z target.[3] This process is known as a projectile fragmentation by a virtual photon from a strong relativistic Coulomb force by a high-Z target.[9] Figure 4 shows the transverse momentum distribution of ^{9}Li fragment from the ^{11}Li + Pb reaction. There can be seen only one wide component (σ = 71 ± 15 MeV/c). Another feature is that the partial cross section for this channel is 2570 ± 300 mb, whereas 215 ± 21 mb for a carbon target. The width of momentum distribution of fragments by EMD can be determined by the excitation energy of projectile nucleus after absorbing photon, which has a peak around the position of E1 giant resonance.[10] Therefore, this process does not give a narrow component which corresponds to 1 MeV or less excitation. The cross section of ^{9}Li fragments for a lead target by nuclear interaction can be estimated from that for a carbon target. It will be several hundred mb at most. This implies the EMD cross section for a lead target is about 2000 mb which is too large to see a narrow component

from nuclear interaction in the experimental error. The estimated EMD cross section is consistent with the prediction of Hansen and Jonson.[3]

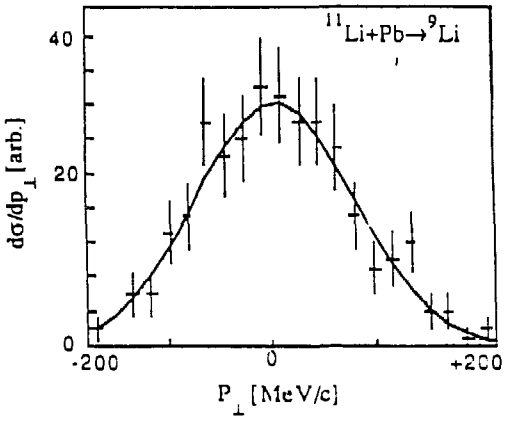

Fig. 4. Transverse momentum distributions of ^{9}Li fragment from ^{11}Li + Pb reaction at 0.8 GeV/nucleon

4. Conclusion

It is shown that the usage of radioactive beams gives us possibilities of studying nuclear structures in a wide range of nuclear chart. Nuclear radii are determined from measurements of nuclear interaction cross section. A study of isospin dependence of *rms* radii in light *p*-shell isobar gives us information on a density dependence of the effective interaction. Exotic features of the fragmentation of a very neutron rich nucleus, ^{11}Li, tell us not only information for the fragmentation process itself but also an exotic structure of ^{11}Li nucleus, *i.e.* existence of large neutron skin.

Although interesting results have been obtained, systematic measurement and quantitative description of data are not enough. As a next step, we have performed experiments to study (a) energy dependence of interaction cross section, (b) total EMD cross section for exotic nucleus through target-mass dependence of interaction cross section, (c) energy dependence of fragmentation of very weakly bound system, (d) isospin symmetry in fragmentation of an exotic mirror pair, (e) giant resonance of radioactive nucleus through EMD process.

Experiments by using radioactive beams will open new features of nuclear structure and nuclear reaction. By choosing various isotope beams, we can change various parameters which relate each other in the stable nuclei. This will give us various points of view how extend the conventional picture by the investigation of stable nuclei.

The author would like to express his great thanks to the colleague who contributed to the experiments (INS-LBL collaboration and INS-Osaka collaboration).

---

* Supported by U.S.DOE under contract No.DE-AC03-76SF00098 and by the Japan-U.S. Cooperative Research Program of the Japan Society for the Promotion of Science.

[1] I. Tanihata, Hyp. Int. **21**, 251 (1985); I. Tanihata *et al.*, Phys. Lett. **160B**, 380 (1985); I. Tanihata *et al.*, Phys. Rev. Lett. **55**, 2676 (1985)

[2] I. Tanihata *et al.*, RIKEN preprint RIKEN-AF-NP-60, July 1987, to be published in Phys. Lett. B

[3] P.G. Hansen and B. Jonson, Europhys. Lett. **4**, 409 (1987)

[4] D.E. Greiner *et al.*, Phys. Rev. Lett. **35**, 152 (1975)

[5] A. Goldhaber, Phys. Lett. **53B**, 306 (1974)

[6] T. Fujita and J. Hüfner, Nuclear Phys. **A343**, 493 (1980); J. Hüfner and M.C. Nemes, Phys. Rev. **C23**, 2538 (1981)

[7] S. Shimoura and I. Tanihata, Contribution to the XI Int. Conf. on Particle and Nuclei (PANIC), Kyoto April 1987. Abstract book p480 (1981)

[8] T. Kobayashi *et al.*, KEK Preprint 87- 78, Sept. 1987.

[9] D.L. Olson *et al.*, Phys. Rev. **C24**, 1529 (1981)

[10] D.L. Olson, private communication

NMR on β-Emitters around the A=40 Region*

K. Matsuta, Y. Noiiri, T. Minamisono, K. Sugimoto, K. Takeyama,
K. Omata#, Y. Shida#, I. Tanihata##, T. Kobayashi**,
S. Nagamiya+,K. Ekuni++, S. Shimoura++, J. R. Alonso@,
G. F. Krebs@, and T. J. M. Symons@

Osaka University, Toyonaka, Osaka 560, Japan
#INS, The University of Tokyo, Tanashi, Tokyo 188, Japan
##RIKEN, Wako, Saitama 351-01, Japan
**National Laboratory for High Energy Physics, Tsukuba,
Ibaragi 305, Japan
+The University of Tokyo, Tokyo 113, Japan
++Kyoto University, Kyoto 606, Japan
@LBL, Berkeley, Ca 94720, USA

1. Introduction

Nowadays radioactive secondary beam opened up the new field of nuclear physics. As an extension of the use of radioactive beam, measurement of the magnetic moment of mirror nuclei in the $f_{7/2}$ shell is in progress. The purpose of the work is to characterize the nuclear structure related to magnetic moment such as meson-exchange current and core polarization.

Since 1965, many active study had been made in the p- and the sd-shell, while this kind of study is very scarce in the $f_{7/2}$ shell. The magnetic moment for almost all the proton rich side nuclei of the $f_{7/2}$ shell mirror doublet which are β^+-emitters are left unknown except for ^{41}Sc whose magnetic moment had been determined by Minamisono et al.[1]. That is mainly because of difficulty in producing the nuclei and also in producing polarization in the nuclei. We developed new NMR technique combined with isotope separator for the purpose. After establishing the technique, systematic work in the region will be performed.

To establish the technique, NMR on β-emitting ^{39}Ca ($I^{\pi}=3/2^+$, $T_{1/2}$= 0.86 s, g=0.681) whose magnetic moment is known[2] were observed. In the experiment, ^{39}Ca was successfully produced

through the projectile fragmentation in heavy-ion reaction and polarized by so called tilted foil technique[3]. The experimental method for the technique is described in the following.

2. On-line isotope separation of short-lived nuclei

Projectile fragmentation in high-energy heavy-ion reaction is suitable for producing short-lived nuclei because of high production efficiency and kinematical momentum focus. Beam line No. 44 at the Bevalac as shown in Fig. 1 was constructed as an isotope separator for the purpose. Advantages in the isotope separation system are 1) high kinetic energy in the nuclei which helps deep implantation of the ions in suitable sample and 2) wide applicability even for short-lived nuclei which has the lifetime ranging from 1 (μs) to 1 (s) because of almost simultaneous isotope separation.

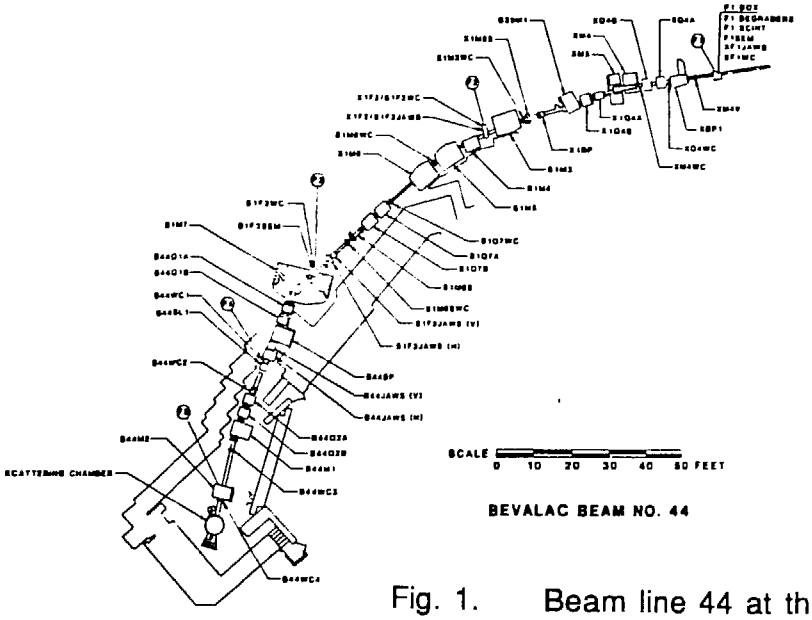

Fig. 1. Beam line 44 at the Bevalac.

In the experiment, ^{39}Ca was produced bombarding 1/2" Be target by the ^{40}Ca beam of 212 (MeV/A) extracted from the Bevatron at the first focus point F1. Various secondary beams produced in the target were rigidity analyzed by a series of magnets and ^{39}Ca of 108 (MeV/A) was selected by slit jaws at dispersive focus point F2 where the dispersion was $x/(\Delta p/p)=1.25$ (cm/%). Separated ^{39}Ca

secondary beam was led to achromatic focus point F3 to be analyzed by the difference in energy loss in the absorber. By the thickness controllable absorber and the analyzing magnet, secondary beam was re-analyzed to eliminate the mixture other than ^{39}Ca in the secondary beam.

In order to reduce the energy spread in the secondary beam, momentum compensator which is essentially the thin plastic wedge was used at F4. By the apparatus, the energy spread which is originally ±2 (MeV/A) was reduced down to ±0.3 (MeV/A). Such energy compensation is necessary for proper utilization of tilted foil technique to polarize the nucleus. After the second analysis, the beam energy was 50 (MeV/A). In order to stop the beam in the suitable sample sitting in the NMR chamber at F5, another thickness controllable energy absorber was used. After final absorber, the energy was about (5 ± 3) (MeV/A).

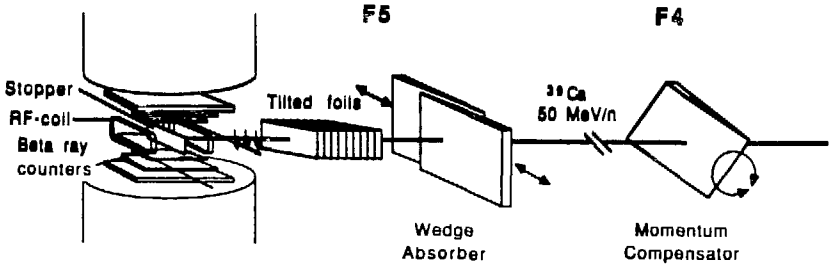

Fig. 2. Schematic view of experimental setup.

3. Tilted foil technique

Tilted foil assembly was instaled right after the final absorber as shown in Fig. 2 to produce the polarization in the ^{39}Ca. Great advantage in the technique is universal applicability for various kind of nuclei.

This technique consist of two steps. first step is to produce the atomic polarization in the beam by the asymmetrical interaction of the atomic beam with the tilted solid surface. Second step is to transfer atomic polarization to the nucleus through hyperfine interaction between atomic and nuclear spin.

In the first process, the charge state of the atomic beam is crucial for the technique. In the experiment, the three electron atom was dominant because of its energy around 5 (MeV/A).

Direction of the produced polarization can be predicted by torque model. In the actual condition as in Fig. 2, the direction of the polarization was downward.

4. NMR technique

Polarized ^{39}Ca beam was implanted into CaF_2 single crystal sample placed in the center of the magnet for external field of 4.8 (kOe) to preserve the polarization.

To detect the polarization, two sets of β-ray telescopes were placed above and below the sample relative to the polarization. Since the β-rays are emitted asymmetrically from the polarized nuclei, we can detect the polarization by the up/down counting rate ratio as

$$R = \frac{\text{Up count}}{\text{Down count}} \sim (1+2AP)G$$

,where P is the polarization, A is the asymmetry parameter which is predicted to be +0.8 for ^{39}Ca, and G is the geometrical asymmetry. In order to achieve NMR, rf magnetic field of 15(Oe) was applied perpendicular to the external field. Center frequency was 2.490 (MHz) and modulation was 100 (kHz) which correspond to g-factor of (0.680±0.027). The NMR effect was observed as a change in counter asymmetry (R).

5. Results and conclusion

β-rays emitted from the sample was measured and the time spectrum was obtained as shown in Fig. 3. Main component in the beam was the ^{39}Ca whose lifetime was determined to be 0.8640±0.0072 (s) which is consistent with the previous data[4]. The NMR effect $2\eta AP$ was obtained as shown in Fig. 4 where the correction factor for finite detector solid angle (η) was (>0.5). It was clearly demonstrated that the polarization was reversed as

inverting the tilt angle (α). Averaging the data from the separate runs, the effect was determined to be $2\eta AP = 0.72 \pm 0.24$ (%).

Thus the isotope separation and the polarization technique has been established. We are now ready for the systematic study of the magnetic moment for mirror doublets in the $f_{7/2}$ shell.

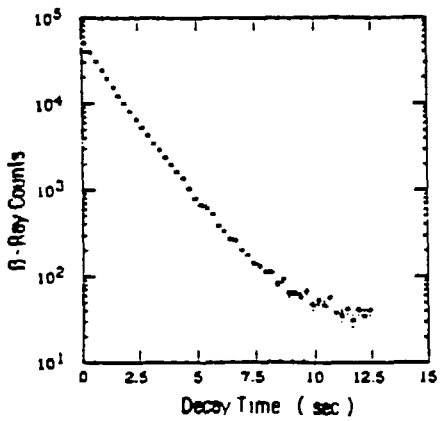

Fig. 3. β-ray time spectrum.

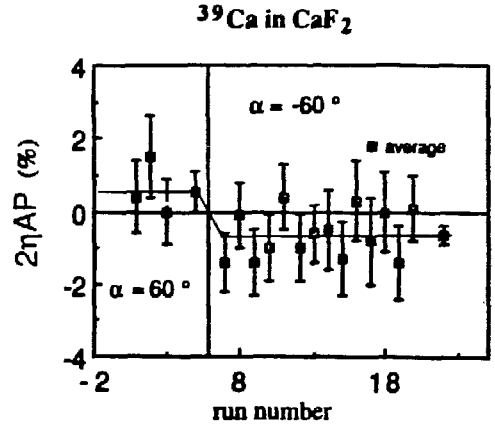

Fig. 4. NMR effect for ^{39}Ca.

Reference

1. T. Minamisono et al., J. Phys. Soc. Japan **34** Suppl.(1973) 158.
2. T. Minamisono et al., Phys. Lett. **61**B (1976) 155.
3. Y. Nojiri et al., Phys. Rev. Lett. **51** (1983) 180.
4. D.E. Alburger et al., Phys. Rev. C**8** (1973) 657.

* Supported by U.S.DOE under contract No. DE-AC03-76SF00098, by the Japan-U.S. Cooperative Research Program from the Japan Society for the Promotion of Science, and from the N.S.F. U.S.A., by the Grant in Aid for Scientific Research from the Ministry of Education, Culture and Science, Japan, and by the Yamada Science Foundation.

ELECTROMAGNETIC PROCESS AT RELATIVISTIC ENERGIES

Hans Emling
Gesellschaft für Schwerionenforschung mbH
6100 Darmstadt, W. Germany

1. Introduction

Electromagnetic excitations in pheripheral heavy ion collisions at (nearly) relativistic energies should yield large cross sections in particular for high-lying collective states. As the excitation probabilities per collision can approach unity, strong multi-step processes are expected which migh allow a study of multi-phonon giant resonances or of the coupling between giant resonances and nuclear surface modes. In addition, the process of electromagnetic excitation at high bombarding energies might give access to in-beam nuclear structure studies using secondary radioactive beams even when obtained with rather low intensities.

A proposal[1] for such a type of studies has been submitted by a collaboration of GSI Darmstadt and the universities at Bochum, Cracow, Frankfurt and Mainz to the program committee for the SIS/ESR facility presently being under construction at GSI. A short summary of that proposal will be presented in this paper.

2. Electromagnetic Excitation at Relativistic Energies

The maximum energy E_m^* that can be transferred by solely electromagnetic interaction at an impact parameter b is determined by the adiabadicity of the collision process i.e. the collision time τ and thus by the ion velocity β (in units of c; $\gamma = \sqrt{1-\beta^{2}}^{-1}$)

$$E^* \cong \hbar/\tau_c \cong \hbar\beta\cdot\gamma/b$$

For relativistic heavy ion collisions under conditions appropriate to SIS ($\gamma \cdot \beta \leq 2$) and at grazing impact ($b = R_1 + R_2$), energies up to about 30 MeV can thus be transferred in a single excitation step. This is quite in contrast to bombarding energies around the barrier for which $E^* \leq 2$ MeV, and therefore high-lying states are efficiently excited only in relativistic heavy ion energies.

Likewise from above expression one can read that for excitation energies below the adiabatic cut-off still large impact parameters contribute to the excitation thus giving a qualitative explanation for the large cross sections to be observed in relativistic heavy ion energies.

Quantitative estimates for excitation probabilities can be obtained in a semiclassical approach[2] or making use of the method of virtual quanta[3]. In fig. 1 we present total cross sections for the excitation of giant resonances of various multipolarities in ^{208}Pb scattered from a Pb target in function of the bombarding energy. Several features should be noted:

- all cross sections are essentially constant above a "threshold" energy around 300 MeV/u which is well within the range of SIS beam energies
- in the lower energy range different multipolarities show a different energy dependence that could be used to distinguish between them
- at higher energies the excitation to the isovector giant dipole (GDR) resonance dominates and even exceeds the geometrical cross section.

Cross sections of heavy-ion induced Coulomb dissociation have been measured by several groups at the BEVALAC[4,5] and also at CERN[6] and the experimental values seem to agree to the semiclassical predictions (see also the compilation of data in ref. 7).

We mention, that the total cross section to the GDR is approximately proportional to $Z_1^2 \cdot Z_2^{5/3}$ (Z_2 being the charge of the excited nucleus) and thus studies using two heavy reaction partners are favourable.

In table 1 we present the excitation probabilities per collision for particular systems at a grazing impact. For both, low-lying as well as high-lying collective states, probabilities close to one are obtained. This indicates on the one hand that the perturbative ansatz of description for such close collisions fails, on the other hand, however, that multistep processs are likely to occur. This seems to us to be the most important aspect because it gives the possibility to study phenomena which cannot be accessed otherwise. Of particular interest are

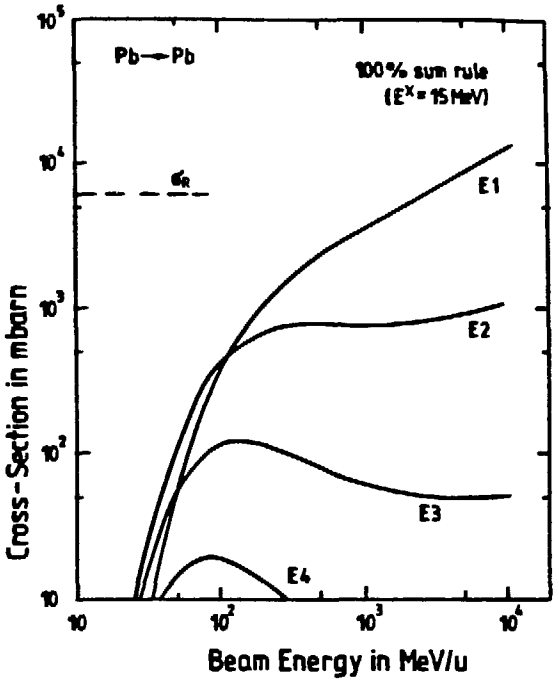

Fig. 1: Total cross sections for the excitation of giant resonances in ^{208}Pb impinging on a Pb target as function of energy. The results were obtained in the semiclassical approximation assuming pure electromagnetic excitation. 100% strength of the energy weighted sum rule was adopted. The geometrical cross section is also indicated.

Table 1:

Excitation probabilities in a grazing collision to nuclear states in projectiles as indicated. A bombarding energy of 200 MeV/u and a Au target was chosen. R.E (Act.) stands for a typical deformed rare earth (actinide) nuclei with a quadrupole moment of 6(10) eb. GDR (GQR) denotes the isovector giant dipol (isoscalar giant quadrupole) resonance; 100% strength of the energy weighted sum-rule was adopted in the calculation.

Nucleus	Exited State	P[%]
^{208}Pb	3^-(2.6 MeV)	1
^{208}Pb	GDR	30
^{208}Pb	GQR	20
R.E.	2^+(.1 MeV)	80
R.E.	GDR	30
R.E.	GQR	20
Act.	2^+(.05 MeV)	100
Act.	GDR	40

- the coupling between surface modes (vibrations, rotations) and giant resonances at low temperature. The coupling between rotations and the GDR has been studied recently by several authors[8], the experimental approach (HI, xn-reactions) however, leads to high nuclear temperatures. Rough estimates for the GDR built on high spin states yield in cross sections in the order of mbarn and are shown in fig. 2 (taken from ref. 9).
- The multiple excitation of the GDR.
  In fig. 3 we show predictions for three different target-projectile combinations and two values of $\gamma = 2$ and $\gamma = 15$. The first γ-value applies to SIS/BEVALAC energies, the latter one to energies available at the AGS facility (Brookhaven) to which a similar study of multiple GDR excitation was proposed by Braun-Munzinger et al. (ref. 10). From fig. 3 it can be seen that several orders of magnitude in cross section are gained for higher-fold GDR excitation in heavy nuclei because the cross section is approximately proportional to $Z^{5/3 \cdot n}$ (Z representing the charge of the excited nucleus and n being the number of absorbed quanta) and measurable yields should be obtained up to $n \cong 6$.

The study of the hitherto unknown multi-phonon states is of interest by itself as the (un)harmonicity of these extreme nuclear state might reveal basic nuclear matter properties. Of particular interest, however, is the spreading width of the multiphonon states and thus their decay channels, on which at present one only can speculate. As a separation of protons and neutrons is induced, however, one might expect that a break-up in fragments with extreme isospin is possible. For light nuclei a complete separation of proton and neutron matter is in principle possible.

3. Applications with Unstable Beams

The strong population of collective states at low as well as high excitation energies provides an excellent tool for standard spectroscopic methods to be applied to unstable beams which will be obtained from the projectile fragment separator[12]. Even very exotic beams - with lifetimes down to 100 ns (a limit placed by the length of the beam transfer line) - can be investgated. It seems to be evident that even intensities of secondary beams of 10^5 p/s are sufficient for standard spectroscopic methods. We like to point out that the decay of the GDR via neutron or charged particle emission leads to a secondary population of a large class of low-lying states including higher spins and thus the basic spectroscopic information (single particle structure, deformation etc.) can be deduced.

For instance, γ-γ-coincidence measurements could be performed. For that purpose a Ge detector array covering a large solid angle would be very helpful. Devices covering

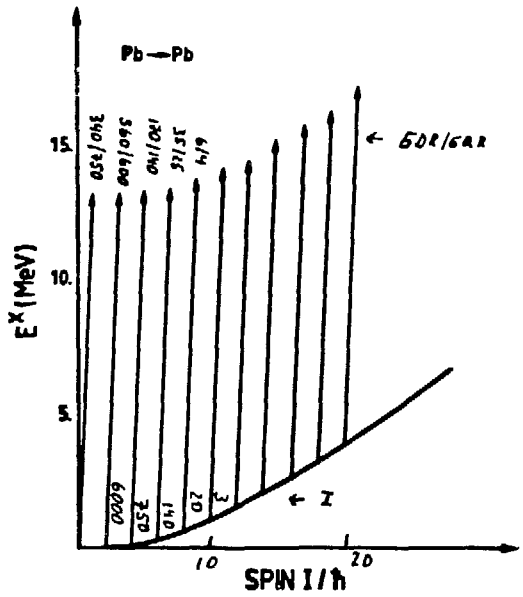

Fig. 2: Cross sections for the excitation of the GDR (GQR) built on high spin states in a deformed Dy nucleus. The excitation is induced by Pb at an incident energy of 100 MeV/u. The estimate is obtained from a semi-classical coupled channel calculation.

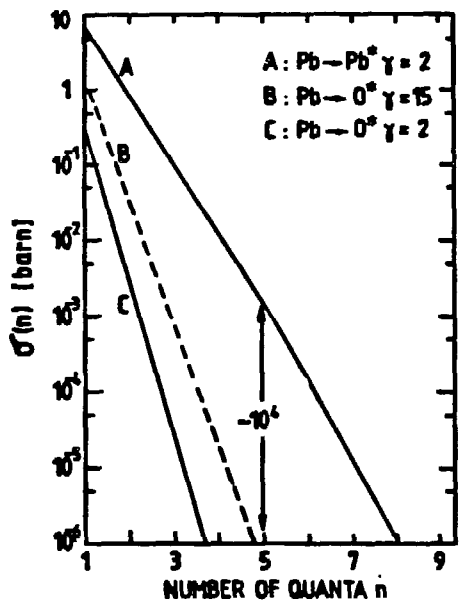

Fig. 3: Cross sections for the multi-phonon excitation of the GDR for collision systems as indicated (* denotes the nucleus excited, n the number of absorbed quanta). The values were estimated based on the method of virtual quanta. Similar results were obtained by Baur and Bertulani within the semiclassical approximation.[11]

50-100% of the total solid angle are presently under discussion both in the United States and in Europe. With a device covering 50% of 4π solid angle for example, a γ-γ-coincidence rate of 10-100 detected photo-peak events is estimated for a medium-mass radioactive beam of 10^5 p/s intensity.

4. Experimental Concept

The studies envisaged will be performed as a complete exclusive measurement of projectile fragmentation. The major components of the proposed set-up are shown in fig. 4. The necessary information of the projectile excitation energy is obtained via reconstruction of the projectile invariant mass. In heavy systems the deexcitation of the excited (multi-phonon) GDR most likely proceeds via evaporation of neutrons. Therefore an efficient neutron detector is needed which allows to measure position and time-of-flight of all neutrons which are emitted in a narrow forward cone of about $\pm 5^0$. Our design studies are based on a sandwich structure of Fe converter material and active plastic paddles covering an area of 2x2 m^2 and being about 1 m deep. A subsystem of the detector has already been tested with neutrons of energies in the range 200-800 MeV which where delivered from the SATURNE accelerator at Saclay, France. For the final detector we expect a detection efficiency of $\geq 90\%$ and position and time resolutions corresponding of $\Delta p/p \approx 10^{-2}$.

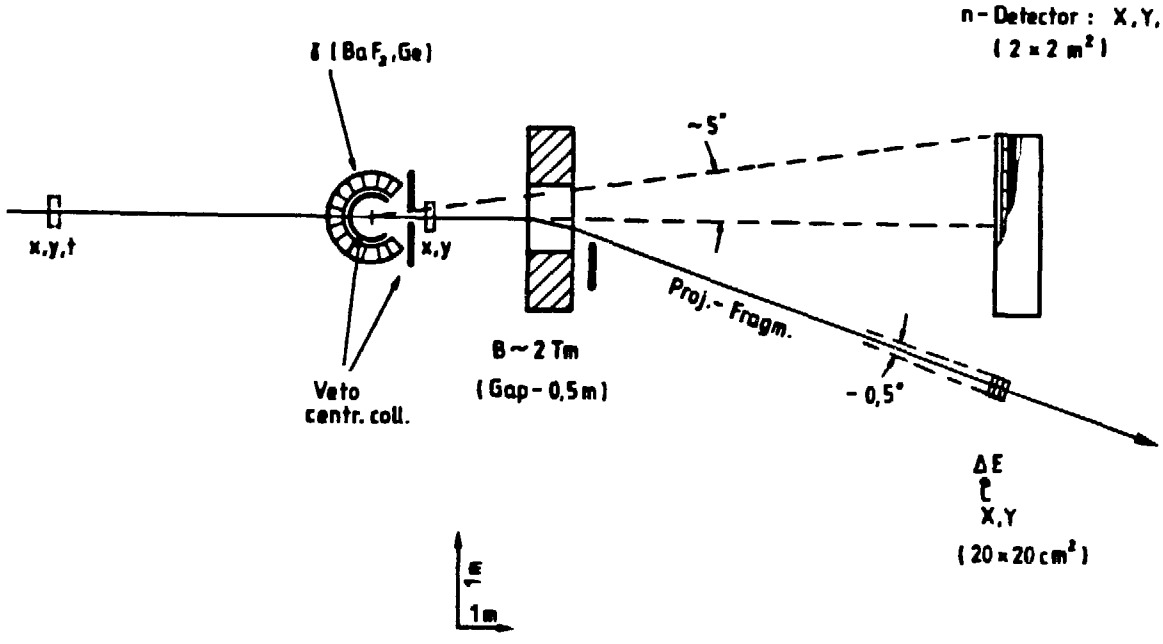

Fig. 4: Schematic view of the experimental set-up as proposed in ref. 1 for the measurements discussed in the text.

The heavy projectile fragment has to be uniquely identified and analyzed making use of a forward magnetic spectrometer and ΔE and Cerenkov counters. A large acceptance angle ($\pm 5^{\circ}$) would be necessary in order not to disturb the neutron measurement. Finally, a target detector system has to be installed covering the total solid angle except the $\pm 5^{\circ}$ forward cone. This detector serves as veto counter for non-pheripheral collisions and for the detection of γ-rays emitted from the excited fragment. Plastic detectors and BaF_2 detectors will be used for the respective purpose.

For the applications with radioactive beams extracted from the projectile fragment separator, the target detector should be replaced by an efficient array of Ge counters as discussed above. In that case, the magnetic spectrometer and the neutron detector can be replaced by less complicated trigger detectors.

References

1. H. Emling et al., Proposal No. 53, to the SIS/ESR program committee, 1987
2. A. Winther and K. Alder, Nucl. Phys. **A319** (1979) 518
3. J.D. Jackson, Classical Electrodynamics (Wiley, New York 1975)
4. M.T. Mercier et al., Phys. Rev. **C35** (1986) 1655
5. D.L. Olson et al., Phys. Rev. **C28** (1983) 1602
6. J.C. Hill, privat communication
7. C.A. Bertulani and G. Baur, Nucl. Phys. **A458** (1986) 775
8. J.O. Newton et al., Phys. Rev. Lett. **46** (1981) 1383
9. H. Emling, Workshop on Experiments at External Beam Lines of SIS and ESR, GSI Darmstadt, 1985
10. P. Braun-Munzinger et al., Proposal to the AGS Program Committee, 1985
11. G. Baur and C.A. Bertulani, Phys. Lett. **B174** (1986) 23
12. G. Münzenberg, proposal to SIS/ESR program committee

Summary and Epilogue

HEAVY ION PRIDE

Philip J. Siemens
Physics Department
University of Tennessee
Knoxville, Tennessee 37996

When we started to study high-energy heavy ion reactions, our primary aim was to study the properties of nuclear matter at a few times nuclear density and a couple of hundred MeV per nucleon excitation energy, hoping to find a chiral phase transition. Since then, we have added more ambitious goals. On one side we have extended the range of conditions under which we try to study nuclear matter: below nuclear density, and at a few to 100 MeV per nucleon excitation energy, looking for a liquid gas phase transition; and at still higher excitation where we hope to find the macroscopic deconfinement of color in a phase transition akin to ionization in gases and to conduction in solids. On the other side we have realized that we also have a lot of interesting physics to learn from the reaction mechanism, about the dynamics of rapid phase transitions: the disassembly of a hot liquid into a hot gas or, perhaps, a liquid-gas mixture via spinodal decomposition or cavitation; and the evolution of the screening of color charges into their complete clustering as the vacuum loses its color conductivity. The challenges have multiplied even more rapidly than the solutions.

The evolution of the experimental situation has been impressive. We now have nearly complete information about the final state of hundreds of reaction products for nuclear collisions at the Bevalac, which has led to a fairly clear picture of the space-time evolution of the colliding nuclei—spectator-participant separation, stopping, splash, etc.—at a qualitative level without reliable quantitative conclusions about nuclear matter properties. In the other regions of higher and lower energies, the experimental data are more fragmentary, leaving open major questions about the nature of the space-time evolution of nuclear collisions in these regimes.

At Bevalac, though, we have a reasonably well-accepted picture of an early division into spectators and participants, with partial penetration of the participant matter, accompanied by some compression, leading to stopping and an approach to local equilibrium, followed by expansion and flow encorporating aspects of both explosion and splash. Why, then, have we not yet been able to reach quantitative conclusions about high-density nuclear matter?

The burden no longer lies only with the experiments. Indeed, we have seen at this meeting impressive demonstrations of their ability to encapsulate their dismayingly multivariate measure-

ments into a few relatively simple parameters and curves which demonstrably are sensitive to the interesting properties of matter. Flow angles (variously parametrized), flow energy, fragment ratios, pion multiplicity, dilepton spectra, and interferometry all contain information about at least some of the key theoretical quantities: cold compression energy, nucleonic effective mass or heat capacity, nucleonic mean free path or viscosity heat conductivity, potential energies of pions and deltas in hot dense matter, and rates or mechanism of pion and delta creation and absorption. There appear, in fact, to be enough measured, readily-interpretable quantities to determine all the theoretically important quantities. Yet quantitative interpretations remain embarrassingly uncertain.

The nature of our misfortune may be understood by comparing our situation to a more familiar paradigm of inductive reasoning. One observes the angle of a diffraction minimum in an angular distribution, then uses a simple formula to obtain an approximate interpretation of the data. Later, more sophisticated analysis with an optical model makes the initial relationship more precise. An initial one-to-one connection between observational and theoretical quantities can be refined to yield more and better information about related aspects.

The reason for our difficulties now emerges. No single experimental result can be uniquely related to a single theoretical quantities: more than one theoretical quantity influences the measurement. Figure 1 shows which theory-experiment sensitivities have been established, most of them by talks at this meeting. We see that everything has to be understood at once. No subset of experimental quantities is influenced only by a smaller or equal subset of theoretical quantities!

This simultaneous interrelation of many quantities places an extraordinary demand on the quantitative reliability of a theory. It is not surprising that our theories so far are not up to the task. We have to look forward to the coming improvements in our theoretical models to give a good account of all the aspects of these important reactions.

Theory \ Experiment	Flow angles / p_t vs. $p_{\parallel}$	Flow energy	Fragment populations	pion multiplicity	dileptons, $\pi\pi$, ρ, etc	Interferometry
Cold compression energy (not $K(n_0)$)	++	++	+	+	?	+?
nucleon effective mass / heat capacity	+/0	+	++	+	?	+?
nucleon mean free path / viscosity	++	++	+	?	+	+
π, Δ potential energy	?	?	+	+	++	?/0
π, Δ absorption / creation / collision broadening	?	?/+	+	+	+	+

Sensitivities of experimental quantities to theoretical quantities

Heavy Ion Physics Challenges at Bevalac/SIS Energies*

M. Gyulassy
Nuclear Science Division
Lawrence Berkeley Laboratory

At the end of the 8^{th} High Energy Heavy Ion Study, it is appropriate to try to put the future physics challenges in this field into perspective. What important milestones have we passed? What experiments and theoretical developments are needed in the next few years to optimize convergence toward our long term objectives? Finally what frontier problems can future high intensity machines (SIS-18/ESR or the Upgraded Bevalac after 1990) address?

First, we recall that the fundamental physics goals of this subfield of nuclear physics can be broadly catagorized as follows:

1. Establish constraints on the *thermodynamic* (P, S, W) and *transport* (η, κ, ξ) properties of nuclear matter over as large a domain as possible of densities, temperatures, neutron/proton ratios, strangeness concentrations, etc.

2. Understand quantitatively the elements of the nuclear reaction mechanism (clustering, fermi motion, mean fields, effective transport cross sections, nuclear disassembly, multifragmentation, etc.) and their effects on specific observables (double and triple differential cross sections, pion and kaon excitation functions, global flow variables, etc.).

3. Produce nuclei near limits of stability $(Z/A \to 1/3, L \to 100\hbar, \text{Strangeness} \to -N)$ and search for novel states of nuclear matter (density isomers, condensates, etc.).

The first ten years of exploration in this field, up to the previous heavy ion study[1] in 1984, resulted in major progress in the second area and extensive (though negative) searches for exotic and anomalous nuclear excitations. During that period only "light" ions ($A < 100$) were available as projectiles. While such light ion experiments were absolutely essential for helping to sort and clarify the complex reaction mechanisms[2], tangible progress on the primary goal had to await experiments with truly heavy ions ($A > 100$) and the simultaneous development of detailed non-equilibrium nuclear transport theories including mean fields. With the development of 4π detectors[1], especially the Ball/Wall and streamer chamber, global event analysis revealed unambiguous evidence for collective nuclear flow for the first time[3] in 1984. However, since nature made nuclei only a few mean free paths thick with diffuse nuclear surfaces, it was found that the nuclear flow was considerably weaker than first predicted by ideal non-viscous hydrodynamics[4]. The difficult task of extracting constraints on the nuclear equation of state from such data on nuclear flow thus had to await the development of Vlasov - (Pauli blocked) Boltzmann (the so called VUU, BUU, or BN) transport codes[5,6] that could address realistically the important non-equilibrium aspects of the problem.

At the last meeting[1] the first tentative attempts to deduce the stiffness of the nuclear energy function, $W(\rho, T = 0)$, were discussed on the basis of the above major developments in both theory and experiment. In the meantime, there has been an impressive series of further developments that were reported in this meeting. The main results pertaining to the primary goal were as follows:

1. Stroebele showed new streamer chamber results[7] based on an improved Danielewicz flow analysis restricted to deuteron fragments. They found the largest in plane flow momentum yet observed, $p_x \approx 150$ Mev/c, in the asymmetric system Ar+Pb at 800 AMeV. For this system, the Cugnon cascade predictions do not even reach 50 MeV/c giving further indications that mean field dynamics are important for understanding the magnitude of the flow momenta. They also confirmed the more modest flow momenta in La+La of $p_x \approx 80$ MeV/c for more peripheral collisions at the same energy. For such peripheral collisions the Cugnon cascade results are much closer (~ 65 Mev/c) to observation. This indicates that while the "corona" physics is adequatly described by simple cascade without mean field effects, central collisions leading to high densities are not.

2. Harris[10] showed new Ball/Wall results on the dependence of flow on fragment mass, A. These new data show that heavier fragments are correlated in azimuthal angle closer to the reaction plane than lighter fragments are. Furthermore, heavier fragments $Z \geq 6$ reveal systematically larger in-plane flow momenta per baryon. A quantitative analysis based on QMD[8,9] by Peilert[11] was able to account for the fragment A dependence of the flow only with an assumed "stiff" (K=400 MeV) equation of state. The momentum dependent "soft" equation of state with in-medium reduced cross section ($\sigma_{eff}/\sigma_{NN} = 0.7$) could only achieve about a third of the observed in-plane momenta.

3. Kampert[12] showed new Ball/Wall data on transverse radial flow in Au+Au. He observed that p,d and t kinetic energy spectra at 90 degrees in the center of mass were virtually identical, in contrast to what was expected if radial flow were present. He^3 and He^4 on the other hand exhibited higher average transverse energies, but the most peculiar result was that He^3 had larger transverse energy than He^4. These results indicate that radial flow, at least in the simple form first suggested by Siemens and Rasmussen, is not achieved in nuclear collisions. The absence of radial flow can be directly attributed to the importance of viscous effects in nuclei. At the previous meeting[1] Kapusta predicted the absence of radial flow through calculations based on the Navier-Stokes equation. This result together with the relative smallness of directed (p_x) flow confirm that the nuclear fluid is very viscous, as expected[13].

4. Keane[14] showed a detailed flow analysis of U+U at 900 AMeV. He observed $p_x \approx 80$ MeV/c as did Stroebele and showed detailed calculations based on the Frankfurt VUU confirming that cascade leads in this case to only ~ 60 MeV/c. However, the VUU results filtered with the streamer chamber acceptance best fit the observations with an assumed "soft" (K=200 MeV) equation of state. The "stiff" equation of state, on the other hand, produced systematically larger flow momenta than observed in this case. This analysis is thus inconsistent with that of Peilert[11], who found that fragment flow[10] required a stiff EOS.

While the above data significantly extend the flow data base, it is clear that consensus on the form of the nuclear equation of state has not yet been reached. At present, the effective compressibility of dense matter remains uncertain to a factor of two ($K = 200 - 400$ MeV).

It is easy to identify several obstacles that hinder the convergence rate toward narrower constraints on the nuclear equation of state.

1. The momentum dependence of the mean field.

2. The uncertainties associated with 4π experimental filters.

3. The uncertain density and temperature dependence of effective transport cross sections.

4. The absence of self-consistent calculations of the equation of state with present nuclear transport models.

5. The uncertain Δ_{33} dynamics and pion absorption mechanisms at high densities.

Last year G. Brown[15] suggested that the apparent stiffness of the equation of state needed in VUU calculations to fit flow data was due to the neglect of the momentum dependence of the nuclear forces. As Brown pointed out at this meeting also, the nuclear mean field involves a cancellation between an attractive scalar field, σ, and a repulsive vector field, ω^0. In the initial phase of a nuclear reaction, momentum space consists of two separated Fermi spheres and thus the vector field is enhanced by a Lorentz boost factor, $\omega^0 \rightarrow 2\gamma_{cm}\omega_F^0$, where ω_F^0 is the vector field value in the ground state. The scalar field is of course invariant to boosts and thus the cancelation between the vector and scalar is reduced in favor of the repulsive vector. This could lead to an apparent hardening of the equation of state. Indeed, detailed calculations[6,9] revealed that the directed flow momenta, p_x differed by only $\sim$ 10% between soft, momentum dependent forces (SM) and hard, momentum independent forces (H).

However, new calculations[11,17] discussed by Stöcker now indicate that the above effect may be too small to explain quantitatively the stiffness needed to fit flow observations. The point is that the momentum distribution of the nucleons is thermalized rapidly due to the large nuclear stopping power at these energies. Thus, the initial free streaming momentum distribution changes rapidly into an approximately thermal one for which no extra gamma factors appear. The calculations of Rosenhauer[17] for Au+Au 800 AMeV showed that up until $\sim$15 fm/c the momentum dependence of the force indeed causes the in plane p_x to increase much more rapidly than that caused by a momentum independent stiff force. However, the final value of p_x is reached only at later time $\sim$ 30 fm/c long after free streaming is over. The p_x reached at 15 fm/c was found to be less than 1/4 of its final value. Most of the final p_x is apparently generated after equilibration. The results of the new study indicate for this system that $p_x \approx 75, 87, 115$ for S,SM, and H respectively. It was not clear why the difference between the SM and H calculations are twice as large as in previous calculations[9], but if these results hold up to future scrutiny, then the apparent contradiction would remain between the softness of the equation of state needed to blow up supernovas and the stiffness needed to explain nuclear flow.

As emphasized by Glendenning[16], in addition to unresolved problems connected with nuclear transport analyses, the problem could lie on the astrophysical side because supernovas provide constraints on the nuclear equation of state only if the prompt mechanism for the bounce is assumed. If Supernova87a liberated less energy than the 1.8 FOE assumed, then neutrino transport could explain the observations. In that case no contraint on the nuclear equation of state would be provided by supernovas and the contradiction with flow data would also disappear. In any case, it is important to keep in mind that the astrophysical constarints are not free of ambiguity either.

The second obstacle in the way of convergence to the equation of state is less basic but practically perhaps more formidable. A generic problem with trying to compare calculations with data taken using complex 4π detectors is that the trigger conditions defining

a particular class of events are often difficult to simulate. Therefore, the theoretical uncertainties associated with using a particular "filter" to simulate experimental biases and acceptances are difficult to assess. Calculations typically produce exclusive events at fixed impact parameters. Experimentally on the other hand only the multiplicity and the momentum distribution in a limited region of phase space can be measured. In the literature this has led to learned theoretical debates over which acceptance filter most closely resembles the actual experimental situation. Since the "filtered" values of p_x differ typically reduced by a factor of two from their values assuming perfect acceptance while the variations of p_x resulting from large variations of the equation of state is tyically less than 50%, this problem is clearly very important to resolve. So what can be done?

In the future, further progress can be made only by simplifying the trigger conditions necessary to constrain the range of impact parameters and the fluctuations of the reaction plane azimuth. At this meeting, Fai discussed several techniques[18] that could simplify the definition and analysis of triple differential cross sections. Next year Madey et. al. will test one of the proposed ideas involving a time-of-flight wall to measure neutron triple differentials. It is important to remember what a triple differential cross section, $\sigma(E, \theta, \phi - \phi_R, M)$, really is. It is a *one* body momentum distribution in three dimensions where the azimuthal angle is measured relative to an estimator, ϕ_R, of the true reaction plane and an estimator, M, e.g. multiplicity, of the magnitude of the impact parameter. Double differentials are simply those one body distributions without a ϕ_R estimator. Of course both ϕ_R and M require a multiparticle detector. However, it is most important that those estimators are well defined and easily simulated. The precision of the estimators as an impact parameter meter is of secondary importance. In the long run, a new 4π device such as the electronic streamer chamber (TPC) proposed by H. Wieman will be required to carry out a full program of one and two particle triple differential measurements. However, in the near future a careful optimization of the ϕ_R and M meters is very much called for.

The third obstacle listed above is the most challenging at present. In the past several years there has been substantial progress on implementing realistic mean field dynamics in transport codes[5,6,8,9]. We note also that a self-consistent treatment of the momentum dependent Vlasov equation including quantum corrections has been formulated in Ref.[19] based on Walecka's Quantum Hadrodynamic Theory (see also contribution by Ko). However, a satisfactory self-consistent treatment of the medium modified Boltzmann part of the transport equations has not yet been formulated. In the past year Malfliet and co-workers have begun to address this problem and have shown[20] that Pauli blocking of *intermediate* states could reduce the effective cross sections in equilibrated systems by 30%. At this meeting, Brown pointed out that density dependent polarization effects can on the other hand even enhance the effective cross sections. Recall the pre-critical scattering[21] phenomena that could arise in dense matter. In extreme cases the NN cross section could be enhanced by a factor of two or more. In actual dynamical situations, it is conceivable that the effective cross sections could start out larger and end up smaller than the free space ones. Thus the transport properties of the system could depend dramatically on time and may have to be calculated self-consistently! What makes the problem of determining the effective cross sections particularly difficult is that unlike the mean fields, which can depend only on the (σ, ω^μ) fields (in spin-isospin symmetric matter), the cross sections involve the exchange of fields with all possible quantum numbers. In particular, while the mean pion field is zero, pion exchange is the dominant contribution to higher partial waves. Thus, a complete theory of the collision term will require as starting point a QHD theory including pions and rho mesons.

The importance of developing a self-consistent theory of effective cross sections was strongly emphasized during this meeting. New calculations[23] reported by Stöcker for directed flow (p_x) using Navier-Stokes with the realistic[13] transport coefficients confirmed the expectation that viscous effects are very large. In fact, p_x was reduced by a factor of two relative to the ideal (Euler) hydrodynamic case. That reduction is absolutely essential to account for the observed magnitude of directed flow. Furthermore, as mentioned above, the absence of radial flow[12] also points to the importance of transport effects. It was thus made very clear at this meeting that no useful constraint on the equilibrium nuclear equation of state could be inferred from nuclear collisions without a simultaneous constraint on the nuclear transport coefficients!

Fortunately, as work proceeds on the theoretical framework needed to handle medium modified collision terms, there are phenomenological steps that could help reduce the height of the third obstacle. As shown by Keane[14] in comparing observed rapidity distributions of baryons to VUU calculations, the U+U data already rules out a constant reduction of the effective cross section by 30%. Also, K. Frankel showed that the double differential cross section in La+La is sensitive to final state Pauli blocking factors, by comparing the old and most recent Cugnon cascade calculations. Thus, single inclusive cross sections are sensitive to the transport cross sections and could be used to constrain at least possible extreme variations of them. There is, however, very little data on inclusive cross sections on heavy systems at this time to study systematically constraints on effective cross sections. The groups, which prior to 1984 measured systematically cross sections for light ion collisions, concentrated on global analysis and left the basic bread and butter double differential cross sections unmeasured. At this meeting we heard repeated calls for return to such basics, i.e. p,d,t, ... spectra (untriggered) for Nb+Nb through U+U in the 100 -1000 AMeV range. Such data are essential if at least phenomenological progress is to be made on the third obstacle.

The fourth obstacle is least difficult in principle but requires an extensive set of new calculations to overcome. For each transport code, as characterized with a definite set of parameters specifying the mean fields and effective cross sections and a set a prescriptions to handle Pauli blocking and two body scattering style, there exists a definite equation of state. Thusfar, the equations of state have not determined by the transport code themselves, but rather inferred indirectly from other work, e.g. Hartree-Fock, using similar forces. It has been known for a long time though[24] that variations of the scattering prescription alone lead to non-ideal equations of state. Thus, simple intranuclear cascade does not correspond to an ideal equation of state. Clearly, calculations of the pressure, entropy, and energy functionals using the transport codes are needed. The main difference from previous calculations is that the initial conditions must be changed from two incoming nuclei to a uniform nuclear matter at given temperature and density using periodic boundary conditions. The expectation of $p^\mu p^\nu$ would then measure the energy momentum tensor.

The fifth obstacle, though not discussed at this meeting, was clearly revealed in recent calculations[25] of delta abundances in dense nuclear matter. At the last meeting there was considerable excitement[26] about the possibility of using the pion excitation function to constrain the nuclear equation of state. Recall that Cugnon and Fraenkel cascade calculations systematically overpredicted the measured pion yields. This led to early estimates that a rather stiff equation of state would be needed to understand the data. The suprising results of Feldmeier and coworkers[25] was that in a self-consistent treatment of deltas and nucleons in QHD, a *softer* EOS could result in *less* deltas than in a system with a rather stiff EOS! This seemingly contradictory result is due to the rapid decrease of the effective

masses of both deltas and nucleons in the model. While definitive conclusions could not be drawn because oversimplified one-dimensional shocks were assumed and multinucleon pion absorption[27] neglected, the results underline that pion yields may eventually teach us more about the unknown properties of deltas in dense matter than about the cold nuclear equation of state.

To advance the understanding of pion dynamics in nuclear collisions, it will be important first to get a better handle on pion absorption mechanisms. Overprediction of the pion yield by cascade already occurs for C+C systems, where certainly no high density equilibrium effects are relevant. There is a need to remeasure directly the pion excitation function in such very light systems since in these systems it will be easiest to isolate the pion absorption physics from the density dependent modifications of the delta and pion dispersion relations. Once the pion excitation function in C+C is understood, then it is worthwhile to return to the heavier systems that will teach us about the interesting delta and pion optical effects in dense media. Secondly, as reported by Odyniec[28], the concave shape of the $p_\perp$ spectra of pions still needs to be understood. Hahn and Glendenning[29] suggested that this observation is due to a complex interplay between effects due to cooling of the source, Bose effects, and collective flow boosts of the spectra. Untangling the reaction mechanism will probably require analysis of *triple* differential pion spectra. Again, there is insufficient data to answer such basic questions.

Part of the present ambiguities on the EOS can also be traced to an uncontrolled proliferation of transport codes. There are at least several versions of the Cugnon cascade code and many versions of VUU codes for example. Different versions differ in details and parameters that are not well documented in the literature. There is a well known and time tested cure for this problem, namely, requiring version numbers and systematic documentation of changes from version to version. A very good example is the series of LUND Monte Carlo programs, JETSET6.3, PYTHIA4.8, etc., used in high energy physics for multiparticle jet fragmentation codes. These programs are found in the CERN program library and a long writeup of each program is updated as necessary. The writeup includes latest Lund and DESY preprints by the authors of the programs and clearly describes all subroutines and common block parameters and includes examples of use. In this field the only example of a well documented code is FREESCO[30]. I suggest that a nuclear code library be established, e.g. on the Lawrence Livermore Lab Cray system, modelled after the CERN program library. Ideally, nuclear dynamics codes ranging from TDHF, Fireball, to Hydrodynamic, Cascade, VUU, QMD, to LUND, DPM, etc. would be included with specific version numbers and long writeups. In addition it would be most useful to have a library of experimental filters, e.g. BallWall84.1, StreamerCham84.1, WA80.1, NA35.1, etc., that are provided by the experimentalists as the best estimate of the acceptance of each particular device. That there is rapid development and modification of transport codes is a good sign that progress is being made. However, I believe that establishing such a library is necessary to ensure a more controlled and disciplined growth of this increasingly complex field.

The proliferation of nuclear transport codes is of course linked to the rapid progress that has been made in understanding many elements of the reaction mechanism. At this meeting there was a great deal of discussion on a new aspect of the reaction mechanism, namely multifragmentation, which poses even greater challenges for both theory and experiment in the future. Broadly speaking, multifragmentation, is the study of the propagation of A body correlations through the process of nuclear dissasembly into many often large fragments. This is obviously a very complex problem on which only the few steps have been

taken. A long range hope is that this phenomenon may shed light on the nuclear gas-liquid phase transition. At this meeting Randrup[31] emphasized the many challenging problems confronting this topic, while Aichelin[11] showed numerical results obtained using QMD. Randrup emphasized the sensitivity of results to inclusion of the density of excited nuclear states and to interactions between the fragments in the expansion phase. Aichelin showed that the characteristic power law for mass yields may have nothing to do with interesting critical exponents but may be simply the accidental form resulting from averaging over impact parameters. These later results again emphasize the necessity of studying reactions with ϕ_R and M impact parameter meters. Inclusive yields are likely to teach very little about such complex phenomena. To make progress experimentally it will be of course necessary to build 4π detectors capable of measuring simultaneously many fragments of large mass over a large kinematical domain. Present detectors and even proposed extensions[32] do not seem adequate to make a dent on this topic. Essentially a more sophisticated Ball-Wall is needed. Theoretically, it is still unclear exactly which multiparticle correlations are most useful to investigate and which are most sensitive to novel dynamical effects. Stöcker suggested that the excitation of topological cross sections, e.g. the cross section for producing at least four $Z > 4$ fragments, may be important to look at. But my general impression at this time is that a proper focus in this area of reaction mechanism studies is still lacking and that such a focus must be found to ensure that the ongoing and scheduled experiments on this topic have long term impact.

As we look toward the physics challenges that new high intensity heavy ion beams and cooler rings will offer in the 1990's, several topics look particularly promising:

1. Exploiting dilepton and photon probes.

2. Using subtreshold K^+ production as a novel probe of dense matter.

3. Using radioactive secondary beams to solve astrophysics problems.

Mosel discussed hard photon yields as a probe of the collective flow and microscopic collision mechanisms. High energy photons, $E \gtrsim 40$ MeV, are mainly sensitive to the rate of neutron-proton scattering in the medium. Hence, these photons may provide an alternate tool to constrain transport cross section. However, high energy photons are also contaminated by π^0 decay. Thus a full exploitation of this probe involves a much better understanding of pion production. Lower energy photons on the other hand become sensitive to coherent radiation of the nuclei, and hence may provide new information on the collective nuclear currents associated with the viscous nuclear flow.

Gale[33] discussed how dilepton yields in the mass range 300 - 800 MeV could shed light on the unknown dispersion relation of pions in dense media. The pion dispersion at high nuclear densities may soften considerably due to P-wave coupling to delta-hole and nucleon-hole excitations. The annihilation of a "$\pi^+\pi^-$" phonon pairs could then yield a dilepton mass distribution that could differ dramatically from the expectation with free space dispersions. Furthermore, since the annihilation occurs inside the matter, the signal will not be so effected by unknown pion absorption processes as the final pion spectra themselves. Thus, dileptons may be unique probe of pion dynamics at high baryon densities and temperatures. On the experimental side, Roche[34] reported the first successful measurements of dilepton pairs at Bevalac energies in p+Be and Ca+Ca at 2 AGeV. Unfortunately, present detectors will not be useful with truly heavy ions and present intensities are too low to permit measurements at lower energies, where more complete nuclear stopping occurs.

Therefore, full exploitation of this probe will require the next generation of detectors at high intensity machines.

Schürmann[35] discussed how subtreshold K^+ production may provide an independent probe of the nuclear equation of state. His calculations showed that while the absolute kaon yields are subject to large uncertainties due to the lack of data on the elementary $pp \rightarrow K+X$ production cross sections, the ratios of the yields $R(A/B) = \sigma(A+A \rightarrow K)/\sigma(B+B \rightarrow K)$ is insensitive to those uncertainties. Furthermore, he found that at 700 AMeV $R(Nb/Ne) = 23$ for a soft EOS while it was 13 for a hard EOS. Thus, this ratio may be more sensitive to the stiffness of the equation of state than p_x flow. A specific advantage of K^+ as a probe is that it has a much larger mean free path than K^-, pions or nucleons, and thus suffers less final state interaction distortion effects. The disadvantage is that experimentally it is more difficult to identify a rare K^+ in a large proton background. Thus, a much more sophisticated detector system is required to exploit this probe. An important open theoretical problem that must be looked into is the sensitivity of K^+ production to the Λ dispersion in dense media. Recall the discussion on pion production. There new calculations[25] revealed that pion production is rather sensitive to the unknown Δ dispersion[25]. I suspect that unambiguous information on the nuclear EOS using kaons will require similarly the simultaneous understanding of Λ dynamics in dense nuclei. Maybe, we can turn this problem around by using kaons mainly as a consistency check on the EOS as deduced from p_x etc. with a primary goal of providing unique information on the properties of hyperons in nuclear matter.

Finally, I want to mention a long term goal of using radioactive secondary beams to address problems of astrophysical interest. As discussed in ref.[36] nucleosynthesis involves many reaction steps where radioctive nuclei participate. For example, to break out of the CNO cycle in order to produce elements up to Fe involves reactions such as $^{15}O(\alpha,\gamma)^{19}Ne(p,\gamma)^{20}Na$ followed by a complicated chain of (p,γ) reactions and weak decays. Very few of the actual reaction rates and decay rates along the chain are known at present. Such reactions could be studied when high intensity primary beams make it possible to produce radioactive secondaries at high rates and when cooler rings will make it possible to store such beams for eventual deceleration to the very low energies of astrophysical interest. For other more conventional applications of secondary beams to the study of nuclear structure see contributions by Shimoura nad Matsuta at this meeting and ref.[36].

In closing, this 8^{th} High Energy Heavy Ion Study clearly demonstrated that since the last meeting, there has been substantial progress on the main objectives in this field. That progress was made possible by an impressive series of experiments utilizing truly heavy ion ($A > 100$) beams for the first time and the simultaneous development of detailed nuclear transport codes. As summarized here and as emphasized in many of the talks, confronting the future challenges will necessitate a great deal more experimental and theoretical work. At this time, when there is a vast expansion of the field of heavy ion physics into the new realm of ultrarelativistic energies at BNL and CERN, the lure of the quark-gluon plasma poses a new sociological challenge that must also be addressed. As both experiments and theoretical work increase vastly in scope, complexity, and commitment of time there is a danger of spreading the approximately conserved number of physicists out too thinly on too many fronts. It is imperative that experiments be chosen and prioritized very carefully and that the development of phenomenological nuclear transport models be brought under stricter control. A concentrated and vigorous effort will ensure that the next meeting, celebrating the opening of the new SIS machine at GSI in 1989, will be as exciting and stimulating as this one.

Acknowledgements: Valuable discussions with J. Aichelin, C. Gale, J. Randrup, B. Schürmann, P. Siemens and H. Stöcker are gratefully acknowledged.

* This work was supported by the Director, Office of Energy Research, Division of Nuclear Physics of the Office of High Energy and Nuclear Physics of the U.S. Department of Energy under Contract No. DE-AC03-76SF00098.

References

[1] Proc. 7th High Energy Heavy Ion Study, Darmstadt, Oct. 1984, GSI-85-10 Report.

[2] S. Nagamiya, M. Gyulassy, Advances in Nuclear Physics, Vol 13, p. 201, (Plenum Pub. Corp. 1984), eds. J.W. Negele, E. Vogt.

[3] H. A. Gustafsson, et. al., Phys. Rev. Lett. 52 (1984) 1590.
R. E. Renfordt, et. al., Phys. Rev. Lett. 53 (1984) 763.
D. Beavis, et. al., Phys. Rev. Lett. 54 (1985) 1652.
K. G. R. Doss, et. al. Phys. Rev. Lett. 57 (1986) 302.

[4] H. Stöcker, W. Greiner, Phys. Rep. 137 (1986) 278.

[5] G. Bertsch, et. al. Phys. Rev. C29 (1984) 673.
H. Kruse, et. al., Phys. Rev. Lett. 54 (1985) 289.
J.J. Molitoris, H.Stocker, Phys. Rev. C32 (1985) 346.

[6] C. Gale, et. al., Phys. Rev. C35 (1987) 1666.

[7] P. Danielewicz, et. al., Warsaw University preprint IFT/42/87 (1987).

[8] J. Aichelin, H. Stöcker, Phys. Lett. B176 (1986) 14.
A. Rosenhauer, et. al., J. Physique C4 (1986) 395.

[9] J. Aichelin, et. al., Phys. Rev. Lett. 58 (1987) 1926.

[10] K. G. R. Doss, et. al., Phys. Rev. Lett. 1987 in press.

[11] G. Peilert, et. al., Frankfurt preprint Nov. 1987.

[12] K. H. Kampert, Univ. Münster Thesis (1986).

[13] A. R. Bodmer, Proc. Top. Conf. on Nuclear Collisions, Fall Creek Falls, Tenn., 1977, Conf-770602, p.309.
J. Blocki, et. al., Ann. Phys. 113 (1977) 330.
P. Danielewicz, Phys. Lett. B146 (1984) 168.

[14] U.C. Riverside streamer chamber collab.

[15] G. Brown, Bevalac Users Meeting 1986. T.L. Ainsworth, et. al., Nucl. Phys. A464 (1987) 740.

[16] N. K. Glendenning, LBL-24249 (1987) preprint.

[17] Rosenhauer, et. al., GSI-preprint 1987.

[18] G. Fai, et.al. Phys. Rev. C36 (1987) 597.

[19] H. Th. Elze, et. al., Mod. Phys. Lett. A2 (1987) 451.

[20] B. ter Haar, R. Malfliet, KVI-643, 651, 654 (1987) preprints.

[21] M. Gyulassy, W. Greiner, Ann. Phys. 109 (1977) 485; Conf-770602 (1977) 457.

[22] B. S. Serot, J. D. Walecka, Adv. Nucl. Sci. 16 (1986) 1.

[23] A. Rentzsch, et. al. Frankfurt preprint.

[24] E. Halbert, Phys. Rev. C23 (1981) 295.
M. Gyulassy, K. Frankel, H. Stöcker, Phys. Lett. 110B (1982) 185.

[25] M. Cubero, M. Schönhofen, H. Feldmeier, W. Norenberg, GSI-87-45 (1987);
B. Waldhauser, J. Maruhn, H. Stocker, W. Greiner, UFTP-194,195 (1987).

[26] J.W. Harris, et. al., Phys. Lett. 153B (1985) 377; Phys. Rev. Lett. 58 (1987) 463.

[27] P. Siemens, G. Brown, Phys. Lett. B (1987) in press.

[28] R. Brockmann, et. al., PRL 53 (1984) 2012; LBL preprint 1987 in preparation.

[29] D. Hahn, N. K. Glendenning, LBL-23864 (1987).

[30] G. Fai, J. Randrup, Comp. Phys. Comm. 42 (1986) 385.

[31] J. Randrup, LBL-24334 (1987).

[32] see contribution of W. Kehoe and L. Moretto.

[33] C. Gale, J. Kapusta, UMSI 87/10 (1987).

[34] G. Roche, et. al., see contribution.

[35] B. Schürmann, W. Zwermann, Phys. Lett. B183 (1987) 31.

[36] I. Tanihata, RIKEN-AF-NP-58 (1987).